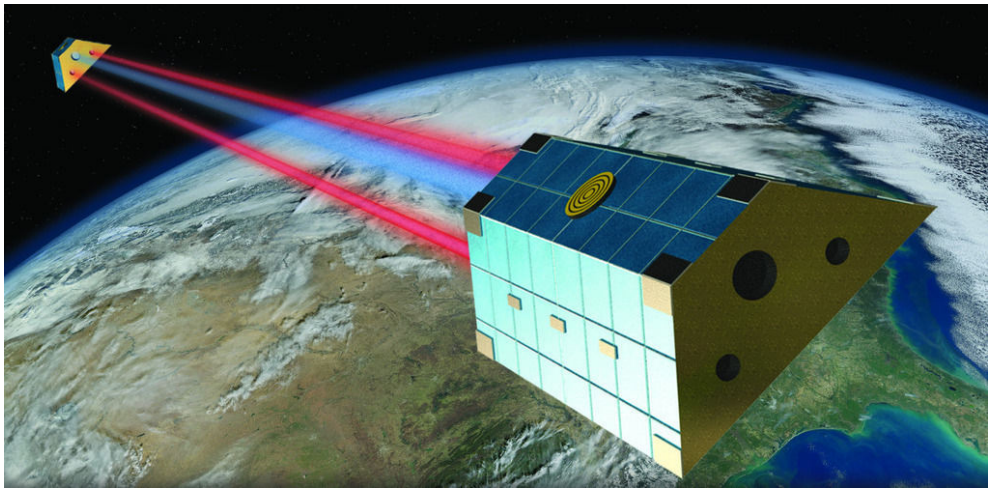


Design Considerations for Future Geodesy Missions and
for Space Laser Interferometry



October 2017

Max Planck Institute for Gravitational Physics
(Albert Einstein Institute)
Gottfried Wilhelm Leibniz Universität Hannover
Germany

Cover picture: Artistic view of the GRACE Follow-On satellites.

Image credit:

Satellites: AEI/Daniel Schütze,

Earth: NASA, “The blue marble”, <http://www.nasa.gov/multimedia/imagegallery>.

Design Considerations for Future Geodesy Missions and
for Space Laser Interferometry

Von der QUEST-Leibniz-Forschungsschule
der Gottfried Wilhelm Leibniz Universität Hannover
zur Erlangung des Grades
Doktor der Naturwissenschaften

- Dr. rer. nat. -

genehmigte Dissertation

von

M. Sc. Vitali Müller
geboren am 06.01.1986 in Omsk/Russland

Oktober 2017

Referent: Prof. Dr. Karsten Danzmann
Institut für Gravitationsphysik (Albert-Einstein-Institut), Hannover, Deutschland

Korreferent: Prof. Dr. Torsten Mayer-Gürr
Institut für Geodäsie, Graz, Österreich

Korreferent: Prof. Dr. Claus Braxmaier
Universität & ZARM, Bremen, Deutschland

Korreferent: Prof. Dr. Gerhard Heinzel
Institut für Gravitationsphysik (Albert-Einstein-Institut), Hannover, Deutschland

Tag der Disputation: 06.10.2017

Kurzzusammenfassung

Der englische Titel dieser Doktorarbeit lautet übersetzt *Konstruktionserwägungen für zukünftige Erdschwerefeld-Satellitenmissionen und zur weltraumbasierten Laser-Interferometrie*. Diese erwähnten Satellitenmissionen messen sehr präzise den Satellitenabstand mittels Laser-Interferometrie, der wiederum genutzt wird um die Erdanziehungskraft und damit die Massenverteilung auf der Erde, weltweit und regelmäßig in bestimmten Zeitabständen, zu kartographieren. Diese Karten sind hilfreich um geophysikalische Phänomene zu studieren, z.B. den Klimawandel oder den Wasserhaushalt der Erde. Der erste Teil dieser Arbeit befasst sich allgemein mit der Nutzlast und dem Zusammenspiel der Instrumente in solchen Satellitenmissionen, während der zweite Teil sich der Laser-Interferometrie widmet.

Der erste Teil beginnt mit einer Einleitung zum Erdschwerefeld und zum Messprinzip der Missionen, sowie einigen Randbedingungen, welche beispielsweise schon durch andere Studien gegeben sind, z.B. die bevorzugten Umlaufbahnen der Satelliten betreffend. Eine kohärente Beschreibung der Distanzmessung, welche die Erdschwereinformation beinhaltet, wird von Grund auf hergeleitet; so werden z.B. die gravitativen Referenzpunkte auf den Satelliten definiert und diskutiert. Die Messmethoden und Genauigkeiten der wichtigsten Nutzlast-Instrumente werden zusammen mit anderen wichtigen Kennzahlen adressiert um mathematische Modelle für die Genauigkeit der späteren Gesamtmessung zu erhalten. Dabei wird Wert darauf gelegt zwischen zufälligem Rauschen und wohldefinierten oszillierenden Fehlerquellen zu unterscheiden. Da letztere Störungen oft vernachlässigt werden, wird deren mögliche Behandlung in der Datenprozessierung angerissen.

Die hergeleiteten Fehler- und Sensitivitätsmodelle für die finale Hauptbeobachtung und für die einzelnen Instrumente werden genutzt, um die Genauigkeit der Erdschwerefeldbestimmung abzuschätzen. Dazu wird der sog. Beschleunigungsansatz verwendet, der im Wesentlichen eine Ende-zu-Ende Simulation liefert und es damit erlaubt, den Einfluss von verschiedenen Missionsszenarien aber auch von unterschiedlichen Instrumenten zu analysieren. Es wird herausgestellt, dass zwei Satellitenpaare mit unterschiedlicher Inklination eine wesentlich genauere Messung des Erdschwerefeldes erlauben und somit eine vielversprechende Option für zukünftige Missionen darstellen. Des Weiteren wird auf die Zentrifugalbeschleunigung der Basislinie zwischen den Satelliten in einem Paar eingegangen, die in aktuellen Konzepten mittels ungenauer GNSS Beobachtungen indirekt bestimmt werden muss. Deshalb werden auch verschiedene Möglichkeiten einer direkteren Bestimmung dieser Beschleunigung evaluiert. Weitere mögliche Verbesserungen in zukünftigen Missionen betreffen die Nutzung sog. Drag-Free Technologie und die Kalibration verschiedener Nutzlast-Instrumente untereinander. Alles in allem beschreibt dieses Kapitel eine Vielzahl von Ideen und Optionen nachfolgende Satellitenmissionen zur Schwerefeldmessung weiterzuentwickeln.

Der zweite Teil dieser Arbeit geht auf die weltraumbasierte Laser-Interferometrie ein und versucht einen systematischen Zugang zu diesem Gebiet zu liefern, welches bislang von der Technologie-Entwicklung für die LISA und GRACE Follow-On Mission geprägt wird. Nach einer kurzen Einführung in die Relativitätstheorie und in die optische Interferometrie, welche Aspekte wie Phasenbestimmung und interferometrische Signale umfasst, wird ein Überblick über die zur Verfügung stehenden und weltraumgeeigneten Teilkomponenten von typischen Interferometern gegeben. Anschließend wird Interferometrie anhand von funktionalen Konzepten, welche u.a. Transponder- und sog. duale Einweg-Systeme einschließen, diskutiert. Dazu werden zuerst Spezifika der optischen Implementierung außen vor gelassen, aber im späteren Verlauf mit einbezogen. Eine detaillierte Beschreibung der Phasen bzw. der äquivalenten Distanzbeobachtung wird für die verschiedenen funktionalen Konzepte hergeleitet und miteinander bezüglich ihrer Sensitivität verglichen. Es wird herausgestellt, dass die Genauigkeit der Instrumente zum einen durch Laserfrequenz-Rauschen und zum anderen durch eine Suszeptibilität zur Satellitenausrichtung limitiert wird. Daneben werden weitere

mögliche Limitierungsfaktoren und deren Lösungsansätze besprochen, wie z.B. die Unsicherheit im Skalierungsfaktor, der einer beschränkten Messgenauigkeit der absoluten Laserfrequenz geschuldet wird.

Weiterhin wird angemerkt, dass eine präzise Beschreibung der Beobachtungsgleichungen relativistische Effekte berücksichtigen muss, die durch die Bewegung der Satelliten und durch das Erdschwerefeld verursacht werden. Dazu wird eine Herleitung und tiefgehende Analyse präsentiert, welche die nötigen Methoden zur Korrektur dieser Effekte in der Datennachverarbeitung liefert und die auch bei GRACE Follow-On Verwendung finden kann.

Zum Schluss wird der optische Aufbau von Interferometern thematisiert. Referenzpunkte werden eingeführt, welche eine elegante Charakterisierung der Abhängigkeit zur Satellitenausrichtung erlauben. Zudem wird die Signalstärke der interferometrischen Messung beschrieben. Verschiedene optische Layouts werden vorgestellt und bewertet. Auf Grundlage dieser Betrachtung werden zwei unterschiedliche Layouts für Schwerefeldmissionen vorgeschlagen, welche auch hinsichtlich ihrer Umsetzbarkeit und optimalen Kennwerte untersucht werden.

Schlagnvorte: Laser-Interferometrie, GRACE, Erdschwerefeld

Abstract

This thesis addresses design considerations for space-borne satellite gravimetry missions, which utilize precise inter-satellite ranging. These missions measure Earth's gravity field and provide valuable snapshots of Earth's mass distribution on a regular basis. The data is used to study geophysical phenomena such as, among others, climate change and the water cycle on large scales. The first part of this thesis is concerned with the overall mission, payload and system design, while the second part discusses space laser interferometry aboard the satellites.

The first part starts with an introduction to the Earth's gravity field, the measurement principles and some boundary conditions on the mission design, which have been derived in previous studies, for example, regarding the favored orbit height of the satellites. A coherent description of the ranging observable, containing the gravity field information, is provided starting from first principles and covering aspects such as the proper definition of the gravitational reference points on the satellites. The measurement methods and accuracies of the main payload instruments are discussed together with other key figures, which are used to derive precise sensitivity models for this type of satellite mission. It is stressed that, in general, two different types of measurement errors need to be distinguished: stochastic fluctuations and deterministic sinusoidal errors. Handling of the latter in post-processing is sketched, because this error type is often neglected in studies.

The derived sensitivity and error models for the final observable and for the individual instruments are used to propagate the errors to the level of the gravity field using the so-called acceleration approach. Thus, an end-to-end simulation is obtained, which is used to assess the effect of different mission scenarios and instrument types onto the gravity field. It is pointed out that the gain in gravity field accuracy with a dual pair mission with different inclinations is significant and, hence, a viable option for future missions. Furthermore, the analysis shows that the centrifugal acceleration of the baseline, formed by the satellite pair, needs to be deduced from relatively imprecise GNSS observations. Different approaches to mitigate this susceptibility by means of direct measurements are discussed. Other aspects regarding potential improvements in future missions are addressed as well, namely, the utilization of drag-free technology and the inter-calibration of different on-board instruments. In summary, this thesis part provides a variety of ideas and option to advance future gravimetric missions.

The second part of this thesis on space laser interferometry attempts to provide a systematic approach to the field, which is mainly shaped by the technology development for the LISA and the GRACE Follow-On mission, so far. After a brief introduction to relativity and optical interferometry, which includes aspects such as phase-tracking and interferometric signals, an overview on the available set of technology for the subsystems of typical laser interferometers is given. Then, interferometry on the level of functional concepts is discussed, which includes transponder-based ranging and dual one-way ranging but leaves out temporarily contributions related to the optical layouts. A detailed description for the phase or equivalent ranging observable is derived for the different functional concepts and they are compared with each other with regard to their sensitivity. It is shown that the precision of the instruments is limited by laser frequency fluctuations and by a dependence on the satellite's attitude. Other potential limiting factors such as the scale factor uncertainty due to the limited absolute laser frequency knowledge are also addressed together with mitigation concepts.

Furthermore, it is noted that an accurate description of the measurements requires the consideration of relativistic effects, which arise due to the motion of the satellites and due to the gravitational field. A derivation and in-depth analysis of these effects is performed, yielding the necessary methods to remove these contributions in post-processing, which can also be applied to the GRACE Follow-On laser ranging instrument.

In the end, the optical layouts and the implementation are thematized. Reference points are introduced to characterize the S/C attitude dependent errors and the signal strength of the phase measurement is discussed. Different optical layouts are assessed and novel layouts based on the previous findings are proposed for future gravimetric missions. These are further analyzed with the help of power budgets regarding their feasibility. Moreover, an exemplary parametric study is performed to obtain the optimal parameters for the instrument design.

Keywords: laser interferometry, GRACE, gravity field

Table of Contents

Kurzzusammenfassung	v
Abstract	vii
Table of Contents	ix
Nomenclature	xiii
List of Figures	xvi
List of Tables	xix
1 Design Considerations for Future Geodesy Missions	1
1.1 Earth's Gravity Field	2
1.1.1 Time-Varying Gravity Field	3
1.1.2 Observation Techniques	3
1.1.3 Geodesy and Fundamental Gravitational Physics	6
1.2 E.motion ² Boundary Conditions	9
1.2.1 Previous Studies	9
1.2.2 Observation Type and Number of Satellites	9
1.2.3 Inclination	10
1.2.4 Altitude and Groundtrack Repeat Cycle	10
1.3 E.motion ² Measurement Principle	11
1.3.1 Properties of Gravity Field Induced Signals	11
1.3.2 Remark on Spectral Densities	12
1.3.3 Projected Differential Gravitational Acceleration (PDGA)	14
1.3.4 Direct Acceleration (DA)	17
1.3.5 Science and Calibration Measurement Bandwidth	17
1.3.6 Definition of the Gravitational Reference Point (GRP)	18
1.3.7 GRP in Servo-Accelerometer Concepts	20
1.3.8 GRP in Drag-Free Concepts	21
1.4 Instruments and Observations	22
1.4.1 GNSS: Global Navigation Satellite System	22
1.4.2 Ranging Interferometer	25
1.4.3 Accelerometer	26
1.4.4 Star Cameras	29
1.4.5 Tone Errors	30
1.4.6 Proposed Data Processing	32
1.5 Baseline State	34
1.5.1 Line-of-Sight Angular Velocity	34
1.5.2 (Reduced-) Dynamic Orbits	35
1.6 Sensitivity Model	38
1.6.1 Direct Acceleration (DA)	38

1.6.2	Projected Differential Gravitational Acceleration (PDGA)	40
1.6.3	Revised PDGA Sensitivity	45
1.7	Gravity Field Recovery	46
1.7.1	Method	46
1.7.2	Handling Tone Errors in Gravity Field Recovery	47
1.7.3	Results: Direct Acceleration (Single Satellite)	47
1.7.4	Results: Single Pair	49
1.7.5	Results: Dual (Bender) Pair	50
1.7.6	Discussion	51
1.8	Centrifugal Acceleration Sensing	52
1.8.1	Accelerometer, Star Camera and Laser Interferometry	53
1.8.2	Sagnac-Interferometry	56
1.8.3	High-Resolution Star Camera	56
1.9	Drag-Free and Drag-Compensation	56
1.9.1	Characteristics of Non-Gravitational Accelerations	57
1.9.2	Requirements on the Accelerometer	59
1.9.3	Selection of Drag Reduction scheme	61
1.9.4	Preliminary Drag-Free Assessment	62
1.9.5	Actuator Technologies	63
1.10	Integrated Instrument Analysis and Calibration	68
1.10.1	Calibration of Accelerometer Scale Factor	70
1.10.2	Calibration of Rotation-to-Ranging Coupling	71
1.10.3	Thermal Monitoring and Control	72
1.11	Summary & Conclusion	73
2	Laser Interferometry in Space	76
2.1	Introduction to Relativity	78
2.1.1	The Geocentric Celestial Reference System (GCRS)	80
2.1.2	Equations of Motion	81
2.2	Introduction to Interferometry	82
2.2.1	Phase Retrieval and Phase Tracking Techniques	84
2.2.2	Optical Detection	88
2.2.3	Differential Wavefront Sensing (DWS)	91
2.2.4	Differential Power Sensing (DPS)	93
2.3	Optical and Interferometer Technology	94
2.3.1	Laser	94
2.3.2	Optical Frequency Standard	95
2.3.3	Photodiodes and Photoreceiver	100
2.3.4	Ultra-Stable Oscillator (USO)	105
2.3.5	Retro-Reflectors	109
2.3.6	Optical Components and Optical Bench	113
2.3.7	Phasemeter	115
2.3.8	Steering Mirror	126
2.3.9	Frequency-Offset PLL and DWS Loops	127
2.3.10	Acquisition Sensor	131
2.4	Functional Concepts	135
2.4.1	Derivation of One-Way Ranging	135
2.4.2	One-Way Ranging	143
2.4.3	Dual One-Way Ranging (DOWR)	144
2.4.4	Derivation of Transponder-based Ranging	150
2.4.5	Transponder-based Ranging	156
2.4.6	Transponder-based Ranging: Low Gain	158
2.4.7	Passive Retro-Reflector Ranging	160

2.4.8	Comparison and Summary	160
2.5	Photon Time of Flight Corrections	164
2.5.1	Local Interferometry	165
2.5.2	Special Relativity	166
2.5.3	General Relativity	169
2.5.4	Ionosphere	172
2.5.5	Atmosphere	175
2.6	Design Principles of Satellite-Satellite Interferometers	181
2.6.1	Gaussian Beam models	181
2.6.2	Transmitter vs. Receiver Pointing	183
2.6.3	Attitude-to-Ranging Coupling	184
2.6.4	RX Reference Points	187
2.6.5	TX Reference Points	190
2.6.6	Validity and Extensions of Reference Points	193
2.6.7	Retro-Reflection, Point-Ahead Direction and Angle	193
2.6.8	Optical Detection Schemes	194
2.6.9	Carrier-To-Noise Density C/N_0	197
2.6.10	Effective Power: RX Beam Power	202
2.6.11	Effective Power: Heterodyne Efficiency	205
2.6.12	Laser Link Acquisition	215
2.7	Optical Layouts	218
2.7.1	On-Axis Interferometry	219
2.7.2	Off-Axis Interferometry	223
2.7.3	Discussion of Layouts	226
2.7.4	Proposed Layouts for NGGM	228
2.8	Laser Link Power Budgets	232
2.8.1	Off-Axis Interferometer	234
2.8.2	On-Axis Interferometer	237
2.8.3	Budget Analysis: Carrier-To-Noise Density	238
2.8.4	Optimal Parameter Selection	242
2.9	Summary & Conclusion	248
Appendix A NGGM Drag Compensation: Accelerometer Saturation and Propellant		252
A.1	Accelerometer	252
A.2	GRACE Level 1B data	252
A.3	Propellant	254
A.4	Summary	255
Appendix B Relativistic Quantities		257
Appendix C General Relativistic Delay of Light		261
Appendix D Polarization and Phase Changes within the GRACE-FO TMA		264
D.1	Setup	264
D.2	Material constants	265
D.3	Polarization Matrices	266
D.4	TMA Polarization Change	267
D.5	TMA Rotation Induced Phase Changes	270

Appendix E Relation between TMA Co-Alignment, Vertex and POMC	272
E.1 Analytical Raytracing	272
E.2 The Nominal Setup	273
E.3 TMA Rotations	274
E.4 TMA mirror misalignment	275
E.4.1 Anti-Parallelism Errors	277
E.4.2 Pathlength errors of a misaligned TMA	278
E.5 Point of Minimal Coupling for a misaligned TMA	280
Appendix F Far-Field of Clipped Gaussian Beams	282
Curriculum Vitae	287
Acknowledgments	289
Bibliography	290

Nomenclature

$\hat{}$	A hat always denotes a matrix
AC	Alternating Current (Oscillating Signal)
ACC	Accelerometer
ACS	Acquisition Sensor
ADC	Analog-Digital-Converter
AEI	Albert-Einstein-Institute
AOCS	Attitude and Orbit Control System
AOD1B	Atmosphere and Ocean De-Aliasing Product by GFZ
AOHIS	Atmosphere, Ocean, Hydrology, Ice, Solid - constituents of time-variable gravity field
AOPL	Accumulated Optical Pathlength
AP	Aperture
AR	Anti-Reflective (Coating)
AS/ASD	Amplitude Spectrum/Amplitude Spectral Density
BOL	Beginning of Life
BS	Beamsplitter
CBE	Current Best Estimate
CCD	Charged-Coupled Device (Camera)
CF	Centrifugal (acceleration)
CMBW	Calibration Measurement Bandwidth
CNR / CN0	Carrier-To-Noise Density
CoC	Center of Phasefront Curvature
CoG	Center of Gravity
CPD	Circular Photodiode
CTE	Coefficient of Thermal Expansion
DAC	Digital-Analog-Converter
DC	Direct Current (not oscillating)
DFT	Discrete Fourier Transform
DOWR	Dual One-Way Ranging
DPLL	Digital Phase Locked Loop
DPS	Differential Power Sensing (Photodiodes)
DWS	Differential Wavefront Sensing
EBC	Extended Body Correction due to non-uniform acceleration
ENBW	Equivalent Noise Bandwidth (effective bin-width in spectral plot)
EOL	End of Life
FGM	Future Gravity Missions
FIA	Fiber Injector Assembly
FoV	Field-Of-View
FPA	Focal Plane Array
FPGA	Field Programmable Gate Array
GCRS/GCRF	Geo-Centric Celestial Reference Frame/System
GFZ	GeoForschungsZentrum Potsdam
GNSS	Global Navigation Satellite System, e.g. GPS

GOCE	Gravity field and steady-state ocean circulation explorer, ESA space mission, 2009-2013
GR	General Theory of Relativity
GRACE	Gravity Recovery and Climate Experiment, American (NASA) / German space mission, launch 2002
GRP	Gravitational Reference Point
GRS	Gravitational Reference Sensor
GW	Gravitational Wave
HCCRR	Hollow Corner-Cube Retro-Reflector
HL-SST	High-Low Satellite-Satellite Tracking, usually by means of GNSS
HM	Higher moments (of gravity field)
HR	Highly-Reflective (Coating)
IFO	Interferometer
IMU	Inertial Measurement Unit
InGaAs	Indium gallium arsenide
IQE	Internal Quantum Efficiency
ITRF/ITRS	International Terrestrial Reference Frame/System
KBR	K/Ka Band Microwave Ranging (Instrument)
L1B	GRACE Level-1B Data
LEO	Low-Earth-Orbit
LFN	Laser Frequency Noise
LISA	Laser Interferometer Space Antenna (Space Mission)
LL-SST	Low-low Satellite-Satellite Tracking, usually by means of ranging
LLF	Local Lorentz Frame
LOS	Line-Of-Sight
LPF	LISA Pathfinder
LPN	Laser Phase Noise (time-integrated LFN)
LRI	Laser Ranging Interferometer
LSQ	Least-Squares fit
NCO	Numerically-Controlled Oscillator
NGGM	Next Generation Geodesy/Gravimetric Missions
NSF	Noise-Shape Function
OB(A)	Optical Bench (Assembly)
OCXO	Oven-Controlled Crystal Oscillators
OWR	One-Way Ranging
PA	Phase Accumulator (in phasemeter)
PBS	Polarizing Beamsplitter
PD, QPD	Photodiode, Quadrant PD
PDGA	Projected Differential Gravitational Acceleration
PER	Polarization Extinction Ratio
PLL	Phase Locked Loop
PM	Phasemeter
POD	Precise Orbit Determination
POMC	Point of Minimal Coupling
PPN	Parameterized Post-Newtonian (Approximation)
PS/PSD	Power Spectrum / Power Spectral Density
PWM	Pulse-Width Modulation
PZT	Piezo-Electric Transducer
RDPOD	Reduced-Dynamic Precise Orbit Determination
RIN	Relative Intensity Noise (laser)
RMS	Root Mean Square
RoC	Radius of Curvature
RP	Reference Point

RR	Retro-Reflector
RSS	Root of Sum of Squares
RX	Receive(r)
SBF, SCF	Satellite Body Frame, Spacecraft Frame
SC, S/C	Spacecraft, Satellite
SCA	Star Camera (Attitude Sensor)
SCF	Scale Factor
SH	Spherical Harmonics, set of basis functions
SLA	Sea Level Atmosphere
SLR	Satellite Laser Ranging, ground-to-satellite
SM	Steering Mirror
SMBW	Science Measurement Bandwidth
SNR	Signal-To-Noise Ratio
SSB	Single Sideband
SSI	Satellite-Satellite Interferometry
SSI	Satellite-to-Satellite Interferometry
TM	Test Mass
TMA	Triple Mirror Assembly, Corner-Cube
TOF	Time of Flight
TRL	Technical Readiness Level
TX	Transmit(ter)
USO	Ultra-Stable Oscillator
w.r.t	with respect to

List of Figures

1.1	SH degree variances: Static gravity field models	4
1.2	SH degree variances: AOHIS constituents of time-variable gravity field	4
1.3	SH degree variances: time-variable gravity field models	5
1.4	Spectral density: Instruments to probe spacetime curvature	8
1.5	Spectral density: PDGA of single C and S coefficients	13
1.6	Spectrum: PDGA for different orbit heights and S/C separations	13
1.7	Spectral density: PDGA with ranging, centrifugal acceleration and numerical errors	16
1.8	Spectral density: PDGA at low frequencies with linear frequency axis	18
1.9	Sketch: Gravitational reference point and ranging	22
1.10	Spectral density: Kinematic orbit precision	24
1.11	Spectral density: Accelerometer noise of different instruments	28
1.12	Flow diagram of a proposed e.motion ² data processing chain	33
1.13	Spectral density: Modeling reduced-dynamic orbit precision	37
1.14	Spectral density: Reduced-dynamic orbit position noise	38
1.15	Spectral density: Direct accelerations (DA) of S/C	40
1.16	Spectral density: PDGA signal and T_i errors	43
1.17	Spectral density: PDGA sensitivity with reduced-dynamic orbits	45
1.18	SH degree variances: Only direct acceleration (single S/C)	48
1.19	Triangular SH plot: Correlations with tone errors	49
1.20	SH degree variances: PDGA single pair	50
1.21	SH degree variances: PDGA single pair, different orbits and separations	51
1.22	SH degree variances: PDGA in Bender pair	52
1.23	Spectral density: LOS angular velocity sensing	55
1.24	Sketch: Drag-free, drag-compensation and servo-accelerometer	58
1.25	Spectral Density: Drag compensation requirement	60
1.26	Spectrum: Residual test-mass motion in drag-free mode	64
1.27	Gain over frequency: Requirement for drag-free AOCS loop gain	64
1.28	Time-series: Angular variations of test-mass in drag-free mode	65
1.29	Spectral density: Angular TM jitter in drag-free mode	65
1.30	Spectral density: Requirement for thruster noise	67
1.31	Spectral density: PWM thruster	68
1.32	Block diagram: Connections between different measurements	69
1.33	Spectral density: Calibration tones within ACC and LRI	71
1.34	Sketch: e.motion ² summary	75
2.1	Block diagram: Phase measurements by means of IQ demodulation	87
2.2	Block diagram: Phase measurements by means of IQ demodulation and phase-tracking	87
2.3	Sketch: Electrical down conversion vs. optical square-law detection	90
2.4	Sketch: DWS working principle	92
2.5	Sketch: Longitudinal phase change upon beam rotation.	93
2.6	Picture: NGGM High-Stability Laser	96

2.7	Picture: NPRO Laser from Tesat	97
2.8	Spectral density: Laser frequency stability of various sources	99
2.9	Photodiode responsivity over wavelength	101
2.10	Picture: Different photodiodes	101
2.11	Plot: Homogeneity measurement of a QPD	102
2.12	SSB Phase Noise of various oscillators including NGGM requirement	106
2.13	Allan deviations: Stability of oscillators including NGGM requirement	107
2.14	Spectral density: Timing jitter of USO and proper time modulation	108
2.15	Sketch: Ray-tracing through corner-cube retro-reflector	110
2.16	Picture/CAD: GRACE Follow-On LRI TMA	111
2.17	Interferogram: Reflected light by corner-cube retro-reflector	112
2.18	Sketch: On-axis retro-reflector types	114
2.19	Picture/CAD: Optical bench types for LISA, GRACE Follow-On and LISA Pathfinder	116
2.20	Picture: Phasemeter electric-circuit board	117
2.21	Block diagram: DPLL phasemeter	118
2.22	Spectral density: Typical input signal for phasemeter	119
2.23	Bode plot: Phasemeter closed-loop transfer function	120
2.24	Spectral density & Bode plot: Phase variations of input signals & decimation filter	121
2.25	Picture: Typical steering mirror	127
2.26	Block diagram: Frequency-offset PLL and DWS loops	128
2.27	Simplified block diagram: Single channel frequency-offset PLL	129
2.28	Loop gain over frequency: Model for frequency-offset PLL	131
2.29	Picture: Typical focal plane array camera for acquisition	132
2.30	Sketch & Minkowski diagram: One-way ranging	137
2.31	Spectral density: One way-ranging laser frequency noise, other noises and signal contributors	143
2.32	Sketch & Minkowski diagram: Dual one-way ranging	145
2.33	Spectral density: Dual one-way ranging laser frequency noise, other noises and signal contributors	147
2.34	Spectral density: Comparison of different noise contributors in laser and mi- crowave ranging	148
2.35	Sketch & Minkowski diagram: Transponder-based ranging	151
2.36	Spectral density: Constituents of the phase on the slave S/C in a high-gain frequency-offset PLL	152
2.37	Spectral density: Constituents of the master's phase in transponder-based ranging	157
2.38	Slide: Executive summary of comparison between DOWR and transponder- based ranging	162
2.39	Spectral density: Special relativistic corrections of the photon time-of-flight for OWR, DOWR and transponder	168
2.40	Spectral density: Validation of analytical formulas for general relativistic pho- ton time of flight correction with respect to numerical results	171
2.41	Spectral density: General relativistic corrections of the photon time of flight for OWR, DOWR and transponder	173
2.42	Spectral density: Ionospheric and special relativistic effects in GRACE Level- 1B data	175
2.43	Spectral density: Ranging noise due to refractive index & variations in refrac- tive index over spatial frequencies	180
2.44	Sketch: Effect of TX beam and RX satellite misalignment	184
2.45	Sketch: Two-way ranging scheme with reference points	185

2.46	Spectral density: S/C pointing variations & ranging noise due to attitude-to-ranging coupling	188
2.47	Sketch: Determination of RX reference points	189
2.48	Sketch: Determination of TX reference points	191
2.49	Optical detection schemes in interferometry	195
2.50	Carrier-to-noise density and phase readout noise of different optical detection schemes	200
2.51	Heterodyne efficiency for a circular photodiode as a function of beam parameters and misalignment	207
2.52	Beam parameters over misalignment angle, where the heterodyne efficiency drops to $1/e^2$	208
2.53	Heterodyne efficiency of photodiode segments over tip and tilt misalignments between phasefronts	209
2.54	Heterodyne efficiency for a segment of a circular quadrant photodiode as a function of beam parameters and misalignment	210
2.55	Drop in heterodyne efficiency due to differential phasefront curvature	211
2.56	Heterodyne efficiency drop due to differential phasefront curvature as a function of beam parameters	213
2.57	Heterodyne efficiency in the presence of a differential phasefront curvature as a function of misalignment angles	214
2.58	Heterodyne efficiency with and without gaps	215
2.59	Sketch: Acquisition strategy in GRACE Follow-On	216
2.60	On-axis optical layout: E.motion concept	221
2.61	On-axis optical layout: NG2 study by Airbus	222
2.62	On-axis optical layout: Alenia concept	222
2.63	Off-axis optical layout: GRACE Follow-On LRI	225
2.64	Sketch: Working principle of a Differential Wavefront Sensing Loop	225
2.65	Proposed optical layout: Off-axis	229
2.66	Proposed optical layout: On-axis interferometer with RX beam power loss	231
2.67	Proposed optical layout: On-axis interferometer without RX beam power loss	233
2.68	Carrier-to-Noise density with units of dB(Hz/m ²) over S/C separation and transmit power	241
2.69	G_{setup} with units of dB(m ²) for the off-axis layout	244
2.70	G_{setup} with units of dB(m ²) for the on-axis layout	247
A.1	Time-series: GRACE-A L1B ACC data (min, max and mean) for 11 years	253
A.2	Time-series: GRACE-B L1B ACC data (min, max and mean) for 11 years	254
A.3	Time-series: Geo-magnetic and solar activity	255
A.4	Time-series: Accelerations (max, min and mean) for e.motion ²	256
D.1	TMA simulation: Coordinate frame, mirrors and beams	265
D.2	Refractive index over wavelength: Gold, silver and aluminum	266
D.3	Electric field vector evolution due to TMA polarization change	267
D.4	Polarization state: Ellipses due to TMA polarization change	268
E.1	Error ellipse for TMA mirror misalignments for a numerical example	278
F.1	Far-field on-axis intensity of clipped Gaussian beams	285
F.2	Far-field intensity over misalignment for clipped Gaussian beams	286
F.3	Far-field divergence of clipped Gaussian beams and model	286

List of Tables

1.1	Assumed tone errors for PDGA	31
1.2	Assumed tone errors for GNSS	31
1.3	Errors within the PDGA	44
1.4	Accelerometer scale factor requirements for different missions	62
2.1	Key figures of a potential NGGM laser system	96
2.2	Allan deviations for potential e.motion ² USO requirement	107
2.3	Physical properties of glass	115
2.4	Key figures of a potential NGGM acquisition sensor	133
2.5	Star magnitude and number of stars for acquisition sensor	134
2.6	Comparison of LISA, LISA Pathfinder and GRACE Follow-On	136
2.7	Calculation of refractive index in LEO	177
2.8	Coefficient of various polynomial functions obtained from fits	207
2.9	Potential negative side effects of additional optical components	220
2.10	Comparison of various laser ranging concepts	228
2.11	Laser Link Power Budget: Part 1/2 for off-axis interferometer	235
2.12	Laser Link Power Budget: Part 2/2 for off-axis interferometer	236
2.13	Laser Link Power Budget: Part 1/2 for on-axis interferometer	239
2.14	Laser Link Power Budget: Part 2/2 for on-axis interferometer	240
2.15	Condensed laser link power budgets	242
D.1	Refractive indices at 1 μm wavelength	266
D.2	Polarization parameters for different TMA materials	269
D.3	Coupling factors: TMA rotations into pathlength via polarization change	271

Part 1

Design Considerations for Future Geodesy Missions

Geodesy is the *science of the measurement and mapping of the Earth's surface* [Helmert, 1880, 1884]. In [Seeber, 2003] the basic aims of geodesy are formulated as

1. Determination of precise global, regional and local three dimensional positions (e.g. establishment of geodetic control).
2. Determination of Earth's gravity field and linear functions of this field (e.g. a precise geoid).
3. Measurement and modeling of geodynamical phenomena (e.g. polar motion, Earth rotation, crustal deformation).

This first part of this thesis deals mainly with the second point, the measurement of Earth's gravity field, although interconnections and overlap also exist with the two other points. Terrestrial measurements using gravimeters provide a good means for this in well-developed regions. Complementary precise orbit determination of satellites in the vicinity to Earth with Satellite Laser Ranging (SLR) from ground and with the Global Navigation Satellite System (GNSS) provide large-scale information of the Earth's gravity field [Bezdek *et al.*, 2014; Jäggi *et al.*, 2011; Baur *et al.*, 2014; Matsuo *et al.*, 2013].

For resolving Earth's small-scale gravity field structure and its temporal variations dedicated missions like GRACE (Gravity Recovery and Climate experiment, launch 2002) and GOCE (Gravity field and steady-state ocean circulation explorer, 2009-2013) have been proven to be vital [Tapley *et al.*, 2004; Johannessen *et al.*, 2003]. GRACE monthly snapshots of Earth's gravity field have provided insights into processes within the *system Earth*, consisting of oceans, solid Earth and atmosphere. The gain in understanding of our planet and the associated importance for society and humankind manifested in the funding of a GRACE Follow-On mission, which is currently being built. It is designed as a low-risk quick successor mission, basically a copy of the GRACE satellites, aiming to provide continuity of data streams with an increased sensitivity due to advances in technology. However, a major change is the integration of a Laser Ranging Interferometer (LRI) technology demonstrator, which shall prove the feasibility of laser interferometry between satellites and verify the increased sensitivity of the ranging observable. The LRI has been developed by an US-German collaboration with involvement of the AEI and the author of this thesis.

Due to the long development and lead times for space missions and space technology, research and studies on future missions are continuously carried out in preparation for the next mission calls by space agencies beyond GRACE Follow-On.

In 2013/2014 a collaborative study involving several institutes of geodesy, geoscience, applied science, and industry partners was conducted and funded by the German Federal Ministry of Research and Technology (BMBF). The efforts led to a comprehensive published report [e.motion² Team, 2014] providing a concept for a future mission with the name

*e.motion*². At first, during the study, scientific requirements and needs were determined and assessed, mission goals in terms of geoid accuracy defined, and technological and mission constraints such as orbit configurations were derived and settled upon. Consequently, the satellite and payload concept was elaborated, providing realistic models for the sensitivity of observables. To complete the study, elaborated full-scale simulations were performed to determine the quality of gravity field solutions and if the mission goals could be achieved. The payload concept of *e.motion*² was worked out as part of this thesis. The author was responsible for the payload concept (work package 400 of the study).

This chapter starts with a short introduction on the structure and constituents of Earth's gravity field, which is the science objective of gravimetric satellite missions, in section 1.1. Then basic concepts are introduced to measure it. In section 1.2, *e.motion*² boundary conditions are addressed, for example, why a particular satellite constellation was selected in the study. In section 1.3 on the measurement principle of GRACE-like missions, the mathematical relation between observations and gravity field is elaborated. This can be based on high-low satellite-satellite tracking (HL-SST), low-low satellite tracking (LL-SST), or a combination of both.

To be able to recover the gravity field different observations by various instruments are required, which are discussed with respect to their important parameters such as sensitivity and errors in section 1.4 (Instruments and Observations). These instrument models are used to derive the noise level in the HL-SST and LL-SST channel (section 1.6), which are finally propagated to the level of gravity fields in section 1.7. This end-to-end simulation, which relates the errors from the very first observation to the final gravity field solution, is used to show the strength of the *e.motion*² concept and to independently verify the result from the study. Additionally, it also allows critical quantities in the processing chain to be revealed, which should be addressed.

It turned out during the analysis that the centrifugal acceleration of the inter-satellite baseline is not measured with sufficient precision, which makes in-situ approaches of gravity field recovery undesirable in LL-SST missions. To circumvent the problem, dynamical reference satellite trajectories are derived, which are again susceptible to errors in the background gravity field models. Hence, a precise direct measurement of the centrifugal acceleration would be beneficial but turns out to be difficult. This is shown in section 1.8.

Another important aspect regarding drag-free utilization was addressed only briefly in the *e.motion*² report, and is therefore supplemented in section 1.9 of this thesis. Finally, section 1.10 presents ideas for the integrated data analysis and calibration of instruments, and section 1.11 completes part one of this thesis with a summary.

1.1 Earth's Gravity Field

Earth's gravity field is static to first order and a pronounced spatial dependency exists due to Earth's oblateness. The gravity acceleration at the poles is roughly 9.832 m/s^2 , while at the equator it is 9.780 m/s^2 [Zhang, 2012, p. 66]. Thus, an object's weight changes by roughly 0.5% between the two locations due to the different distances to the geocenter and the change in centrifugal acceleration. If a best-fit ellipsoidal gravity field is subtracted from the actual gravity field, the remaining spatial structure is of the order of $\pm 100 \text{ mgal} = \pm 1.0 \text{ mm/s}^2$ (peak-peak), a factor of 10^{-4} smaller. Commonly, Earth's gravity field is expressed as a particular equipotential surface, the so-called geoid. The geoid undulation (height) w.r.t. a reference ellipsoid is globally between approximately -100 m and $+85 \text{ m}$. The distribution of geoid height signal as a function of spatial frequencies, expressed as equivalent spherical harmonic degrees, is shown by the upper dark blue trace in figure 1.1.

1.1.1 Time-Varying Gravity Field

In addition to a large static part there are temporal variations of Earth’s gravity field. They are of special interest, since they can be used to study mass transport within the system Earth, e.g. ice mass losses at polar regions, sudden mass shifts due to earthquakes, changing water resources and so on. In general, one should distinguish between tidal and non-tidal temporal variations. Tidal variations of the gravity field are caused by gravitational pull from other celestial bodies, especially from the Moon. The well-known ocean tides, which reach water elevations of 60 cm over oceans and even higher in shallow regions, have, next to the principal semi-diurnal component, several constituents with lower frequencies. The solid Earth and atmosphere are also affected by tides. For example, the solid Earth tides result in a periodic land uplift with 20-30 cm magnitude, which can be measured e.g. by means of GNSS. If tidal effects are subtracted from the gravity field, non-tidal variations become visible, which are often categorized as *AOHIS* [Gruber *et al.*, 2011] :

- **Atmosphere:** e.g. distribution and propagation of pressure systems,
- **Ocean:** e.g. mass variations due to atmospheric and continental freshwater fluxes and evaporation, changes in temperature, salinity, or surface height changes due to currents
- **Hydrology:** e.g. terrestrial water storage such as basins, rivers and groundwater,
- **Ice:** e.g. ice mass change in polar regions,
- **Solid Earth:** e.g. glacial isostatic adjustment and seismic deformations.

Many of these effects have a strong connection to weather phenomena and contain high frequency signals with periods of hours to days. Space-borne gravimetry is sampling Earth’s gravity field on a global scale and spatial coverage of measurement points is only sufficient after a few weeks of integration for a gravity field map update. Higher frequencies in the time-variable gravity field need to be subtracted using background models to avoid aliasing of the high-frequency content into the (low-frequency) measurement. For this, the GeoForschungsZentrum Potsdam (GFZ) is providing an *atmosphere and ocean de-aliasing product* (AOD1B), which consists of a set of spherical harmonic coefficients (cf. next subsection), which are updated every 6 hours and are derived from meteorological and ocean models. The mean monthly non-tidal AOHIS signal is shown in figure 1.2. It was obtained by forward-modeling [Gruber *et al.*, 2011]. These traces indicate the time-variable components of the gravity field, which one aims to measure with GRACE-like missions. The typical precision of gravity field solutions derived on a periodic basis is illustrated in figure 1.3. Please note that figure 1.3 shows the difference between a static gravity field (Eigen-6c4) and, for example, monthly gravity field solutions. As is apparent from the plot, the GRACE monthly gravity field solutions can recover the AOHIS signal up to SH degree ≈ 40 .

1.1.2 Observation Techniques

Space-borne geodesy aims to map Earth’s static and temporal gravity field on a global scale. The gravity field is dependent on the mass distribution within the system Earth. One goal of geodesy is to determine the gravitational potential function, $V(t, x, y, z)$, which is in general a function with spatial and temporal dependency. For simplification it is often assumed that all mass is concentrated within a sphere (with mean Earth radius a), so that the potential fulfills the Laplacian equation $\nabla^2 V = 0$ for exterior points. In this type of boundary condition the gravity field outside the sphere is fully determined by a potential function defined on the sphere. This function is often expressed in terms of a series expansion of global spherical harmonics (SH) [Barthelmes, 2009] with degree l and order m :

$$V(r, \varphi, \theta) = \frac{GM}{r} \cdot \sum_{l=0}^{\infty} \sum_{m=0}^l \left(\frac{a}{r}\right)^l P_{l,m}(\cos(\theta)) \cdot [\cos(m\varphi) \cdot C_{l,m} + \sin(m\varphi) \cdot S_{l,m}]. \quad (1.1)$$

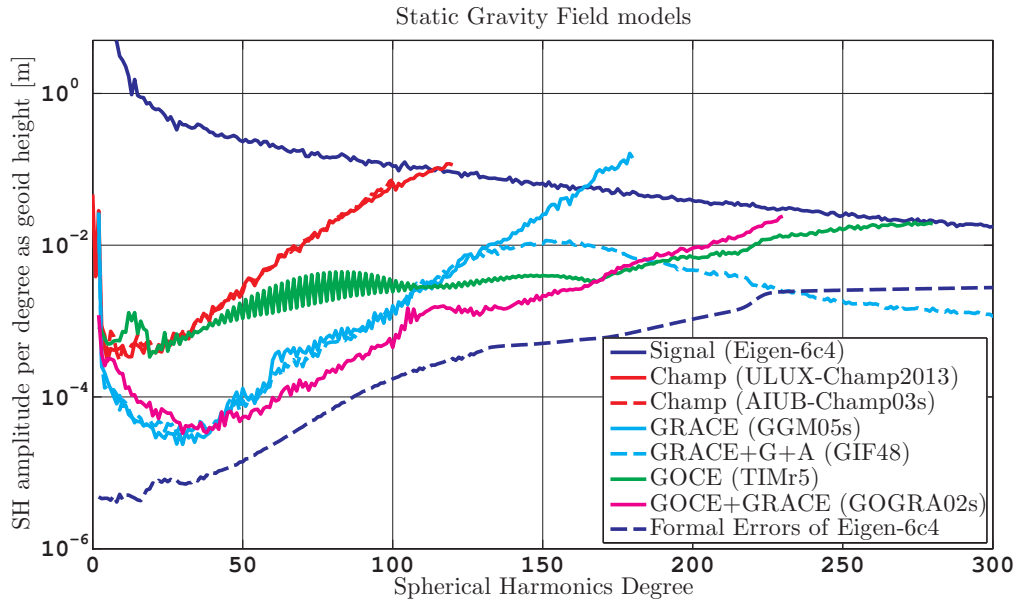


Figure 1.1: Static gravity field models derived by GRACE, Champ, GOCE, Gravimetry (G) and Altimetry (A). The upper dark blue trace is the signal of the Eigen-6c4 model, which contains GRACE, GOCE, Gravimetry and Altimetry information. The other traces are computed as the difference to the Eigen-6c4 model.

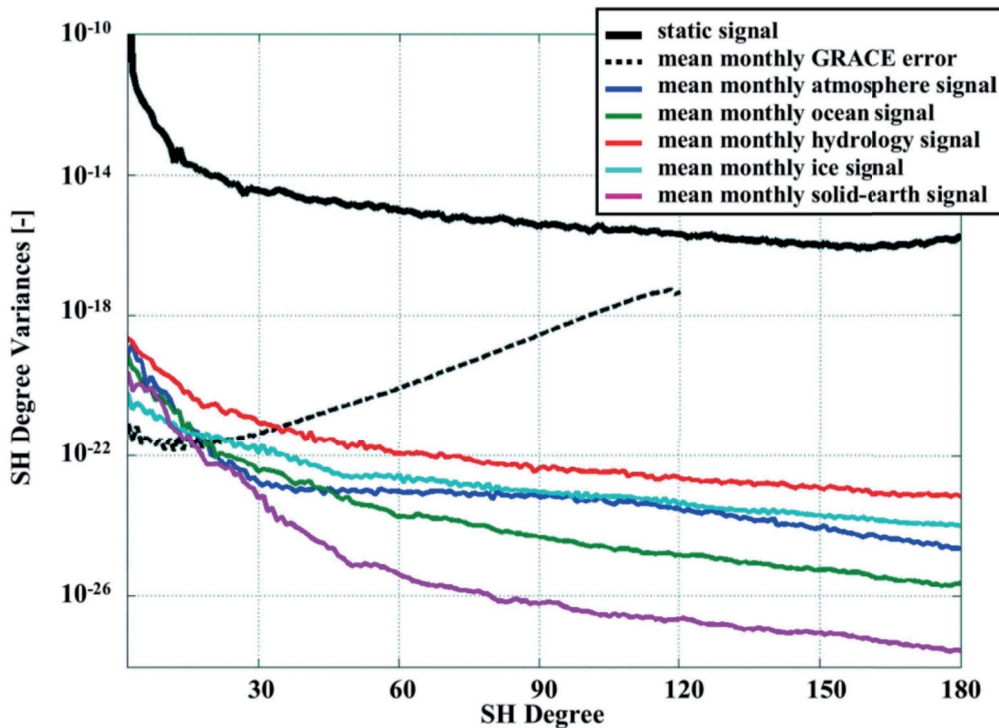


Figure 1.2: Mean of monthly signal in terms of spherical harmonic degree variances for different AOHIS components (colored traces) compared to mean monthly error of GRACE derived fields (dashed black line). Plot from [Gruber *et al.*, 2011] under Creative Commons Attribution 3.0 License.

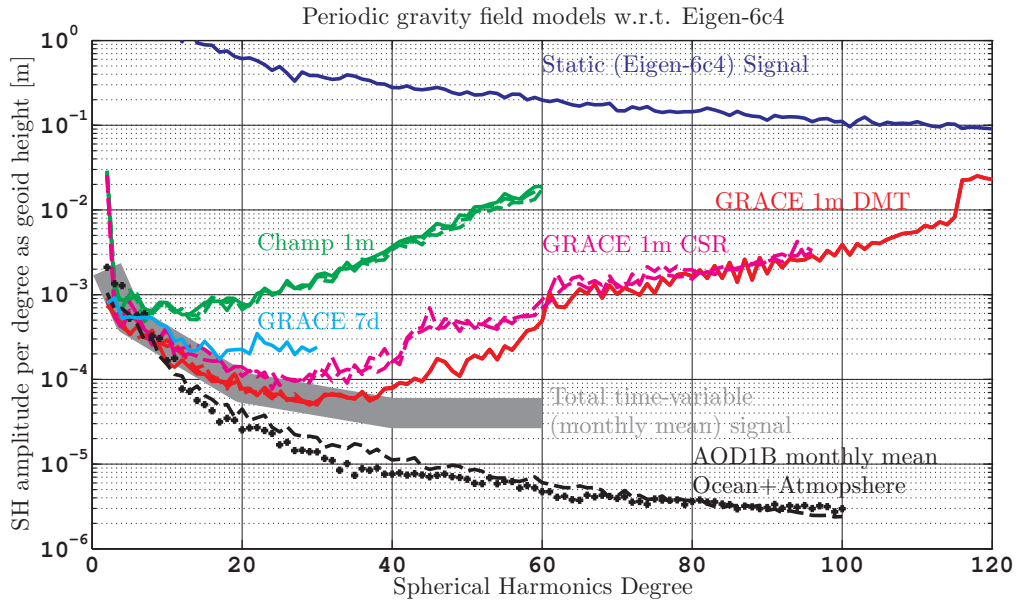


Figure 1.3: Typical signal and error content in gravity field solutions derived on a regular basis with different integration times, e.g., 7 days and 1 month, for CHAMP (green trace) and for GRACE (red, magenta and light blue traces). The black traces indicate the monthly variability of the gravity field due to ocean and atmospheric effects derived from AOD1B. The gray bold trace indicates an upper limit for the time-variable gravity field averaged over one month, which is the sum of the single components shown in figure 1.2. CSR and DMT denote two different processing centers and schemes.

However, in recent years expansions or supplementations with local basis functions also came into focus [Naeimi, 2013]. The SH-coefficients $C_{l,m}(t)$ and $S_{l,m}(t)$ fully determine the gravity field. The equation refers to a co-rotating Earth-fixed coordinate frame and the coordinates r, λ, θ denote spherical coordinates. One should note that the orbit height or radial distance r attenuates coefficients of degree l with $1/r^l$ in the potential V , while the acceleration, defined as the spatial gradient of the potential $\vec{\nabla}V$, is attenuated already by $1/r^{l+1}$. The gravity gradient, the second spatial derivative of the gravity potential, is attenuated by $1/r^{l+2}$, where r is measured from the center of the Earth.

If one aims to compute the physically correct acceleration of a satellite in an Earth-fixed frame, eq. (1.1) needs to be supplemented by the non-harmonic centrifugal potential [Barthelmes, 2009, eq. (4)], which accounts for the centrifugal acceleration present in a rotating frame, as well as by the Coriolis acceleration if the object is moving in the Earth-fixed frame. The Euler acceleration needs to be considered if the angular velocity of the frame is not constant.

Several means exist to access the potential or its functionals. The three most prominent principles of space-borne gravimetry are introduced in the following sections:

Gravity Field from Orbit Trajectory

A free-falling satellite within a spherically symmetric gravity field, without disturbances from atmosphere and other celestial bodies, will orbit the central body in a closed elliptical (Keplerian) trajectory, if relativistic effects are neglected. Higher moments of the gravity field, small deviations from the sphericity of the gravity field, induce disturbances in the trajectory, which can be measured by means of SLR or GNSS. From these, low degree coefficients $C_{l,m}(t)$ and $S_{l,m}(t)$ can be computed, as shown in the case of the LAGEOS and CHAMP satellites [Jäggi *et al.*, 2012]. The limited accuracy of orbit tracking of millimeter to centimeter and

disturbances such as atmospheric drag allow only large-scale features of the gravity field to be retrieved. The temporal variations of these coefficients have seasonal and annual components as well as long-term drifts. The residual atmosphere produces drag accelerations, which can be mitigated by flying at higher altitudes with the detrimental effect of a lower gravity signal amplitude. Alternatively, the drag acceleration can be measured using accelerometers and subtracted later in post-processing.

Gravity Field from Satellite-Satellite Tracking

The determination of absolute 3-d positions w.r.t. the Earth is, in general, less accurate than the measurement of distance changes between close objects, e.g. a pair of satellites. The distance between close free-falling satellites is influenced by gravitational and non-gravitational effects and can be read out with high precision via low-low satellite-satellite tracking (LL-SST). The non-gravitational part can be measured with accelerometers and removed from the observations. With GRACE one can retrieve spherical harmonic coefficients for the static field up to degree 180, which corresponds to a spatial (half-wavelength) resolution of approximately 110 km. Monthly solutions are usually determined up to degree 90 [Dahle *et al.*, 2012, GFZ RL05], which corresponds to approximately 220 km spatial half-wavelength resolution. In case of GRACE, the satellites are separated by approx. 220 km.

Gravity Field from Gradiometry

The concept of differential measurements can be extended to multiple close objects, e.g. test-masses on a single satellite. By measuring their relative acceleration, or equivalent distance changes, one can form a short-arm gradiometer. Such a setup with six accelerometers has been used in the GOCE mission, which was capable of retrieving all six degrees of the gravity gradient tensor. The short baseline nature yields the best sensitivity for high-degree coefficients. However, a lower orbit and longer integration times compared to GRACE are essential in order to resolve the weak fine-structure of the static gravity field. The temporal AOHIS signals of such high-degree coefficients (up to $l \approx 1800$) are below the instrument sensitivity. The sensitivity at low degrees (below 50) for an integration time of one month is insufficient for resolving the time-variable gravity field. However, use of gradiometry for resolving the time-variable gravity field is under investigation, for example, within the collaborative research center *geo-Q* at the Leibniz University of Hannover¹.

Data Fusion

Generally, the measurement quality benefits from an increased number of independent observations. A GRACE-like mission can exploit information from the precise satellite-satellite link as well as from orbit trajectory to retrieve the gravity field. The combination of gradiometry and satellite-satellite tracking could be considered. The most accurate gravity models are obtained from a combination of satellite measurements with terrestrial observations.

However, from a satellite mission design perspective, it is also necessary to justify a space mission by pointing out a stand-alone benefit to science and society. Therefore, *e.motion*² and other studies usually define science objectives in terms of geophysical phenomena to be observed, or in terms of gravity field resolution. Since this thesis focuses on technology aspects and system design, the interested reader is referred to [*e.motion*² Team, 2014, chapter 2] for detailed scientific objectives.

1.1.3 Geodesy and Fundamental Gravitational Physics

Measuring the gravity field unavoidably leads to the question on the nature of gravitation. For most terrestrial applications, the Newtonian description from 1687 as an instantaneous force

¹Project B07: <http://www.geoq.uni-hannover.de/>

acting between masses is sufficient. However, the Newtonian formalism is prone to deficiencies (e.g. perihelion shift of Mercury), which were resolved by Albert Einstein’s General Theory of relativity (GR) in the beginning of the 20th century. In the framework of GR, space and time are merged to a four-dimensional spacetime and gravitation is a fictitious force arising from the curvature of spacetime. This curvature is caused by mass, or equivalently by energy, through $E = mc^2$. Thus, measuring Earth’s gravity field is equivalent to the determination of the curvature of spacetime.

Newton’s first axiom states that force-free objects rest or move with constant velocity along a straight line. In the Euclidean space, a straight line is the shortest connection between two points. In GR, a free-falling object is moving along so-called geodesics, which are the shortest connection between arbitrary points in the 4d-spacetime. The metric of the spacetime, which defines distances and therefore the trajectory, is connected through Einstein’s field equations directly to the mass (and energy).

By tracking the orbital trajectory of an ideally free-falling satellite, in other words by recording its position at certain times, one obtains the 4-dimensional spacetime trajectory, the geodesic. With this, one can derive the spacetime curvature, known as the gravity field. The same is achieved by measuring distance changes between free-falling test-masses, e.g. between GRACE satellites or within a GOCE gradiometer. Earth’s static and time variable gravity field is equivalent to a static and time-variable spacetime curvature.

Recall that distances, and therefore also positions, are defined by the speed of light c , i.e. pathlength of light rays in vacuum. In the case of GNSS, position is determined by means of the travel time of electromagnetic waves. Electromagnetic waves, in particular light, is our ruler for spacetime. Much research at the AEI is focused on building instruments, which can read this ruler with ever higher precision.

One such instrument is the planned Laser Interferometer Space Antenna (LISA) [Danzmann *et al.*, 2017] mission. It will measure tiny ripples in space-time, so-called gravitational waves (GW), which propagate through the universe at the speed of light and are generated by accelerated masses. Due to spacetime’s stiffness, only massive cosmic bodies like stars and black holes are supposed to produce GW with sufficient amplitude to be detected in our solar system.

Such waves were predicted by Einstein in 1916 [Einstein, 1916]. Their existence has been shown indirectly by Hulse-Taylor in 1974 [Hulse & Taylor, 1975], who were rewarded with a Nobel prize in 1993. On 14th September 2015, the ground-based LIGO detectors succeeded in the first direct measurement [LSC, 2016]. However, such ground-based detectors are limited to frequencies above ≈ 10 Hz, where disturbances from Earth are manageable. The low-frequency regime containing most of the gravitational wave sources can be covered by LISA. LISA can be placed far away from Earth, such that variations in spacetime curvature due to Earth are sufficiently small.

The spacetime measurements mentioned in this section rely on the measurement of distance or length changes. The ratio of sensitivity of length measurement, expressed as $m/\sqrt{\text{Hz}}$, and the actual distance between the probing masses, yields the so-called strain sensitivity with units of $1/\sqrt{\text{Hz}}$. It is a measure of the sensitivity of the spacetime curvature measurements. In figure 1.4, the acceleration noise and corresponding strain sensitivity are depicted for different instruments. This illustrates that fundamental physics, such as gravitational wave physics, and the science of precise determination of Earth’s gravity field are closely related.

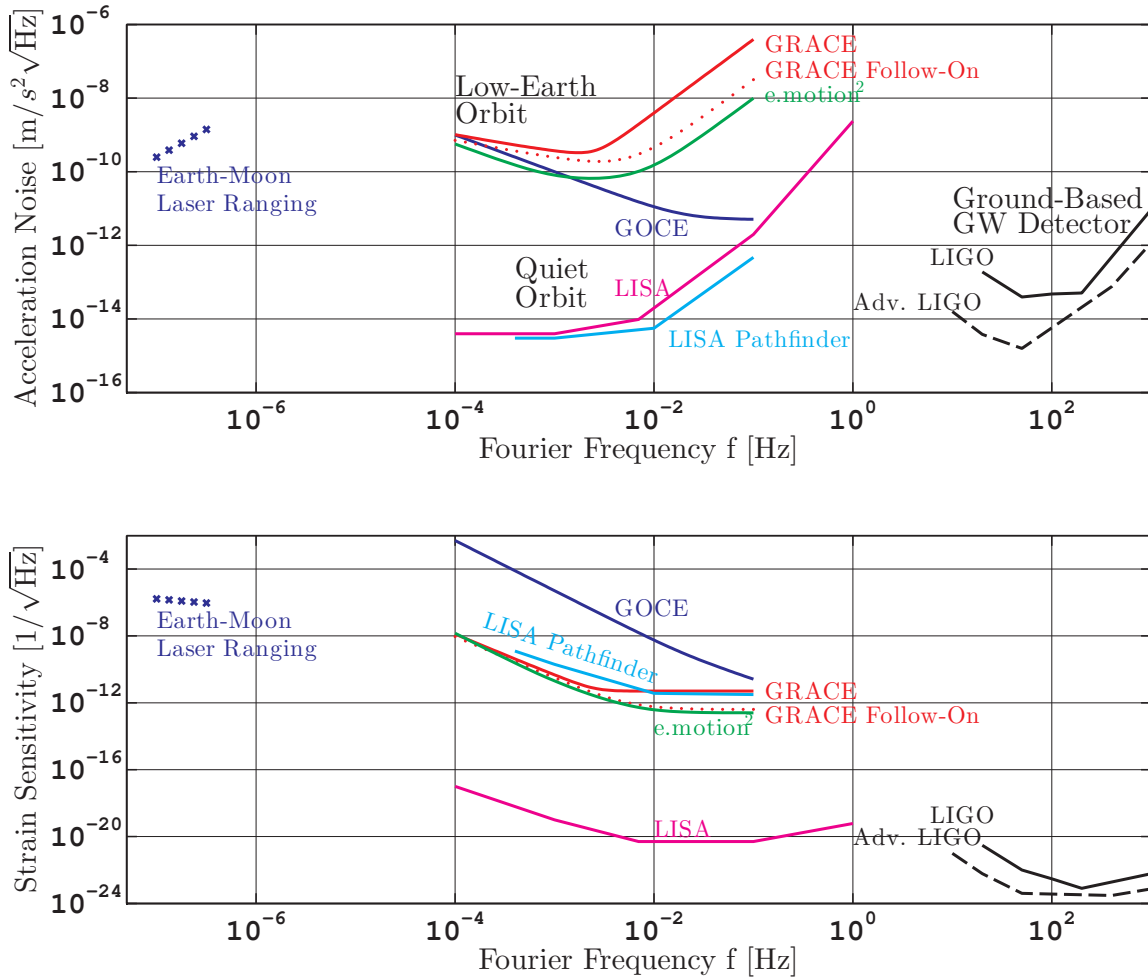


Figure 1.4: (Top:) Sensitivity of different instruments and means to probe spacetime curvature expressed as acceleration noise. One should keep in mind that the different instruments aim to measure different effects (signals) of spacetime curvature, i.e. Earth gravity missions map the spatial form/distribution, while gravitational wave instruments detect propagating waves. (Bottom:) Upper plot rescaled to strain sensitivity.

1.2 E.motion² Boundary Conditions

1.2.1 Previous Studies

The satellite gravimetry missions GRACE, CHAMP, GOCE and GRACE Follow-On have resulted in over 1700² scientific publications to date. Continuously, papers are released concerning ideas, concepts and analysis of future geodesy missions. For example, [Sneeuw *et al.* \[2005\]](#) pointed out various (geophysical) science objectives and corresponding sensitivity requirements and, furthermore, simulated different cases of high-altitude, gradiometry, GRACE-like and other satellite formation missions with a quick-look tool. The analysis is limited to static gravity field recovery and uses various simplifications (e.g. no accelerometer noise). [Bender *et al.* \[2003\]](#) suggested laser interferometry along a single axis in a GRACE-like configuration and along two axes in a Cartwheel configuration. In a later paper, a dual pair GRACE concept with inclinations of 90° and 63° was suggested for an improved temporal resolution and therefore a reduction of temporal aliasing [[Bender *et al.*, 2008](#)]. [Elsaka \[2010\]](#) analyzed various formations in his PhD thesis, e.g. Pendulum, Cartwheel, LISA-like, Bender, with regard to the retrieval of the static and temporal gravity field by means of satellite-to-satellite tracking. He emphasized that pure along-track measurements as in GRACE introduce anisotropy and are therefore suboptimal and should be complemented by measurements along the radial or cross-track component. In addition, it is stated that the proper selection of orbits can suppress errors induced by temporal aliasing. [Loomis *et al.* \[2012\]](#) used different accelerometer and ranging noise levels to assess the gain by advanced missions. He concluded that a gain solely in ranging sensitivity does not improve gravity field solutions. Instead, a reduction of accelerometer errors, e.g. a drag-free mission, and the reduction of temporal aliasing is required. In [[Flechtner *et al.*, 2016](#)] the expected enhancement of gravity field solutions due to the laser interferometer was analyzed for the GRACE Follow-On mission. The simulation spanning 5 years predicts a modest gain for the fine structure due to the interferometer, but accelerometer noise and background model errors are still major contributors to the overall error.

Other comprehensive resources concerning science objectives and conceptual mission designs are [[Rummel *et al.*, 2003](#)] and [[Koop & Rummel, 2007](#)].

Additionally, specific studies containing derivation of scientific requirements, formulation of mission scenarios and of instrument concepts, and end-to-end simulations have been conducted [[Alenia-Team, 2010](#); [NG2-Team, 2011](#); [Reubelt *et al.*, 2014](#)]. The precursor of the e.motion² study, on which this thesis focuses, was the e.motion study [[e.motion Team, 2010](#)]. In Europe, the term Next Generation Geodesy/Gravimetric Missions (NGGM) is coined for such future missions, with e.motion² being the German *NGGM-D* study.

1.2.2 Observation Type and Number of Satellites

The e.motion² mission concept is designed to study the mass transport within the system Earth, in particular to track mass changes on Earth over a long period of 10 years with monthly sampling. As pointed out in previous sections, the strength of a GOCE-like gradiometry mission is its ability to provide a finely resolved global gravity field map, but it requires a long period to obtain global coverage. Hence, it is well suited for the static gravity field. In addition, the low altitude of a GOCE-like mission requires drag-compensation, which limits the mission lifetime due to propellant constraints. Therefore, the e.motion² concept was based on GRACE-like low-low satellite-satellite tracking (LL-SST). Different pendulum constellations, as well as a dual-GRACE, so-called “Bender” configuration [[Bender *et al.*, 2008](#)], were considered in the study. More sophisticated formations such as a Cartwheel have been suggested in literature [[Bender *et al.*, 2003](#)] but impose technological challenges,

²1369 for GRACE and 11 for GRACE Follow-On according to GFZ website (<http://www.gfz-potsdam.de/sektion/globales-geomonitoring-und-schwerefeld/publikationen/>), 333 for GOCE according to ISI Web of Knowledge search (<http://apps.webofknowledge.com/>)

e.g. due to higher relative velocities and formation control, and were therefore not considered for e.motion².

As various analyses have shown [Elsaka, 2010; Pour *et al.*, 2013], pendulum formations with two satellites, as well as the Bender configuration with four satellites, outperform the classical GRACE concept. However, since a Heisenberg-like uncertainty relation holds, the product of spatial resolution D_{space} and temporal resolution D_{time} of gravity field maps is bounded for a fixed number of measurement links or SST pairs [Pour *et al.*, 2013],

$$D_{\text{space}} \cdot D_{\text{time}} \geq \text{const.} \quad (1.2)$$

Thus, further improvement requires an increase in measurements, e.g. by a second pair. A dual pair GRACE mission doubles the measurement points, thus, leading to an improvement of a factor of $\sqrt{2}$ at least, compared to a single GRACE pair. The gain is even larger due to reduction in temporal aliasing. Pour *et al.* [2013] claim a gain factor between 10 and 15 for a Bender configuration over a single in-line pair for 6-day short-period gravity field solutions.

The superior sensitivity of the Bender configuration w.r.t. a Pendulum for degrees below 60, which contain most of the time-variable signal, was identified in [e.motion² Team, 2014, Figure 3-5, p. 25]. Furthermore, the fact that the Pendulum configuration has already been analyzed in the precursor e.motion study [e.motion Team, 2010] led to a selection of the Bender configuration as baseline for e.motion².

1.2.3 Inclination

The inclination of a single satellite pair in a gravimetry missions is usually close to 90°. Such a polar orbit ensures coverage of the poles, which are of special interest for geoscience e.g. due to ice mass loss by global warming. Due to the rotation of the Earth underneath the satellites, the ground-track pattern can achieve global coverage. One should note that the poles are crossed at each orbital revolution, while a particular point on the equator may have long periods between subsequent passes. Usually, the orbits are not exactly polar to avoid numerical difficulties. Moreover, a small polar gap can increase the coverage in non-polar regions and can even improve retrieval of particular spherical harmonic coefficients [Elsaka, 2010].

The inclination of a second pair should be significantly smaller to achieve a more homogeneous global distribution of data points and, in addition, add measurements along the East-West direction, which helps to reduce the anisotropy and striping in GRACE gravity field solutions.

Obviously, a four satellite mission is rather demanding concerning funding aspects, so that a collaborative mission between different space agencies should be envisaged. In the e.motion² study the inclination of the second pair was chosen based on a parametric analysis [e.motion² Team, 2014, sec. 3.3] such that the second pair can still provide a stand-alone benefit by means of global gravity field maps, e.g. significant portions of ice mass regions are covered. Finally, an inclination of 70° was selected for the second pair.

1.2.4 Altitude and Groundtrack Repeat Cycle

The selection of altitude and inclination determines the ground-track pattern or equivalently, the distribution of measurement points over the sphere. While the GRACE altitude is naturally decaying, the pattern changes and might result in short repeat cycles, whereas the e.motion² concept envisions an orbit control with a fixed repeat pattern and homogeneous distribution of measurements over the sphere during the whole mission lifetime. In addition, as shown for example in [Murböck *et al.*, 2014], the effect of temporal aliasing by tidal and non-tidal effects in gravity field maps can be suppressed by using particular altitude bands, e.g. 294 km–309 km, 360 km–370 km, 416 km–426 km or 479 km–495 km. This is based on the idea of shifting the strongest orbital resonances to high SH orders and therefore SH degrees, such that the low degrees and orders containing the monthly time-variable gravity field

are less affected by temporal aliasing. These orbital resonances are also discussed in [Sneeuw, 2000].

The orbital repeat pattern is usually denoted as the ratio of an integer number of orbital revolutions β over a period of integer nodal days α . For the e.motion² concept, long-term repeat cycles of $\beta/\alpha = 478/31$ for the polar pair and $\beta/\alpha = 474/31$ for the second pair were selected. These cycles are achieved at orbital altitudes of 434 km and 441 km, respectively. In addition, Pour *et al.* [2013] showed that such ground-tracks have subcycles, which also allow retrieval of 6-day snapshots of Earth’s gravity field, which in turn can help to de-alias the monthly solutions [Wiese *et al.*, 2011].

In the e.motion² study technological feasibility with regard to drag compensation and maintenance of orbit height over a decade was analyzed for altitudes around 455 km and 366 km. For an altitude of 366 km a combination of cold-gas propulsion for attitude control and electric propulsion (μ RIT) for drag compensation was suggested, with propellant demand of approx. 22 kg for nitrogen and xenon for 10 years. A pure cold-gas system seems feasible at orbit heights above 400 km with approx. 60 kg propellant, and was selected as baseline in the e.motion² study.

1.3 E.motion² Measurement Principle

The rationale behind the selection of two satellite pairs in a LEO orbits for the e.motion² study was pointed out in previous sections. Each satellite can exploit high-low satellite tracking, while each pair enables low-low satellite tracking, as introduced in section 1.1.2 (Observation Techniques) to determine Earth’s gravity field. In the following subsections, the relation between observations and SH coefficients of Earth’s gravity field is elaborated.

1.3.1 Properties of Gravity Field Induced Signals

The determination of Earth’s gravity field by means of low-low satellite tracking (LL-SST) can be described by the measurement of a differential gravitational acceleration between two satellites projected onto the line-of-sight given as

$$\delta a_g(t) = \left(\hat{R} \cdot \vec{\nabla} V(\vec{r}_{\text{GRP2}}) - \hat{R} \cdot \vec{\nabla} V(\vec{r}_{\text{GRP1}}) \right) \cdot \vec{e}_{12}, \quad (1.3)$$

with $\vec{r}_{\text{GRP1,2}}$ denoting the position of the gravitational reference point (GRP) of each spacecraft and where \hat{R} is a rotation matrix, transforming the Earth-fixed pseudo-acceleration³ to an inertial frame. An idealized case is assumed, where the spacecraft are point masses and the GRP coincides with the center-of-mass and center-of-gravity. Non-conservative forces and gravitational perturbations from other celestial bodies are omitted. The vector \vec{e}_{12} is the normalized direction vector between the two GRPs in the inertial frame. The functional in eq. (1.3) is denoted as “projected differential gravitational acceleration” (PDGA) from now on. It can be evaluated using the spherical harmonic expansion from eq. (1.1) and the relation $\vec{a}_g(\vec{r}) = +\vec{\nabla} V(\vec{r})$ with geodesy-typical sign convention, in contrast to the common expression $\vec{a}_g(\vec{r}) = -\vec{\nabla} V(\vec{r})$ in physics.

The result can be written as Fourier sum of the form

$$\delta a_g(t) = \sum_{l=0}^{l_{\max}} \sum_{m=0}^l \sum_{q=0}^{q_{l,m}} \left(\cos(2\pi f_{l,m,q}t + \alpha_{l,m,q}) \cdot C_{l,m} \cdot \bar{c}_{l,m,q} + \sin(2\pi g_{l,m,q}t + \beta_{l,m,q}) \cdot S_{l,m} \cdot \bar{s}_{l,m,q} \right), \quad (1.4)$$

where the amplitudes ($\bar{c}_{l,m,q}$, $\bar{s}_{l,m,q}$), frequencies ($f_{l,m,q}$, $g_{l,m,q}$) and phases ($\alpha_{l,m,q}$, $\beta_{l,m,q}$) are dependent on the orbits of the satellites. Each spherical harmonic coefficient of particular

³This is a pseudo-acceleration, because the gradient of the SH potential does not include the centrifugal acceleration apparent in a rotating Earth-fixed frame.

degree l and order m produces a comb of sinusoidal signals in the PDGA, as illustrated in figure 1.5 for a particular polar orbit. The magnitude of each trace in figure 1.5 is already scaled by the SH coefficient of a typical Earth gravity field (model). However, if the traces are normalized to unity SH coefficients, these traces can be understood as a basis for the PDGA signal. Decomposition of the PDGA signal into this basis yields the SH coefficients.

Another approach for space gravimetry is to use high-low satellite tracking (HL-SST) of individual satellites by means of GNSS. This allows to retrieve the 3-d position. Forming time-derivatives yields velocity and acceleration. Assuming that the state vector \vec{r}_{GRP1} is given in the inertial frame, the gravitational acceleration $\ddot{\vec{r}}_{1,g}(t)$ can be written as:

$$\ddot{\vec{r}}_{1,g}(t) = \hat{R} \cdot \vec{\nabla} V(\vec{r}_{\text{GRP1}}). \quad (1.5)$$

Each vector component can be expanded in the same manner as in eq. (1.4) into a Fourier sum, and a very similar plot to figure 1.5 can be obtained. Expression (1.5) will be denoted as “direct acceleration” (DA).

Since the spatial (full-wavelength) resolution Λ of coefficients with degree l on Earth’s surface is [Barthelmes, 2009]

$$\Lambda(l) \approx \frac{40000 \text{ km}}{l}, \quad (1.6)$$

the gravitational signals $\delta a_g(t)$ and $\ddot{\vec{r}}_{1,g}(t)$ contain information with frequencies smaller than

$$f < \frac{v}{\Lambda(l)}, \quad (1.7)$$

where v is the mean spacecraft velocity of approximately 7.6 km/s in LEO. This provides an approximate relation between SH degree l and the measurement frequency. For $l = 52$, the full-wavelength resolution is 770 km and the frequency cut-off is at roughly 9.8 mHz, as shown in figure 1.5. In contrast, $l = 200$ has a full-wavelength resolution of 200 km and frequencies below 38 mHz (not shown).

The PDGA observation $\delta a_g(t)$ and the DA observation $\ddot{\vec{r}}_{1,g}(t)$ do not consist of single coefficients but of a superposition of several thousand coefficients at the same time. This produces a quasi-continuous signal in the frequency domain. Exemplary spectra of the projected gravitational acceleration (PDGA) for different satellite separations L and orbit heights h are shown in figure 1.6. They are based on pure gravitational accelerations derived from the static EGM96 gravity field model. One can see that the signal amplitude scales with the satellite separation (baseline length) L , which is expected as long as the spatial resolution of SH coefficients is larger than the baseline length L . If the baseline length approaches the spatial wavelength of particular coefficients, a common-mode suppression appears (cf. [Sneeuw, 2000, Section 4.4]), but this is usually not very pronounced in the final gravity field solutions.

The satellite altitude alters the roll-off frequency in figure 1.6, which is known in geodesy as *upward continuation* acting as strong low-pass filter [Zhu & Jekeli, 2007]. With lower altitude, one can resolve higher frequencies and thus higher spherical harmonic coefficients. In case of the direct gravitational acceleration $\ddot{\vec{r}}_{1,g}(t)$, *upward continuation* is also present. However, the signal is obviously independent of the baseline length L .

1.3.2 Remark on Spectral Densities

A remark is given on the difference between the representation of data as *spectrum* and as *spectral density*: The PDGA signal in figure 1.6 is plotted as a spectrum and not as a spectral density, because the PDGA signal is the superposition of several thousand single tones and the tone amplitude and power is correctly displayed in an amplitude spectrum (AS) or power spectrum (PS), as long as the spectral resolution of the spectrum is sufficient. If the bin-width of a spectral estimation is larger than the frequency separation between two tones, they

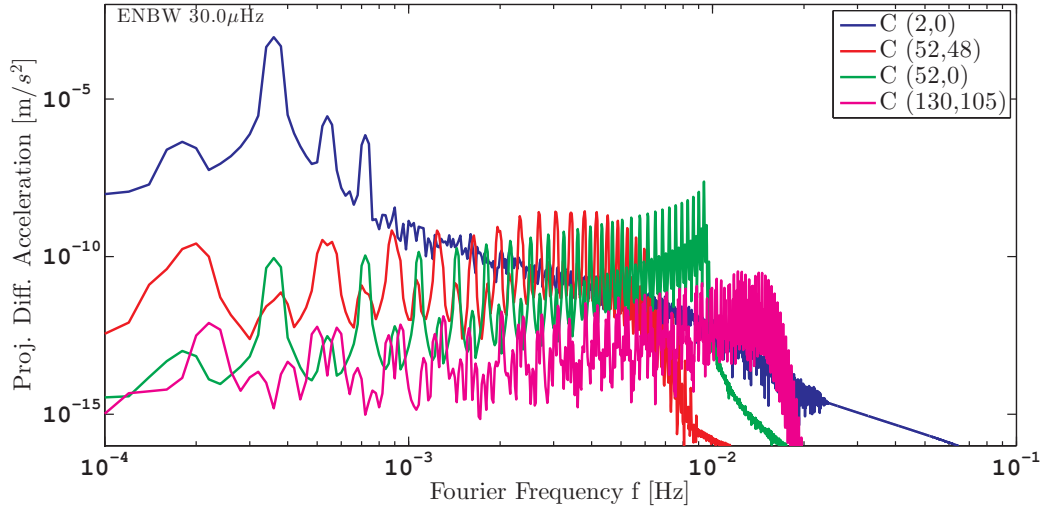


Figure 1.5: Signal in the projected differential gravitational acceleration due to particular spherical harmonic coefficients shown as a spectrum. The spacecraft separation is 200 km at an orbit height of 400 km. The magnitude of the individual traces/coefficients is based on a typical Earth gravity field (EGM96 model).

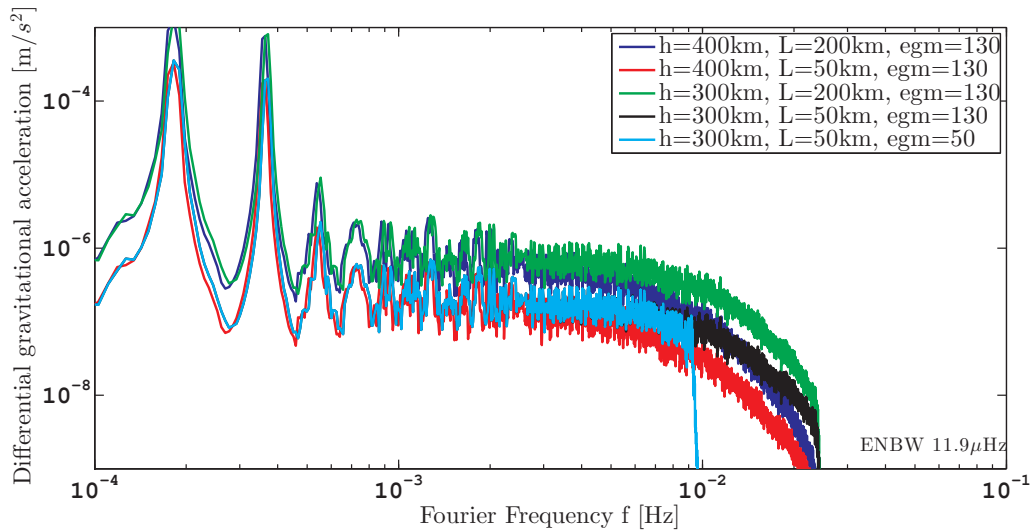


Figure 1.6: Typical spectra of projected differential gravitational acceleration for different satellite separations L , orbit height h and truncation degree of the SH expansion. A lower altitude increases the roll-off frequency, such that higher degrees of spherical harmonics are observable. The light blue trace contains only spherical harmonics up to degree 50.

may fall into the same frequency bin and are shown as a single peak with the combined tone power. Ideally, a power spectrum is the visualization of the integrated power in a frequency bin, and the amplitude spectrum is simply the square root of the power spectrum.

Recall that noise is a stochastic process and is characterized by a well-defined power spectral density, i.e. power at particular Fourier frequency in a 1 Hertz bandwidth. Noise has a continuous distribution of power in the frequency domain, while the power of sinusoidal tones is concentrated at single discrete frequencies. Hence, the noise level in a spectrum is proportional to the frequency resolution, while the peak height of tones is independent of the frequency resolution.

Thus, a spectrum is not the correct means for visualizing noise in the frequency domain and *spectral densities* are used. Loosely speaking, a power spectral density (PSD) is a power spectrum (PS) divided by the frequency resolution, which is the bin-width of the spectral estimation. The frequency resolution f_{res} of a single periodogram, consisting of a single discrete Fourier transformation of a discrete time-series, is given by

$$f_{\text{res}} = N/f_s = 1/T, \quad (1.8)$$

where N is the number of samples, f_s the sampling frequency and T the total duration of the time-series.

Noise in a spectral density plot is independent of the frequency resolution. However, the peak height of sinusoidal signals is proportional to $T = 1/f_{\text{res}}$ in a power spectral density plot or proportional to \sqrt{T} in an amplitude spectral density plot. Thus, it is not possible to display signal (tones) and noise meaningful in a single frequency domain plot, unless the frequency resolution is provided to recover the corresponding amplitude without ambiguity.

Correct spectral estimation is even more complicated, as the frequency response of a discrete Fourier transform is widened due to the finite time series. Hence, for precise spectral estimates, one needs to apply window functions, which can either be optimized for obtaining the correct noise spectral density or for obtaining the correct peak height of tone signals. For a detailed description of the topic, the reader is referred to [Heinzel *et al.*, 2002].

With window functions, the important quantity to convert from a spectrum to a spectral density and vice versa is not the frequency resolution f_{res} but the so-called “equivalent noise bandwidth” (ENBW):

$$\text{ASD}^2 = \text{PSD} = \text{PS}/\text{ENBW} = \text{AS}^2/\text{ENBW}. \quad (1.9)$$

As a good practice, all spectral domain plots within this thesis show the ENBW.

The distinction between a sinusoidal tone signal and noise becomes unclear, if the signal contains so many tones that its power can be considered quasi-continuous in frequency, as it is the case for the PDGA signal in figure 1.6. The frequency resolution of the spectral estimate is larger than the mean separation between tone frequencies and the power in most frequency bins is **not** dominated by a single tone frequency but by various tone frequencies within each bin. In such a case it makes sense to also use a spectral density, as it provides the average power per bandwidth and a quantity, which is independent of the frequency resolution, i.e. length of time-series.

However, the large peaks apparent at the first integer multiples of the orbital frequency in figure 1.6 are dominating the corresponding bin power at these frequencies, so that the peak height needs to be derived from a spectrum in units of m/s^2 instead of $\text{m}/(\text{s}^2\sqrt{\text{Hz}})$.

1.3.3 Projected Differential Gravitational Acceleration (PDGA)

The PDGA definition from eq. (1.3) needs to be related to the observations, in particular the ranging observable. For this purpose one considers

- the gravitational reference point (GRP) trajectories $\vec{r}_1(t)$ and $\vec{r}_2(t)$ of both S/C,

- the connecting line $\vec{r}_{12}(t) = \vec{r}_2(t) - \vec{r}_1(t)$, $\vec{e}_{12}(t) = \vec{r}_{12}(t)/|\vec{r}_{12}(t)|$
- the inter-satellite distance $\rho(t) = |\vec{r}_{12}(t)| = \sqrt{\vec{r}_{12} \cdot \vec{r}_{12}}$,
- the non-gravitational accelerations $\vec{a}_{\text{ng},1}(t)$ and $\vec{a}_{\text{ng},2}(t)$ acting on the GRP and caused e.g. by atmospheric drag,

Computing the first time-derivative of the inter-satellite distance ρ yields

$$\dot{\rho} = \frac{\vec{r}_{12} \cdot \dot{\vec{r}}_{12}}{\sqrt{\vec{r}_{12} \cdot \vec{r}_{12}}} = \vec{e}_{12} \cdot \dot{\vec{r}}_{12}, \quad (1.10)$$

while the second-time derivative can be expressed as

$$\ddot{\rho} = \vec{e}_{12} \cdot \ddot{\vec{r}}_{12} + \dot{\vec{e}}_{12} \cdot \dot{\vec{r}}_{12}, \quad (1.11)$$

where the acceleration vector between the two satellites $\ddot{\vec{r}}_{12}$ is influenced by gravitational and non-gravitational effects:

$$\begin{aligned} \ddot{\vec{r}}_{12} &= \hat{R} \cdot \vec{\nabla} V(\vec{r}_1) + \vec{a}_{\text{ng},1} - \hat{R} \cdot \vec{\nabla} V(\vec{r}_2) - \vec{a}_{\text{ng},2} \\ &= \hat{R} \cdot \widehat{M}(\vec{r}_1, \vec{r}_2) \cdot \overline{CS} + \vec{a}_{\text{ng},1} - \vec{a}_{\text{ng},2}, \end{aligned} \quad (1.12)$$

where \hat{R} is simply a rotation matrix transforming from the Earth fixed to the inertial frame. Since the gravitational acceleration (and potential) is a linear function of the SH coefficients, one can write all spherical harmonics coefficients into a vector \overline{CS} and use a convenient matrix-vector notation to compute the potential V or the gradient of the potential $\vec{\nabla} V$. The matrix \widehat{M} is the so-called design matrix. Finally, by exploiting $\dot{\vec{e}}_{12} = \dot{\vec{r}}_{12}/\rho - \vec{r}_{12} \cdot \dot{\rho}/\rho^2$ and by re-arranging the desired SH coefficients to the left-hand-side one easily arrives at

$$\underbrace{\vec{e}_{12} \cdot \hat{R} \cdot \widehat{M}(\vec{r}_1, \vec{r}_2) \cdot \overline{CS}}_{\text{PDGA}} = \ddot{\rho} - a_{\text{ng},1,\text{LOS}} + a_{\text{ng},2,\text{LOS}} - \left(\frac{|\dot{\vec{r}}_{12}|^2}{\rho} - \frac{\dot{\rho}^2}{\rho} \right) \quad (1.13)$$

$$= \ddot{\rho} - (a_{\text{ng},2,\text{LOS}} - a_{\text{ng},1,\text{LOS}}) - \frac{\dot{\vec{r}}_{12,\perp}^2}{\rho} \quad (1.14)$$

$$= \ddot{\rho} - (a_{\text{ng},2,\text{LOS}} - a_{\text{ng},1,\text{LOS}}) - |\vec{\omega}_{\text{LOS}}|^2 \cdot \rho, \quad (1.15)$$

where $\dot{\vec{r}}_{12,\perp}$ is the relative transversal velocity between the spacecraft, i.e. perpendicular to the line-of-sight, and $a_{\text{ng},\text{LOS}} = \vec{a}_{\text{ng}} \cdot \vec{e}_{12}$ is the non-gravitational acceleration along the line-of-sight. The third term on the right hand side can also be written in terms of the angular velocity $\vec{\omega}_{\text{LOS}} = (\vec{r}_{12} \times \dot{\vec{r}}_{12})/|\vec{r}_{12}|^2$ of the constellation baseline (cf. eq. (1.15)), showing that the third term is a centrifugal acceleration. Eqs. (1.13)-(1.15) are powerful, since they provide a linear relation via the design matrix $\widehat{M}(\vec{r}_1, \vec{r}_2)$ between spherical harmonic coefficients \overline{CS} and observables such as ranging and accelerometer data at each point in time. In the so-called *classical acceleration approach*, the gravity field SH coefficients are determined by solving the linear equations (1.13)-(1.15) in a least-squares sense for \overline{CS} , which also allows the easy propagation of errors and noise from the observations into the final gravity field solutions. Due to the epoch-wise and in-situ nature, the acceleration approach is also well suited to handle data gaps.

The typical magnitudes of the first ranging and third centrifugal term on the right hand side of eq. (1.15) are illustrated with red and green traces in figure 1.7. One notices that the magnitude of the ranging term and centrifugal acceleration is comparable at low frequencies, while at high frequencies the latter rolls off more quickly.

Unfortunately, the relative transversal velocity $\dot{\vec{r}}_{12,\perp}$ or the angular velocity $\vec{\omega}_{\text{LOS}}$ cannot be measured with sufficient sensitivity, as will be discussed in subsequent sections, making this straightforward approach impractical for real mission data processing [Ellmer, 2011; Naeimi,

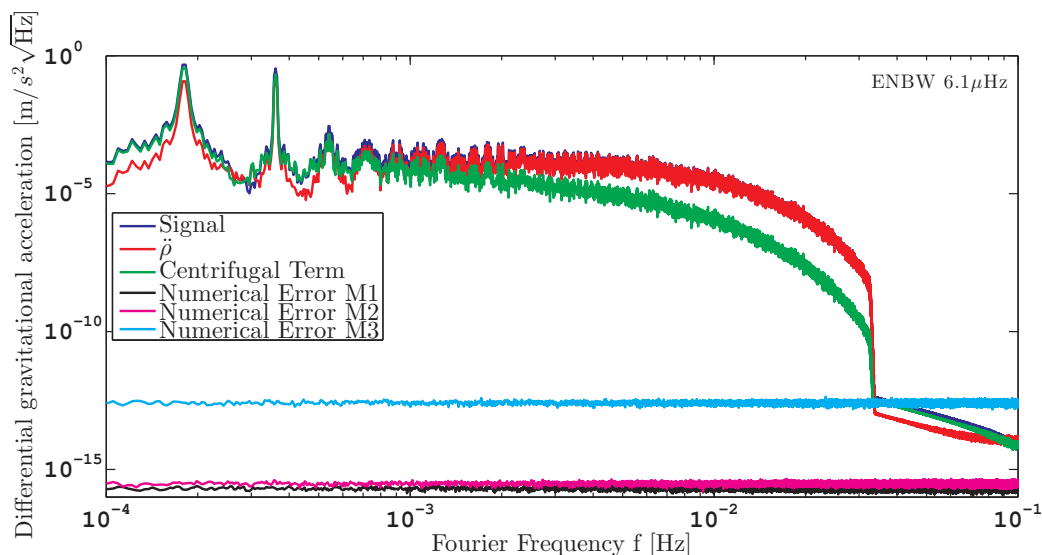


Figure 1.7: Typical spectral density of the projected differential gravitational acceleration (green trace) using a static gravity field model up to degree 180, spacecraft separation of 200 km and orbit height of 400 km. The range acceleration $\ddot{\rho}$ is shown in red, while non-gravitational accelerations are omitted. The centrifugal part is comparable in magnitude to the ranging content for frequencies below 1 mHz. The numerical accuracy of the floating point arithmetic is shown in black (i.e. orbit integration, computation of range ρ and acceleration from spherical harmonics).

2013]. More sophisticated methods like variational-equation approaches (used by CSR, JPL and GFZ), a short-arc (integral-equation) approach [Mayer-Gürr, 2006] or modified acceleration approaches [Liu, 2008] can reduce the negative effect resulting, however, in increased complexity and computational costs. These approaches typically compute dynamic orbits based on a-priori force models, e.g. static and temporal gravity field models, and with empirical parameters, such that these dynamic orbits or arcs match the observations. The residuals are further minimized by adjusting the spherical harmonics coefficients. Sometimes, the high-quality gravity fields are obtained by iterative methods, which additionally complicates error propagation from observations to final gravity field solutions.

If inter-satellite ranging information is used to derive the gravity field, information on the centrifugal acceleration needs to enter the processing chain at some point, since the baseline is rotating (cf. GOCE data processing in [Stummer, 2013]). Analysis by Ditmar *et al.* [2012] using a modified acceleration approach showed that orbit and centrifugal acceleration errors can explain the noise level in the Delft Mass Transport (DMT-1) monthly gravity field solutions for Fourier frequencies between 0.1 mHz and 1 mHz.

One can derive an alternative expression for the centrifugal term using energy conservation as shown in [Jekeli, 1999] and [Visser *et al.*, 2003], which yields the following result for the all-important magnitude of relative velocity in eq. (1.15)

$$|\dot{\vec{r}}_{12}(t)|^2 = 2 \cdot E_1(t) + 2 \cdot E_2(t) - 4\sqrt{E_1(t) \cdot E_2(t)} \cos(\alpha(t)), \quad (1.16)$$

with E_1 and E_2 being the specific energy of satellite 1 and 2, respectively, while $\alpha(t)$ is the angle between the two velocity vectors $\alpha(t) = \sphericalangle(\dot{\vec{r}}_1, \dot{\vec{r}}_2)$. One can express the specific energy, i.e. the energy per unit mass, of one satellite in the inertial (space-fixed) frame as [Visser *et al.*, 2003]

$$E_i(t) = \frac{1}{2} |\dot{\vec{r}}_i|^2 = V(\vec{r}_i) + (\vec{\omega}_e \times \vec{r}_i) \cdot \dot{\vec{r}}_i + \int_{t_0}^t \vec{a}_{\text{ng},i} \cdot \dot{\vec{r}}_i dt - E_c, \quad (1.17)$$

where the first term is the geopotential with geodetic sign convention, the second term accounts for the rotation of the potential with $\vec{\omega}_e$ being Earth's angular velocity. The third term accounts for energy dissipation, e.g. due to drag, and can be expressed in terms of accelerometer measurements, while the last term is an energy constant describing the energy at initial time t_0 .

In summary, three different methods to describe the centrifugal acceleration can be identified. The first method (M1) uses eq. (1.13), where $|\dot{\vec{r}}_{12}|^2$ is directly taken from GNSS observations. The second method (M2) using the angular velocity $\vec{\omega}_{\text{LOS}}$ from eq. (1.15) is equivalent to M1, if the same GNSS observation is used. However, alternative approaches to determine $\vec{\omega}_{\text{LOS}}$ are discussed later in section 1.5.1, which might allow for higher precision. The third method (M3) is based on the specific energy of the spacecraft (cf. eq. (1.16)).

The equivalence of all three methods in the error-free case is shown in figure 1.7, where the residuals of each method are depicted (lower three traces). The implementation of method M3 seems to be less precise, with the white noise floor suggesting it is limited by rounding errors and numerical precision. Later, in section 1.6.2, the susceptibility of the three methods to noise and error contributions is analyzed.

1.3.4 Direct Acceleration (DA)

The PDGA provides one observation of the gravity field at each epoch for a satellite pair, while the second time-derivative of the satellite trajectory (sec. 1.1.2) provides additionally three equations for each vector component per S/C

$$\hat{R} \cdot \vec{\nabla} V(\vec{r}_{\text{GRP}}) = \hat{R} \cdot \widehat{M}(\vec{r}_{\text{GRP}}) \cdot \vec{CS} = \ddot{\vec{r}}_{\text{GRP}} - \vec{a}_{\text{ng}}, \quad (1.18)$$

where non-gravitational accelerations \vec{a}_{ng} should be subtracted. The matrix $\widehat{M}(\vec{r})$ is the design matrix relating the observations on the right hand side linearly to the SH coefficients \vec{CS} . \hat{R} is a rotation matrix transforming the pseudo-acceleration to an inertial frame. \hat{R} could be as well absorbed in the design matrix \widehat{M} . Again, the SH coefficients of the gravity field can be obtained in a least-squares sense by inverting eq. (1.18), where $\ddot{\vec{r}}$ and \vec{a}_{ng} on the right-hand-side can be derived from GNSS and accelerometer, respectively.

1.3.5 Science and Calibration Measurement Bandwidth

The science measurement bandwidth should be selected such that it contains most of the gravity field signal. As is apparent from figure 1.7, the gravity field signal in the PDGA (and DA, not shown in the plot) falls off at high frequencies. At some point, the signal to noise ratio reaches unity and higher frequencies contain only noise. Recording and transmitting these frequencies to ground should be avoided to save resources.

However, it should be kept in mind that the noise at high frequencies can be used to assess the sensitivity of instruments and can indicate abnormal instrument behavior.

The upper bound of the science measurement bandwidth is typically given by the Nyquist theorem as $f_s/2$, where f_s is the sampling frequency of the data. Recording data every 5 s yields an upper resolvable frequency of 0.1 Hz, which contains SH degree coefficients up to degree 500. This is considered to be sufficient, in particular because it turns out in later sections that unity signal to noise ratio is reached at approx. 0.04 Hz for e.motion².

The lower frequency bound is a trade-off between scientific return and complexity of instrument development, verification and costs. For an instrument, a lower bound of 0.1 mHz requires that all sub-systems and components are verified down to that frequency, implying a single measurement of approx. 10 hours⁴ to state definitely the noise level at 0.1 mHz. For e.motion² a natural lower bound at the orbital frequency of 0.18 mHz was selected, since all SH coefficients produce signals above this frequency.

⁴0.1 mHz corresponds to 2.7 hours, however, due to artifacts in a spectral estimation a longer measurement is recommended.

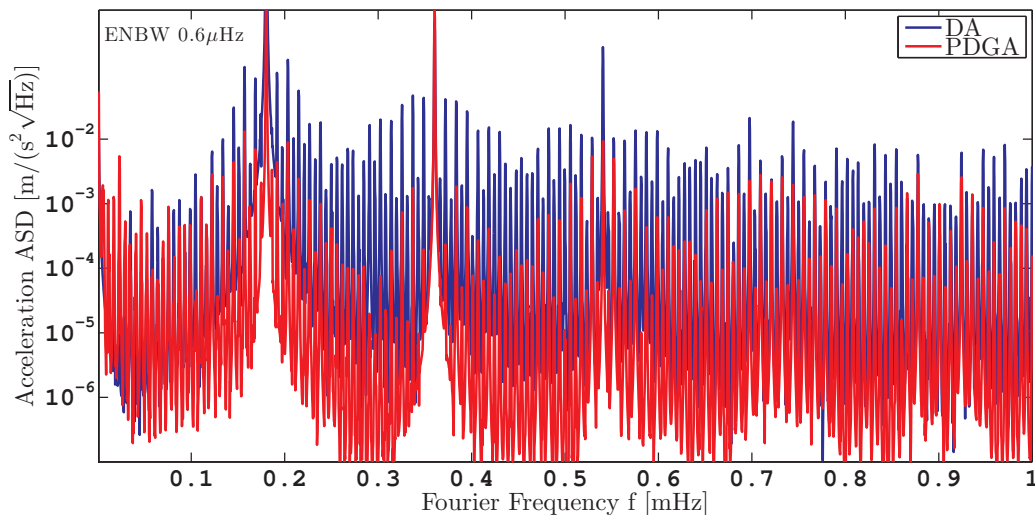


Figure 1.8: Typical PDGA and DA signals at low frequencies expressed as acceleration amplitude spectral density on a linear frequency axis.

With a science measurement bandwidth (SMBW) of

$$\text{SMBW} : 0.18 \text{ mHz} < f < 0.1 \text{ Hz} \quad (1.19)$$

all SH coefficients containing interesting gravity field information can be recovered. However, there is still some gravity signal at $f < 0.18$ mHz, as indicated in figure 1.8, because the orbit repeat frequency w.r.t. the rotating Earth, i.e. the ground-track repeat cycle, is $\ll 0.18$ mHz.

Furthermore, it is pointed out that temporal gravity field variations at monthly time scales and longer, e.g. frequencies $f_t \ll 1$ μ Hz, do not show up at these frequencies in the Fourier domain of the PDGA and DA signal. It is not required to extend the measurement bandwidth to measure these variations. Temporal variations of the SH coefficients produce sidebands at $\pm f_t$ w.r.t. the tone frequencies within the SMBW.

In the e.motion² study, a novel technique was suggested to continuously calibrate instruments, in particular the accelerometer, with the help of the LRI. The idea is discussed later in section 1.10. For this, an extension of the higher frequency end by a so-called calibration measurement bandwidth (CMBW) is suggested

$$\text{CMBW} : 0.1 \text{ Hz} < f < 0.3 \text{ Hz}. \quad (1.20)$$

At these frequencies, all instruments should be limited by intrinsic noise, which means there is no gravity signal in the ranging data and no drag signal in the accelerometer data present. Hence, sinusoidal signals injected for calibration purposes in the CMBW can be recovered by the instruments.

1.3.6 Definition of the Gravitational Reference Point (GRP)

The GRP is the point used to evaluate the PDGA (eqs. (1.13)-(1.15)) and DA (eq. (1.18)) equations. It is usually defined for GRACE-like missions as the center-of-mass (CoM) or as center-of-gravity (CoG) of the satellite. Ideally, all on-board measurements (GNSS, Accelerometer, Ranging Interferometer) are referred to the GRP, which simplifies gravity field retrieval.

However, although CoG and CoM are often used interchangeably in literature, the CoG is defined as the position where the resultant (gravity gradient) torque \vec{T} vanishes [Feynman

et al., 2013], i.e.

$$\vec{T} = \int_V \rho(\vec{r}) \cdot (\vec{r} - \vec{r}_{\text{CoG}}) \times \vec{g}(\vec{r}) d^3\vec{r} \stackrel{!}{=} 0, \quad (1.21)$$

with ρ being the satellite's mass density and $\vec{g}(\vec{r}) = -\vec{\nabla}V(\vec{r})$ being the gravitational acceleration. There is no general solution for this equation. In particular, if a solution exists, it may be non-unique, i.e. a so-called *line-of-action* may exist. An alternative but equivalent implicit definition of the center of gravity \vec{r}_{CoG} is given by

$$m_{\text{sat}} \cdot \vec{g}(\vec{r}_{\text{CoG}}) = \int_V \rho(\vec{r}) \cdot \vec{g}(\vec{r}) d^3\vec{r}, \quad (1.22)$$

with m_{sat} being the satellite's total mass. For a parallel (uniform) gravity field over the volume of the satellite or rigid body, the CoG and CoM coincide, causing confusion due to their interchangeable appearance in literature. If a unique CoG exists, it is located within the rigid body and depends on the gravity field, the body's mass distribution and orientation.

Considering the dependence on attitude and gravity, the author of this thesis does not see a benefit in using the CoG as a reference point and encourages the use of the CoM, since it depends only on the mass distribution but not on external properties such as attitude or gravity field. In addition, the motion of the satellite can be separated into a translational and a rotational part around the CoM, which is not true if the equations of motion are written w.r.t. the CoG [Kasdin & Paley, 2011, p. 229].

However, using the CoM to solve the translational equations of motion for a spatially extended rigid body requires a correction for the non-uniform gravitational field. To derive the correction, one can expand the gravitational acceleration \vec{g} around the center of mass in a Taylor series

$$\vec{g}(\vec{r}_{\text{CoM}} + \vec{r}) \approx \vec{g}(\vec{r}_{\text{CoM}}) + g_{mn} \cdot r_n + \frac{g_{kmn} \cdot r_m \cdot r_n}{2}, \quad (1.23)$$

where $g_{mn} = g_{mn}(\vec{r}_{\text{CoM}})$ is the gravity gradient matrix \hat{G} and the Einstein summation convention is used, i.e. the expression $g_{mn} \cdot r_n$ can be written as matrix-vector multiplication $\hat{G} \cdot \vec{r}$. The vector \vec{r} points from the CoM to other parts of the satellite. The latin indices m, n, k take values 1..3. The tensor $g_{kmn} = g_{kmn}(\vec{r}_{\text{CoM}})$ contains the third spatial derivatives of the geopotential. The gravitational force acting on a satellite is therefore

$$m_{\text{sat}} \cdot \vec{g}_{\text{sat}} = \int_V \rho(\vec{r}_{\text{CoM}} + \vec{r}) \cdot \vec{g}(\vec{r}_{\text{CoM}} + \vec{r}) d^3\vec{r} \quad (1.24)$$

$$\approx m_{\text{sat}} \cdot \vec{g}(\vec{r}_{\text{CoM}}) + g_{mn} \cdot \int_V \rho(\vec{r}) \cdot r_n d^3\vec{r} + \frac{g_{kmn}}{2} \cdot \int_V \rho(\vec{r}) \cdot r_n \cdot r_m d^3\vec{r}. \quad (1.25)$$

Without loss of generality, one can assume the coordinate frame to be centered in the CoM, thus, the second term vanishes. The third term can be related to the moment of inertia tensor \hat{I} , which is defined as

$$\hat{I} = I_{mn} = \int_V \rho(\vec{r}) \cdot ((r_1^2 + r_2^2 + r_3^2)\delta_{mn} - r_n \cdot r_m) d^3\vec{r}, \quad (1.26)$$

with δ_{nm} being the Kronecker delta. We define the 3×3 matrix \hat{P} as

$$\hat{P} = \int_V \rho \cdot r_n \cdot r_m d^3\vec{r} = \hat{I} - \frac{1}{2} \begin{pmatrix} I_{22} + I_{33} - I_{11} & 0 & 0 \\ 0 & I_{11} + I_{33} - I_{22} & 0 \\ 0 & 0 & I_{11} + I_{22} - I_{33} \end{pmatrix} \quad (1.27)$$

The moments of inertia tensor \hat{I} and \hat{P} are antisymmetric, while the tensor g_{kmn} is symmetric due to Schwarz' theorem. Due to this symmetry, many terms cancel out in the product

$g_{kmn} \cdot P_{mn}$. Finally, one can write the gravitational force acting on the satellite as

$$m_{\text{sat}} \cdot \vec{g}_{\text{sat}} \approx m_{\text{sat}} \cdot \vec{g}(\vec{r}_{\text{CoM}}) + \frac{g_{kmn} \cdot P_{nm}}{2} \quad (1.28)$$

$$= m_{\text{sat}} \cdot \vec{g}(\vec{r}_{\text{CoM}}) + \frac{1}{2} \begin{pmatrix} g_{111} \cdot P_{11} + g_{122} \cdot P_{22} + g_{133} \cdot P_{33} \\ g_{211} \cdot P_{11} + g_{222} \cdot P_{22} + g_{233} \cdot P_{33} \\ g_{311} \cdot P_{11} + g_{322} \cdot P_{22} + g_{333} \cdot P_{33} \end{pmatrix}. \quad (1.29)$$

The second term, the extended body correction (EBC), can be written in the case of a GM/r monopole field as

$$\vec{a}_{\text{EBC}} = \frac{3 \cdot GM}{2r^7} \begin{pmatrix} x^2 r^2 \cdot (3P_{11} + P_{22} + P_{33}) - 5x^2 \cdot (P_{11}x^2 + P_{22}y^2 + P_{33}z^2) \\ y^2 r^2 \cdot (P_{11} + 3P_{22} + P_{33}) - 5y^2 \cdot (P_{11}x^2 + P_{22}y^2 + P_{33}z^2) \\ z^2 r^2 \cdot (P_{11} + P_{22} + 3P_{33}) - 5z^2 \cdot (P_{11}x^2 + P_{22}y^2 + P_{33}z^2) \end{pmatrix} \quad (1.30)$$

$$= \frac{6 \cdot GM}{2r^7} \begin{pmatrix} x^2 r^2 \cdot (3I_{11} + I_{22} + I_{33}) - 5x^2 \cdot (I_{11}x^2 + I_{22}y^2 + I_{33}z^2) \\ y^2 r^2 \cdot (I_{11} + 3I_{22} + I_{33}) - 5y^2 \cdot (I_{11}x^2 + I_{22}y^2 + I_{33}z^2) \\ z^2 r^2 \cdot (I_{11} + I_{22} + 3I_{33}) - 5z^2 \cdot (I_{11}x^2 + I_{22}y^2 + I_{33}z^2) \end{pmatrix}, \quad (1.31)$$

where (x, y, z) is the CoM position and $r^2 = x^2 + y^2 + z^2$.

The moments of inertia are referred to the inertial frame and are therefore dependent on the S/C attitude. Taking the numerical values for GRACE from [Wang, 2003, p. 23] and considering nominal S/C pointing along the velocity vector, the moments of inertia are approximately $I_{rr} = 390 \text{ kg} \cdot \text{m}^2$, $I_{aa} = 70 \text{ kg} \cdot \text{m}^2$, $I_{cc} = 340 \text{ kg} \cdot \text{m}^2$, where r , a and c denote the radial, along-track and cross-track direction, respectively. For an orbital altitude of $h = 400 \text{ km}$ ($R = 6771 \text{ km}$) and total mass of 420 kg , eq. (1.31) has a magnitude of $5 \cdot 10^{-13} \text{ m/s}^2$ in the direction of the geocenter. Temporal variations are considered to be even smaller, and can be evaluated using eq. (1.31) but are beyond the scope of this section.

With the gravity gradient being $2.56 \cdot 10^{-6} \text{ s}^{-2}$, this yields an effective separation between the CoM and CoG of $(5 \cdot 10^{-13} \text{ m/s}^2)/(2.56 \cdot 10^{-6} \text{ s}^{-2}) \approx 0.2 \mu\text{m}$. A sub-micrometer difference was also obtained by the derivation in [Wang, 2003, p. 23]. Although the magnitude of this effect is rather small, a correct physical model should account for the \vec{a}_{EBC} effect, in particular with regard to future missions with higher sensitivity.

It is emphasized that satellite rotations induced by a pure torque, e.g. by magneto-torquers, keep the CoM and not the CoG constant and therefore allow rotational and translational motion of a satellite or a rigid body to be separated.

However, the CoM of a satellite should not be considered as fixed, as it changes due to propellant consumption or the differential thermal expansion of the satellite structure. In addition, the accelerometer type has implications on the optimal GRP definition, making the discussion cumbersome.

In this thesis, two different accelerometer concepts are discussed in the following sections.

1.3.7 GRP in Servo-Accelerometer Concepts

The first accelerometer concept utilizes a servo-accelerometer, as in GRACE(-FO), which has also been selected as the basis for the e.motion² study. For such a concept, the GRP is defined as the time-averaged S/C CoM position. Furthermore, we define the servo-accelerometer reference point (RP) as the pivot point of rotations, where pure angular accelerations and zero linear accelerations are measured by the servo-accelerometer. In the ideal case, this point is given by the test-mass CoM inside the accelerometer.

If the accelerometer RP and the GRP, i.e. the test-mass and S/C CoM, are co-located, rotations of the S/C will not disturb the linear acceleration measurement. In addition, fictitious accelerations discussed in sec. 1.4.3 on the accelerometer are minimized. However, the accelerometer will measure a small bias, because the test-mass CoG and S/C CoG are not co-located due to the different offset from the corresponding CoM. Nonetheless, resolving

this small effect is challenging due to the inherent uncertainty in the bias of accelerometers (cf. sec. 1.4.3).

It is remarked that a mass-trim maneuver by means of magneto-torquers, as performed in GRACE [Wang, 2003, p. 17], rotates around the CoM. According to [Wang, 2003] and [Wang *et al.*, 2010], the CoM can be co-located with the accelerometer in-orbit to better than 100 μm . To determine the CoG, a mass-trim maneuver by means of the gravity gradient torque would be required, which is difficult to realize due to the small magnitude and interference with other non-gravitational torques.

Recalling the PDGA and DA combination, the dynamics of the GRP are governed by

$$\ddot{\vec{r}}_{\text{GRP}} \approx \vec{a}_{\text{grav}} + \vec{a}_{\text{ng}} + \vec{a}_{\text{EBC, SC}}, \quad (1.32)$$

while the servo-accelerometer discussed in sec. 1.4.3 provides ideally linear accelerations,

$$\vec{\Gamma} \sim \vec{a}_{\text{ng}} + \vec{a}_{\text{EBC, SC}} - \vec{a}_{\text{EBC, TM}}. \quad (1.33)$$

Hence, the DA from eq. (1.18) appears slightly modified

$$\ddot{\vec{r}}_{\text{GRP}} - \vec{\Gamma} - \vec{a}_{\text{EBC, TM}} = \hat{R} \cdot \hat{M}(\vec{r}_{\text{GRP}}) \cdot \overline{C}\vec{S}. \quad (1.34)$$

However, $\vec{a}_{\text{EBC, TM}} \approx 0$ is a valid approximation, considering that the correction for the S/C was already at $|\vec{a}_{\text{EBC, SC}}| \approx 10^{-13} \text{ m/s}^2$ level. This implies that the projected differential gravitational acceleration (PDGA) from eqs.(1.13)-(1.15) also remains valid, if the non-gravitational acceleration \vec{a}_{ng} is replaced by the servo-accelerometer measurement $\vec{\Gamma}$.

1.3.8 GRP in Drag-Free Concepts

The time-varying S/C center-of-mass location and the difficulty in measuring it can be overcome by utilizing a drag-free concept (discussed in sec. 1.9). In such a concept, the GRP is defined as the test-mass CoM, which is physically well-defined and stable w.r.t. the test-mass geometry. The accelerometer is operated in open-loop mode without suspending the internal test-mass electro-statically at least not in the sensitive axis. However, the accelerometer precisely determines the six degrees of freedom of the free-floating test-mass, i.e. position \vec{x}_{TM} with respect to an accelerometer fiducial (reference point) and orientation. Collision of the test-mass with the accelerometer housing is prevented by actuating the whole satellite in the translational degrees of freedom, whereby electro-static suspension may be used in the rotational degrees of freedom to ensure correct pointing of the S/C.

The geometry between the accelerometer reference point and the ranging (interferometer) reference point needs to be stable. In particular, the vector $\vec{\Delta}$ connecting both points needs to be known.

The dynamics of the GRP is influenced by gravitational accelerations \vec{a}_{grav} and small electro-static corrections \vec{a}_{es} , e.g. to ensure inter-S/C pointing and to remove long-term drifts,

$$\ddot{\vec{r}}_{\text{GRP}} \approx \vec{a}_{\text{grav}} + \vec{a}_{\text{es}}. \quad (1.35)$$

Non-gravitational accelerations such as drag are acting on the S/C but not on the test-mass, except for the residual \vec{a}_{es} .

The ranging observation ρ between the two GRPs is obtained by combining the ranging observable between the ranging interferometer reference points ρ_{ifo} with the position sensing from the accelerometers, i.e.

$$\rho = \rho_{\text{ifo}} + \vec{\Delta}_1 \cdot \vec{e}_{12} + \vec{\Delta}_2 \cdot \vec{e}_{12} - \vec{x}_{\text{TM},1} \cdot \vec{e}_{12} - \vec{x}_{\text{TM},2} \cdot \vec{e}_{12}, \quad (1.36)$$

which is illustrated in figure 1.9.

The quantity ρ can be determined with low noise and is independent of the inherently unstable S/C CoM. The PDGA and DA observables in the form of eqs. (1.13)-(1.15) and eq. (1.18) remain valid, if the non-gravitational acceleration \vec{a}_{ng} is replaced by \vec{a}_{es} .

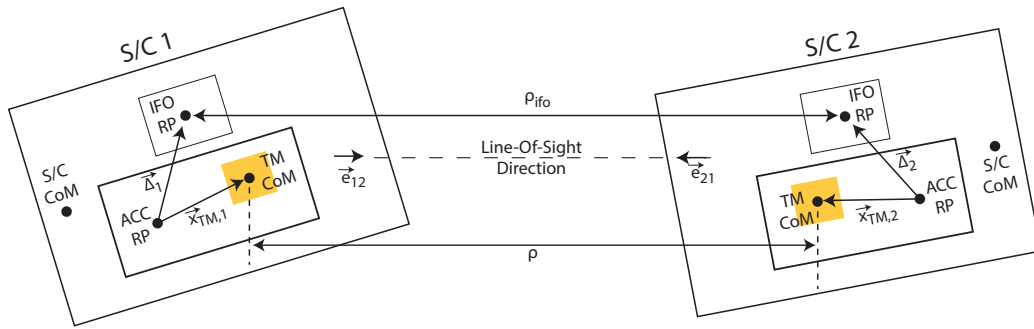


Figure 1.9: In a drag-free concept, the gravitational reference point (GRP) is defined as the center-of-mass (CoM) of the test-mass on a satellite. By combining precise position information from the accelerometer $\vec{x}_{\text{TM},1}$ and $\vec{x}_{\text{TM},2}$ with the ranging information ρ_{ifo} one can obtain the ranging observation ρ between both GRPs. The misalignment between the satellites is exaggerated in this schematic.

In a drag-free concept, the accelerometer can be placed close to the S/C CoM, which might simplify the analysis and control, since a pure S/C torque will not result in a large translation of the test-mass. But it is not required, as shown by the LISA and LISA Pathfinder mission concepts [Danzmann *et al.*, 2017; eLISA/NGO Team, 2012; Danzmann *et al.*, 2007]. For redundancy concerns, one might consider two accelerometers close to the S/C CoM.

The interested reader is referred to [Reubelt *et al.*, 2014], where the positioning of accelerometers is also discussed.

1.4 Instruments and Observations

In the previous section, the measurement principle of the e.motion² concept and GRACE-like missions was introduced. In particular, how the gravity field can be obtained from on-board measurements was demonstrated. It is important to clearly define the instruments, their observables and expected sensitivity levels to avoid a discrepancy between predicted and actual sensitivity, as present in the GRACE mission⁵.

The aim of this section is to provide sufficient information, such that a realistic overall sensitivity and error model for the PDGA and DA channel can be obtained, which will then be propagated to the level of gravity fields.

1.4.1 GNSS: Global Navigation Satellite System

Each e.motion² satellite requires a high-quality GNSS receiver which can deliver code, phase and optional Doppler measurements of the GNSS satellites in view. The GNSS processing unit is connected to an ultra-stable oscillator (cf. sec. 2.3.4 on USO) and will be capable of deriving a navigation solution consisting of a 3-d position and velocity vector in real-time. The accuracy of the on-board real-time navigation solution is required to be better than

$$\sigma_{3d} < 30 \text{ m}, \quad (1.37)$$

for the laser link acquisition and the on-board line-of-sight estimation. Code, phase and Doppler measurements for all satellites in view are recorded and down-linked as science data for gravity field recovery. Additional measurements such as radio occultation for atmospheric studies could be envisioned.

⁵The errors in current monthly gravity fields [Dahle *et al.*, 2014, GFZ RL05] are a factor 6 higher than the pre-launch GRACE *baseline sensitivity* derived in [Kim, 2000]. This factor was steadily decreased in the past by advances in data processing.

During the gravity field recovery, GNSS information is used to derive kinematic time-resolved 3-d position and velocity vectors of the GNSS antenna phase center. This requires solving phase ambiguities, corrections for the ionosphere, precise GNSS satellite ephemeris and so forth. Using S/C attitude information and calibration data, the kinematic position and velocity of the GRP can be derived from the kinematic position and velocity of the GNSS antenna phase center.

Kinematic orbits are determined geometrically by the distance to the GNSS satellites, but they do not exploit additional information, for example, from the gravity field. In this thesis, the following simplified frequency-dependent isotropic position noise is used

$$\begin{aligned} \text{ASD}[\vec{r}_{\text{GNSS,E}}] &= (1, 1, 1)^\top \cdot \text{ASD}[r_{\text{GNSS,E}}] \\ &= (1, 1, 1)^\top \cdot \sqrt{\left(\frac{8 \text{ cm}/\sqrt{\text{Hz}}}{1 + f/1 \text{ mHz}}\right)^2 + (1 \text{ cm}/\sqrt{\text{Hz}})^2}, \end{aligned} \quad (1.38)$$

where the subscript E indicates the error part and is based on the logic that a measurement can be composed into an error-free signal and an error.

The ASD model is shown in figure 1.10 together with true GRACE kinematic orbits derived by TU Graz [Zehentner & Mayer-Gürr, 2013] for two different days. Since the epoch-wise covariance information is provided, formal error estimates are also shown. The rms-value in each component of the noise model is 4 mm with $f_s = 0.1 \text{ Hz}$, which might seem low considering that an rms-value of the order of a centimeter is normally given in literature [Weigelt *et al.*, 2013; Montenbruck *et al.*, 2005]. However, the author assumes that these rms-values are usually driven by tones or excess noise at the orbital frequency and higher harmonics, as shown in a plot in [Zehentner & Mayer-Gürr, 2013], and by outliers or non-Gaussian noise, which is difficult to handle with PSDs. For further information on GNSS receiver precision and kinematic orbit determination in gravimetric satellite missions, the reader is referred to [Van Helleputte, 2011].

As will become obvious in subsequent parts of the thesis, precise GNSS observations are essential for exploiting the full sensitivity of future GRACE-like missions, e.g. of e.motion². The author would like to emphasize the following aspects, which may lead to improved kinematic orbits:

- Availability of low-level data and pre-processing: Commercial GNSS receivers often perform proprietary pre-processing of measurements, which hampers advances by a broad scientific community. Thus, declaring low-level data streams as scientific data in early stages of the mission design could circumvent this issue. Moreover, pre-processing algorithms within the receiver and on-ground need to be documented well and made available for users.
- Number of channels: As opposed to terrestrial GNSS observations, satellites in a LEO usually do not have obstacles, which may decrease the visibility of GNSS satellites, with the exception being the Earth. However, due to the increased velocity, LEO satellites usually observe a particular satellite only for a short time, which complicates solving integer ambiguities. A high number of simultaneous readout channels should be envisaged, such that all visible GNSS satellites can be tracked. The maximum number of 10 GPS satellites from GRACE [Montenbruck *et al.*, 2005] is not sufficient nowadays.
- New bands and networks: Tracking of additional bands (e.g. L5 in GPS) and use of the European GALILEO GNSS network, which is being deployed by the time of writing, and other networks like GLONASS, BeiDou and QZSS may also improve the measurement.
- Advanced data analysis: e.g. GNSS receiver clock modeling, as suggested in [Weinbach & Schön, 2013], or modeling of relativistic clock effects, as discussed in section 2.5 of this thesis.

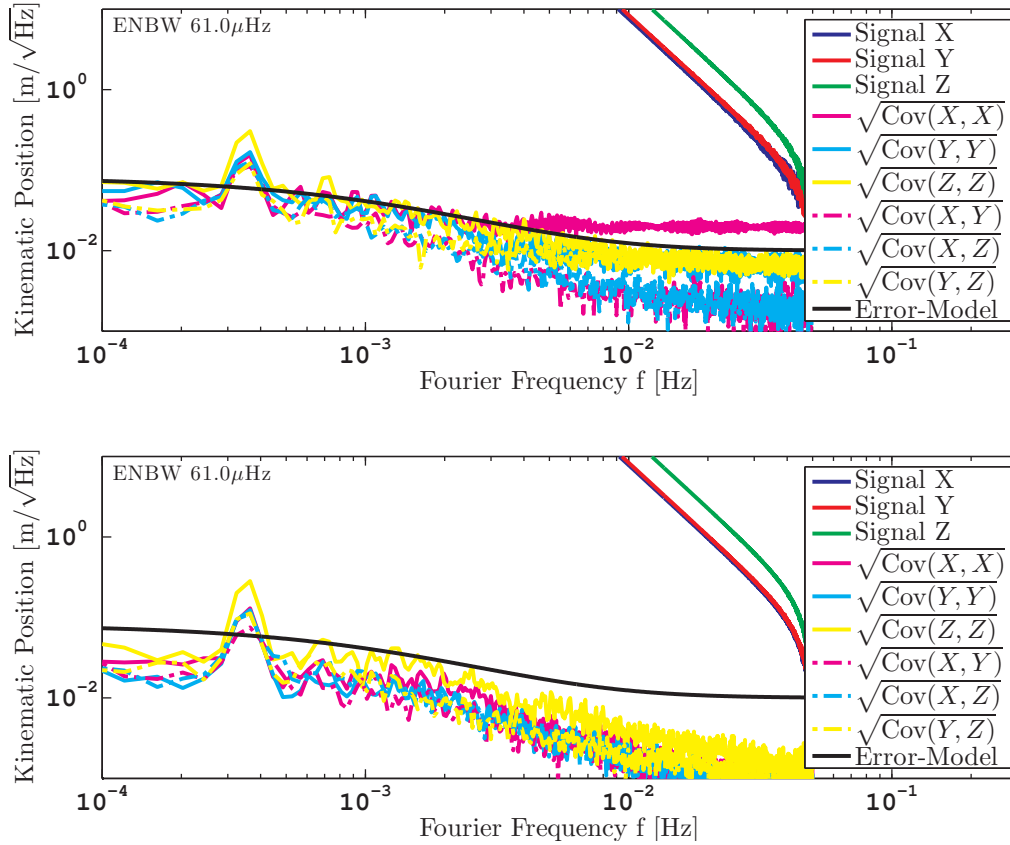


Figure 1.10: Kinematic positions and covariance information from [Zehentner & Mayer-Gürr, 2013] plotted as an ASD. The upper figure is a GRACE-A orbit from 2008-01-01, while the lower plot shows day 2006-02-06. The coordinate frame is ITRF (IGS05). The noticeable variability in the magnitude of the co-variance estimates between both days was not investigated further, but may be caused by ionospheric disturbances driven from solar activity or by changes in the receiver configuration, e.g. activated occultation antenna.

- Reduction of GNSS multipath effects by selecting appropriate materials for S/C structure and optimizing S/C structure design and antenna positioning.
- Thorough on-ground characterization of the GNSS receivers and antennas on the fully-assembled spacecraft, e.g. phase-center variation maps, delays and cross-talk between channels.
- Two tilted main POD antennas: Due to orbital dynamics of the GNSS receiver, tracked GNSS satellites appear at low elevation mainly in the ram direction, propagate to the GNSS antenna zenith and leave at the aft. Two tilted antennas could enhance the overall field-of-view, while parallel observation of a GNSS satellite with both antennas could reduce antenna related errors. Furthermore, GNSS-derived attitude information can be correlated with star camera data. A larger field-of-view enables longer tracking of satellites, which helps to reduce the number of phase integer ambiguities. Such a concept was recently analyzed in [Wallat & Schön, 2016].
- Availability of velocity information: To the knowledge of the author, Doppler frequency measurements were not available in GRACE. Thus, a kinematic velocity could only be obtained by (imprecise) numerical differentiation of the phase observations at low sampling rate. Time-differenced phase observations at high rate on the receiver or at least the Doppler observation from the receiver’s tracking loops might improve the kinematic solutions.

A potential candidate receiver for an e.motion² mission is the state-of-the-art TriG receiver [Esterhuizen *et al.*, 2009], which will also be used in GRACE Follow-On [Meehan *et al.*, 2012]. It is a dual processor GNSS receiver with up to 16 antenna input ports and with up to 300 configurable satellite signal processing channels [Tien *et al.*, 2012].

1.4.2 Ranging Interferometer

A laser ranging interferometer is capable of measuring inter-satellite distance variations with a sensitivity of a few tens of nm/ $\sqrt{\text{Hz}}$ along the line-of-sight. In general, each interferometer has a point or an axis of minimal coupling (POMC), where interferometric pathlength changes upon rotation are minimized. These POMCs are nominally designed to coincide with the respective satellite GRP. The interferometer provides only biased ranging ρ_{biased} due to integer phase ambiguity. The overall noise with contributions from laser frequency noise, spacecraft attitude jitter, parasitic Sagnac effect, readout noise and many other sources is assumed to be covered by the following straw man sensitivity formula within the SMBW

$$\text{ASD}[\rho_{\text{biased,E}}](f) = 25 \frac{\text{nm}}{\sqrt{\text{Hz}}} \cdot \sqrt{1 + \left(\frac{10 \text{ mHz}}{f}\right)^2} \cdot \frac{L}{100 \text{ km}}, \quad 0.18 \text{ mHz} < f < 0.1 \text{ Hz}, \quad (1.39)$$

where L is the absolute spacecraft separation and the $\sqrt{\cdot}$ -term is called the Noise-Shape-Function (NSF). The latter accounts for an increased noise at low frequency, mostly driven by temperature fluctuations and by $1/f$ noise present in many electrical components.

An additional error is induced by the limited knowledge of the DC-scale factor $\mathcal{S}_{DC,E}$, in other words, knowledge of absolute laser frequency, which relates the interferometric phase measurement to a physical length. The corresponding noise can be described with the spectral density

$$\text{ASD}[\rho_{\text{biased,DC-SCF,E}}](f) = \mathcal{S}_{DC,E}^{(\text{IFO})} \cdot \text{ASD}[\rho_{\text{biased,M}}]. \quad (1.40)$$

This noise is proportional to the actual (measured) signal amplitude $\rho_{\text{biased,M}}$ and the proportionality factor is the fractional laser frequency knowledge $\mathcal{S}_{DC,E}^{(\text{IFO})} \approx 10^{-6}$, which will be further discussed in section 2.3.2 of the thesis. The time variability of the scale factor (AC

part) is accounted for by eq. (1.39). It might be possible to fit the DC scale factor in the process of gravity field retrieval. However, a strong correlation between the interferometer DC scale factor and a common scale factor of SH coefficients may complicate the correction. In addition, the large post-fit ranging residuals, e.g. from deficiencies in background gravity field models, make such an approach difficult. Direct correlation of GNSS observations, i.e. GNSS-derived range, with the interferometry observation is another option. However, the detailed estimation of the DC scale factor was beyond the scope of this thesis.

In addition to ranging, laser interferometry is capable of providing a measurement of the local S/C misalignment w.r.t. the line-of-sight by the so-called Differential Wavefront Sensing (DWS) technique, which is assumed to deliver yaw and pitch misalignment with a noise lower than

$$\text{ASD}[\text{DWS}_{\text{Yaw,E}}] \approx \text{ASD}[\text{DWS}_{\text{Pitch,E}}] \lesssim 1 \mu\text{rad}/\sqrt{\text{Hz}} \cdot \text{NSF}(f), \quad (1.41)$$

where the same noise shape function (NSF) as in eq. (1.39) is considered.

Moreover, a static offset of less than

$$\text{Yaw}_{\text{bias}} \approx \text{Pitch}_{\text{bias}} < 10 \mu\text{rad} \quad (1.42)$$

in the interferometer reference frame seems realistic.

GRACE-like microwave dual one-way ranging (DOWR) achieves a sensitivity of the order of [Kim, 2000, p. 144]

$$\text{ASD}[\rho_{\text{biased,E}}](f) \approx \sqrt{\left(\frac{L}{200 \text{ km}}\right)^2 + \left(\frac{1.8 \text{ mHz}}{f}\right)^4} \frac{\mu\text{m}}{\sqrt{\text{Hz}}}, \quad 0.18 \text{ mHz} < f < 0.1 \text{ Hz}, \quad (1.43)$$

which is given here for the sake of completeness. The microwave instrument is limited at high frequencies by the readout noise, which scales with the carrier-to-noise density and can be assumed to be linearly dependent on the spacecraft separation [Kim, 2000, p. 112]. For a detailed description of interferometry, the reader is referred to part 2 of this thesis.

1.4.3 Accelerometer

Each e.motion² S/C requires an accelerometer, which is capable of measuring linear and angular non-gravitational accelerations acting on the satellites, e.g. due to atmospheric drag, thruster, solar radiation pressure, Earth's albedo radiation pressure, Lorentz forces and other unexpected disturbances.

Potential candidates are classical electro-static servo-accelerometers from ONERA, which have been used in CHAMP, GRACE, GRACE Follow-On and GOCE. Alternatively, a LISA Pathfinder (LPF)-like gravity reference sensor (GRS) [Danzmann *et al.*, 2007] could be utilized in a drag-free concept. All of these inertial measurement devices utilize a metallic high-density cuboid test-mass, which is located well shielded inside the accelerometer housing with a gap to the walls. ONERA instruments prefer a few micron thin wire to charge the test-mass at AC frequencies ($\approx 100 \text{ kHz}$) and to polarize it at DC [Frommknecht *et al.*, 2003], while the LPF GRS test-mass is kept neutral without physical contact using UV light discharge [Danzmann *et al.*, 2007, p. 12]. Electrodes in the housing can be used either to sense the position and orientation of the test-mass (also called proof-mass) by capacitive means, or to apply a force or torque by electro-static means. Usually, the electrodes are arranged pair-wise on the axes, such that the common signal provides linear accelerations and the differential signal the angular quantity.

ONERA accelerometers are typically servo-controlled in all degrees of freedom, meaning that the test-mass is centered and aligned with high gain and bandwidth in the accelerometer housing. The actuator signal is calibrated and provides a measure of the linear and angular non-gravitational acceleration. Obviously, the proof-mass will not follow a geodesic, but will

follow the accelerometer housing and S/C. However, the deviation from the geodesic can be derived from the actuator signal.

If a drag-free system is utilized, some degrees of freedom are operated open-loop without electro-static suspension. In this case, the non-gravitational acceleration is given by the second time-derivative of the capacitive position sensing. However, to avoid physical contact between proof-mass and housing, the S/C utilizes a drag-free control loop, which actuates thrusters to re-center the S/C and accelerometer housing w.r.t. the proof mass. Typically, such a geodesic (free-fall) motion of the test-mass cannot be realized in all degrees of freedom due to constraints, e.g. in e.motion² due to inter-S/C pointing. A further challenge is to suppress cross-talk between servo-controlled and drag-free degrees of freedom.

In the LISA Pathfinder mission, one of the GRS units is operated in the sensitive axis in drag-free mode [Armano *et al.*, 2016b], while the second GRS uses electro-static forces only at very low frequencies out of measurement band to avoid long-term drifts. Both GRS units feature an optical readout of the respective test-mass along the sensitive axis which provides, in combination with DWS, three degrees of freedom out of six. Capacitive sensing is used for the other degrees of freedom as well, in parallel to the interferometric readout. A high sensitivity of capacitive sensing can, in general, be achieved with a small gap and high voltages between test-mass and electrode housing [Danzmann *et al.*, 2007, p. 7], although a larger gap is favorable for drag-free operation due to the low bandwidth of thrusters and the accompanied motion of the test-mass.

For e.motion², a servo-accelerometer was considered sufficient with a sensitivity half-way between the GRACE Follow-On accelerometer and the GOCE in-orbit accelerometer performance (cf. figure 1.11), under the premise that drag-compensation is available (cf. sec. 1.9). As the GOCE mission utilized six accelerometers mounted on a common platform, with each instrument providing readout for six degrees of freedom, sufficient redundancy is present to assess the in-orbit accelerometer noise floor [Stummer, 2013, sec. 5.1.3] also at low frequencies. The obtained noise level of $\approx 10^{-11} \text{ m/s}^2\sqrt{\text{Hz}}$ does not agree with the pre-launch predicted sensitivity of $\approx 10^{-12} \text{ m/s}^2\sqrt{\text{Hz}}$ [Marque *et al.*, 2010; Christophe, 2013] to the understanding of the author of this thesis. One potential explanation could be that the pre-launch predicted sensitivity considers only intrinsic instrument noise, while the total noise may be larger, as will be discussed. In the e.motion² study, the conservative sensitivity of in-orbit GOCE accelerometers was considered.

At high frequencies, the e.motion² accelerometer requirement was relaxed (cf. black trace in figure 1.11), since ranging is dominating the PDGA observation at high frequencies anyway.

The dashed green line at the top of figure 1.11 indicates the GOCE drag-free performance [Sechi *et al.*, 2011], i.e. the deviation of the proof-mass trajectory from a geodesic. In 2016, the LISA Pathfinder mission showed a superb in-orbit drag-free sensing noise of $\approx 3 \text{ fm}/(\text{s}^2\sqrt{\text{Hz}})$, measured optically between the two free-falling test-masses on-board [Armano *et al.*, 2016b]. For LISA Pathfinder, the actual deviation from geodesic motion, e.g. due to electro-static suspension and perturbing forces, can be considered to be (far) below $\approx 10^{-12} \text{ m}/(\text{s}^2\sqrt{\text{Hz}})$ for all frequencies $f > 0.1 \text{ mHz}$ (priv. comm. Sarah Paczkowski, AEI).

Such a performance is not directly transferable to LEO gravimetric missions. On one hand, the thermal, magnetic, gravitational and non-gravitational disturbances are higher for LEO missions. On the other hand, LISA Pathfinder was designed to push the limits of available technology and to act as experimental scientific platform with, for example, a well-balanced self-gravity field [Armano *et al.*, 2016a], low noise truster and high complexity, which was accompanied by notable costs.

However, the benefit and feasibility of a gravimetric drag-free mission is still a key topic for future geodesy missions. Hence, this aspect is revisited in section 1.9.

For now, a servo-controlled accelerometer is considered, with the accelerometer reference point co-located with the S/C CoM. It is emphasized that such a measurement of non-gravitational accelerations in a rotating S/C frame is susceptible to various fictitious accelerations. A simplified model for the accelerometer measurement of linear accelerations

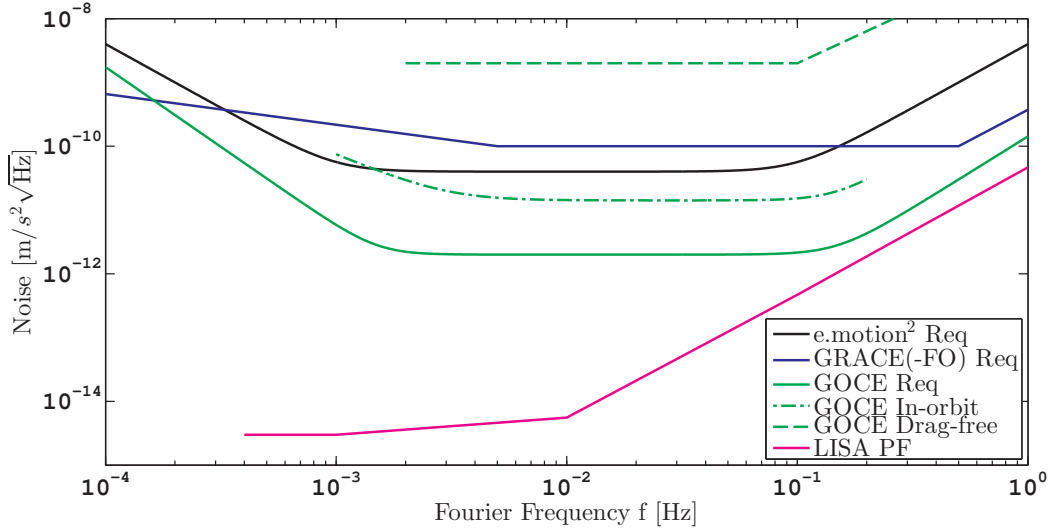


Figure 1.11: Noise levels of accelerometers along the sensitive axis for various missions (solid lines). The GOCE drag-free trace (dashed green) denotes the precision of geodesic motion, while all other lines denote the sensing performance.

$\vec{\Gamma}_{\text{meas,SRF}}$ in the spacecraft (science) reference frame (SRF) can be written in the following form [Klinger & Mayer-Gürr, 2016; Frommknecht *et al.*, 2003]

$$\vec{\Gamma}_{\text{meas,SRF}} = \delta \hat{R}_{\text{ARF}} \cdot \hat{S} \cdot \left(\hat{G} \cdot \vec{r} - \hat{\omega}^2 \cdot \vec{r} - 2\hat{\omega} \cdot \dot{\vec{r}} - \dot{\hat{\omega}} \cdot \vec{r} + \hat{R}_{\text{ARF}} \cdot \vec{a}_{\text{ng}} + \vec{k}_2 + \vec{a}_{\text{EBC}} \right) + \vec{b} + \vec{n}, \quad (1.44)$$

where \vec{a}_{ng} contains the non-gravitational linear accelerations in the inertial frame acting on the S/C, \vec{n} is the intrinsic instrument noise, \vec{b} contains biases, \hat{S} is a scale factor or geometry matrix, which is ideally the unity matrix, but may contain scale factors and cross-coupling between the axes [Klinger & Mayer-Gürr, 2016, eq. 3]. \hat{R}_{ARF} is the rotation matrix transforming from the inertial frame into the accelerometer reference frame (ARF), while $\delta \hat{R}_{\text{ARF}}$ denotes the uncertainty in the ARF axes w.r.t. the SRF. \hat{G} is the gravity gradient, $\hat{\omega}$ the angular velocity tensor of the ARF and SRF frame and \vec{r} is the offset between test-mass CoM and S/C CoM. \vec{k}_2 is the quadratic coupling, which can be written as

$$\vec{k}_2 = (\hat{R}_{\text{ARF}} \cdot \vec{a}_{\text{ng}})^{\text{T}} \cdot \hat{K}_2 \cdot \hat{R}_{\text{ARF}} \cdot \vec{a}_{\text{ng}}, \quad (1.45)$$

with \hat{K}_2 containing the quadratic coupling terms as diagonal elements. The extended body correction \vec{a}_{EBC} accounts for non-uniform gravitational acceleration of the S/C and test-mass

$$\vec{a}_{\text{EBC}} = \vec{a}_{\text{EBC, SC}} - \vec{a}_{\text{EBC, TM}}, \quad (1.46)$$

which has been introduced in section 1.3.6.

The e.motion² accelerometer requirement from figure 1.11 is considered to account for all potential error contributions from eq. (1.44), and in particular for the fictitious accelerations, and not only for the intrinsic noise \vec{n} . It is defined for the science measurement bandwidth from 0.18 mHz to 0.1 Hz along the two sensitive accelerometer axes in radial and along-track direction by

$$\begin{aligned} \text{ASD}[\Gamma_{\text{X,E}}] &= \text{ASD}[\Gamma_{\text{Y,E}}] \\ &= 4 \cdot 10^{-11} \frac{\text{m}}{\text{s}^2 \sqrt{\text{Hz}}} \cdot \sqrt{\left(\frac{1 \text{ mHz}}{f} \right)^4 + 1 + \left(\frac{f}{10 \text{ mHz}} \right)^4}. \end{aligned} \quad (1.47)$$

The requirement for the less sensitive cross-track axis is relaxed by one order of magnitude to

$$\text{ASD}[\Gamma_{Z,E}] = 4 \cdot 10^{-10} \frac{\text{m}}{\text{s}^2\sqrt{\text{Hz}}} \cdot \sqrt{\left(\frac{1 \text{ mHz}}{f}\right)^4 + 1 + \left(\frac{f}{10 \text{ mHz}}\right)^4}. \quad (1.48)$$

The axes X,Y,Z refer to the accelerometer reference frame (ARF), but are roughly aligned with radial, along and cross-track direction, respectively. For the angular acceleration sensitivity an effective lever-arm of $d_l = 10 \text{ mm}$ between the sensing electrodes is assumed and only the less-sensitive axis is taken into account as baseline for all axes

$$\begin{aligned} \text{ASD}[\dot{\omega}_{X,E}] &= \text{ASD}[\dot{\omega}_{Y,E}] = \text{ASD}[\dot{\omega}_{Z,E}] = \frac{\text{ASD}[\Gamma_{Z,E}]}{d_l} \\ &= 4 \cdot 10^{-8} \frac{\text{rad}}{\text{s}^2\sqrt{\text{Hz}}} \cdot \sqrt{\left(\frac{1 \text{ mHz}}{f}\right)^4 + 1 + \left(\frac{f}{10 \text{ mHz}}\right)^4}. \end{aligned} \quad (1.49)$$

The matrix \hat{S} in eq. (1.44) is a critical component and requires particular attention. Consider the along-track x-axis of the accelerometer to be independent of the other axes. The ratio between the true in-orbit value $S_{xx,\text{true}}$ and the best estimate $S_{xx,\text{estim.}}$, determined e.g. from on-ground calibration, is a fractional scale factor

$$\mathcal{S} = \frac{S_{xx,\text{true}}}{S_{xx,\text{estim.}}} = \mathcal{S}_S^{(\text{ACC})} + \mathcal{S}_E^{(\text{ACC})} \approx 1 + \mathcal{S}_E^{(\text{ACC})}, \quad (1.50)$$

ideally close to unity. The subscripts S and E stand for the signal and unknown error, respectively.

It is recommended to distinguish between the DC (zero frequency, mean) part and fluctuations (AC) within the measurement band, i.e.

$$\mathcal{S}_E^{(\text{ACC})}(f) = \mathcal{S}_{\text{DC,E}}^{(\text{ACC})} + \mathcal{S}_{\text{AC,E}}^{(\text{ACC})}(f). \quad (1.51)$$

The noise coupling into the measured acceleration Γ from the DC scale factor uncertainty depends on the measured signal, while the AC scale factor fluctuations are multiplied in a worst-case assessment by the maximum non-gravitational acceleration Γ_{max} , i.e.

$$\text{PSD}[\Gamma_{S,E}] = (\mathcal{S}_{\text{DC,E}}^{(\text{ACC})})^2 \cdot \text{PSD}[\Gamma_{\text{meas}}] + \Gamma_{\text{max}}^2 \cdot \text{PSD}[\mathcal{S}_{\text{AC,E}}^{(\text{ACC})}]. \quad (1.52)$$

For example, the second contribution does not show up in typical noise measurements, where one tries to measure zero acceleration.

For the PDGA signal, the non-gravitational acceleration along the line-of-sight is of importance. Hence, cross-talk from other axes due to a misaligned accelerometer need to be prevented. A misalignment would also show up as change in the DC scale factor $\mathcal{S}_{\text{DC,E}}^{(\text{ACC})}$. Other important aspects such as accelerometer saturation and requirements for the scale factors are taken into account later in section 1.9, which deals with drag-free operation and drag compensation.

1.4.4 Star Cameras

A star camera typically consists of one or several sensor heads and a processing unit. The sensor heads image the starry sky onto a photosensitive array (e.g. CCD), which provides a two-dimensional digital picture. The processing unit compares the location of the stars on the picture with a star catalog and derives the orientation of the sensor head w.r.t. the starry sky, which is practically an inertial frame. For an overview of the working principle and data processing of star cameras, the reader is referred to [Frommknecht, 2008] and [Bandikova, 2015]. Multiple sensor heads are required, since illumination by the Sun or Moon can blind

the sensor head. GRACE used two sensor heads, while GRACE Follow-On will utilize three sensor heads to avoid parallel blinding of all heads by Sun and Moon. It is also evident that future missions should utilize at least three sensor heads. Analyses of star camera noise and errors as well as of camera head data fusion in the context of GRACE can be found in [Inácio *et al.*, 2015; Harvey, 2016] and [Bandikova & Flury, 2014].

The information provided in [Bandikova & Flury, 2014] was used to assess the sensitivity of the measurement. A noise of approximately 10^{-5} rad/(s $\sqrt{\text{Hz}}$) at 0.1 Hz and proportionality to the Fourier frequency f , i.e. blue noise in angular rate ASD domain, is considered for the two sensitive axes. Integration yields a white noise level of approx. $16 \mu\text{rad}/\sqrt{\text{Hz}}$.

The orientation of the star camera heads in GRACE allows the S/C roll axis to be retrieved with highest precision in hot redundant operation of heads, while the other axes are degraded due to influences from the less-precise sensor head boresight axes [Bandikova, 2015, Fig. 5.2], in particular in case of non-optimal sensor head fusion. With recent advances, e.g. optimal fusion [Bandikova, 2015, Fig. 5.5] and debugged stellar aberration correction routines [Harvey, 2016], a simplified isotropic noise model for the angles (α, β, γ) , relating the satellite attitude to an inertial frame, is considered for e.motion²

$$\text{ASD}[(\alpha, \beta, \gamma)^T] = (1, 1, 1)^T \cdot 16 \mu\text{rad}/\sqrt{\text{Hz}} \cdot \sqrt{1 + \left(\frac{0.01 \text{ Hz}}{f}\right)^2}, \quad (1.53)$$

where a noise-shape function was introduced to allow for an increased noise at low frequencies due to thermal variations and drifts.

It is noted that angular biases between star camera frames, satellite (science) frame and other instrument frames, arising from thermal or launch load effects, need to be calibrated in-orbit. A typical magnitude of a few milliradian can impose operational challenges for instruments with tight pointing requirements, e.g. laser ranging interferometers.

1.4.5 Tone Errors

The recent sections focused on stochastic error models, i.e. noise, and partly on errors with systematic behavior such as biases or scale factors. However, measurement errors can also have a deterministic origin, e.g. they may be caused by periodic excitation of temperature. Noise shows a continuous distribution of power over frequency, while sinusoidal signals have power at a particular discrete frequency, i.e. delta peaks. Noise is characterized by a power or amplitude spectral density with units of e.g. meter/ $\sqrt{\text{Hz}}$, while tones are described by an amplitude unit e.g. meter.

Tone errors are modulations of the instrument output driven by periodic excitations of environmental quantities such as

- Temperature
- Magnetic field
- Atmosphere / Ionosphere
- Gravitational Potential
- S/C inertial attitude

All of these environmental quantities have a pronounced variation at the orbital or twice the orbital frequency for a LEO satellite and, thus, can be written as

$$\mathcal{E}(t) = \sum_{n=1}^{\infty} (a_{c,n} \cdot \cos(2\pi f_{\text{orb}} n t) + a_{s,n} \cdot \sin(2\pi f_{\text{orb}} n t)), \quad (1.54)$$

where two amplitudes $(a_{c,n}, a_{s,n})$ per frequency were used instead of the equivalent representation of one phase and one amplitude (cf. eq. 5-8 in [e.motion² Team, 2014]).

n/rev	PDGA _E	ρ_E [μm]	Γ_E [pm/s^2]
1	$100 \mu\text{m} \cong 126 \text{ pm/s}^2$	25	32
2	$20 \mu\text{m} \cong 101 \text{ pm/s}^2$	5	25.5
3	$5 \mu\text{m} \cong 46 \text{ pm/s}^2$	1	11.5
4	$0.8 \mu\text{m} \cong 16 \text{ pm/s}^2$	0.2	4
5	$0.16 \mu\text{m} \cong 5.1 \text{ pm/s}^2$	0.04	1.25
6	$0.032 \mu\text{m} \cong 1.5 \text{ pm/s}^2$	0.008	0.25

Table 1.1: Tone error requirement for the PDGA observation of a SST link (second column), and flow-down onto S/C instrument level (third and fourth column). The ranging values ρ_E are half-roundtrip requirements for a single LRI-instruments (per S/C). The accelerometer values Γ_E are given per instrument (or per S/C).

n/rev	GNSS [mm]
1	4
2	4

Table 1.2: Tone error assumption for GNSS and orbit determination.

Usually, the susceptibility of an instrument to this environmental quantity \mathcal{E} can be described by a coupling factor $c_{M,\mathcal{E}}$, which may be time or frequency dependent, such that the measurement error $M_{\mathcal{E}}$ is given by

$$M_{\mathcal{E}} = c_{M,\mathcal{E}} \cdot \mathcal{E}, \quad (1.55)$$

with the equation being deployed in the frequency or the time domain. One should also recall that non-linearities in a dynamic system produce higher-harmonics at integer multiples of the excitation frequency, yielding a comb of tones with decreasing amplitude. Since Earth's gravity also produces a comb of sinusoidal signals in the PDGA as well as in the direct satellite acceleration (DA), it is important to study the effect of tones on gravity field retrieval in order to be able to set proper requirements at instrument level and to develop strategies to mitigate this error in gravity field recovery.

A first, but preliminary, step in this direction has been done in [e.motion² Team, 2014, sec. 5.1.5]. Gravity field recovery has been performed twice, with and without induced tones. From these results, tone amplitude requirements were derived, such that science objectives in terms of gravity field precision are met. The instrument tone requirements for the two prime instruments of the PDGA, accelerometer and interferometer, are adopted from the e.motion² study and shown in table 1.1. The tone error in the final PDGA observation is distributed equally on the four instruments per link, two accelerometers and two interferometers, with following formula

$$\text{PDGA}_E = 2 \cdot \rho_E + 2 \cdot \Gamma_E \cdot (2\pi f_{\text{orb}} \cdot n)^2, \quad [\text{m}]. \quad (1.56)$$

However, the approach did not take into account an adopted gravity field recovery algorithm, which is capable of handling tone errors. Hence, it is very likely that these requirements can be relaxed with algorithms taking tone errors into account, as will be discussed in section 1.7.2.

Tone errors in the orbit determination have not been handled in the e.motion² study. However, based on the covariance information of the kinematic orbit as shown in figure 1.10, a tone error of 4 mm at 2/rev frequency is assumed here. Interestingly, the covariance information does not show an increased error at 1/rev frequency, which might be caused by deficiencies in the error modeling. In this thesis, an additional tone amplitude of 4 mm at 1/rev frequency is assumed, as summarized in table 1.2.

It is beyond the scope of this thesis to derive and justify tone error requirements for all instruments. However, the author of this thesis would like to outline a roadmap on this issue for future studies. As these satellite gravity mission studies usually consist of different groups, which are concerned, for example, with gravity field recovery, instrument design, spacecraft design and so on, it is advised to provide separated dedicated work packages, which can be performed in parallel.

First, the time series of environmental quantities at the S/C position like magnetic field strength, temperature (or incident solar irradiation) and S/C attitude needs to be determined for the particular mission design baseline. From these, the sinusoidal characteristics such as amplitude and frequency can be determined for each environmental parameter.

The remaining tasks

3. Gravity field recovery: development of potential strategies to cope with tone errors and the definition of maximum acceptable tone error in the instruments for the different strategies
2. Instrument design: deriving the transfer functions of the instruments from environmental parameters such as temperature, magnetic field and attitude to the measurements such as ranging or accelerations
1. Spacecraft design: derivation of transfer functions from environmental quantities in-orbit to instrument boxes using a S/C model

need to be iterated with respect to the spacecraft design, such that the final tone errors permit the science objectives to be met.

1.4.6 Proposed Data Processing

Many instruments on-board a GRACE-like mission are capable of measuring the same physical quantities, e.g. attitude, baseline angular velocity, inter-spacecraft distance. This redundancy should be exploited to validate and calibrate the different instruments against each other and to optimally combine the data streams to obtain the *baseline state* with least errors. A *baseline state* means here quantities which fully describe an e.motion² link, consisting of two satellites, for the gravity field recovery. The baseline state is ideally derived by an integrated parameter estimation and serves as the interface to gravity field recovery. From a time-series of baseline state quantities, as illustrated in the scheme in figure 1.12, the SH coefficients can be computed. However, the (co)variance information of SH coefficients contains information on deficiencies in the a-priori information of the integrated parameter estimate and should be fed back, resulting in a recursive approach.

Although this strategy might be a matter of dispute, as some groups prefer to use directly low-level or raw observations, the author of this thesis prefers a clear separation between baseline state parameter estimation and gravity field recovery. The complexity of both steps individually is already enormous, making a single step procedure from raw observations to SH coefficients almost impossible to follow. Additionally, the two step procedure from figure 1.12 allows the easy comparison, validation and improvement of different methods of gravity field recovery without bothering with low-level corrections, e.g. from temperature.

However, the first step of baseline state parameter estimation needs to be open for a broad scientific community, well documented, replicable and should be improved steadily and frequently, considering input from gravity field recovery groups. An open question in data processing remains regarding the use of a-priori gravity field information in the first step, which has not been addressed here.

The interested reader is also referred to the section on Integrated Instrument Analysis and Calibration (sec. 1.10 on page 68).

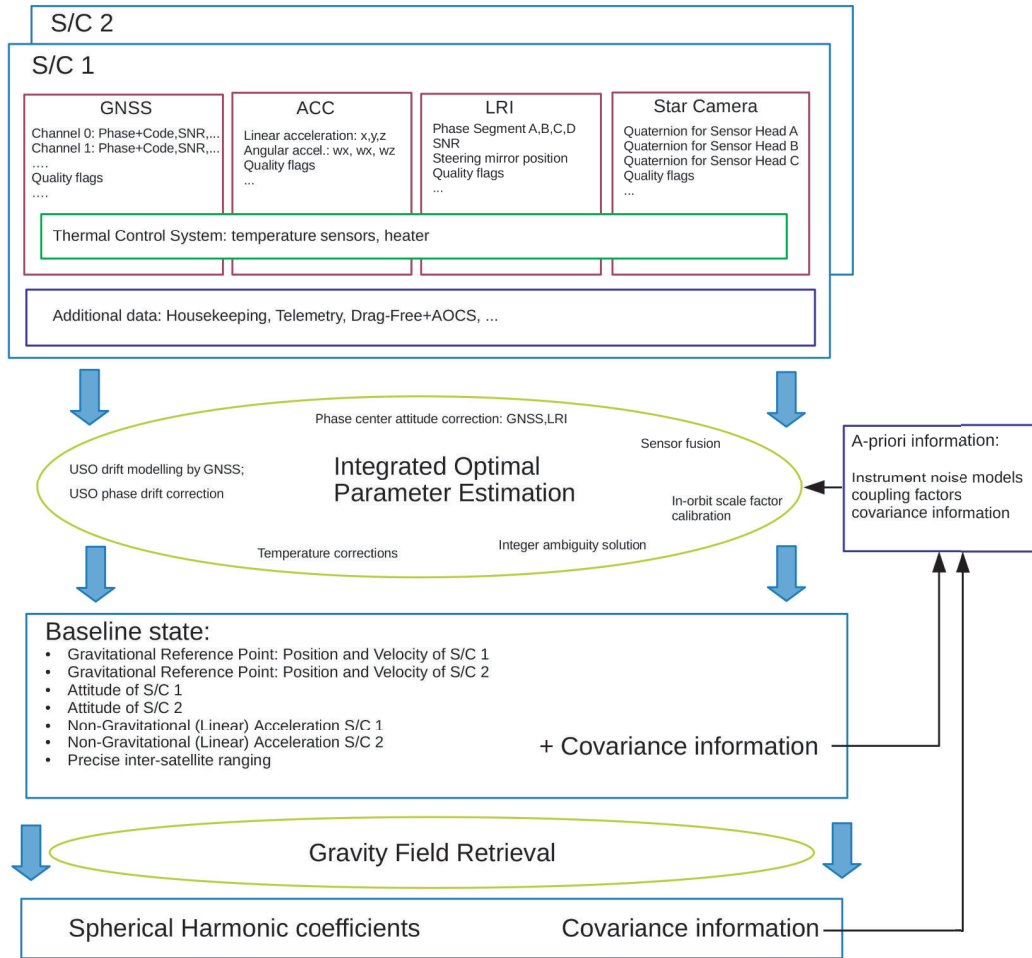


Figure 1.12: Flow diagram of the proposed e.motion² data processing chain.

1.5 Baseline State

The next sections address the recovery of Earth's gravity field from simulated observations. This requires that baseline state quantities, in particular the gravitational reference points, are determined from instrument observations. For the purpose of this thesis, a simplified approach was selected instead of the integrated parameter estimation introduced in sec. 1.4.6. An idealized servo-accelerometer concept is considered, where the accelerometer reference point, interferometer reference point and S/C CoM coincide. Furthermore, the GNSS observations refer to the S/C CoM instead of the GNSS antenna phase center.

The following straightforward formulas for the GRP have been used

$$\vec{r}_{\text{GRP},1,\text{GNSS+IFO}} \approx \frac{\vec{r}_{\text{GRP},1,\text{GNSS}} + \vec{r}_{\text{GRP},2,\text{GNSS}}}{2} - \vec{e}_{12,\text{GNSS}} \cdot \frac{\rho_{\text{unbiased}}}{2}, \quad (1.57)$$

$$\vec{r}_{\text{GRP},2,\text{GNSS+IFO}} \approx \frac{\vec{r}_{\text{GRP},1,\text{GNSS}} + \vec{r}_{\text{GRP},2,\text{GNSS}}}{2} + \vec{e}_{12,\text{GNSS}} \cdot \frac{\rho_{\text{unbiased}}}{2}, \quad (1.58)$$

where $\vec{r}_{\text{GRP},1/2,\text{GNSS}}$ is the GRP (=S/C CoM) position derived solely from GNSS kinematic orbits. Such a definition of the GRP incorporates a low noise distance between the GRPs. This is important, because the GRPs are used to evaluate the potential function on the left hand side of the PDGA observation equation (eq. (1.13)) and the right hand side contains the precise ranging information.

The offset, which is required to transform the interferometrically measured biased ranging $\rho_{\text{biased}}(t)$ into a correct (unbiased) distance, is computed with

$$\rho_{\text{unbiased}}(t) = \rho_{\text{biased}}(t) - \underbrace{\langle \rho_{\text{biased}} \rangle + \langle |\vec{r}_{\text{GRP},1,\text{GNSS}} - \vec{r}_{\text{GRP},2,\text{GNSS}}| \rangle}_{\text{offset}}, \quad (1.59)$$

where $\langle \rangle$ denotes temporal averaging.

The line-of-sight - the baseline - is estimated here from GNSS observations at each epoch according to

$$\vec{e}_{12,M} \approx \frac{\vec{r}_{\text{GRP},2,\text{GNSS}} - \vec{r}_{\text{GRP},1,\text{GNSS}}}{|\vec{r}_{\text{GRP},2,\text{GNSS}} - \vec{r}_{\text{GRP},1,\text{GNSS}}|}. \quad (1.60)$$

Since the GNSS-derived GRP position is known at the $\text{cm}/\sqrt{\text{Hz}}$ level and the satellite separation is of the order of 100 km, the angular jitter of the GNSS-derived baseline is of the order of $0.1 \mu\text{rad}/\sqrt{\text{Hz}}$.

The previous equations are, in many aspects, simplified and hence suboptimal. For example, they do not consider the different noise characteristics of GNSS and ranging interferometer observations, e.g. at very low frequencies the interferometric ranging may become less accurate due to drifts compared to GNSS-derived distance. Additionally, the line-of-sight estimation dismisses attitude information from other instruments, e.g. DWS, accelerometer and star camera with respective noise characteristics.

However, these simplifications allow analytical formulas for the expected noise level in the PDGA channel to be derived in subsequent sections.

1.5.1 Line-of-Sight Angular Velocity

The line-of-sight or baseline angular velocity has been defined by (cf. sec. 1.3.3)

$$\vec{\omega}_{\text{LOS}} = \vec{e}_{12} \times \dot{\vec{e}}_{12} = \frac{\vec{r}_{12} \times \dot{\vec{r}}_{12}}{|\vec{r}_{12}|^2} = \frac{\dot{\vec{r}}_{12,\perp}}{|\vec{r}_{12}|},$$

where $\dot{\vec{r}}_{12,\perp}$ is the relative velocity between both S/C GRPs perpendicular to the LOS. It can be computed straightforward from the GRP position (eq. (1.58)), however, alternative ways to determine it will be discussed in sec. 1.8. Since precise ranging information is only available

along the LOS, the precision of the angular velocity is dominated by GNSS uncertainties (cf. eq. (1.38)) and the error (denoted with subscript E) in the angular velocity can be considered in the PSD domain as

$$\text{PSD}[\vec{\omega}_{\text{LOS,E}}] \approx (1, 1, 1)^\top \cdot \frac{2 \cdot (2\pi f)^2 \cdot \text{PSD}[r_{\text{GNSS,E}}]}{L^2}, \quad (1.61)$$

where L is the inter-spacecraft separation. Because the assumed position noise is isotropic, i.e. each vector component has the same PSD, the noise in the angular velocity is isotropic as well.

It will turn out subsequently, that $\vec{\omega}_{\text{LOS}}$ is a critical quantity. The precision of $\vec{\omega}_{\text{LOS}}$ can be improved by utilizing more precise orbits than directly available from GNSS observations, which are introduced next.

1.5.2 (Reduced-) Dynamic Orbits

The GNSS-derived kinematic orbits are based on multilateration and do not exploit information on the dynamics of the GNSS receiver. The errors in the kinematic orbits can be understood as readout noise, which can be decreased by using additional information or constraints, e.g. from

- **Energy conservation:** The energy of the satellite as the sum of kinematic, potential, rotational and dissipated energy is preserved along the orbit. Evaluating the potential energy requires a-priori knowledge of the gravity field.
- **Accordance with ranging:** The ranging instrument provides precise distance measurements along the line-of-sight, which can constrain the GNSS observation error along one axis.
- **System dynamics and a-priori-knowledge of the gravity field:** Approximate a-priori knowledge of the gravity field can constrain the GNSS observation error significantly, if the satellite's equations of motion are utilized. If the non-gravitational accelerations are considered in the dynamics, this approach complies typically with the energy conservation constraints.

Some caution is required, since one aims to measure the gravity field but tries to incorporate some a-priori knowledge of the gravity field, which might bias the solution. However, with GRACE-like missions, one aims to measure a small time-variable gravity field signal on an approximately 10.000 times larger static field, which should be well known.

A straightforward approach is to use an orbit integrator in combination with best-knowledge force models to derive an orbit trajectory, which approximates the GNSS (kinematic) observations, i.e. best-fit to the kinematic orbit. This so-called *dynamic precise orbit determination* uses only a few free parameters such as the initial state vector of the satellite and a few quantities describing the force models (e.g. drag coefficient) [Bertiger *et al.*, 1994]. In the so-called *reduced-dynamic precise orbit determination* (RDPOD) additional free parameters are introduced to account for errors in force models as well, and to allow *an optimal synthesis of dynamic and geometrical information* [Bertiger *et al.*, 1994].

The accuracy of the (reduced-)dynamic orbits is limited by the knowledge of the forces acting on the satellite and by the accuracy of the kinematic orbits. Such forces can have a non-gravitational origin, e.g. atmospheric drag, solar radiation pressure, but also a gravitational origin, which has a large static part, high-frequency contributions (periods of hours and days) and a monthly signal, which one actually tries to measure. The latter one cannot be assumed to be a-priori knowledge. The high-frequency tidal and non-tidal content, as well as non-gravitational accelerations, need to be reduced from observations by background models.

An estimation of the errors in the (reduced-)dynamic orbits with regard to the true trajectory is not straightforward, since the true trajectory is not known for real orbits. The

precision of the accelerometer and the ranging instrument are usually sufficient, such that these errors are not dominating the dynamic orbit determination.

In this thesis, the position noise in (reduced-)dynamic orbits $\vec{r}_{\text{RDPOD,E}}$ is approximated by colored noise with spectral density obtained by finding the values for the corner-frequency f_c and n in

$$\text{ASD}[\vec{r}_{\text{RDPOD,E}}] = \text{ASD}[\vec{r}_{\text{GRP,E}}] \cdot \frac{1}{1 + (f/f_c)^n} \quad (1.62)$$

with the help of simulated orbits.

Therefore, it is assumed that the accuracy of gravitational and non-gravitational background models can be expressed as equivalent SH geoid error. For different accuracy levels of this a-priori gravity field, the best-fit orbital arcs are computed using a numerical integrator and multi-dimensional numerical optimization to find the initial state vector. The best-fit arcs minimize the rms 3-d distance to the kinematic GRP orbits over the arc period, which is approximately half of the orbital period. The assumed a-priori gravity field knowledge is shown in the upper-left plot of figure 1.13. Case 1 does not contain errors in the a-priori gravity field, hence only the noise from GNSS observations is present. Case 4 is adopted as realistic baseline for the error in the background modeling.

Typical differences between true simulated orbit position and (reduced-)dynamic orbit position are shown in Figure 1.14, where also a model with $f_c = 1$ mHz and $n = 3$ is shown.

In the same manner, the angular velocity of the baseline is determined. The resulting model reads

$$\text{ASD}[\omega_{\text{LOS,E,RDPOD}}](f) \approx 2 \cdot 10^{-10} \text{ rad}/(\text{s}\sqrt{\text{Hz}}) \cdot \frac{\sqrt{200 \text{ km}/\rho}}{(1 + f/5 \text{ mHz})^2 \cdot (1 + f/10 \text{ mHz})^4} \quad (1.63)$$

and is shown on the two lowest panels in figure 1.13. The lower left panel indicates the fluctuations in the angular rate, determined as the difference $\vec{\omega}_{\text{LOS,RDPOD}} - \vec{\omega}_{\text{LOS,True}}$ and rss'ed after spectral estimation over the x, y, z components for the four different cases. The actual signal $\vec{\omega}_{\text{LOS,True}}$ is shown as the dark blue trace, while the light blue trace is the angular velocity noise derived from pure GNSS errors. One can conclude that (reduced-)dynamic orbits provide baseline angular velocities with significantly lower noise compared to the GNSS-based angular velocity. The lower right panel shows the angular velocity components in the RTN frame (see caption) for the noise in case 4 and the actual signal. The signal and noise in the tangential (T) component, i.e. along the LOS, is significantly smaller and should actually vanish as per its definition but is likely caused by numerical inaccuracies⁶. The model (eq. (1.63)) approximates the noise for the normal (cross-track) and radial direction.

It should be noted that the dependence on the baseline length ρ in eq. (1.63) was estimated from reproducing the plots for satellite separations of 10 km, 50 km and 100 km.

The plot on the upper right of figure 1.13 shows the acceleration error of the (reduced-)dynamic orbit w.r.t. the true orbit. Even if no background model errors are present, as in the magenta case 1 trace, the (reduced-)dynamic orbit does not correspond to the true orbit due to the GNSS noise. As a result of common-mode rejection of errors, since both satellites experience a similar environment, the relative acceleration noise between the satellites is lower (middle left plot) than the absolute acceleration error of one satellite (upper right plot). The error in the relative acceleration $\ddot{\vec{r}}_{12}$ is strongly connected to the centrifugal term $|\dot{\vec{\omega}}_{\text{LOS}}|^2 \cdot \rho$ in the PDGA, as the first time derivative of the baseline angular velocity $\dot{\vec{\omega}}_{\text{LOS}}$ contains $\ddot{\vec{r}}_{12}$:

$$\dot{\vec{\omega}}_{\text{LOS}} = \frac{\vec{e}_{12} \times \ddot{\vec{r}}_{12} - 2 \cdot \vec{\omega}_{\text{LOS}} \cdot \dot{\rho}}{\rho} \quad (1.64)$$

The middle right plot shows the noise in the centrifugal acceleration $|\dot{\vec{\omega}}_{\text{LOS}}|^2 \cdot \rho$.

⁶The RTN frame of one of the S/C was used instead of the RTN frame of the baseline.

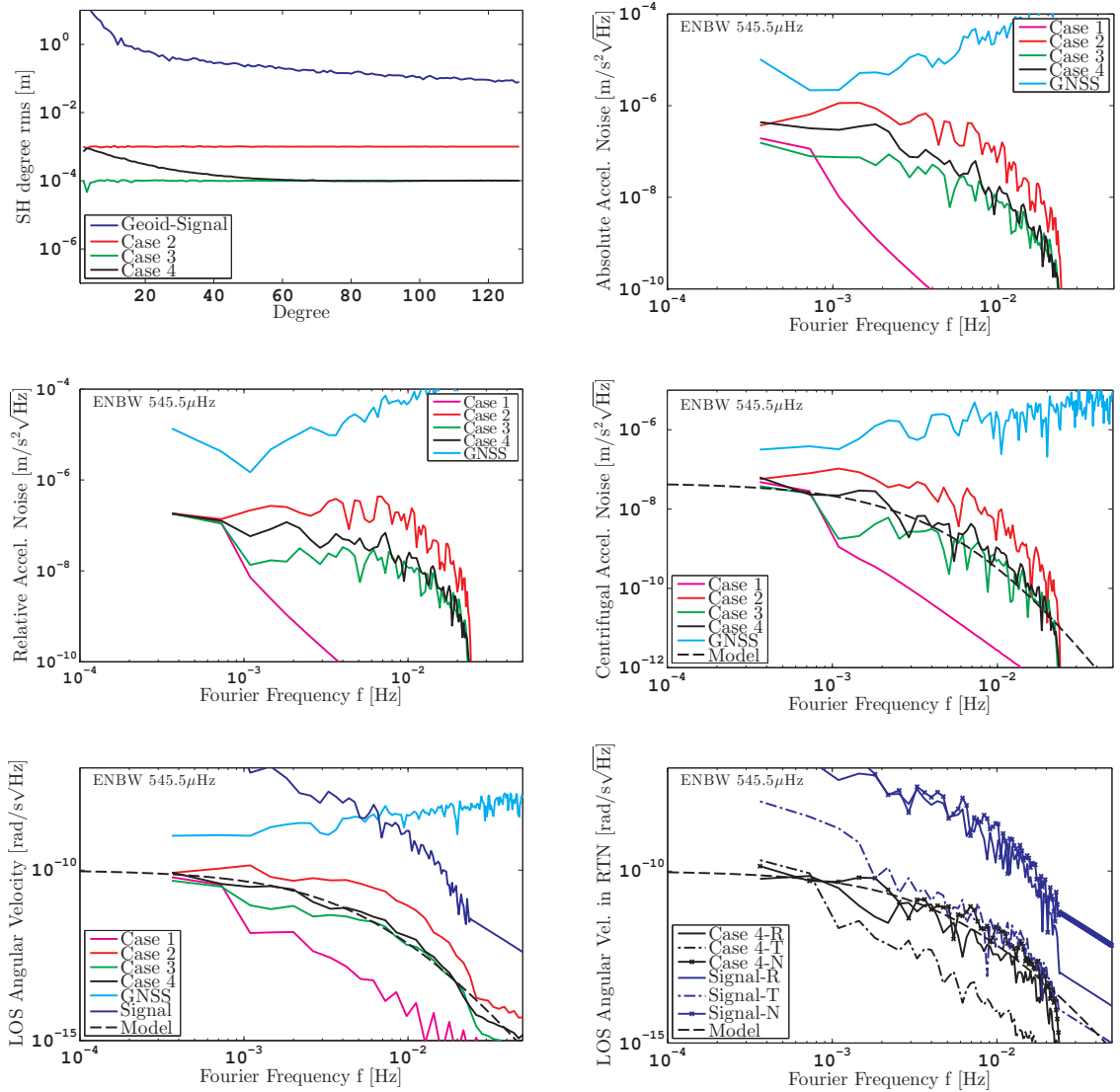


Figure 1.13: (**Upper Left:**) Different cases of accuracy for the a-priori gravity field, used to derive (reduced-)dynamic orbits from kinematic orbits. A lower error in the a-priori field implies a lower error in the (reduced-)dynamic orbit. Case 1 is not shown, since it has no error. (**Upper Right:**) Error in acceleration (root of sum of squares - rss'ed - over x, y, z) for a single satellite for the different cases. The acceleration noise in the kinematic orbits (GNSS) is shown in light blue. (**Middle Left:**) Relative acceleration (rss'ed over x, y, z) between the two satellites for the different cases. (**Middle Right:**) Errors in the centrifugal acceleration term of the PDGA for the different cases. (**Lower Left:**) Error in the angular velocity (root of sum of squares over x, y, z). (**Lower Right:**) Error in the angular velocity for case 4 and the signal in a local orbit frame (RTN: Radial, Tangential/Along-Track, Normal/Cross-Track). All plots assume an orbit height of 400 km and a spacecraft separation of 200 km. The gravity field is considered up to degree 180.

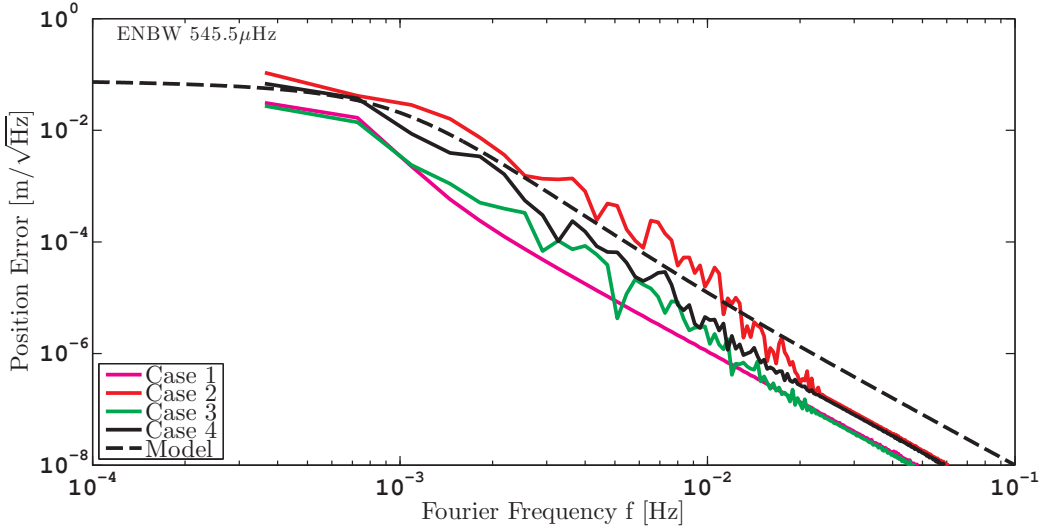


Figure 1.14: The simulated precision of (reduced-)dynamic orbits for a satellite at height $h = 400$ km height and with the background model errors from the cases given in figure 1.13 (upper left). The traces correspond to the root of sum of squared values over x, y, z in the spectral domain.

The propagation of tones into the (reduced-)dynamic orbit and the corresponding angular velocity is done in the following way: It is assumed that differential transverse position, e.g. radial or cross track direction, is subject to common-mode rejection between the (nearby) satellites in a link, such that the 4 mm tone amplitude of kinematic orbits (cf. sec. 1.4.5) is suppressed to amplitudes of $a_1 = 0.3$ mm and $a_2 = 0.1$ mm at 1/rev and 2/rev frequency, respectively, in the (reduced-)dynamic orbits. From these amplitudes a_n , the following formula is used to obtain an error in the angular velocity

$$\omega_{\text{LOS,E,Tones}} = \sum_{n=1}^2 \frac{a_{n,s} \cdot \sin(2\pi f_{\text{orb}} t \cdot n) + a_{n,c} \cdot \cos(2\pi f_{\text{orb}} t \cdot n)}{\rho} \cdot 2\pi f_{\text{orb}} \cdot n, \quad (1.65)$$

which translates into the following error in the centrifugal acceleration term:

$$|\vec{\omega}|^2 \cdot \rho \approx 2 \cdot |\vec{\omega}_{DC}| \cdot \omega_{\text{LOS,E,Tones}} \cdot \rho = \frac{4\pi}{T_{\text{orb}}} \cdot \omega_{\text{LOS,E,Tones}} \cdot \rho. \quad (1.66)$$

1.6 Sensitivity Model

In section 1.3, the two primary relations between the Earth gravity field and observables were derived: On the one hand, one can obtain the SH coefficients from the projected differential gravitational acceleration (PDGA, LL-SST) and on the other hand, directly from the orbit trajectory (direct acceleration, DA, HL-SST). In section 1.4, error models of the measurements were introduced. In this section, measurement errors are propagated into PDGA and DA, such that rigorous sensitivity models for PDGA and DA are obtained. In the subsequent section 1.7, the errors are then related to gravity field solutions.

1.6.1 Direct Acceleration (DA)

Let us denote the error-free, i.e. true, satellite GRP position with the subscript “T,GRP”. Measurements and errors are denoted with the subscripts “M” and “E”, respectively, such that one obtains

$$\vec{r}_{\text{T,GRP}} = \vec{r}_{\text{M,GRP}} - \vec{r}_{\text{E,GRP}} = \vec{r}_{\text{M}} - \vec{r}_{\text{E}} \quad (1.67)$$

The term $\vec{r}_{E,GRP}$ contain errors in the determination of the GRP, i.e. GNSS errors. From eq. (1.18), one easily arrives at an expression for the satellite's 3-d direct gravitational acceleration \overrightarrow{DA} in an inertial frame

$$\overrightarrow{DA}_{\text{True}}(t) = \widehat{M}(\vec{r}_{T,GRP}) \cdot \overrightarrow{CS} + \vec{a}_{\text{ng},T} = \widehat{M}(\vec{r}_{M,GRP}) \cdot \overrightarrow{CS} - \widehat{G} \cdot \vec{r}_E + \vec{a}_{\text{ng},T} \quad (1.68)$$

$$= \underbrace{\ddot{\vec{r}}_M + \vec{a}_{\text{ng},M}}_{\text{Measurement}} - \underbrace{\widehat{G} \cdot \vec{r}_E - \ddot{\vec{r}}_E - \vec{a}_{\text{ng},E}}_{\text{Errors}}, \quad (1.69)$$

where the gravity gradient \widehat{G} relates a position error to an acceleration. The non-gravitational accelerations are given by \vec{a}_{ng} . The noise in the observation of the direct acceleration (DA) can be approximatively expressed as power spectral density by

$$\begin{aligned} \text{PSD}[\overrightarrow{DA}_E](f) &\approx \|\widehat{G}\|_\infty^2 \cdot \text{PSD}[\vec{r}_E] + (2\pi f)^4 \cdot \text{PSD}[\vec{r}_E] + \text{PSD}[\vec{a}_{\text{ng},E}] \\ &\approx \left(\left(\frac{8\pi^2}{T_{\text{Orb}}^2} \right)^2 + (2\pi f)^4 \right) \cdot \text{PSD}[\vec{r}_E] + \text{PSD}[\vec{a}_{\text{ng},E}], \end{aligned} \quad (1.70)$$

where several approximations were used to derive a handy equation. The square root of the expression is visualized in fig. 1.15 as light blue dashed trace, which has a white noise floor at low frequencies and is increasing with f^2 (in the ASD domain) due to the double-differentiation.

In general, the gravity gradient \widehat{G} in eq. (1.69) is time-dependent and it is mixing the different vector components. The dominating part of the gravity gradient \widehat{G} is due to the zero degree term (point-mass, PM), which is typically written as [Seefelder, 2002, eq. 4-16]

$$\widehat{G}_{\text{PM}}(\vec{r}) = \frac{GM}{r^3} \left(3 \frac{\vec{r} \cdot \vec{r}^\top}{r^2} - \frac{\vec{r}^\top \cdot \vec{r}}{r^2} \cdot \mathbb{1}_{3 \times 3} \right) = \frac{4\pi^2}{T_{\text{orb}}^2} \left(3 \frac{\vec{r} \cdot \vec{r}^\top}{r^2} - \frac{\vec{r}^\top \cdot \vec{r}}{r^2} \cdot \mathbb{1}_{3 \times 3} \right) \quad (1.71)$$

where $\mathbb{1}_{3 \times 3}$ is the identity matrix and $T_{\text{orb}} = 2\pi \cdot \sqrt{r^3/GM}$ is the orbital period of a circular orbit at height $|\vec{r}|$. The eigenvalues of \widehat{G}_{PM} are

$$(\|\widehat{G}\|_\infty, -\|\widehat{G}\|_\infty/2, -\|\widehat{G}\|_\infty/2) \quad (1.72)$$

with the matrix norm $\|\widehat{G}\|_\infty \approx 8\pi^2/T_{\text{Orb}}^2 \approx 2.5 \cdot 10^{-6} \text{ s}^{-2}$ for a LEO satellite, which corresponds to the value for the gravity gradient in radial direction. Eq. (1.70) assumes the worst-case coupling along the radial direction and is valid as long as the noise in \vec{r}_E is isotropic, which has been assumed for the GNSS observations (cf. eq. (1.38)). The validity of the simplified model in eq. (1.70) is shown in figure 1.15, where the direct acceleration vector components of a satellite at 400 km orbit height are depicted together with the errors.

The error traces are based on instrument GNSS noise, which is differentiated twice to yield the acceleration noise plus the contribution due to evaluating the acceleration at the wrong position, which is depending on \widehat{G} . The latter is not a direct measurement error but rather a disturbance of the gravity retrieval process that shows up, for example, if post-fit residuals are computed. It is an error in *independent variables* in the context of least-squares estimation. In contrast to *ordinary least squares*, where the independent variables are considered as error-free, the so-called *total least squares estimation* considers errors in both dependent and independent variables and is therefore favored within this thesis. The total least squares estimation uses a modified covariance matrix for data weighting. The error model represented by eq. (1.69) can be understood as covariance information for the total least-squares problem (cf. sec. 1.7.1). However, the difference between a total least-squares and an ordinary least-squares estimation is expected to be rather small for the DA, since the white noise from the independent variables is dominant only for frequencies below 3 mHz.

The signal trace in y direction in figure 1.15 has a lower amplitude level, because the orbital plane is oriented in the xz -plane in the inertial frame in this particular example.

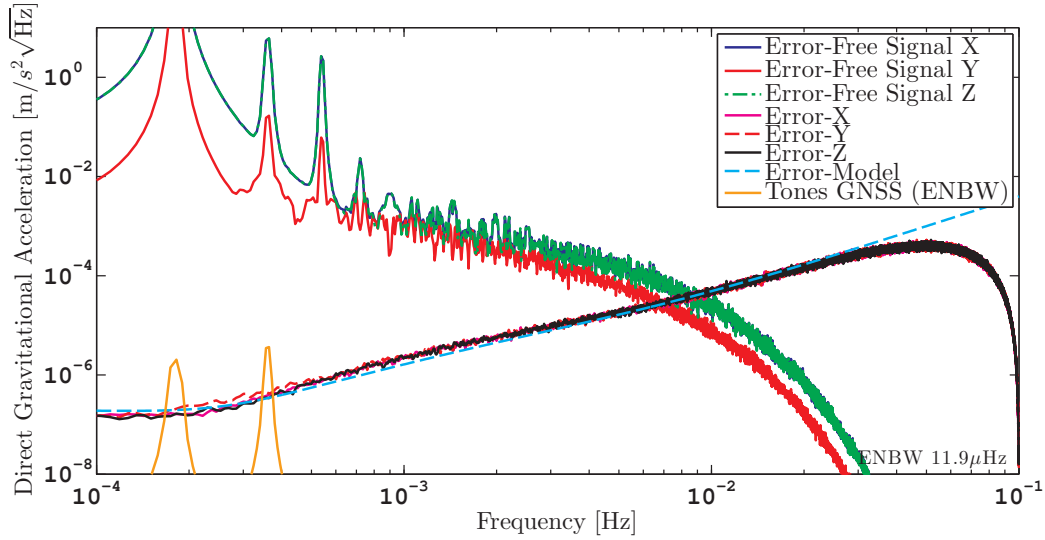


Figure 1.15: ASD of the direct satellite acceleration in x, y and z directions in an inertial frame. The errors in x, y and z in the acceleration induced by position (and according acceleration) errors agree with the model shown as light blue dashed trace. An orbit height of 400 km was used. Only gravitational accelerations from a static field (EGM96) were considered.

1.6.2 Projected Differential Gravitational Acceleration (PDGA)

The procedure of the previous subsection is used to derive the errors for the projected differential gravitational acceleration as well, starting with the error-free expression as given by the left-hand side of eq. (1.13)

$$\delta a_g = \vec{e}_{12T,GRP} \cdot \hat{R} \cdot \vec{\nabla} V_{12T,GRP}, \quad (1.73)$$

where the subscript “T” indicates true (error-free) quantities.

The true line-of-sight vector $\vec{e}_{12T,GRP}$ and the true differential potential $V_{12T,GRP}$ are not accessible and can only be determined from measurements (subscript “M”), thus measurement errors (subscript “E”) are present. Using eq. (1.67) for both satellites and the gravity gradient \hat{G} , one arrives at the following expression, which considers errors in the potential term:

$$\begin{aligned} \delta a_g &= \vec{e}_{12T,GRP} \cdot \hat{R} \cdot \vec{\nabla} V_{12T,GRP} \\ &\approx \vec{e}_{12T,GRP} \cdot \hat{R} \cdot \vec{\nabla} V_{12M} - \vec{e}_{12T,GRP} \cdot \hat{R} \cdot \left(\hat{G}(\vec{r}_{1M}) \cdot \vec{r}_{1E} - \hat{G}(\vec{r}_{2M}) \cdot \vec{r}_{2E} \right). \end{aligned} \quad (1.74)$$

The rotation matrix \hat{R} transforms vectorial quantities from the Earth-fixed to the Space-fixed frame. By introducing directly the inertial quantities with the following tilde-notation, one reduces the complexity of subsequent equations:

$$\vec{\nabla} \tilde{V}_{12} := \hat{R} \cdot \vec{\nabla} V_{12}, \quad (1.75)$$

$$\hat{\tilde{G}} := \hat{R} \cdot \hat{G}. \quad (1.76)$$

To consider errors in the true line-of-sight vector $\vec{e}_{12T,GRP}$, one can exploit that $\vec{e}_{12T,GRP}$ and $\vec{e}_{12M,GRP} = \vec{e}_{12M}$ are normalized and that $\cos(x + \delta x) \approx \cos(x) - \delta x \cdot \sin(x)$, which provides

$$\begin{aligned} \delta a_g &\approx \vec{e}_{12M} \cdot \vec{\nabla} \tilde{V}_{12M} - \vec{e}_{12M} \cdot \left(\hat{\tilde{G}}(\vec{r}_{1M}) \cdot \vec{r}_{1E} - \hat{\tilde{G}}(\vec{r}_{2M}) \cdot \vec{r}_{2E} \right) \\ &\quad - \alpha_E \cdot |\vec{e}_{12M} \times \vec{\nabla} \tilde{V}_{12M}| \end{aligned} \quad (1.77)$$

with the angle $\alpha_E = \angle(\vec{e}_{12M,GRP}, \vec{e}_{12T,GRP})$ denoting the angle between the true LOS and the measured LOS. The magnitude of this angle can be approximated as $|\alpha_E| \approx |\vec{r}_{12E,\perp}|/|\vec{r}_{12M}|$, with $\vec{r}_{12E,\perp}$ being the relative transverse position error w.r.t. the line of sight. The first term in eq. (1.77) is the measured projected differential gravitational acceleration. The next two terms are caused by errors in the position: the second term accounts for errors in the gravitational potential, while the third term accounts for an error in the LOS direction (α_E). It is sufficient to approximate the potential difference \tilde{V}_{12M} (in the third term) and the inertial gravity gradient \hat{G} in eq. (1.77) to first order by a spherical gravity field of a point-mass (PM) Earth, since it is by far the dominating contribution and these quantities are additionally multiplied with small errors terms. For clarity, a subscript ‘‘PM’’ is added to these quantities. One should note that with this approximation, one does not need to express $\tilde{V}_{12M,PM}$ and \hat{G}_{PM} explicitly in terms of SH coefficients \overline{CS} , which one aims to determine later on.

For a spherical gravity field and circular satellite orbits, the expression $|\vec{e}_{12M} \times \vec{\nabla} \tilde{V}_{12M,PM}|$ vanishes. However, it is kept as variable c_α to remind that elliptic orbits or non GRACE-like constellations may lead to a coupling of LOS-direction estimation errors into the PDGA:

$$c_\alpha(t) := |\vec{e}_{12M}(t) \times \vec{\nabla} \tilde{V}_{12M,PM}(t)|. \quad (1.78)$$

Hence, one obtains

$$\delta a_g \approx \vec{e}_{12M} \cdot \vec{\nabla} \tilde{V}_{12M} - \underbrace{\vec{e}_{12M} \cdot \left(\hat{G}_{PM}(\vec{r}_{1M}) \cdot \vec{r}_{1E} - \hat{G}_{PM}(\vec{r}_{2M}) \cdot \vec{r}_{2E} \right)}_{\text{errors}} - \alpha_E \cdot c_\alpha, \quad (1.79)$$

where the errors are often ignored in the literature, because they are contained in the independent variables, e.g. on the left-hand side of a linear equation $\hat{A} \cdot \vec{x} = \vec{b}$.

In the same manner, one can expand the right hand side of eq. (1.13)

$$\begin{aligned} \delta a_g &= \ddot{\rho}_T - (\vec{a}_{ng2,T} - \vec{a}_{ng1,T}) \cdot \vec{e}_{12T} - X_T \\ &= \ddot{\rho}_M - \ddot{\rho}_E - (\vec{a}_{ng2,M} - \vec{a}_{ng1,M}) \cdot \vec{e}_{12M} + (\vec{a}_{ng2,E} - \vec{a}_{ng1,E}) \cdot \vec{e}_{12M} \\ &\quad + |\vec{e}_{12M} \times (\vec{a}_{ng2,M} - \vec{a}_{ng1,M})| \cdot \alpha_E - X_M + X_E, \end{aligned} \quad (1.80)$$

where the centrifugal part is kept in the variable ‘‘X’’. By combining eq. (1.77) and eq. (1.80) and collecting all error terms one ends up with

$$\begin{aligned} \text{PDGA}(t) &= \ddot{\rho}_M - a_{ng2,M,LOS} + a_{ng1,M,LOS} - X_M \\ &\quad - \ddot{\rho}_E + a_{ng2,E,LOS} - a_{ng1,E,LOS} + |\vec{e}_{12M} \times (\vec{a}_{ng2,M} - \vec{a}_{ng1,M})| \cdot \alpha_E \\ &\quad + \vec{e}_{12M} \cdot \left(\hat{G}_{PM}(\vec{r}_{1M}) \cdot \vec{r}_{1E} - \hat{G}_{PM}(\vec{r}_{2M}) \cdot \vec{r}_{2E} \right) + \alpha_E \cdot c_\alpha + X_E. \end{aligned} \quad (1.81)$$

The first line contains the pure measurements. The two other lines are error terms in the observations. The measurement of the centrifugal part denoted as X_M and the error in the measurement X_E may be expressed in three different ways, based on eqs. (1.13), (1.15) and (1.16) as discussed in sec. 1.3.3

$$X_M^{(1)} = \frac{|\dot{\vec{r}}_{12M}|^2}{\rho_M} - \frac{\dot{\rho}_M^2}{\rho_M} \quad (1.82)$$

$$\begin{aligned} X_E^{(1)} &= -\rho_E \cdot \left(\frac{|\dot{\vec{r}}_{12M}|^2}{\rho_M^2} - \frac{\dot{\rho}_M^2}{\rho_M^2} \right) + 2 \cdot |\dot{\vec{r}}_{12E}| \cdot \frac{|\dot{\vec{r}}_{12M}|}{\rho_M} - 2 \cdot \dot{\rho}_E \cdot \frac{\dot{\rho}_M}{\rho_M} \\ &= -\rho_E \cdot \frac{X_M^{(1)}}{\rho_M} + 2 \cdot |\dot{\vec{r}}_{12E}| \cdot \frac{|\dot{\vec{r}}_{12M}|}{\rho_M} - 2 \cdot \dot{\rho}_E \cdot \frac{\dot{\rho}_M}{\rho_M} \end{aligned} \quad (1.83)$$

$$X_M^{(2)} = |\vec{\omega}_{LOS,M}|^2 \cdot \rho_M \quad (1.84)$$

$$X_E^{(2)} = 2 \cdot |\vec{\omega}_{LOS,M}| \cdot \rho_M \cdot |\vec{\omega}_{LOS,E}| + |\vec{\omega}_{LOS,M}|^2 \cdot \rho_E \quad (1.85)$$

$$X_M^{(3)} = 2 \cdot \frac{E_{1M} + E_{2M} - 2\sqrt{E_{1M} \cdot E_{2M}} \cos(\beta_M)}{\rho_M} - \frac{\dot{\rho}_M^2}{\rho_M} \quad (1.86)$$

with

$$E_{iM} = V(\vec{r}_{iM}) + (\vec{\omega}_e \times \vec{r}_{iM}) \cdot \dot{\vec{r}}_{iM} + \int_{t_0}^t \vec{a}_{ng,iM} \cdot \dot{\vec{r}}_{iM} dt - E_{cM}, \quad i \in \{1, 2\} \quad (1.87)$$

$$\beta_M = \nabla(\dot{\vec{r}}_{1M}, \dot{\vec{r}}_{2M}). \quad (1.88)$$

A rigorous derivation of the error for the energy-based centrifugal term $X_E^{(3)}$ is not given here, since it is cumbersome with lengthy expressions. As will be seen subsequently, all three representation are dominated by GNSS velocity errors. Other authors have also shown that energy-based gravity field retrieval is dominated by GNSS velocity errors [Jekeli, 1999; Visser *et al.*, 2003]. To improve readability, all error terms are numbered as T_i by rewriting eq. (1.81)

$$\text{PDGA}(t) = \ddot{\rho}_M - a_{ng2,M,LOS} + a_{ng1,M,LOS} - X_M + \sum_i T_i. \quad (1.89)$$

An approximative noise model for the PDGA is provided as

$$\text{PSD}[\text{PDGA}_E](f) = \sum_i \text{PSD}[T_i], \quad (1.90)$$

where the single terms are summarized in table 1.3 and visualized for a typical parameter set in figure 1.16. The ranging noise term has been complemented by scale factor variations, as discussed in sec. 1.4.2

$$\ddot{\rho}_E(t) \longrightarrow \ddot{\rho}_E(t) + \mathcal{S}_{DC}^{(IFO)} \cdot \ddot{\rho}_M(t). \quad (1.91)$$

Furthermore the accelerometer measurement Γ_i on the i -th S/C has replaced $\vec{a}_{i,ng}$ and is supplemented with scale factor terms, as discussed in sec. 1.4.3,

$$a_{ng,i,E,LOS}(t) \approx \Gamma_{i,E,LOS}(t) + \mathcal{S}_{DC,i,E}^{(ACC)} \cdot \Gamma_{i,M,LOS}(t) + \mathcal{S}_{AC,i,E}^{(ACC)}(t) \cdot \Gamma_{i,M,LOS}(t). \quad (1.92)$$

In many studies on future geodesy missions, in particular in the ones which are based on quick-look simulations, only the first two terms from the table 1.3 are considered: T_1 , the ranging noise along the LOS, and T_2 , the accelerometer noise along the LOS. For GRACE- and GRACE Follow-On-like sensitivity levels, this might be sufficient. However, for further advanced missions it is not sufficient to simply state that an decrease in ranging and accelerometer noise yields a better gravity field, as complex interdependencies start to play a role.

One should note that the centrifugal part of the PDGA decreases faster with frequency than the ranging part (solid black and dark blue traces in figure 1.16). All three methods to describe the baseline centrifugal acceleration (M1, M2, M3) yield the same precision for the centrifugal acceleration (red, green and black dots overlap in the plot). The precision is determined by GNSS (velocity) errors. The analytic noise models for the centrifugal term, eqs. (1.83) and (1.85) shown as solid red and dashed dark blue traces, agree well with the numerical data (red, green and black dots in figure 1.16). A unity signal-to-noise ratio for the centrifugal acceleration is reached at ≈ 10 mHz in figure 1.16.

Position uncertainties of the kinematic GRP, as assumed in eqs. (1.38) and (1.58), lead to a non-negligible effective noise of the order of $10^{-8} \text{ m/s}^2 \sqrt{\text{Hz}}$ in the PDGA measurement (green trace T_4). It arises due to the fact that the evaluation point (position) of the SH gravity field is fluctuating and is an error in the *independent variable* in the context of least-squares adjustment. One has to use the GRP as defined in sec. 1.5 instead of the GNSS position for the evaluation of the gravity field, if one wants to utilize precise ranging observables, because the GNSS errors along the LOS are significantly higher than the ranging noise. T_5 is also an error in the independent variable and is caused by inaccuracies in the measured LOS direction, as well as T_3 , which is coupling non-gravitational accelerations into the PDGA.

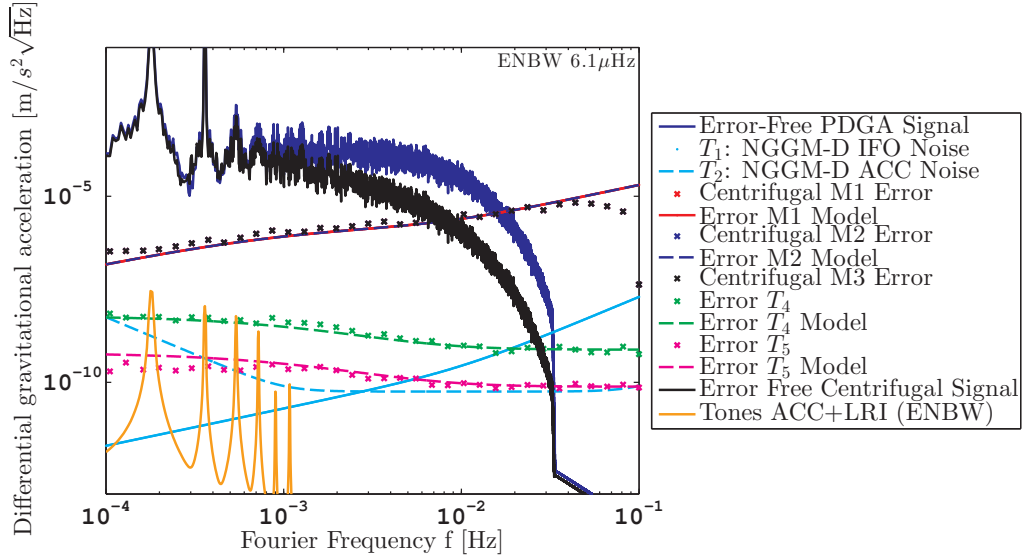


Figure 1.16: Spectral density of the PDGA signal and error contributions for an orbit height of 400 km and $L = 200$ km. Non-gravitational accelerations have been omitted. The upper dark blue and dashed black trace indicate the PDGA signal and the centrifugal acceleration, respectively. The centrifugal acceleration is part of the PDGA signal. The measurement error in the centrifugal acceleration for all methods (M1, M2, M3) is the same (overlap in the plot) and crosses the centrifugal acceleration signal at roughly 10 mHz. The green traces show the error contribution from orbit position errors (T_4), which is also above the instrument noise of accelerometer and interferometer proposed in the NGGM-D (e.motion²) study. Traces labeled with *model* are the simplified analytic expressions from table 1.3.

T_7 describes the uncertainty in the absolute knowledge of frequency or wavelength of the ranging instrument, which relates the phase measurement to a physical length. T_8 accounts for the similar scale factor uncertainty in the accelerometer. T_9 considers fluctuations of the accelerometer scale factor within the measurement band and should actually be covered by requirements on instrument level as in the LRI. T_{10} is the effect of an offset in the unbiased ranging observable (cf. eq. (1.59)), which is typically negligible, as it is of the order of $\Delta L/L \approx 10^{-7}$. Thus, it is smaller than the DC scale factor uncertainty of the ranging interferometer, which will be discussed in the second part of this thesis. T_7, T_8, T_9, T_{10} are not shown in figure 1.16 for the sake of readability.

Furthermore, one can conclude that the here presented analytic (simplified) PSD models in table 1.3 match the PSDs from numerical (time-series) data in figure 1.16.

The sensitivity of the direct acceleration (DA) is limited by GNSS errors. This is expected, since the gravity field is derived from the orbit trajectory and accelerometer data is only used to correct for non-gravitational effects. However, in the analysis so far the PDGA approach cannot utilize its precise ranging or accelerometer measurement, due to the noise in the centrifugal acceleration term caused by inaccuracies of kinematic orbits (denoted within this thesis often as GNSS or GRP position noise). For energy-based gravity field retrieval, this error is usually expressed in terms of velocity. Expressing the centrifugal term in terms of the baseline angular velocity did not provide better results, since the baseline angular velocity $\vec{\omega}_{\text{LOS}}$ is determined most precisely by means of GNSS (cf. section 1.5.1). This is the reason why in-situ approaches such as the acceleration approach or energy-balance approach cannot be applied directly to data processing of real missions, as mentioned in sec. 1.3.3.

In the next section, many noise contributors are reduced by utilizing reduced-dynamic orbits, which have been introduced in sec. 1.5.2.

i	Term description	Time-Domain T_i	Spectral Domain, approx. $\text{PSD}[T_i]$
1	Ranging Noise, 2nd time derivative	$-\ddot{\rho}_E$	$(2\pi f)^4 \cdot \text{PSD}[\rho_E]$
2	Accelerometer Noise along LOS	$+\Gamma_{2,E,LOS} - \Gamma_{1,E,LOS}$	$2 \cdot \text{PSD}[\Gamma_{E,LOS}]$
3	LOS error into non-grav. acc.	$ \vec{e}_{12M} \times (\vec{\Gamma}_{2,M} - \vec{\Gamma}_{1,M}) \cdot \alpha_E$	$\frac{4 \cdot \Gamma_{DC}^2}{\rho_{DC}^2} \cdot \text{PSD}[r_{E,GNSS}]$
4	GRP position error in potential	$\vec{e}_{12M} \cdot \hat{\hat{C}}_{PM}(\vec{r}_{1M}) \cdot \vec{r}_{1E}$ $-\vec{e}_{12M} \cdot \hat{C}_{PM}(\vec{r}_{2M}) \cdot \vec{r}_{2E}$	$\frac{4GM^2 \rho_{DC}^2}{R_{orb}^8} \cdot \text{PSD}[r_{E,GNSS}]$
5	LOS error in grav. potential	$\alpha_E \cdot c_\alpha$	$\frac{2c_{\alpha,DC}^2}{\rho_{DC}^2} \cdot \text{PSD}[r_{E,GNSS}]$
6a	Centrifugal acc. error M1	$X_E^{(1)}$ from eq. (1.83)	$\frac{128\pi^4 f^2}{T_{orb}^2} \cdot \text{PSD}[r_{E,GNSS}]$
6b	Centrifugal acc. error M2	$X_E^{(2)}$ from eq. (1.85)	$\frac{16\pi^2 \cdot \rho_{DC}^2}{T_{orb}^2} \cdot \text{PSD}[\omega_{E,LOS}]$
7	Ranging DC-scale error	$-\mathcal{S}_{DC,E}^{(FO)} \cdot \ddot{\rho}_M$	$\left(\mathcal{S}_{DC,E}^{(FO)}\right)^2 \cdot (2\pi f)^4 \text{PSD}[\rho_M]$
8	Accelerometer DC scale factor error	$\mathcal{S}_{DC,E}^{(ACC)} \cdot \Gamma_{2,M,LOS}$ $-\mathcal{S}_{DC1,E}^{(ACC)} \cdot \Gamma_{1,M,LOS}$	$2 \cdot \left(\mathcal{S}_{DC,E}^{(ACC)}\right)^2 \cdot \text{PSD}[\Gamma_{M,max,LOS}]$
9	Accelerometer AC scale factor variations	$\mathcal{S}_{AC2,E}^{(ACC)} \cdot \Gamma_{2,M,LOS}$ $-\mathcal{S}_{AC1,E}^{(ACC)} \cdot \Gamma_{1,M,LOS}$	$2 \cdot \text{ACC}_{DC,M,LOS} \cdot \text{PSD}[\mathcal{S}_{AC,E}^{(ACC)}]$
10	Ranging Bias Error	$\text{PDGAM} \cdot \frac{\Delta L}{L}$	$\text{PSD}[\text{PDGAM}] \cdot \frac{\Delta L}{L}$

Table 1.3: Error terms of the projected differential gravitational acceleration (PDGGA) and dominating power spectral densities (PSD) for a GRACE-like configuration. R_{orb} is the orbit height w.r.t. the geocenter. T_{orb} is the orbital period given by $T_{orb} = 2\pi \cdot \left(\frac{GM}{(6371 \text{ km} + R_{orb})^3}\right)^{-1/2}$. The assumed GNSS noise $\text{PSD}[r_{E,GNSS}]$ is given in eq. (1.38).

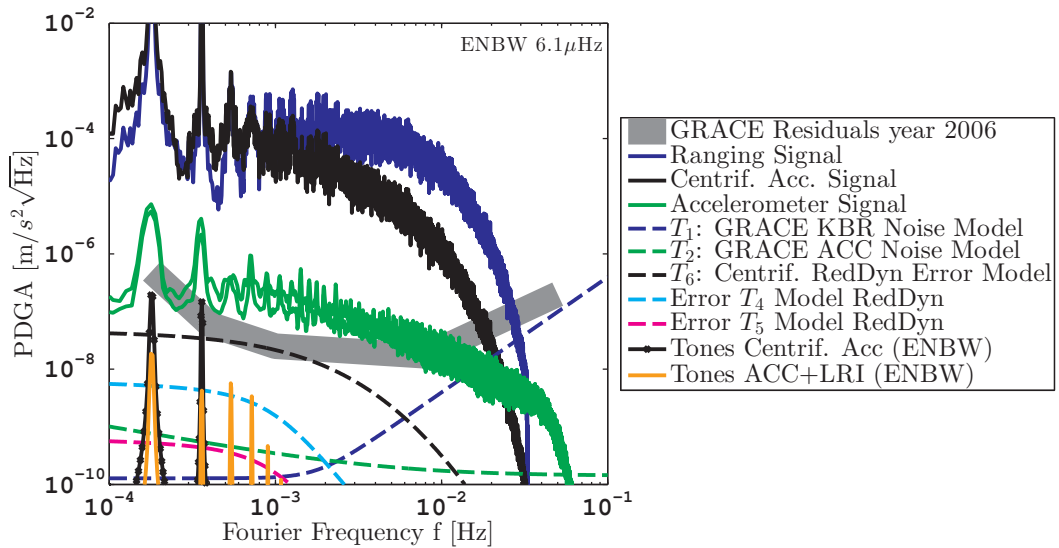


Figure 1.17: Spectral density of the PDGA signal and error contributions for an orbit height of 400 km and $L = 200$ km. The PDGA signal is composed of the sum of ranging, centrifugal acceleration and non-gravitational accelerations shown as solid dark blue, black and green traces, respectively. Two green traces are depicted to indicate the signal variability between different days and are direct plots of the GRACE Level-1B accelerometer data. The observation noise of each contribution is shown as dashed dark blue, black and green line. The gray thick line roughly indicates the GRACE (post-fit) residuals for the year 2006 as given in [Ditmar *et al.*, 2012]. The light blue and magenta traces are additional error contributions, as given in table 1.3. The model of the centrifugal acceleration and position noise is based on reduced-dynamic short arcs, as discussed in section 1.5.2.

1.6.3 Revised PDGA Sensitivity

Figure 1.16 is reproduced with GRACE instrument noise levels instead of with e.motion² noise levels by utilizing the models from sec. 1.3.3. The results and additionally the real GRACE residuals as given in [Ditmar *et al.*, 2012] are plotted in figure 1.17. These post-fit residuals can be compared to the noise models.

It is noted that the residual noise in GRACE for frequencies between 0.2 mHz and 2 mHz can be explained by errors in the centrifugal term (dashed black trace in figure 1.17), which are due to the limited accuracy of force models, in particular of the gravitational background models. Such inaccuracies also manifest as an error in the precise orbit determination (position and velocity of satellites). However, the noise model is based on the simple assumption that the background models are as good as the monthly mean gravity signal (for SH degrees < 60). A more precise analysis would require the assessment of the errors in actual background models and propagating them into short arcs of reduced-dynamic satellite orbits. Also, stationarity of the signals needs to be considered. Such an analysis is beyond the scope of this section.

Frequency regions higher than approximately 14 mHz are dominated by microwave ranging instrument noise, as also stated in [Ditmar *et al.*, 2012]. Particularly, above 30 mHz, the ranging signal should contain only noise, since gravitational and non-gravitational signals are below the noise level. The noise in GRACE residuals for intermediate frequencies, roughly between approximately 2 mHz and 14 mHz, cannot be explained by the models derived in this thesis. Ditmar *et al.* [2012] also assigned the noise in this region to *unknown physical origin*. The excess noise observed at the orbital frequency of 0.18 mHz is likely caused by deterministic excitation and tone errors of all instruments.

1.7 Gravity Field Recovery

In the previous section 1.6, the error and noise terms in the projected differential gravitational acceleration (PDGA) as well as in the direct satellite acceleration (DA) were analyzed, which are used to derive Earth's gravity field. In this section, the different noise contributions are assessed at the level of spherical harmonics.

1.7.1 Method

In this thesis a linear relation between the gravity field SH coefficients \overrightarrow{CS} and the measurement vector \overrightarrow{M} , either the PDGA or the DA, is utilized

$$\overrightarrow{M} = \hat{D} \cdot \overrightarrow{CS}, \quad (1.93)$$

where each element of the vector \overrightarrow{M} is a measurement at a particular epoch. The matrix \hat{D} is the design matrix. The well-known ordinary least-squares (LSQ) solution obtained by inverting the normal matrix $\hat{N} = \hat{D}^\top \hat{D}$ yields

$$\overrightarrow{CS}_{\text{LSQ}} = \hat{N}^{-1} \cdot \hat{D}^\top \cdot \overrightarrow{M}, \quad (1.94)$$

which minimizes the Euclidean norm of (post-fit) residuals

$$\|\hat{A} \cdot \overrightarrow{CS}_{\text{LSQ}} - \overrightarrow{M}\|^2. \quad (1.95)$$

This least-squares solution is a so-called *best linear unbiased estimate* (BLUE, cf. Gauss-Markov-Theorem) if the noise in the measurement vector \overrightarrow{M} is uncorrelated, i.e. Gaussian white, with variance σ^2 and vanishing mean. The (co-)variance matrix of estimates $\hat{C}_{\text{fit}} = \sigma^2 \cdot \hat{N}^{-1}$ [Björck, 1996, p. 4] contains the variances for each fit parameter, i.e. SH coefficients, on the diagonal as well as the co-variance information as off-diagonal elements.

If the noise in the measurement vector is correlated, one can obtain a BLUE by considering the (co-)variance matrix \hat{C}_M of measurements/observations. The LSQ solution is then given as the weighted least squares solution [Gans, 1992, p. 28]

$$\overrightarrow{CS}_{\text{LSQ}} = \left(\hat{D}^\top \cdot \hat{W} \cdot \hat{D} \right)^{-1} \hat{D}^\top \cdot \hat{W} \cdot \overrightarrow{M}, \quad (1.96)$$

with the weight matrix $\hat{W} = \hat{C}_M^{-1}$ and the (co-)variance matrix of estimates as $\hat{C}_{\text{fit}} = \left(\hat{D}^\top \cdot \hat{W} \cdot \hat{D} \right)^{-1}$. A drawback of the ordinary LSQ is the assumption of an error-free design matrix \hat{D} , which is derived from error-free *independent variables*. By using the total least-squares estimation, also errors in the independent variables can be considered. Then the weight matrix is complemented by (co-)variance information of the independent variables \hat{C}_{IV} [Gans, 1992, p. 33]

$$\hat{W} = \left(\hat{K}_M \cdot \hat{C}_M \cdot \hat{K}_M^\top + \hat{K}_{\text{IV}} \cdot \hat{C}_{\text{IV}} \cdot \hat{K}_{\text{IV}}^\top \right)^{-1}, \quad (1.97)$$

where the matrices \hat{K} contain partial derivatives, such that \hat{K}_M is the identity matrix for a linear problem as discussed here (eq. (1.93)).

Usually, additional assumptions and simplifications are applied, such that the weight matrix \hat{W} becomes a Toeplitz form or sparse, which can simplify computations. Alternatively, various methods exist to estimate the measurement (co-)variance matrix iteratively by analysis of post-fit residuals (cf. Variance Component Estimation [Kusche, 2003; Mayer-Gürr, 2006] [Liu, 2008, sec. 3.4]). Additionally, decorrelation of (post-fit) SH coefficients is widely used [Kusche, 2007; Kusche *et al.*, 2009], e.g. since an estimation of the measurement co-variance matrix in the presence of errors in the time-variable gravity background models is non-trivial.

Also striping in GRACE gravity field maps is associated with correlations of SH and can be reduced by decorrelation filtering [Swenson & Wahr, 2006].

It is noted that the measurement (co-)variance matrix can contain information on stochastic as well as on non-stochastic errors. The latter ones could be caused for example by tone errors in the instruments.

1.7.2 Handling Tone Errors in Gravity Field Recovery

Tone errors have been introduced in section 1.4.5 and are sinusoidal errors in measurements. Tone errors cannot be treated with the same means as noise, since noise is a stochastic process and tone errors are deterministic errors, which, for example, do not average out. Different ways for mitigation of tones in gravity field recovery are sketched here:

- **Correction of data in pre-processing:** If the exciting physical process variables (e.g. temperature) are measured or can be deduced from background models and if the a-priori coupling factor knowledge is sufficient, the corresponding data streams can be corrected in pre-processing for tone effects.
- **Fitting of tone amplitudes:** If knowledge of the tones is insufficient, tone amplitudes can be fitted together with SH coefficients. Ideally, tone errors with a drifting phase should be considered. Such an approach can absorb the combined error of several instruments and the post-fit (co-)variance matrix provides correlations between the tones and particular SH coefficients. Such correlations are expected, since for example the zonal coefficients have most of their signal at integer multiples of the orbital frequency, as shown for $C_{2,0}$ and $C_{52,0}$ in figure 1.5.
- **Notching of frequencies:** By assuming a high stochastic noise at tone frequencies as (a-priori) instrument (co-)variance information, signals at these frequencies are down-weighted in the gravity field recovery. Although it is not the correct way of handling deterministic errors, it may still provide sufficient results and does not require additional parameters to be fitted.

In this thesis, the second approach of these approaches, fitting of tone amplitudes, is exploited, which basically declares the tone errors as a type of signal one aims to recover together with SH coefficients. Since errors in the time-variable background models are considered in the form of a simplified stochastic model, the (co-)variance information for the DA or PDGA measurement can be described by stochastic means, in particular in terms of PSDs. Whitening filters (cf. [Monsky, 2010, sec. 4.6.5]) are used in this thesis for decorrelating the measurements and the design matrix before constructing and inverting the normal matrices.

Since the sensitivity models derived in section 1.6 contain also the errors due to independent variables, e.g. the gravity gradient term in eq. (1.70) and the T_4 term in table 1.3, the weighting filter uses the (co)variance information from eq. (1.97). Thus, the SH coefficient estimation is performed in a total least-squares sense.

1.7.3 Results: Direct Acceleration (Single Satellite)

The gravity fields obtainable from pure kinematic orbits (no dynamic POD) of one polar satellite at 400 km height with repeat cycle $\beta/\alpha = 466/30$ are shown in figure 1.18 for a typical 30-day solution with $30 \cdot 86400 \text{ s} \cdot 0.2 \text{ Hz} \cdot 3 \approx 1.5 \cdot 10^6$ observations (all xyz components). The lowest trace is a sanity check and is a closed-loop simulation without any measurement errors. The trace has been enhanced by a factor of 10^6 to improve readability of the figure. Considering GNSS noise as shown in figure 1.15 yields traces with an error of 5 mm at degree 30, which is comparable to results from [Zehentner & Mayer-Gürr, 2013] shown as black crosses. When noise whitening (decorrelation of measurements) is used, reasonable results are obtained for the formal errors (magenta dashed trace), which coincide with the true errors

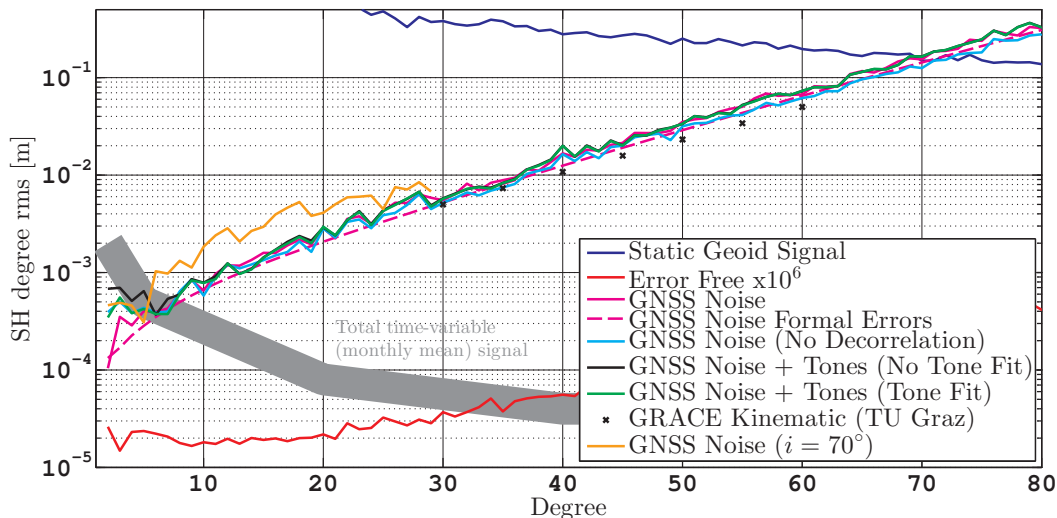


Figure 1.18: Geoid rms-error per SH degree for gravity fields from kinematic trajectory (direct acceleration, HL-SST) of a single polar satellite at $h = 400$ km. The thick time-variable gravity field trace has been replotted from fig. 1.3.

(magenta solid) as one would expect. In particular, the very low SH degrees improve, since they gain weight in the fit due to the low noise of the measurement at low frequencies. If tone errors are included in the GNSS measurement, the low degree coefficients degrade (black solid trace), in particular the C20 coefficient. The tones at $1/\text{rev}$ and $2/\text{rev}$ frequency have a high correlation with the C20 and other zonal coefficient, as one can already see on figure 1.5 on page 13 and by evaluating the inverse normal matrix, if tone amplitudes are a fit parameter (cf. fig. 1.19). The error in the C20 coefficient without tones is $\approx 9 \cdot 10^{-12}$, while tones with 4 mm amplitude increase the error to above 10^{-10} . Fitting tone amplitudes together with SH coefficients reduces the error by a factor of 2 in the simulations performed here.

It is well known that monthly GRACE gravity field solutions cannot resolve the C20 coefficient very well and it is recommended to obtain this coefficient from SLR measurements based on multiple satellites [Cheng *et al.*, 2011]. Due to geophysical effects, the C20 coefficient oscillates with annual and semi-annual periods with an amplitude of approx. 10^{-10} [Chen & Wilson, 2008]. Errors in the tide background models, in particular in the solar tide S_2 constituent, are supposed to appear aliased at these frequencies and complicate retrieval of this signal [Ray *et al.*, 2003; Chen *et al.*, 2009]. One should note that also the β' angle, the angle between sun vector and orbital plane, changes with semi-annual period. This likely leads to cyclic thermal changes at semi-annual and annual periods and possibly modulating tone errors within GNSS, KBR and ACC at these periods. Also the decreased sensitivity of monthly C20 estimates [Ogawa, 2010, Fig. 2.3] could be produced by tone errors at $1/\text{rev}$ and $2/\text{rev}$ frequency, as pointed out here. It might be beneficial to evaluate if GRACE gravity fields based on pure kinematic orbits exhibit the same degraded sensitivity for C20 as the full solutions containing PDGA and DA information to pinpoint the origin of the decreased sensitivity for C20.

Adding kinematic information from a second (close-by) satellite would reduce the rms of SH coefficients by a factor of $\sqrt{2}$ in figure 1.18 (not shown), since the number of observations is doubled. A 70° inclined satellite, e.g. of the Bender configuration as proposed in the e.motion² study, shows degraded sensitivity for a global gravity field (orange trace) due to the polar gaps.

A non-polar mission will in general show poor global SH geoid rms values and the metric should be adopted, e.g. a latitude dependent weighting in the spatial domain could be used. In addition, regularization methods are required, since the least-squares adjustment of SH

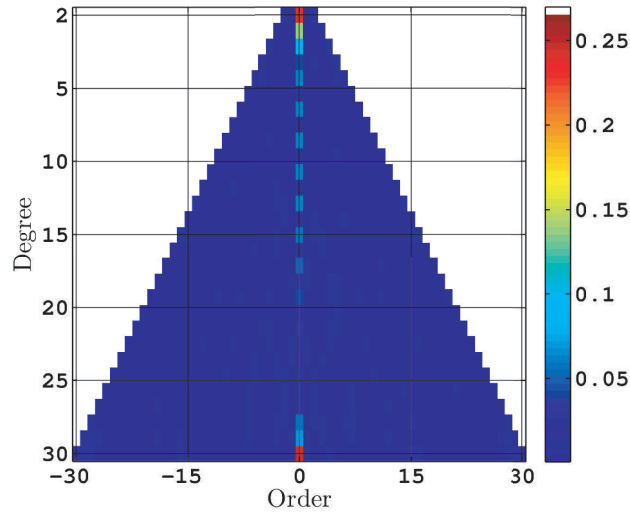


Figure 1.19: Correlations between SH coefficients and twelve tone fit parameters t_i , which are sine and cosine components in x, y and z direction for frequencies at once and twice the orbital frequency. For each SH coefficients α in the triangular plot, the color value in the plot has been computed as $\sqrt{\sum_{i=1}^{12} \text{cov}(\alpha, t_i)^2 / (\text{cov}(\alpha, \alpha) \cdot \text{cov}(t_i, t_i))}$ from the inverse normal matrix. Negative orders denote S coefficients, while positive orders denote C coefficients.

coefficients (up to high degrees) is ill-posed for a non-polar satellite [van Lonkhuyzen *et al.*, 2002]. Therefore, the scenario described by the orange trace considered only a gravity field up to degree 30, since it was solvable without regularization.

1.7.4 Results: Single Pair

The sensitivity of the direct acceleration (HL-SST) allows to retrieve the geoid at degree 10 with approximately 1 mm rms-error, while degree 35 has an rms-error of 1 cm in figure 1.18. The PDGA sensitivity in terms of geoid error is shown in figure 1.20 for different individual noise contributions. The ranging instruments (KBR or LRI, black traces) show the lowest noise. The accelerometer noise is comparable to the noise induced by uncertainties in the LOS direction, denoted as T_5 within this thesis, which is in good agreement with figure 1.16 on page 43. The uncertainties in the GRP position, mainly caused by GNSS (kinematic) errors and imprecision in background gravity field models, picked up via the (reduced-) dynamic orbit determination, are denoted as T_4 (solid magenta trace). Keeping this in mind, a comparison with results from [e.motion² Team, 2014, Fig. 7-22] reveals that other gravity retrieval approaches from different institutes yield a similar geoid rms-error of 0.1 mm for degree 90, if errors in background-models are omitted.

The geoid errors from the uncertainty in the centrifugal acceleration is dominating in figure 1.20. Recall, that this error was modelled based on (reduced-) dynamic orbits and an assumption for the knowledge of the background models. Often, as in the e.motion² study, the analysis of GRACE-like mission studies starts with simplified simulations, which do not consider background model errors, and is concluded with realistic (full-scale) simulations, which consider background model errors. Comparison with [e.motion² Team, 2014, Fig. 7-23] for the two-satellite case shows that the centrifugal acceleration error model used here is in agreement with the results from full-scale simulations, given by 0.1 mm at degree 15 and 2 mm at degree 90.

Although the centrifugal acceleration error rolls off quickly between 1 mHz and 10 mHz in figure 1.17, it still spoils high degrees of SH in gravity field solutions. One should keep in mind that noise at high frequencies degrades only the high SH degree coefficients. However, noise at low frequencies affects both low and high SH degree coefficients (cf. figure 1.5 on

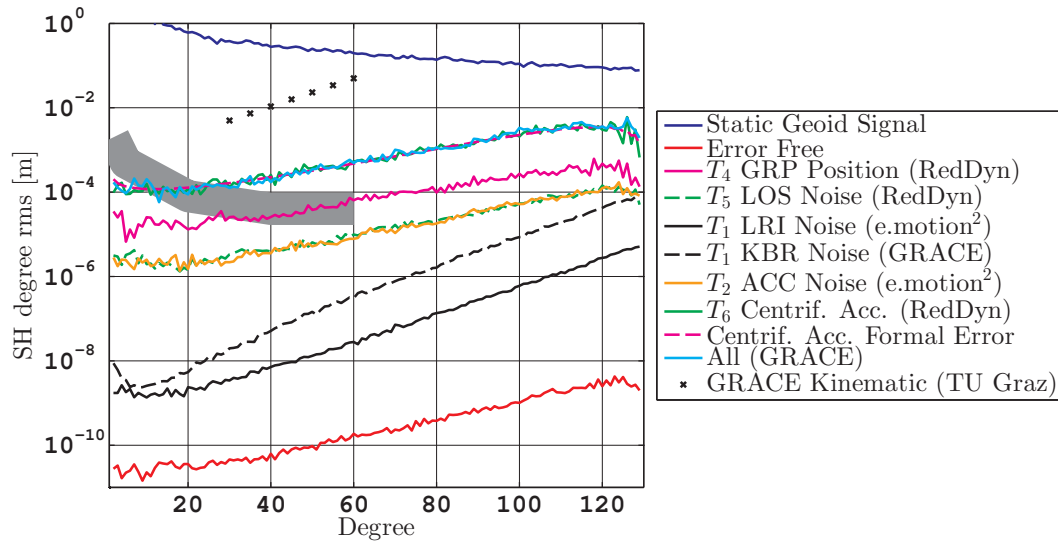


Figure 1.20: Geoid rms-error per SH degree for gravity fields from projected differential gravitational acceleration (PDGA, LL-SST) of a polar GRACE-like pair with 400 km orbit height, 200 km spacecraft separation and with $\beta/\alpha = 466/30$ repeat-orbit. The thick gray trace denotes the time-variable monthly gravity field and has been replotted from fig. 1.3. The different traces labeled T_i refer to the error terms from table 1.3 on page 44.

page 13).

Tone errors in the PDGA as shown in figure 1.17 on page 45 yield an error of $\approx 0.6 \cdot 10^{-10}$ in the C20 coefficient (not shown in the plots), which is roughly of the same order of magnitude as the geophysical signal. However, if tone amplitudes are fitted together with SH coefficients, the error could be reduced by a factor of 2. The free parameters are the tone amplitude and phase, but both parameter are considered to be constant over one month of data.

The dependency of geoid errors on orbit height and S/C separation is illustrated in figure 1.21, which considers the instrument and noise models within this thesis. For higher S/C altitude, the higher SH degree coefficients start to degrade, while a shorter S/C separation increases the error in all degrees. Combination of PDGA and DA information on the level of normal equations improves the gravity field solution slightly for SH degrees between 20 and 60, although the geoid error of pure DA observations is always higher than the PDGA error (cf. figure 1.18). However, as shown by the red trace in figure 1.21, the DA noise falsifies the geoid slightly at high SH degrees above 100, which might be caused in this thesis by non-optimal data weighting and decorrelation.

1.7.5 Results: Dual (Bender) Pair

The results for the single polar pair constellation obtained in this thesis are compatible with the results from the e.motion² study obtained by various institutes. Finally, the gravity field results from the combination of two satellite pairs in a Bender configuration are shown in figure 1.22. The results are obtained by combining the normal matrices and are compared to full-scale simulations from the e.motion² study. The magenta traces are the results for a single polar pair from the previous section. Adding information from an additional 70° inclined satellite pair does not simply improve the noise in the gravity field by a factor of $\sqrt{2}$ but rather by an order of magnitude in the shown root-mean-square error per SH degree. For SH degrees between 20 and 60, the geoid error is at 0.02 mm and comparable with the e.motion² results.

Unfortunately, for higher SH degrees, the approach followed here to consider background model errors as a stationary noise within the centrifugal acceleration with a particular PSD

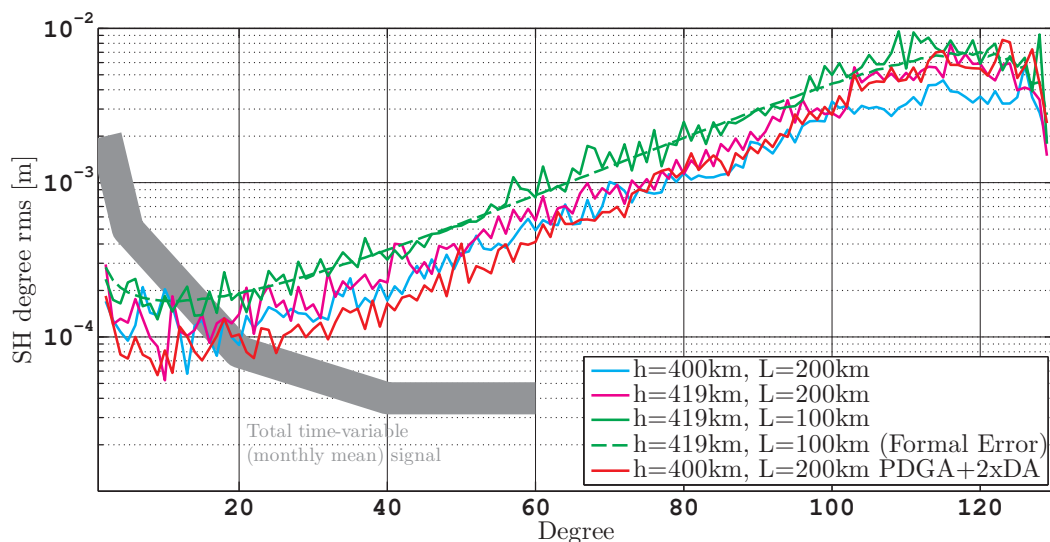


Figure 1.21: Geoid rms-error per SH degree from PDGA measurement of a single polar pair for different orbit heights (h) and spacecraft separation (L). All traces contain accelerometer, ranging and centrifugal acceleration noise. The red trace indicates the combination of PDGA and DA measurements from both satellites.

produces too optimistic results. One main outcome of the e.motion² study was the feasibility of 1 mm geoid rms error at degree 130 for the suggested Bender configuration, whereby the results here show 0.2 mm geoid error at SH degree 130. However, this circumstance has not yet been investigated further.

1.7.6 Discussion

The previous sections contain a derivation of the gravity field measurement from first principles. The sensitivity of the main instruments was discussed together with methods to obtain baseline state quantities from measurements. From these an error analysis of the projected differential gravitational acceleration (PDGA or LL-SST) and of the direct acceleration (DA, HL-SST) was performed. Finally, the sensitivity was transferred to the level of SH coefficients, yielding an end-to-end simulation.

It was shown that a Bender configuration, as proposed in the e.motion² study, significantly reduces the errors in Earth gravity field estimates compared to a single pair mission. Furthermore, aspects such as the ability to determine the C20 coefficient were addressed. The acceleration approach was favored in the analysis, because it establishes a linear relation between observations and SH coefficients. This linearity leads also to a straightforward error propagation from observations to gravity field. However, the drawback of the acceleration approach is a deficiency in the centrifugal acceleration term. It was stated that the centrifugal acceleration term can be written in terms of a transverse relative velocity, in terms of the baseline angular velocity $\vec{\omega}_{\text{LOS}}$ or in terms of energy. However, all three representations turned out to be equivalent.

To overcome the issue, the derivation of more precise orbits, i.e. reduced dynamic orbits, is inevitable but requires a-priori information of the force models and of the (instantaneous) gravity field. The problem of gravity field determination needs to be solved in combination with precise orbit determination (POD). This entanglement complicates the analysis, since errors in the POD and of the gravity background models propagate into other quantities such as the S/C position and then finally into the final gravity field solution in a non-trivial way. However, it is indisputable that gravity field retrieval in combination with precise orbit determination can provide high resolution gravity maps, as has been demonstrated even in

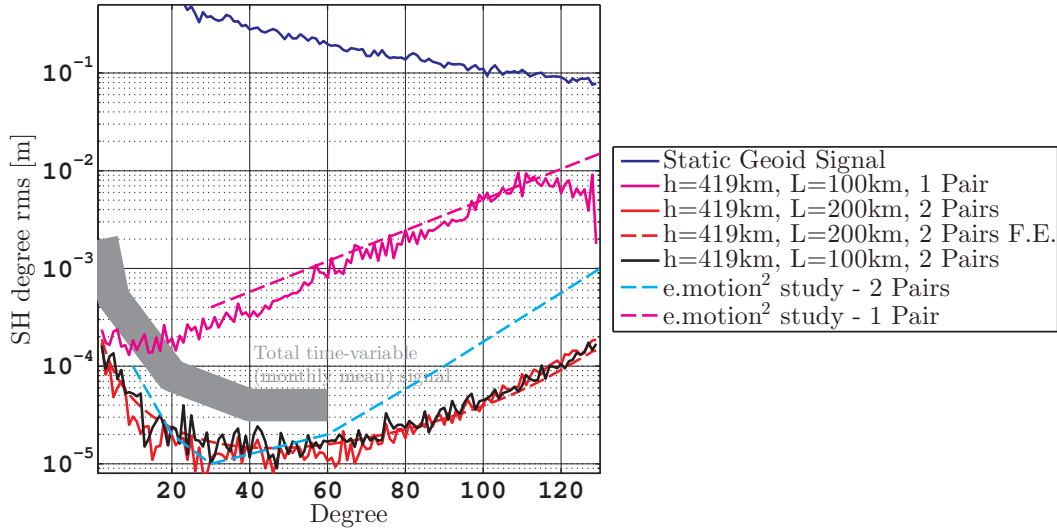


Figure 1.22: Geoid rms-error per SH degree from PDGA measurement of a single polar pair at an orbit height of 419 km, $\beta/\alpha = 464/30$ and 100 km spacecraft separation (in magenta), compared to the Bender configuration with an additional 70° inclined satellite pair ($\beta/\alpha = 461/30$) in red and black. F.E. denotes formal errors. The dashed lines are independent results as obtained in the e.motion² study.

the lunar GRAIL mission [Konopliv *et al.*, 2013].

In this thesis, the error in the POD-part was considered by deriving a stationary noise model for the centrifugal acceleration term based on an assumption for the knowledge of an a-priori gravity field and based on an orbit fit of short arcs. This is a strong simplification but allowed to use the acceleration approach with its benefits, e.g. no linearized equations as in (reduced-)dynamic orbit determination. The results for the single polar pair are compliant with current GRACE post-fit residuals and provide an understanding of critical parameters for future missions. Unfortunately, the results for the double Bender pair are too optimistic (at high SH degrees) compared to full-scale simulations with proper consideration of background model errors, but the significant benefit of a second inclined pair could be demonstrated.

1.8 Centrifugal Acceleration Sensing

The observation technique for GRACE and GRACE Follow-On as well as various mission proposals for future SST geodesy missions is based on precise ranging between satellites, measurement of non-gravitational accelerations by means of an accelerometer, orbit determination using a GNSS receiver and other auxiliary measurements such as star cameras to measure spacecraft attitude. As discussed in the previous sections, the centrifugal (CF) acceleration of the baseline cannot be measured with sufficient precision with current techniques and needs to be derived by means of (reduced-)dynamic orbit determination, usually implicitly in the gravity retrieval process. The author of this thesis is convinced that a precise measurement of the baseline centrifugal acceleration would simplify the gravity retrieval and would reduce the effect of background model errors in the gravity field solutions. Therefore, this section is dedicated to a brief feasibility assessment of different ways to measure this baseline centrifugal acceleration.

The baseline centrifugal acceleration $PDGA_{CF}$ can be written in accordance to eq. (1.13)

as

$$\text{PDGA}_{\text{CF}} = \frac{|\dot{\vec{r}}_{12}|^2}{\rho} - \frac{\dot{\rho}^2}{\rho} = \frac{\dot{\vec{r}}_{12,\perp}^2}{\rho} = |\vec{\omega}_{\text{LOS}}|^2 \cdot \rho, \quad (1.98)$$

where the precise (unbiased) inter-satellite ranging ρ is combined with less precise velocity information. Obviously, an improvement of GNSS observations would provide better absolute S/C positions as well as a more precise relative position vector \vec{r}_{12} and therefore more precise centrifugal accelerations. Strategies to improve the kinematic GNSS orbits have been addressed in section 1.4.1 but are likely only capable to provide an incremental improvement.

By linearizing eq. (1.98) and using L for the time-averaged unbiased ranging $\rho(t)$, one can derive the noise in terms of the power spectral density in the centrifugal acceleration term,

$$\text{PSD}[\text{PDGA}_{\text{CF,E}}](f) \approx 2 \cdot L \cdot \begin{pmatrix} |\omega_{\text{LOS,DC,x}}|^2 \\ |\omega_{\text{LOS,DC,y}}|^2 \\ |\omega_{\text{LOS,DC,z}}|^2 \end{pmatrix}^{\text{T}} \cdot \text{PSD}[\vec{\omega}_{\text{LOS,E}}](f), \quad (1.99)$$

which is a vector product and forms together with the noise in the accelerometer and range acceleration the main contributors of the overall PDGA (LL-SST) sensitivity. We can assume here that the mean angular velocity $\vec{\omega}_{\text{LOS,DC}}$ is constant in an inertial frame, e.g. for GRACE-like missions it points in cross-track direction of both S/C with a magnitude of $2\pi/T_{\text{orb}}$. Without loss of generality one can choose a coordinate frame, such that only a single component is non-zero in $\vec{\omega}_{\text{LOS,DC}}$, and hence, only a single component of $\text{PSD}[\vec{\omega}_{\text{LOS,E}}]$ is of importance.

Recalling figure 1.16 on page 43, the centrifugal acceleration noise should be ideally at the sensitivity level of the accelerometer and ranging instrument. For simplicity, the accelerometer is taken as reference, because it is the dominating noise source at low frequencies. Thus, a requirement for the measurement noise of the angular velocity along the sensitive axis would be based on the noise of the accelerometer $\Gamma_{\text{X,E}}$ (cf. eq.(1.47)), i.e.

$$\text{ASD}[\omega_{\text{req}}](f) := \frac{\text{ASD}[\Gamma_{\text{X,E}}](f)}{2 \cdot L \cdot 2\pi/T_{\text{orb}}}. \quad (1.100)$$

Evaluation of the required sensitivity for $L = 200$ km and $T_{\text{orb}} \approx 5550$ s, which corresponds to $h \approx 400$ km, yields values of

$$\begin{aligned} \text{ASD}[\omega_{\text{req}}](f = 10^{-4} \text{ Hz}) &\approx 1 \cdot 10^{-11} \text{ rad}/(\text{s}\sqrt{\text{Hz}}) \\ \text{ASD}[\omega_{\text{req}}](f = 10^{-3} \text{ Hz}) &\approx 2 \cdot 10^{-13} \text{ rad}/(\text{s}\sqrt{\text{Hz}}). \end{aligned} \quad (1.101)$$

As will turn out in the next paragraphs, where different methods to determine or measure $\vec{\omega}_{\text{LOS}}$ are discussed, reaching such a sensitivity is extremely challenging, if not impossible.

It is remarked that the baseline angular velocity in an e.motion² or GRACE-like missions is equivalent to the GOCE S/C angular velocity. However, as the baseline length between accelerometers in GOCE is approx. 10^6 times smaller than $L = 200$ km, the sensitivity for the angular velocity can be relaxed by this factor. In the GOCE mission, the gradiometer and S/C attitude was measured by star cameras and by the gradiometer (accelerometer pairs), with a pre-launch specified peak-sensitivity of $1 \cdot 10^{-9}$ rad/(s $\sqrt{\text{Hz}}$) at 5 mHz [Stummer, 2013, Fig. 6.3].

1.8.1 Accelerometer, Star Camera and Laser Interferometry

An alternative method to derive the baseline angular velocity $\vec{\omega}_{\text{LOS}}$ other than by satellite velocities is possible by a combination of measurements from an inertial measurement unit (IMU) and LRI pointing information, typically via Differential Wavefront Sensing (DWS). The IMU can be an accelerometer, star cameras, a gyroscope or a sensor fusion result of all of them.

Each IMU measures the angular rate of the corresponding satellite w.r.t. an inertial frame, while information on the LOS direction is available from LRI pointing measurements. If both satellites perfectly faced each other, the LRI pointing signal would be zero (or constant) along the orbit, while the measured angular rate of the IMU on both satellites is equal to the baseline angular velocity. However, as the satellites are prone to attitude jitter, the accelerometer and star camera angular rate measurements are contaminated by jitter noise. This attitude jitter is measured by the LRI on each satellite and can be used as correction in post-processing.

We wish to derive the sensitivity of the combination of the IMU measurement and LRI pointing. Consider an IMU capable to measure the orientation of the satellite body frame (SBF) w.r.t. the inertial frame (IF) in all 3 degrees of freedom, e.g. a star camera, a gyroscope or an accelerometer (angular accelerations). Note that only the star camera is capable to measure an unbiased attitude w.r.t. the inertial starry sky, while gyroscope and accelerometer need additional information to resolve an initial bias, e.g. from sensor fusion.

Such an IMU measurement provides a rotation matrix relating the SBF to the IF

$$\hat{R}_{\text{SBF} \rightarrow \text{IF}} = \hat{R}_x(\alpha) \cdot \hat{R}_y(\beta) \cdot \hat{R}_z(\gamma), \quad (1.102)$$

where α, β and γ describe the rotation angles for rotations around the x , y and z axes, respectively.

Without loss of generality it is assumed that the orbital planes are oriented such that the angular velocity predominantly points in y -direction, i.e.

$$\beta(t) = \omega_{\text{DC}} \cdot t + \delta\beta(t). \quad (1.103)$$

Additionally, the LRI measures the line-of-sight (LOS) with respect to the SBF on each S/C. The DWS-derived LOS $\vec{e}_{12|\text{SBF}}$ can be written as

$$\vec{e}_{12|\text{SBF}} = \hat{R}_y(\text{DWS}_v) \cdot \hat{R}_z(\text{DWS}_h) \cdot \begin{pmatrix} 1 \\ 0 \\ 0 \end{pmatrix}_{|\text{SBF}}. \quad (1.104)$$

It was assumed without loss of generality that the nominal LOS direction is along the x -axis in the SBF. Furthermore, the DWS measurement angles DWS_v , DWS_h were used. Finally, the line-of-sight vector in the inertial frame is given by

$$\vec{e}_{12|\text{IF}} = \hat{R}_{\text{SBF} \rightarrow \text{IF}} \cdot \vec{e}_{12|\text{SBF}}. \quad (1.105)$$

With these definitions, one arrives with the help of an algebraic software such as *Mathematica* at a linearized formula for the angular velocity vector

$$\vec{\omega}_{\text{LOS}} = \vec{e}_{12|\text{IF}} \times \dot{\vec{e}}_{12|\text{IF}} \approx \underbrace{\begin{pmatrix} 0 \\ \omega_{\text{DC}} \\ 0 \end{pmatrix}}_{\vec{\omega}_{\text{LOS,DC}}} + \underbrace{\begin{pmatrix} -(\delta\gamma + \delta\text{DWS}_h) \cdot \omega_{\text{DC}} \\ \delta\dot{\beta} + \delta\text{DWS}_v \\ \delta\dot{\gamma} + \delta\text{DWS}_h + \delta\alpha \cdot \omega_{\text{DC}} \end{pmatrix}}_{\vec{\omega}_{\text{LOS,E}}}. \quad (1.106)$$

This formula shows the coupling of errors (denoted with δ) into the final angular velocity. Using this eq. (1.106) in eq. (1.99), one notices that the y -component is the linear dominant component in the power spectral density. The noise in this sensitive angular velocity component can be described in the power spectral domain as

$$\text{PSD}[\omega_{\text{LOS,E}}] = \text{PSD}[\omega_{\text{IMU}}] + (2\pi f)^2 \cdot \text{PSD}[\delta\text{DWS}_v], \quad (1.107)$$

where the first term is the noise in the angular rate derived from the IMU, i.e. $\dot{\beta}$ in eq. (1.106), and the second term is the noise in the LRI pointing measurement.

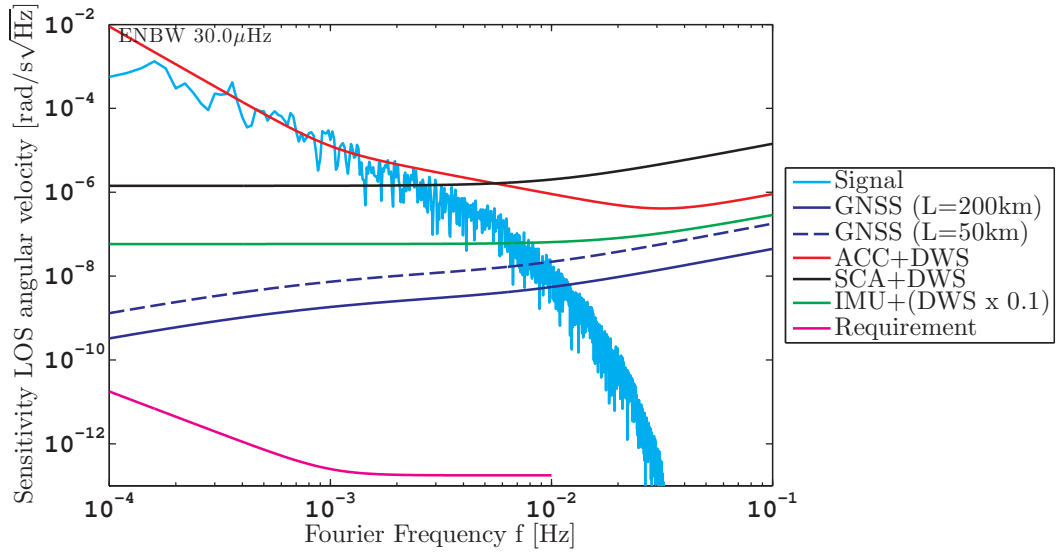


Figure 1.23: Sensitivity of different measurements of LOS angular velocity expressed as spectral density. The signal is given for a GRACE-like constellation at 400 km height and with 200 km separation. The magenta requirement trace corresponds to eq. (1.100). IMU: Inertial Measurement Unit (Laser Fiber Gyroscope), SCA: Star Camera, DWS: Pointing measurement of the LRI

The corresponding numerical models are given in eq. (1.49) and eq. (1.41), which yields for the accelerometer IMU

$$\text{PSD}[\omega_{\text{LOS,E,ACC+LRI}}] \approx 2 \cdot \frac{\text{PSD}[\dot{\omega}_{\text{ACC,E}}]}{(2\pi f)^2} + 2 \cdot (2\pi f)^2 \cdot \text{PSD}[\text{DWS,E}] \quad (1.108)$$

$$\begin{aligned} & \left(4 \cdot 10^{-8} \text{ rad}/(\text{s}^2\sqrt{\text{Hz}}) \cdot \sqrt{\left(\frac{1 \text{ mHz}}{f}\right)^4 + 1 + \left(\frac{f}{10 \text{ mHz}}\right)^4} \right)^2 \\ & \approx 2 \cdot \frac{\quad}{(2\pi f)^2} \\ & + 2 \cdot (2\pi f)^2 \cdot 10^{-12} \text{ rad}^2/\text{Hz} \cdot \text{NSF}^2(f) \end{aligned} \quad (1.109)$$

and for the star camera IMU (cf. eq. (1.53))

$$\text{PSD}[\omega_{\text{LOS,E,SCA+LRI}}] \approx 2 \cdot (2\pi f)^2 \cdot \text{PSD}[\alpha_{\text{SCA,E}}] + 2 \cdot (2\pi f)^2 \cdot \text{PSD}[\text{DWS,E}] \quad (1.110)$$

$$\begin{aligned} & \approx 2 \cdot (2\pi f)^2 \cdot \left(16 \mu\text{rad}/\sqrt{\text{Hz}} \cdot \sqrt{1 + \left(\frac{0.01 \text{ Hz}}{f}\right)^2} \right)^2 \\ & + 2 \cdot (2\pi f)^2 \cdot 10^{-12} \text{ rad}^2/\text{Hz} \cdot \text{NSF}^2(f) \end{aligned} \quad (1.111)$$

The numerical values over frequency are visualized in figure 1.23. For comparison, the sensitivity of the commercially available laser gyroscope ASTRIX[®]200 from Airbus⁷ is shown as green trace. According to the specifications, the instrument is capable to reach an angular-random-walk noise of $0.00012^\circ/\sqrt{\text{hr}}$, which translates to approx. $3.6 \cdot 10^{-8} \text{ rad}/(\text{s}\sqrt{\text{Hz}})$. Since the LRI pointing information would be the dominant noise source, it was assumed that the DWS or pointing readout (eq. (1.41)) can be improved from $1 \mu\text{rad}/\sqrt{\text{Hz}}$ by one order of magnitude to $0.1 \mu\text{rad}/\sqrt{\text{Hz}}$ for the green trace. Even potential Sagnac atom interferometers [Barrett *et al.*, 2014] would not provide better sensitivity than the GNSS kinematic-derived baseline angular velocity.

⁷<http://www.space-airbusds.com/en/equipment/astrix-200.html>

One can conclude that with currently available instruments one can not perform an independent measurement of the baseline angular velocity with a noise level better than the required eq. (1.101) shown as magenta trace in figure 1.23.

1.8.2 Sagnac-Interferometry

A very prominent way to measure angular velocities is to exploit the Sagnac effect, which causes an accumulation of a phase difference between a clockwise and a counter-clockwise propagating wave, if the setup is rotating in inertial space [Malykin, 2000]. The phase difference expressed as pathlength Δx can be computed from

$$\Delta x = \frac{\vec{\omega} \cdot \vec{n} \cdot A}{c}, \quad (1.112)$$

where c is the speed of light and \vec{n} the normal vector of the area A . A laser ranging interferometer is in general susceptible to the Sagnac effect and one needs to ensure that it is sufficiently small to not disturb the ranging measurement. In the GRACE Follow-On LRI the area A is approximately $200 \text{ km} \cdot 0.6 \text{ m}$ due to the racetrack configuration. The angular velocity signal, which is caused by the gravity field with an amplitude of approx. $10^{-3} \text{ rad}/(\text{s}\sqrt{\text{Hz}})$ at a Fourier frequency of 10^{-4} Hz (cf. figure 1.23 on page 55), produces a parasitic ranging-signal of the order of $400 \text{ nm}/\sqrt{\text{Hz}} \cdot \sin(\theta)$, where θ is the angle between the normal vector of the area A and $\vec{\omega}$. Since $\sin(\theta)$ is close to zero in the GRACE Follow-On concept, the parasitic Sagnac contribution is below the sensitivity requirement of the LRI.

One could consider to develop a more sophisticated laser ranging interferometer, which is capable of distinguishing between the Sagnac effect and ranging (longitudinal displacement). Such a concept would be beneficial, since it directly measures the angular velocity of the baseline. However, to reach a sensitivity of $1 \cdot 10^{-11} \text{ rad}/(\text{s}\sqrt{\text{Hz}})$ in the angular velocity with the optimal case of $\sin(\theta) \approx 1$, one would still need a ranging sensitivity of $10^{-15} \text{ m}/\sqrt{\text{Hz}}$, which is far beyond feasibility for low frequencies.

Also sophisticated large ground-based ring laser gyroscopes [Schreiber *et al.*, 2001, 2009], which exploit the Sagnac effect and can be used to monitor Earth's rotation rate, hardly achieve the sensitivity in eq. (1.101).

1.8.3 High-Resolution Star Camera

An alternative approach could be to utilize additional high-resolution star cameras on each S/C, which are aligned with respect to the nominal line-of-sight direction. The idea is to measure star positions with high precision as well as laser light from the distant S/C. Since the distant S/C is co-moving, it will appear as fixed star, while the (real) stars in the background appear to move with the orbital rate ω_{DC} . The required angular velocity sensitivity translates to an attitude sensitivity of $16 \text{ nrad}/\sqrt{\text{Hz}}$ at low frequencies. Assuming a star position readout sensitivity of $0.1 \text{ pixel}/\sqrt{\text{Hz}}$ and a sensor with 4096×4096 pixels, the required field-of-view for the high-resolution star camera would be $650 \mu\text{rad} \times 650 \mu\text{rad}$. However, this requires resolving very faint stars in order to have at least a few objects in the field-of-view and therefore feasibility is rather questionable. More details can be found in the section on the acquisition sensor in the second part of this thesis (cf. sec. 2.3.10).

In summary, no suitable method could not be identified within this thesis, which would improve the centrifugal acceleration measurement. The best mean remains to be based on precise orbit determination due to the very large S/C separation.

1.9 Drag-Free and Drag-Compensation

The GRACE and the GRACE Follow-On missions do not utilize drag compensation with high duty cycle. However, sporadic thruster activations are required for orbit and constellation

maintenance [Yoon *et al.*, 2006]. The GOCE mission used an ion propulsion system to compensate non-gravitational accelerations [Canuto, 2008]. For space-based interferometers such as LISA and LISA Pathfinder, a drag-free system is essential. Although the terms *drag-free* and *drag-compensation* are used interchangeably in literature, here, the following distinction is introduced: A *drag-free* system has a test-mass (or proof mass) following a so-called geodesic, meaning that it is influenced only by gravitational forces, i.e., it is free-falling. In particular, the coupling between spacecraft and proof-mass is very weak within a particular frequency band, which is usually the (science) measurement bandwidth (MBW). Typically, a drag-free mode can be realized only in a few degrees-of-freedom of a test-mass, especially if several drag-free test-masses are present in a satellite [Danzmann *et al.*, 2007, LISA Pathfinder] or if the satellites form a constellation and inter S/C pointing is required [eLISA/NGO Team, 2012; Danzmann *et al.*, 2017].

Position sensors measure the position and orientation of the test-mass within the spacecraft or accelerometer, either capacitively or laser interferometrically. The signal is fed back into a controller, which commands actuators of the satellite to produce a linear and/or angular acceleration to keep the proof-mass centered within a housing. However, at very low frequencies, i.e. below the interesting measurement band, drifts of the test-mass and S/C need to be reduced by electro-static suspension, e.g. for orbit and formation maintenance. The non-gravitational accelerations Γ are obtained by differentiating the position information. A drag-free concept is illustrated in figure 1.24 (bottom). Accelerometers in the context of drag-free systems are often called inertial sensors or drag-free sensors.

In contrast, *drag-compensation* usually utilizes a servo-accelerometer, where the proof-mass position is measured by capacitive sensing and the proof mass is centered within the accelerometer with high control-loop gain and high bandwidth by electro-static means (cf. upper panel in figure 1.24). The actuation signal (voltage), which is ideally proportional to the electro-static force applied to the test-mass, provides the non-gravitational accelerations. The accelerometers by the French company Onera used in CHAMP, GRACE, GRACE-Follow-On and GOCE are of the latter servo-controlled type. For a *drag-compensation* concept, the measured non-gravitational accelerations, which are derived from the electrostatic feedback signals acting on the test-mass, are fed back into another outer control loop, which actuates the satellite by means of thruster and torquers to counteract the non-gravitational accelerations (cf. center panel in figure 1.24).

The main difference between drag-compensating and drag-free systems is the bandwidth of the electro-static suspension, which is a continuous parameter. Hence, the difference between both concepts is gradual and not black-and-white. Drag-compensation uses two nested control-loops within the measurement bandwidth, while drag-free operation utilizes only the Attitude and Orbit Control System (AOCS) loop within the measurement bandwidth. In an ideal drag-free concept, the proof-mass follows a geodesic. While in drag-compensation, the proof-mass follows a geodesic only in case of infinite AOCS loop gain. In the case of finite AOCS loop gain, the high electro-static suspension couples the proof-mass and the S/C strongly. Any disturbance on the S/C produces a deviation from geodesic motion of the test-mass, which is, however, suppressed by the finite AOCS loop gain.

Because the proof-mass has non-negligible motion inside the accelerometer housing in case of drag-free operation, the definition of the gravitational reference point for gravity recovery was adopted in sec. 1.3.6 (and following). In a drag-free mission, the well-defined and stable proof-mass CoM needs to serve as ranging reference point. As the S/C shields the non-gravitational disturbances such as drag and solar radiation pressure, the proof-mass is ideally only influenced by gravitational accelerations.

1.9.1 Characteristics of Non-Gravitational Accelerations

A potential drag reduction system, either drag-compensating or drag-free, needs to counteract the non-gravitational accelerations caused by residual atmospheric drag, by radiation

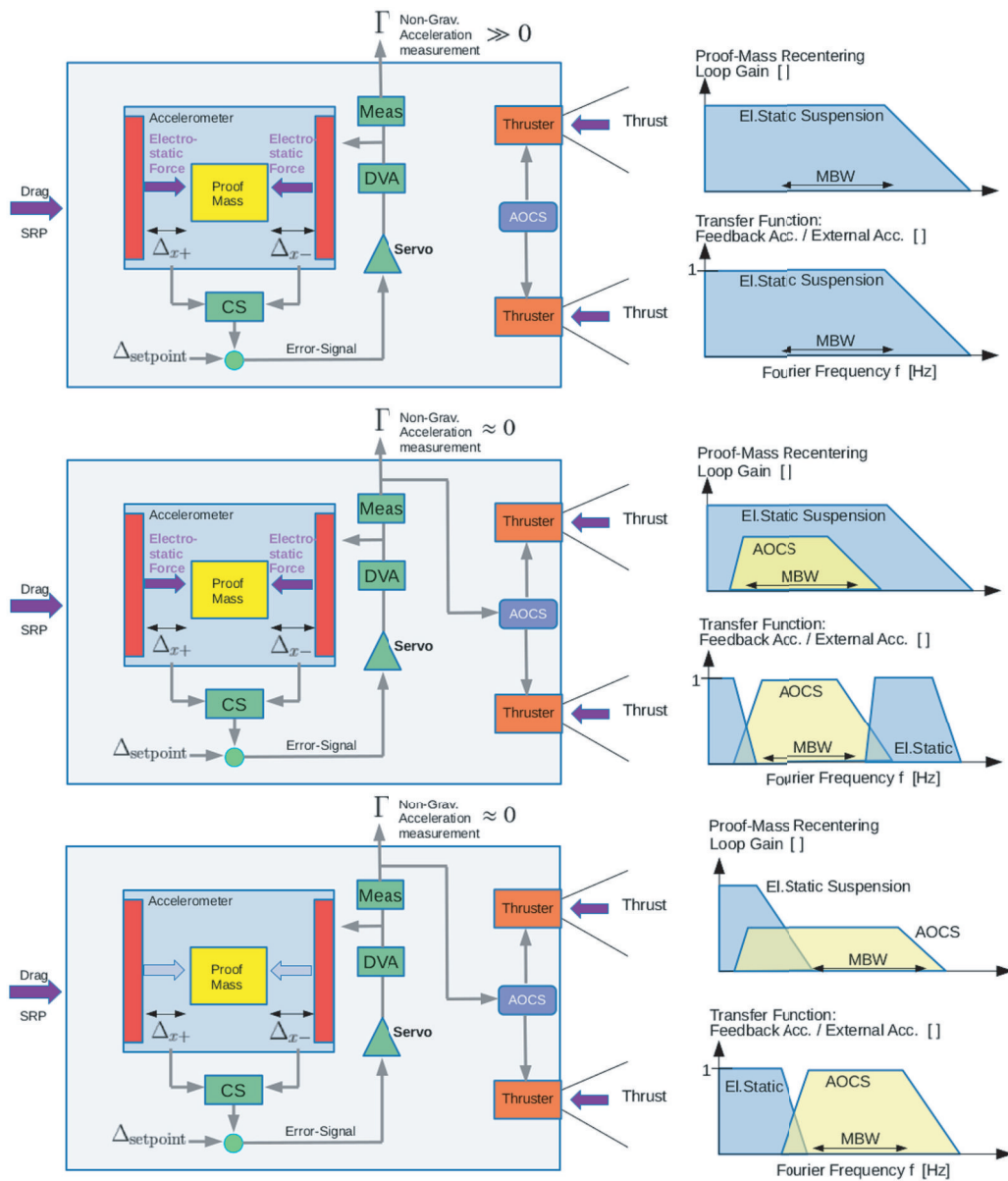


Figure 1.24: (Top:) Servo-Accelerometer concept as in GRACE and GRACE Follow-On simplified for one degree-of-freedom. (Center:) Servo-Accelerometer with feed-back into the AOCS system, which reduces the measured non-gravitational accelerations Γ . This so-called drag-compensation scheme has been utilized in the GOCE mission. (Bottom:) Drag-Free concept with undisturbed proof-mass within the measurement bandwidth. Abbreviations: CS (Capacitive Sensing), DVA (Drive Voltage Amplifier), Meas (Measurement), AOCS (Attitude and Orbit Control System), MBW (Measurement Bandwidth)

e.g. solar or Earth's albedo radiation pressure, and by Lorentz force. Atmospheric drag is considered dominant, as future gravity missions will most likely utilize a lower altitude than GRACE. The drag force can be computed according to [Montenbruck & Gill, 2000, eq. 3.97].

$$\vec{F}_{\text{drag,ITRF}} = -\frac{1}{2} \cdot C_D \cdot A \cdot \rho \cdot |\dot{\vec{r}}_{\text{ITRF}}|^2 \cdot \frac{\dot{\vec{r}}_{\text{ITRF}}}{|\dot{\vec{r}}_{\text{ITRF}}|}, \quad (1.113)$$

where ITRF refers to an Earth-fixed frame, A is the cross-section area of the S/C, C_D is the drag coefficient and ρ is the atmospheric density. The density ρ is a function of the satellite's altitude and position and it depends strongly on the solar activity, usually characterized by F10.7 flux, and geo-magnetic activity, usually characterized by K_p or A_p coefficients [Montenbruck & Gill, 2000]. The solar activity exhibits a 11-year cycle. Based on figure 3-20 from [e.motion² Team, 2014], the following approximate formula for the atmospheric density ρ between 300 km and 500 km altitude can be derived

$$\rho(h = 400 \text{ km} + \Delta h) \approx 10^{-12} \text{ kg/m}^3 \cdot \begin{cases} 10.0 \cdot 3^{-\Delta h/100 \text{ km}} & \text{(high case)} \\ 0.4 \cdot 10^{-\Delta h/100 \text{ km}} & \text{(low case)} \end{cases}. \quad (1.114)$$

With $C_D = 2.2$, $A = 0.97 \text{ m}^2$ and $\dot{\vec{r}} = 7600 \text{ m/s}$ this translates to a drag force of

$$F(h = 400 \text{ km} + \Delta h) \approx \begin{cases} 0.616 \text{ mN} \cdot 3^{-\Delta h/100 \text{ km}} & \text{(high case)} \\ 0.002 \text{ mN} \cdot 10^{-\Delta h/100 \text{ km}} & \text{(low case)} \end{cases}. \quad (1.115)$$

The result illustrates the large range between high and low solar activity. Spectral analysis of the atmospheric drag on a LEO satellite reveals that next to a static part, the signal power is concentrated at (low) integer multiples of the fundamental orbital frequency [Frommknecht, 2008, p. 53]. Moreover, Zijlstra *et al.* [2005] pointed out that atmospheric models lack frequency-continuous signals when compared to accelerometer data and suggested a method to model short-term variations by producing an appropriate filter. For a comprehensive report on atmospheric density models, also in comparison with satellite accelerometer data, the reader is referred to [Doornbos *et al.*, 2009].

In this thesis, the spectral behavior of worst-case non-gravitational accelerations for e.motion² was approximated rigorously based on the green trace in figure 1.25 by

$$\text{PSD}[a_{\text{ng,max}}](f) = 3 \cdot 10^{-11} \frac{\text{m}^2}{\text{s}^4 \cdot \text{Hz}} \cdot \frac{1}{1 + (f/0.2 \text{ mHz})^2}, \quad (1.116)$$

which is shown as dashed light blue trace in the same figure.

It is remarked here that accelerometry in GRACE is perturbed by short twangs, which might be caused by vibrations, probably induced by insulator foil at the nadir side of the S/C [Peterseim, 2014]. Also, electro-magnetic susceptibility of the accelerometer, e.g. to heater switching, has been reported [Peterseim, 2014]. The design of the GRACE Follow-On satellites was partly optimized to reduce these effects. A potential NGGM mission needs to address these issues as well, in particular if the accelerometer data is used in a control loop for drag reduction.

Other non-gravitational disturbances from solar radiation pressure, Earth's and Moon's albedo radiation, unexpected disturbances and Lorentz effects, where the charged S/C interacts with the geomagnetic field, are not covered here in detail. The interested reader is referred to [Frommknecht, 2008]. It is assumed that all these effects are covered by eq. (1.116).

In this section only linear accelerations are considered, a similar analysis needs to be performed for angular accelerations.

1.9.2 Requirements on the Accelerometer

The characteristics of non-gravitational accelerations can be used to derive requirements on the accelerometer. The maximum mean force as given by eq. (1.115) at 400 km height is

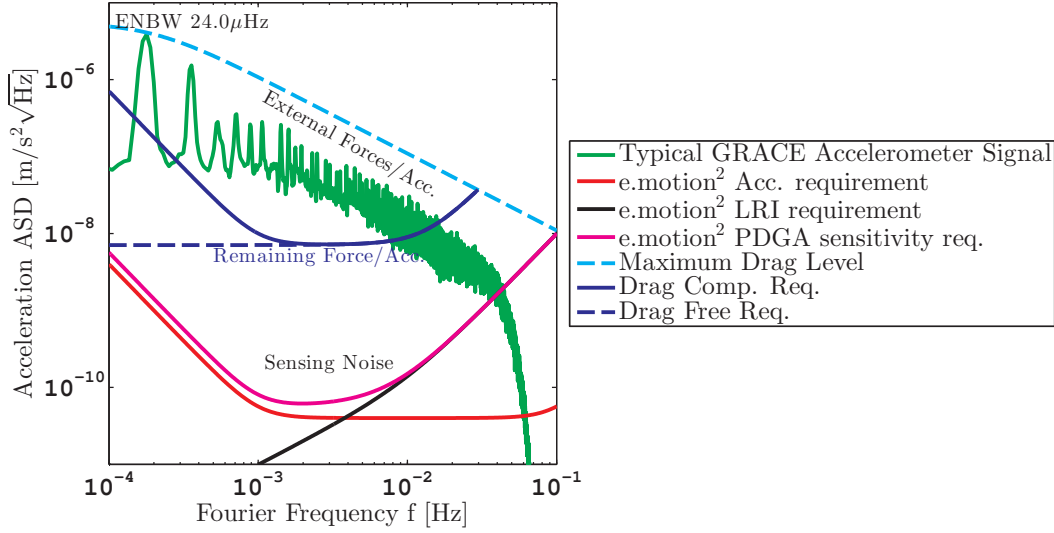


Figure 1.25: Drag compensation requirement (dark blue trace) expressed as residual non-gravitational acceleration ASD along the LOS. The dashed light blue trace is a worst-case assumption for the maximum level of non-gravitational accelerations at e.motion² orbit height (≈ 400 km). Drag compensation is not required above $4 \cdot 10^{-2}$ Hz, since even under worst-case assumptions, the non-suppressed acceleration would be sufficiently small. The green trace of a typical GRACE accelerometer signal corresponds to L1B data from the year 2007.

0.6 mN, which corresponds to $7.5 \cdot 10^{-7}$ m/s² with a satellite mass of 800 kg. With margin and converting to peak values, an accelerometer dynamic range of $\pm 6 \cdot 10^{-6}$ m/s² has been specified for e.motion².

Due to the quantization noise arising from the finite number of bits in analogue-to-digital converter, e.g. high-end 24-bit ADCs, the resulting quantization noise is of the order of (cf. eq. 2.314)

$$\frac{12 \cdot 10^{-6} \text{m/s}^2 \cdot 2^{-N}}{\sqrt{6 \cdot f_s}} \approx \frac{12 \cdot 10^{-6} \text{m/s}^2 \cdot 2^{-24}}{\sqrt{6 \cdot 10 \text{Hz}}} \approx 10^{-13} \text{m/s}^2 \sqrt{\text{Hz}} \quad (1.117)$$

for such a dynamic range.

The amplitude spectral density of non-gravitational accelerations in the worst-case assumption is approximately 10^{-6} m/s²√Hz at 1 mHz (cf. figure 1.25). The sensitivity of the accelerometer is at approx. $4 \cdot 10^{-11}$ m/s²√Hz, yielding a signal-to-noise ratio of 25000.

However, this implies that the accelerometer mean (DC) scale factor $\mathcal{S}_{\text{DC}}^{(\text{ACC})}$ (cf. sec. 1.4.3 on accelerometers) needs to be known to one part in 25000 or to $4 \cdot 10^{-5}$. A survey of scale factor requirements in missions and studies is given in table 1.4. Current accelerometers, e.g. the one used in GRACE Follow-On, achieve an absolute knowledge of about 2%. Although some concepts state a knowledge at the parts-per-million (ppm) level, details on the technical realization are not provided.

Recall that the scale factor induced noise in the accelerometer measurement is governed by (cf. eq. (1.52))

$$\text{PSD}[\Gamma_{S,E}] = (\mathcal{S}_{\text{DC},E}^{(\text{ACC})})^2 \cdot \text{PSD}[\Gamma_{\text{meas}}] + \Gamma_{\text{max}}^2 \cdot \text{PSD}[\mathcal{S}_{\text{AC},E}^{(\text{ACC})}], \quad (1.118)$$

which shall be below the overall accelerometer noise $\text{PSD}[\Gamma_{X,E}]$ or at least below the PDGA sensitivity, which is limited at high frequencies by the ranging instrument. One needs to define values, i.e. requirements, on all of the four terms in eq. (1.118). These need to be iterated, until suitable and achievable values are obtained for all of the quantities.

In the e.motion² study, a DC scale factor knowledge requirement was proposed by the author of this thesis as

$$\mathcal{S}_{\text{DC, req}}^{(\text{ACC})} = 2 \cdot 10^{-3} = 0.2\%, \quad (1.119)$$

which was considered already demanding. However, with a dedicated continuous in-orbit calibration, which will be discussed in the subsequent section 1.10, such a value is achievable.

A requirement for the AC scale factor $\mathcal{S}_{\text{AC,E}}^{(\text{ACC})}$ stability within the measurement bandwidth is proposed as

$$\mathcal{S}_{\text{AC, req}}^{(\text{ACC})} = 10^{-3} \frac{1}{\sqrt{\text{Hz}}} \cdot \sqrt{\left(\frac{1 \text{ mHz}}{f}\right)^2 + 1}, \quad 0.18 \text{ mHz} < f < 0.1 \text{ Hz}, \quad (1.120)$$

which is considered achievable by the author of this thesis. From this requirement, one can state that maximum in-orbit non-gravitational accelerations Γ_{max} of less than

$$\Gamma_{\text{max, req}} = a_{\text{ng, max, req}} = 10^{-8} \text{ m/s}^2, \quad (1.121)$$

will comply with the accelerometer sensitivity requirement. Thus, a drag-reduction scheme is required on both S/C, which reduces the in-orbit non-gravitational accelerations below this value.

The last missing requirement from eq. (1.118) is the one for $\text{PSD}[\Gamma_{\text{meas}}]$, i.e. on the highest level of in-orbit non-gravitational accelerations within the science frequency band. An expression, which is compliant with the PDGA sensitivity and $\mathcal{S}_{\text{DC, req}}^{(\text{ACC})}$, is proposed here as

$$\begin{aligned} & \sqrt{\text{PSD}[\Gamma_{\text{meas, req}}](f)} \\ &= \text{ASD}[a_{\text{ng, DCO, req}}](f) = \frac{1}{4 \cdot 0.2\%} \cdot \sqrt{2 \cdot \text{PSD}[\Gamma](f) + (2\pi f)^4 \cdot \text{PSD}[\text{LRI}](f) \cdot 0.1} \end{aligned} \quad (1.122)$$

for frequencies $0.18 \text{ mHz} < f < 40 \text{ mHz}$. The factor $1/4$ accounts for two satellites and margin, while the factor 0.1 in the square-root is also a margin, which ensures that the accelerometer scale factor is not limiting the PDGA sensitivity, even if the LRI noise is one order of magnitude below the requirement $\text{PSD}[\text{LRI}]$. The sensitivity along the sensitive axis of the accelerometer is labeled as $\text{PSD}[\Gamma] = \text{PSD}[\Gamma_{\text{X,E}}]$ (cf. eq. (1.47)).

Numerical values for eq. (1.122) are shown as solid dark blue trace in figure 1.25. The frequency band for the requirement ranges from the fundamental orbital frequency up to the unity gain frequency, where non-gravitational disturbances reach the sensitivity of the PDGA sensitivity ($\approx 40 \text{ mHz}$). For comparison, the drag-reduction requirement in the [Alenia-Team \[2010\]](#) study was at $10^{-8} \text{ m/s}^2 \sqrt{\text{Hz}}$ between 1 mHz and 100 mHz , which is stricter at higher frequencies. A similar requirement to eq. (1.122) has been suggested by the author of this thesis during the e.motion² study, but was revised for this thesis.

It will turn out subsequently that eq. (1.122) is a design driver for drag-reduction schemes based on *drag-compensation*, while *drag-free* requires smaller fluctuations at low Fourier frequencies (cf. dashed dark blue trace in figure 1.25).

1.9.3 Selection of Drag Reduction scheme

If drag compensation, i.e. reduction of non-gravitational accelerations, is required only to

- maintain the orbit height and therefore the ground track repeat cycle,
- avoid accelerometer saturation due to constant along-track atmospheric drag,

Concept/Mission/Study	Knowledge	Stability within MBW
Alenia [Alenia-Team, 2008]	0.02 %	$5 \cdot 10^{-8} 1/\sqrt{\text{Hz}}$
FGM [Reubelt <i>et al.</i> , 2014]	0.01 %	$1 \cdot 10^{-6} 1/\sqrt{\text{Hz}}$
e.motion [e.motion Team, 2010]	-	-
NG2 [NG2-Team, 2011]	0.001 %	$1 \cdot 10^{-6}$
GRACE-FO [Foulon, 2013]	2 %	unknown
GOCE spec [Kramer, 2002]	0.1 %	$1 \cdot 10^{-2}$
GOCE diff. [Cesare, 2002]	0.01 %	$< 1 \cdot 10^{-5} 1/\sqrt{\text{Hz}}$

Table 1.4: Accelerometer scale factor requirements in different missions and studies. The column labeled “Knowledge” refers to the DC (mean) scale factor accuracy.

a feed-forward or DC-compensation approach can be utilized. This means that the attitude and orbit control system (AOCS) of the S/C is commanded to produce a constant (DC) linear acceleration, which compensates the average along-track drag over time-scales of days to months. As shown in the technical note in Appendix A, the accelerometer dynamic range of an Onera-type accelerometer is sufficiently large, such that saturation due to drag does not occur at orbit heights greater than 420 km. However, there might be scientific or technical reasons to use drag compensation within the measurement band, such as the limited knowledge of the accelerometer scale factor. This led to the derivation of the drag-compensation requirement in eq. (1.122) and finally to a selection of an e.motion² baseline [e.motion² Team, 2014], where the S/C compensate non-gravitational accelerations with a control loop, i.e. within the (science) measurement frequency band.

The use of a drag-free concept was only briefly addressed in the e.motion² study. The feasibility of a drag-free system as in LISA and LISA Pathfinder has not been shown, to the author’s knowledge, for a LEO orbit. Drag-free offers the advantage of a well-defined gravitational reference point and a weak coupling between test-mass and S/C, which results in a weak coupling of actuator and sensor errors into the motion of the test-mass. Decoupling the spacecraft from the measurement and using a well-shielded proof-mass as reference point as done in LISA and LISA Pathfinder should therefore be further investigated for LEO gravity missions. A starting point for this is provided in the next subsection.

1.9.4 Preliminary Drag-Free Assessment

An important aspect for the assessment of the feasibility of a drag-free system is the residual test-mass motion, i.e. translation and rotation, within the inertial sensor, as it needs to be sufficiently small to avoid collision of the proof-mass with the housing. For simplicity we consider in the following the motion only in the line-of-sight direction, as the non-gravitational accelerations are considered to be pre-dominant in this direction. The maximum displacement δx can be computed from a spectral density of (residual) non-gravitational accelerations $a_{\text{ng,res}}$ as a function of the bandwidth corner frequency f_{dco} by

$$\delta x_{\text{pk}} \approx 3 \cdot \sqrt{\int_{f_{\text{dco}}}^{\infty} (2\pi f)^{-4} \cdot \text{PSD}[a_{\text{ng,res}}](f) \, df}, \quad (1.123)$$

where the pre-factor 3 converts the rms-value to a zero-peak (99.7 % probability) value under the worst-case assumption of a completely Gaussian residual acceleration. The factor would be $\sqrt{2}$ for sinusoidal residual accelerations. f_{dco} denotes here the upper frequency bound of the electro-static actuation band or the lower frequency bound of the AOCS bandwidth (cf. the transfer function at the bottom in figure 1.24).

Figure 1.26 shows the residual test-mass motion as a function of the frequency bound f_{dco} for different levels of residual non-gravitational accelerations, which are taken from figure 1.25. As the solid dark blue trace in figure 1.26 shows, if non-gravitational accelerations

are compensated according to the solid dark blue trace in figure 1.25 and the test-mass is not electro-statically actuated at frequencies higher than 0.18 mHz, the proof-mass CoM motion within the housing is of the order of 2 mm. One could reduce the test-mass motion by choosing a smaller drag-free bandwidth and actuating electro-statically at higher frequencies. However, this would lead to a servo-accelerometer with the aforementioned drawbacks. Alternatively, the level of the residual non-gravitational forces needs to be reduced, i.e. by increasing the AOCS loop gain. Therefore, a drag-free requirement has been derived and is shown as dashed dark blue trace in figure 1.25 with flat low-frequency shape, which leads to a residual test-mass motion of approx. 120 μm . Such a motion could be tolerable and electro-static actuation of the test-mass would then be required for frequencies below 0.18 mHz, which are below the (science) measurement band.

The required AOCS loop gain for the drag-compensation and drag-free case is depicted in figure 1.27, which is the minimum required suppression factor of non-gravitational disturbances. As thrusters can typically provide sufficient linear momentum at low frequencies, the shown loop gain is considered to be realistic.

The requirements for drag-compensation and drag-free systems have been formulated along the line-of-sight. In principle this is sufficient, as the gravity field is sensed along the line-of-sight. Practically, the orthogonal axes need to be considered as well, as cross-coupling between axes cannot be neglected, but a relaxation by a factor of 10 to 100 is likely possible. Also the cross-talk between rotational and translational degrees as well as the exact equations of motions of the test-mass needs to be taken into account, but such an analysis is beyond scope of this thesis.

Regarding the angular degrees of freedom, the plot shown in figure 1.28 illustrates the variation of the test-mass orientation within the housing. The plot assumes that the e.motion² S/C points exactly along the line-of-sight. The line-of-sight rotates with a mean angular rate of $2\pi/T_{\text{orb}}$ in the inertial frame but has also variations within the science measurement band due to oblateness of Earth and higher moments of the gravity field. The test-mass is considered to rotate with constant angular velocity, i.e. no torques from gravity gradient or electro-static suspension occur. The variation of 1 mrad per orbital revolution suggests that a 300 μm gap size for a cuboid test-mass with a 50 millimeter side length is sufficient to cope with the angular variation and translation. Moreover, strong electro-static suspension of the angular degrees of freedom is likely not required within the measurement bandwidth. The traces from figure 1.28 have been converted into spectral densities, which are shown in figure 1.29 for the sake of completeness.

In summary, no obvious show stopper for a LEO drag-free concept could be identified, however, the analysis is restricted to a very simplified domain. For example, it was assumed that the sensitivity and characteristics of the servo-accelerometer hold as well for a drag-free position sensor. The sensitivity of such position sensing accelerometers was not discussed. However, these preliminary positive results can hopefully stimulate further research on drag-free concepts in the context of gravimetric missions.

The here derived information on the AOCS loop gain and the remaining non-gravitational acceleration after drag-reduction (eq. (1.122)) can be used to derive further requirements on the thrusters, which are addressed in the next section and apply to drag-compensation with a classical servo-accelerometer and to drag-free concepts using position sensing.

1.9.5 Actuator Technologies

The linear and angular accelerations required to compensate non-gravitational disturbances can be produced by various actuators. Pure torque on a satellite can be generated by means of magnetorquers, also called *torque rods*, which are based on electromagnetic coils. They produce a magnetic field, which generates a torque in the geomagnetic field. Usually, an additional magnetometer is used to measure the geomagnetic field at the satellite. The GOCE, GRACE and the future GRACE Follow-On missions utilize these actuators. Mo-

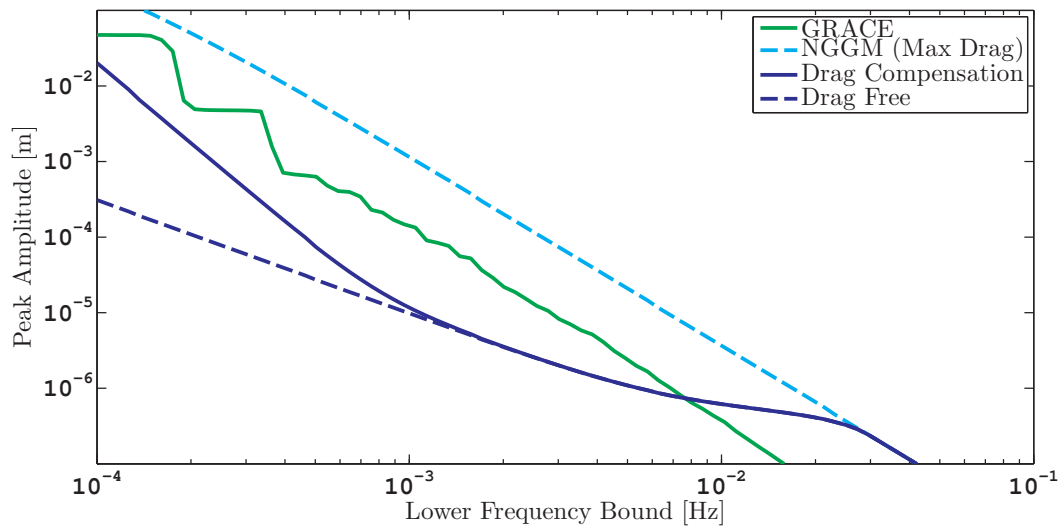


Figure 1.26: Residual test-mass motion δx along the LOS for a drag-free concept, where the test-mass is not electro-statically actuated within a drag-free frequency band, as a function of the drag-free bandwidth and for different levels of (residual) non-gravitational accelerations.

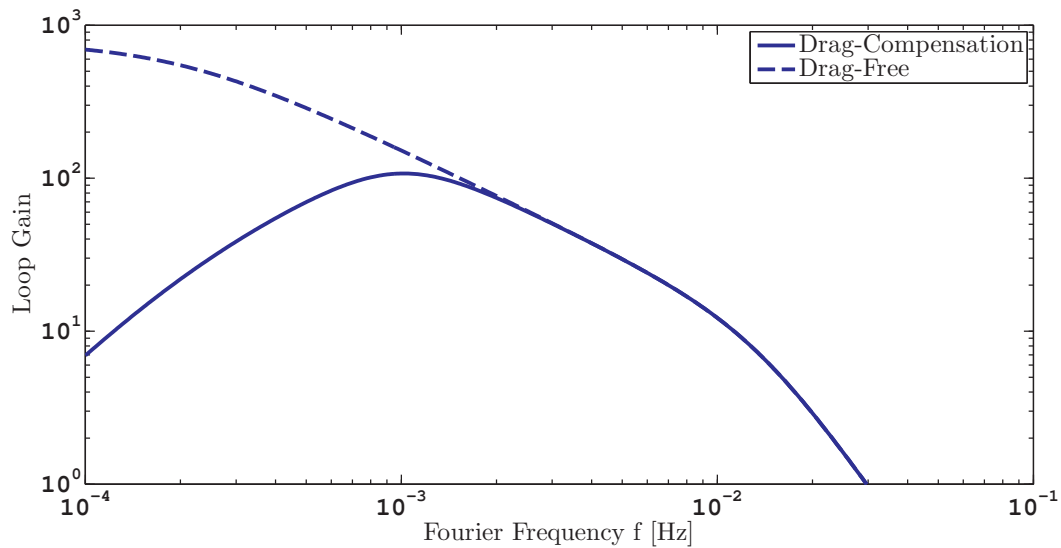


Figure 1.27: Required AOCS loop gain for the drag-free and drag-compensation case according to figure 1.25, i.e. the ratio of the maximum external acceleration (light blue dashed curve) over the dark blue traces in the figure.

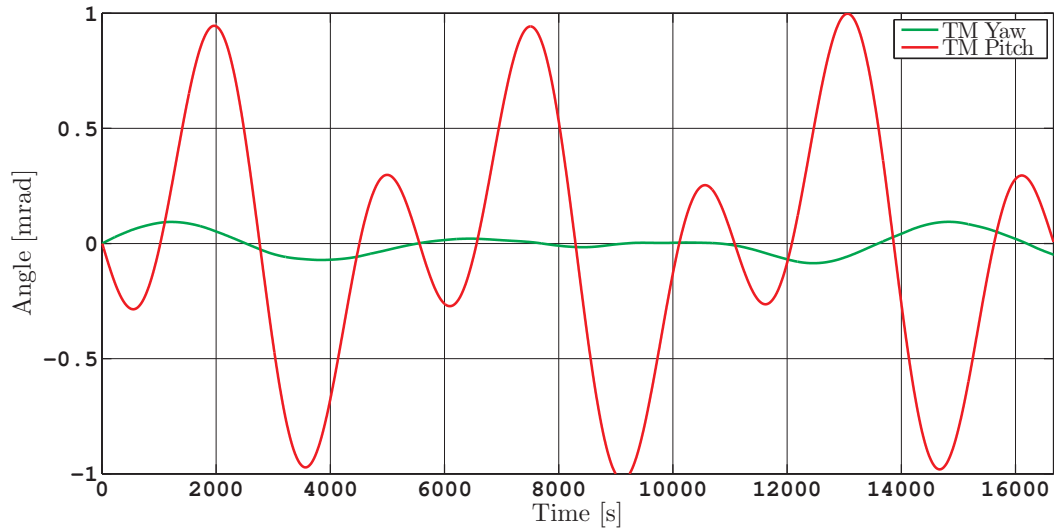


Figure 1.28: Angular variations of the test-mass w.r.t. the accelerometer housing for the drag-free case. The S/C is considered to point exactly along the line-of-sight. The test-mass rotates torque-free with a particular initial angular velocity. The shown period corresponds to three orbital revolutions.

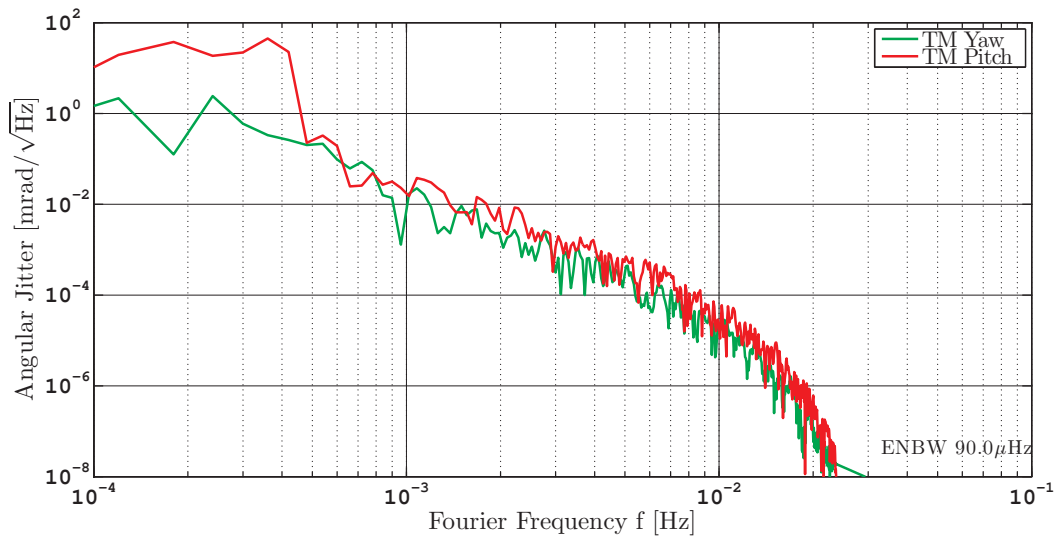


Figure 1.29: Spectral densities of angular jitter of the test-mass as shown in figure 1.28.

mentum wheels are considered as problematic, as vibrations may disturb the accelerometer measurement. Potential thruster technologies are

- **Continuous Cold Gas:** A pressurized gas tank is connected to a thruster, consisting basically of a nozzle. A valve controls the flux. This type of thrusters is used in, among others, GRACE and GRACE Follow-On and provides usually a specific impulse I_{sp} around 65 s for nitrogen. Micro-Newton N_2 cold-gas thrusters manufactured by TAS-I have been characterized for the GAIA mission [Jarrige *et al.*, 2014]. The thrust noise was below $1 \mu\text{N}/\sqrt{\text{Hz}}$ for frequencies below 2 mHz at a thrust level of 500 μN . The overall tested thrust range was 1 μN ($I_{sp} \approx 50$ s) up to 1 mN ($I_{sp} \approx 63$ s). These thrusters are being used on LISA Pathfinder [Armano *et al.*, 2015] as well as the Colloid thrusters⁸.
- **PWM Cold Gas:** The Formosat-5 satellite utilizes a cold-gas system with pulse-width modulation developed by the German company AST⁹. Over 10^9 actuation cycles have been demonstrated, resulting in a > 10 year lifetime for a PWM switching frequency of 3 Hz.
- **Kaufman Ion Thruster:** Such gridded ion thrusters ionize the propellant atoms (usually xenon) in a chamber with electrons, which are generated by a cathode and accelerated towards an anode. The ions are accelerated as well in an electrostatic field between two grids and ejected, providing the recoil momentum transfer. Charging of the satellite is counter-acted by a neutralizer, which emits electrons to neutralize the ejected plasma. The GOCE mission utilized such a type of thruster with 100 mm diameter grid manufactured by QinetiQ Ltd. The thrust range from 0.6 mN to 20.6 mN [Wallace *et al.*, 2011] can be achieved with specific impulses from 500 s to 3500 s over the thrust range, while the electrical power demand is specified from 55 W to 585 W over the thrust range [Edwards *et al.*, 2004]. The thrust noise level is 1.2 mN/ $\sqrt{\text{Hz}}$ at 1 mHz and 12 $\mu\text{N}/\sqrt{\text{Hz}}$ at high frequencies.
- **RIT:** Radio-frequency gridded ion thrusters use conducting coils to produce electromagnetic fields (with MHz frequencies) in the discharge chamber, which accelerate free electrons and ionize the propellant. No cathode in the discharge chamber is required as for the Kaufman type. These thruster are capable to achieve super high bandwidths, i.e. they have short reaction times. An extensive description and performance analysis is provided in [e.motion² Team, 2014, section 4.4]. A maximum thrust of 2 mN should be sufficient for a gravimetric mission at > 400 km altitude (cf. eq. (1.115)), which can be achieved with a 35 mm diameter grid. Measurements of a 25 mm unit exist and show a thrust noise of 10 $\mu\text{N}/\sqrt{\text{Hz}}$ at 10 mHz and at 200 μN setpoint [e.motion² Team, 2014, Fig. 4-20]. The ASD decays towards higher frequencies with $1/f$. A specific impulse between 500 s to 4000 s over a thrust range from 50 μN to 2 mN is specified in [e.motion² Team, 2014, p. 54].
- **Colloid Thruster:** These micro-newton ion thrusters are also called electrospray thrusters and emit ionized liquid droplets of propellant. The LISA Pathfinder mission utilizes this type of thruster, which has been a US contribution, next to the cold-gas system. The specified thrust ranges from 5 μN up to 30 μN with $I_{sp} > 150$ s and with a specified noise level of 0.1 $\mu\text{N}/\sqrt{\text{Hz}}$ for frequencies below 1 mHz [Ziemer *et al.*, 2007], whereby the actual noise performance is significantly better according to the publication.

Due to their higher specific impulse I_{sp} , ion thrusters require significantly less propellant (mass) with the drawback of higher electrical power consumption. The preliminary assessment of propellant demand for a 10 year mission lifetime shows that a N_2 cold-gas propulsion

⁸Initially, it was intended to use Colloid and FEEP thrusters, but the latter were changed to cold gas.

⁹<http://www.advancedspacetechologies.de/>

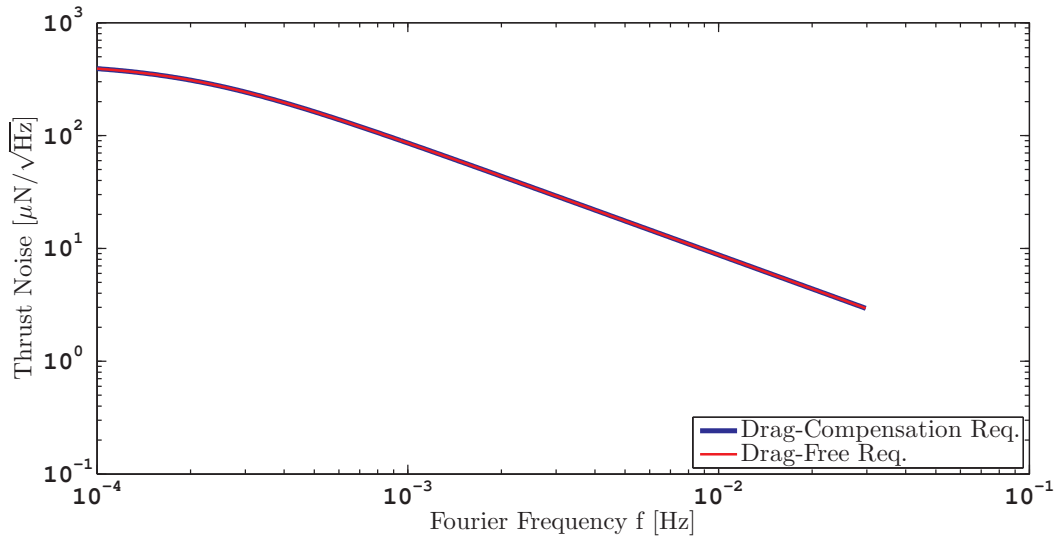


Figure 1.30: Requirement for thrust noise to reach the drag-compensation or drag-free requirement in figure 1.25. The thrust noise is referred to a set-point of 0.6 mN.

for the e.motion² baseline of 420 km altitude is sufficient, where 43 kg are required for drag compensation and 14 kg for attitude control [e.motion² Team, 2014, p. 42]. For a constellation at 360 km altitude a combination of cold-gas and electric propulsion was suggested.

In closed-loop operation of a drag-reduction system, the actuator noise is suppressed by the loop gain in the same way as the external disturbances. Since the requirement for the residual non-gravitational accelerations $\text{ASD}[a_{\text{ng,DCO,req}}](f)$ with active drag-reduction has been defined (cf. figure 1.25) as well as the AOCs loop gain $K(f)$ (cf. figure 1.27), one can derive a requirement for the thruster noise $\text{ASD}[F_{\text{ThN,req}}](f)$ according to

$$\text{ASD}[F_{\text{ThN,req}}](f) = \frac{1}{10} \cdot \text{ASD}[a_{\text{ng,DCO,req}}](f) \cdot K(f) \cdot m_{\text{sat}}. \quad (1.124)$$

Scaling by factor of 1/10 is assumed to account for several active thrusters, thrust vector variations and sufficient margin. The results in figure 1.30 for a satellite mass of $m_{\text{sat}} = 800$ kg are equal for the drag-compensation as well as for the drag-free case. The thrust noise requirement holds for the set-point of 0.6 mN corresponding to the maximum expected thrust (eq. 1.115), while lower setpoints are considered to have a lower noise.

Pulse-width modulation (PWM) thrusters need some precautions concerning the accelerometer design, as the accelerometer internally resolves the PWM signal. A PWM signal appears as a comb of spikes, which decay in amplitude to high frequencies. The roll-off is enhanced as the pulses are not perfectly rectangular, but the actual shape depends strongly on the characteristics of the thruster. A theoretical example is shown in figure 1.31. The internal accelerometer bandwidth needs to be sufficiently high, such that all signals are processed. Otherwise, they could alias into the science measurement band (0.18 mHz to 0.1 Hz). In other words, the accelerometer needs to resolve internally each PWM switching cycle sufficiently well. In a digital processing context, this means that the sampling frequency needs to be sufficiently high to avoid aliasing due to undersampling. Another concern regards aliasing by downsampling: The internal accelerometer signal needs to be downsampled to a convenient rate for down-link transmission, e.g. to 1 Hz. Therefore, a strong anti-aliasing filter (AAF) is required, as it needs to suppress the signal in the AAF band in figure 1.31 below the measurement sensitivity, e.g. to $10^{-12} \text{ m}/(\text{s}^2\sqrt{\text{Hz}})$.

In summary, different thruster types exist with key figures such as maximum thrust, which depends on the final selected orbit and solar activity, the specific impulse, which drives the propellant mass demand, and thrust noise, which needs to comply with the residual level of

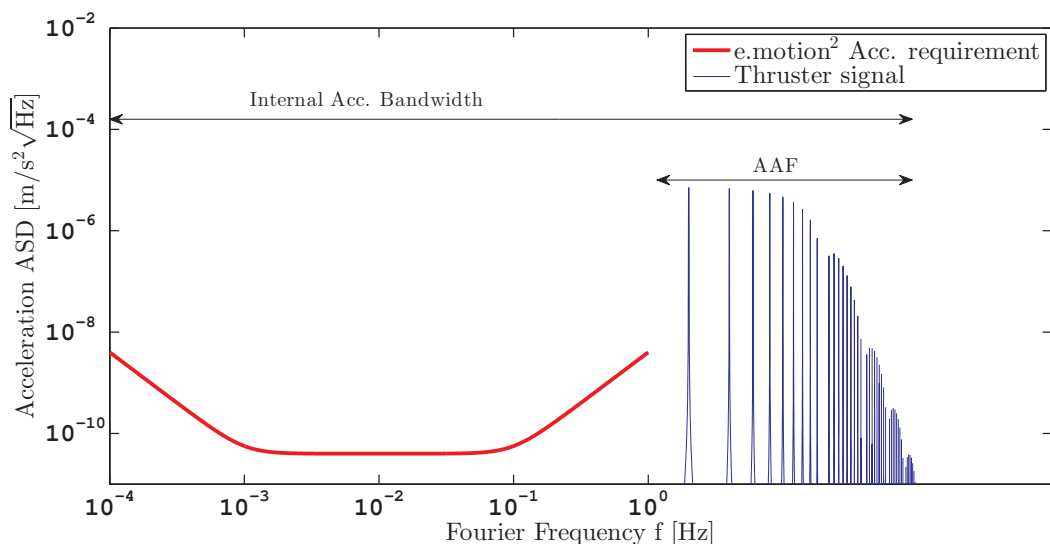


Figure 1.31: Pulse Width Modulation signal of thruster with switching frequency of 2 Hz (dark blue trace) with the e.motion² accelerometer sensitivity requirement shown in red. Higher frequencies are not labelled as the roll-off frequency of the PWM signal is not known.

non-gravitational accelerations after drag-reduction. The here derived requirement for the thrust noise is demanding, but can be fulfilled by the low-noise cold gas system or colloid thrusters. RIT thrusters are close to the thrust noise requirement and further iteration of the drag-reduction concept might lead to a relaxation of the requirement, e.g. the maximum non-gravitational acceleration level includes ample of margin, which might be too conservative.

1.10 Integrated Instrument Analysis and Calibration

For future gravimetric missions, an integrated instrument analysis and calibration becomes more important, because more measurements of the same physical quantities are available. This is depicted in figure 1.32, where the upper part shows the main scientific measurement instruments (green boxes) and the physical baseline state quantities (blue boxes, cf. sec. 1.5) for GRACE and the lower part for the e.motion² concept. As shown in the figure, both missions can obtain ranging information from GNSS and a dedicated ranging instrument (KBR or LRI). The precision and accuracy of the measurements is not shown in the plot. However, this cross-link can be used to improve the kinematic orbit determination or to estimate the offset in the biased inter-satellite ranging. In the e.motion² concept, the additional channel of attitude information from laser interferometric DWS and steering mirror orientation leads to an increased density of interconnections. For example, the precise GNSS-derived line-of-sight can be compared to the line-of-sight estimate on each satellite, which is based on DWS and star camera information.

In the data processing scheme proposed in section 1.4.6 on page 32, the baseline state quantities (blue boxes in figure 1.32) are obtained by solving a single system of equations, taking into account all available information. Note that the block diagram in figure 1.32 is simplified in many aspects and does not reflect all interconnections and steps, as various calibrations are missing, e.g. temperature, scale factors, offsets and so forth.

Two major calibrations will be addressed in the next sub-sections. One is regarding the accelerometer (DC) scale factor, and the other is the attitude correction for the laser ranging instrument (box labeled A.C. next to to the LRI in figure 1.32), which causes a coupling of rotations into the ranging measurement. The last sub-section addresses briefly thermal aspects in the design of future missions.

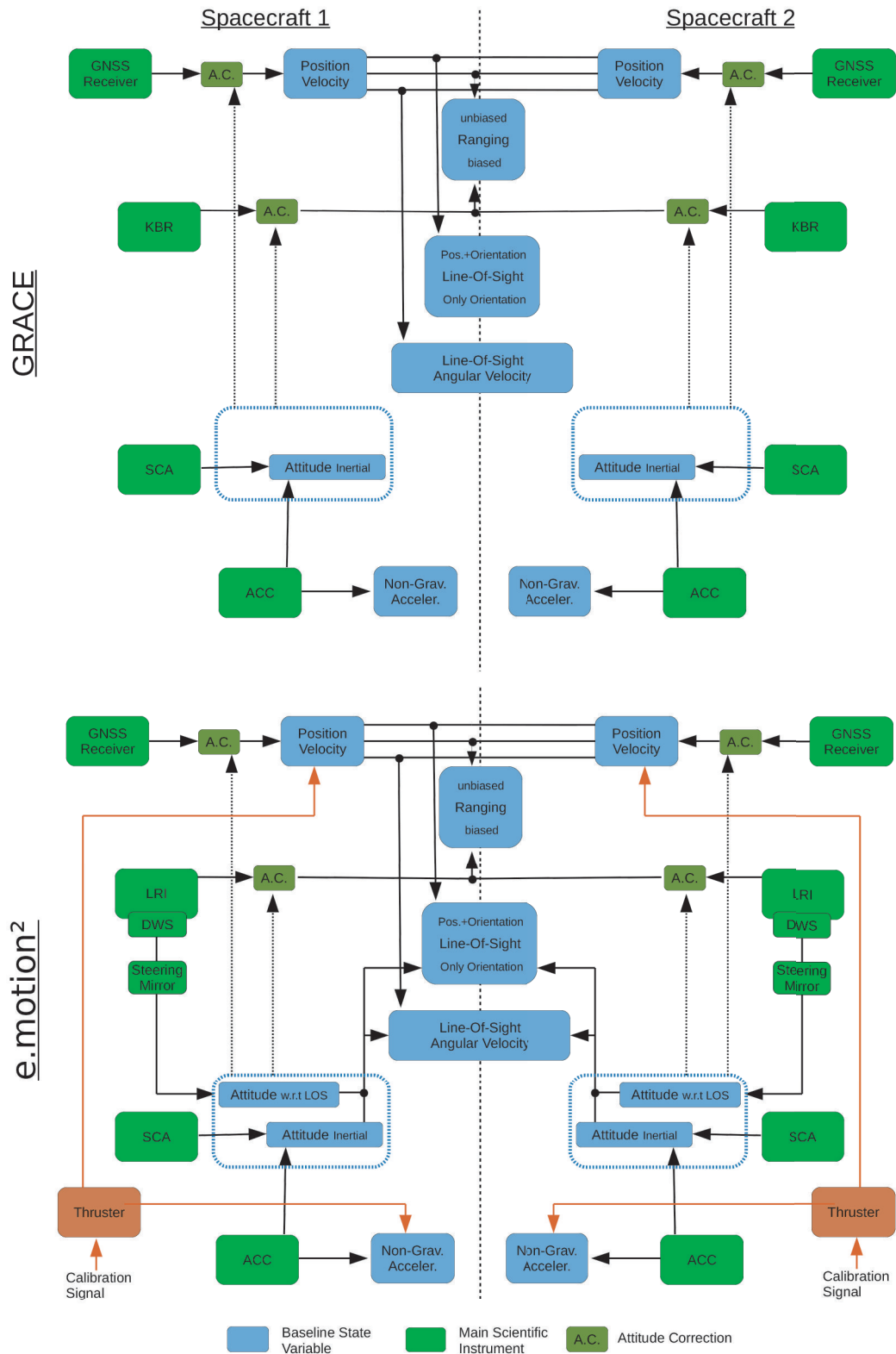


Figure 1.32: Block diagram of instruments (measurements) and baseline state variables for the GRACE mission (top) and e.motion² (bottom). Abbreviations: SCA: Star Cameras, ACC: Accelerometer, LRI: Laser Ranging Instrument

1.10.1 Calibration of Accelerometer Scale Factor

This calibration is driven by the necessity to determine the accelerometer DC scale factor $S_{DC}^{(ACC)}$ precisely to a level of $2 \cdot 10^{-3}$ in-flight (cf. sec. 1.9.2), which is assumed to be beyond the capability of predictions based calibrations made on ground.

In the e.motion² proposal, the use of dedicated calibration tones was suggested by the author of this thesis [e.motion² Team, 2014, sec. 5.2.4], which can be conveniently implemented in a drag-compensation or drag-free control loop. A natural idea is to produce a signal which can be measured simultaneously by accelerometer and LRI. The ratio of both measurements provides the scale factor of the accelerometer, as the LRI scale factor can be assumed to be accurate to approx. 10^{-6} . The sinusoidal calibration signal, which is fed to the thruster, is shown in orange in figure 1.32. Ideally, the calibration frequency (band) should not overlap with the science measurement band, which is used for gravity field determination, as this simplifies data analysis.

For a future gravimetric mission with approx. 400 km orbit height, a calibration band between 0.10 Hz and 0.30 Hz is suitable, since only instrument noise and no signal is expected in the accelerometer and ranging measurement (cf. figure 1.33). The modulation of thrust by the calibration signal, injected into the AOCS loop used for drag-reduction, is directly measured by the accelerometer. However, it also changes the satellite dynamics, e.g. position, and therefore the inter-satellite distance, which is measured by the LRI. By using calibration signals with different frequencies on both satellites, a continuous calibration of both accelerometers in a link is possible with the LRI.

The calibration tones do not require additional propellant if the mean of the calibration tone is used to compensate the average (DC) atmospheric drag. Consider an average drag force of $50 \mu\text{N}$, which can be compensated by an oscillating thrust between $5 \mu\text{N}$ and $95 \mu\text{N}$. This yields an acceleration rms-peak amplitude of $3.98 \cdot 10^{-8} \text{ m/s}^2$ at the calibration frequency in the accelerometer measurement and an equivalent 100 nm rms ranging distance variation in the LRI, if the calibration tone frequency is 0.1 Hz and a satellite mass of 800 kg is assumed. Averaging for three orbital periods ($T \approx 16600 \text{ s}$) yields a spectral density peak magnitude of $5.13 \cdot 10^{-6} \text{ m}/(\text{s}^2\sqrt{\text{Hz}})$ or equivalently $13 \mu\text{m}/\sqrt{\text{Hz}}$. To reach a signal-to-noise ratio of 500, which is equivalent to estimating the accelerometer scale factor to $2 \cdot 10^{-3}$, the ranging measurement noise needs to be $\lesssim 25 \text{ nm}/\sqrt{\text{Hz}}$, corresponding to the actual sensitivity requirement (cf. eq. (1.39)) at the high end of the science measurement band. A tightening of the LRI requirement for the calibration band could be envisioned, as the two main noise contributors of the LRI roll-off at high frequencies. The following requirement

$$\text{ASD}[\rho_{\text{biased,E}}](f) = 25 \frac{\text{nm}}{\sqrt{\text{Hz}}} \cdot \sqrt{\left(\frac{0.1 \text{ Hz}}{f}\right)^4} \cdot \frac{L}{100 \text{ km}}, \quad 0.1 \text{ Hz} < f < 0.3 \text{ Hz} \quad (1.125)$$

allows to measure the accelerometer scale factor with an accuracy of $2 \cdot 10^{-3}$ for all frequencies in the calibration band (0.1 Hz...0.3 Hz).

The instrument sensitivity level of interferometer and accelerometer in e.motion², the respective expected signal level and the calibration tones are depicted in figure 1.33.

Although the calibration modulates the position of the satellites, the precision of the GNSS observations is not sufficient to resolve the sub-mm effect. The calibration tone amplitude in the range-domain could be enhanced by a higher thrust variation or by using lower frequencies. However, the first option would result in an increased propellant demand and the second option yields a superposition of calibration signal and a high signal from orbital dynamics, i.e. gravity field, and is therefore considered unfeasible.

The here discussed accelerometer scale factor calibration was initially introduced for a drag-compensation concept with servo-accelerometer and neglects any non-linearities or quadratic coupling. However, in a drag-free concept with a test-mass motion of $\pm 120 \mu\text{m}$ and $\pm 1 \text{ mrad}$ (cf. sec. 1.9.4) such effects might be non-negligible.

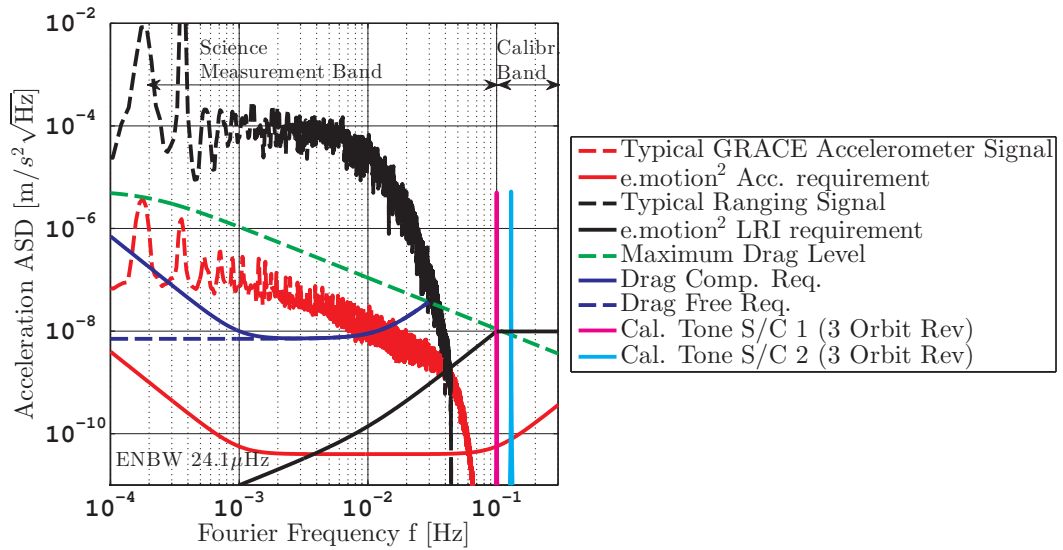


Figure 1.33: Calibration tones within a calibration band, induced by the drag-reduction control loop, are measured by accelerometer and LRI. This allows one to retrieve the accelerometer scale factor. The stated ENBW is valid for the calibration tones but not for the traces labeled with “typical” in the legend.

1.10.2 Calibration of Rotation-to-Ranging Coupling

The spacecraft rotation-to-ranging (or pathlength) coupling is one of the major error contributors in the ranging observation, either with laser or microwave radiation. It mainly results from the non-perfect pointing of the S/C along the line-of-sight due to disturbance torques and forces in orbit in combination with an offset between the center-of-rotation and ranging reference point, e.g. microwave antenna phase center or TMA vertex in GRACE-FO like laser interferometry. In addition, the baseline (line-of-sight) is not rotating at a constant angular rate (cf. light blue trace in figure 1.23), which requires active steering of the S/C. If the satellite misalignment in yaw ($y(t)$), pitch ($p(t)$) and roll ($r(t)$) is written as a vector $\vec{u} = (y(t), p(t), r(t))^T$, the error coupling into the ranging observation ρ due to one spacecraft can be expanded as a power series to quadratic order as

$$\delta\rho(t) \approx (c_y, c_p, c_r) \cdot \vec{u} + \vec{u}^T \cdot \begin{pmatrix} c_{yy} & 0 & 0 \\ c_{py} & c_{pp} & 0 \\ c_{ry} & c_{rp} & c_{rr} \end{pmatrix} \cdot \vec{u}. \quad (1.126)$$

The critical coupling angles are yaw and pitch, corresponding to an offset between ranging reference point and CoM perpendicular to the line-of-sight, while the interferometer is less susceptible to roll rotations and offsets along the line-of-sight. A coupling of 1 mm/rad corresponds to an offset of 1 mm in non-LOS direction.

Detailed discussion of the coupling is postponed until section 2.6. It is remarked here that the linear (and quadratic) coupling is minimized by design in the case of the GRACE Follow-On and e.motion² LRI to $\lesssim 0.1$ mm/rad, while the GRACE (FO) microwave system has a linear coupling of the order of a few mm/rad [Horwath *et al.*, 2010]. Unfortunately, the coupling factors cannot be determined credibly to a precision better than approx. 0.1 mm/rad on-ground in case of the LRI, while the microwave precision is even lower due to the approx. 1.5 m offset in LOS direction.

Thus, in-orbit estimation is typically performed by correlating attitude information with the range measurement in the process of gravity field recovery. However, due to the large unmodelled signal in the ranging data, i.e. post-fit residuals, the determination of the coupling coefficients to a level of better than 0.1 mm/rad is questionable. One should also consider

that the S/C CoM may be unstable at the level of 0.1 mm/rad due to differential thermal expansion, thermo-elastic deformations and other effects.

A promising approach for a calibration would be based again on calibration signals in form of periodic pointing variations with magnitude u_c in yaw and pitch, potentially also in roll, and at high frequencies, where no gravity signal is present, e.g. around 0.15 Hz. The accuracy for estimating the yaw c_y or pitch c_p coupling factor can be computed with

$$\delta c = \frac{\text{ASD}[\rho_E]}{u_{c,\text{rms}} \cdot \sqrt{T}}, \quad (1.127)$$

where $\text{ASD}[\rho_E]$ is the sensitivity of the ranging measurement. Considering an integration time of $T = 45$ min and a pointing excitation of $u_c = 25 \mu\text{rad}_{\text{rms}} = 35.4 \mu\text{rad}_{\text{pk}}$, one arrives at a sensitivity of $\delta c \approx 20 \mu\text{m}/\text{rad}$. This means the offset between ranging reference point and CoM can be determined to 20 μm every 45 min in the plane perpendicular to the line-of-sight.

Such an excitation would also allow one to compare continuously the angular measurements from accelerometer, star cameras and LRI DWS and in particular track the S/C CoM quasi-continuously, instead of sporadically as currently performed in GRACE [Wang, 2003].

As linear accelerations falsify the calibration, pure torque actuators like magneto-torquer or reaction wheels should be envisioned. The maximum torque T_{max} required to produce the sinusoidal excitation u_c is simply given in case of linearized Euler equations by $T_{\text{max}} = I \cdot u_{c,\text{pk}} \cdot (2\pi f_c)^2$, where $f_c = 0.15$ Hz is the excitation frequency. In a worst-case assumption with a S/C moment of inertia of $I = 500 \text{ kg} \cdot \text{m}^2$, one obtains $T_{\text{max}} = 0.015 \text{ kg} \cdot \text{m}^2/\text{s}^2$. Such a torque can be produced by rotating a solid disk with $m = 2$ kg and 20 cm diameter sinusoidally with frequency f_c by 100 degrees (forth and back). These reaction wheels, which should be distinguished from fast-spinning momentum wheels, could produce the required sinusoidal pointing excitation, but one needs to ensure that the induced micro-vibrations are negligible.

A potential calibration or validation of the accelerometer by a well-defined torque might be considered as well but requires further analysis.

Alternatively, the torque $T_{\text{max}} = 0.015 \text{ kg} \cdot \text{m}^2/\text{s}^2$ can also be exerted with a magnetic linear dipole moment of approx. $600 \text{ A} \cdot \text{m}^2$ in Earth's magnetic field with $B = 2.6 \cdot 10^{-5}$ Tesla (worst-case at 400 km height). However, such dipole moment would require likely several magneto-torquers, remarkable electric power and mass resources and special means to mitigate electro-magnetic interference with other instruments. In addition, the simultaneous availability of the torque in all required axes, due to the 3-d structure of the geo-magnetic field, needs further analysis.

1.10.3 Thermal Monitoring and Control

An aspect of the integrated instrument analysis is the correction of scientific measurements for temperature effects, either temperature fluctuations with resulting measurement noise or periodic temperature variations with resulting tone errors. Temperature-induced errors have been reported for the star cameras, e.g. angles between the sensor heads [Harvey, 2016], for the accelerometer in terms of a susceptibility of the order of $10^{-10} \text{ m}/(\text{s}^2 \cdot \text{K})$ [Foulon, 2013] and for the ranging interferometer (cf. sec. 2.3.6).

The temperature sensitive parts of the main scientific instruments, e.g. laser frequency stabilization or accelerometer electronics, need to be located in a thermally stabilized zone. Proper selection of passive and active thermal control in several stages needs to ensure a thermal stability of better than $10 \text{ mK}/\sqrt{\text{Hz}}$ for the LRI [e.motion² Team, 2014, sec. 5.3.7.3] within the science measurement band, which is demanding due to the LEO orbit with changing sun incidence angle and open paths to space for the optical instruments. Furthermore, the variation in temperature should not exceed 0.1 K per orbital revolution in the thermally stabilized zone to suppress tone errors.

To verify the in-orbit thermal stability, and to enable precise corrections of science data in post-processing, high-performance temperature sensors have been suggested as scientific pay-

load on e.motion² [e.motion² Team, 2014, sec. 5.5.1]. They shall be read out at a sufficiently high sampling rate, e.g. 0.1 Hz. Suitable sensors with electronics have been developed for the LISA Pathfinder mission [Sanjuán, 2009] and reach a sensitivity of better than $1 \text{ mK}/\sqrt{\text{Hz}}$ at a Fourier frequency of 1 mHz.

In general, it is recommended to consider the temperature stability already in early stages of the S/C design and to account for a precise measurement of temperature.

1.11 Summary & Conclusion

The first part of this thesis revisited and extended the e.motion² concept as a future gravimetric satellite mission, consisting of two satellite pairs in low Earth orbits in a so-called Bender configuration. The aim of the mission is the measurement of Earth's time-varying gravity field on a monthly basis. In the beginning, the composition of Earth's gravity field has been introduced (sec. 1.1.1), together with the basic concepts to measure it (sec. 1.1.2). The e.motion² proposal is based on a combination of GNSS-based high-low satellite-satellite-tracking and ranging-based low-low satellite-satellite tracking.

In many aspects, gravimetric missions with accelerometry and ranging have overlap with missions from fundamental gravitational physics, which can yield fruitful technology transfer as demonstrated by laser ranging interferometry (sec. 1.1.3). From a gravitational physics perspective, Earth's gravity field produces a curvature in the fabric of space-time, which is measured by e.motion².

Some boundary conditions of e.motion², e.g. the rationale behind the selection of orbits or altitude, have been explained (sec. 1.2), prior to a mathematical description of the gravity field measurement (sec. 1.3). It was discussed that each spherical harmonic (SH) coefficient of the gravity field induces a comb of sinusoidal signals at different frequencies in the observables. However, as the gravity field is composed of an infinite number of coefficients, the power distribution is quasi-continuous over frequency. By selecting a science measurement band from 0.18 Hz to 0.1 Hz, most of the gravity field signal can be recorded for later gravity field recovery.

The definition of the gravitational reference point (GRP) was addressed in section 1.3.6, which is, loosely speaking, the reference point of the satellite which all measurements are referred to. The difference between center-of-gravity and center-of-mass GRP was pointed out, as well as the fact that missions utilizing drag-free control should choose a different GRP compared to missions utilizing servo-accelerometers.

The characteristics of the different scientific instruments and their sensitivity models were introduced (sec. 1.6) and propagated to the final observables of the projected differential gravitational acceleration (PDGA) and the direct acceleration (DA). Comprehensive error models with various contributions revealed that the pure intrinsic instrument noise level of accelerometer and interferometer are not sufficient to assess the final sensitivity of gravity field observations. Instead, errors in gravity background models, in GNSS observations as well as instrument errors beyond simple noise, e.g. scale factors, need to be considered. It was shown that the analysis is compatible with the GRACE gravity field post-fit residuals (sec. 1.6.2), providing confidence on the validity for the future e.motion² mission.

The baseline (or line-of-sight) centrifugal acceleration was identified as a critical component. It can be written in terms of the baseline angular velocity, which can be derived from GNSS observations only with insufficient precision. This issue was completely neglected in the initial e.motion² study but was overcome here by replacing the kinematic orbits with more precise reduced-dynamic orbits. However, the simulation of the full dynamic-orbit determination, which accounts for realistic background gravity field models, was beyond the scope of this thesis and the precision was derived by a simplified model (sec. 1.5.2).

In sec. 1.7, the sensitivity models of PDGA and DA have been translated to gravity fields and SH degree variances. The acceleration approach was preferred due to its linear relation, which allows to easily propagate errors from observation to SH coefficients. For example,

different strategies to handle tone errors have been considered (sec. 1.7.2), which improve the measurement of particular SH coefficients being highly correlated with tone errors, e.g. C20. The gravity field results for a single polar satellite pair obtained by the here-presented method was comparable to the results obtained previously in the e.motion² study by independent other groups. In case of the e.motion² Bender constellation with two pairs, a significant improvement over a single-pair constellation could be demonstrated, making an e.motion²-like mission favorable. Unfortunately, the here-obtained result was significantly better and probably over-optimistic compared to full-scale simulations from the initial e.motion² study, which is possibly due to the simplified handling of errors in reduced-dynamic orbits.

However, the simulation approach from first principles, via instrument sensitivity models to the final SH gravity field coefficients, allowed to identify critical aspects of the mission design. One is the aforementioned centrifugal acceleration, which is not measured directly with high precision by instruments but contains almost as much gravity field information as the ranging data. A dedicated measurement would certainly improve gravity field solutions, and was hence discussed in sec. 1.8. However, the here-suggested different methods showed that it is non-trivial to measure this quantity more precisely than with GNSS or precise orbit determination.

Another interesting aspect for future missions is the consideration of drag-reduction schemes (sec. 1.9), which are required generally to maintain the orbit repeat cycles and to avoid accelerometer saturation. The latter fact does not apply for the e.motion² parameters as shown in Appendix A. Another benefit of drag-reduction, or more precisely reduction of non-gravitational forces, is a decreased susceptibility for accelerometer scale factor variations. These have been identified as a driving requirement and made drag-reduction within the measurement band mandatory for e.motion².

Although the initial e.motion² study used servo-accelerometers and drag compensation as baseline, the feasibility of a drag-free concept for a LEO gravimetric mission remains an open interesting question. In particular, the demonstrated superb sensitivity of the LISA Pathfinder spacecraft [Armano *et al.*, 2016b], orders of magnitude below the noise of servo-accelerometers, in combination with other advantages such as physically well-defined GRP, advertise the promising technology for future gravimetric missions. For e.motion², a preliminary assessment on feasibility in sec. 1.9.4 showed positive results and first requirements on thruster noise and AOCS loop gain were provided but require more thorough analysis in the next years.

The last section 1.10 elaborated means of in-orbit calibrations and corrections of measurements for e.motion² and potentially other future gravity missions. Two calibration schemes were introduced. The first one due to the need to determine the absolute accelerometer scale factor to a level of 0.2%. It is based on sinusoidal thrust modulations in the calibration band (0.1 Hz to 0.3 Hz) injected via the AOCS control loop. It is found that this would not increase the average propellant consumption required to maintain the (roughly) geodesic orbit and corresponding repeat pattern. The idea behind the scheme is to measure the calibration tones on both S/C in a link with the accelerometer and with the ranging instrument in parallel, which allows one to derive the accelerometer scale factors, in particular because the LRI scale factor is more stable. With the precise scale factor, the accelerometer measurements can be converted into actual physical non-gravitational accelerations at the specified e.motion² accelerometer sensitivity level.

The second calibration scheme (sec. 1.10.2) regards the S/C rotation-to-ranging coupling, which is a major error contributor in the range observation. With small sinusoidal pointing excitations of the S/C in the calibration band, the coupling coefficients can be determined sufficiently well, providing the ability to correct the ranging data for gravity field recovery and to validate other angular measurements from star cameras and accelerometer.

Furthermore, the third correction scheme (sec. 1.10.3) attempts to utilize high-performance temperature sensors, since the temperature correction of science data will become more important in the context of an integrated data analysis in future gravity missions with advanced

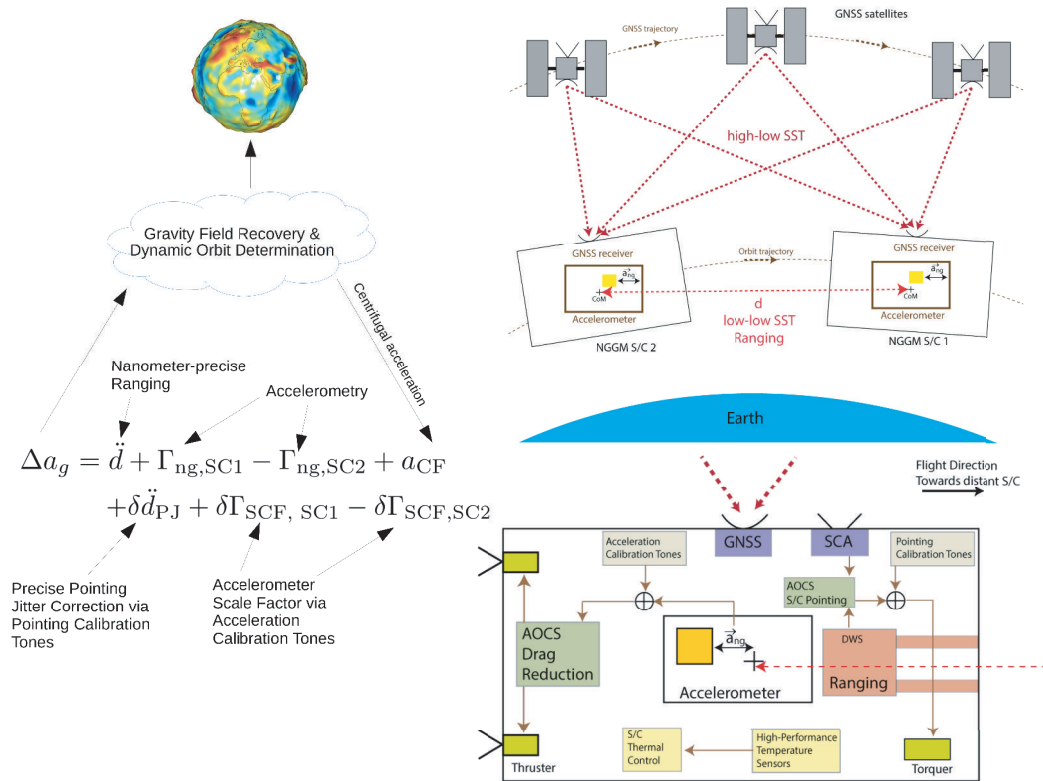


Figure 1.34: Overview of the e.motion² concept as presented within this thesis.

sensitivity. However, such corrections cannot circumvent solid thermal design of the S/C.

This first thesis part is concluded with figure 1.34, which summarizes the e.motion² instrument concept.

Part 2

Laser Interferometry in Space

Distance and distance changes can best be determined precisely by means of electro-magnetic radiation simply because length is defined by the propagation velocity, the speed of light c_0 , of such radiation in vacuum (cf. SI definition of length¹). Two commonly used techniques are:

- The measurement of the propagation time Δt of a laser pulse or of a modulation feature on the light. This can provide the absolute distance d via the relation

$$d = c_0 \cdot \Delta t. \quad (2.1)$$

Such a direct time of flight measurement requires precise clocks and precise time stamping of the emission and arrival of the light pulse. Absolute accuracies at millimeter level are currently achievable, e.g. by laser rangefinder [Eisele, 2014]. This technique is also used, for example, in lunar laser ranging to determine the absolute distance between Earth and Moon.

- The continuous measurement of the phase of electro-magnetic radiation by means of interferometry. Electro-magnetic waves are described by an oscillating electro-magnetic field vector. The phase is part of the state of the electro-magnetic field vector and is a repetitive feature propagating with the speed of light. For light, the phase can not be directly measured, since it changes too quickly, but by using interferometry the phase can be indirectly determined by overlapping the measurement wave with a reference wave. This allows the phase difference between the measurement wave, which traversed the distance one aims to measure, and the known reference wave to be determined. The phase difference can be directly converted to a pathlength difference via the wave's frequency or wavelength. However, the repetitive or oscillating nature of the phase prevents the determination of the absolute distance. Instead, a time-resolved biased distance, which means the time-varying distance up to an unknown constant offset, can be measured. Loosely speaking, in interferometry, one determines the distance with the help of a ladder. The separation between the rungs of the ladder is the electro-magnetic wavelength. The distance to the next rung of the ladder, which can be understood as the phase, can be measured precisely. However, the actual rung number is unknown.

Both techniques can also be combined, as it is widely used in Global Navigational Satellite System (GNSS) applications with a rough absolute but unprecise code measurement and a precise but biased phase measurement. Radio and microwave signals are routinely used for ranging purposes, but are less suited for high precision metrology due to the long wavelength. Lasers in the visible or near-IR part of the spectrum enable relative measurements in the nano-, pico-, and even femtometer regime using interferometry.

Optical interferometers as high precision inter-satellite ranging instruments have been developed in the context of the LISA mission since the 1990s [Bender *et al.*, 1998; Danzmann

¹General Conference on Weights and Measures 1983, Comptes rendus de la 17e CGPM (1983), 1984, 97

et al., 2017]. The LISA mission aims to resolve inter-satellite distance variations with a noise level of a few picometers (10^{-12} m/ $\sqrt{\text{Hz}}$) at millihertz frequencies between satellites in a quiet deep-space environment with approx. 2.5 million km ($2.5 \cdot 10^9$ m) separation between spacecraft. Nowadays, such sensitivities are routinely achieved in laboratories at short time scales, but stabilization of the optical setups and of the readout electronics over long timescales (millihertz regime) is demanding. In addition, LISA technology is capable of determining the absolute inter-satellite distance to sub-meter accuracy by applying additional modulations on the laser link.

In the last decade, optical space interferometry was also considered for space missions to measure Earth's gravity field and resulted in the Laser Ranging Interferometer (LRI) onboard GRACE Follow-On. The LRI is a technical demonstrator to be launched in 2018 with a sensitivity requirement of 80 nm/ $\sqrt{\text{Hz}}$ for Fourier frequencies above 10 mHz. For future gravimetric missions this technology is expected to be used as the primary inter-satellite ranging instrument. In these missions, determination of the absolute inter-satellite distance is performed by means of GNSS and dedicated absolute ranging is not considered necessary.

This second thesis chapter provides an overview of the current state of inter-satellite laser ranging interferometry and addresses potential improvements for future instruments. The author of this thesis has been and is still involved in the development of the GRACE Follow-On LRI, which is the first inter-satellite laser ranging interferometer, and the author has provided substantial input within the e.motion² mission study on the general payload concept and on the laser interferometry, which resulted in a published comprehensive report [e.motion² Team, 2014]. For this thesis, many of the ideas have been revisited, advanced and embedded in a broader context together with completely new aspects.

The outline of this chapter is as follows. The basics of the theory of relativity are reviewed in section 2.1, as relativistic effects need to be considered in the data analysis and are crucial for a precise understanding of the range measurement. The next section 2.2 is used to introduce fundamental interferometer techniques such as phase retrieval methods and interferometric observables, e.g. longitudinal phase, differential wavefront sensing (DWS) and differential power sensing (DPS). The third section 2.3 is concerned with the technology for subsystems of laser interferometers, e.g. laser sources, photodiodes, phasometers, clocks, and so forth. The main specifications, figures of merit and driving requirements are introduced as they set the boundary conditions for the following study and discussion of interferometers.

Although the field of optical inter-satellite ranging interferometry is just emerging, various optical layouts and designs have already been suggested in literature for gravimetric missions [Kawamura *et al.*, 2009; eLISA/NGO Team, 2012; Danzmann *et al.*, 2017; e.motion Team, 2010; e.motion² Team, 2014; Dehne *et al.*, 2009; Sheard *et al.*, 2012; NG2-Team, 2011; Alenia-Team, 2010] and for the gravitational-wave mission LISA [Bender *et al.*, 1998; d'Arcio *et al.*, 2010]. A systematic approach to the field has been attempted here by categorizing the concepts at different levels, namely at the level of functional concepts and at the level of optical layouts. The former one includes one-way ranging, dual-one way ranging, transponder-based ranging and, briefly, passive retro-reflectors, while the latter one is divided into on-axis and off-axis layouts. The different functional concepts, which are to a large extent independent of the actual interferometer design, are studied in section 2.4. Mathematical models of the phase observables are derived for the main functional concepts and the potential error contributors are discussed including laser frequency noise, relativistic effects and timing errors. In addition, the relation between phase observables and the instantaneous range between the satellites, which is typically used in the data analysis of gravimetric missions, is established. Although optical interferometry differs in many aspects from ranging by means of radio-waves, e.g. microwaves, some parallels exist and are stressed in this section.

Important contributors to the phase-derived biased range measurement are effects due to the inter-satellite propagation, which include relativistic effects due to the finite speed of light and fluctuations from the ionosphere or atmosphere. These are called photon time of

flight corrections in this thesis, and are addressed in sec. 2.5. Within sec. 2.4 and 2.5 one obtains the precise relation of the phase measurement to the instantaneous range, so that the equations and provided corrections, e.g. for relativistic effects, can be readily used in actual flight-data processing and in the simulation of realistic data streams for studies of future missions.

Section 2.6 addresses principles of the actual instrument design that can be roughly separated into aspects regarding the minimization of ranging errors and into aspects regarding the optimization of the signal strength and signal-to-noise ratio, the so-called carrier-to-noise density. One major contributor to the ranging errors is the so-called attitude-to-ranging coupling, which is described in this thesis with the help of reference points of the interferometer. These reference points attempt to provide a geometrical representation of the typical coupling factors of S/C attitude into the phase-derived range measurement. It turns out that these points can be used as a figure of merit and characterization criteria for designs, e.g. off-axis vs. on-axis designs. Moreover, the well-definedness and the stability of these points are important aspects, since these points can be understood as the fiducial points for the biased range measurement. The second half of section 2.6 is concerned with the carrier-to-noise density, which is driven on the one hand by the received power and on the other hand by the wavefront overlap within the interferometer. Detailed models are derived for both quantities.

Section 2.7 contains a survey of optical layouts, which have been proposed so far for space laser ranging instruments. The location of the reference points in the different layouts is discussed and it is pointed out that the optical design should include a retro-reflection property of the light. An off-axis layout with a corner-cube retro-reflector, which is well understood from previous work and which offers various advantages, is suggested for a future e.motion²/NGGM mission. It incorporates various learned lessons. Moreover, an on-axis layout could be derived and proposed as alternative for future missions, which offers the same advantages as the off-axis concept, however, with the capability to include a telescope in the laser link.

Both proposed optical layouts have various free parameters, such as beam sizes or telescope magnification, which are optimized with the help of optical power link budgets and parametric studies in section 2.8. The budgets are a helpful tool to ensure that the carrier-to-noise density (discussed in sec. 2.6) is sufficiently high and, thus, the instrument can perform the phase measurement in the operational conditions including satellite misalignments. It turns out that an on-axis design with a telescope does not provide much benefit in a gravimetric satellite mission. However, the proposed on-axis layout may still be a viable option even without a dedicated telescope as it may show a reduced complexity due to the lack of a corner-cube retro-reflector.

Finally, section 2.9 concludes this thesis part with a summary and some finishing remarks.

2.1 Introduction to Relativity

Ranging interferometry in GRACE-like missions and even in GNSS would not work without proper consideration of relativistic effects, which manifest as delays due to the finite speed of light and due to gravity, as the time dilation of clocks on-board the satellites or simply as relativistic corrections to the equations of motion. Most effects can be described as corrections to the classical Newtonian theory. Here, the basic concepts and ideas of special and general relativity are recalled, but an in-depth introduction to relativity is beyond the scope of this section and the interested reader is referred to [Misner *et al.*, 1973], [Kopeikin *et al.*, 2011] and [Schutz, 2009].

In the classical Newtonian theory, the motion of a rigid body, such as a GRACE-like satellite, can be decomposed into the translation of the center of mass and the rotations of the body around the center of mass. The translations are governed by Newton's law of

motion

$$\vec{a}_i(t) = \frac{d^2 \vec{r}_i(t)}{dt^2} = \vec{F}_i(t)/m, \quad (2.2)$$

while the rotation can be described with Euler's equations. Equation (2.2) states that the second time derivative of the center of mass position $\vec{r}_i(t)$ of the i -th S/C, i.e. the acceleration \vec{a}_i , is proportional to the force \vec{F} acting on the satellite. The symbol m denotes the mass of the satellite. It is noted that the acceleration contains gravitational and non-gravitational contributions. The force and acceleration show a dependency on the S/C attitude, which means that for precise simulations and calculations all six degrees of freedom need to be considered simultaneously.

In Newtonian and Galilean theory, the time t is an absolute global parameter. However, since Einstein's theory of relativity, it is known that time is not an absolute parameter. Even ideal error-free clocks accumulate the time at different rates depending on various factors such as their speed or gravitational potential. In the context of relativity, it is advantageous to describe the trajectory of a point-mass or a particle through space and time as a four-vector

$$x_i^\alpha(t) = (x_i^0, x_i^1, x_i^2, x_i^3) = (c_0 \cdot t, \vec{r}_i(t))^\top, \quad (2.3)$$

which is called the *world line*. The 3-dimensional trajectory or orbit \vec{r}_i through space is now supplemented by the coordinate time t . Moreover, there exists the proper time $\tau_i(t)$, which an error-free and co-moving clock would display for the particle. The proper time is the error-free on-board time of the satellites in the context of this thesis. The symbol c_0 is the constant proper speed of light in vacuum, which is nowadays defined as exactly 299 792 458 m/s [Petit *et al.*, 2010]. Recall that the components of the position \vec{r}_i indicate the distances along different axes from the coordinate frame origin, and distances are in general defined via the propagation time of light and the constant c_0 .

The theory of general relativity currently provides the most precise means with which to describe gravitation on macroscopic scales. It can be accessed from a geometrical perspective, where it states that an object with a particular initial position and velocity and solely under the influence of gravitation will follow the *shortest* world line through the four dimensional space-time. The term *short* with regard to a world line requires the definition of a distance in the four dimensional space-time, which differs from the classical Euclidean distance for purely spatial trajectories. The squared length of an infinitesimally short section of the world line, the so-called interval ds^2 , is defined in general relativity (GR) by the metric tensor $g_{\mu\nu}$ as

$$ds^2 = g_{\mu\nu}(x_i^\alpha) \cdot dx^\mu \cdot dx^\nu, \quad (2.4)$$

where the Einstein summing convention was used, meaning that the expression on the right hand side is summed over each index that appears once up and once down. Greek indices such as α , β , μ and ν can range from 0..3. Thus, the previous equation can be written as a left- and right-sided multiplication of the vector $\vec{x}_i = x_i^\alpha$ with the 4×4 matrix $\hat{g}_{\mu\nu}$. It should be noted that world lines can be categorized into time-like ($s^2 < 0$), light-like ($s^2 = 0$) or space-like ($s^2 > 0$) curves.

The metric tensor $g_{\mu\nu}$ is, in general, a function of the time and position x_i^α and of the matter and energy content in space-time. In the absence of matter and energy², the space-time is said to be flat and can be described in Cartesian coordinates by the metric tensor

$$\hat{g}_{\mu\nu} = \hat{\eta}_{\mu\nu} = \hat{\eta}^{\mu\nu} = \begin{pmatrix} -1 & 0 & 0 & 0 \\ 0 & 1 & 0 & 0 \\ 0 & 0 & 1 & 0 \\ 0 & 0 & 0 & 1 \end{pmatrix}. \quad (2.5)$$

²and in absence of exotic objects such as black holes

This is the so-called Minkowski metric and represents the domain of special relativity (SR). In the presence of matter and energy, i.e. with gravitation, the space-time is curved and the metric tensor deviates from eq. (2.5). For the rather small mass and energy density present in our solar system or in the vicinity of Earth, it is beneficial to express the metric tensor $g_{\mu\nu}$ with a perturbation $h_{\mu\nu}$ as

$$g_{\mu\nu}(x_i^\alpha) = \eta_{\mu\nu} + h_{\mu\nu}(x_i^\alpha). \quad (2.6)$$

The metric perturbation can be understood as a generalization of the gravitational potential from Newtonian theory. With this perturbation, the shortest world line, for example, results in an elliptic trajectory in the case of a satellite orbiting the Earth.

Although SR seems to be restricted to a small domain of validity, it is of great importance due to the fact that locally, in a sufficiently small region around the origin of a coordinate system, the metric tensor can be made flat by a proper choice of the coordinate system. This is a consequence of relativity, which means that the equations describing the laws of physics are the same in all admissible frames. For example, the physics within a (small) satellite can be considered in a flat spacetime, e.g. relativistic effects between on-board instruments are negligible, light propagation obeys the classical rules on the satellite, and so forth.

In this thesis, relativistic effects become important for the definition of the on-board time (sec. 2.3.4), the derivation of the phase observable (sec. 2.4) for different functional concepts, and for relativistic corrections of the light propagation time (sec. 2.5). For the computation of the orbit trajectory and relativistic effects of LEO satellites, an Earth-centered and quasi-inertial coordinate system is advantageous, which will be introduced next.

2.1.1 The Geocentric Celestial Reference System (GCRS)

The GCRS, or the realization denoted as Geocentric Celestial Reference Frame (GCRF), is well-suited for describing the motion of satellites around the Earth and to simulate interferometric ranging observations in a gravimetric mission. It is a kinematically non-rotating frame with respect to the solar system barycentric coordinate system (BCRS). The origin of the GCRS is co-located with Earth's center of mass and the z -axis is roughly along Earth's angular velocity vector. The exact orientation of the GCRS axes w.r.t. the BCRS is not relevant for the purpose of this thesis.

Transformations between the GCRS and the rotating Earth-fixed International Terrestrial Reference System (ITRS), where Earth's geopotential is (almost) constant, are specified in the IERS conventions [Petit *et al.*, 2010].

The coordinate time t of the GCRS is a theoretical time, which an ideal clock would provide far away from Earth, i.e. in the absence of a gravitational field, and co-moving with Earth's center, i.e. at rest in the GCRS. Although the initial epoch $t = 0$ is irrelevant for the purpose of this thesis, the so-called Geocentric Coordinate Time (TCG) has been established [Petit *et al.*, 2010, sec. 10.1]. The TCG time is related to the terrestrial time (TT) by the constant L_G [Petit *et al.*, 2010, sec. 10.1] by

$$\frac{dt_{\text{TT}}}{dt_{\text{TCG}}} = 1 - L_G = 1 - 6.969290134 \cdot 10^{-10}. \quad (2.7)$$

The terrestrial time is realized, for example, by the Terrestrial Atomic Time (TAI) or by the GPS time and both time scales have (approximately) the same rate as the SI second on the geoid. Thus, the TCG time used to derive the satellite's trajectory and simulated observations is different from the time typically used on Earth. Hence, all constants relying on the second need to be properly scaled for simulations to account for the correct time system, e.g. the GM value of a gravity field model [Gurfil & Seidelmann, 2016, sec. 3.8].

The commonly used metric tensor for the GCRS is given in eq. (B.4) in the appendix B.

2.1.2 Equations of Motion

The equations of motion for a massive or massless test-particle in a gravitational field are governed, in the context of general relativity and in absence of other forces, by the geodesic equation

$$\frac{d^2 x^\mu}{d\lambda^2} = -\Gamma^\mu_{\alpha\beta}(x_i^\nu) \cdot \frac{dx^\alpha}{d\lambda} \cdot \frac{dx^\beta}{d\lambda}, \quad (2.8)$$

where the Einstein summing convention was used again. The so-called Christoffel symbols $\Gamma^\mu_{\alpha\beta}(x_i^\nu)$ are defined in appendix B and depend on the metric tensor and, hence, on the four-dimensional position x_i^ν , which is commonly called an *event*. The symbol λ is a scalar parameter of the motion such as the proper time τ_i . An equivalent equation with respect to the coordinate time t instead of parameter λ is [Kopeikin *et al.*, 2011]

$$\frac{d^2 x^k}{dt^2} = -\Gamma^k_{\alpha\beta} \cdot \frac{dx^\alpha}{dt} \cdot \frac{dx^\beta}{dt} + \frac{1}{c_0} \Gamma^0_{\alpha\beta} \cdot \frac{dx^\alpha}{dt} \cdot \frac{dx^\beta}{dt} \cdot \frac{dx^k}{dt} \quad \text{with } k = 1..3 \quad (2.9)$$

The geodesic equation is the analogon to Newton's equation of motion. As the mass and energy density in our solar system is rather small in terms of relativistic effects, such relativistic effects can be described by so-called Parameterized Post-Newtonian (PPN) approximations [Misner *et al.*, 1973, §39.11 PPN Equations of Motion] [Kopeikin *et al.*, 2011, sec. 6.1.5], where one can write the spatial equations of motion as a function of the coordinate time t by

$$\frac{d^2 \vec{r}_i(t)}{dt^2} = \vec{a}_i(\vec{r}_i, \vec{v}_i, t) + \vec{a}_{\text{PPN}}(\vec{r}_i, \vec{v}_i, t). \quad (2.10)$$

A derivation of \vec{a}_{PPN} can be found in appendix B with the final solution given in eq. (B.28) to eq. (B.30). Thus, the satellite trajectory can still be obtained by numerical integration, but requires some additional computational effort.

The proper time τ of a particle or satellite can be determined from the relation [Soffel & Langhans, 2012, p. 54]

$$d\tau^2 = -\frac{1}{c_0^2} ds^2, \quad (2.11)$$

which allows the proper time of the satellite τ_i to be written as a line integral along the geodesic world line [Kopeikin *et al.*, 2011, eq. 3.225]

$$\tau_i(t') = \int_0^{t'} \frac{d\tau_i(t)}{dt} dt = \frac{1}{c_0} \int_0^{t'} \sqrt{-g_{\mu\nu}(x_i^\alpha(t)) \cdot \frac{dx_i^\mu}{dt} \cdot \frac{dx_i^\nu}{dt}} dt \quad (2.12)$$

$$\stackrel{\text{SR}}{\approx} \int_0^{t'} \sqrt{1 - |\dot{\vec{r}}_i(t)|^2/c_0^2} dt. \quad (2.13)$$

The proper time τ of a LEO satellite deviates slowly from the GCRS coordinate time t . The small drift is mainly caused by the absolute velocity of the S/C within the GCRS and by the gravitational time dilation. The magnitude of the drift of the proper time in a LEO can be derived from the previous definition as

$$\frac{d\tau_i}{dt} - 1 \approx -\frac{|\dot{\vec{r}}_i(t)|^2}{2 \cdot c_0^2} - \frac{GM}{r \cdot c_0^2} \approx -3.21 \cdot 10^{-10} - 0.65 \cdot 10^{-9} \approx -1 \cdot 10^{-9}, \quad (2.14)$$

which assumed $|\dot{\vec{r}}_i(t)|^2 \approx 7600 \text{ m/s}$, $GM = 3.986 \cdot 10^{14} \text{ m}^3/\text{s}^2$ and $r = (6378 + 400) \text{ km}$. Although the effect seems small, it is still measurable, as will be discussed in sec. 2.3.4 on USO clocks. In addition, a modulation of the proper time also implies a modulation of the apparent laser frequency, which can yield non-negligible phase variations in interferometry.

It is remarked that the equations of motion (cf. eq. (2.10)) are also valid for a photon. A photon follows a so-called null-geodesic, i.e. the interval ds^2 vanishes along a photon world line. Since interferometry measures the phase of electro-magnetic waves, it is necessary to understand how the phase evolves through space-time. In [Misner *et al.*, 1973] it is shown that the phasefront of an electro-magnetic wave also follows such a geodesic, thus, it seems natural to switch between the equivalent wave and photon interpretations of light, where required. With proper selection of initial conditions for position and velocity one can numerically integrate eq. (2.10) in the GCRS to obtain the light path. However, one has to note that the coordinate velocity of a photon is not equal to the proper vacuum speed of light c_0 in general relativity. It equals c_0 in a flat space-time metric (cf. eq. (2.5)), and thus, in any local Lorentz frame along the light path. In general relativity, one can find at each point in space-time a coordinate frame, the local Lorentz frame, where the metric is flat close to the point, i.e. one has a Minkowski metric as in special relativity in the neighborhood of the point.

A derivation of the coordinate speed of light c_n in the metric of the GCRS is given in appendix B and can be written as a function of the photon position \vec{r} , the normalized propagation direction \vec{d} and the GCRS coordinate time t :

$$c_n(t, \vec{r}, \vec{d}) = c_0/n_{\text{gr}}(t, \vec{r}, \vec{d}). \quad (2.15)$$

One could write the apparent slow down due to the space-time curvature in the form of an equivalent refractive index $n_{\text{gr}}(t, \vec{r}, \vec{d})$. The proper time and the coordinate speed of light are of importance, as they influence the ranging observables obtained by laser interferometry.

2.2 Introduction to Interferometry

An interferometer utilizes the process of interference, which means the coherent superposition, i.e. addition, of waves with subsequent detection of the intensity. The resulting intensity pattern is different from the intensity patterns of the individual waves. Interference can be observed for acoustic waves, matter waves, surface water waves as well as with electro-magnetic radiation such as light, microwave or radio waves. Waves can interfere destructively, meaning a local annihilation, which can be used, for example, for active acoustic noise cancellation [Hansen, 2002]. Due to conservation of energy, destructive interference at one location is accompanied by constructive interference at another location. The interference result at a particular detection point depends on the state of the involved wave, i.e. on the phase and polarization of the waves at the point.

This thesis chapter focuses on interference of electro-magnetic waves, light in particular. Such waves can be described by the real-valued electric field vector $\vec{E}(\vec{r}, t)$ and the real-valued magnetic field strength $\vec{H}(\vec{r}, t)$, which both depend on the evaluation point \vec{r} and time t . There exists a connection between both field quantities, which will be introduced later. For the moment, only the electric field is considered and it is assumed that the coordinate system originates at the source of the electro-magnetic field, i.e. it is the rest-frame. Furthermore, general relativistic effects are omitted, which means that the space-time is flat.

Under such conditions one can write a generic model for a monochromatic vectorial electric field as

$$\vec{E}(\vec{r}, t) = \vec{P}(\vec{r}, t) \cdot E_0(\vec{r}) \cdot \cos(2\pi\nu t + \Psi(\vec{r})) = \text{Re} \left(\vec{E}^c(\vec{r}, t) \right), \quad (2.16)$$

which contains the normalized polarization direction \vec{P} , the amplitude E_0 , the phase $\Psi(\vec{r})$ and the frequency ν . For the sake of easing some algebraic operations, a complex electrical field \vec{E}^c can be defined analogously as

$$\vec{E}^c(\vec{r}, t) = \vec{P}^c(\vec{r}) \cdot E_0(\vec{r}) \cdot e^{i \cdot (2\pi\nu t + \Psi(\vec{r}))} = \vec{E}^c(\vec{r}) \cdot e^{i \cdot (2\pi\nu t + \Psi(\vec{r}))}, \quad (2.17)$$

where the time-dependence of the polarization vector was dropped, because circular or elliptical polarizations can be achieved by a phase difference between the vector components of \vec{P}^c . Throughout this thesis, quantities in the complex domain show a superscript c .

The phasefronts of a wave are the surfaces of constant phase, i.e. all \vec{r} fulfilling $\Psi(\vec{r}) = \text{const.}$ Such a phasefront propagates locally and in vacuum with the speed of light c_0 along the direction of the local wave vector \vec{k} :

$$\vec{k}(\vec{r}) = \vec{\nabla}\Psi(\vec{r}). \quad (2.18)$$

In general, the field quantities such as \vec{E} and \vec{E}^c obey Maxwell's equations. However, in optics the radiation typically shows a preferred direction and forms a beam. Many (analytical) beam models fulfill Maxwell's equations only under paraxial approximations, which means for points close to the preferred axis.

The phase Ψ for many beam or wave models can be written in the form of

$$\Psi(\vec{r}) = -\vec{k}_0 \cdot \vec{r} - \phi_E(\vec{r}), \quad (2.19)$$

with a constant wave vector \vec{k}_0 defining the preferred direction and with another slowly changing and model-dependent phase term ϕ_E . The local wave vector \vec{k} and the constant wave vector \vec{k}_0 have the norm

$$k = |\vec{k}_0| = |\vec{k}| = 2\pi n/\lambda_0 = 2\pi n\nu/c_0, \quad (2.20)$$

where λ_0 is the vacuum wavelength and n is the refractive index of the medium. The phase term $\phi_E(\vec{r})$ is a constant for plane waves and has a parabolic form in the case of Gaussian beams, for example.

The instantaneous phase $\Phi(\vec{r}, t)$ of any electro-magnetic wave is defined here as the argument of the cosine function in eq. (2.16), i.e.

$$\Phi(\vec{r}, t) = 2\pi\nu t + \Psi(\vec{r}) = 2\pi\nu t - \vec{k}_0 \cdot \vec{r} - \phi_E(\vec{r}). \quad (2.21)$$

One can show [Zhou *et al.*, 2007; Carter, 1972] that the phase Φ approaches spherical phasefronts, i.e.

$$\Phi^{\text{ff}}(r, t) = 2\pi\nu t - k \cdot r = 2\pi\nu t - \frac{2\pi n \cdot r}{\lambda_0}, \quad (2.22)$$

in the far-field along the direction of \vec{k}_0 , where $|\vec{r}| = r$ is much larger than the transverse spatial extension of the electric field.

Thus, the instantaneous phase of the electric field increases monotonically with time. Furthermore, the phase is proportional to the distance between the source and evaluation point \vec{r} in the far-field, i.e. spherical phasefronts are formed. The proportionality factor is the wave number k . This linear relationship is exploited in (laser) ranging interferometry to measure distance changes.

It is important to note that the time-derivative of the phase is an instantaneous frequency ν or an instantaneous angular frequency ω , i.e.

$$\omega = \frac{d}{dt}\Phi = 2\pi\nu. \quad (2.23)$$

The instantaneous phase Φ as introduced and discussed here is a purely theoretical quantity, which can not be measured directly, because only the electric field vector \vec{E} and the cosine of the phase is accessible. The cosine function is an even function, which makes the sign of the phase physically irrelevant. Moreover, the cosine function is a periodic function with 2π periodicity. Hence, the phase can only be determined modulo 2π , which is commonly called phase wrapping as values larger than 2π appear wrapped into the interval $0..2\pi$.

However, sufficiently dense consecutive measurements of the phase allow the phase jumps to be unwrapped as long as the phase change between consecutive measurements is sufficiently small, which will be utilized in the next subsection on phase retrieval and tracking.

The instantaneous phase value Φ of the wave \vec{E} propagates along the wave vector $\vec{k}(\vec{r})$ through space. This allows the phase value at a particular time t and position \vec{r} to be written in the form of a retarded time, i.e.

$$\Phi(\vec{r}, t) \stackrel{!}{=} \Phi(\vec{r}', t - \Delta t) = \Phi(\vec{r}', t) + 2\pi\nu \cdot \Delta t + \delta\phi_E, \quad (2.24)$$

where Δt is the propagation time of the phase value, i.e. the time of flight of a photon from the position \vec{r}' to the detection point \vec{r} . The last summand $\delta\phi_E$ is the phase change in the model-dependent phase ϕ_E between the emission point \vec{r}' and the evaluation point \vec{r} , which can often be omitted, since it is usually sufficiently constant. For example, for classical Gaussian beams $\delta\phi_E$ is the change in the Gouy phase. This method of rewriting the phase at the detection point \vec{r} and time t as the phase value at the location \vec{r}' and time $t' = t - \Delta t$ is essential for the precise description of the ranging observables in subsequent sections.

It is insightful to form the time-derivative of the first two terms of the previous equation. The derivative of the first term $\Phi(\vec{r}(t), t)$ can be written with the help of eq. (2.21) as

$$\frac{1}{2\pi} \frac{d\Phi(\vec{r}(t), t)}{dt} = \frac{1}{2\pi} \cdot \frac{\partial\Phi(\vec{r}(t), t)}{\partial\vec{r}} \cdot \frac{\partial\vec{r}}{\partial t} + \frac{1}{2\pi} \cdot \frac{\partial\Phi(\vec{r}(t), t)}{\partial t} = \frac{1}{2\pi} \cdot \vec{k} \cdot \vec{v} + \nu, \quad (2.25)$$

while the second term $\Phi(\vec{r}', t - \Delta t)$ yields

$$\frac{1}{2\pi} \frac{d\Phi(\vec{r}', t - \Delta t)}{dt} = \nu \cdot \frac{d\Delta t}{dt} + \nu. \quad (2.26)$$

In the first result, the Doppler effect is expressed with the velocity \vec{v} of the detection point \vec{r} , while in the second result the same Doppler shift is expressed with the time derivative of the propagation time $\Delta t = \Delta t(\vec{r}(t), \vec{r}')$. Both descriptions are equivalent.

In the next sections, radio waves are considered. They are electro-magnetic waves with frequencies up to several gigahertz or, in other words, with wavelengths larger than a few millimeters. Such waves can be directly converted to electrical signals by antennas and processed with electronics. It is assumed that an antenna converts the electrical field vector \vec{E} into a scalar voltage or current signal $y(t)$, i.e.

$$\vec{E}(\vec{r}, t) \rightarrow y(t) = a_y \cdot \cos(\Phi_y(t)). \quad (2.27)$$

For radio waves, the frequency of the voltage $y(t)$ is equal to the electric field frequency ν and the amplitude a_y is assumed to change only very slowly w.r.t. the oscillation period of $y(t)$. The relation between the phase Φ_y of the scalar signal and the instantaneous phase Φ of the electro-magnetic wave will be addressed in a subsequent section for light fields (cf. sec. 2.2.2). As a first step, different techniques to recover the phase, i.e. the argument of the cosine, for a single scalar input are addressed in the following section.

2.2.1 Phase Retrieval and Phase Tracking Techniques

Phase retrieval and tracking of a measured oscillating signal $y(t)$ means the determination of the phase φ_y and Φ_y in

$$y(t) = a_y \cdot \cos(\Phi_y(t)) = a_y \cdot \cos(2\pi f_y t + \varphi_y(t)). \quad (2.28)$$

Here, Φ_y is decomposed into a time-proportional part $2\pi f_y t$, which describes most of the repetitive structure of $y(t)$, and the much smaller phase variations $\varphi_y(t)$, which typically contains the desired ranging information.

The frequency of electric signals in this section is denoted with the symbol f , while the previous section used the symbol ν for frequencies of electro-magnetic waves, e.g. for light.

The word *phase* is a vague word, as it may refer to the instantaneous phase Φ_y , which is monotonically increasing with time, or it may refer to phase variations $\varphi_y(t)$, where a constant phase ramp is already removed. Sometimes, phase is limited to a range of π or 2π , and sometimes it is an unwrapped phase with the domain of real numbers. In most cases, the meaning can be deduced from the context.

Phase retrieval and tracking is typically performed in the digital domain. It is therefore assumed that the signal $y(t)$ is digitized with a sampling frequency f_{sample} larger than twice the oscillation frequency $\dot{\Phi}_y/(2\pi)$, i.e.

$$\text{Nyquist theorem : } f_{\text{sample}} > 2 \cdot f_{\text{signal}} = 2 \cdot \frac{1}{2\pi} \cdot \frac{d\Phi_y}{dt}. \quad (2.29)$$

The most common technique for recovering the phase of $y(t)$ is to demodulate it into the in-phase I component and the out-of-phase quadrature Q . The demodulation is performed by multiplicative mixing with a reference oscillation at a frequency f_r , so-called *heterodyning*, i.e.

$$\begin{aligned} I(t) &:= y(t) \cdot \cos(2\pi f_r t) \\ &= \frac{\alpha}{2} \cdot (\cos(2\pi(f_y + f_r)t + \varphi_y) + \cos(2\pi(f_y - f_r)t + \varphi_y)), \end{aligned} \quad (2.30)$$

$$\begin{aligned} Q(t) &:= y(t) \cdot \sin(2\pi f_r t) \\ &= \frac{\alpha}{2} \cdot (\sin(2\pi(f_y + f_r)t + \varphi_y) + \sin(2\pi(f_y - f_r)t + \varphi_y)). \end{aligned} \quad (2.31)$$

The scheme is illustrated in fig. 2.1. The I and Q signals are low-pass filtered (LF) to remove the oscillations at the sum frequency. If the input signal has a non-vanishing mean value, one needs to filter out f_r and f_y as well. The phase of $y(t)$ with respect to the reference frequency f_r can be obtained with

$$\varphi_{IQ}(t) = \arctan2(\text{LF}(Q(t)), \text{LF}(I(t))), \quad (2.32)$$

while the rms-amplitude is

$$a_{IQ,\text{rms}}(t) = \sqrt{\text{LF}(I(t))^2 + \text{LF}(Q(t))^2}. \quad (2.33)$$

The two argument $\arctan2$ function considers the sign of both I and Q to determine the phase in all four quadrants with a range of 2π compared to the classical $\arctan(Q/I)$ with a range of π . The bounded or wrapped phase $\varphi_{IQ}(t)$ is the result of the phase retrieval. For the purpose of ranging interferometry, the phase can be unwrapped by tracking the phase changes and removing the phase jumps. This yields the measured instantaneous phase Φ_{meas} of the signal y as

$$\Phi_{\text{meas}}(t) = 2\pi f_r t + \text{unwrap}[\varphi_{IQ}(t)] = 2\pi f_r t + \varphi_{IQ}(t) + 2\pi \cdot m(t), \quad (2.34)$$

where $m(t)$ is a time-varying integer determined by an unwrapping algorithm [Wand, 2007, sec. D.2].

The phase Φ_{meas} differs from the true instantaneous phase Φ_y by an integer multiple of 2π :

$$\Phi_{\text{meas}}(t) = \Phi_y(t) + \underbrace{2\pi \cdot n}_{\text{offset}}, \quad n \in \mathbb{N}. \quad (2.35)$$

This offset is inaccessible, as the considered electric field model (cf. eq. (2.16)) is periodic with time. In some applications with transient effects of electro-magnetic waves, e.g. generation of waves, it might be useful to define the absolute value of the phase. However, within the scope of this thesis, the absolute value of the instantaneous phase is irrelevant.

The reference frequency f_r can differ slightly from the actual frequency of the signal $y(t)$, because a small mismatch appears as a phase ramp within the phase $\varphi_{IQ}(t)$.

The I and Q demodulation, i.e. multiplication with sine and cosines, is the foundation of the Fourier theory. For example, the complex Fourier coefficient c^c is given by

$$c^c = \text{LF}(I(t)) + i \cdot \text{LF}(Q(t)), \quad (2.36)$$

if the low-pass filtering consists of forming the average and f_r is an integer multiple of f_{sample}/N with N being the number of samples forming a batch of samples. N is the so-called length or size of the Discrete Fourier Transform (DFT). If one uses a single frequency f_r to demodulate the signal, it is denoted as a Single-Bin Discrete Fourier Transform (SBDFT). The more general DFT computes an equally spaced spectrum with N bins by demodulating the input with N equally spaced frequencies in parallel.

The phase obtained by a SBDFT is the average phase within the batch of N samples. Thus, the phase φ_{IQ} is available with a sampling rate of f_{sample}/N and variations of $\varphi_{IQ}(t)$ on time scales shorter than N/f_{sample} can not be recovered. SBDFT is well suited for signals where the frequency of the signal $y(t)$ is known a-priori and quite stable, i.e. only small phase variations $\varphi_y(t)$ are expected (cf. eq. (2.28)):

$$\frac{d\varphi_y}{dt} \ll \frac{d\Phi_y}{dt}. \quad (2.37)$$

Furthermore, phase unwrapping typically requires the phase change between consecutive phase samples to be smaller than π :

$$\frac{N}{f_{\text{sample}}} \cdot \frac{d\varphi_y}{dt} < \pi. \quad (2.38)$$

Both requirements are met for the laser interferometry on-board the LISA Pathfinder satellite and, in fact, the on-board phasometers use the SBDFT at a fixed reference frequency f_r of 1.0 kHz.

However, the variations of φ_y are typically large in inter-satellite ranging interferometry due to the relative velocity of the satellites. Thus, the limitations imposed by eq. (2.37) and (2.38) are severe and the SBDFT is not well suited. One can overcome the limitations with an extension of the $I&Q$ demodulation, which is phase tracking by means of a (digital) phase-locked loop (DPLL). This scheme is illustrated in fig. 2.2 and utilizes a variable frequency f_r , which is stored in a so-called phase increment register (PIR). It is derived from the feedback of φ_{IQ} . The variable and instantaneous frequency in the PIR is continuously integrated within the numerically controlled oscillator (NCO) and the resulting phase is stored in a phase accumulator (PA), which is used to derive the sine and cosine components for the $I&Q$ demodulation through a look-up table.

For ranging interferometry, this phase tracking system can be designed with a high gain and bandwidth of the feedback control loop, such that the internally measured error signal φ_{IQ} is close to zero. Thus, the value of the phase accumulator directly provides a continuous and unwrapped phase Φ_{meas} . An analytical model for the phase observation of an ideal DPLL is

$$\Phi_{\text{meas}}(t') = 2\pi \int_{t=0}^{t'} |f_r| dt = \int_{t=0}^{t'} \left| \frac{d\Phi_y}{dt} \right| dt, \quad (2.39)$$

which is always positive and monotonically increasing.

DPLL phase tracking is a common and well-established technique and can be implemented conveniently in digital FPGA circuits [Gerberding, 2014]. It will be utilized in the GRACE Follow-On mission for laser ranging as well as microwave ranging, is commonly used in GNSS receivers and is also foreseen in the LISA mission.

More details and alternative methods such as zero-crossing detection for phase retrieval are addressed in the section 2.3.7 on phasometers.

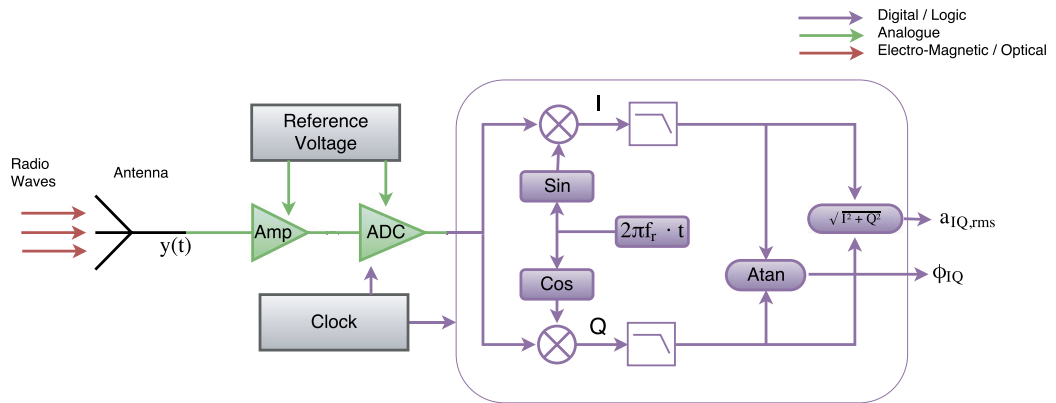


Figure 2.1: The electro-magnetic radio waves are transformed into an oscillatory voltage $y(t)$, amplified, digitized and IQ-demodulated to obtain the phase φ_{IQ} and amplitude $a_{IQ,rms}$

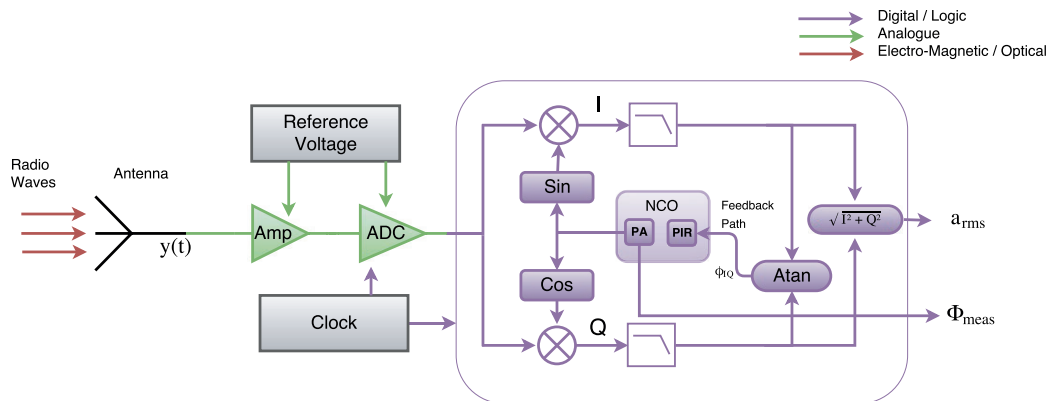


Figure 2.2: Working principle of a digital phase-locked loop (DPLL) used for phase retrieval and tracking. The electro-magnetic radio waves are transformed into an oscillatory voltage $y(t)$, amplified, digitized and IQ-demodulated to obtain the phase φ_{IQ} , which is fed back to the numerically controlled oscillator (NCO). A more realistic scheme can be found in sec. 2.3.7 on the phasemeter.

2.2.2 Optical Detection

So far, phase retrieval was discussed for electro-magnetic radiation with wavelengths larger than a few millimeters and for electrical signals. The other side of the electro-magnetic spectrum, with wavelengths smaller than 1 mm, is usually denoted as the optical part of the spectrum, where the oscillation frequency is larger than 30 terahertz and too fast to be resolved directly by electrical signals. For the sake of completeness, it is noted that the frequency range between 300 GHz and 30 THz is commonly called the *terahertz gap*, as neither conventional detectors nor sources from optics or electronics can be used at these frequencies. However, bridging the gap is being attempted as described in the overview article by [Sirtori \[2002\]](#).

The photoelectric effect provides a means of accessing the intensity of electro-magnetic radiation, i.e. the time-averaged energy flux. The directional instantaneous energy flux is typically expressed as the Poynting vector $\vec{S}(t)$, which has units of watt per square meter (W/m^2) and is defined by

$$\vec{S}(\vec{r}, t) = \vec{E}(\vec{r}, t) \times \vec{H}(\vec{r}, t) = \text{Re}(\vec{E}^c(\vec{r}, t)) \times \text{Re}(\vec{H}^c(\vec{r}, t)) \quad (2.40)$$

where \vec{H} is the magnetic field vector of the light field with units of A/m and \vec{E} has units of V/m. The norm of the time-averaged Poynting vector is the intensity with units of W/m^2 . For time harmonic fields with temporal dependency $e^{i2\pi\nu t}$, it is given by [[Träger, 2012](#), eq. 3.65]:

$$\langle \vec{S} \rangle(\vec{r}, t) = \frac{1}{2} \cdot \text{Re} \left(\vec{E}^c(\vec{r}, t) \times \vec{H}^{c*}(\vec{r}, t) \right) \propto \langle |\vec{E}(\vec{r}, t)|^2 \rangle \cdot \vec{e}_S. \quad (2.41)$$

The star * denotes complex conjugation. The vector $\langle \vec{S} \rangle$ is proportional to the squared electric field $|\vec{E}|^2$, because the magnetic field \vec{H} can be expressed in terms of the electric field \vec{E} as

$$\vec{H}(\vec{r}, t) = \frac{1}{c_0 \cdot \mu_0 \cdot \mu} \cdot \frac{\vec{k}}{k} \times \vec{E}(\vec{r}, t) = \frac{1}{c_0 \cdot \mu_0 \cdot \mu} \cdot \vec{e}_S \times \vec{E}(\vec{r}, t), \quad (2.42)$$

where μ_0 is the magnetic permeability of vacuum and μ is the permeability of the medium. The direction of the time-averaged Poynting vector \vec{e}_S is parallel to the local wave vector \vec{k} in isotropic non-conducting dielectric media, i.e. parallel to the gradient of the phase function or phasefront. This can be easily shown for plane waves [[Träger, 2012](#), eq. 3.65] or spherical waves, but a general proof for arbitrary vector fields from Maxwell's first principles seems to be non-trivial, because the local wave vector \vec{k} is not well-defined.

In fact, a general method to define a scalar phase function Φ and the local wave vector $\vec{k}(\vec{r})$ from vector field quantities \vec{E} and \vec{H} may be a relation in the form of³

$$\vec{e}_S = \frac{\langle \vec{S} \rangle(\vec{r}, t)}{|\langle \vec{S} \rangle(\vec{r}, t)|} = \frac{\vec{\nabla} \Phi(\vec{r})}{k} = \frac{\vec{k}}{k}. \quad (2.43)$$

Since the energy flux is proportional to the squared electric field, light detectors such as e.g. those using the photoelectric effect are referred to as *square-law detectors*. For example, a photodiode provides a photocurrent I_{ph} ,

$$I_{\text{ph}} = \eta_{\text{PD}} \int_{\text{PD}} \langle \vec{S} \rangle \cdot d\vec{n}, \quad (2.44)$$

where η_{PD} is the photodiode responsivity with units of A/W and the brackets denote temporal averaging. The domain of spatial integration in eq. (2.44) is the active area of the photodiode,

³More generally, one should use the cross product of electric displacement \vec{D} and \vec{H} instead of \vec{S} , since \vec{E} is not perpendicular to \vec{k} in birefringent media [[Träger, 2012](#), eq. 5.77]. This also means that the energy is not transported along the electric phase normals \vec{k} in such media.

where \vec{n} is the normal vector of the active area surface. Detectors in the optical domain can not resolve the fast oscillation at optical frequencies and can provide only the intensity, in contrast to antennas and radio waves.

If a light field \vec{E} with single frequency ν and constant amplitude is impinging on the photodiode, the resulting photocurrent is constant and proportional to the optical power P within the active area. However, if two electric fields \vec{E}_r and \vec{E}_y with nearby frequencies ν_r and ν_y are overlapped, i.e.

$$\begin{aligned}\vec{E}^c(\vec{r}, t) &= \vec{E}_y^c(\vec{r}) \cdot e^{i2\pi\nu_y t + i\varphi_y} + \vec{E}_r^c(\vec{r}) \cdot e^{i2\pi\nu_r t + i\varphi_r} \\ \vec{H}^c(\vec{r}, t) &= \vec{H}_y^c(\vec{r}) \cdot e^{i2\pi\nu_y t + i\varphi_y} + \vec{H}_r^c(\vec{r}) \cdot e^{i2\pi\nu_r t + i\varphi_r},\end{aligned}\quad (2.45)$$

they produce a photocurrent given by

$$\begin{aligned}I_{\text{ph}}(t) &= \eta_{\text{PD}} \cdot \frac{1}{2} \cdot \text{Re} \left[\int_{\text{PD}} \vec{E}_y^c(\vec{r}) \times \vec{H}_y^{c*}(\vec{r}) + \vec{E}_r^c(\vec{r}) \times \vec{H}_r^{c*}(\vec{r}) \right. \\ &\quad + e^{i2\pi\delta\nu t + i\delta\varphi} \cdot \vec{E}_r^c(\vec{r}) \times \vec{H}_y^{c*}(\vec{r}) \\ &\quad \left. + e^{-i2\pi\delta\nu t - i\delta\varphi} \cdot \vec{E}_y^c(\vec{r}) \times \vec{H}_r^{c*}(\vec{r}) \, d\vec{n} \right].\end{aligned}\quad (2.46)$$

The first line is time-independent and yields the sum of the incident light power of both beams, i.e. $P_y + P_r$, where P_y and P_r are the light power levels of \vec{E}_y and \vec{E}_r , respectively. These values would be measured in the absence of interference, i.e. if only a single beam is present (cf. eq. (2.44)). The difference phase $\delta\varphi = \varphi_y - \varphi_r$ and difference frequency $\delta\nu = \nu_y - \nu_r$ have been introduced as abbreviations. One can show that the integrand in the second and third line is oscillating at the difference frequency $\delta\nu$, e.g.

$$\text{Re} \left[e^{i2\pi\delta\nu t + i\delta\varphi} \cdot \vec{E}_r^c(\vec{r}) \times \vec{H}_y^{c*}(\vec{r}) + e^{-i2\pi\delta\nu t - i\delta\varphi} \cdot \vec{E}_y^c(\vec{r}) \times \vec{H}_r^{c*}(\vec{r}) \right] \quad (2.47)$$

$$\begin{aligned}&= \cos(2\pi\delta\nu t + \delta\varphi) \cdot \text{Re}(\vec{E}_r^c \times \vec{H}_y^{c*}) - \sin(2\pi\delta\nu t + \delta\varphi) \cdot \text{Im}(\vec{E}_r^c \times \vec{H}_y^{c*}) \\ &\quad + \cos(2\pi\delta\nu t + \delta\varphi) \cdot \text{Re}(\vec{E}_y^c \times \vec{H}_r^{c*}) + \sin(2\pi\delta\nu t + \delta\varphi) \cdot \text{Im}(\vec{E}_y^c \times \vec{H}_r^{c*})\end{aligned}\quad (2.48)$$

$$\begin{aligned}&= \cos(2\pi\delta\nu t + \delta\varphi) \cdot \text{Re}(\vec{E}_r^{c*} \times \vec{H}_y^c) + \sin(2\pi\delta\nu t + \delta\varphi) \cdot \text{Im}(\vec{E}_r^{c*} \times \vec{H}_y^c) \\ &\quad + \cos(2\pi\delta\nu t + i\delta\varphi) \cdot \text{Re}(\vec{E}_y^c \times \vec{H}_r^{c*}) + \sin(2\pi\delta\nu t + \delta\varphi) \cdot \text{Im}(\vec{E}_y^c \times \vec{H}_r^{c*})\end{aligned}\quad (2.49)$$

$$\begin{aligned}&= \cos(2\pi\delta\nu t + \delta\varphi) \cdot \text{Re}(\vec{E}_r^{c*} \times \vec{H}_y^c + \vec{E}_y^c \times \vec{H}_r^{c*}) \\ &\quad + \sin(2\pi\delta\nu t + \delta\varphi) \cdot \text{Im}(\vec{E}_r^{c*} \times \vec{H}_y^c + \vec{E}_y^c \times \vec{H}_r^{c*})\end{aligned}\quad (2.50)$$

$$= \text{Re} \left[e^{i2\pi\delta\nu t + i\delta\varphi} \cdot (\vec{E}_r^{c*} \times \vec{H}_y^c + \vec{E}_y^c \times \vec{H}_r^{c*}) \right]. \quad (2.51)$$

Using the result eq. (2.51) in eq. (2.46) allows the final photocurrent to be written in the common forms

$$I_{\text{ph}}(t) = \eta_{\text{PD}} \cdot \left(P_y + P_r + \text{Re}(e^{i2\pi\delta\nu t + i\delta\varphi} \cdot a^c) \right) \quad (2.52)$$

$$= \eta_{\text{PD}} \cdot (P_y + P_r) \cdot (1 + c \cdot \cos(2\pi\delta\nu t + \delta\varphi + \vartheta)), \quad (2.53)$$

$$= \eta_{\text{PD}} \cdot (P_y + P_r + 2 \cdot \sqrt{P_y \cdot P_r} \cdot \eta \cdot \cos(2\pi\delta\nu t + \delta\varphi + \vartheta)), \quad (2.54)$$

where a^c denotes the complex oscillation amplitude, $c \in [0..1]$ is the so-called interferometric contrast defined by

$$c = \frac{2 \cdot \sqrt{P_y \cdot P_r} \cdot \eta}{P_y + P_r} = |a^c|, \quad (2.55)$$

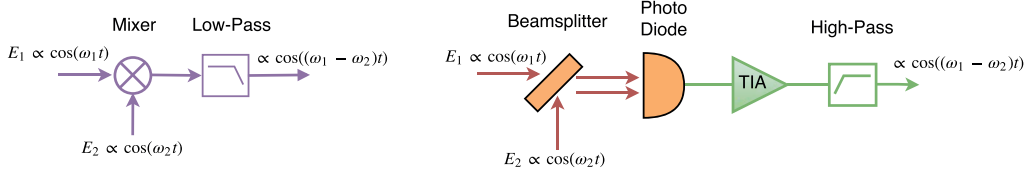


Figure 2.3: These block diagrams illustrate frequency down conversion by electrical mixing (left) and by optical square-law detection (right). High-pass filtering is used to remove a bias in the electric signal.

and η and ϑ are the amplitude and phase obtained by the complex overlap integral

$$\sqrt{\eta}e^{i\vartheta} = \frac{\frac{1}{2} \int_{\text{PD}} \vec{E}_r^{c*} \times \vec{H}_y^c + \vec{E}_y^c \times \vec{H}_r^{c*} \, d\vec{n}}{\sqrt{P_y \cdot P_r}} \quad (2.56)$$

$$= \frac{\frac{1}{2} \int_{\text{PD}} (\vec{E}_r^{c*} \cdot \vec{E}_y^c) \cdot \left(\frac{\vec{k}_r}{k_r} + \frac{\vec{k}_y}{k_y} \right) - (\vec{E}_r^{c*} \cdot \vec{k}_y) \cdot \vec{E}_y^c - (\vec{E}_y^c \cdot \vec{k}_r) \cdot \vec{E}_r^{c*} \, d\vec{n}}{\sqrt{P_y \cdot P_r}} \quad (2.57)$$

$$\approx \frac{\int_{\text{PD}} \vec{E}_r^{c*} \cdot \vec{E}_y^c \, dS}{\sqrt{P_y \cdot P_r}}, \quad (2.58)$$

where dS denotes the surface element. It was assumed here that the beat frequency $\delta\nu$ can be resolved by the photodiode.

The η is often called the heterodyne efficiency and is a measure of the similarity of both electric fields. It is independent of the absolute power level of each beam due to the normalization by P_y and P_r . Eq. (2.56) is a general expression considering the vectorial nature of light, which is not commonly found in literature to the knowledge of the author. The last approximation in eq. (2.58) considers that the phasefronts are almost parallel to the photodiode surface, i.e. \vec{k}_y and \vec{k}_r are parallel to \vec{n} , which implies that $\vec{E} \perp \vec{n}$.

In the derivation of the photocurrent $I_{\text{ph}}(t)$ (cf. eq. (2.54) and (2.45)) an artificial separation between the phase ϑ and $\delta\varphi = \varphi_y - \varphi_r$ has been introduced. Such an approach typically eases the computation, because φ_y and φ_r can be used to describe the macroscopic phase, which includes the effect due to the accumulated optical pathlength traversed by the light field, while ϑ accounts for a smaller phase effect due to the geometry of the wavefronts. However, these phases can not be distinguished in the measurement.

The oscillatory photocurrent $I_{\text{ph}}(t)$ is usually amplified and converted into a voltage using a transimpedance amplifier (TIA). If the voltage (or current) is high-pass filtered, such that the static part is removed, one can say that the optical frequencies ν have been down-converted to a new frequency $\delta\nu$ similar to the process in electrical mixing (cf. fig. 2.3).

In a subsequent stage, the phase of the voltage (or current) can be recovered with the aforementioned phase measurement techniques (cf. sec. 2.2.1).

Thus, in optical interferometry, the phase of the light field \vec{E}_y is obtained by optical mixing with an optical reference field \vec{E}_r to produce an oscillation frequency accessible to electronics, followed by electrical mixing within the DPLL to zero frequency for phase retrieval. Therefore, the measured phase depends on the stability of the optical reference field \vec{E}_r and on the stability of the clock driving the reference oscillation within the DPLL.

Eq. (2.54) is also applicable in the case of homodyne interferometry, when the reference and measurement fields have the same carrier frequency, i.e. $\delta\nu = 0$. This type of readout has no oscillatory time-dependence. In such a scheme, a change in the phase φ_y of the light field is related to a phase change in the photocurrent, whereby the sensitivity

$$\frac{dI_{\text{ph}}}{d\varphi_y} \propto 2 \cdot \sqrt{P_y \cdot P_r \cdot \eta} \cdot \sin(\varphi_y - \varphi_r + \vartheta) \quad (2.59)$$

vanishes for $\varphi_y - \varphi_r + \vartheta = 0$, at the so-called *bright-fringe* or *dark-fringe* setpoints, where the cosine term in eq. (2.54) is maximal or minimal, respectively. The sensitivity is maximized at the *mid-fringe*, i.e. $\varphi_y - \varphi_r + \vartheta = \pi/2$. The direct relation between measured power and phase can be advantageous for the detection of tiny phase changes, as the sensitivity can be enhanced by increasing the light power, but requires an optical power stabilization and the ability to handle higher optical powers. In addition, homodyne interferometers require that the dynamics of the tracked object, and hence the changes in the optical phase φ_y , are slow enough, such that the optical reference phase φ_r can follow it to maintain the setpoint.

On the first glance, a homodyne scheme seems beneficial, as only single mixing in the optical domain is performed. In fact, homodyne schemes for gravimetric inter-satellite ranging have been considered experimentally by Nagano *et al.* [2004, 2005] and Yeh *et al.* [2011], who state a dynamic range of cm/s for the relative velocity. However, this would require well-matched satellite orbits and most likely an active control of the relative velocity between satellites in a gravimetric mission.

Another difficulty with homodyne schemes is that the DC photocurrent, and hence the phase readout, is falsified by omni-present low-frequency electronic noise and variations of the optical power, the reference voltage and the wavefront overlap η . In a heterodyne readout scheme, the desired phase is encoded at a convenient (sub-)radio frequency $\delta\nu$, where most error contributions are sufficiently small. The demodulation to a DC “frequency” for phase retrieval is performed digitally within the PLL in the phasemeter, where a phase-value can be stored and transmitted mostly unaffected by low-frequency variations.

Heterodyne phase readout with phase tracking by means of a digital PLL is considered in this thesis as the baseline for future gravimetric missions, mainly due to the mature technology and significant heritage from the development of the LISA and GRACE Follow-On missions. Such a readout is capable of handling low received light power, e.g. in the picowatt regime, which is typically encountered in inter-satellite ranging. The sensitivity of the phase readout is sufficient even under these low-light conditions, which means that several other noise sources are limiting the ranging sensitivity. Another advantage is the dynamic range in terms of the maximum relative velocity between satellites, which has been so far designed to handle a few m/s, corresponding to Doppler shifts of a few MHz in the optical frequency. However, a potential extension to a larger dynamic range is considered possible [e.motion² Team, 2014, sec. 5.3.2.3]. This is an important aspect for future gravity missions with advanced satellite constellations and orbits, e.g. pendulum [Elsaka, 2010] or even precise (optical) high-low satellite ranging [Schlie *et al.*, 2015].

2.2.3 Differential Wavefront Sensing (DWS)

Differential Wavefront Sensing [Morrison *et al.*, 1994] is a technique for measuring the relative phasefront tilt between two laser beams or light fields. It utilizes a segmented photodiode as shown in fig. 2.4. If the interfering light fields are tilted with respect to each other, the phase of the left two segments (*A* and *C*) differs from the phase of the right two segments (*B* and *D*). The phase differs between upper and lower segments if a phasefront tip is present, The linear combinations

$$\text{DWS}_{\text{tilt}} = \frac{\varphi_A + \varphi_C - \varphi_B - \varphi_D}{2}, \quad \text{DWS}_{\text{tip}} = \frac{\varphi_A + \varphi_B - \varphi_C - \varphi_D}{2} \quad (2.60)$$

are called *DWS signals* and have units of radian, where the radian refers to the phase of the photocurrent. Unfortunately, various conventions with different signs and normalization factors exist. Therefore, clear documentation of the used implementation in hard- or software is mandatory. A coherent combination of the different segments is also possible, where the

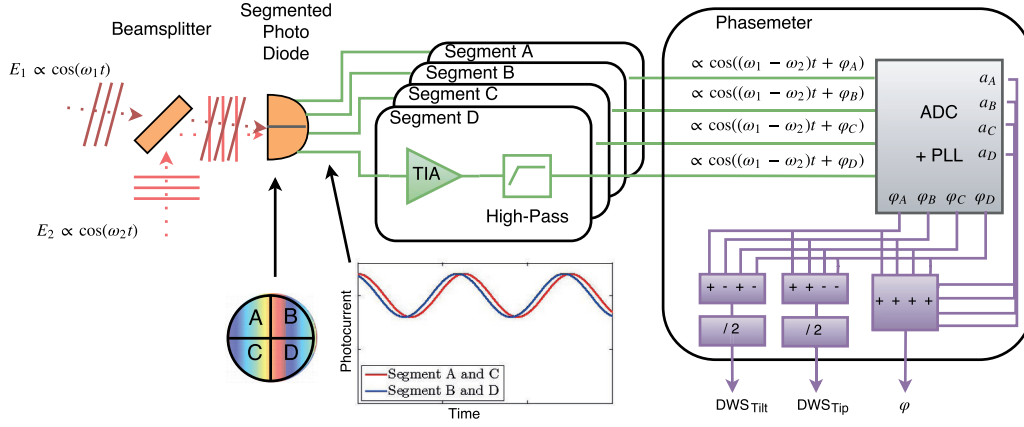


Figure 2.4: Working principle of Differential Wavefront Sensing (DWS) with a segmented photodiode. The phasemeter returns the DWS signals DWS_{tilt} and DWS_{tip} as well as the longitudinal phase φ , which contains the ranging information.

phase is weighted with the heterodyne amplitude, i.e.

$$\begin{aligned} DWS_{\text{tilt}} &= \arg(a_A^c + a_B^{c*} + a_C^c + a_D^{c*}) \\ &= \arg(a_A \cdot e^{i\varphi_A} + a_B \cdot e^{-i\varphi_B} + a_C \cdot e^{i\varphi_C} + a_D \cdot e^{-i\varphi_D}), \end{aligned} \quad (2.61)$$

$$\begin{aligned} DWS_{\text{tip}} &= \arg(a_A^c + a_B^c + a_C^{c*} + a_D^{c*}) \\ &= \arg(a_A \cdot e^{i\varphi_A} + a_B \cdot e^{i\varphi_B} + a_C \cdot e^{-i\varphi_C} + a_D \cdot e^{-i\varphi_D}), \end{aligned} \quad (2.62)$$

which is equivalent to eq. (2.60) up to a factor of 2, if all segments have the same heterodyne magnitude. The complex oscillation coefficient a_X^c with $X \in \{A, B, C, D\}$ was defined in eq. (2.52), whereby the magnitude is $a_X = |a_X^c|$.

The relation between the differential geometrical phasefront tip and tilt directly in front of the photodiode and the DWS signal is, in general, dependent on the wavefront (amplitude and phase) of both light fields, the area and orientation of the segments and the slit width between segments. Proper selection of beam parameters yields a linear relation between geometrical tilt and DWS around a working point with aligned phasefronts. For example, the linear coupling factor for plane waves impinging on a photodiode with radius r_{PD} is [Sheard *et al.*, 2012]

$$m_{\text{DWS}} = \frac{16 \cdot r_{\text{PD}}}{3 \cdot \lambda}, \quad (2.63)$$

which has units of rad/rad, meaning an electrical phase (angle) over a geometrical angle. For a typical photodiode size of $r_{\text{PD}} = 0.5 \text{ mm}$ and $\lambda = 1064 \text{ nm}$, this results in $m_{\text{DWS}} = 2506 \text{ rad/rad}$. For more realistic beams with non-flat intensity, the coupling is of similar magnitude and can be computed numerically by eq. (2.58). This large magnification m_{DWS} allows tiny differential phasefront tilts to be resolved. In particular, if m_{DWS} and the orientation of the reference phasefront is known, DWS provides a precise measure for the orientation of the measurement beam. Another reason for the excellent DWS performance is the common mode rejection of errors among different segment channels.

The longitudinal phase φ_{long} , i.e. the ranging information, can be obtained from the phase of the coherent sum of all segments, i.e.

$$\varphi_{\text{long}} = \arg(a_A \cdot e^{i\varphi_A} + a_B \cdot e^{i\varphi_B} + a_C \cdot e^{i\varphi_C} + a_D \cdot e^{i\varphi_D}), \quad (2.64)$$

which is equal to the phase obtained by a single element photodiode in the limit of vanishing slit (gap) width.

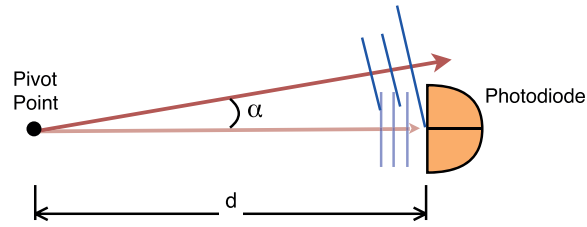


Figure 2.5: The average phase on the photodiode, i.e. the longitudinal phase, changes from $d \cdot 2\pi/\lambda$ to $d \cdot \cos(\alpha) \cdot 2\pi/\lambda$ by rotating the plane waves around the pivot point. For plane waves, the average phase over the circular photodiode is the same as the phase at the center of the diode.

It is noted that zeroing DWS in the case of typical laser beams implies a maximization of the wavefront overlap η of the coherent sum of all segments. This maximizes the heterodyne amplitude and the signal-to-noise ratio of the longitudinal (ranging) phase measurement.

Another remark concerns the coupling between phasefront misalignment and the longitudinal phase. In general, the DWS signals couple strongly to the longitudinal phase φ_{long} if rotations of the phasefront are not performed around the photodiode center. This is shown in fig. 2.5, where the effective lever arm d yields a rotation-to-phase coupling according to

$$\Delta\varphi = d \cdot (1 - \cos(\alpha)) \cdot 2\pi/\lambda \approx -d \cdot \alpha^2/2 \cdot 2\pi/\lambda. \quad (2.65)$$

In the plane wave approximation, d is simply the length given by the projection of the wave propagation direction \vec{k} onto the vector from the photodiode center to the pivot point. The quadratic coupling vanishes if the reference beam is rotated by the same amount around the same pivot point, such that DWS is zeroed again. In practice, an imaging system is often used to image the rotation pivot point onto the photodiode center, which reduces the effective lever arm d to a value close to zero.

2.2.4 Differential Power Sensing (DPS)

In the same manner as DWS utilizes a linear combination of the phases from different segments of a quadrant photodiode, the DPS readout is formed by a linear combination of the DC photocurrents P of each segment

$$\begin{aligned} \text{DPS}_X &= \frac{P_{\text{left}} - P_{\text{right}}}{P_{\text{total}}} = \frac{P_A + P_C - P_B - P_D}{P_A + P_B + P_C + P_D}, \\ \text{DPS}_Y &= \frac{P_{\text{top}} - P_{\text{bottom}}}{P_{\text{total}}} = \frac{P_A + P_B - P_C - P_D}{P_A + P_B + P_C + P_D}. \end{aligned} \quad (2.66)$$

Normalizing the DPS signal to the total beam power makes it independent of beam power fluctuations. If a single circular Gaussian beam is centered on a quadrant photodiode, each segment receives approximately one quarter of the total light power. A slight de-centering results in an imbalance between the segments. DPS is a useful tool for centering a beam on a photodiode or vice versa, to center the photodiode w.r.t. a beam. After calibrating the DPS signal with well-known translations, DPS can be used to measure beam walk on a photodiode in terms of physical length, with a common resolution at the micrometer level.

The DPS signals are linear in the displacement for a nearly centered beam [Wanner, 2010], but non-linearities appear for considerable offsets. The linearity factor depends on the actual beam shape and size, as well as on the photodiode size and gaps. If two beams with comparable power levels are impinging on the diode and both are subject to beam walk, DPS in its simple form cannot provide useful information. However, since inter-satellite interferometers are typically operated with one powerful and one weak beam, DPS approximately indicates the beam position of the powerful beam.

In summary, in laser (ranging) interferometry the phase of the light fields is used to measure distance changes, because the phase at a receiver depends on the traversed distance of the light, or in other words, on the propagation time of the light field. Since the phase at optical frequencies is not directly accessible to electronics, one compares in an interferometer the measurement light field, which contains the ranging information, to a reference light field with stable phase and frequency. The case with two fields of equal frequencies yields a homodyne interferometer. However, due to the orbital dynamics in inter-satellite ranging one prefers a heterodyne scheme with slightly different optical frequencies. This difference in frequency corresponds to different slopes in the instantaneous phase of the light fields (with respect to time). By overlapping the light fields and subsequent photodetection one obtains an oscillating photocurrent at the difference frequency which contains the ranging information encoded in its phase. The phase of the oscillating photocurrent, which is the phase difference between both light fields, can be retrieved by a digital phase-locked loop (DPLL) within a phasemeter. By using segmented photodiodes one can obtain the ranging signal, which is often called the longitudinal phase, from the average phase of all photodiode segments, while differential combinations of the segments allows information on the phase-front tilt between the light fields, so called DWS signals, and on the position of the light beams on the photodiode, so-called DPS signals, to be retrieved.

2.3 Optical and Interferometer Technology

The following subsections introduce the currently available technology and subsystems which are typically required and used to build laser ranging interferometers. The basic working principle of the subsystems and the relevant figures of merit and design drivers with regard to ranging interferometry are introduced. The information in these subsections allow to study the sensitivity limits of ranging instruments in the following parts of this thesis.

2.3.1 Laser

Optical inter-satellite interferometry requires a source of continuous, coherent, single frequency light. Two key parameters are the wavelength and the optical power. The field of gravitational wave detection by means of optical interferometry prefers 1064 nm light, which has grown historically, as optical components out of fused silica show low absorption at this wavelength [Schnabel *et al.*, 2010]. In particular, solid-state Nd:YAG (Neodymium doped Yttrium Aluminum Garnet) laser crystals with a non-planar ring oscillator (NPRO) structure advanced in the last decades yielding a high mechanical stability, a narrow line-bandwidth of a few kHz and a large separation between longitudinal modes. The actual laser crystal is usually pumped optically by dedicated pump laser diodes at another wavelength. Space-qualified lasers of this type are commercially available from the company Tesat-Spacecom GmbH, which also delivered the LISA Pathfinder and the GRACE Follow-On lasers, both with an optical output power of a few tens of milliwatt. A higher output power can be achieved by laser amplifiers as used, for example, in the Laser Communication Terminals [Muehlnikel *et al.*, 2012].

ESA recently started activities in the development of a NGGM-High Stability Laser [Nicklaus *et al.*, 2014a], which is specified to provide up to 500 mW frequency stabilized 1064 nm laser light for future gravimetric missions (cf. fig. 2.6). A laser system for space-applications ideally delivers the light in a single-mode polarization maintaining fiber with a high polarization extinction ratio or as a free beam in a TEM₀₀ mode with a linear or well defined polarization. As the intrinsic, free-running frequency stability of lasers is generally insufficient for precise ranging, the lasers need the capability to tune the frequency with high bandwidth, so that they can be locked to an external frequency standard. For example, an NPRO crystal can be tuned at low-frequencies via a typical temperature coupling of

approx. 3 GHz/K and with higher bandwidth via a piezo-electric transducer with typical coupling of approx. 1 MHz/V. Other candidate technologies are the Distributed Brag Reflector (DBR) laser, the Distributed Feedback (DFB) laser or a fiber laser [Numata *et al.*, 2010; Tröbs *et al.*, 2009], which can also provide radiation with a wavelength of 1064 nm.

Although the use of semiconductor DBR or DFB laser diodes seems advantageous due to the lower mass and lower power consumption, these laser types usually emit strongly elliptical beams, which require additional beam shaping or acceptance of significant losses in the fiber coupling efficiency. An additional concern is the relative intensity noise (RIN) at frequencies used for the phase readout (> 4 MHz). Therefore, the final complexity of such new systems needs to be assessed and compared to an NPRO laser. It is noted that in [Alnis *et al.*, 2008] diode lasers at 972 nm have been locked to cavities using AOMs and in [Tröbs, 2005] a DFB laser has been locked to a cavity with residual (in-loop) frequency noise of $1 \text{ kHz}/\sqrt{\text{Hz}}$ at 10 mHz.

Preliminary requirements and key figures for an e.motion² laser, which can serve as a starting point for further discussion and iteration, are shown in table 2.1. A critical issue is the required long lifetime of the laser system, as optical systems are susceptible to degradation due to contamination, radiation, space corrosion and premature aging. In particular, laser diodes such as the pump diodes for an NPRO gain medium have shown failures on a previous mission [Ott *et al.*, 2006] and efforts have focused on improving their reliability, also driven by the rising need in optical communication applications. Space-qualified hermetically-sealed arrays of pump diodes with multimode fiber output and utilizing cold-redundancy have been reported [Traub *et al.*, 2007; Hildebrand, 2005] together with a reliability of 0.9998 over a 10 years lifetime and with 10 W of optical pump power (cf. fig. 2.7). In general, it is recommended to operate laser diodes at low electrical and thermal load, which corresponds to a low optical output power, as this enhances the lifetime (cf. so-called Arrhenius model [Gale, 2008]). Additional engineering efforts are required regarding the thermal dissipation of a high power laser subsystem on a satellite, but this is considered less critical for a laser output power < 1 W in gravimetric missions.

One can consider other common wavelengths such as 1550 nm or 532 nm for the laser. The wavelength influences the divergence of a Gaussian beam, in particular the spot size at the distant satellite, as well as the photodiode responsivity or more precisely the photodiode quantum efficiency. The divergence of the beam can also be adjusted using the waist size of a Gaussian beam, while the quantum efficiency can be improved from approx. 60% at 1064 nm to above 90% under ideal conditions (cf. sec. 2.3.3 on photodiodes). The latter is beneficial for the signal-to-noise ratio of the instrument, but it does not reduce the noise in the range measurement. Although a smaller wavelength implies a higher ranging precision for a fixed phase readout sensitivity, interferometry in gravimetric missions is currently limited by laser frequency noise and spacecraft attitude jitter noise, which does not improve with a shorter laser wavelength. Therefore, the author of this thesis currently does not think it is necessary to change the well-established wavelength and discard the associated mature technology.

2.3.2 Optical Frequency Standard

The optical frequency ν of a laser is important, because it sets the scale for converting a physical displacement Δd to an optical phase change $\Delta\varphi$ measured by interferometry:

$$\Delta d = \frac{\Delta\varphi}{2\pi} \cdot \frac{c_0}{\nu} = \frac{\Delta\varphi}{2\pi} \cdot \lambda. \quad (2.67)$$

Precise knowledge of the physical distance (in meters) is required in gravimetric missions, since the ranging data is processed with other physical observations such as accelerations. Thus, an error in the absolute value of the frequency or wavelength appears as a static scale factor error. In addition, fluctuations of the frequency are of importance as these appear as a noise in the interferometric distance measurement. However, the exact coupling of frequency

Parameter	Value	Comment
Laser Wavelength λ	1064 nm	
Operation Mode	CW	Continuous wave
Laser Power in SM-PM Fiber	500 mW 400 mW	Beginning of Life End of Life
RIN for $f > 4$ MHz	$< 10^{-15}$ 1/Hz	For Phase Readout Noise (cf. sec. 2.6.9)
RO RIN Peak	TBD	Avoidance of AC saturation
Knowledge of λ	1 ppm	In-orbit scale factor for converting phase to length
LFN at 1 mHz	$< 10^8$ Hz/ $\sqrt{\text{Hz}}$	
LFN at 1 Hz	$< 10^6$ Hz/ $\sqrt{\text{Hz}}$	
Lifetime	> 10 years	Mission lifetime

Table 2.1: Key figures and requirements of a laser system for a potential e.motion² mission. Abbreviations: SM-PM: Single Mode and Polarization Maintaining; LFN: (Free-Running) Laser Frequency Noise; RIN: Relative Intensity Noise; RO: Relaxation Oscillation

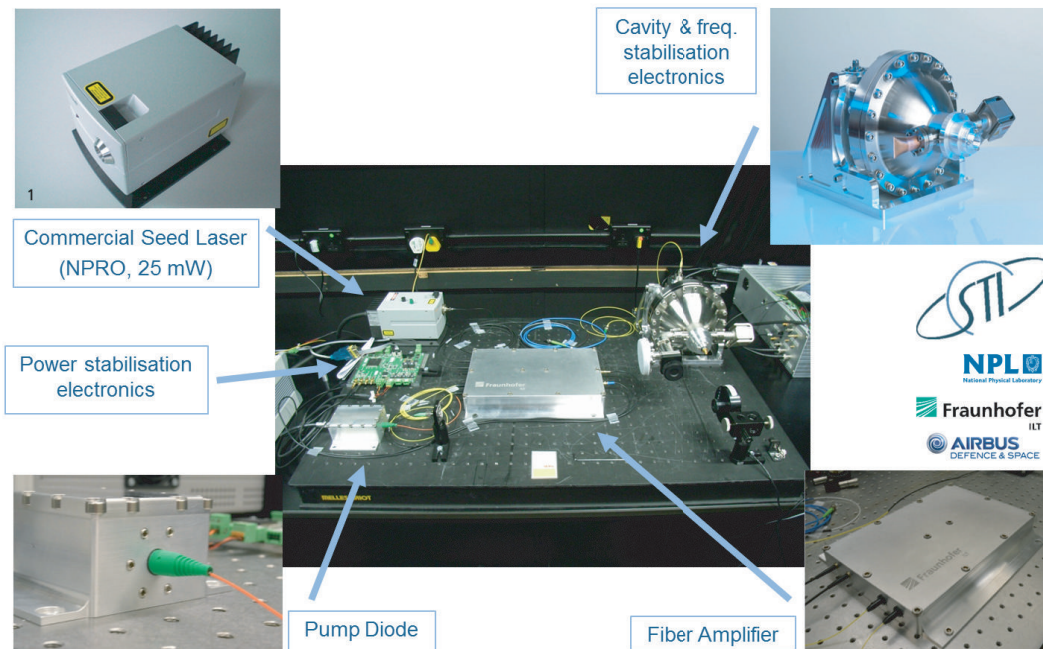


Figure 2.6: Breadboard of the NGGM High Stability Laser. Image courtesy of SpaceTech Immenstaad GmbH, Germany.

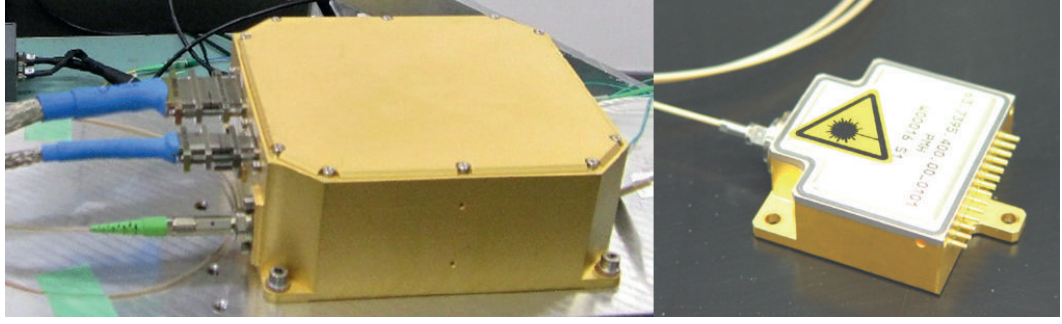


Figure 2.7: (Left:) NPRO laser for LISA Pathfinder from Tesat-Spacecom GmbH with approx. 35 mW optical output power at 1064 nm. (Right:) Tesat Pump Module with physical dimensions of 40x40x25 mm³ and a mass of 150 grams. The unit can deliver up to 5 W optical power at a wavelength of 808 nm [Schwander, 2006]. Image courtesy of Tesat-Spacecom GmbH.

fluctuations into the observations depends on the interferometer concept and this discussion is postponed until section 2.4, which introduces functional concepts.

The true frequency ν_{true} of the laser light, which may be stabilized by an external frequency standard, can be expressed as

$$\nu_{\text{true}}(\tau) = \nu_{\text{design}} + \delta\nu_{\text{DC}} + \delta\nu_{\text{LFN}}(\tau), \quad (2.68)$$

where ν_{design} is the known design frequency, $\delta\nu_{\text{DC}}$ is a small static error in the frequency, and $\delta\nu_{\text{LFN}}(\tau)$ are the small time-variable fluctuations with zero mean. The time τ denotes the proper time for objects on the satellite, which may differ from the coordinate time t , but the difference is only of importance in later sections. With this notation, one can approximate the true wavelength λ_{true} as

$$\lambda_{\text{true}} = \frac{c_0}{\nu_{\text{true}}(\tau)} \approx \lambda_{\text{design}} \cdot \left(1 - \frac{\delta\nu_{\text{DC}}}{\nu_{\text{design}}} - \frac{\delta\nu_{\text{LFN}}(\tau)}{\nu_{\text{design}}} \right), \quad (2.69)$$

which shows that the fractional and not the absolute frequency errors are of importance for the fractional error of the wavelength.

Recall that the instantaneous phase Φ of a light field $\vec{E}^c \propto e^{i \cdot \Phi}$ was defined for a monochromatic light field at constant frequency as (cf. eq. (2.21))

$$\Phi(\vec{r}, \tau) = 2\pi\nu\tau + \Psi(\vec{r}). \quad (2.70)$$

Using this, one can write the phase of a light field from an error-prone laser source as

$$\Phi(\vec{r}, \tau') = 2\pi \int_{\tau=0}^{\tau'} \nu_{\text{true}}(\tau) d\tau + \Psi(\vec{r}) \quad (2.71)$$

$$= 2\pi \cdot \underbrace{(\nu_{\text{design}} + \delta\nu_{\text{DC}})}_{\nu_{\text{true,mean}}} \cdot \tau' + 2\pi \underbrace{\int_{\tau=0}^{\tau'} \delta\nu_{\text{LFN}}(\tau) d\tau}_{\Phi_{\text{LFN}}(\tau)} + \Psi(\vec{r}), \quad (2.72)$$

which is a phase ramp with a slope proportional to $\nu_{\text{true,mean}}$ and which is increasing monotonically with time τ . Furthermore, it contains phase fluctuations Φ_{LFN} due to laser frequency noise. The spatial dependence of the phase $\Psi(\vec{r})$ has no relevance here.

A first indicator of the frequency stability of laser light is the linewidth, but more informative is the spectral density of the frequency noise, i.e. $\text{ASD}[\delta\nu_{\text{LFN}}](f)$ with units of $\text{Hz}/\sqrt{\text{Hz}}$, which can be easily converted to a fractional stability or Allan variances.

Frequency standards are commonly categorized into macroscopic and microscopic. Macroscopic standards are usually cavities, where the frequency is defined by the separation between two mirrors. A fraction of the light to be stabilized is injected into the cavity and kept resonant using the so-called Pound-Drever-Hall technique [Drever *et al.*, 1983]. Resonances occur not at a single particular frequency, but whenever the round-trip distance is an integer multiple of the wavelength. The frequency separation between adjacent resonances is called the free-spectral range (FSR), $\nu_{\text{FSR}} = c/(2 \cdot L_{\text{cav}})$, and is approximately 1.5 GHz for a 10 cm long cavity. Therefore, a cavity can provide only stability but not accuracy, i.e. the absolute frequency value needs to be determined by other means, e.g. from calibration of the laser wavelength w.r.t. set-points of the laser such as the crystal temperature.

Relevant noise sources for the frequency stability of cavities are shot noise and readout noise, residual laser amplitude modulations, intrinsic thermal noise and environmental contributions such as accelerations, vibrations and temperature variations. The intrinsic thermal noise of cavities can be computed by means of the fluctuation-dissipation theorem [Numata *et al.*, 2004; Kessler *et al.*, 2012] and contributions from the spacer, the mirror coating and substrate need to be taken into account. For room-temperature, the frequency noise limit from thermal noise (TN) of a mature cavity design is given approximately by

$$\text{ASD}[\delta\nu_{\text{LFN,TN}}](f) \approx 0.2 \text{ Hz}/\sqrt{\text{Hz}} \cdot \sqrt{\frac{1 \text{ Hz}}{f}} \cdot \frac{\lambda}{1064 \text{ nm}} \quad (2.73)$$

$$= 7 \cdot 10^{-16} \text{ 1}/\sqrt{\text{Hz}} \cdot \sqrt{\frac{1 \text{ Hz}}{f}} \cdot \nu, \quad (2.74)$$

which is shown as red solid trace in fig. 2.8. Experimental verification of this limit is provided, for example, by Notcutt *et al.* [2006] and Chen *et al.* [2013] and it is shown by the solid light blue trace. One has to mention that such a stability can be achieved in well-shielded ground-experiments but may not be attainable in a low Earth orbit with constraints on mass, dimensions and temperature stability.

The GRACE Follow-On LRI frequency noise requirement

$$30 \text{ Hz}/\sqrt{\text{Hz}} \cdot \sqrt{(1 + (3 \text{ mHz}/f)^2) \cdot (1 + (10 \text{ mHz}/f)^2)}, \quad 2 \text{ mHz} < f < 100 \text{ mHz} \quad (2.75)$$

has been fulfilled by an ultra-low expansion (ULE) glass cavity with a 77.5 mm spacer from *Ball Aerospace and Technologies Corporation* [Thompson *et al.*, 2011]. Alternatives to linear cavities, which are often called Fabry-Pérot cavities, are long fiber interferometers. These have shown a stability of $30 \text{ Hz}/\sqrt{\text{Hz}}$ at Fourier frequencies $f > 15 \text{ mHz}$ [McRae *et al.*, 2013]. In such a concept, the long fiber is used to form an unequal arm interferometer that measures the laser frequency fluctuations. These measured fluctuations are used to control the laser frequency, which effectively stabilizes the laser frequency or wavelength to the length of the fiber.

Instead of stabilizing the wavelength to a macroscopic length, microscopic frequency standards use the energy transition levels of atoms or molecules. A prominent example is an iodine cell, containing molecular iodine $^{127}\text{I}_2$, which has absorbing hyperfine transitions near 532 nm. A 1064 nm laser can be frequency-doubled and locked to such a transition, providing a precise absolute frequency. Breadboard setups for space-applications have demonstrated a stability below the GRACE Follow-On LRI requirement [Doringshoff *et al.*, 2010; Schuldt *et al.*, 2012] (cf. dashed light blue trace in fig. 2.8). As the frequency of the transition $R(56)32 - 0$ is known with a relative uncertainty $< 10^{-11}$ [BIPM, 2007], the laser frequency is known to much better than the required 1 ppm from table 2.1, once the frequency is locked to such standard.

For comparison, the frequency stability of current clocks is depicted in fig. 2.8, which is given for the Pharaoh cesium space clock in terms of Allan deviations by $\sigma_y(\tau_{\text{avg}}) = 10^{-13}/\sqrt{\tau_{\text{avg}}}$ [Delva *et al.*, 2012] and for the most precise clock in 2015 by $\sigma_y(\tau_{\text{avg}}) =$

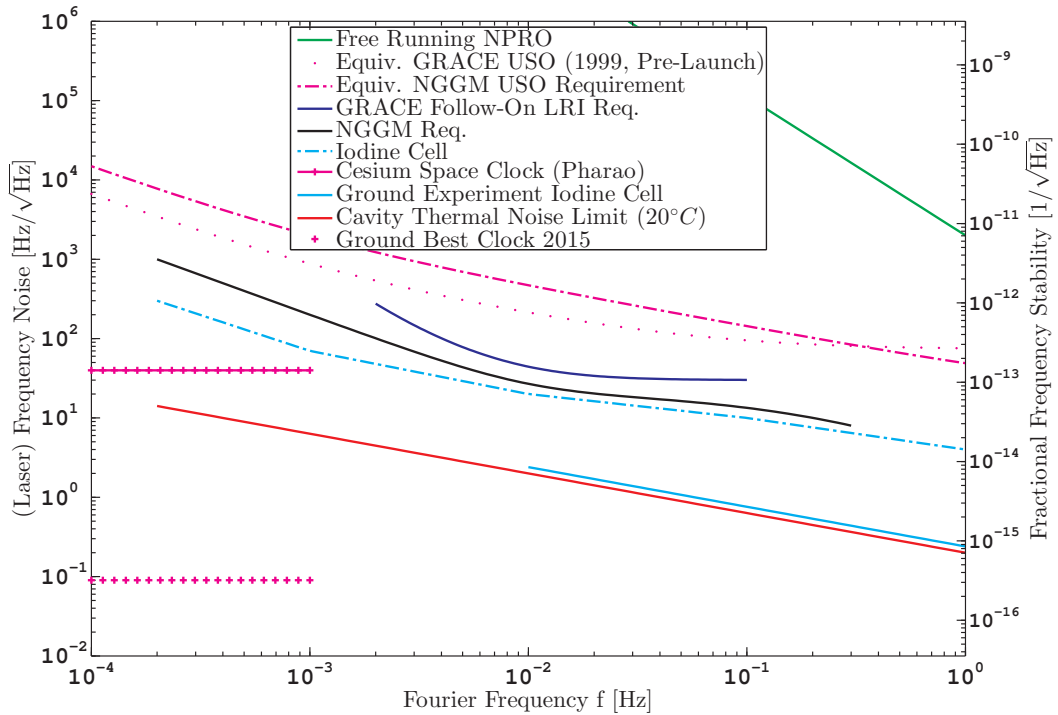


Figure 2.8: Laser frequency stability requirement in the GRACE Follow-On mission (dark blue trace) and for NGGM (black trace). A typical free-running NPRO frequency noise (green trace) is approximately reproduced from [Tröbs, 2005]. The thermal noise limit (red trace) agrees well with experimental data as given in [Chen *et al.*, 2013] (light blue trace). The iodine cell performance is from [Doringshoff *et al.*, 2010]. The corresponding fractional stability with units of $1/\sqrt{\text{Hz}}$ is given on the right axis of the plot. For comparison, the stability of current clocks is shown in magenta: (i) the Pharao cesium clock [Delva *et al.*, 2012] in the ACES experiment on the ISS, (ii) an optical lattice clock in a ground laboratory experiment [Nicholson *et al.*, 2015] (iii) the GRACE USO and a NGGM USO stability (see sec. 2.3.4). The frequency noise for all traces is referred to 1064 nm wavelength, i.e. rescaled to a carrier frequency of 282 THz.

$2.2 \cdot 10^{-16}/\sqrt{\tau_{\text{avg}}}$ [Nicholson *et al.*, 2015]. The Allan deviations are translated into spectral densities according to [Ferre-Pikal & Walls, 2001, Table 1]

$$\text{ASD}[\delta\nu](f) \approx \sigma_y \cdot \sqrt{\tau_{\text{avg}}} \cdot \sqrt{2} \cdot \nu, \quad \text{if } \sigma_y(\tau_{\text{avg}}) \propto 1/\sqrt{\tau_{\text{avg}}}. \quad (2.76)$$

An iodine cell, as well as a linear rigid Fabry-Perot cavity, seem to be the most promising candidates for optical frequency standards in a NGGM mission. The following requirement for the frequency stability of the frequency standard in a NGGM mission is proposed:

$$\text{ASD}[\delta\nu_{\text{LFN,req}}](f) = 20 \text{ Hz}/\sqrt{\text{Hz}} \cdot \sqrt{1 + (10 \text{ mHz}/f)^2} \cdot \frac{1}{1 + f/200 \text{ mHz}}. \quad (2.77)$$

It is compulsory for $1 \text{ mHz} < f < 300 \text{ mHz}$ and is a goal for $f < 1 \text{ mHz}$, as the interferometer is not the limiting instrument in the line-of-sight acceleration (PDGA) sensitivity at these frequencies. Compared to eq. (5-31) in [e.motion² Team, 2014], a second factor has been added to describe a decreasing frequency noise at Fourier frequencies $f \gtrsim 30 \text{ mHz}$ (cf. black trace in fig. 2.8), which is required for the calibration of the accelerometer with the LRI in the frequency band $100 \text{ mHz} < f < 300 \text{ mHz}$ (cf. section 1.10).

In general, the frequency stability needs to be achieved under the environmental conditions on the satellite. Thus, the susceptibility to temperature, magnetic and electric fields as well as rotations needs to be taken into account. For example, centrifugal forces deform the cavity

and induce a frequency change [Herrmann, 2008], which depends on the cavity geometry and position of the cavity within the satellite. Even if the pointing of the satellite is ideal along the line-of-sight, the baseline angular velocity of $10^{-5} \text{ rad/s}\sqrt{\text{Hz}}$ at 1 mHz (cf. fig. 1.23) can lead to a centrifugal acceleration of $6.3 \cdot 10^{-8} \text{ rad/s}^2\sqrt{\text{Hz}}$ at 1 mHz, which shall not change the fractional cavity length of the order of 10^{-13} . Detailed structural, mechanical and thermal analysis is therefore essential.

2.3.3 Photodiodes and Photoreceiver

Photodiodes convert an optical power into an electric current by exploiting the inner photoelectric effect. In so-called semiconductor PIN diodes with an undoped intrinsic (I) layer between a p- and n-doped layer, the absorption of most photons takes place in the intrinsic region. The material, and in particular the bandgap energy, of the semiconducting I-layer defines the spectral response or wavelength dependent responsivity $\eta_{\text{PD}}(\lambda)$ of diodes. For a 1064 nm wavelength, detectors made of Indium gallium arsenide (InGaAs) offer the highest responsivity of approx. 0.67 A/W. Silicon sensors usually achieve only approx. 0.4 A/W or less at this wavelength, but are better suited for the visible spectrum as shown in fig. 2.9. The internal quantum efficiency (IQE), i.e. the ratio of produced primary electrons over absorbed photons, cannot exceed unity, because the photodiodes are operated in a regime where the photon energy roughly matches the bandgap energy, which excludes multi-photon absorption. Therefore, the responsivity $\eta_{\text{PD}}(\lambda)$ is limited to approx. 0.85 A/W for 1064 nm light, which can be computed with

$$\eta_{\text{PD}}(\lambda) = \frac{\text{EQE} \cdot \lambda \cdot e}{h \cdot c_0} \quad (2.78)$$

where h is the Planck's constant, c_0 is the speed of light, e is the elementary charge and EQE is the external quantum efficiency. An IQE < 1 implies additional internal losses e.g. due to electron-hole recombination. External losses such as reflection or transmission of photons need also to be considered and are accounted for by the EQE, which is the ratio of photoelectrons over incident photons. For example, the refractive index of $\text{In}_{0.53}\text{Ga}_{0.47}\text{As}$ [Dinges *et al.*, 1992] is roughly $n(\lambda = 1064 \text{ nm}) \approx 3.65 - 0.26i$ and results via the Fresnel equation in a normal incidence power reflectivity of $R = |n - 1|^2 / |n + 1|^2 \approx 32.6\%$. Impedance matching by means of an anti-reflection coating on the active area mitigates this effect and can yield an overall external quantum efficiency of $> 80\%$. It is noted that a non-negligible part of the light is still reflected at the photodiode, which needs to be considered in the optical stray light analysis.

Another important photodiode property is the bandwidth f_{BW} , where the photocurrent response from an oscillatory optical stimulus drops below 3 dB. It is usually limited by the junction capacitance C_J , since the cut-off frequency f_{BW} is inversely proportional to the square-root of the capacity

$$f_{\text{BW}} \propto \frac{1}{\sqrt{C_J}}. \quad (2.79)$$

The junction capacity depends on the area of the detector. If signals up to 20 MHz need to be detected, an area below 1 mm^2 should be envisaged. Typical capacities are in the region of a few tens of picofarads for satellite interferometric applications, where the diodes are operated in photoconductive mode with a reverse bias voltage, which additionally reduces the capacitance. High-speed single element photodiodes with gigahertz bandwidth exist, but have the size of only a few ten micron.

With regard to the space environment and the space qualification of diodes, radiation induced increase of dark current and changes in responsivity have been reported [Gill *et al.*, 2005]. However, these issues have been addressed and are nowadays not substantive [Joshi *et al.*, 2006].

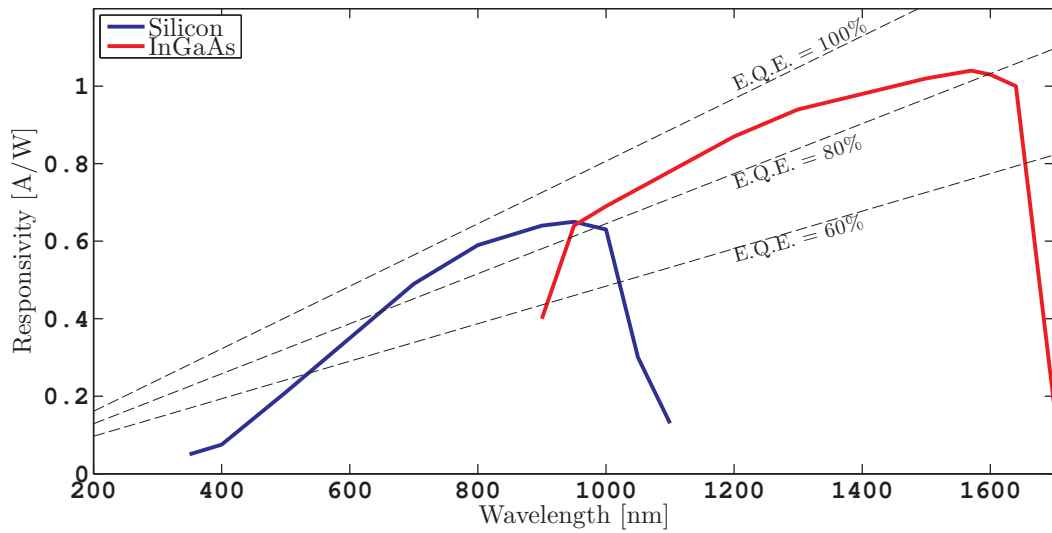


Figure 2.9: Typical spectral responsivity $\eta_{PD}(\lambda)$ for silicon and InGaAs photodiodes. The black dashed lines indicate different values of the external quantum efficiency (EQE) given as the ratio of produced primary photoelectrons over incident photons.



Figure 2.10: Photograph of a large circular single-element photodiode (center), a small quadrant-photodiode with barely visible gaps (bottom), and a large quadrant photodiode (right).

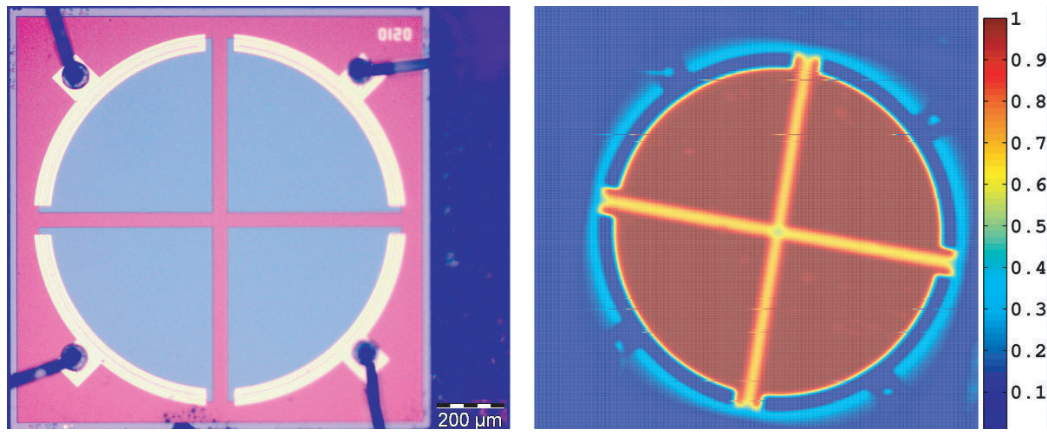


Figure 2.11: (Left:) A typical microscope image of a 1 mm diameter quadrant photodiode with four segments. The yellow-white outer parts are the electrodes, which are connected via wires at the four edges. The pale blue parts denote the active area of the segments. The gap size between the segments is roughly $50\ \mu\text{m}$ in this image. (Right:) A typical DC homogeneity of a segmented quadrant photodiode is shown as determined from the photocurrent. A small laser beam was used to perform a two-dimensional scan over the diode and the colorfunction indicates the summed photocurrent of all segments. Image courtesy of Germán Fernández Barranco (AEI).

Furthermore, for silicon photodiodes used at 1064 nm wavelength, an abnormal low bandwidth has been reported [Diekmann, 2013, sec. 4.2], which might require further investigation.

A remark is given on avalanche photodiodes, which can achieve a significantly higher spectral responsivity due to the generation of secondary electrons in an avalanche process, which might appear beneficial. However, secondary electrons do not enhance the signal to noise ratio of (photon) shot noise limited interferometers such as in the LISA mission. In addition, avalanche photodiodes are typically operated at a high reverse bias voltage $\gg 30\ \text{V}$, which increases the complexity of the electronics and the dark current. Moreover, the excess noise due to the inherently unstable gain makes this type of photodiode less favorable for low-noise phase tracking interferometry, where a large DC photocurrent and a small AC modulation is present. Nevertheless, these devices might be of interest for detecting weak light fields in the initial link acquisition, such as in the LITE mission [Boroson, 1993].

Several quadrant photodiodes have been space qualified for the GRACE Follow-On mission. A typical diode is the commercially available FCI-InGaAs-Q1000 by OSI Optoelectronics Inc., which offers low cross-talk between neighboring segments and low dark current $< 15\ \text{nA}$. It has a diameter of 1 mm and a gap size of $45\ \mu\text{m}$. A typical measurement of response uniformity over the active area is shown in fig. 2.11 (right), where issues such as asymmetry between segments, occultation by objects such as wires or parasitic reflections, e.g. from the housing, are not apparent.

In heterodyne interferometry, the photocurrent consists of a bias and a small modulation from the optical beatnote, which needs to be converted to a voltage by a transimpedance amplifier, typically in several stages. In the first stage a split into a DC and an AC path is recommended to simplify electronic design. A variable gain for the AC and DC path can ensure an optimal digitization of the AC and DC signals over mission lifetime, considering degradation in laser power and the uncertainties in the power link budget, for example. A characteristic of the whole photoreceiver, formed by the electronic amplifier and the photodiode, is the equivalent input current noise [Cervantes *et al.*, 2011]. A typical performance of

$$\text{ASD}[I_{\text{PR}}](f) = 5\ \text{pA}/\sqrt{\text{Hz}}, \quad 4\ \text{MHz} < f < 20\ \text{MHz} \quad (2.80)$$

has been shown in laboratories and in the GRACE Follow-On LRI on-ground testing. The

equivalent input current noise can be modeled for an active operational amplifier as [Cervantes *et al.*, 2011]

$$\text{PSD}[I_{\text{PR}}](f) = \text{PSD}[I_{\text{n}}](f) + \text{PSD}[I_{\text{j}}](f) + \text{PSD}[I_{\text{d}}](f) + \text{PSD}[I_{\text{v}}](f), \quad (2.81)$$

where $\text{PSD}[I_{\text{n}}]$ is the amplifier current noise, $\text{PSD}[I_{\text{j}}]$ is the thermal Johnson noise (of the feedback resistor), $\text{PSD}[I_{\text{d}}]$ is the shot-noise from photodiode dark current and the last term $\text{PSD}[I_{\text{v}}]$ accounts for the amplifier voltage noise, which couples into the equivalent input current noise. It is noted that the equivalent input current noise $\text{PSD}[I_{\text{PR}}](f)$ increases towards higher frequencies due to $\text{PSD}[I_{\text{v}}](f)$ [Cervantes *et al.*, 2011, cf. eq. 4], which is in a well-designed photoreceiver driven by the intrinsic capacitance of the photodiode segment.

The overall current noise $\text{PSD}[I_{\text{PR}}]$ can be converted to a noise equivalent optical power (NEP) via the responsivity or to a voltage noise via the transimpedance gain. Other figures of merit to be considered are, for example, the phase stability over temperature and frequency, electrical power consumption and channel cross talk.

An analytical model for the photoreceiver, which converts two optical fields such as $\vec{E}_r^c(\vec{r}, \tau) \propto e^{i\Phi_r(\tau)}$ and $\vec{E}_y^c(\vec{r}, \tau) \propto e^{i\Phi_y(\tau)}$ impinging on the photodiode (segment) into voltages $y(\tau)$, can be written as

$$y_{\text{DC}}(\tau) \approx G_{\text{DC}} \cdot \eta_{\text{PD}} \cdot (P_y + P_r) + \delta y_{\text{PR, DC}} \quad (2.82)$$

$$y_{\text{AC}}(\tau) \approx G_{\text{AC}} \cdot \mathcal{H}_{\text{PR}} \left[\eta_{\text{PD}} \cdot 2 \cdot \sqrt{P_y \cdot P_r \cdot \eta} \cdot \cos(\Phi_r(\tau) - \Phi_y(\tau) + \vartheta) \right] + \delta y_{\text{PR, AC}} \quad (2.83)$$

$$\approx G_{\text{AC}} \cdot \eta_{\text{PD}} \cdot 2 \cdot \sqrt{P_y \cdot P_r \cdot \eta} \cdot \cos(\Phi_r(\tau) - \Phi_y(\tau) + \vartheta + \Upsilon_{\text{PR}}) + \delta y_{\text{PR, AC}}, \quad (2.84)$$

where P_y and P_r are the total power values of the impinging individual light fields on the active area, and which have been defined in sec. 2.2.2 on optical detection. The photodiode responsivity with units of A/W is denoted as η_{PD} . The transimpedance gains with units of V/A for the DC and AC paths are labeled G_{DC} and G_{AC} , respectively. The spatially averaged overlap between both fields $\sqrt{\eta}e^{i\vartheta}$ has been specified in eq. (2.58). Compared to sec. 2.2.2, the expressions are supplemented here by the term Υ_{PR} , accounting for the effect of the photoreceiver transfer function and additional noise $\delta y_{\text{PR, AC/DC}}$.

The GRACE Follow-On photoreceivers [Barranco *et al.*, 2017], and photoreceivers in general, are complex analog electronic systems. They are optimized to have a flat amplitude response within the photoreceiver measurement band, e.g. 4 MHz..20 MHz, and to have a high suppression out of this band. A transfer function is a good means with which to characterize photoreceivers for ranging interferometry. This is the ratio of output over input in the frequency domain and is commonly expressed in terms of the (discrete) Z transform $H^c(z)$, in terms of the Laplace transform $H^c(s)$ or in terms of the Fourier transform $H^c(f)$. Recall that in this thesis, complex quantities are supplemented with the superscript c . The \mathcal{H}_{PR} operator in eq. (2.83) denotes the application of the photoreceiver transfer function onto the time series in the argument. It is assumed that the transfer function \mathcal{H}_{PR} is normalized to unity at low frequencies. However, in practice, the product of gain and transfer function ($G_{\text{AC}} \cdot \mathcal{H}_{\text{PR}}$) is difficult to separate. Moreover, under the assumption that the transfer function has a flat amplitude response, it is justified to consider only the phase response of the transfer function, which was used in the recast from eq. (2.83) to (2.84).

Although transfer functions offer an accurate way to describe and compute the output from a given input and they provide much insight and information, they are sometimes impractical and need to be approximated. Here, the transfer function of the photoreceiver (or subsequently of the phasemeter) is impractical, because it describes the behavior of the device in the operational frequency band, e.g. 4 MHz..20 MHz, which is decades away from the science measurement band of the actual ranging data, e.g. 0.18 mHz to 0.1 Hz. This is advantageous for the ranging sensitivity, because the ranging information is encoded at high frequencies where it is less susceptible to omni-present low-frequency noise. However, in principle, the precise simulation of ranging data requires data streams at a MHz sampling rate, where one can apply the transfer function. Fortunately, this can be avoided by exploiting

the fact that the input signals are stationary to a good approximation on the time scale of the sampling rate of the science data, i.e. the input signal has a fixed frequency on a time scale of 1 or 10 seconds. This allows the effect of the photoreceiver transfer function to be written as an additive term $\Upsilon_{\text{PR}}(f_{\text{beat}})$ in the phase, depending on the input frequency of the signal f_{beat} , rather than the more general form as a convolution of the transfer function impulse response with the time-series. In some sections of this thesis, e.g. when the working principle of the phase-locked loop is explained in sec. 2.3.9, this justification does not hold, and the general transfer function formalism from control loop theory is used.

A generic description of the photoreceiver transfer function is given by a polynomial formula, e.g.

$$\Upsilon_{\text{PR}}(f_{\text{beat}}) = \alpha_{\text{PR,off}} + \alpha_{\text{PR,lin}} \cdot |f_{\text{beat}}| + \alpha_{\text{PR,quad}} \cdot |f_{\text{beat}}|^2 + \dots, \quad (2.85)$$

where the beatnote frequency, i.e. the input frequency to the photoreceiver, can be derived from eq. (2.84) as

$$f_{\text{beat}} = \frac{1}{2\pi} \cdot \frac{d|\Phi_r(\tau) - \Phi_y(\tau) + \vartheta|}{d\tau}. \quad (2.86)$$

The linear term $\alpha_{\text{PR,lin}}$ denotes the delay of the output signal w.r.t. the input signal, i.e. a time shift by a frequency-independent amount $\Delta\tau_{\text{PR}}$. This can easily be shown in the frequency domain by using the time-shift rule, e.g.

$$\frac{\text{signal output}}{\text{signal input}} = \frac{g(\tau - \Delta\tau_{\text{PR}})}{g(\tau)} \xrightarrow{\mathcal{F}} \frac{e^{-i2\pi f \Delta\tau_{\text{PR}}} \cdot \mathcal{F}[g(\tau)]}{\mathcal{F}[g(\tau)]} = H^c(f) \quad (2.87)$$

$$= e^{-i2\pi f \Delta\tau_{\text{PR}}}. \quad (2.88)$$

The result in the last line represents a linearly decreasing slope in a Bode phase plot of $H^c(f)$, which allows the delay time with units of seconds to be written as $\Delta\tau_{\text{PR}} = -\alpha_{\text{PR,lin}}/(2\pi \text{ rad})$.

The GRACE Follow-On photoreceivers exhibit $\alpha_{\text{PR,lin}} \approx -0.2 \text{ rad/MHz}$ [Barranco *et al.*, 2017] and have a negligible quadratic term $\alpha_{\text{PR,quad}}$. A similar magnitude can also be considered for future missions. This corresponds to an equivalent delay of $\Delta\tau_{\text{PR}} \approx 32 \text{ ns}$. The constant phase offset $\alpha_{\text{PR,off}}$ can be neglected, because it is simply a further offset in the biased range.

The linear delay $\alpha_{\text{PR,lin}}$ is mostly common mode between the channels of the photoreceiver, if the same cables and cable lengths are used and if the channels are designed symmetrically, e.g. on the electric circuit board. However, a non-negligible phase difference among channels in the combined photoreceiver and phasemeter chain might remain. This phase difference needs to be calibrated on-ground and removed within the computation of the DWS signals in the phasemeter, as it would falsify the DWS signals.

The DWS signals are not susceptible to a common phase change in all four channels. It is often sufficient to apply a static phase-offset correction for each channel in the DWS calculation, i.e. up to the first term in eq. (2.85). In theory, the second linear term could also be corrected by a phasemeter, however, this was not utilized so far to the knowledge of the author.

Thus, the longitudinal phase and ranging information contains the average effect of $\alpha_{\text{PR,lin}}$ of all channels, which needs to be removed in post-processing. A conservative accuracy of 10% is assumed for the correction in this thesis, i.e. the remaining effect of the photoreceiver transfer function is

$$\Upsilon_{\text{PR,PP}}(\tau) \approx -2\pi \cdot 0.1 \cdot \Delta\tau_{\text{PR}} \cdot f_{\text{beat}}(\tau), \quad (2.89)$$

which corresponds to a delay of approx. 3.2 ns.

2.3.4 Ultra-Stable Oscillator (USO)

The USO is an electrical frequency reference, similar to the optical frequency standards discussed in sec. 2.3.2. It is also used as a clock that triggers all on-board satellite instruments and that provides the time-tag to the measurements. Fluctuations in the frequency correspond to a timing jitter. Typically, satellite USOs consist of a quartz crystal, which is a piezoelectric resonator with mechanical eigen-frequencies ranging from kHz to several hundred MHz depending on the crystal geometry and harmonic number. The electrical signal is generated by an oscillatory circuit, which is kept in resonance with the mechanical eigen-frequency or its harmonic.

The USOs in GRACE and GRACE Follow-On are used to generate the microwave carrier for the microwave ranging instrument via electrical frequency multiplication. Hence, the USOs act as a length reference for the microwave ranging instrument, in the same way as the cavity is a length reference for the laser ranging instrument. The typical science-grade USO frequency stability with units of Hz/ $\sqrt{\text{Hz}}$, e.g. in GRACE, is approximately 1 order of magnitude worse than the optical frequency stability (requirement) of a cavity, as shown in fig. 2.8.

Oscillators are usually characterized by their short-term stability in terms of the IEEE recommended single-sideband phase noise $\mathcal{L}(f)$ and by their long-term stability in terms of an Allan variance $\sigma_y^2(\tau)$. The single-sideband (SSB) phase noise $\mathcal{L}(f)$ is nowadays defined as one half of the one-sided power spectral density of phase fluctuations $\text{PSD}[\varphi_{\text{USO}}]$ [IEEE, 1999, table A.1] or frequency fluctuations $\text{PSD}[f_{\text{USO}}]$:

$$2 \cdot \mathcal{L}(f) = \text{PSD}[\varphi_{\text{USO}}](f) = \frac{\text{PSD}[\omega_{\text{USO}}](f)}{(2\pi f)^2} = \frac{\text{PSD}[f_{\text{USO}}](f)}{f^2}. \quad (2.90)$$

The SSB phase noise $\mathcal{L}(f)$ is commonly expressed in units of dBc/Hz, which is the relative power in decibels with respect to the carrier in a 1 Hz bandwidth. It was historically the power of the noise in one sideband due to phase fluctuations in a 1 Hz bandwidth and normalized to the total signal power consisting of carrier plus sidebands. The old definition required that amplitude fluctuations were negligible and that the total noise power was small, such that a small angle approximation was valid. However, with the new definition, the phase noise can be expressed unambiguously [IEEE, 1999] and the SSB phase noise is trivially related to a spectral density

$$\text{PSD}[\varphi_{\text{USO}}](f) = \frac{1}{2} \cdot 1 \frac{\text{rad}^2}{\text{Hz}} \cdot 10^{\frac{\mathcal{L}(f)}{10}}, \quad [\mathcal{L}] = \text{dBc/Hz}, \quad (2.91)$$

where, for example, a single-sideband phase noise of $\mathcal{L} = 50 \text{ dBc/Hz}$ corresponds to a one-sided power spectral density of $50 \cdot 10^3 \text{ rad}^2/\text{Hz}$.

The GRACE mission utilized oven-controlled quartz oscillators (OCXO) manufactured by JHU/APL with a mass of 3.2 kg, 2.3 W electrical power demand and a phase noise of $\mathcal{L}(f = 10 \text{ Hz}) = -112 \text{ dBc/Hz} = 6.3 \cdot 10^{-12} \text{ rad}^2/\text{Hz}$ for a carrier at 76 MHz [Weaver *et al.*, 2004]. This translates to a phase noise of $\mathcal{L}(f = 10 \text{ Hz}) = -135 \text{ dBc/Hz}$ at a carrier frequency of 5 MHz and is comparable with commercial compact ultra-low noise oscillators such as the OCXO 8607 from OSCILLOQUARTZ, however, this model is now deprecated and no longer available. A similar performance can be considered for a potential NGGM USO, which is depicted together with various other oscillator types in fig. 2.12. The functional model of the here proposed NGGM USO requirement can be written as

$$\mathcal{L}(f) = \sum_{\alpha=0}^4 h_{\alpha} \cdot \frac{f^{-\alpha}}{(1 \text{ Hz})^{-\alpha}} \quad (2.92)$$

with $h_0 = 1.0 \cdot 10^{-15} \text{ rad}^2/\text{Hz}$, $h_1 = 1.0 \cdot 10^{-14} \text{ rad}^2/\text{Hz}$, $h_2 = 5.0 \cdot 10^{-15} \text{ rad}^2/\text{Hz}$, $h_3 = 3.2 \cdot 10^{-13} \text{ rad}^2/\text{Hz}$ and $h_4 = 3.2 \cdot 10^{-16} \text{ rad}^2/\text{Hz}$. This requirement has been derived from

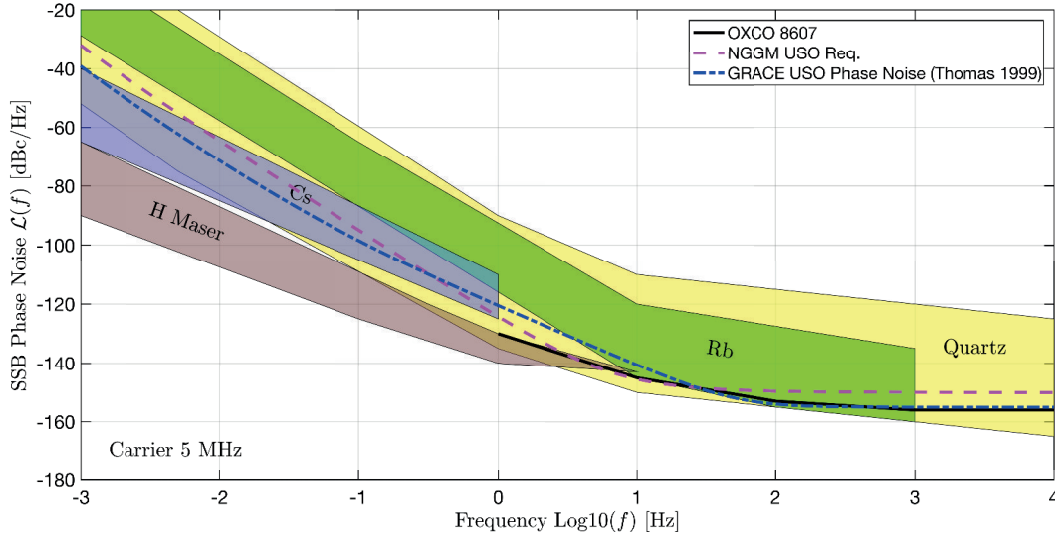


Figure 2.12: Typical single-sideband (SSB) phase noise of oscillators. All values have been rescaled for a 5 MHz carrier. This figure is an updated and modified version of a plot shown in a tutorial by John R. Vig [Vig, 2014].

a relaxation of the OXCO 8607 specification at high frequencies and, at low frequencies, from values given in Thomas [1999] on the estimated GRACE USO performance before the launch, which were a bit optimistic. The spectrum of phase fluctuations $\text{PSD}[\varphi_{\text{USO}}](f)$ can be converted to an Allan variance $\sigma_y^2(\tau)$ by [Ferre-Pikal & Walls, 2001]

$$\sigma_y^2(\tau) = \frac{2}{(\pi\tau)^2} \int_0^{f_h} \frac{\text{PSD}[f_{\text{USO}}](f)}{f_0^2} \cdot \frac{\sin^4(\pi\tau f)}{f^2} df \quad (2.93)$$

$$= \frac{2}{(\pi\tau)^2} \int_0^{f_h} \frac{\text{PSD}[\varphi_{\text{USO}}](f)}{f_0^2} \cdot \sin^4(\pi\tau f) df, \quad (2.94)$$

where f_0 is the carrier (USO) frequency and f_h is the measurement system bandwidth. The inverse transformation from Allan variances to low-frequency (< 1 Hz) phase noise is non-trivial, as knowledge of the high-frequency phase noise (> 1 Hz) and knowledge of f_h , which is usually not provided, are required. Furthermore, one needs to assume a particular shape (functional model) of the low-frequency phase noise. A derivation of the phase noise from Allan variances for the GRACE USO is given in [Thomas, 1999] and it is shown in fig. 2.12 as a blue dashed-dotted trace.

The Allan deviation of the NGGM USO requirement is shown as a magenta trace in the lower panel of fig. 2.13, which is comparable with the red trace of the GRACE USO performance as specified in table 2.2 and with the GRAIL USO stability. The dark blue trace indicates the timing accuracy of GNSS in post-processing, where a position uncertainty at centimeter level (white noise) yields a timing uncertainty at a 10^{-10} s/ τ level. The lower panel of fig. 2.13 shows that the satellite clock should only be steered in-orbit or in the ground processing towards GNSS time at low frequencies or at averaging times higher than few hundred seconds. In fact, the USO clock offset correction in the GRACE data is provided every 300 sec [Ko & Tapley, 2010; Fackler, 2005].

The red dashed line in the upper panel of fig. 2.13 shows the laser frequency noise of the optical cavity as defined by eq. (2.77), while the dashed green line is the thermal noise limit of cavities at room temperature. Although optical frequency standards can reach a higher stability, the transformation of optical frequencies to electrical signals usually requires a complex frequency comb. Hence, utilizing a single optical frequency standard for laser interferometry and as on-board clock is a non-trivial task.

The amplitude spectral density of USO phase fluctuations $\text{ASD}[\varphi_{\text{USO}}](f)$ can be con-

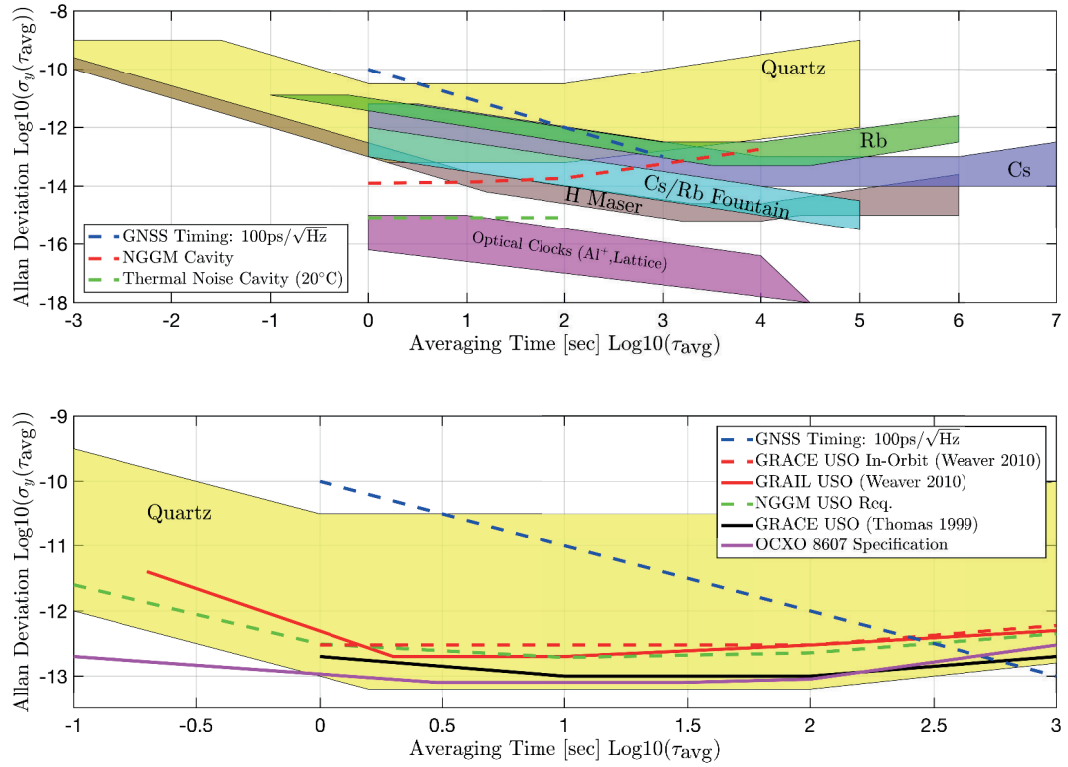


Figure 2.13: Typical Allan deviations (square root of Allan variance) for various oscillators. The upper panel is an updated and modified version of a plot shown in a tutorial by John R. Vig [Vig, 2014]. The lower panel shows the potential NGGM USO requirement with respect to other comparable USOs.

τ_{avg}	NGGM USO Requirement	GRACE USO
0.2 s	$1.3 \cdot 10^{-12}$ ($1.2 \cdot 10^{-13}$)	$4 \cdot 10^{-12}$
2 s	$2.3 \cdot 10^{-13}$ ($1.9 \cdot 10^{-13}$)	$2 \cdot 10^{-13}$
10 s	$1.9 \cdot 10^{-13}$ ($1.9 \cdot 10^{-13}$)	$2 \cdot 10^{-13}$
100 s	$2.3 \cdot 10^{-13}$ ($2.3 \cdot 10^{-13}$)	$3 \cdot 10^{-13}$
1000 s	$4.5 \cdot 10^{-13}$ ($4.5 \cdot 10^{-13}$)	$5 \cdot 10^{-13}$
10000 s	$1.3 \cdot 10^{-12}$ ($1.3 \cdot 10^{-12}$)	-

Table 2.2: Allan deviation $\sigma_y(\tau_{\text{avg}})$ of USO fractional frequency stability computed for a measurement system bandwidth $f_h = 10$ kHz and in brackets for $f_h = 10$ Hz. The GRACE USO performance is taken from Weaver *et al.* [2010].

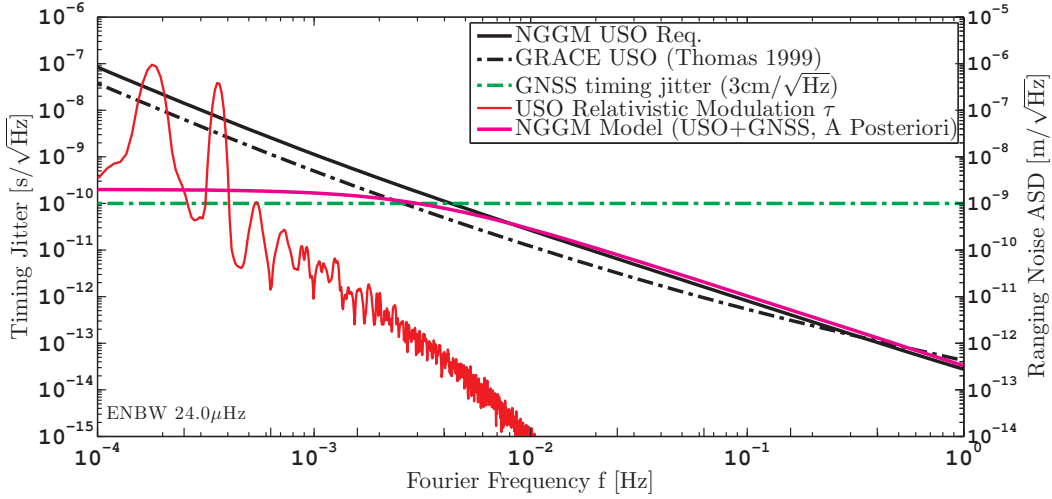


Figure 2.14: The amplitude spectral density of the proper time $\tau(t)$ of a GRACE-like satellite (red trace) due to relativistic effects, in comparison with GNSS timing jitter (green trace) and USO clock stability (black traces). The magenta trace is a (rough) analytical model for the timing error after post-processing on ground. The axis on the right side is the timing jitter multiplied with 20 m/s.

verted to the equivalent timing jitter $\delta\tau_{\text{USO}}$ by

$$\text{ASD}[\delta\tau_{\text{USO}}](f) = \frac{\text{ASD}[\varphi_{\text{USO}}](f)}{2\pi f_0}, \quad (2.95)$$

where f_0 is again the nominal USO frequency. Every non-static on-board measurement is falsified by timing jitter. For example, if the relative velocity between two satellites is 1 m/s, a timing jitter of $1 \text{ ns}/\sqrt{\text{Hz}}$ leads to a noise of $1 \text{ nm}/\sqrt{\text{Hz}}$ in a range measurement. This error is caused by the inability to correctly determine the sampling time in the desired time frame.

For further discussion of the on-board time it is necessary to consider relativistic effects and to introduce the time frames correctly. The satellite dynamics, the instantaneous inter-satellite range and the gravity field recovery are typically performed or defined in the GCRS coordinate system (cf. sec. 2.1.1). The coordinate time t of the GCRS is the so-called Geocentric Coordinate Time (TCG). The ideal error-free time of a satellite and of all on-board instruments, as measured by error-free clocks on the satellite, is given by the proper time τ_i on the i -th S/C (cf. eq. (2.12)). The proper time can be expressed as a function of the coordinate time t and it can be computed in simulations by a numerical integration of eq. (2.12).

The general definition of a time from an oscillator is

$$\tau_{i,\text{USO}}(\tau_i) = \frac{2\pi \int_0^{\tau_i} f_{i,\text{USO,true}}(\tau'_i) d\tau'_i}{2\pi f_{i,\text{USO,nom}}}, \quad (2.96)$$

where $f_{i,\text{USO,nom}}$ is the nominal oscillator frequency and $f_{i,\text{USO,true}}(\tau)$ is the true but unknown instantaneous frequency of the oscillator, which is prone to noise and errors. For the purpose of this thesis, it is sufficient to write the solution of eq. (2.96) as

$$\tau_{i,\text{USO}}(\tau_i(t)) = \tau_i(t) + \delta\tau_{i,\text{USO}}(\tau_i(t)) + \delta\tau_{i,\text{USO,off}}, \quad (2.97)$$

where $\delta\tau_{i,\text{USO}}$ is the timing jitter of the USO (cf. eq. (2.95)) with zero mean and $\delta\tau_{i,\text{USO,off}}$ is a static or very slowly varying offset.

A typical result of the proper-time $\tau_i(t)$ w.r.t. the coordinate time t for a GRACE like satellite is shown as a red trace in fig. 2.14 in terms of an amplitude spectral density. The shown signal arises due to the time dilation caused by the orbital velocity and the gravitational potential. In addition, the black traces show the USO timing jitter noise $\delta\tau_{i,\text{USO}}$ discussed

here. The USO error can be estimated and corrected by the GNSS-based precise orbit determination for low Fourier frequencies ($f < 4 \text{ mHz} \approx 1/250 \text{ s}$). The precision of the GNSS-based timing can be computed from $c_0 \cdot \Delta\tau = \Delta r$, which is shown as the green trace for an assumed position noise of $\text{ASD}[\Delta r] = 3 \text{ cm}/\sqrt{\text{Hz}}$. However, this correction works only in post-processing on ground, since the in-orbit derived GNSS position, the so-called navigation solution, is accurate to a few ten meters only.

It is apparent from fig. 2.14 that the pronounced peaks of the proper time τ_i and hence of the USO time $\tau_{i,\text{USO}}$ (red trace) at the orbital frequency and higher harmonics can be resolved by the clock time solution of the GNSS-based precise orbit determination.

An analytical model for the timing jitter with incorporated GNSS clock error estimates from post-processing (PP) can be formulated as

$$\text{ASD}[\delta\tau_{i,\text{USO,PP}}](f) = \frac{2 \cdot 10^{-10} \text{ s}/\sqrt{\text{Hz}}}{1 + (f/3 \text{ mHz})^{1.5}}, \quad (2.98)$$

which is shown as the magenta trace in fig. 2.14. This expression is used later to estimate the sensitivity of ranging instruments more realistically.

The USO timing offset $\delta\tau_{i,\text{USO,off}}$ from eq. (2.97) is assumed to be of the order of

$$\delta\tau_{i,\text{USO,off}} \approx 100 \text{ ps}, \quad (2.99)$$

which corresponds to 3 cm. This offset induces a delay, but is uncritical for laser interferometry as will be shown in later sections, since other digital delays and delay uncertainties exceed the 100 ps value.

A further remark is given here on a statement found in [Yeh *et al.*, 2011], where it was claimed that the USO becomes obsolete in a homodyne interferometer, because the coupling of timing jitter into the ranging observation via the phase ramp from the frequency offset is removed. Indeed, the susceptibility to timing jitter can be reduced, however, as the frequency offset and the Doppler shift due to the range rate are of the same order, the advantage is rather incremental. Moreover, precise clocks improve the orbit determination, and gravimetric missions should still use a high-performance low-noise science grade USO clock.

Finally, it is noted that additional requirements for the USO regarding spurs (tones), radiation hardness and magnetic and electric susceptibility need to be assessed, but are beyond the scope of this section.

2.3.5 Retro-Reflectors

Hollow Corner-Cube Retro-Reflectors (HCCRR)

A retro-reflector is typically a passive optical system which reverses the propagation direction of a ray, independent of the angle of incidence, as long as it is within the field-of-view of the retro-reflector. In general, the exiting ray will be offset laterally w.r.t. the incident ray. A widely used type of retro-reflector is the corner-cube, which consists of three mutually orthogonal plane mirrors. The intersection point of all three mirror planes is the so-called vertex. Corner-cubes can be further classified into *solid* and *hollow* types.

In the solid case, the three mirror planes can be obtained by cutting a solid glass cube diagonally and applying a highly-reflective (HR) coating on the outer planes. The diagonal face is anti-reflective (AR) coated and serves as entrance aperture. Solid corner-cubes have the advantage of a higher acceptance angle (field-of-view) [Yang & Friedsam, 1999] due to refraction compared to hollow corner-cubes, which consist simply of three well aligned mirrors (cf. top part in fig. 2.16). Due to the absence of light propagation in glass and its purely reflective nature, hollow corner-cube retro-reflectors (HCCRR) are preferred by the author of this thesis for precise ranging interferometry. In addition, they offer interesting properties regarding the optical pathlength, which is illustrated in fig. 2.15 (for two dimensions). The

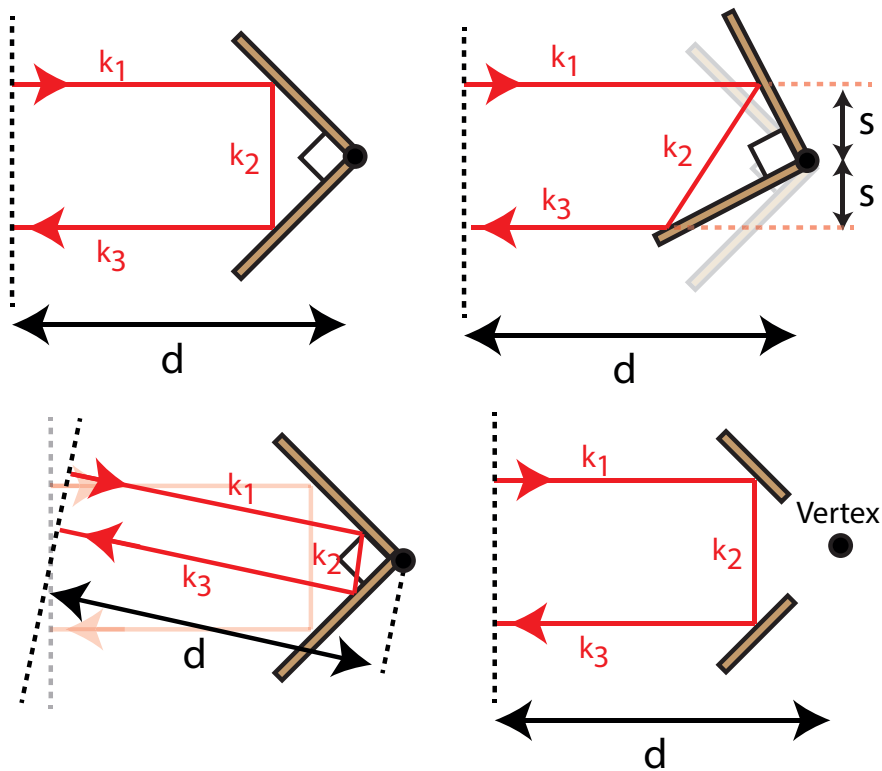


Figure 2.15: Ray-tracing through a right-angled prism, which is the 2-d equivalent of a 3-d hollow corner-cube retro-reflector (HCCR). The accumulated geometrical pathlength $k_1 + k_2 + k_3$ is twice the separation d between vertex and virtual plane in all four sub-plots. (**Upper left:**) Nominal light path. (**Upper right:**) HCCR rotated around its vertex. The lateral separation between ingoing and outgoing ray remains as $2 \cdot s$. (**Lower left:**) The ingoing beam is rotated. (**Lower right:**) Non-required portions of the HCCR may be removed to provide a physically accessible virtual vertex point.

accumulated geometrical and optical pathlength through a HCCR is invariant under rotations of the HCCR around the vertex, i.e. under changes of the direction of the incident ray. However, one should note that the virtual detection plane defining the pathlength has to stay normal to the ray direction. Not-required portions of the mirrors can be removed, such that the vertex becomes a virtual point well-defined by the intersection of the mirror planes, as sketched on the lower-right panel in fig. 2.15. This allows collocation of the HCCR vertex with the accelerometer reference point and S/C center of mass. Furthermore, it should be noted that a HCCR is the generalization of a two-dimensional right-angled prism into three dimensions.

The lateral separation between the ingoing and outgoing ray is determined by the lateral separation between ingoing ray and the vertex (cf. upper-right panel in fig. 2.15). The HCCR in the GRACE Follow-On LRI with a 60 cm lateral offset is called the Triple Mirror Assembly (TMA). It is mounted together with the accelerometer and star cameras, as shown in fig. 2.16. The tube-like design maximizes the free space between the TMA structure and vertex to almost the maximal possible value of approximately one half of the lateral offset. In addition, the hollow tube acts as a protection for the light path. The nominal incidence angles of the light on the three TMA mirrors are 60° , 60° and 45° . This changing angle in combination with the fact that the mirror normal vectors are not located in a single plane requires special attention regarding polarization changes as analyzed diversely in literature [Liu & Azzam, 1997; Player, 1988; Scholl, 1995; Bieg, 2015; He *et al.*, 2013]. A corresponding analysis for the GRACE Follow-On TMA and potential future missions can be found in

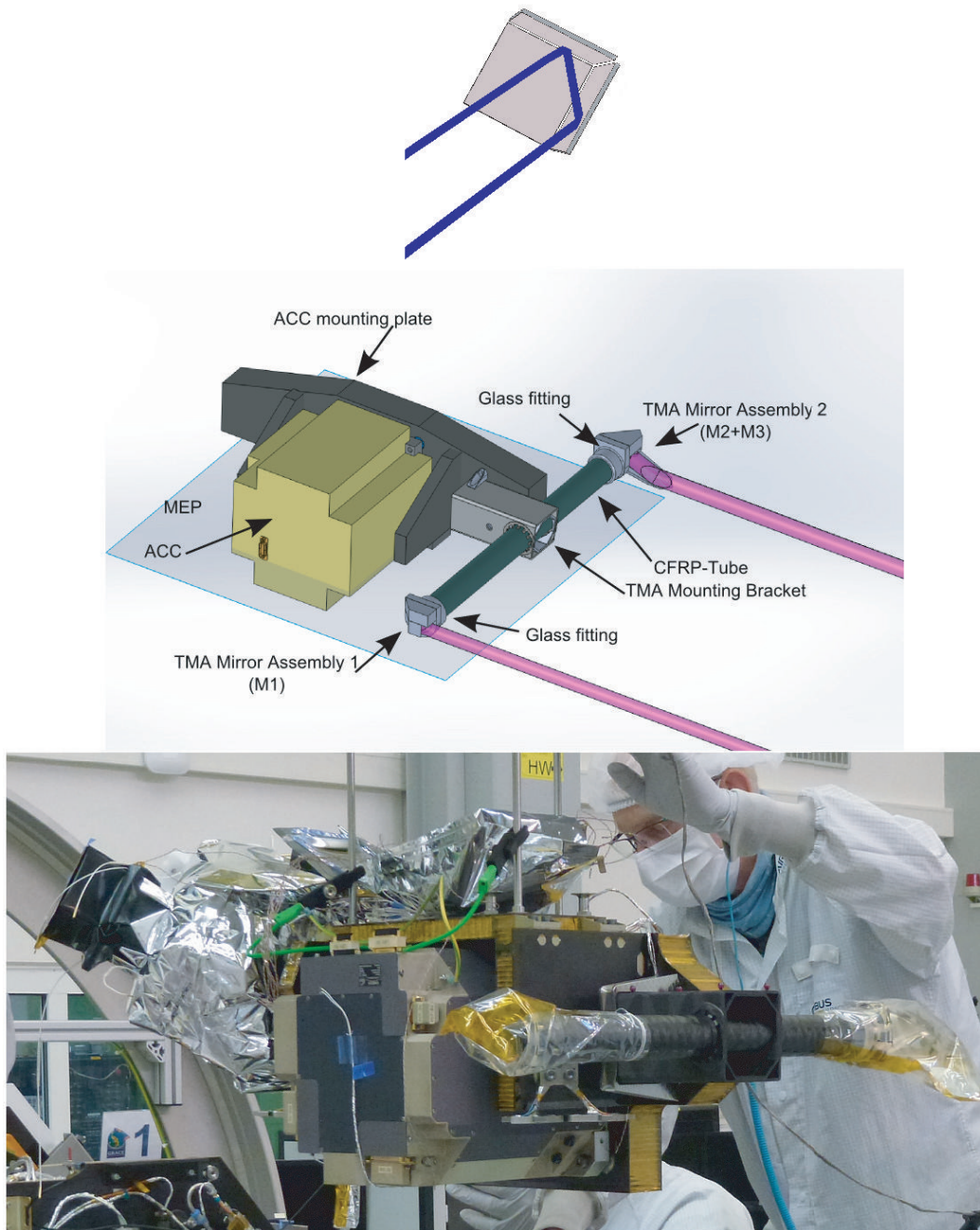


Figure 2.16: (Top:) A ray-tracing path through a hollow corner-cube retro-reflector (HC-CRR) consisting of three mutually perpendicular mirrors. (Center:) An early CAD-model of the accelerometer and triple-mirror assembly (TMA) without star cameras on the main equipment platform (MEP) in GRACE Follow-On. Image courtesy of SpaceTech GmbH Immenstaad. (Bottom:) Photo of final assembly consisting of accelerometer, TMA and star cameras prior to integration into the GRACE Follow-On S/C. Image courtesy of Airbus Defence and Space GmbH.

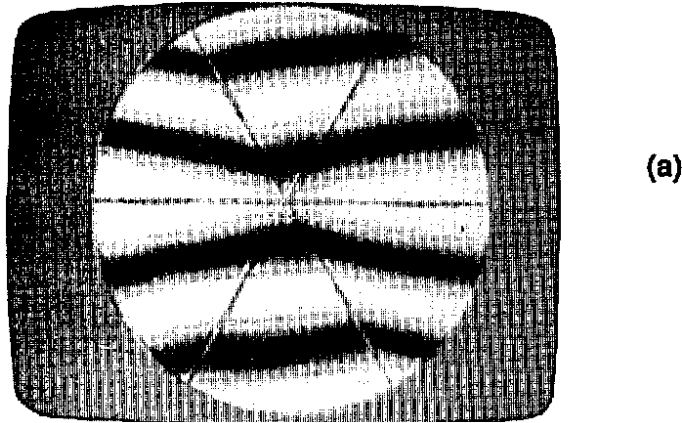


Figure 2.17: An exemplary interferogram of a hollow corner-cube retro-reflector with circular open aperture from [Ai & Smith, 1992]. The center point is the vertex. Three physical edges exist in a corner-cube, but due to reflection six segments appear with different deflection angles due to imperfect alignment of the mirror planes. Image courtesy of OSA Publishing with granted permission for *fair use* under US copyright law.

appendix D.

The GRACE Follow-On LRI is designed such that the light is reflected three times in a particular order at the mirrors. However, if a full (non-virtual) corner-cube is used with light entering closely to the vertex, there are in total six different possible paths with three reflections through a HCCR, depending on the location of the first reflection [Liu & Azzam, 1997]. Hence, different portions of an extended beam may travel different paths and yield a mixture of different polarization states for the retro-reflected field. This polarization change makes HCCR not straight-forward to use in optical cavities [Peck, 1962].

Moreover, the output directions of the different portions are altered in the presence of manufacturing tolerances of a HCCR, as shown in an exemplary interferogram in fig. 2.17. The sharp edges yield a segmented structure, whereby each segment is caused by a different path through the HCCR. Similar interferograms have been used to measure the anti-parallelism of the GRACE Follow-On TMA [Schütze, 2014]. It is non-trivial to measure parallelism over a separation of 600 mm due to the difficulty to obtain or manufacture flat bars or mirrors of sufficient size, which can serve as a reference.

If a HCCR is used as an on-axis retro-reflector, the segmentation of the beam with the associated polarization and direction changes needs to be considered. Furthermore, the influence of the non-reflective vertex needs to be taken into account. High-quality HCCR can reach a co-alignment error of less than an arcsecond ($<4.84 \mu\text{rad}$) with a wavefront quality close to that of a flat mirror. The physically compact tube-shaped retro-reflector of GRACE Follow-On has been designed to reach a co-alignment error of less than $50 \mu\text{rad}$ with error contributions from temperature variations, zero-G effects, moisture release, reference flat bar uncertainties and manufacturing (alignment) tolerances. The *Retroreflector in Space* (RIS), a full HCCR with an open aperture of 50 cm, reached an accuracy of a few μrad [Sugimoto & Minato, 1996].

The geometrical and optical pathlength through an ideal error-free HCCR is twice the distance to the vertex (cf. caption of fig. 2.15). Furthermore, rotations around the vertex do not change the pathlength. However, if the HCCR has non-perfectly aligned mirror planes, rotations around the vertex yield a rotation-to-pathlength coupling, whereby the vertex is still the intersection point of the mirror planes. This error coupling is analyzed in appendix E together with anti-parallelism errors of a TMA.

For a potential future NGGM mission, where the accommodation of an interferometer in the S/C can be considered unconstrained and in an early stage, a more compact retro-reflector design is recommended. This would allow the use of a highly rigid structure with enhanced anti-parallelism, most likely of the order of a few arcseconds.

Alternative Retro-Reflector Designs

Another well-known type of retro-reflector is the cat's eye. It is typically designed out of a primary lens and a secondary reflective curved or flat surface. Types with two half spheres as shown in fig. 2.18 have also been analyzed [Goldman, 1996]. A good starting point for the analysis of such retro-reflector is the paraxial ABCD formalism, as performed by Snyder [1975]. A retro-reflector ABCD matrix is given by

$$\widehat{M}_{\text{RR}} = \begin{pmatrix} -1 & 0 \\ 0 & -1 \end{pmatrix}, \quad (2.100)$$

which can be used as the target expression for finding the correct focal lengths or distances in the design phase. The two diagonal elements in the matrix indicate a pure reflection of the ray's lateral displacement at the optical axis and the inversion of the ray direction. This might suggest that such cat's eye retro-reflectors can be used to produce a large lateral offset, however, the ABCD formalism holds only in the paraxial approximation, i.e. when the ratio of lateral offset over lens curvature radius is small.

The negative identity matrix \widehat{M}_{RR} implies that the beam mode, e.g. the complex q -parameter of a Gaussian beam, is not changed by a retro-reflector, i.e.

$$q_{\text{new}}^c = \frac{A \cdot q^c + B}{C \cdot q^c + d} = \frac{-q^c}{-1} = q^c \quad (2.101)$$

at least in the paraxial approximation, which is the domain of validity for the ABCD formalism. However, aberrations and imperfections of the curved surface alter the wavefront quality, making flat surfaces preferable where applicable. A suggestion for an on-axis retro-reflector, naturally arising after studying the paper by Snyder [1975], is shown at the bottom of fig. 2.18. It consists of a lens and a flat surface. The ray's origin and the flat surface are located in the focal planes of the lens. The focal length of the lens should be as large as possible to mitigate aberrations.

It is noted that the accumulated optical pathlength for the on-axis ray and the tilted ray are equal because they traverse different paths in glass (cf. black and red rays in the bottom part of fig. 2.18). This becomes especially obvious if the optical system is unfolded at the mirror, which yields an ideal 1:1 imaging system. A wavefront tilt at the entrance plane results in a pure tilt at the exit plane without changing the absolute phase in an ideal imaging system. Equivalent is the statement that spherical wavefronts are reproduced in the image plane. Hence, the shown origin of the rays in the focal plane is the pivot point of zero rotation coupling, similar to the vertex in a HCCRR.

Such an on-axis retro-reflector is used in a later section for the optical layout of an on-axis interferometer.

2.3.6 Optical Components and Optical Bench

The main optical components in an interferometer are beamsplitters, fiber couplers, photodiodes, polarizing beamsplitters, mirrors, lenses, waveplates and polarization filters. Most consist of a substrate on which an optical coating is deposited. Transmissive optical components such as beamsplitters and lenses are composed of a transparent isotropic substrate, typically glass, with a wavelength dependent refractive index between 1.4 and 1.9. BK7 and fused silica are commonly used glass types in off-the-shelf components with some typical physical properties shown in table 2.3.

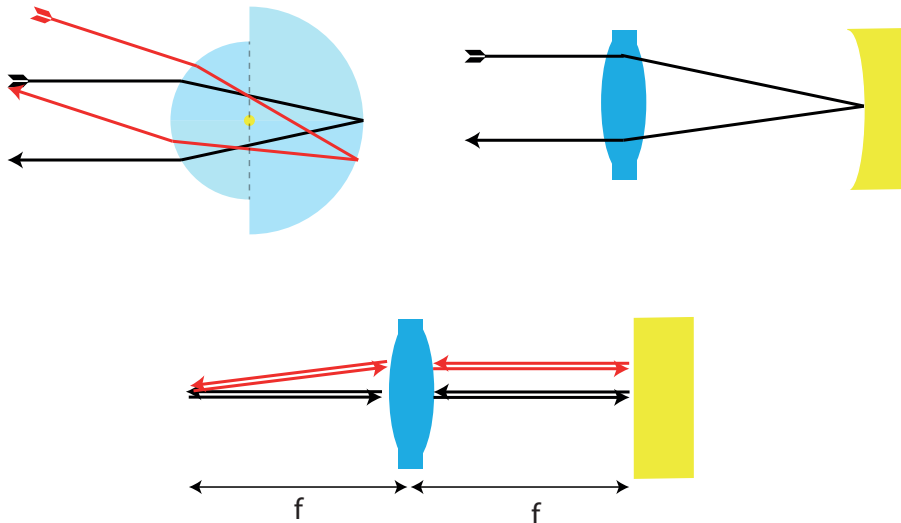


Figure 2.18: (Upper left:) Ray-tracing through a spherical ball retro-reflector consisting of two half spheres constructed out of the same material. (Upper right:) Ray paths through a cat's eye retro-reflector with a lens and a reflective curved surface. (Bottom:) A retro-reflector design with a lens and flat reflecting surface.

An important aspect for the interferometer design is the temperature dependence of the refractive index dn/dT , which is typically accompanied by a mechanical linear expansion with coefficient α . This coefficient of thermal expansion (CTE) of the substrates should be compatible with the mounts and baseplates of the components. The optical pathlength change Δs upon temperature change ΔT can be computed with [Träger, 2012, eq. 5.127]

$$\Delta s = \Delta T \cdot L \cdot G = \Delta T \cdot L \cdot (dn/dT + \alpha \cdot (n - 1)). \quad (2.102)$$

If the total pathlength through the glass in the sensitive path of the interferometer is $L = 10$ cm and the temperature fluctuations at the components are $\delta T(f) = 10 \text{ mK}/\sqrt{\text{Hz}}$, one obtains a resulting pathlength and ranging noise of $8.3 \text{ nm}/\sqrt{\text{Hz}}$ for fused silica. Glasses with minimal $\Delta s/\Delta T$ coupling are called *athermal glasses*, e.g. Ohara S-PHM52, but they have the disadvantage of being more difficult to polish and shape due to brittleness [Heinzel, 2002, LTP].

The variety of optical payloads that have been launched and used in space [Qian, 2016] provides sufficient technology heritage such that effects from the space environment on components out of glass or birefringent materials, e.g. for wave plates, are well understood and considered uncritical. Most prominent of these effects are radiation induced absorption and density (refractive index) changes in glasses [Gusarov *et al.*, 2002]. Space-qualified optical coatings are also available and need to withstand the radiation and the atomic oxygen flow if directly or indirectly exposed to sun light or space in a LEO.

As most of the interferometer setups are planar, it is natural to use a common baseplate for the optical layout. High-precision interferometers such as those in LISA Pathfinder and planned for LISA use a glass ceramic with ultra-low CTE and superb flatness, such as the ULE-glasses by Cornig, Ohara Clearceram-Z or Zerodur with $\alpha < 0.1 \text{ ppm/K}$ (cf. fig. 2.19). Substrates can be fixed permanently with a space-qualified technique called hydroxide catalysis bonding [Elliffe *et al.*, 2005], yielding a quasi-monolithic structure which can survive the launch loads and resist temperature variations. An alternative to bonding is gluing of components, which is easier to manufacture and which can also provide stable optical systems if the glue layer is thin.

Glass	n	dn/dT [ppm/K]	α [ppm/K]	G [$\mu\text{m}/(\text{K} \cdot \text{m})$]
N-BK7	1.5067	1.1	7.1	4.7
Fused Silica	1.4496	8.1	0.55	8.3

Table 2.3: Properties of glass in vacuum for $\lambda \approx 1064$ nm. The linear thermal coefficient of expansion is denoted with α , while G is the temperature coefficient of optical pathlength change for a substrate with 1 meter length, i.e. $G = dL \cdot d(\Delta s)^2/dT$. All values are taken from the SCHOTT AG product catalogue.

For the gravimetric GRACE-FO LRI a costly ultra-low CTE bench was not required. This is because, on one hand, the sensitivity requirement is relaxed to nanometers compared to picometers, and on the other hand, the LRI design cancels many phase fluctuations on the bench in the final ranging observable. The optical components in the LRI are tightly enclosed and fixed in a titanium block, which reduces the thermal fluctuations due to the large surrounding thermal mass (cf. lower-right part of fig. 2.19). The CTE of titanium is well matched to the CTE of the BK7 glass used in the LRI [Nicklaus *et al.*, 2014b]. In addition, the nearly sealed design minimizes contamination of optics. Mitigation of particulate and molecular contamination should already be addressed in early stages of a potential NGGM interferometer design, as it might be beneficial to operate some sensitive components at a higher temperature, which can reduce the contamination, or to budget for some decontamination heaters, as in the LRI.

A metal optical bench, e.g. out of titanium, is a viable option for an NGGM-like laser interferometer as suggested in the e.motion² proposal [e.motion² Team, 2014].

2.3.7 Phasemeter

The main purpose of a phasemeter is the tracking of the phase of the MHz signals provided by each photodiode segment and photoreceiver (cf. eq. (2.84)). Fast electronics based on Field-Programmable-Gate-Arrays (FPGAs) have proven to be suitable [Shaddock *et al.*, 2006; Gerberding, 2014], and FPGAs have been optimized for space applications at least since the late 1990s [Mavis *et al.*, 1998]. Additional electronics such as Digital-to-Analog and Analog-to-Digital (DAC/ADC) converters are required to control a potential steering mirror, the laser, the frequency stabilization, and to read in additional signals such as the AC and DC channels of the photoreceiver, steering mirror and laser sensors. Additionally, a phasemeter needs to support different modes, for example, science operation or signal acquisition, which requires complex logic [Ales *et al.*, 2015].

The GRACE Follow-On LRI phasemeter has been developed by JPL/NASA. A European study for the LISA Metrology System developed a phasemeter up to TRL 4 [Barke *et al.*, 2014]. Such a LISA-like phasemeter (cf. fig. 2.20) offers additional features to reach the desired $\text{pm}/\sqrt{\text{Hz}}$ sensitivity in a deep-space environment, e.g. corrections for USO drifts, ADC timing jitter subtraction, capability for data transfer via modulation of the laser light and absolute ranging with a pseudo-random code.

In a low Earth orbit with available GNSS and with a ranging sensitivity goal of $\text{nm}/\sqrt{\text{Hz}}$, such features are not required. Therefore, a NGGM phasemeter can be based on the LISA metrology system, however, with a substantial reduction in complexity. Some effort is still required to reach TRL 6 or higher, in particular, to achieve a decrease in power consumption and dissipation, as well as improved thermal stability.

The frequency band of the phase tracking is a key figure that typically ranges from 4 MHz to 20 MHz [Bykov *et al.*, 2009]. The lower limit should be sufficiently high so as to stay above frequency regions with significant laser relative intensity noise (cf. section 2.3.1 on lasers) and other omni-present low frequency noise sources, which might otherwise lead to a saturation of the phasemeter ADC channels. The phase retrieval already requires an oscillatory (AC) signal with zero mean. Hence, the high-pass filter can be designed to define the lower frequency of

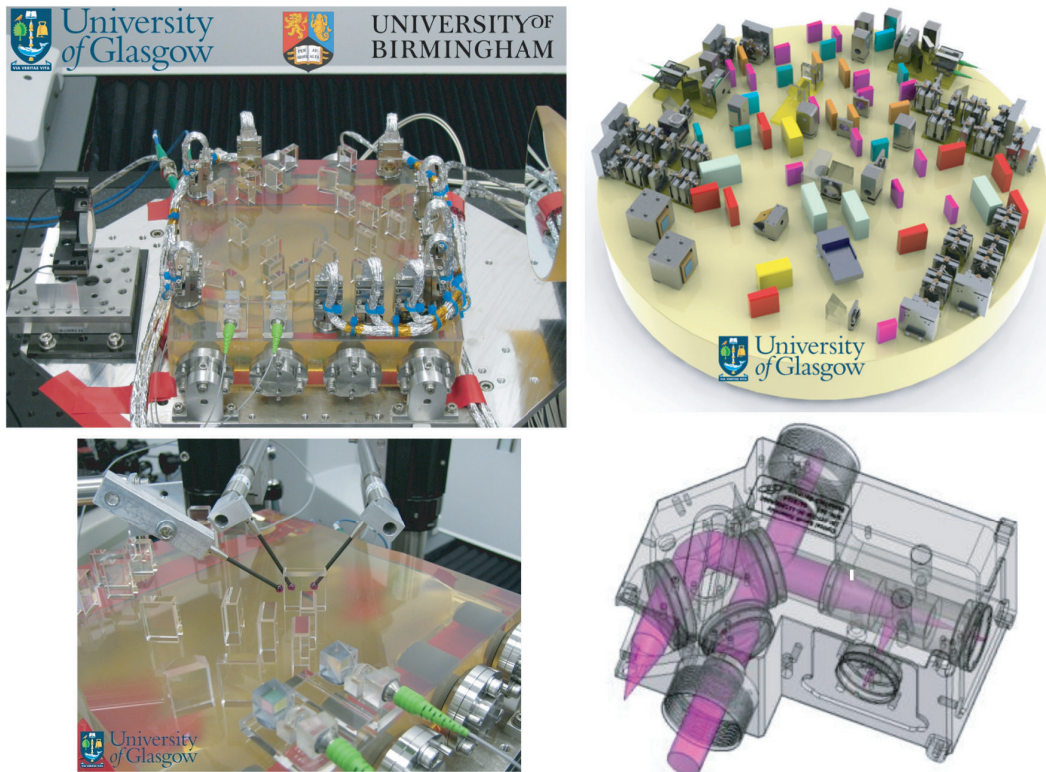


Figure 2.19: (**Upper left:**) The flight optical bench of LISA Pathfinder (**Upper right:**) An optical bench CAD model for LISA (**Lower left:**) Bonding of optical components of the LISA Pathfinder optical bench. The three fingers define the position of the component while the bond is established. (**Lower right:**) A model of the optical bench in the GRACE Follow-On LRI. This subfigure image courtesy of SpaceTech Immenstaad GmbH.

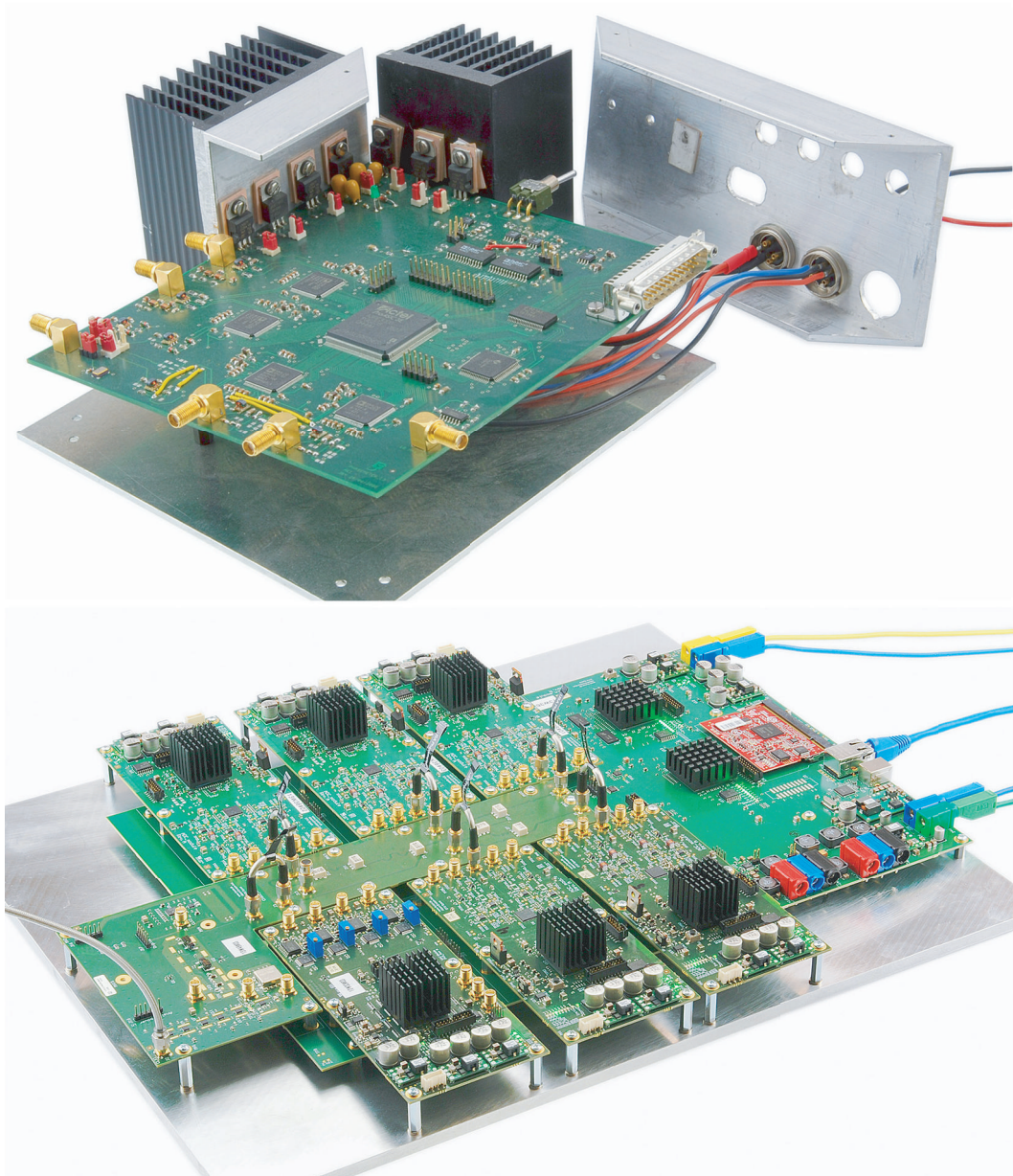


Figure 2.20: (Top:) A typical FPGA-based 4-channel phasemeter for laboratory experiments developed at the AEI Hannover. (Bottom:) An engineering breadboard of a LISA-like phasemeter developed by DTU Space (Denmark), Axcon ApS (Denmark) and the AEI (Germany). It is based on FPGAs and a modular design. The mainboard is equipped with a clock module, five ADC module with 4 channels each and a DAC module (4 channels). Images from [Barke *et al.*, 2014].

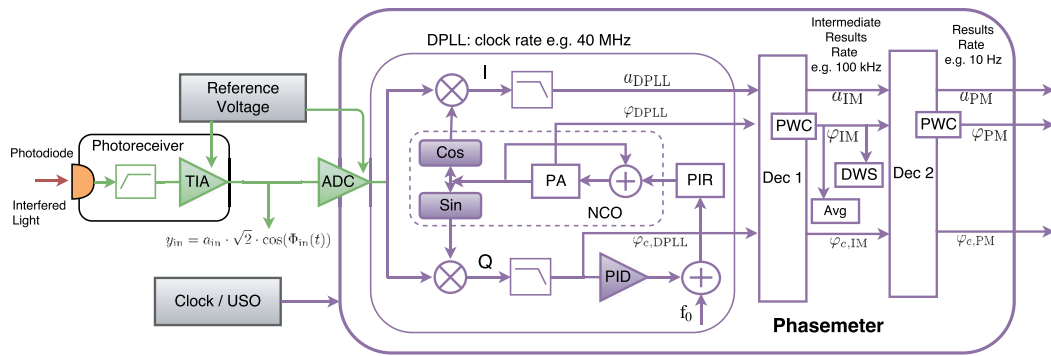


Figure 2.21: Block diagram of a single channel of a digital phase-locked loop (DPLL) phasemeter. The quadrature (Q) component is used as an error signal $\varphi_{e,DPLL}$, which in turn is used to derive the phase increment register (PIR), containing the current frequency of the digital reference signal. Integrating the PIR yields the phase accumulator (PA), which is the phase of the digital local oscillator within the phasemeter. Decimation of the phase accumulator, for example, by means of cascaded integrator combs (CIC), yields the final phase output φ_{PM} of the single phasemeter channel. A phase-wrapping correction (PWC) is applied to remove negative side-effects arising from filtering a noncontinuous signal, such as smoothing and ringing. The average phase (Avg.) and the DWS signals are formed from multiple channels.

the band prior to digitization (cf. fig. 2.21). If the beatnote frequency approaches zero, which in the limit corresponds to homodyne detection, the signal amplitude is attenuated by the filter until the phase lock is lost.

The upper limit of 20 MHz is given by the bandwidth of the photoreceiver, in particular of the photodiode itself, as it acts as a low-pass filter (cf. section 2.3.3 on photodiodes) and by the increasing noise of the photoreceiver towards higher frequencies. If the upper limit is increased, e.g. by using smaller photodiodes and choosing appropriate analogue electronic components, the clock frequency of the FPGAs and the associated sampling frequency of the digital part becomes the limiting factor. Typically, a low-pass anti-aliasing filter (AAF) is implemented prior to digitization, which removes frequencies higher than half the sampling frequency (Nyquist-theorem) or even lower. This avoids aliasing of high frequency noise into the measurement band during digitization.

Although a larger bandwidth appears beneficial, one should keep in mind that it is more complicated to ensure a well-behaved amplitude and phase response of the photoreceiver and phasemeter in a larger bandwidth. If the inter-satellite dynamics require a very high bandwidth of the phasemeter and the clock frequency is limiting, one can consider using the aliased beatnote. This desired undersampling is a technique that is used in the LISA metrology system for the 75 MHz pilot tone measurement [Barke *et al.*, 2014, p. 27], for example. But this has far-reaching consequences on laser link acquisition and overall performance, and, to the knowledge of the author, was not well studied yet.

The phase tracking algorithm within a phasemeter is typically based on a digital phase-locked loop (DPLL) as depicted in fig. 2.21. Compared to fig. 2.2 in the section on optical detection and phase retrieval, the scheme here shows some additional parts and the arctangent was removed, because for a sufficiently strong phase-lock one can utilize the small phase approximation ($\arctan(x) \approx x$). In the following, an accurate analytical model for the phase observable φ_{PM} for a single channel of the phasemeter is derived, which is later used to compute more complex interferometer signals as well as the longitudinal phase given by the average of several segments.

It should be recalled that the input to the phasemeter, i.e. the output of the photoreceiver,

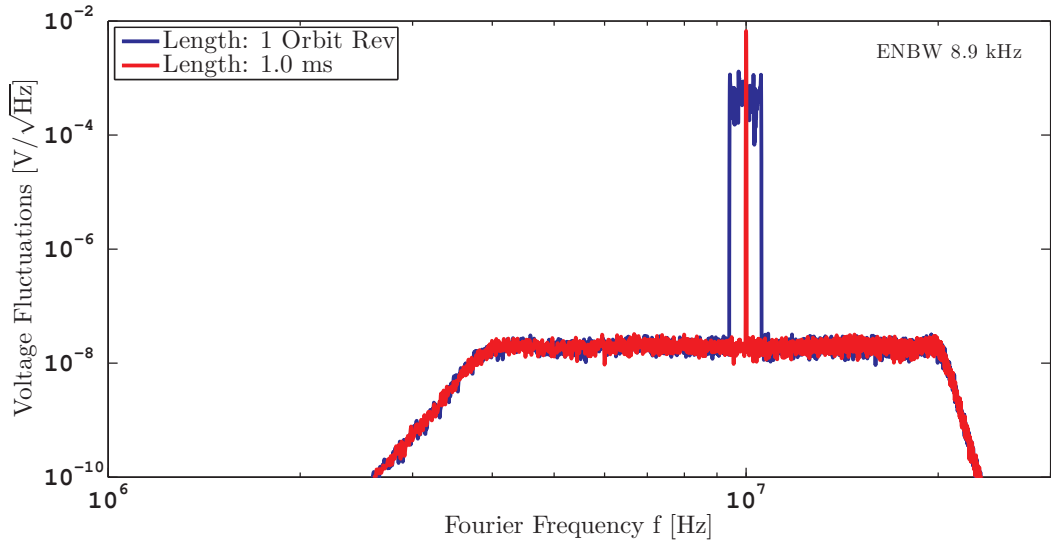


Figure 2.22: Exemplary spectral density of the photoreceiver AC channel, i.e. the phasemeter input y_{in} . For a time series much shorter than the orbital period, the signal appears quasi-monochromatic with a single frequency (red trace). Laser phase noise and ranging induced phase changes widen the peak. The frequency is time-varying in a long time series (dark blue trace). The noise floor is shaped by the band-pass filter in the photoreceiver with corner frequencies at 4 MHz and 20 MHz.

can be written for the purpose of this thesis as

$$y_{\text{in}}(\tau) = \sqrt{2} \cdot a_{\text{in}} \cdot \cos(\Phi_{\text{in}}(\tau)) = \sqrt{2} \cdot a_{\text{in}} \cdot \cos(\omega_{\text{mean}} \cdot \tau + \delta\varphi_{\text{in}}(\tau)), \quad (2.103)$$

where the mean angular beatnote frequency $\omega_{\text{mean}} = 2\pi f_{\text{beat,mean}}$ is of the order of MHz times 2π . The mean is formed over a few orbital periods. Of course, the apportioning of the phase Φ_{in} into $\omega_{\text{mean}} \cdot \tau$ and $\delta\varphi_{\text{in}}$ is performed artificially for the sake of the analysis. The phase variations Φ_{in} and $\delta\varphi_{\text{in}}$ contain the ranging signal with frequency content below 1 Hz and laser phase noise with frequency content below 100 kHz, e.g. for a free-running laser. These two contributions are depicted in terms of the spectral density in the upper panel of fig. 2.24. The only difference between Φ_{in} and $\delta\varphi_{\text{in}}$ is a phase ramp, which is usually not visible in frequency-domain plots.

The rms-amplitude a_{in} is considered to vary only very slowly, e.g. below 1 Hz, and is rescaled by $\sqrt{2}$ to form the peak value in eq. (2.103). The proper time τ is used instead of the GCRS coordinate time t , which indicates that signals are defined in the local Lorentz frame of the S/C.

The input signal y_{in} defined by eq. (2.103), which is exemplarily shown in terms of a spectral density in fig. 2.22, is demodulated within the digital phase-locked loop (DPLL) into an in-phase (I) component and an out-of-phase (quadrature Q) component by multiplication with a digital reference signal (cf. fig. 2.21). The low-pass filtered Q component is proportional to $\sin(\varphi_{e,\text{DPLL}}) \approx \varphi_{e,\text{DPLL}}$ if the reference sinusoid has a similar frequency and phase as the input signal. This error signal $\varphi_{e,\text{DPLL}}$ is used in a feedback control loop to adjust the digital reference frequency in the phase increment register (PIR), such that $\varphi_{e,\text{DPLL}}$ is zeroed. The I component contains the magnitude of the input signal, if the error signal is zero. The PIR is quasi-continuously integrated by the numerically controlled oscillator (NCO) and yields the phase of the reference signal, which is stored in the phase accumulator (PA). The phase accumulator is a register with a finite number of bits, and hence the ever increasing phase causes regular overflows of the PA. These result in jumps in the phase and would cause ringing of the filtered and decimated output. To resolve this issue, one can deliberately introduce a phase-reducing jump by a well-defined amount in the PA prior to overflow and then correct

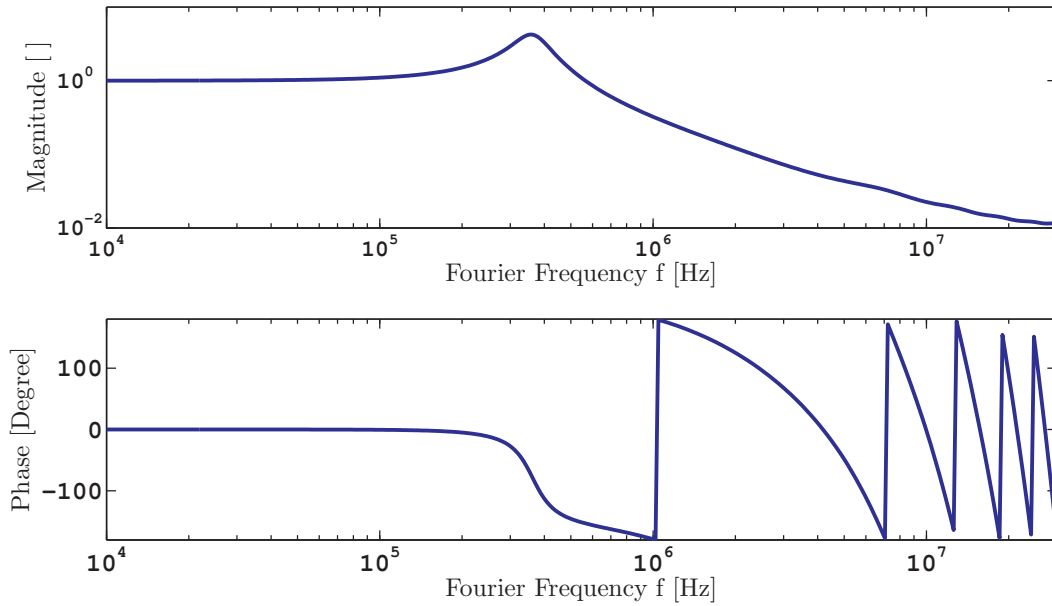


Figure 2.23: Bode plot of an exemplary closed-loop transfer function $H_2^c(s)$ of a digital phase-locked loop (DPLL). It has been (approximately) reproduced from fig. 4.3 in [Gerberding, 2014].

for the filter response of the jump directly in the phasemeter⁴. This is called phase-wrapping correction (PWC) in fig. 2.21. As a result, the filtered output contains a sharp jump and no artifacts such as ringing.

Alternatively, one can also use the digital frequency in the PIR, which is not subject to wrapping, for decimation and as science data. This requires a (trivial) integration in on-ground processing. However, since the JPL phasemeter in GRACE Follow-On utilizes the phase as science data, the analysis in this thesis follows the same approach.

A DPLL is, in general, a non-linear system due to the presence of a mixer. Furthermore, it provides several outputs from a single scalar input, such as the amplitude a_{DPLL} , the phase φ_{DPLL} and often the error signal $\varphi_{e,\text{DPLL}}$. However, one can synthesize a single scalar output y_{DPLL} according to

$$y_{\text{DPLL}} = a_{\text{DPLL}} \cdot \cos(\varphi_{\text{DPLL}} + \varphi_{e,\text{DPLL}}) \quad (2.104)$$

$$\approx a_{\text{DPLL}} \cdot \cos(\varphi_{\text{DPLL}}) = a_{\text{DPLL}} \cdot \cos\left(2\pi \int f_{\text{DPLL}}(\tau) d\tau\right). \quad (2.105)$$

Thus, the DPLL performs a phase measurement by fitting a digital sinusoid to the input signal. The digital copy is typically cleaner, since most of the noise power at frequencies other than the oscillation frequency is rejected by the DPLL. This digital copy allows an effective transfer function for the DPLL in the Laplace domain to be defined as

$$H_1^c(s) = \frac{y_{\text{DPLL}}^c(s)}{y_{\text{in}}^c(s)} \quad (2.106)$$

which includes contributions from the analog-to-digital converters (ADCs) and the DPLL itself. This transfer function is defined only for the MHz band shown in fig. 2.22. Similarly, one can define a transfer function for the phase variations, i.e.

$$H_2^c(s) = \frac{\delta\varphi_{\text{DPLL}}^c(s)}{\delta\Phi_{\text{in}}^c(s)} \quad (2.107)$$

⁴To the knowledge of the author, this principle originates from the GRACE-FO LRI team at JPL

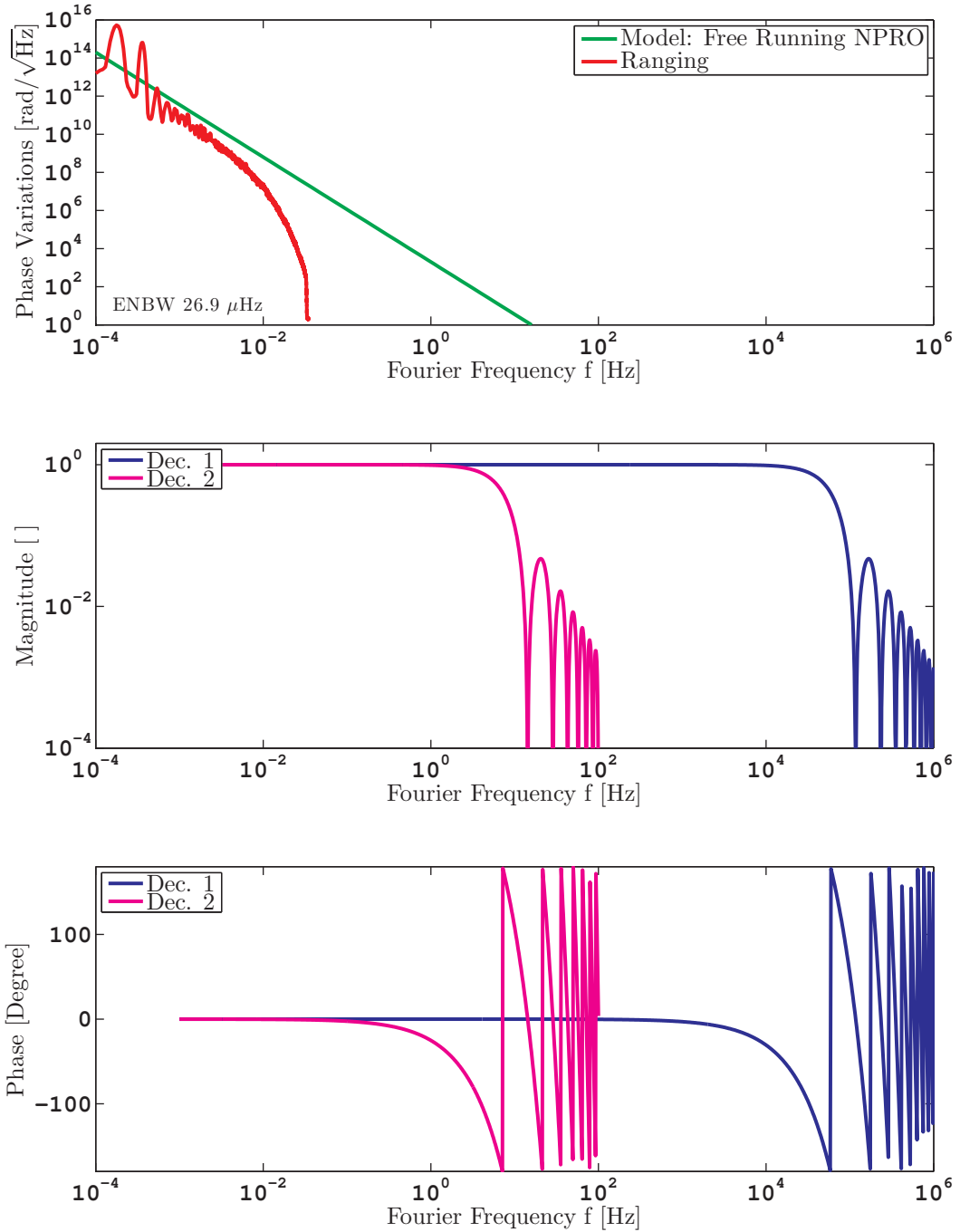


Figure 2.24: (**Upper panel:**) The two dominating constituents of $\delta\varphi_{\text{in}}$ and Φ_{in} . (**Central panel:**) The magnitude of typical decimation filters used to decrease the sampling rate in a phasemeter. (**Lower panel:**) The phase response of typical decimation filters is (ideally) linear, i.e. it is a delay, which appears non-linear in the semi-logarithmic plot shown here. The decimation filters shown are cascaded-integrator combs (CIC) with $N = 2$ and are only examples.

which has typically a flat amplitude and phase response up to the bandwidth of the DPLL, for example, $f_{\text{loop,DPLL}} \approx 50$ kHz. An exemplary Bode plot of the closed-loop transfer function $H_2^c(s)$ with a higher DPLL bandwidth of 300 kHz is given in fig. 2.23. The open-loop gain (not shown in the figure) crosses unity at the Fourier frequency $f_{\text{loop,DPLL}}$ and phase fluctuations in $\delta\varphi_{e,\text{DPLL}}$ (cf. fig. 2.21) at lower frequencies are suppressed by the loop. It should be noted that the open-loop and the closed-loop transfer function $H_2^c(s)$ depend on the amplitude a_{in} and on the instantaneous beatnote frequency f_{beat} , i.e.

$$f_{\text{beat}}(\tau) = \frac{1}{2\pi} \left| \frac{d\Phi_{\text{in}}(\tau)}{d\tau} \right|. \quad (2.108)$$

The transfer function $H_2^c(s)$ is defined up to the MHz band, but it is well defined also for low frequencies, where the ranging information is encoded (cf. red trace in upper panel of fig. 2.24). It is sufficient to use a sampling rate of the order of 1 Hz or 10 Hz to record the ranging data in-orbit or to simulate such observations. Since the transfer function of the DPLL, here $H_2^c(s)$, is basically unity at such low frequencies, one can approximate the effect of the DPLL transfer function as an additive term Υ_{DPLL} . This has also been done for the transfer function of the photoreceiver (cf. sec. 2.3.3), i.e.

$$\varphi_{\text{DPLL}}(\tau') = 2\pi \cdot \int_{\tau'_0}^{\tau'} f_{\text{DPLL}}(\tau) d\tau \approx \Phi_{\text{in}}(\tau') + \text{const.} + \Upsilon_{\text{DPLL}}(f_{\text{beat}}(\tau')) + \delta\varphi_{\text{PM}}, \quad (2.109)$$

where f_{beat} is the beatnote frequency and where the noise due to imprecise phase tracking was accounted for by the addend $\delta\varphi_{\text{PM}}$. The effect of the DPLL transfer function on the phase Υ_{DPLL} is the argument of $H_1^c(s)$ and can be described in a general way as a polynomial (cf. eq. (2.85)) in the phasemeter measurement bandwidth. The linear part in Υ_{DPLL} w.r.t. f_{beat} corresponds to a phase delay by a time $\Delta\tau_{\text{USO,DPLL}}$, which is always non-zero due to the finite clock frequency of the digital logic. This delay is generally defined with respect to the USO time, since the USO clock is driving the digital logic.

So far, the derivation did not properly consider the USO clock driving the phasemeter. The USO clock time τ_{USO} relates the apparent (digital) frequency in the phasemeter f_{DPLL} , which is measured with respect to the USO time, to the proper true frequency of the input signal $f_{\text{beat}}(\tau)$, which is measured with respect to the proper time τ , via

$$\frac{f_{\text{beat}}(\tau)}{f_{\text{DPLL}}(\tau_{\text{USO}})} \approx \frac{d\tau_{\text{USO}}}{d\tau}. \quad (2.110)$$

The relation is only approximative, as it is assumed that f_{DPLL} contains noise and minor effects due to transfer functions.

Hence, a more precise description of the DPLL phase, which yields the same result as eq. (2.109), reads as follows

$$\varphi_{\text{DPLL}}(\tau'_{\text{USO}}) = 2\pi \cdot \int_{\tau_{\text{PM,on}}}^{\tau'_{\text{USO}}} f_{\text{DPLL}}(\tau_{\text{USO}}) d\tau_{\text{USO}} \quad (2.111)$$

$$= 2\pi \cdot \int_{\tau_{\text{PM,on}}}^{\tau'_{\text{USO}}} \underbrace{f_{\text{beat}}(\tau) \cdot \left(\frac{d\tau_{\text{USO}}}{d\tau} \right)^{-1}}_{\text{apparent freq. in phasemeter}} d\tau_{\text{USO}} + \delta\varphi_{\text{PM}} + \Upsilon_{\text{DPLL}} \quad (2.112)$$

$$\approx \Phi_{\text{in}}(\tau = \tau_{\text{USO}}^{-1}(\tau'_{\text{USO}})) + \text{const.} + \delta\varphi_{\text{PM}} + \Upsilon_{\text{DPLL}}, \quad (2.113)$$

where the arbitrary start time of phase tracking $\tau_{\text{PM,on}}$ yields the constant in the last line and is a manifestation of the fact that interferometry can only measure a biased range. In fact, the constant is ideally an integer multiple of 2π , since the reference signal in the DPLL is in-phase with the input signal. This condition can not be easily incorporated in the integral form (eq. (2.112)) and was not explicitly written in the last line, because many effects can

cause a deviation of the constant from an integer multiple of 2π . The integer ambiguity can often be resolved in GNSS applications, however, for space interferometry with a wavelength of $1\ \mu\text{m}$ or less, this is normally impossible and not necessary due to the limited accuracy of absolute ranging.

The equivalence of eq. (2.109) and (2.113) implies that a *wrong* USO time does not falsify the phase-tracking result directly, e.g. the digital reference oscillation within the DPLL still follows the input oscillation. However, a *wrong* USO time falsifies the result indirectly due to a changed sampling of the results, thus, one does not assign the correct time to the digital phase samples. For example, the received phase values φ_{DPLL} are taken at specific USO instants of time ($\tau_{\text{USO}} = 0, 1, 2, 3, \dots$), however, one is interested in the corresponding GCRS coordinate time t , because most of the higher-level data analysis is performed with respect to the coordinate time t . One can assume that the USO time $\tau_{\text{USO}}(t)$ is estimated by computing the relativistic effects, i.e. proper time τ of the S/C, and by applying corrections for drifts and low-frequency variations of the USO with respect to GNSS observations. This estimated and best-knowledge USO time $\tau_{\text{USO,est}}(t)$ contains an USO timing jitter noise and an offset with respect to the real USO time, i.e.

$$\tau_{\text{USO,est}}(\tau(t)) = \tau(t) - \delta\tau_{\text{USO}}(\tau(t)) - \delta\tau_{\text{USO,off}} \quad (2.114)$$

This can be approximated as

$$\tau = \tau_{\text{USO,est}}(\tau) + \delta\tau_{\text{USO}}(\tau) + \delta\tau_{\text{USO,off}} \Rightarrow \tau(\tau_{\text{USO,est}}) \approx \tau_{\text{USO,est}} + \delta\tau_{\text{USO}}(\tau_{\text{USO,est}}) + \delta\tau_{\text{USO,off}} \quad (2.115)$$

which allows the phase in eq. (2.113) to be written as

$$\Phi_{\text{in}}(\tau) \approx \Phi_{\text{in}}(\tau_{\text{USO,est}} + \delta\tau_{\text{USO}} + \delta\tau_{\text{USO,off}}) \approx \Phi_{\text{in}}(\tau_{\text{USO,est}}) + \delta\varphi_{\text{PM,USO}} \quad (2.116)$$

where the phase $\Phi_{\text{in}}(\tau_{\text{USO,est}})$ is, for example, the received phase sample from the S/C, which is to our best knowledge taken at the proper time $\tau_{\text{USO,est}}$. However, the errors in the estimate, $\delta\tau_{\text{USO}}$ and $\delta\tau_{\text{USO,off}}$, are the USO timing jitter and the timing offset, respectively (cf. sec. 2.3.4 on USO). Both contributions are combined into the phasemeter USO error $\delta\varphi_{\text{PM,USO}}$, which is given by

$$\delta\varphi_{\text{PM,USO}} \approx \frac{d\Phi_{\text{in}}}{d\tau} \cdot (\delta\tau_{\text{USO}}(\tau(t)) + \delta\tau_{\text{USO,off}}) \quad (2.117)$$

$$= 2\pi f_{\text{beat}}(\tau(t)) \cdot \delta\tau_{\text{USO}}(\tau(t)) + 2\pi f_{\text{beat}}(\tau(t)) \cdot \delta\tau_{\text{USO,off}}. \quad (2.118)$$

This error is not a classical measurement error but arises from the limited accuracy of the sample time. In addition, the error includes assumptions on the accuracy of the final orbital positions from GNSS observations, since these are used to reduce the magnitude of $\delta\tau_{\text{USO}}$.

Another step to be considered for the realistic modeling of the phasemeter output is the decimation. The internal phase φ_{DPLL} from the phase accumulator is decimated in two (or even more) stages to a rate of approx. 10 Hz for transmission to ground. Decimation means here anti-aliasing filtering and downsampling of the data (cf. fig. 2.21). The effect of two typical decimation filters is shown as a Bode plot in the middle and lower panels of fig. 2.24. One can conclude that the magnitude of the ranging data is almost unaffected by decimation filtering, since the ranging data is at frequencies well below to the first notch frequency. More complicated filters as in the GRACE Follow-On LRI can achieve a deviation from unity of less than 10^{-9} in the science measurement band between 0.1 mHz to 0.1 Hz. The phase response of these filters is linear, i.e. they cause only a delay by a time $\Delta\tau_{\text{USO,Dec}}$, which needs to be defined with respect to the USO time, because it is a digital decimation filter.

Thus, it is reasonable to model the effect of the decimation filters by

$$\varphi_{\text{PM}}(\tau_{\text{USO}}) = \mathcal{H}_{\text{Dec2}} [\mathcal{H}_{\text{Dec1}} [\varphi_{\text{DPLL}}(\tau_{\text{USO}})]] \approx \varphi_{\text{DPLL}}(\tau_{\text{USO}}) + \Upsilon_{\text{Dec}}, \quad (2.119)$$

with

$$\Upsilon_{\text{Dec}} \approx \Upsilon_{\text{Dec}}(\tau) = 2\pi f_{\text{beat}}(\tau) \cdot \Delta\tau_{\text{USO,Dec}}, \quad f < 0.1 \text{ Hz}, \quad (2.120)$$

which holds only for Fourier frequencies below 0.1 Hz. For higher frequencies, the decimation filters also change the amplitude of the phase, however, this is of little interest as these frequencies are noise dominated in gravimetric missions.

The effect of the decimation filters is deterministic and can be easily determined from the phasemeter implementation. Hence, one can correct the received phase values φ_{PM} in on-ground post-processing. However, the term Υ_{Dec} is kept in the equations as a reminder of this issue.

With the decimation and the USO induced phase errors, one can finally write the phase observable φ_{PM} in terms of the coordinate time t as

$$\varphi_{\text{PM}}(t) = \Phi_{\text{in}}(\tau(t)) + \delta\varphi_{\text{PM,USO}} + \underbrace{\Upsilon_{\text{DPLL}} + \Upsilon_{\text{Dec}}}_{\Upsilon_{\text{PM}}} + \delta\varphi_{\text{PM}} + \text{const.}, \quad (2.121)$$

The output of the phasemeter $\varphi_{\text{PM}}(t)$ in eq. (2.121) is the input phase Φ_{in} of y_{in} , but falsified by phase errors due to the USO timing uncertainty $\delta\varphi_{\text{PM,USO}}$ and by the phasemeter transfer function Υ_{PM} . The latter is predominantly a delay by a time $\Delta\tau_{\text{USO,PM}}$, which means that the phase Υ_{PM} has a strong linear dependence on the input frequency f_{beat} . The delay time $\Delta\tau_{\text{USO,PM}}$ is driven by the decimation filters (Υ_{Dec}), while the delay from Υ_{DPLL} is negligible, because the DPLL is a fast control loop. In the following, it is assumed that the effect of the transfer function Υ_{PM} is a pure delay. This is non-trivial to achieve in practice, as it requires a highly-developed and mature phasemeter.

Under this assumption one can use an alternative expression for the phasemeter output:

$$\varphi_{\text{PM}}(t) = \Phi_{\text{in}}(\tau(t) - \Delta\tau_{\text{USO,PM}}) + \delta\varphi_{\text{PM,USO}} + \underbrace{\delta\Upsilon_{\text{PM}}}_{\approx 0} + \delta\varphi_{\text{PM}} + \text{const.}, \quad (2.122)$$

with a total delay time $\Delta\tau_{\text{USO,PM}} = \Delta\tau_{\text{USO,DPLL}} + \Delta\tau_{\text{USO,Dec}}$. The effects of the transfer functions are deterministic and can be reversed in ground-based post-processing. This raises the question on the potential accuracy of a post-processing (PP) reduction of the term Υ_{PM} in eq. (2.121), or of the delay time $\Delta\tau_{\text{USO,PM}}$ in eq. (2.122). Here, we simply assume that the delay $\Delta\tau_{\text{USO,PM}}$ can be determined to 25 ns, which corresponds to one clock cycle of a 40 MHz phasemeter, such that one obtains

$$\delta\Upsilon_{\text{PM,PP}} \approx 2\pi f_{\text{beat}}(\tau(t)) \cdot 25 \text{ ns}, \quad f < 0.1 \text{ Hz}, \quad (2.123)$$

for the error of the correction in post-processing.

In the following, the magnitude of the noise terms $\delta\varphi_{\text{PM,USO}}$ and $\delta\varphi_{\text{PM}}$ is addressed. An upper bound for the former, the USO timing errors, can be given by taking into account a maximum fixed frequency $f_{\text{beat,max}}$, which yields

$$\begin{aligned} \text{PSD}[\delta\varphi_{\text{PM,USO}}](f) &\approx (2\pi \cdot f_{\text{beat,max}})^2 \cdot \text{PSD}[\delta\tau_{\text{USO,PP}}](f) \\ &+ (2\pi \cdot f \cdot \delta\tau_{\text{USO,off}})^2 \cdot \text{PSD}[\Phi_{\text{in}}](f), \end{aligned} \quad (2.124)$$

where $\text{PSD}[\delta\tau_{\text{USO,PP}}]$ is a spectral density of USO timing jitter. A maximum frequency of 20 MHz in combination with eq. (2.98) yields an USO jitter induced phase noise of less than 6 mrad/ $\sqrt{\text{Hz}}$. This is equivalent to a ranging noise of less than 1 nm/ $\sqrt{\text{Hz}}$ (cf. the magenta trace with the right axis in fig. 2.14). The second summand, depending on $\text{PSD}[\Phi_{\text{in}}](f)$ and on the timing offset $\delta\tau_{i,\text{USO,off}} \approx 100 \text{ ps}$ (cf. eq. (2.99)), is a delay that has the same effect as the delay uncertainty of the phasemeter transfer function in eq. (2.123), but a different physical origin. The delay uncertainty of the phasemeter transfer function and the delay due to the USO timing offset are indistinguishable in the model for the phasemeter observable

discussed here, and as the assumed uncertainty in the delay of the transfer function is much larger than the USO timing offset, one could omit the USO timing offset, though it is kept in this thesis for the sake of generality and completeness. In addition, it is remarked that the $\text{PSD}[\delta\tau_{\text{USO,PP}}]$ is based on assumptions on the final accuracy of the satellite orbits in the GCRS. In the context of GRACE microwave ranging, the error term $\delta\varphi_{\text{PM,USO}}$ is called the *time-tag correction* error [Kim, 2000].

The sensitivity of the phase readout of a phasemeter $\text{PSD}[\delta\varphi_{\text{PM}}]$, expressed as power spectral density with units of rad^2/Hz , is given by the inverse carrier-to-noise density C/N_0 , i.e.

$$\text{PSD}[\delta\varphi_{\text{PM}}] = \frac{1 \text{ rad}^2}{C/N_0}, \quad (2.125)$$

which also holds for the phase-tracking within GPS receivers [Langley, 1997, eq. 16]. This expression is called *system noise* in the context of GRACE KBR ranging [Kim, 2000].

The carrier-to-noise density C/N_0 is the sinusoidal beatnote rms power, usually expressed in terms of the input photocurrent with units of A_{rms}^2 in the context of laser interferometry, divided by the noise power spectral density of the photocurrent, evaluated at the beatnote frequency and with units of $A_{\text{rms}}^2/\text{Hz}$,

$$C/N_0 = \text{CNR} = \frac{\text{Signal RMS Power}}{\text{Noise PSD}}. \quad (2.126)$$

The C/N_0 , often also abbreviated as CNR, has units of Hz, but is commonly expressed as dB-Hz.

At low C/N_0 , the PLL within the phasemeter may be susceptible to cycle slips and shows an increased readout noise, while even lower C/N_0 may result in loss of the phase lock. Hence, a phasemeter should be able to continuously track the phase of input signals without cycle slips for signals with a C/N_0 higher than, for example,

$$C/N_{0,\text{req}} = 70.0 \text{ dB-Hz} = 10^{70.0/10} \text{ Hz}, \quad (2.127)$$

which is the required minimum during science mode in the GRACE Follow-On LRI project. This requirement corresponds, via eq. (2.125), to a phase readout noise of $0.3 \text{ mrad}/\sqrt{\text{Hz}}$ or a ranging equivalent fluctuation of $53 \text{ pm}/\sqrt{\text{Hz}}$ with 1064 nm radiation. Thus, even if the interferometer is operated at the minimum C/N_0 value, the phase readout noise is not limiting the ranging sensitivity of current and future gravimetric missions, which also means that these interferometers are not shot-noise limited.

A phasemeter can operate at lower C/N_0 , if the PLL bandwidth and hence the integrated noise in the PLL bandwidth is reduced. However, this implies a lower loop gain and a slower control loop, thus, the dynamics of the tracked phase need to be smaller. The author of this thesis currently sees no necessity for investigating such modifications.

An automatic gain control in the photoreceiver chain is recommended in order to avoid saturation and profusion of the dynamic range of the ADCs. The resolution in terms of bit-depth of ADCs and the high sampling rate should be selected such that quantization noise of ADCs is not limiting the phase readout performance (cf. sec. 2.6.9 on the carrier-to-noise density)

Alternative methods for phase retrieval and tracking such as zero-crossing phasemeters have been investigated in the context of the LISA mission [Pollack & Stebbins, 2006], where effectively the integer and fractional number of zero-crossing of the oscillating signal are counted in a time interval. Although the LISA phase readout sensitivity ($\approx 1 \text{ } \mu\text{cycle}/\sqrt{\text{Hz}}$) was demonstrated in a breadboard experiment, some questions regarding low-frequency noise, aliasing and (optical) intensity fluctuations remain open, at least to the knowledge of the author of this thesis. Moreover, a zero-crossing phasemeter completely discards information between the zero-crossings and is not capable of tracking a superposition of several beatnotes.

Furthermore, as stated in [Barke *et al.*, 2014, p. 40], such a zero crossing phasemeter would require a challenging 2.7 GHz reference clock frequency to reach LISA-like sensitivity for a 20 MHz beatnote frequency.

2.3.8 Steering Mirror

A steering mirror in the context of satellite laser interferometry is typically a glass substrate with a highly reflective coating mounted onto a tip and tilt actuator. Figures of merit are the dynamic range, precision and the actuation bandwidth. Typically, one is interested in fine and fast steering mirrors in inter-satellite laser interferometry. The two main available technologies are voice-coil or piezo-electric actuators, while sensing of the orientation can be performed by optical, capacitive or inductive means. A closed-loop operation using a servo-controller and feedback of the sensing signal is recommended, as it reduces overshoots, effects due to mechanical resonances and hysteresis.

Fast steering capability is required for a potential laser link acquisition search in particular, where the laser beam is deflected in a pattern to scan an uncertainty cone. Phase and amplitude fidelity, or at least stability of the transfer function with respect to on-ground calibration over the operational frequency band, is important in order to avoid distortions between the commanded and the actual pattern. The electrical power demand and thermal loads due to dissipation are additional constraints especially in the laser link acquisition phase.

After successful link acquisition, the pointing signal for the steering mirror can be derived with the desired precision with the Differential Wavefront Sensing technique by the interferometer. As such a control loop minimizes the DWS signal, pointing information is not present in the DWS anymore but instead in the commanded steering mirror position or its integrated sensor. Hence, these sensors need to be sufficiently accurate in terms of absolute angles and precise in terms of noise.

More general requirements on robustness against radiation, mechanical and thermal loads as well as against electro-magnetic interference need to be taken into account. Since the steering mirror is a moving part within the S/C, one needs to ensure that induced micro-vibrations are tolerable. This includes assessment of potential side-effects on an accelerometer or test-mass.

The GRACE Follow-On LRI Fine Steering Mirrors, with a mechanical range of approx. ± 5 mrad, are provided by Airbus Defence and Space GmbH. They have flight heritage and utilize voice-coil based actuators with Eddy current sensors from Kaman Aerospace Corp. The servo-controller for closed-loop operation is implemented in two nested stages in the LRI. The servo-controller of the inner loop, which stabilizes the mirror orientation to a particular setpoint with the Kaman sensors, is implemented in the Optical Bench Electronics (OBE). The outer loop, the actual DWS pointing loop, is implemented in the Laser Ranging Processor (phasemeter). A typical steering mirror for laboratory experiments is shown in fig. 2.25.

In general, a steering mirror produces a significant rotation-to-pathlength coupling, often called rotation-to-piston coupling, when used for precise interferometric applications. This holds even for gimbaled setups, where the pivot point is nominally located on the front mirror surface. Three axis actuators with tilt, tip and piston degrees of freedom are available and used, for example, in astronomical telescopes [Alloin & Mariotti, 1994]. However, they require a dedicated approach for measuring the piston (pathlength) change. The rotation-to-pathlength coupling has been extensively studied in the LISA context [Chwalla *et al.*, 2016; Schuster *et al.*, 2016], e.g. for the in-field pointing [Brugger *et al.*, 2014] of the LISA telescopes. The coupling can be minimized by an interferometer design that is to a large extent immune to longitudinal motion of a steering mirror, such as the GRACE Follow-On LRI or the concepts discussed later in this thesis.

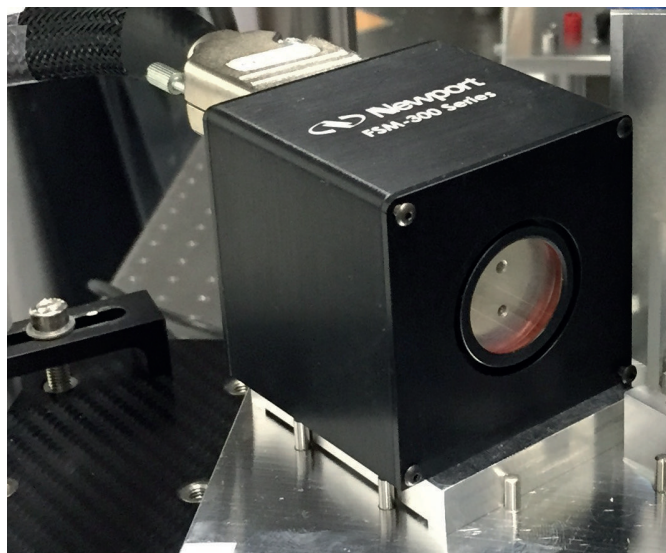


Figure 2.25: A voice-coil based fast steering mirror FSM-300 from Newport Inc. as used in an AEI laboratory.

2.3.9 Frequency-Offset PLL and DWS Loops

In subsequent sections, transponder-based ranging schemes are discussed, as optical interferometers in the LISA and GRACE Follow-On missions utilize this concept. A transponder receives light (or signals) and transmits an amplified version of the light (or signals). Optical transponders for interferometry need to achieve a stable and well-known relation between the optical phase of the received light and the phase of the transmitted light. Moreover, the direction of the transmitted light needs to be controlled in most interferometers, such that the emitted light of the transponder returns to the sender. In principle, both aspects can be fulfilled with an extension of the phasemeter functionality and with additional actuators, as shown in the block diagram in fig. 2.26. Two interfered light fields are impinging on a quadrant photodiode and each segment of the photodiode provides a photocurrent, which is amplified and converted to a voltage by the photoreceiver. The phasemeter tracks the phase of each segment. An average phase of all channels yields the longitudinal phase, i.e. the ranging information, while the differential phase between segments (DWS_v and DWS_h) measures the differential phasefront tilt and tip between both interfered light fields (cf. sec. 2.2.3 on DWS).

In addition to the digital phase-locked loop (DPLL) used to track the phase, extra control loops are present in fig. 2.26. The two loops shown in the figure are called *DWS loops*. They use the DWS signals as the input and derive the error signals from a comparison with set-points $DWS_{h,0}$ and $DWS_{v,0}$. The resulting error signals are used in a controller to derive the actuator signals in two directions, for example, for a steering mirror. The steering mirror changes the direction of the local laser beam, and hence the differential phasefront tilt and tip at the photodiode, until the DWS signals match the desired set-points. Typically, these set-points are zero and the phasefronts are parallel at the photodiode. Parallel phasefronts at the photodiode output port of the recombination beamsplitter also cause parallel phasefronts at the other beamsplitter port, which is labeled *TX light* in fig. 2.26, due to reciprocity of light. Instead of deflecting the local laser light with a steering mirror, one can also actuate the attitude of the S/C, which changes the direction of RX light in a S/C fixed coordinate frame. Different beam pointing schemes will be discussed in detail in sec. 2.7 on optical layouts.

The other control loop shown in fig. 2.26 is called the *frequency-offset PLL*, which uses the average phase of all segments. This longitudinal phase is compared to a phase-ramp stored in the register $PAref$, which is simply the integral of a constant frequency f_{off} . The resulting

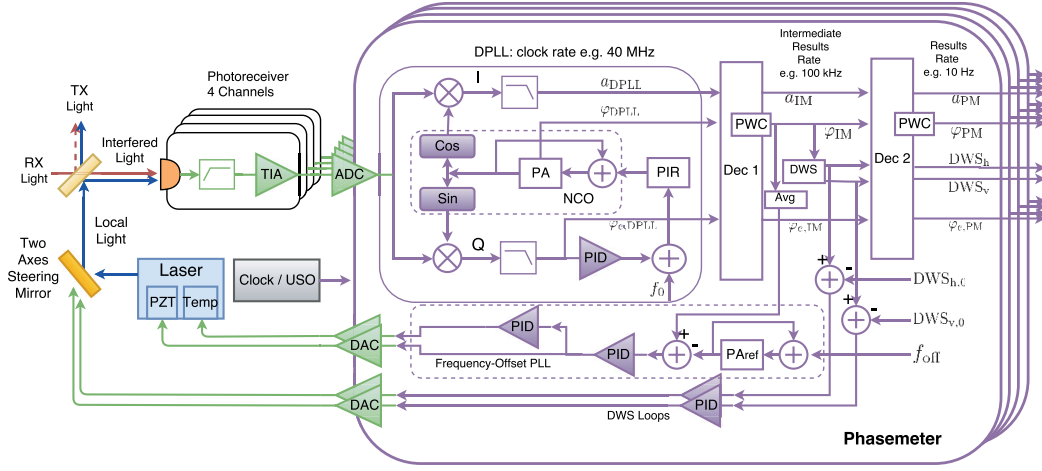


Figure 2.26: A block diagram of a DPLL phasemeter with a frequency-offset phase-locked loop (PLL) and a DWS control loop. The frequency-offset PLL shown here uses a temperature actuator and a piezoelectric transducer (PZT) to control the frequency of the local laser. The DWS control loop utilizes a tip and tilt steering mirror as an actuator. The science data telemetry contains the ranging information as the phase of the channel φ_{PM} , the heterodyne amplitude a_{PM} , which is the I-value, and the phase error signal $\varphi_{e,PM}$, i.e. the Q quadrature value, for each phasemeter channel.

error signal is used in a controller to derive an actuator signal for the frequency actuators of the laser, e.g. typically a piezoelectric-transducer (PZT) and temperature actuators such as Peltier elements for an NPRO laser. Temperature actuators are required, as PZTs have only a limited actuation range. Temperature control is used at low frequencies, while PZTs have a high bandwidth. Both actuators change the frequency and phase of the local laser. As will be derived subsequently, this loop forces the measured longitudinal (average) phase to follow a constant phase ramp with frequency f_{off} , which implies that the phase of the local laser follows the phase of the received light, offset, however, by the frequency f_{off} . Thus, it enables the above mentioned operation as a transponder.

In principle, the frequency-offset PLL can be modeled with a single element photodiode and with reduced complexity, as shown in the block diagram in fig. 2.27. The phasemeter output without feedback, i.e. the loop is opened by setting $H_{PLL,PZT}^c = 0$, can be readily derived from the block diagram in the Laplace domain as

$$\begin{aligned} \varphi_{PM}^{(OL)}(s) = & (\Phi_{RX}^c - \Phi_{LO}^c + \vartheta^c) \cdot H_{PR}^c \cdot H_{ADC}^c \cdot H_{DPLL}^c \cdot H_{Dec1}^c \cdot H_{Dec2}^c \\ & + \delta\varphi_{PM,USO}^c + \delta\varphi_{PM}^c \cdot H_{Dec1}^c \cdot H_{Dec2}^c, \end{aligned} \quad (2.128)$$

where each quantity is a complex-valued function (superscript c) of the complex frequency parameter $s = \sigma + i\omega$. The DPLL transfer function H_{DPLL}^c has been introduced as H_2^c in sec. 2.3.7. The term ϑ accounts for a phase change due to the wavefront overlap over the active area of the photodiode and $\delta\varphi_{PM,USO}^c$ denotes noise due to USO timing jitter. Although physically not completely correct, it is assumed that the quantity propagating in the overall block diagram is a phase, which is sufficient for the purpose of this section. It is remarked that the phases Φ_{RX}^c and Φ_{LO}^c are defined here at the (relativistic) event A , i.e. the position and time, which means the instance of interference and reception at the photodiode. Another event B for the light emission at the laser is marked in the figure, which will be used in a later section. The symbol D_{AB} means a delay from event A to B .

It is advisable to compare the previous Laplace representation to the previously derived time-domain form, which can be obtained from eq. (2.84) and eq. (2.121) as

$$\varphi_{PM}^{(OL)}(\tau) = |\Phi_{RX}(\tau) - \Phi_{LO}(\tau) + \vartheta + \Upsilon_{PR}| + \delta\varphi_{PM,USO} + \Upsilon_{PM} + \delta\varphi_{PM} + \text{const.} \quad (2.129)$$

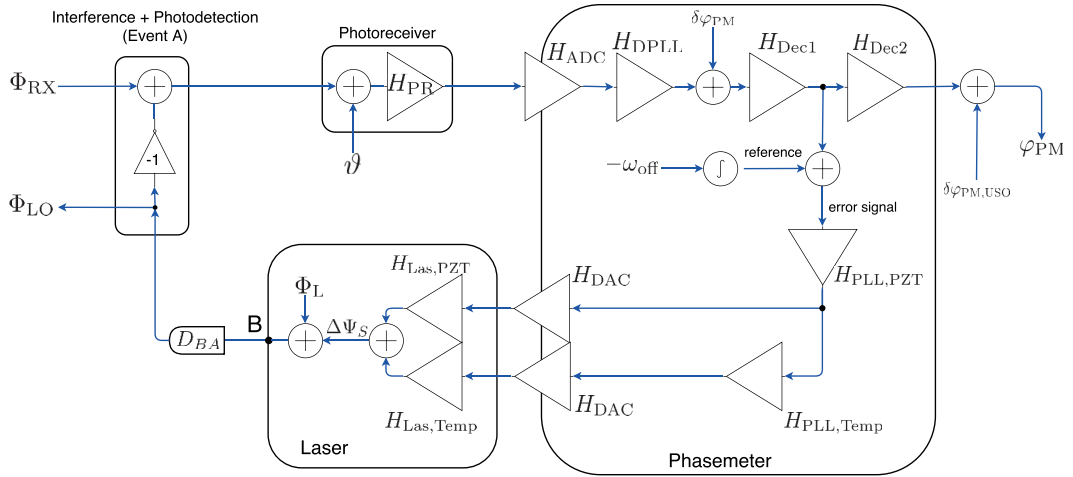


Figure 2.27: A simplified block diagram of the frequency-offset PLL, where the measured phase is used to lock the phase of the local laser with an offset frequency ω_{off} to the incoming light field.

One should notice that the transfer functions H^c from ADC, DPLL, and the two decimation filters correspond in the time-domain to the term Υ_{PM} , which holds only under the assumptions discussed in sec. 2.3.7 on the phasemeter. Otherwise, both representations are equivalent.

In addition, it should be noted that the optical phase of the local oscillator (LO) laser beam can be written as

$$\Phi_{\text{LO}}^c(s) = (\Phi_{\text{L}}^c(s) + \Delta\Psi^c(s)) \cdot D_{\text{BA}}^c(s), \quad (2.130)$$

where Φ_{L}^c is the optical phase of the laser, and includes laser phase fluctuations, e.g. due to laser frequency noise. The phase $\Delta\Psi^c(s)$ due the temperature and PZT actuators vanishes in case of an open loop. However, in the closed-loop case, one can express $\Delta\Psi^c$ as a function of Φ_{RX} and Φ_{LO} by taking into account the loop contributions (in counter-clockwise direction in the block diagram). This yields an implicit equation for the local oscillator phase of the form

$$\Phi_{\text{LO}}^c(s) = (\Phi_{\text{L}}^c(s) + \Delta\Psi^c(s, \Phi_{\text{LO}}^c)) \cdot D_{\text{BA}}^c(s), \quad (2.131)$$

which can be analytically solved for $\Phi_{\text{LO}}^c(s)$. It is anticipated that the open loop gain of the frequency-offset PLL is large, i.e.

$$|H_{\text{PZT+Temp}}^c(s)| = |H_{\text{PZT}}^c(s) + H_{\text{Temp}}^c(s)| \gg 1, \quad (2.132)$$

where the following abbreviations for the individual loop contributors are introduced:

$$H_{\text{PZT}}^c(s) = H_{\text{Las,PZT}}^c(s) \cdot H_{\text{DAC}}^c(s) \cdot H_{\text{PLL,PZT}}^c(s) \quad (2.133)$$

$$H_{\text{Temp}}^c(s) = H_{\text{Las,Temp}}^c(s) \cdot H_{\text{DAC}}^c(s) \cdot H_{\text{PLL,Temp}}^c(s) \cdot H_{\text{PLL,PZT}}^c(s). \quad (2.134)$$

Further useful abbreviations are

$$H_p^c(s) = H_{\text{PR}}^c(s) \cdot H_{\text{ADC}}^c(s) \cdot H_{\text{DPLL}}^c(s) \cdot H_{\text{Dec1}}^c(s) \quad (2.135)$$

$$H_{\text{Loop}}^c(s) = H_{\text{PZT+Temp}}^c(s) \cdot H_p^c(s) \cdot D_{\text{BA}}^c(s) \quad (2.136)$$

$$H_{\text{CLG}}^c(s) = \frac{H_{\text{Loop}}^c(s)}{1 + H_{\text{Loop}}^c(s)}, \quad (2.137)$$

where $H_{\text{Loop}}^c(s)$ is the large total open loop gain, while the closed-loop transfer functions $H_{\text{CLG}}^c(s)$ and $H_p^c(s)$ have a magnitude close to one. With these definitions one can write the phase Φ_{LO} as

$$\Phi_{\text{LO}}^c(s) = H_{\text{CLG}}^c \cdot \left(\Phi_{\text{RX}}^c + \vartheta^c + \frac{-\omega_{\text{off}}/s + \delta\varphi_{\text{PM}}^c \cdot H_{\text{Dec1}}^c}{H_p^c} \right) + \frac{\Phi_L^c \cdot D_{\text{BA}}^c}{1 + H_{\text{Loop}}^c} \quad (2.138)$$

$$\begin{aligned} &\approx \Phi_{\text{RX}}^c + \vartheta^c + \frac{-\omega_{\text{off}}/s + \delta\varphi_{\text{PM}}^c \cdot H_{\text{Dec1}}^c}{H_p^c} \\ &+ \frac{1}{H_{\text{Loop}}^c} \cdot (\Phi_L^c \cdot D_{\text{BA}}^c - \Phi_{\text{RX}}^c - \vartheta^c) \\ &+ \frac{1}{H_{\text{Loop}}^c} \cdot \left(\frac{\omega_{\text{off}}/s - \delta\varphi_{\text{PM}}^c \cdot H_{\text{Dec1}}^c}{H_p^c} \right) \end{aligned} \quad (2.139)$$

where the last approximation holds for a large open loop gain, i.e. $H_{\text{CLG}}^c \approx 1 - 1/H_{\text{Loop}}^c$. All terms except the constant ω_{off} are a function of the complex frequency parameter s . The first line in the approximation represents the infinite gain limit ($|H_{\text{Loop}}^c(s)| \rightarrow \infty$), where the phase of the LO light Φ_{LO} corresponds to the phase of the RX light Φ_{RX} but shifted in frequency by ω_{off} . Furthermore, Φ_{LO} contains a contribution from ϑ , which is a slowly-varying phase term arising from averaging the electric fields over the active area of the photodiode. The second line is proportional to the inverse open loop gain and is a correction for a high but finite open loop gain. This line contains the phase noise of the laser Φ_L^c and the phase of the RX light Φ_{RX}^c , both of which might have a high magnitude. The third line is another correction for a high but finite open loop gain, which can be neglected, because $\delta\varphi_{\text{PM,USO}}$ is a small phase readout noise and the ω_{off}/s term has only a DC component.

It is remarked that the LO phase at the event of emission at the laser B (cf. fig. 2.27) can be readily derived from the previous equation as

$$\Phi_B^c(s) = \frac{\Phi_{\text{LO}}^c(s)}{D_{\text{BA}}^c(s)}, \quad (2.140)$$

which will be used in a later section to derive the phase of the transmitted beam.

In the same manner, it is straightforward to compute the phasemeter output in case of closed-loop operation as

$$\varphi_{\text{PM}}^{(\text{CL})}(s) = H_{\text{CLG}}^c(s) \cdot \frac{H_{\text{Dec2}}^c(s) \cdot \omega_{\text{off}}}{s} + \delta\varphi_{\text{PM,USO}}(s) + \frac{\varphi_{\text{PM}}^{(\text{OL})}(s)}{1 + H_{\text{Loop}}^c(s)}. \quad (2.141)$$

The first summand in eq. (2.141) is the constant phase ramp, the second term accounts for USO timing jitter and the third term is the highly suppressed open loop phase (cf. eq. (2.128)).

Under the assumptions of high loop gain H_{Loop}^c and of a pure constant phase delay in H_{Dec2}^c by $\Delta\tau_{\text{USO,Dec2}}$, one can obtain the following time-domain expression

$$\varphi_{\text{PM}}^{(\text{CL})}(\tau) \approx \omega_{\text{off}} \cdot (\tau_{\text{USO}}(\tau) - \Delta\tau_{\text{USO,Dec2}}) + \delta\varphi_{\text{PM,USO}} + \text{const.} + \mathcal{O}\left(\frac{1}{H_{\text{Loop}}^c}\right), \quad (2.142)$$

which contains in the first summand the constant phase ramp, which is delayed by the delay of the second decimation filter, and the USO timing jitter.

It will be shown in sec. 2.4.4 on the transponder-based ranging concepts that the loop gain is sufficiently high for the approximation and that the $\mathcal{O}(1/H_{\text{Loop}}^c)$ term can be omitted if, for example, the following open loop gain is assumed

$$|H_{\text{Loop}}(f)| \approx |H_{\text{PZT+Temp}}(f)| \approx \frac{1646 \text{ Hz}^3 \cdot \sqrt{360000 + 1.4 \cdot 10^7 \text{ Hz}^{-2} \cdot f^2 + 40 \text{ Hz}^{-4} \cdot f^4}}{f^3}, \quad (2.143)$$

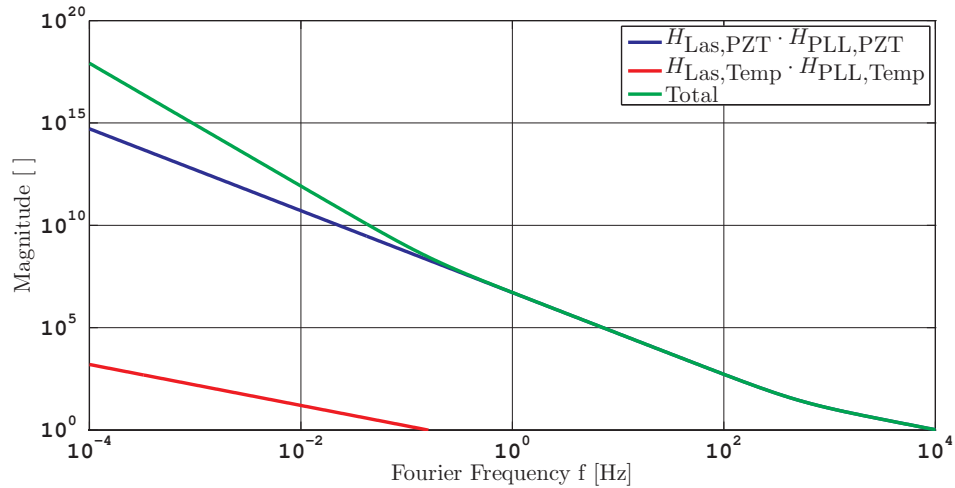


Figure 2.28: A model of the open loop gain of the frequency-offset PLL, as specified by eq. (2.143).

which is depicted by the green trace in fig. 2.28. This total loop gain has been derived from the transfer functions of the PZT and temperature loop, which are the red and dark blue traces in the plot. The open loop gain within the GRACE Follow-On LRI can be considered to be even higher⁵. Thus, the frequency-offset PLL can be designed such that phase variations, as measured by the phasemeter in open loop, are suppressed at 1 mHz by a factor of 10^{15} or more.

The model of the frequency-offset PLL discussed here will be used in section 2.4 on functional concepts to derive a model for the phase observable in transponder-based ranging schemes.

2.3.10 Acquisition Sensor

Laser interferometers have a narrow angular field of view, which is why precise pointing of laser beams along the line-of-sight and with an eventual point-ahead angle is crucial to enable tracking of the light's phase. This is particularly challenging, since mechanical loads from launch and thermo-elastic deformations yield misalignments between the on-board instruments that differ from on-ground calibrations before launch. Furthermore, the real-time estimates of the line-of-sight direction on the satellites depend on the accuracy of the local S/C position, the local S/C attitude as well as on the accurate knowledge of the distant S/C position.

Once the link is closed and the DPLL in the phasemeter is locked, precise DWS signals can be used to minimize residual misalignments and to optimize the signal-to-noise ratio of the interferometric link. Although the GRACE Follow-On LRI is capable of acquiring the link without a dedicated acquisition sensor, such a device can significantly reduce the complexity of the acquisition phase. This sensor is typically called a *focal plane array* (FPA) and can be based on common CMOS (Complementary metal-oxide-semiconductor) or on common CCD (charged coupled device) technology. Its function is the same as a digital camera sensor with a moderate number of pixels.

Light from the distant S/C is focused by an focusing system, e.g. by a simple lens, onto the two-dimensional CMOS/CCD pixel array. A tip or tilt of wavefronts in front of the focusing system due to local S/C or instrument misalignment yields an offset in the spot location from the nominal position at the FPA, similar to the working principle of a Shack-Hartmann sensor, autocollimator or star camera. This measured misalignment can be minimized by

⁵priv. comm. with Kirk McKenzie, JPL/NASA, February 2017

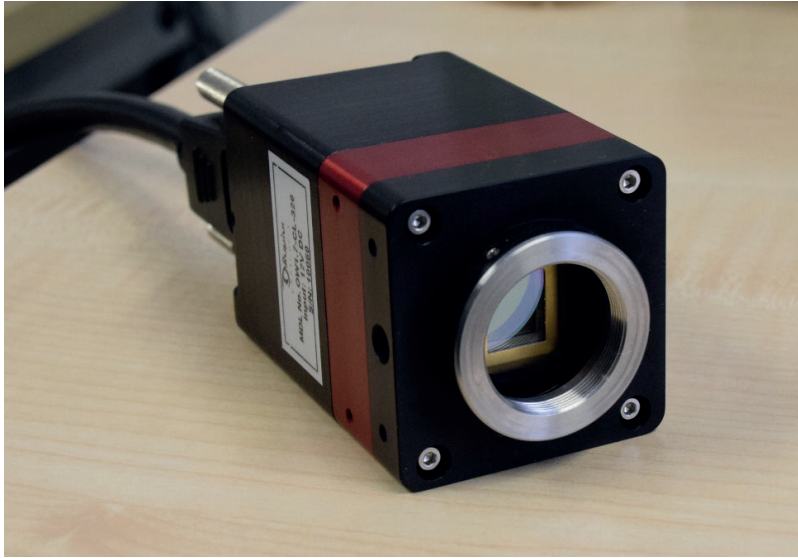


Figure 2.29: The OWL SWIR 320 focal plane array from Raptor Photonics with an InGaAs chip.

S/C actuators or fed forward into laser beam steering actuators.

As pointing information from the acquisition sensor needs to be referred to the optical axis of the interferometer, accommodation of the sensor on the optical bench is recommended to mitigate effects of misalignments.

A potential candidate device is the compact OWL SWIR 320 camera from Raptor Photonics with specifications shown in table 2.4 and a photograph in fig. 2.29. The camera dissipates less than 10 W of electrical power with activated thermo-electric cooling of the chip. Cooling of the chip is recommended in order to reduce the dark current driven by thermal generation of electrons, which is a major noise contributor in low-light cameras. An alternative device is the SU320KTS-1.7RT from Goodrich Corp, which also utilizes InGaAs for photodetection and is also sensitive at 1064 nm for this reason.

A typical CCD dark current density j_d for InGaAs of [Boisvert *et al.*, 2008]

$$j_d = 3.06 \cdot 10^{13} \text{ nA/cm}^2 \cdot e^{-0.73 \text{ eV}/kT}, \quad (2.144)$$

implies that a pixel of the size $30 \mu\text{m} \times 30 \mu\text{m}$ produces on average approx. $n_{\text{dark}} = 10^4$ dark current electrons per second at $T = 253 \text{ K} = -20^\circ \text{ C}$. According to the well-known shot noise formula for Poisson processes, this dark current fluctuates with a variance $\sigma_{n,\text{shot}}^2$ of

$$\sigma_{n,\text{shot}}^2 = n_{\text{dark}} + n_{\text{PE}}, \quad (2.145)$$

where n_{PE} is the number of actual photo-electrons. The dark current electrons accumulate in the pixel bins, even if no light is incident, and produce shot noise.

The overall camera noise (rms) per pixel in terms of electrons consisting of shot-noise, readout noise and ADC quantization noise can be written as [Holst & Lomheim, 2011]

$$\sigma_{n,\text{sys}}^2 \approx \sigma_{n,\text{shot}}^2 + \sigma_{n,\text{readout}}^2 + \sigma_{n,\text{ADC}}^2, \quad (2.146)$$

where other noise sources such as reset-noise, on-chip and off-chip amplifier noise and pattern noise are omitted. Furthermore, it was assumed that a background image and hence the average dark current is subtracted. The readout noise $\sigma_{n,\text{readout}}$ is typically specified by the manufacturers, while the quantization noise $\sigma_{n,\text{ADC}}$ is [Holst & Lomheim, 2011]

$$\sigma_{n,\text{ADC}} = \frac{n_{\text{well}}}{2^b \cdot \sqrt{12}}, \quad (2.147)$$

Sensor Type	InGaAs PIN-Photodiode
Active Pixel	320 × 256
Pixel Pitch	30 μm × 30 μm
Active Area	9.6 mm × 7.68 mm
Quantum Efficiency @ 1064 nm	> 60 %
Noise (RMS)	< 700 e ⁻ (Low Gain), < 150 e ⁻ (High Gain)
Pixel Well Depth	> 3 Me ⁻ (Low Gain), > 120 ke ⁻ (High Gain)
ADC	14 bit
Exposure Time	500 ns to 40 ms
Interface	CameraLink

Table 2.4: Specifications of the OWL SWIR 320 camera from Raptor Photonics.

where b denotes the number of available ADC bits and n_{well} is the full-well capacity in terms of electrons.

Finally, the signal-to-noise ratio (SNR) of a pixel can be defined by

$$\text{SNR} = \frac{n_{\text{PE}}}{\sigma_{\text{n,sys}}}. \quad (2.148)$$

Further aspects regarding the optics and the design of the acquisition sensor, calculation of SNR and the discussion of the expected accuracy of the angular measurement is postponed to sec. 2.6.12 on laser link acquisition.

It is remarked that an acquisition sensor could be operated as a narrow field of view (FoV) star tracker, if the software is extended. This would allow the device to be used continuously and not only for sporadic acquisition events. However, this only makes sense, if the acquisition sensor FoV is large enough to detect several stars for most of the time. While star trackers are typically designed to have a FoV of $>100 \text{ deg}^2$ [Lindh, 2014, p. 4], an acquisition sensor requires a small FoV or a high number of pixels to precisely resolve the direction of the incoming laser wavefront.

The angular density of stars on the celestial sphere up to a certain apparent magnitude is shown in table 2.5. The highest detectable apparent magnitude for a sensor depends on various aspects, e.g. sensor spectral responsivity, intrinsic noise and coatings of the optics that direct incoming light onto the sensor. A narrow bandwidth coating centered at the laser wavelength is certainly beneficial for laser link acquisition as it reduces stray light and can mitigate risks from over-exposure, e.g. induced by blinding due to the Sun or Moon. On the other hand, such a coating reduces the available optical power of the stars for star tracking.

Although using the acquisition sensor as a star tracker is a viable option, it adds significant complexity and constraints on the acquisition sensor subsystem. As such an acquisition sensor has not been designed nor utilized in inter-satellite interferometry, this thesis does not consider a star-tracking mode as a baseline in order to reduce the complexity in this early phase.

Furthermore, the author recommends the revision of the LISA acquisition sensor design, which has a very narrow FoV with a low resolution in terms of pixels [AEI-TN, 2011], regarding the expected average number of stars within the FoV in star-tracking mode.

Apparent Magnitude	N	stars / degree ²
..
6	4958	0.120
7	15256	0.370
8	44772	1.085
9	128421	3.113
10	349741	8.478
..

Table 2.5: The typical star density on the celestial sphere from http://www.hnsky.org/star_count.htm. The total sphere has 41253 degree². N is the total number of Tycho2 or UCAC4 catalogued stars up to the apparent visible magnitude. The table assumes a uniform distribution of stars over the celestial sphere.

2.4 Functional Concepts

In general, inter-satellite ranging interferometry measures distance variations between satellites by exchanging laser light. Before designing the interferometer, some boundary conditions need to be clarified, e.g. the expected maximum and minimum inter-satellite distance and the expected relative velocity along the connection line and transversally. These aspects are determined by the satellite constellation and orbits. A comparative tabular overview for the missions LISA, LISA Pathfinder and GRACE Follow-On is given in table 2.6, which also addresses other interferometric aspects such as the phase readout method. The GRACE Follow-On column is exemplary for a gravimetric in-line satellite formation and most of the numbers are applicable to the e.motion² concept.

For LISA and GRACE-like missions the inter-satellite distance ρ can be approximated by

$$\rho(t) = \rho_0 + \rho_{\text{mod}} \cdot \sin(2\pi t/T_{\text{mod}}) + \delta\rho(t), \quad (2.149)$$

which consists of a constant bias ρ_0 , an approximately sinusoidal modulation with amplitude ρ_{mod} and $\delta\rho(t)$ containing small variations compared to ρ_{mod} . The variations $\delta\rho(t)$ contain most of the scientific information, e.g. on the fine gravity field structure in case of e.motion² and GRACE or on gravitational waves in case of LISA. The modulation period is usually given by the orbital period, whereby a second strong modulation at twice the period may be present due to eccentric orbits or orbit mismatch between the satellites. Thus, the spectrum of $\rho(t)$ contains a few dominating tones, which might be even not in the frequency band of the science data, and a quasi-continuous distribution of signal power over frequencies as the interesting science data ($\delta\rho(t)$).

The quantity $\rho(t)$ is the instantaneous range between the gravitational reference points (cf. sec. 1.3.6 on GRP) on each S/C, which can be considered here as the center of mass of each S/C, i.e.

$$\rho(t) = \rho_{\text{inst}}(t) = |\vec{r}_1(t) - \vec{r}_2(t)|. \quad (2.150)$$

This equation and the constituents are defined in the GCRS, which is a quasi-inertial non-rotating system.

As already discussed in the first part of this thesis, future gravimetric missions require inter-satellite range measurements over a distance of 100 km..200 km with a sensitivity between $25 \text{ nm}/\sqrt{\text{Hz}}$ and $50 \text{ nm}/\sqrt{\text{Hz}}$ at a Fourier frequency of 0.1 Hz. The science measurement band ranges from approx. 0.18 mHz to 0.1 Hz. The maximum range rate, i.e. the relative velocity along the line-of-sight, is below 5 m/s. With clarified boundary conditions, different functional concepts for inter-satellite interferometry can be assessed. In the next sections, the most common concepts, namely one-way ranging, dual one-way ranging, transponder and retro-reflector based ranging, are introduced and their respective sensitivity limits and constraints are discussed.

At first, the general one-way ranging phase observable is derived, which can be written in terms of the instantaneous range $\rho_{\text{inst}}(t)$. However, the phase is only to first order proportional to the range, and many corrections and errors are present due to special and general relativistic effects, due to errors arising from the specifics of the optical interferometer design (sec. 2.6) and due to other effects such as clock errors and laser frequency noise.

2.4.1 Derivation of One-Way Ranging

The simplest form of a displacement measurement can be realized by measuring radio-waves or light, both electro-magnetic waves, emitted by a laser aboard a S/C. If emitter and receiver are in relative motion, the apparent frequency of the wave at the receiver is shifted due to the Doppler effect (cf. eq. (2.26) in sec. 2.2). By integrating the Doppler shift frequency in a phase tracking loop, one obtains a phase (cf. eq. (2.121)), which is to first order proportional to the biased distance in ranging interferometry (cf. eq. (2.22)). A sketch of a one-way ranging

	LISA	LISA Pathfinder	GRACE F.O.
# of Spacecraft	3	1	2
Avg. ρ	≈ 2.5 Mkm	38 cm	200 km
Max. $\dot{\rho}$	5 m/s	≈ 0	5 m/s
Max. Doppler Shift	5 MHz	≈ 0	5 MHz
Max. ρ_{mod}	10000 km	≈ 0	4 km
Modulation Period	1 year		93 min
Max. $\ddot{\rho}$	1 $\mu\text{m}/\text{s}^2$	≈ 0	6 mm/s^2
Max. Doppler Rate	1 Hz/s	≈ 0	6 kHz/s
Max. $v_{12,\perp}$	200 m/s	≈ 0	250 m/s
Point Ahead Angle	1.4 μrad	≈ 0	1.6 μrad
Beam Div. θ_{TX}	≈ 2 μrad	n.a.	≈ 140 μrad
Environm. Condition	Deep-Space	Deep-Space, LP	LEO
Concept	Transponder	Several MZ IFOs	Transponder
Readout Scheme	Heterodyne	Heterodyne	Heterodyne
Phase Retrieval	DPLL	SBDFT	DPLL
Beatnote Frequency	4..20 MHz	1.0 kHz	4...20 MHz
Laser Wavelength	1064 nm	1064 nm	1064 nm
Science Meas. Band	0.1 mHz..0.1 Hz	1 mHz..0.1 Hz	0.1 mHz..0.1 Hz
Ranging Sensitivity \ddagger	≈ 10 pm/ $\sqrt{\text{Hz}}$ $\hat{=} 9$ $\mu\text{cycl.}/\sqrt{\text{Hz}}$	$\lesssim 10$ pm/ $\sqrt{\text{Hz}}$ $\hat{=} 9$ $\mu\text{cycl.}/\sqrt{\text{Hz}}$	80 nm/ $\sqrt{\text{Hz}}$ $\hat{=} 75$ mcycl./ $\sqrt{\text{Hz}}$
On-Orbit Ranging Sensitiv.		35 fm/ $\sqrt{\text{Hz}}$	
LFN Reduction	Transponder TDI	\ddagger Equal-Arm IFO	Transponder
Time Reference	USO per S/C + CTT	USO Single Common	USO per S/C GNSS avail.
Ranging Ref. Point(s)	Test-Mass	Test-Mass	Virtual at CoM
Absol. Laser Ranging	Yes, ≈ 1 m accuracy	Not Req.	Not Req. (GNSS avail.)
(Optical) Data Transm.	Yes	Not Req.	Not Req.

Table 2.6: Comparison of three missions utilizing laser interferometric distance measurements. The relative velocity along the line of sight is denoted as $\dot{\rho}$, while $\ddot{\rho}$ is the corresponding acceleration. The transversal relative velocity between the satellites $v_{12,\perp}$ is measured perpendicular to the line of sight. Further abbreviations: LFN: Laser Frequency Noise, LP: Lagrangian Point; θ_{TX} : Gaussian beam divergence of TX beam; CTT: Clock Tone Transfer; \ddagger : Pre-launch requirement; MZ: Mach Zehnder; \ddagger : Measure and subtract

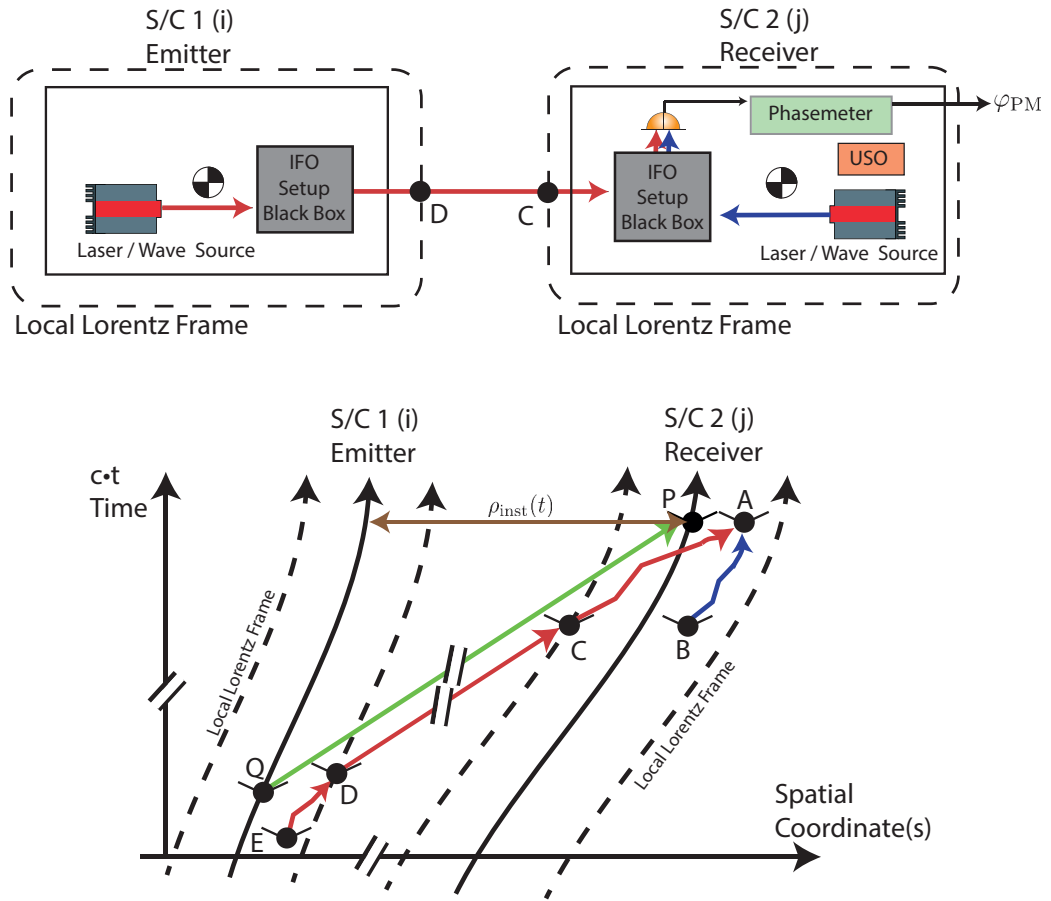


Figure 2.30: (**Upper Part:**) Simplified one-way ranging scheme by means of (optical) interferometry. (**Lower Part:**) Minkowski diagram of the light path in a one-way ranging scheme. At each event A, B, C, \dots the future light cone was indicated with two lines, since light can reach only these regions. Within the interferometer setup, i.e. in the local Lorentz frame (LLF) of the S/C, the light is deflected and hence not a straight line. Inter S/C propagation in free space between events D and C is shown as straight line. The instantaneous range ρ_{inst} and the photon path of an ideal range measurement between both CoM (green arrow) are shown as well.

scheme by means of optical interferometry is shown in the upper panel of fig. 2.30, whereby it is also applicable in similar form to electro-magnetic waves, e.g. microwaves.

The specifics of the optical implementation of the interferometer are not considered in this section, i.e. the interferometer is simply a black box with input and output laser beams. With eq. (2.121) one can write the observed phase φ_{PM} of the phasemeter as

$$\varphi_{PM|j}(t_A) = |\Phi_{in,j}(\tau_j(t_A))| + \delta\varphi_{PM,USO,j} + \delta\varphi_{PM,j} + \Upsilon_{PM,j} + \text{const.} \quad (2.151)$$

where t_A is the GCRS coordinate time of the measured phase sample, as provided by the phasemeter. The emitter satellite is labeled with subscript i , while the receiver is S/C j as shown in fig. 2.30. It is reminded that the phase $\varphi_{PM|j}$ is actually recorded in the local Lorentz frame (LLF) of the receiver S/C j . The time associated with a particular phase value is given in the time frame of the on-board USO, however, for the formula, the time has been converted to the GCRS coordinate time. Errors due to the conversion are covered by $\delta\varphi_{PM,USO,j}$. The digital phase sample at time t_A from the phasemeter is equal to the phase $\Phi_{in}(\tau(t_A))$, which is the phase of the input signal to the phasemeter up to the effect of the transfer function $\Upsilon_{PM,j}$ and the errors $\delta\varphi_{PM,USO,j} + \delta\varphi_{PM,j}$.

The phase of the phasemeter input, which is the photoreceiver output, can be written as

(cf. eq. (2.84))

$$|\Phi_{\text{in},j}(\tau_j(t_A))| = |\Phi_{i|j}(\tau_j(t_A)) - \Phi_{j|j}(\tau_j(t_A)) + \vartheta_j + \Upsilon_{\text{PR},j}| \quad (2.152)$$

$$= \pm (\Phi_{i|j}(\tau_j(t_A)) - \Phi_{j|j}(\tau_j(t_A))) \pm \vartheta_j + \Upsilon_{\text{PR},j} + \text{const.} \quad (2.153)$$

where $\Phi_{i|j}$ and $\Phi_{j|j}$ are the absolute optical phase values of the light from S/C i and S/C j , respectively, expressed in the local Lorentz frame of S/C j and with respect to the proper time τ_j . These are the phase values of the light fields at the center of the active area of the photodiode. The phase term ϑ_j is obtained from the overlap integral of wavefronts over the active area and is expected to change only very slowly. It accounts for the effect of spatially averaging the phase of the light fields over a macroscopic active area. The phase change due to the transfer function of the photoreceiver is denoted with $\Upsilon_{\text{PR},j}$.

The absolute value (magnitude) was removed in the second line (eq. (2.153)), which eases the equations later on. Recall that the sign of the phase of a scalar signal such as Φ_{in} is ill-defined, because only the cosine of the phase is physically accessible and the cosine function is an even function. The measured phase of the phasemeter φ_{PM} starts at zero, when the instrument is turned on, and it increase monotonically with time. However, the input to the phasemeter Φ_{in} is defined here analytically as a phase difference and can be positive or negative. One can replace the magnitude by the sign \pm without loss of generality, if the upper sign is selected for $\Phi_{i|j} > \Phi_{j|j}$, which practically means that the frequency of the received light is higher than the frequency of the local laser light of the receiver. Such a frequency ordering is well defined and can not swap during normal operation of the phasemeter, because the phasemeter is not capable of handling zero crossings of the beatnote frequency, i.e. of the frequency difference (cf. sec. 2.3.7 on phasemeter).

The phasemeter output φ_{PM} can be described in good approximation as the difference of the phase of the two optical fields impinging onto the photodiode. The event of impinging light fields in the GCRS is labeled in the following as $\mathcal{T}_A|_{\text{GCRS}} = (c_0 \cdot t_A, \vec{r}_{j,\text{PD}}(t_A))^{\text{T}}$, which is a point in the four dimensional space-time. The position of the photodiode in the GCRS is denoted with $\vec{r}_{j,\text{PD}}$. Events offer the advantage that they fix the time and position and they can be converted unambiguously with transformations between different coordinate systems. Thus, one can use a simplified notation \mathcal{T}_A and express arguments of functions with a shorter notation, e.g. $f(\mathcal{T}_A) = f(t_A, \vec{r}_A)$.

The paths or world lines of the light fields are shown in the Minkowski diagram in the lower panel of fig. 2.30 as red and blue lines. Several events (A, B, C, \dots) are marked: the reception of light and measurement of phase (A), light emission on the receiver and emitter (B and E) and the free space propagation between C and D .

The phase of the light fields at \mathcal{T}_A had to propagate through space-time to reach that event, i.e. one can think of photons carrying or forming the phase information. The light field of the local laser on the receiver S/C has an electric-field vector $\vec{E}_j^c \propto e^{i\Phi_{j|j}}$ and it's phase can be described with the help of eq. (2.72) at the event of emission \mathcal{T}_B by

$$\Phi_{j|j}(\mathcal{T}_B) = 2\pi\bar{\nu}_{j|j} \cdot \tau_j(t_B) + \Phi_{\text{LFN},j}(\tau_j(t_B)) + \Delta\Psi_{B,j}, \quad (2.154)$$

where $\bar{\nu}_{j|j}$ is the true and mean laser frequency with units of Hertz of the laser on S/C j as measured in the S/C j LLF, i.e. in the rest frame. One can reduce the number of symbols in subsequent equations by using the corresponding angular frequency $\bar{\omega} = 2\pi\bar{\nu}$. The laser frequency fluctuations are expressed in terms of a phase noise $\Phi_{\text{LFN},j}$, while all other phase contributions to the laser light are covered by $\Delta\Psi_{B,j}$.

However, since the photon path denotes the path of a constant phase⁶, the phase at the event of emission and the phase at the event of reception are equal, i.e.

$$\Phi_{j|j}(\tau_j(t_A)) = \Phi_{j|j}(\mathcal{T}_A) = \Phi_{j|j}(\tau_j(t_B)) = \Phi_{j|j}(\mathcal{T}_B) \quad (2.155)$$

$$= \bar{\omega}_{j|j} \cdot \tau_j(t_A - \Delta t_{BA}) + \Phi_{\text{LFN},j}(\tau_j(t_A - \Delta t_{BA})) + \Delta\Psi_{B,j} \quad (2.156)$$

⁶In [Misner *et al.*, 1973] it is shown that the phasefront of an electro-magnetic wave follows a null-geodesic, i.e. it is a photon path.

where $\Delta t_{BA} = t_A - t_B$ was used to denote the time difference in the GCRS system between both events. Some second order phase effects arising from the evolution of non-trivial wave-fronts (keyword Gouy phase) are omitted here, i.e. a plane wave approximation is used. Such effects are not of relevance for this section and are introduced when more realistic light beam models are considered.

With eq. (2.156) one obtains the light's phase from the local receiver laser at the photodiode of the receiver S/C. This worked out easily, because all the quantities are defined in the same local Lorentz frame. However, for the phase of the light from the emitter, one needs to transform the optical light phase from the LLF of S/C i into the LLF of S/C j . For this, one can use the fact that the light's phase is Lorentz invariant, i.e. it does not change upon transformations. This can be easily shown for plane and spherical waves, because the phase can be written as the invariant product of the four-wave vector and the four-position [Shiozawa, 2013, sec. 2.5]. However, it also holds for more complex waves. The value of the phase is simply the number of passed wave crests, and hence, independent of the frame. Furthermore, the instantaneous real electric and magnetic field vectors vanish for particular values of the phase, which suggests that they are zero in all frames.

It is interesting to note that the electric field vector \vec{E} , the magnetic field vector \vec{H} and the Poynting vector \vec{S} are not Lorentz invariant. Thus, the polarization vector changes upon transformation from one to the other S/C ⁷.

The Lorentz invariance of the phase states that the phase in the coordinate system of the emitter S/C i is equal to the phase in the coordinate system of S/C j at the same event, e.g. for \mathcal{T}_A :

$$\Phi_{i|j}(\mathcal{T}_A) = \Phi_{i|i}(\mathcal{T}_A) \quad (2.157)$$

The right-hand-side can be expressed in the same way as eq. (2.156) with Δt_{EA} denoting the propagation time of the phase from the event of emission \mathcal{T}_E to the event of reception \mathcal{T}_A , while the left-hand-side can be expressed in the most general form as an integral over a time-variable instantaneous observed angular frequency $\omega_{i|j}(\tau_j)$. Hence, one can re-write the previous equation as

$$\Phi_{i|j}(\tau_j(t_A)) = \int^{\tau_j(t_A)} \omega_{i|j}(\tau_j) d\tau_j + \text{const.} \quad (2.158)$$

$$= \bar{\omega}_{i|i} \cdot \tau_i(t_A - \Delta t_{EA}) + \Phi_{\text{LFN},i}(\tau_i(t_A - \Delta t_{EA})) + \Delta \Psi_{E,i}, \quad (2.159)$$

where the integral start time was omitted and accounted for by an arbitrary constant. This equation can be considered as a definition for the instantaneous observed angular frequency $\omega_{i|j}(\tau_j)$. The arbitrary constant arises from the lacking (relativistic) synchronizations of the proper times τ_i and τ_j and is not of importance here.

The reception event \mathcal{T}_A and the event time t_A were used for the derivation, however, it is obvious that for a continuous measurement one can set $t = t_A$. Now it is easy to determine the apparent frequency of the received light for the receiver S/C $\nu_{i|j}(\tau_j(t))$ as

$$\frac{1}{2\pi} \cdot \frac{d\Phi_{i|j}(\tau_j(t))}{d\tau_j} = \bar{\nu}_{i|i} \frac{d\tau_i(t - \Delta t_{EA})}{d\tau_j} + \frac{1}{2\pi} \cdot \frac{d\Phi_{\text{LFN},i}(\tau_i(t - \Delta t_{EA}))}{d\tau_j} \quad (2.160)$$

$$= \left(\bar{\nu}_{i|i} \frac{d\tau_i(t - \Delta t_{EA})}{dt} + \frac{1}{2\pi} \cdot \frac{d\Phi_{\text{LFN},i}(\tau_i(t - \Delta t_{EA}))}{dt} \right) \cdot \frac{dt}{d\tau_j} \quad (2.161)$$

$$= \left(\bar{\nu}_{i|i} \frac{d\tau_i}{dt} + \frac{1}{2\pi} \cdot \frac{d\Phi_{\text{LFN},i}}{d\tau_i} \cdot \frac{d\tau_i}{dt} \right) \cdot \left(1 - \frac{d\Delta t_{EA}}{dt} \right) \cdot \frac{dt}{d\tau_j} \quad (2.162)$$

$$= \left(\bar{\nu}_{i|i} + \frac{1}{2\pi} \cdot \frac{d\Phi_{\text{LFN},i}}{d\tau_i} \Big|_{t_E} \right) \cdot \left(1 - \frac{d\Delta t_{EA}}{dt} \Big|_t \right) \cdot \frac{d\tau_i}{dt} \Big|_{t_E} \cdot \left(\frac{d\tau_j}{dt} \Big|_t \right)^{-1}, \quad (2.163)$$

⁷A Lorentz boost mixes the electric and magnetic field vectors. However, since both vectors are in-phase for linearly polarized light, the phase of the oscillation does not change.

where the first bracket in the last line shows the instantaneous laser frequency at the time of emission (t_E) in the LLF of the emitter S/C. The second bracket is the classical Doppler shift, which becomes obvious due to $\Delta t_{EA} = \Delta t_{EA}(t) \approx \rho_{\text{inst}}(t)/c_0$ with the instantaneous S/C distance $\rho_{\text{inst}}(t)$ in the GCRS. The last two terms are present in a relativistic Doppler theory and give rise to effects such as the so-called transverse Doppler effect, where a frequency change is observed only from transverse motion due to time dilation [Rindler, 2012, sec. 3.2]. Eq. (2.163) can be readily employed in simulations, since all the quantities can be determined.

Finally, by using eqs. (2.151), (2.153), (2.156) and (2.159), one can formulate a single expression for the phasemeter observation of the receiver S/C as:

$$\begin{aligned} \varphi_{\text{PM}|j}(t) &= \pm \bar{\omega}_{i|i} \cdot \tau_i(t - \Delta t_{EA}) \pm \Phi_{\text{LFN},i}(\tau_i(t - \Delta t_{EA})) \pm \Delta \Psi_{E,i} \\ &\mp \bar{\omega}_{j|j} \cdot \tau_j(t - \Delta t_{BA}) \mp \Phi_{\text{LFN},j}(\tau_j(t - \Delta t_{BA})) \mp \Delta \Psi_{B,j} \\ &\pm \vartheta_j + \Upsilon_{\text{PR},j} + \delta\varphi_{\text{PM,USO},j} + \delta\varphi_{\text{PM},j} + \Upsilon_{\text{PM},j} + \text{const.} \end{aligned} \quad (2.164)$$

The first line contains the phase of the light from the emitting S/C, the second line contains the phase of the local laser light, and the third line contains the phase contributions due to the wavefront overlap ϑ , the photoreceiver Υ_{PR} , the USO timing error $\delta\varphi_{\text{PM,USO}}$, the phasemeter delay Υ_{PM} , and the phase readout noise $\delta\varphi_{\text{PM}}$. The first two lines were expressed in terms of the propagation time between the photon emission and reception event.

Eq. (2.164) is a generic one-way or single path ranging observation, which is expressed in terms of photon time of flight Δt between events. It accounts for relativistic effects, which manifest in the appearance of the proper time τ and as changes in Δt . In the following, some algebraic manipulations are performed to partly separate the relativistic from non-relativistic effects. For this reason one can define a *delta proper time* $\delta\tau$ according to

$$\delta\tau(t) = t - \tau(t), \quad (2.165)$$

which increases only slowly with a rate of $d\tau/dt = \delta\dot{\tau}(t) \approx 10^{-9}$ s/s (cf. eq.(2.14)). A spectral density plot of τ , which is also applicable to $\delta\tau$, is shown as the red trace in fig. 2.14. It is remarked that $\delta\tau$ has practically no signal at frequencies higher than 1 Hz. Thus, with the definition, one can approximate the delayed proper time as

$$\tau(t - \Delta t) = t - \Delta t - \delta\tau(t - \Delta t) \quad (2.166)$$

$$\approx t - \Delta t - \delta\tau(t) + \Delta t \cdot \delta\dot{\tau}(t), \quad (2.167)$$

which is justified and accurate, because the delay due to the photon time of flight Δt is always much smaller than 1 second in gravimetric missions.

The laser phase noise can be approximated rigorously as well:

$$\begin{aligned} \Phi_{\text{LFN},i}(\tau_i(t - \Delta t)) &= \Phi_{\text{LFN},i}(t - \Delta t - \underbrace{\delta\tau(t) + \Delta t \cdot \delta\dot{\tau}(t)}_{\approx 0}) \\ &\approx \Phi_{\text{LFN},i}(t) - \delta\omega_{\text{LFN}}(t) \cdot \Delta t, \end{aligned} \quad (2.168)$$

because it decays towards high frequencies and the delay Δt is small. The quantity $\delta\omega_{\text{LFN}} = 2\pi\delta\nu_{\text{LFN}}$ is the angular laser frequency noise. Furthermore, it is noticed that Φ_{LFN} is a stationary stochastic variable with zero mean, which means that spectral properties are invariant under time-shifts.

Moreover, a second definition concerning the optical angular frequencies $\bar{\omega}_{i|i}$ and $\bar{\omega}_{j|j}$ is introduced:

$$\bar{\omega}_{i|i} = \tilde{\omega} \pm \frac{\Delta\tilde{\omega}}{2} \quad (2.169)$$

$$\bar{\omega}_{j|j} = \tilde{\omega} \mp \frac{\Delta\tilde{\omega}}{2}, \quad (2.170)$$

where $\tilde{\omega}$ denotes the mean frequency and $\Delta\tilde{\omega} = |\tilde{\omega}_{|i} - \tilde{\omega}_{|j}|$ is the positive difference frequency, which is the positive angular beatnote frequency. If these new quantities are used in the phasemeter observable, it is helpful to use the assumption that the Doppler shift from $\tilde{\omega}_{|i}$ to $\tilde{\omega}_{|j}$ is smaller than the difference frequency $\Delta\tilde{\omega}$, which makes the statements $\tilde{\omega}_{|i} > \tilde{\omega}_{|j}$ ($= \Phi_{|i} > \Phi_{|j}$) and $\tilde{\omega}_{|i} > \tilde{\omega}_{|j}$ equivalent. Initially, the upper sign of \pm and \mp was used for $\tilde{\omega}_{|i} > \tilde{\omega}_{|j}$, but with the new assumption it also holds for $\tilde{\omega}_{|i} > \tilde{\omega}_{|j}$, which is much easier to handle for practical calculations.

In summary, one can approximate the carrier phase terms in $\varphi_{\text{PM}|j}$ as

$$\begin{aligned}
 & \pm \tilde{\omega}_{|i} \cdot \tau_i(t - \Delta t_{EA}) \mp \tilde{\omega}_{|j} \cdot \tau_j(t - \Delta t_{BA}) \\
 & \approx \pm \tilde{\omega} t \mp \tilde{\omega} \Delta t_{EA} + \frac{\Delta\tilde{\omega}}{2} t - \frac{\Delta\tilde{\omega}}{2} \Delta t_{EA} \mp \tilde{\omega} \delta\tau_i(t - \Delta t_{EA}) - \frac{\Delta\tilde{\omega}}{2} \delta\tau_i(t - \Delta t_{EA}) \\
 & \quad \mp \tilde{\omega} t \pm \tilde{\omega} \Delta t_{BA} + \frac{\Delta\tilde{\omega}}{2} t - \frac{\Delta\tilde{\omega}}{2} \Delta t_{BA} \pm \tilde{\omega} \delta\tau_j(t - \Delta t_{BA}) - \frac{\Delta\tilde{\omega}}{2} \delta\tau_j(t - \Delta t_{BA}) \\
 & = +\Delta\tilde{\omega} \cdot t \mp \tilde{\omega} \cdot \Delta t_{EB} - \frac{\Delta\tilde{\omega}}{2} \cdot (\Delta t_{EA} + \Delta t_{BA}) \\
 & \quad \mp \tilde{\omega} \cdot (\delta\tau_i(t - \Delta t_{EA}) - \delta\tau_j(t - \Delta t_{BA})) - \frac{\Delta\tilde{\omega}}{2} (\delta\tau_i(t - \Delta t_{EA}) + \delta\tau_j(t - \Delta t_{BA})) \\
 & = +\Delta\tilde{\omega} \cdot t \mp \tilde{\omega} \cdot \Delta t_{EB} - \frac{\Delta\tilde{\omega}}{2} \cdot (\Delta t_{EA} + \Delta t_{BA}) \\
 & \quad \mp \tilde{\omega} \cdot (\delta\tau_i - \delta\dot{\tau}_i \Delta t_{EA} - \delta\tau_j + \delta\dot{\tau}_j \Delta t_{BA}) - \frac{\Delta\tilde{\omega}}{2} \cdot (\delta\tau_i - \delta\dot{\tau}_i \Delta t_{EA} + \delta\tau_j - \delta\dot{\tau}_j \Delta t_{BA}),
 \end{aligned} \tag{2.171}$$

where the new propagation time $\Delta t_{EB} = \Delta t_{EA} - \Delta t_{BA}$ appeared. It is the time difference between the photon emission on the emitting S/C and photon emission of the local laser on the receiving S/C in the GCRS system (cf. fig. 2.30). The laser phase noise terms can be written as

$$\begin{aligned}
 & \pm \Phi_{\text{LFN},i}(\tau_i(t - \Delta t_{EA})) \mp \Phi_{\text{LFN},j}(\tau_j(t - \Delta t_{BA})) \\
 & \approx \pm \Phi_{\text{LFN},i}(t) \mp \delta\omega_{\text{LFN},i} \cdot \Delta t_{EA} \mp \Phi_{\text{LFN},j}(t) \pm \delta\omega_{\text{LFN},j} \cdot \Delta t_{BA},
 \end{aligned} \tag{2.172}$$

which is a sufficient approximation for the purpose of this section.

Combining the previous approximations into $\varphi_{\text{PM}|j}$ yields

$$\begin{aligned}
 \varphi_{\text{PM}|j}(t) & = +\Delta\tilde{\omega} \cdot t \mp \tilde{\omega} \cdot \Delta t_{EB} \pm \Phi_{\text{LFN},i}(t) \mp \Phi_{\text{LFN},j}(t) \\
 & \quad \mp \delta\omega_{\text{LFN},i} \cdot \Delta t_{EA} \pm \delta\omega_{\text{LFN},j} \cdot \Delta t_{BA} \\
 & \quad \mp \tilde{\omega} \cdot (\delta\tau_i - \delta\tau_j) \\
 & \quad \mp \tilde{\omega} \cdot (+\delta\dot{\tau}_j \cdot \Delta t_{BA} - \delta\dot{\tau}_i \cdot \Delta t_{EA}) \\
 & \quad - \frac{\Delta\tilde{\omega}}{2} \cdot (\Delta t_{EA} + \Delta t_{BA}) - \frac{\Delta\tilde{\omega}}{2} \cdot (\delta\tau_i - \delta\dot{\tau}_i \Delta t_{EA} + \delta\tau_j - \delta\dot{\tau}_j \Delta t_{BA}) \\
 & \quad \pm \Delta\Psi_{E,i} \mp \Delta\Psi_{B,j} \pm \vartheta_j + \Upsilon_{\text{PR},j} + \delta\varphi_{\text{PM,USO},j} + \delta\varphi_{\text{PM},j} + \Upsilon_{\text{PM},j} \\
 & \quad + \text{const.},
 \end{aligned} \tag{2.173}$$

with upper signs applying for the frequency ordering $\tilde{\omega}_{|i} > \tilde{\omega}_{|j}$. The first term in the first line contains a monotonically increasing phase ramp, given by the beatnote frequency $\Delta\tilde{\omega}$. The second term is typically the ranging observation, which will be addressed subsequently. The next two terms indicate the laser phase noise Φ_{LFN} of both S/C. The second line contains further fluctuations of the laser, which are expressed as laser frequency noise $\delta\omega_{\text{LFN}}$. The third line includes the effect of time dilation and is responsible for a transverse Doppler effect. The fourth line describes further relativistic corrections, which are multiplied with the mean optical frequency $\tilde{\omega}$. The fifth line has terms proportional to the beatnote frequency $\Delta\tilde{\omega}$, while the terms on the last lines have been addressed previously and contain effects due to

wavefront overlap ϑ_j , photoreceiver transfer function $\Upsilon_{PR,j}$, USO timing error $\delta\varphi_{PM,USO,j}$, interferometric phase readout noise $\delta\varphi_{PM,j}$ and phasemeter transfer function $\Upsilon_{PM,j}$. The constant bias indicates that with laser interferometry one can not determine the absolute inter-satellite distance but only a biased range.

So far, the observation equation for $\varphi_{PM|j}(t)$ is independent of the actual desired measurement, i.e. the instantaneous range $\rho_{inst}(t)$ between both S/C CoM in the GCRS. It is important to state the coordinate system, because the instantaneous range, and distance in general, is a quantity depending on the coordinate system due to relativistic effects such as length contraction. The ranging information in a phase observation shows typically up as a product of an optical frequency $\tilde{\omega}$ times a propagation time Δt , here, it is the second term in the first line in eq. (2.173). The time difference Δt_{EB} is the photon time of flight from emission on the sender S/C to the photodiode at the receiver S/C minus the time of flight from the local laser to the photodiode on the receiver craft. It can be separated into three contributions, namely into the desired instantaneous range ρ_{inst} , into contributions from the interferometer instrument $\delta t_{EB,ifo}$ and into corrections to the inter-satellite time of flight $\Delta t_{PQ,corr}$:

$$\Delta t_{EB} = \Delta t_{EA} - \Delta t_{BA} \quad (2.174)$$

$$= \underbrace{\rho_{inst}(t)/c_0 + \Delta t_{PQ,corr}(t)}_{\Delta t_{PQ}} + \delta t_{EB,ifo}(t). \quad (2.175)$$

The term Δt_{PQ} expresses the light propagation time between the hypothetical events P and Q (cf. fig. 2.30), which means between emission of the light wave at the emitter CoM and reception of the light at the receiver CoM at GCRS coordinate time t . This would be the ideal, error-free, and relativistically correct ranging measurement. However, Δt_{PQ} differs from the actual measurement Δt_{EB} by $\delta t_{EB,ifo}$, which is the error due to the interferometer instrument. The proper vacuum speed of light is labeled as c_0 . Eq. (2.175) is revisited in subsequent sec. 2.5 on photon time of flight corrections.

It is remarked that the delta terms $\Delta\tilde{\omega}, \delta\tau$ and $\delta\dot{\tau}$ in eq. (2.173) are orders of magnitude smaller than the mean optical frequency $\tilde{\omega}$, hence, mutual products of these delta terms are even smaller and can be approximated or neglected. Furthermore, the magnitude of Δt terms expressing the time of flight between both S/C, such as Δt_{EB} or Δt_{EA} , is dominated by $\rho_{inst}(t)/c_0$. For this reason one can approximate terms in $\varphi_{PM|j}$, which have a small magnitude and which contain a light propagation time Δt . With this in mind one obtains from eq. (2.173) the following final expression for the one-way ranging (OWR) phase observable

$$\begin{aligned} \varphi_{PM|j}^{(OWR)}(t) = & +\Delta\tilde{\omega} \cdot t \mp \tilde{\omega} \cdot \rho_{inst}(t)/c_0 \mp \tilde{\omega} \cdot \delta t_{EB,ifo}(t) \pm \Phi_{LFN,i}(t) \mp \Phi_{LFN,j}(t) \\ & \mp \delta\omega_{LFN,i} \cdot \rho_{inst}(t)/c_0 \pm \delta\omega_{LFN,j} \cdot \Delta t_{BA} - \frac{\Delta\tilde{\omega}}{2} \cdot \rho_{inst}(t)/c_0 \\ & \mp \tilde{\omega} \cdot (\delta\tau_i - \delta\tau_j) \mp \tilde{\omega} \cdot \Delta t_{PQ,corr} - \frac{\Delta\tilde{\omega}}{2} (\delta\tau_i + \delta\tau_j) \pm \tilde{\omega} \cdot \delta\dot{\tau}_i \cdot \rho_{inst}(t)/c_0 \\ & \pm \Delta\Psi_{E,i} \mp \Delta\Psi_{B,j} \pm \vartheta_j + \Upsilon_{PR,j} + \delta\varphi_{PM,USO,j} + \delta\varphi_{PM,j} + \Upsilon_{PM,j} \\ & + \text{const.}, \end{aligned} \quad (2.176)$$

where the terms with small magnitude were omitted, i.e.

$$\Delta t_{BA} \cdot \Delta\tilde{\omega} \approx \Delta\tilde{\omega} \cdot \delta\dot{\tau}_i \cdot \Delta t_{EA} \approx \delta\dot{\tau}_j \cdot \Delta t_{BA} \approx \pm\delta\omega_{LFN,j} \cdot \Delta t_{BA} \approx 0. \quad (2.177)$$

The first and second line in eq. (2.176) contain the non-relativistic terms, while the third line accounts for the relativistic effects. One aim of this thesis chapter is to show that all the constituents in eq. (2.176) are understood and can be removed in post-processing, so that one can recover the instantaneous range between both S/C center of mass or GRPs. Similar equations will be derived in the subsequent sections for the other and more relevant functional concepts such as the transponder scheme. However, at first, the relevance of some terms in eq. (2.176) is analyzed.

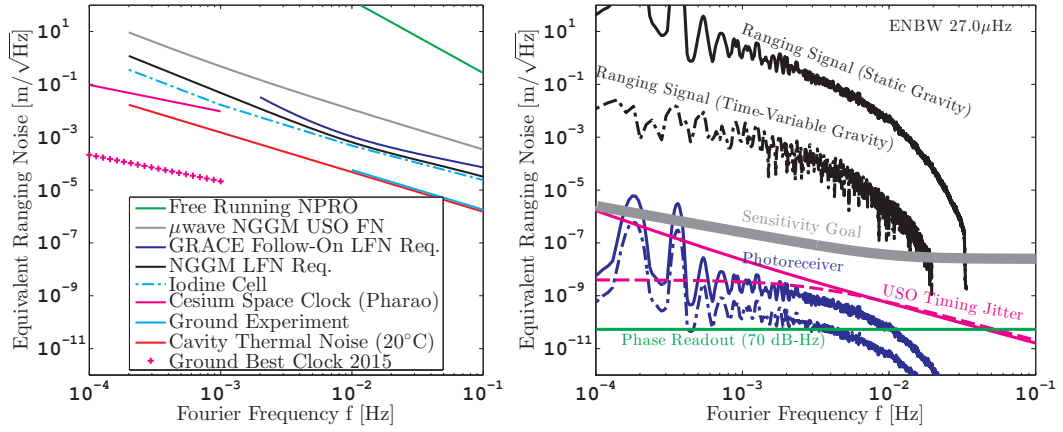


Figure 2.31: (Left panel:) One-way ranging noise due to (laser) frequency noise (LFN) for different frequency standards or requirements with a S/C separation of $L = 100$ km. The equivalent laser frequency noise with units of $\text{Hz}/\sqrt{\text{Hz}}$ is shown in fig. 2.8. The gray trace indicates the frequency noise of microwaves, which are derived from the USO stability discussed in sec. 2.3.4 on the USO. (Right panel:) The black lines at the top show the expected ranging signals of a GRACE-like constellation with $L = 100$ km and $h = 400$ km. The total ranging signal consists of the sum of time-variable plus static gravity field, however, both contributions have been separated for illustration. The time-variable signal was derived from the ESA ESM model [Dobslaw *et al.*, 2015]. The gray bold line indicates the sensitivity goal of $25 \text{ nm}/\sqrt{\text{Hz}} \times \text{NSF}(f)$. The blue, magenta and green traces show noise contributions present in (laser) interferometry. All traces consider an optical wavelength of $\lambda = 1064$ nm.

2.4.2 One-Way Ranging

The one-way ranging scheme as shown in fig. 2.30 is the most simple ranging approach. The ranging phase observable, i.e. the phasemeter output, was derived in the previous section with final result for $\varphi_{\text{PM}|j}^{(\text{OWR})}$ given in eq. (2.176). It is anticipated that the dominant noise sources are the laser phase noises from the emitter $\Phi_{\text{LFN},i}(t)$ and from the receiver $\Phi_{\text{LFN},j}(t)$. In the following, it is assumed that the wave sources on both S/C have a similar frequency stability and are uncorrelated, which allows the spectral density of phase fluctuations to be written as

$$\text{ASD}[\Phi_{\text{LFN},i} - \Phi_{\text{LFN},j}](f) = \sqrt{2} \cdot \text{ASD}[\Phi_{\text{LFN}}](f) = \sqrt{2} \cdot \frac{2\pi \cdot \text{ASD}[\delta\nu_{\text{LFN}}](f)}{2\pi f}. \quad (2.178)$$

The phase fluctuations and the phase $\varphi_{\text{PM}|j}^{(\text{OWR})}$ can be converted to a length by dividing the phase (fluctuations) with the wave number $2\pi/\lambda = 2\pi\bar{\nu}_{i|i}/c_0$, whereby it is neglected for the moment that the true and mean in-orbit frequency $\bar{\nu}_{i|i}$ is only known with limited accuracy.

The (laser) frequency noise (LFN) of various sources has been discussed in sec. 2.3.2 on optical frequency standards and was shown in fig. 2.8. One can use this information and apply eq. (2.178) to produce the plot shown in the left panel of fig. 2.31. The plot can be compared to the right panel, where the goal sensitivity of $25 \text{ nm}/\sqrt{\text{Hz}} \times \text{NSF}(f)$ for a NGGM ranging instrument is depicted (cf. eq. (1.39)). The black traces on the right side show the expected ranging signal. In addition, three noise contributors present in $\varphi_{\text{PM}|j}^{(\text{OWR})}$ are shown as the dark blue, magenta and green traces, which correspond to $\Upsilon_{\text{PR},j}$, $\delta\varphi_{\text{PM},\text{USO},j}$ and $\delta\varphi_{\text{PM},j}$, respectively. Since the one-way ranging scheme utilizes a single interferometer and phasemeter, these contributions are solely caused on the receiver side.

The green trace on the right panel of fig. 2.31 indicates the phase readout noise denoted as $\text{ASD}[\delta\varphi_{\text{PM},j}]$, which is given by the inverse carrier-to-noise density and has been discussed in the sec. 2.3.7 on the phasemeter (cf. eq. (2.125)). Here, the shown trace uses a carrier-

to-noise density of 70.0 dB-Hz, which is a worst-case assumption. This noise would be even lower for a higher carrier-to-noise density or higher signal-to-noise ratio.

The magenta traces show the phase noise due to USO timing jitter $\delta\varphi_{\text{PM,USO},j}$, which has been defined in eq. (2.124). The two different magenta traces indicate different underlying timing jitter ASD $[\delta\tau_{\text{USO}}]$. The solid magenta line considers a stability as specified for the NGGM USO in sec. 2.3.4. The dashed magenta line assumes the post-processed timing jitter ASD $[\delta\tau_{\text{USO,PP}}]$, which also includes information from GNSS and was defined in eq. (2.98). Both magenta traces are based on a worst-case beatnote frequency of 20 MHz, which can be considered as an upper limit for the jitter noise contributor. The noise due to the USO timing offset (cf. eq. (2.124)) has been omitted here, but will be shown in a subsequent section.

The dark blue traces on the right panel of fig. 2.30 cover the effect of the photoreceiver transfer function ASD $[\Upsilon_{\text{PR},j}]$, which is predominantly a phase delay. The solid blue line indicates the raw coupling (cf. eq. (2.85)), while the dashed blue trace includes the effect of a post-processing correction (cf. eq. (2.89)).

It should be noted that even the best frequency standards can not reach the goal sensitivity, which makes this functional concept unpractical for a GRACE-like or NGGM gravimetric mission. The laser noise can be significantly reduced by two-way ranging schemes, which will be introduced in the next subsections.

In addition, there are some other technical difficulties, which arise in one-way schemes. For example, the laser frequency on emitter and receiver needs to be stabilized to similar absolute values, shifted only by a few MHz, in order to avoid zero-crossings of the beatnote frequency at the photodiode (cf. sec. 2.3.7 on phasemeter). Moreover, the emitter satellite has no information on the correct pointing of the laser beam and would require divergent beams to strike the distant S/C.

However, one-way microwave ranging is commonly used in satellite Doppler tracking. The sensitivity of such microwave Doppler tracking can be assessed with the gray trace on the left panel of fig. 2.30, where the NGGM USO frequency stability (cf. table 2.2 and the magenta solid-dotted trace in fig. 2.8) were used to plot the equivalent ranging noise due to phase fluctuations. This means the USO acts as frequency standard and source to produce the radiation. The noise spectral density of roughly $5 \mu\text{m}/\sqrt{\text{Hz}} \cdot (1 \text{ Hz}/f)^{1.3}$ at high frequencies ($f \approx 1 \text{ Hz}$, not shown in the plot anymore) corresponds after averaging for 60 s with a sampling rate of 1 Hz to a line-of-sight (1σ) rms velocity error of

$$\sigma = \frac{1}{\sqrt{2}} \cdot \left(\int_{1/60\text{Hz}}^{1/2\text{Hz}} \left(5 \mu\text{m}/\sqrt{\text{Hz}} \cdot (1 \text{ Hz}/f)^{1.3} \cdot (2\pi f) \right)^2 df \right)^{1/2} \approx 26 \mu\text{m/s}, \quad (2.179)$$

which agrees well with the typical performance in one-way Doppler tracking of $30 \mu\text{m/s}$ [Iess *et al.*, 2012]. In eq. (2.179), the $1/\sqrt{2}$ rescales the dual USO noise level from fig. 2.31 to a single USO level, since the ground station can utilize a more precise clock.

2.4.3 Dual One-Way Ranging (DOWR)

The dual one-way ranging scheme is basically a duplication of the one-way ranging scheme as shown in the sketch (cf. upper panel of fig. 2.32) and in the Minkowski diagram (lower panel). Both S/C emit, receive and interfere light. Phasemeter on-board of each S/C track the phase. The DOWR is characterized by a common reception time $t_A = t_{A'} = t$, which is achieved in post-processing by interpolating the data streams.

For the analysis of the DOWR phase observable Θ one can directly use eq. (2.176) for $\varphi_{\text{PM},j}^{(\text{OWR})}$. To derive the observation on S/C i , the following rules can be applied. First, all indices i and j are exchanged. Secondly, the signs \pm and \mp are exchanged, because the frequency ordering is opposite on the other S/C. Furthermore, all event labels A, B, \dots are replaced by the corresponding primed quantities (cf. fig. 2.32)). One arrives at the following

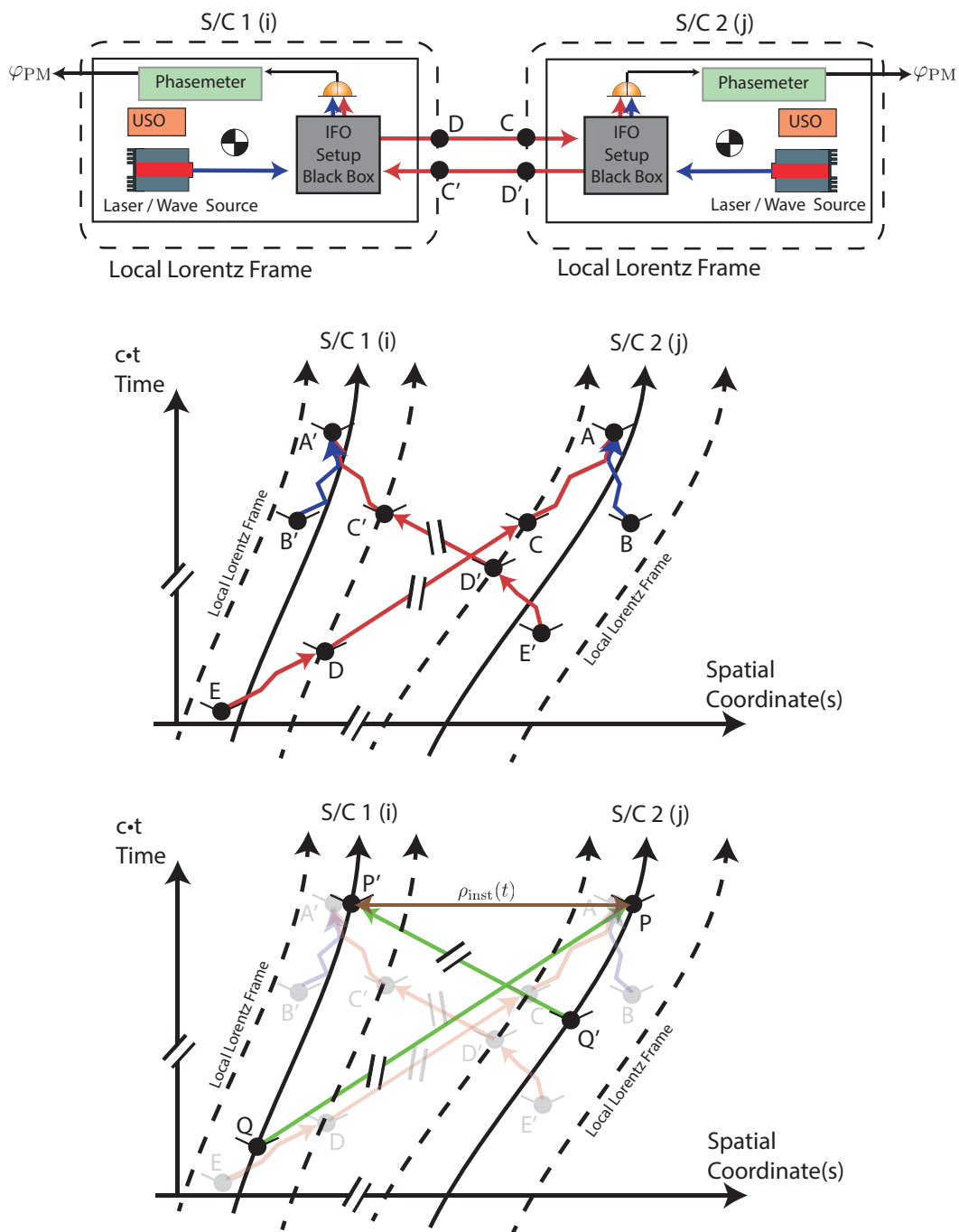


Figure 2.32: A sketch of a dual one-way ranging interferometer. The Minkowski diagram in the central panel shows the actual light paths, while the bottom panel shows the light paths (green) of an ideal range measurement between the two CoM or GRP of the S/C. Furthermore, the instantaneous range ρ_{inst} is depicted.

expression for S/C i

$$\begin{aligned}
 \varphi_{\text{PM}|i}^{(\text{OWR})}(t) = & +\Delta\tilde{\omega} \cdot t \pm \tilde{\omega} \cdot \rho_{\text{inst}}(t)/c_0 \pm \tilde{\omega} \cdot \delta t_{E'B',\text{ifo}}(t) \mp \Phi_{\text{LFN},j}(t) \pm \Phi_{\text{LFN},i}(t) \\
 & \pm \delta\omega_{\text{LFN},j} \cdot \rho_{\text{inst}}(t)/c_0 - \frac{\Delta\tilde{\omega}}{2} \cdot \rho_{\text{inst}}(t)/c_0 \\
 & \mp \tilde{\omega} \cdot (\delta\tau_i - \delta\tau_j) \pm \tilde{\omega} \cdot \Delta t_{P'Q',\text{corr}} - \frac{\Delta\tilde{\omega}}{2} \cdot (\delta\tau_j + \delta\tau_i) \\
 & \mp \tilde{\omega} \cdot \delta\dot{\tau}_j \cdot \rho_{\text{inst}}(t)/c_0 \\
 & \mp \Delta\Psi_{E',j} \pm \Delta\Psi_{B',i} \mp \vartheta_i + \Upsilon_{\text{PR},i} + \delta\varphi_{\text{PM,USO},i} + \delta\varphi_{\text{PM},i} \\
 & + \Upsilon_{\text{PM},i} + \text{const.}, \tag{2.180}
 \end{aligned}$$

which can be combined with $\varphi_{\text{PM},j}^{(\text{OWR})}$ to cancel the major laser phase noise terms Φ_{LFN} and to provide the DOWR phase:

$$\begin{aligned}
 \Theta(t) = & \varphi_{\text{PM}|i}^{(\text{OWR})}(t) - \varphi_{\text{PM}|j}^{(\text{OWR})}(t) \\
 = & \pm 2 \cdot \tilde{\omega} \cdot \rho_{\text{inst}}(t)/c_0 \pm \tilde{\omega} \cdot (\delta t_{EB,\text{ifo}}(t) + \delta t_{E'B',\text{ifo}}(t)) \\
 & \pm (\delta\omega_{\text{LFN},i} + \delta\omega_{\text{LFN},j}) \cdot \rho_{\text{inst}}(t)/c_0 \\
 & \pm \tilde{\omega} \cdot (\Delta t_{PQ,\text{corr}} + \Delta t_{P'Q',\text{corr}}) \mp \tilde{\omega} \cdot (\delta\dot{\tau}_i + \delta\dot{\tau}_j) \cdot \rho_{\text{inst}}(t)/c_0 \\
 & \pm (\Delta\Psi_{E,i} - \Delta\Psi_{E',j}) \mp (\Delta\Psi_{B,j} - \Delta\Psi_{B',i}) \pm \vartheta_j \mp \vartheta_i \\
 & - \Upsilon_{\text{PR},j} - \delta\varphi_{\text{PM,USO},j} - \delta\varphi_{\text{PM},j} + \Upsilon_{\text{PR},i} + \delta\varphi_{\text{PM,USO},i} + \delta\varphi_{\text{PM},i} \\
 & - \Upsilon_{\text{PM},j} + \Upsilon_{\text{PM},i} + \text{const.} \tag{2.181}
 \end{aligned}$$

The first summand in the first line in eq. (2.181) contains the ranging information, i.e. twice the instantaneous distance between both S/C CoM. The second summand accounts for interferometer instrument errors (δt_{ifo}), such as attitude-to-ranging coupling in both OWR paths. The second line contains the laser frequency noise of both lasers. The third line contains delays due to relativistic effects and ionosphere ($\Delta t_{PQ,\text{corr}} + \Delta t_{P'Q',\text{corr}}$), which will be addressed in sec. 2.5. The second addend in the third line is a relativistic modulation ($\propto \delta\dot{\tau}$). Line four contains the static or only very slowly varying laser phase variations ($\Delta\Psi$), which are highly suppressed due to the difference of unprimed and primed quantities. Furthermore, ϑ accounts for the phase variations of the light fields over the active area of the photodiode, which is determined by the overlap integral of the electric fields. The next line contains further contributors, which have been discussed in the previous one-way ranging section. The last line contains the phasemeter transfer function $\Upsilon_{\text{PM},j}$ and the constant bias, which should remind the reader that one can not determine the absolute inter-satellite distance, but only a biased range.

The DOWR phase observable $\Theta(t)$ contains twice the inter-satellite distance. However, it can be converted to a (phase) equivalent distance $\rho_{\Theta}(t)$ by

$$\rho_{\Theta}(t) = \frac{c_0 \cdot \Theta(t)}{\mp 2 \cdot \tilde{\omega}_{\text{est.}}} + \epsilon_{\text{SCF}}, \tag{2.182}$$

where $\tilde{\omega}_{\text{est.}}$ is the best-knowledge mean angular frequency of both S/C, since the true mean in-orbit frequency $\tilde{\omega} = (\bar{\omega}_{i|i} + \bar{\omega}_{j|j})/2$ is not known. This introduces a small scale factor error ϵ_{SCF} , which depends on the magnitude of $\Theta(t)$. In sec. 2.3.1 on the laser, an in-orbit knowledge for λ of 1 ppm was stated as realistic for cavity-based frequency standards with NPRO laser. Thus, the range with unit of meters can be obtained from the phase with an accuracy of 1 ppm. This is not a classical noise source but a multiplicative error. It is depicted by the orange trace in the lower panel of fig. 2.33.

The (phase) equivalent distance ρ_{Θ} is to first order the desired instantaneous inter-S/C distance ρ_{inst} . However, deviations are present due to noise, errors and relativistic effects. One major noise source is laser frequency noise, which is shown in the upper panel of fig. 2.33

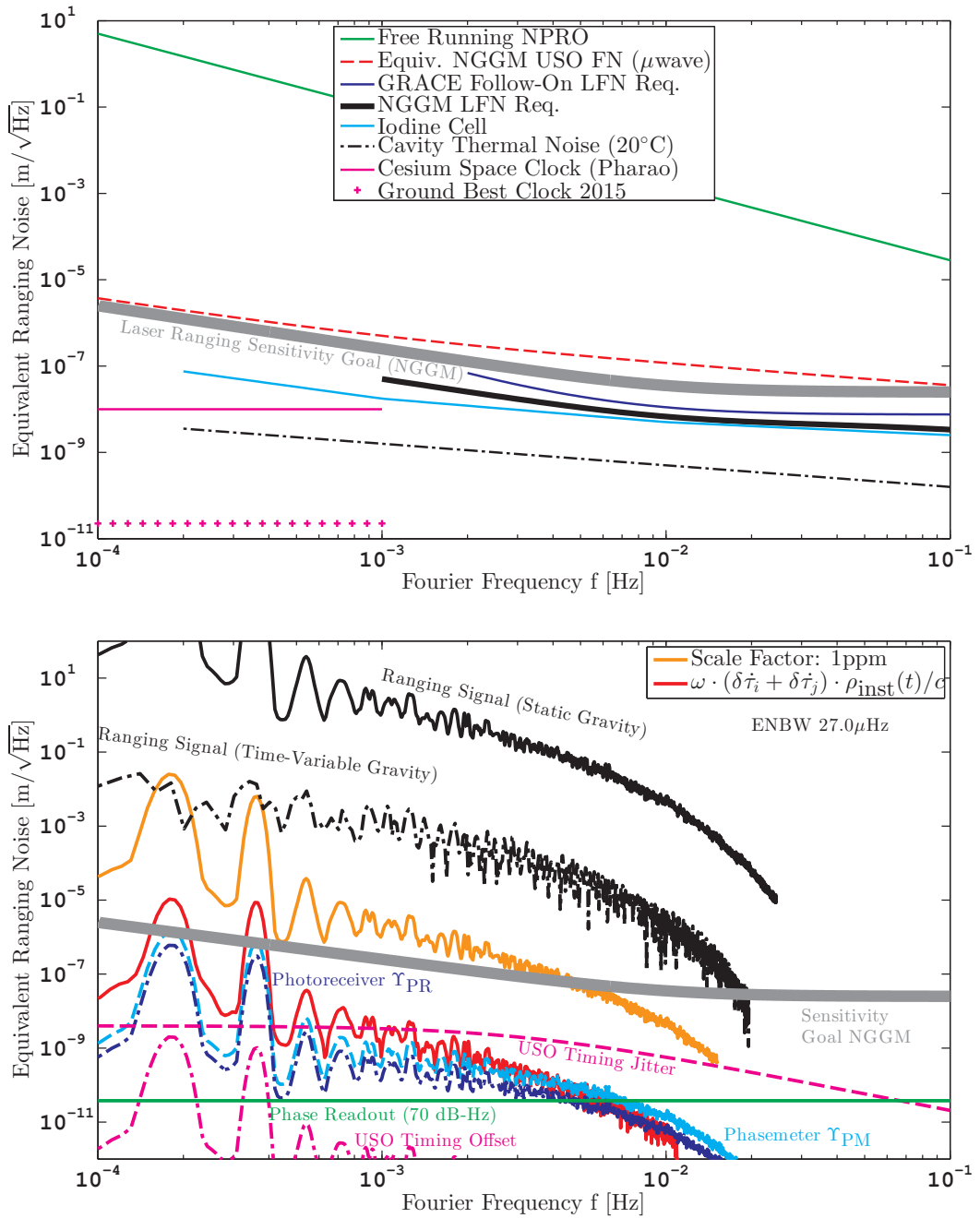


Figure 2.33: (Upper panel:) Dual one-way ranging (DOWR) noise due to (laser) frequency noise (LFN) for different frequency standards or requirements with a S/C separation of $L = 100$ km. The equivalent laser frequency noise with units of $\text{Hz}/\sqrt{\text{Hz}}$ is shown in fig. 2.8. (Lower panel:) The black lines at the top show the expected ranging signals of a GRACE-like constellation with $L = 100$ km and $h = 400$ km. The total ranging signal consists of the time-variable plus static gravity field, however, both contributions have been separated for illustration. The time-variable signal was derived from the ESA ESM model [Dobslaw *et al.*, 2015]. The gray bold line indicates the NGGM sensitivity goal of $25 \text{ nm}/\sqrt{\text{Hz}} \times \text{NSF}(f)$. All traces consider an optical wavelength of $\lambda = 1064$ nm and refer to a single-way distance, i.e. they are summands in $\rho_\Theta(t)$ (cf. eq. (2.182)).

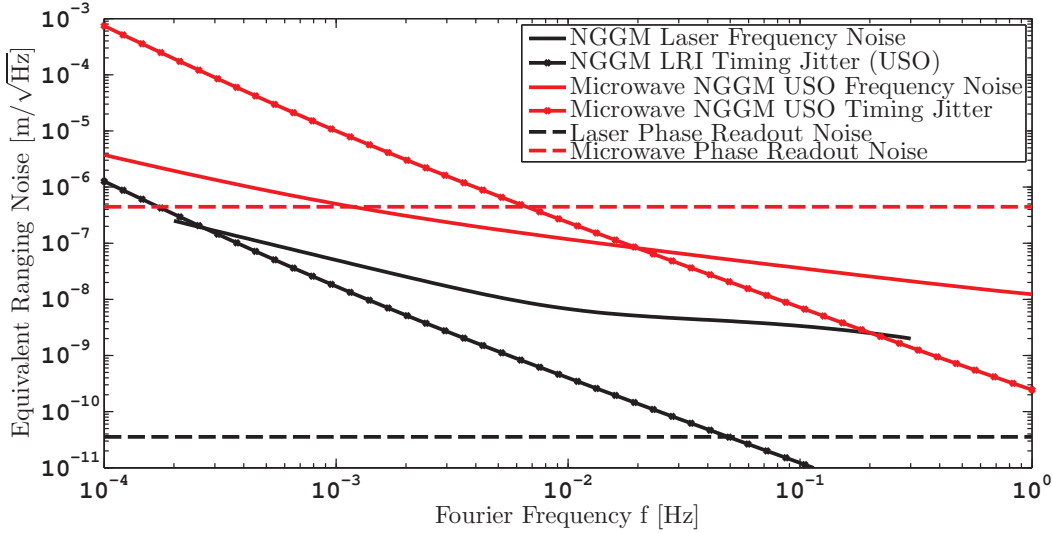


Figure 2.34: Amplitude spectral density of different noise contributions in a dual one-way ranging measurement. The y -axis refers to the (single-way) distance fluctuations, although the DOWR phase is to first order proportional to twice the distance. This plot assumes an inter-satellite distance of $L = 100$ km. Other parameters for this plot are $\lambda_{\text{microwave}} = c/24 \text{ GHz} = 1.25 \text{ cm}$, $\lambda_{\text{laser}} = 1064 \text{ nm}$, $C/N_0 = 70.0 \text{ dB-Hz}$ and maximum beatnote frequencies (for timing jitter) of 20 MHz and 1 MHz for laser and microwave, respectively.

for various frequency standards or experiments. The thick black trace is the NGGM laser frequency noise requirement (cf. eq. (2.77)), which will be assumed as baseline in the further discussion. It is below the gray sensitivity goal curve, which is $25 \text{ nm}/\sqrt{\text{Hz}} \times \text{NSF}(f)$ (cf. eq. (1.39)). One should note that the frequency stability of a free-running NPRO laser is insufficient (green trace) and needs to be improved with a dedicated frequency standard.

The lower panel of fig. 2.33 shows other constituents of $\Theta(t)$ and $\rho_{\Theta}(t)$ in the spectral domain. The magnitudes of the phase readout noise $\delta\varphi_{\text{PM}}$ and of the timing jitter noise in $\delta\varphi_{\text{PM,USO}}$ are scaled by $1/\sqrt{2}$ in the ASD plot compared to the one-way ranging scheme, since two uncorrelated phasemeters and USOs are present in DOWR. The effect of the phasemeter transfer function Υ_{PM} can be corrected in post-processing (cf. sec. 2.3.7). The dashed light blue trace illustrates already the effect of the error in the correction $\delta\Upsilon_{\text{PM,PP}}$, which is modeled here as a simple delay of the phase output by 25 ns per phasemeter (cf. eq. (2.123)). Since the effect of the transfer functions Υ from phasemeter and photoreceiver are not stochastically driven, they are assumed to add up linearly and are hence not rescaled by $\sqrt{2}$. The shown dark blue photoreceiver Υ_{PR} line is based on the post-processing correction (cf. eq. (2.89) as well.

The second magenta line at the bottom illustrates the negligible effect from the USO timing offset $\delta\tau_{\text{USO,off}}$, which is a second term in the USO induced phase error $\delta\varphi_{\text{PM,USO}}$ (cf. eq. (2.118) and (2.124)) with the following PSD expression in the DOWR case:

$$(2\pi \cdot f \cdot \delta\tau_{\text{USO,off,j}})^2 \cdot \text{PSD}[\varphi_{\text{PM}|j}^{(\text{OWR})}] + (2\pi \cdot f \cdot \delta\tau_{\text{USO,off,i}})^2 \cdot \text{PSD}[\varphi_{\text{PM}|i}^{(\text{OWR})}]. \quad (2.183)$$

For this trace, an offset of $\delta\tau_{\text{USO,off}} = 100 \text{ ps}$ was assumed per S/C, which can be understood as the systematic bias or slowly varying offset in the time stamping of phase samples. In contrast, the timing jitter accounts for fluctuations within the science measurement frequency band. The offsets $\delta\tau_{\text{USO,off}}$ can be caused by errors in the required interpolation of phase samples to a common reception time. However, this offset corresponds to a further delay next to delays from the uncertainty in the phasemeter and photoreceiver transfer functions, which are assumed to be larger. The three lines showing the errors due to delays (Υ_{PM} , Υ_{PR}

and USO time offset) in fig. 2.33 are based on the assumption that the DOWR is realized with a frequency standard and not by a free-running laser, such that the actual phase measurement is dominated at low frequencies by the ranging (Doppler) signal on both S/C. If free-running lasers would be used, laser phase noise would dominate the phase measurement and the errors due to delays would be driven by the laser phase noise. Thus, DOWR with free-running lasers is more demanding in terms of requirements on delays and timing offsets.

Many relativistic contributions related to the proper time cancel out in eq. (2.181) for Θ compared to the one-way ranging observable $\varphi_{\text{PM}}^{(\text{OWR})}$, for example, the terms related to the transverse Doppler effect or, more generally, to the gravitational and special relativistic frequency shift. These are proportional to the product of optical frequency and proper time ($\tilde{\omega} \cdot \delta\tau$). The typical magnitude of the remaining term $\tilde{\omega} \cdot (\delta\dot{\tau}_i + \delta\dot{\tau}_j) \cdot \rho_{\text{inst}}(t)/c_0$ in eq. (2.181) is shown by the red trace in the lower panel of fig. 2.33, which can be regarded as uncritical. Moreover, it can be corrected in post-processing due to its non-stochastic nature. This term can be understood as the remaining effect of the gravitational and special relativistic frequency shift in the DOWR combination, whereby most of the effect ($\tilde{\omega} \cdot \delta\tau$) is canceled by the two-way ranging combination. Many other relativistic contributions on the propagation time between the satellites are absorbed in $\Delta t_{PQ,\text{corr}} + \Delta t_{P'Q',\text{corr}}$ and will be addressed in a subsequent section.

The DOWR scheme is used by the microwave ranging instrument in GRACE and GRACE Follow-On. An approximate frequency stability of microwave radiation is indicated by the dashed red trace in the upper panel of fig. 2.33, which was derived from the USO stability discussed in sec. 2.3.4. It is remarked that the frequency stability of the microwave radiation is approximately one order of magnitude lower than the stability of the laser light. Hence, the anticipated larger gain in sensitivity of a laser interferometer cannot solely be caused by the frequency or phase noise of the radiation with units of $\text{rad}/\sqrt{\text{Hz}}$ or $\text{Hz}/\sqrt{\text{Hz}}$. The sensitivity difference between a microwave and a laser ranging system is illustrated in fig. 2.34, where the laser frequency noise $\delta\omega_{\text{LFN}}$, the phase readout noise $\delta\varphi_{\text{PM}}$ and the timing jitter noise $\delta\varphi_{\text{PM,USO}}$ are shown for microwave (red traces) and for a laser instrument (black traces). One should notice that the microwave instrument is limited by phase readout noise $\delta\varphi_{\text{PM}}$, which is called in the GRACE KBR context *system noise* [Kim, 2000], and timing jitter $\delta\varphi_{\text{PM,USO}}$, while the interferometer is limited by frequency noise $\delta\omega_{\text{LFN}}$. The timing jitter and phase readout noise scale with the wavelength, which is a factor $\lambda_{\text{microwave}}/\lambda_{\text{laser}} \approx 10^4$ smaller for the laser light. The used worst-case value for the carrier-to-noise density of 70.0 dB-Hz in the plot is in agreement with the value from [Kim, 2000, p. 112] for the microwave instrument and is also realistic for a laser ranging instrument (see sec. 2.3.7 on phasemeter). However, it is stressed that other important noise contributions such as the spacecraft pointing jitter and the ionospheric noise have been neglected in this comparison.

Another difference due to the wavelength concerns the beatnote frequencies on both satellites. A range rate of 5 m/s between the satellites induces a frequency Doppler shift of approx. 5 MHz for 1064 nm laser light, while the same rate causes 400 Hz at a wavelength of 1.25 cm. To avoid zero crossings of the beatnote frequency, the USOs on-board of each GRACE satellite are detuned by 99 Hz [Dunn *et al.*, 2003], which corresponds to approx. 20 ppm or 0.5 MHz at the 24.5 GHz K band. A crystal oscillator frequency can be easily altered by a change in the geometry. As laser interferometry exhibits larger Doppler shifts in terms of Hertz, the offset frequency needs to be higher, e.g. at 10 MHz, but the fractional detuning is smaller around 0.035 ppm, if a 1064 nm laser wavelength is assumed. Such a small but well-defined detuning is difficult to achieve directly with laser frequency standards and would likely require additional frequency shifting components to the author's knowledge.

A transponder scheme can be envisioned to circumvent this issue, which will be explained in the next sections.

2.4.4 Derivation of Transponder-based Ranging

In this functional concept both S/C receive and emit laser light and both perform an interferometric phase readout, as in the DOWR case. One satellite emits frequency stabilized light at an event E in the Minkowski diagram in fig. 2.35. This S/C with active frequency stabilization is denoted as *master* (M). The distant S/C denoted as *slave* receives the light at coordinate time t_A and performs a phase readout with the interferometer and phasemeter, which can be written as (cf. eq. (2.164)):

$$\begin{aligned} \varphi_{\text{PM}|S}^{(\text{OL})}(t_A) &= \pm \bar{\omega}_{M|M} \cdot \tau_M(t_A - \Delta t_{EA}) \pm \Phi_{\text{LFN},M}(\tau_M(t_A - \Delta t_{EA})) \pm \Delta \Psi_{E,M} \\ &\mp \bar{\omega}_{S|S} \cdot \tau_S(t_A - \Delta t_{BA}) \mp \Phi_{\text{LFN},S}(\tau_S(t_A - \Delta t_{BA})) \mp \Delta \Psi_{B,S} \\ &\pm \vartheta_S(t_A) + \Upsilon_{\text{PR},S} + \delta\varphi_{\text{PM},\text{USO},S} + \delta\varphi_{\text{PM},S} + \Upsilon_{\text{PM},S} + \text{const.}, \end{aligned} \quad (2.184)$$

where the first line contains the phase of the light received from the master, the second line contains the phase of the local light and the third line contains additional contributions from interferometry, such as the phase due to wavefront overlap (ϑ_S), contributions from the transfer function of the photoreceiver and phasemeter (Υ) as well as USO timing errors $\delta\varphi_{\text{PM},\text{USO},S}$. The previous expression can be approximated as (cf. eq. (2.176))

$$\begin{aligned} \varphi_{\text{PM}|S}^{(\text{OL})} &= +\Delta\tilde{\omega} \cdot t_A \mp \tilde{\omega} \cdot \rho_{\text{inst}}(t_A)/c_0 \mp \tilde{\omega} \cdot \delta t_{EB,\text{ifo}}(t_A) \pm \Phi_{\text{LFN},M}(t_A) \mp \Phi_{\text{LFN},S}(t_A) \\ &\mp \delta\omega_{\text{LFN},M} \cdot \rho_{\text{inst}}(t_A)/c_0 \pm \delta\omega_{\text{LFN},S} \cdot \Delta t_{BA} - \frac{\Delta\tilde{\omega}}{2} \cdot \rho_{\text{inst}}(t_A)/c_0 \\ &\mp \tilde{\omega} \cdot (\delta\tau_M - \delta\tau_S) \mp \tilde{\omega} \cdot \Delta t_{PQ,\text{corr}} - \frac{\Delta\tilde{\omega}}{2} (\delta\tau_M + \delta\tau_S) \pm \tilde{\omega} \cdot \delta\dot{\tau}_M \cdot \rho_{\text{inst}}(t_A)/c_0 \\ &\pm \Delta\Psi_{E,M} \mp \Delta\Psi_{B,S} \pm \vartheta_S + \Upsilon_{\text{PR},S} + \delta\varphi_{\text{PM},\text{USO},S} + \delta\varphi_{\text{PM},S} + \Upsilon_{\text{PM},S} \\ &+ \text{const.}, \end{aligned} \quad (2.185)$$

The upper sign applies in the expression, if the laser frequency of the master laser $\bar{\omega}_{M|M}$ is higher than the frequency of the slave S/C $\bar{\omega}_{S|S}$. Furthermore, as in the DOWR case, it is assumed that the relative velocity between both S/C along the line of sight $\dot{\rho}_{\text{inst}}$ is low enough such that the Doppler induced frequency shift does not change the frequency ordering, i.e.

$$\dot{\rho}_{\text{inst}}/c_0 \cdot \bar{\omega}_{M|M} < |\bar{\omega}_{S|S} - \bar{\omega}_{M|M}| \quad (2.186)$$

However, the slave S/C uses the measured phase in a feedback control loop, the so-called frequency offset phase-locked loop (PLL) as explained in sec. 2.3.9, to zero the difference between the measured phase and a reference phase $\varphi_{\text{ref}} = \omega_{\text{off}} \cdot \tau_{\text{USO}} + \text{const.}$ This is achieved by actuating the laser frequency, which can be modeled here by an adjustment of $\Delta\Psi_S$, which was so far simply a slowly-varying phase term of the laser. The actual measured closed-loop phase has been derived in the frequency domain in eq. (2.141) in sec. 2.3.9. If the loop gain H_{Loop} is sufficiently high, one can obtain a simple time-domain expression of the closed-loop phase measurement as (cf. eq. (2.142))

$$\begin{aligned} \varphi_{\text{PM}|S}^{(\text{CL})}(\tau_S(t_A)) &\approx \omega_{\text{off},S} \cdot \tau_{\text{USO},S}(\tau_S(t_A)) - \omega_{\text{off},S} \cdot \Delta\tau_{\text{USO},\text{Dec}2,S}(\tau_S(t_A)) \\ &+ \delta\varphi_{\text{PM},\text{USO},S} + \text{const.} + \mathcal{O}\left(\frac{1}{H_{\text{Loop}}}\right) \end{aligned} \quad (2.187)$$

where the first term is a phase ramp with constant frequency $\omega_{\text{off},S}$, the second summand depends on the delay time of the second decimation filter in the phasemeter. This term is almost constant, however, it may contain a small relativistic modulation and is for this reason kept for further analysis. The third addend denotes the USO timing error of the phase measurement, which arises from the conversion of the on-board phase measurement to the GCRS coordinate time t . It contains the effect of timing jitter and of the timing offset. The

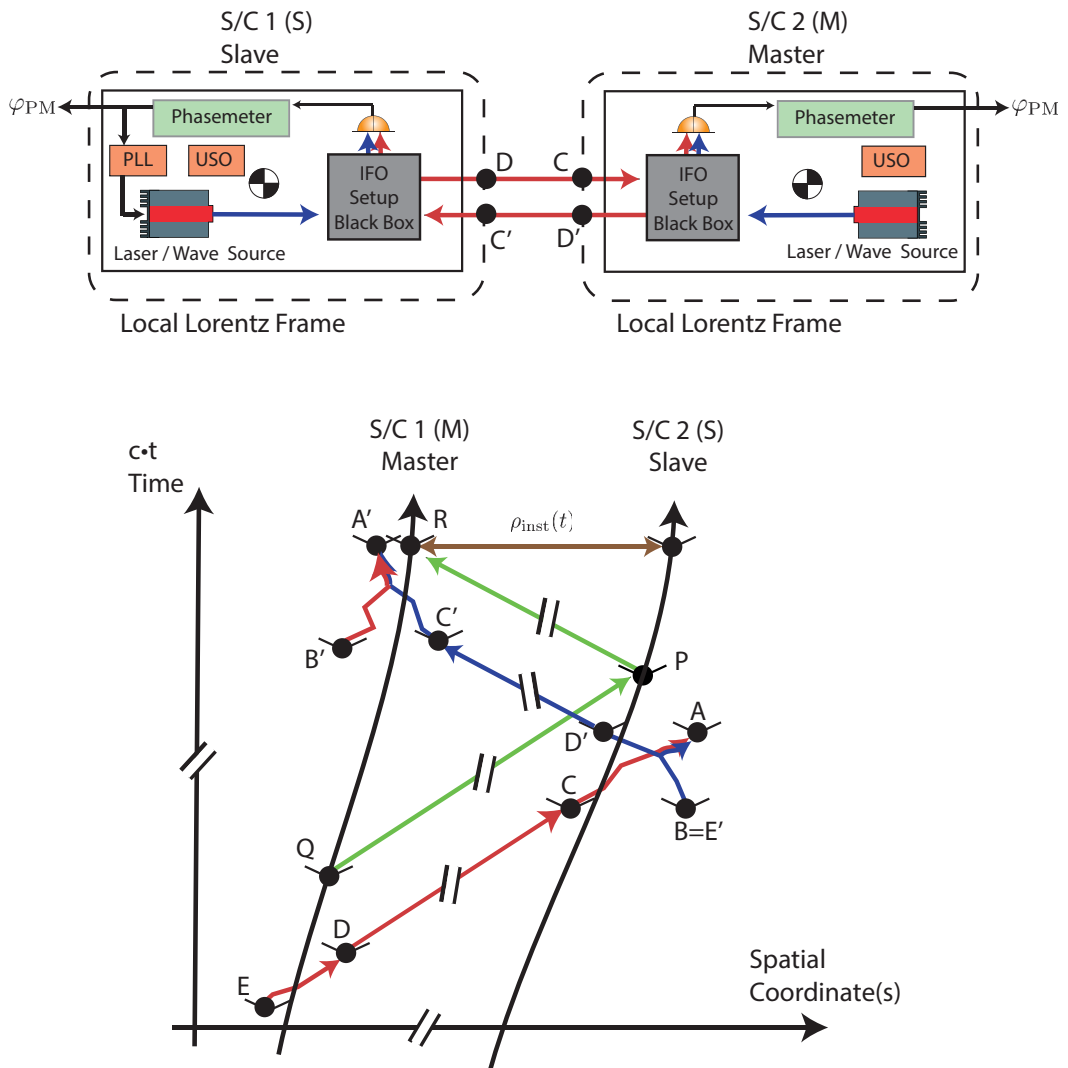


Figure 2.35: Transponder ranging scheme, where the slave spacecraft locks its laser with an offset frequency to the incoming light field. The lower plot shows the corresponding Minkowski diagram of light paths (red and blue arrows) in a transponder concept. The green arrows indicate the light world lines of an ideal range measurement between the CoM of both S/C.

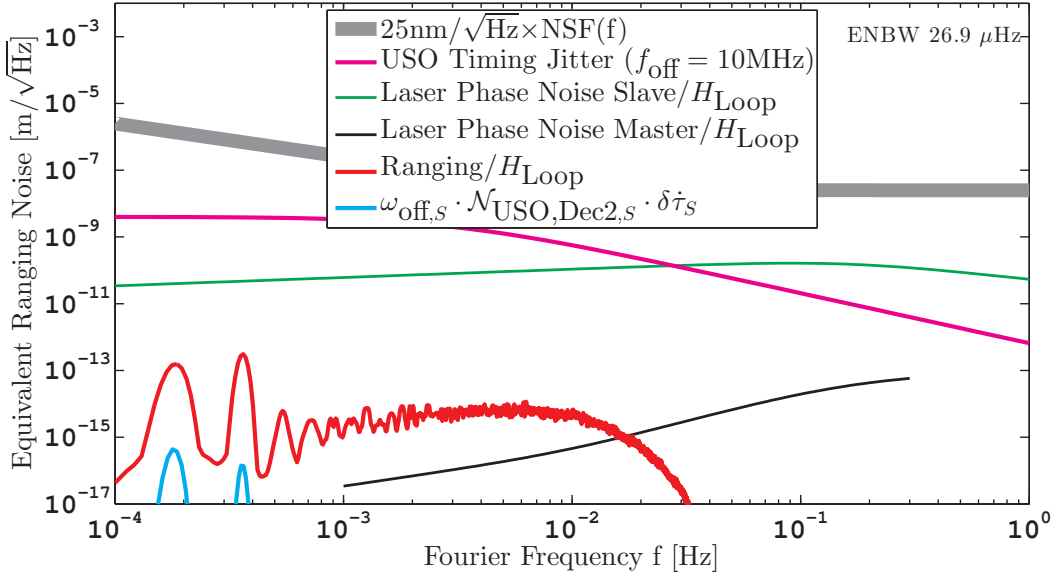


Figure 2.36: Constituents of the closed-loop phase $\varphi_{\text{PM},S}^{(\text{CL})}$ on the slave S/C. The frequency offset PLL open loop gain H_{Loop} has been defined in eq. (2.143). The laser phase noise for master and slave is based on the NGGM frequency standard and on the free-running NPRO stability, respectively, shown by the green and black trace in fig. 2.8. The magenta trace considers already post-processing corrections (cf. eq. (2.124)). The phase variations have been converted to equivalent displacement spectral densities under the assumption of a wavelength of $\lambda = 1064 \text{ nm}$.

jitter induced phase noise depends on the frequency of the beatnote, which is ω_{off} and can be considered of the order of $2\pi \cdot 10 \text{ MHz}$ for the slave S/C. The phase noise induced by the static offset $\Delta\tau_{\text{USO,off}}$ depends on the measured phase variations in the measurement band, which are suppressed and negligible in closed-loop operation on the slave satellite. Thus, as in the DOWR case, the term $\delta\varphi_{\text{PM,USO,S}}$ is dominated by timing jitter and is shown in terms of the equivalent displacement noise as magenta line in fig. 2.36.

To justify the omission of the $\mathcal{O}(1/H_{\text{Loop}})$ term in eq. (2.187), one needs to ensure that the open loop phase contributions are suppressed by the open loop gain H_{Loop} to a negligible level, which is shown in fig. 2.36 as well. The dominant contributors to $\varphi_{\text{PM},S}^{(\text{OL})}$ are the free-running laser phase noise from the slave S/C ($\Phi_{\text{LFN},S}$, green trace), the laser phase noise from the frequency-stabilized master laser ($\Phi_{\text{LFN},M}$, black trace) and the actual ranging signal arising from the Doppler shift ($\rho_{\text{inst}}(t)$, red trace), which is implicitly given by the propagation time between both S/C (Δt_{EA}) in eq. (2.184). Thus, the open loop phase variations $\varphi_{\text{PM},S}^{(\text{OL})}$ are suppressed by the control loop to a level below $1 \text{ nm}/\sqrt{\text{Hz}}$ as apparent from fig. 2.36.

The delay term $\omega_{\text{off},S} \cdot \Delta\tau_{\text{USO,Dec2},S}$ in eq. (2.187) is a pure digital delay of the second decimation filter, and hence it is dependent on the USO clock rate. However, as the USO clock time is a good approximation for the proper time, one can approximate it rigorously with the help of the delta proper time (cf. eq. (2.165)):

$$\begin{aligned} \omega_{\text{off},S} \cdot \Delta\tau_{\text{USO,Dec2},S} &\approx \omega_{\text{off},S} \cdot \mathcal{N}_{\text{USO,Dec2},S} \cdot (1 - \delta\tau_S) \\ &= \text{const.} - \omega_{\text{off},S} \cdot \mathcal{N}_{\text{USO,Dec2},S} \cdot \delta\tau_S, \end{aligned} \quad (2.188)$$

where $\mathcal{N}_{\text{USO,Dec2},S}$ is the proper delay in the local Lorentz frame of the S/C. The magnitude of $\mathcal{N}_{\text{USO,Dec2},S}$ is determined by the sampling rate of the science data, which is the output of the second decimation filter. The effect of this term on the phase is negligible even with a worst-case assumption of $\mathcal{N}_{\text{USO,Dec2},S} \approx 1 \text{ s}$ and with $\omega_{\text{off},S} = 2\pi \cdot 10 \text{ MHz}$, which is indicated by the light blue trace in fig. 2.36. Thus, a post-processing correction of this term is not

required but would be possible.

In summary, the phase readout at the slave S/C is in good approximation a constant ramp over time without ranging information. This zero measurement was obtained by imprinting the phase information from the received light of the master satellite onto the laser light of the slave S/C. It is important to notice that the same light used for interference and photodetection on the slave S/C is also transmitted back to the master. The phase of the light at the emission event B on the slave S/C in fig. 2.35 can be directly deduced from eq. (2.140) and (2.138) as

$$\begin{aligned} \Phi_B(\tau_S(t_B)) &= +\Phi_{\text{RX}}(\tau_S(t_B) + \Delta\tau_{\text{BA},S}) + \vartheta_S(\tau_S(t_B) + \Delta\tau_{\text{BA},S}) + \delta\varphi_{\text{PM},S} \\ &\quad \mp \omega_{\text{off},S} \cdot (\tau_{\text{USO},S}(t_B) + \Delta\tau_{p,S}(t_B) + \Delta\tau_{\text{BA},S}) + \mathcal{O}(1/H_{\text{Loop},S}) \end{aligned} \quad (2.189)$$

$$\begin{aligned} &= +\Phi_{\text{RX}}(\tau_S(t_A)) \\ &\quad + \vartheta_S(\tau_S(t_A)) + \delta\varphi_{\text{PM},S}(\tau_S(t_A)) \mp \omega_{\text{off},S} \cdot \tau_{\text{USO},S}(\tau_S(t_A)) \\ &\quad \mp \omega_{\text{off},S} \cdot \Delta\tau_{p,S}(t_B) + \mathcal{O}(1/H_{\text{Loop},S}) \end{aligned} \quad (2.190)$$

$$\begin{aligned} &= +\bar{\omega}_{M|M} \cdot \tau_M(t_E) + \Phi_{\text{LFN},M}(\tau_M(t_E)) + \Delta\Psi_{E,M} \\ &\quad + \vartheta_S(\tau_S(t_A)) + \delta\varphi_{\text{PM},S}(\tau_S(t_A)) \mp \omega_{\text{off},S} \cdot \tau_{\text{USO},S}(\tau_S(t_A)) \\ &\quad \mp \omega_{\text{off},S} \cdot \Delta\tau_{p,S}(t_B) + \mathcal{O}(1/H_{\text{Loop},S}) \end{aligned} \quad (2.191)$$

where $\Phi_{\text{RX}}(\tau(t_A))$ is the received phase at event A , i.e. the first line of eq. (2.184), which was used in the recast to obtain eq. (2.191). The phase of the emitted light Φ_B at the slave S/C does not contain contributions from the slave laser, e.g. no carrier phase $\bar{\omega}_{S|S} \cdot \tau_S$ and no laser phase noise $\Phi_{\text{LFN},S}$, because these are suppressed by the control loop and absorbed together with other terms in $\mathcal{O}(1/H_{\text{Loop},S})$. The light phase Φ_B is positive, however, the sign of the frequency shift $\omega_{\text{off},S}$ depends on the frequency ordering between master and slave laser. Furthermore, as in the DOWR case, it is required that the Doppler frequency shift is smaller than the offset frequency, such that the frequency order can not be reversed by the relative motion between S/C. This means that eq. (2.186) is equivalent to

$$\dot{\rho}_{\text{inst}}/c_0 \cdot \bar{\omega}_{M|M} < \omega_{\text{off},S} \quad (2.192)$$

which provides an operational lower limit for the selection of the offset frequency $\omega_{\text{off},S}$ depending on the (maximum) expected relative velocity $\dot{\rho}_{\text{inst}}$. In the following discussion, the generic value of $\omega_{\text{off},S} = 2\pi \cdot 10 \text{ MHz}$ is kept, which fulfills the condition in eq. (2.192) for the gravimetric mission concepts discussed in this thesis.

The term $\Delta\tau_{p,S}$ in eq. (2.191) is a delay due to the effect of the transfer functions from photoreceiver, ADC, DPLL and first decimation filter on the slave S/C (cf. transfer function H_p^c in sec. 2.3.9). Although this delay is constant in the local Lorentz frame of the slave S/C, i.e. the proper delay with respect to the proper time of the satellite, it may show a small variation in the GCRS coordinate time t . Therefore, the term is kept for a subsequent evaluation.

The emitted light of the slave S/C propagates back to the master, where it is interfered with the local laser light and the phase of the beatnote is read out. Again, one can exploit the Lorentz invariance of the phase, which allows the phase at the reception event A' on the master satellite to be written simply as the phase at the emission event Φ_B on the slave

satellite. This yields

$$\begin{aligned}
 \varphi_{PM|M}(t_{A'}) &= \pm \bar{\omega}_{M|M} \cdot \tau_M(t_{A'} - \Delta t_{B'A'}) \pm \Phi_{LFN,M}(\tau_M(t_{A'} - \Delta t_{B'A'})) \pm \Delta \Psi_{B',M} \\
 &\mp \Phi_B(\tau_S(t_B)) \\
 &\mp \vartheta_M(t_{A'}) + \Upsilon_{PR,M}(t_{A'}) + \delta\varphi_{PM,USO,M}(t_{A'}) + \delta\varphi_{PM,M}(t_{A'}) \\
 &+ \Upsilon_{PM,M}(t_{A'}) + \text{const.} \tag{2.193}
 \end{aligned}$$

$$\begin{aligned}
 &= \pm \bar{\omega}_{M|M} \cdot \tau_M(t_{A'} - \Delta t_{B'A'}) \pm \Phi_{LFN,M}(\tau_M(t_{A'} - \Delta t_{B'A'})) \pm \Delta \Psi_{B',M} \\
 &\mp \bar{\omega}_{M|M} \cdot \tau_M(t_{A'} - \Delta t_{EA'}) \mp \Phi_{LFN,M}(\tau_M(t_{A'} - \Delta t_{EA'})) \mp \Delta \Psi_{E,M} \\
 &\mp \vartheta_S(\tau_S(t_{A'} - \Delta t_{AA'})) \mp \delta\varphi_{PM,S}(\tau_S(t_{A'} - \Delta t_{AA'})) \\
 &+ \omega_{\text{off},S} \cdot \tau_{USO,S}(\tau_S(t_{A'} - \Delta t_{AA'})) + \omega_{\text{off},S} \cdot \Delta\tau_{p,S}(t_{A'} - \Delta t_{BA'}) \\
 &\mp \vartheta_M(t_{A'}) + \Upsilon_{PR,M}(t_{A'}) + \delta\varphi_{PM,USO,M}(t_{A'}) + \delta\varphi_{PM,M}(t_{A'}) \\
 &+ \Upsilon_{PM,M}(t_{A'}) + \text{const.} \mp \mathcal{O}(1/H_{\text{Loop},S}), \tag{2.194}
 \end{aligned}$$

which is a very generic description of the phase observable on the master S/C. It is noted that the proper time of the master (τ_M) as well as of the slave (τ_S) S/C appear in the equation. Furthermore, one-way photon propagation times from the slave to the master, such as $\Delta t_{AA'}$, and round-trip delays, e.g. $\Delta t_{EA'}$, are present.

The same approximations as in sec. 2.4.1 on the one-way ranging can be used to assess the magnitude of the single contributors and to derive a relation to the instantaneous range ρ_{inst} . At first, terms with the optical frequency $\bar{\omega}_{M|M} \gg 10^{10}$ rad/s are considered. It is recalled that the proper time τ is increasing with a rate of almost 1 s/s in the GCRS, while the delta proper time is $\delta\tau = t - \tau$ (cf. eq. (2.165)) and has a rate of the order of $\delta\dot{\tau}(t) \approx 10^{-9}$ s/s (cf. eq.(2.14)). Furthermore, the photon propagation time Δt for distances on a single S/C, one-way between both S/C and round-trip between both S/C are of the order of 10^{-8} s, 0.33 ms and 0.66 ms, respectively, for an assumed satellite separation of 100 km.

Thus, one can approximate the terms depending on the optical frequency as

$$\begin{aligned}
 &\bar{\omega}_{M|M} \cdot (\tau_M(t_{A'} - \Delta t_{B'A'}) - \tau_M(t_{A'} - \Delta t_{EA'})) \\
 &= \bar{\omega}_{M|M} \cdot [t_{A'} - \Delta t_{B'A'} - \delta\tau_M(t_{A'} - \Delta t_{B'A'}) - (t_{A'} - \Delta t_{EA'} - \delta\tau_M(t_{A'} - \Delta t_{EA'}))] \tag{2.195}
 \end{aligned}$$

$$\begin{aligned}
 &= \bar{\omega}_{M|M} \cdot \left(\underbrace{-\Delta t_{B'A'} + \Delta t_{EA'}}_{=\Delta t_{EB'}} + \delta\tau_M(t_{A'} - \Delta t_{EA'}) - \delta\tau_M(t_{A'} - \Delta t_{B'A'}) \right) \tag{2.196}
 \end{aligned}$$

$$\approx \bar{\omega}_{M|M} \cdot (\Delta t_{EB'} + \delta\tau_M(t_{A'}) - \delta\dot{\tau}_M(t_{A'}) \cdot \Delta t_{EA'} - \delta\tau_M(t_{A'}) + \delta\dot{\tau}_M(t_{A'}) \cdot \Delta t_{B'A'}) \tag{2.197}$$

$$\approx \bar{\omega}_{M|M} \cdot \Delta t_{EB'} - \bar{\omega}_{M|M} \cdot \delta\dot{\tau}_M(t_{A'}) \cdot 2 \cdot \rho_{\text{inst}}(t_{A'})/c, \tag{2.198}$$

where the time difference $\Delta t_{EB'}$ contains mainly the ranging information. This quantity is a difference between $\Delta t_{EA'}$ and $\Delta t_{BA'}$, where $\Delta t_{EA'}$ is the time of flight of a photon from the emission event on the master S/C to the reception event at the photodiode after the round-trip path, while $\Delta t_{BA'}$ is the time of flight of another local oscillator photon from the master laser to the master photodiode. One can write the propagation time $\Delta t_{EB'}$ in terms of the instantaneous range and correction terms:

$$\Delta t_{EB'} = \Delta t_{EA'} - \Delta t_{BA'} \tag{2.199}$$

$$\begin{aligned}
 &= 2 \cdot \underbrace{\rho_{\text{inst}}(t)/c_0 + \Delta t_{QPR,\text{corr}}}_{\Delta t_{QPR}} + \delta t_{\text{ifo}}(t), \tag{2.200}
 \end{aligned}$$

where δt_{ifo} contains corrections due to the interferometer instruments on both S/C, e.g. due to attitude-to-ranging coupling and other pathlength couplings, while $\Delta t_{QPR,\text{corr}}$ denotes corrections for the inter-satellite round-trip time, e.g. due to relativistic delays or ionospheric effects. The term Δt_{QPR} is the ideal and relativistically correct round-trip propagation time

between both S/C CoM shown by the green arrows in the Minkowski diagram in fig. 2.35. The previous equation is discussed in detail in the subsequent sec. 2.5 on corrections to the photon time of flight.

The second summand in eq. (2.198) is a relativistic effect, which appeared in similar form in the DOWR scheme and turned out to be uncritical. It is the remaining effect of a gravitational and special relativistic frequency shift between the locally used photon for interference and the round-trip delayed photon. It is pointed out that terms of the form of optical frequency times delta proper time ($\omega \cdot \delta\tau$), which contain most of the gravitational and special relativistic frequency shift, canceled out as in the DOWR scheme. Thus, also the transverse Doppler effect [Rindler, 2012, sec. 3.2] at the optical (carrier) frequency is highly suppressed in a transponder concept.

The laser phase noise in eq. (2.194) can be rigorously approximated with the help of eq. (2.168) as

$$\Phi_{\text{LFN},M}(\tau_M(t_{A'} - \Delta t_{B'A'})) - \Phi_{\text{LFN},M}(\tau_M(t_{A'} - \Delta t_{EA'})) \quad (2.201)$$

$$= \Phi_{\text{LFN},M}(t_{A'} - \Delta t_{B'A'} - \delta\tau_M(t_{A'} - \Delta t_{B'A'})) \\ - \Phi_{\text{LFN},M}(t_{A'} - \Delta t_{EA'} - \delta\tau_M(t_{A'} - \Delta t_{EA'})) \quad (2.202)$$

$$\approx \Phi_{\text{LFN},M}(t_{A'}) - 2\pi\delta\nu_{\text{LFN},M} \cdot (\Delta t_{B'A'} + \delta\tau_M(t_{A'} - \Delta t_{B'A'})) \\ - (\Phi_{\text{LFN},M}(t_{A'}) - 2\pi\delta\nu_{\text{LFN},M} \cdot (\Delta t_{EA'} + \delta\tau_M(t_{A'} - \Delta t_{EA'}))) \quad (2.203)$$

$$\approx -2\pi\delta\nu_{\text{LFN},M} \cdot (-\Delta t_{EB'} + \delta\tau_M(t_{A'}) - \delta\tau_M(t_{A'} - \Delta t_{EA'})) \quad (2.204)$$

$$\approx 2\pi \cdot \delta\nu_{\text{LFN},M}(t_{A'}) \cdot (+\Delta t_{EB'} - \delta\dot{\tau}_M(t_{A'}) \cdot \Delta t_{EA'}) \quad (2.205)$$

$$\approx 2\pi \cdot \delta\nu_{\text{LFN},M}(t_{A'}) \cdot 2 \cdot \rho_{\text{inst}}(t_{A'})/c. \quad (2.206)$$

The laser phase variations almost cancel each other, since the phase (noise) is compared to itself with a small delay. The remaining frequency variations $\delta\nu_{\text{LFN},M}$ couple via the round-trip distance (or delay). The round-trip delay $\Delta t_{EA'}$ was omitted from eq. (2.205) to (2.206), because it is multiplied with the small $\delta\dot{\tau}$ and with $\delta\nu_{\text{LFN},M}$, which is also much smaller than the optical frequency ($2\pi \cdot \delta\nu_{\text{LFN},M} \ll \bar{\omega}_{M|M}$).

The phase ramp due to the frequency offset $\omega_{\text{off},S}$ on the slave S/C in eq. (2.194) is driven by the USO on the slave S/C, which can be rewritten with the help of eq. (2.97) as

$$\omega_{\text{off},S} \cdot \tau_{\text{USO},S}(\tau_S(t_{A'} - \Delta t_{AA'})) \quad (2.207)$$

$$= \omega_{\text{off},S} \cdot \tau_S(t_{A'} - \Delta t_{AA'}) + \omega_{\text{off},S} \cdot \delta\tau_{\text{USO},S}(\tau_S(t_{A'} - \Delta t_{AA'})) \quad (2.208)$$

$$= \omega_{\text{off},S} \cdot (t_{A'} - \Delta t_{AA'} - \delta\tau_S(t_{A'} - \Delta t_{AA'})) + \omega_{\text{off},S} \cdot \delta\tau_{\text{USO},S}(\tau_S(t_{A'} - \Delta t_{AA'})) \quad (2.209)$$

$$\approx \underbrace{\omega_{\text{off},S} \cdot t_{A'} - \omega_{\text{off},S} \cdot \delta\tau_S(t_{A'})}_{\omega_{\text{off},S} \cdot \tau_S(t_{A'})} - \omega_{\text{off},S} \cdot \Delta t_{AA'} + \omega_{\text{off},S} \cdot \delta\tau_{\text{USO},S}(\tau_S(t_{A'})) \quad (2.210)$$

$$\approx \omega_{\text{off},S} \cdot t_{A'} - \omega_{\text{off},S} \cdot \delta\tau_S(t_{A'}) - \omega_{\text{off},S} \cdot \rho_{\text{inst}}(t_{A'})/c_0 + \delta\varphi_{\text{off},\text{USO},S}. \quad (2.211)$$

It contains a constant phase ramp $\omega_{\text{off},S} \cdot t$, which should be ideally modeled via the proper time, i.e. $\omega_{\text{off},S} \cdot \tau_S$. Because this term depends on the proper time of the slave S/C, it gives rise to a transverse Doppler effect, however, only for the offset frequency, which is typically of the order of $\omega_{\text{off}}/\bar{\omega}_{M|M} \approx 10^{-7}$ compared to the optical carrier frequency. Furthermore, a one-way delay $\Delta t_{AA'} \approx \rho_{\text{inst}}(t_{A'})/c_0$ is present, which also causes a longitudinal Doppler effect in the offset frequency with a small magnitude ($\approx 10^{-7}$) relative to the primary ranging information. These terms appear in the phase of the master S/C and may cancel with a proper combination with the slave data stream in a final ranging measurement, which will be addressed in the next subsection.

The last approximation concerns the delay term $\omega_{\text{off},S} \cdot \Delta\tau_{p,S}$ from the frequency offset PLL, which appeared in eq. (2.194). It is the delay from photoreceiver, phasemeter DPLL and first decimation filter on the slave S/C. This delay is constant in the local Lorentz frame of the slave S/C, where it is denoted as $\mathcal{N}_{p,S}$. However, in the GCRS, the delay appears

modulated with the proper time of the slave satellite, which can be written as

$$\omega_{\text{off},S} \cdot \Delta\tau_{p,S} \approx \omega_{\text{off},S} \cdot \mathcal{N}_{p,S} \cdot (1 - \delta\tau_S) = \text{const.} - \omega_{\text{off},S} \cdot \mathcal{N}_{p,S} \cdot \delta\dot{\tau}_S. \quad (2.212)$$

This approximation has been already used in eq. (2.188) for the delay of the second decimation filter $\mathcal{N}_{\text{USO,Dec2},S}$, which in fact is much larger than $\mathcal{N}_{p,S}$, because $\mathcal{N}_{p,S}$ is part of the fast high-bandwidth DPLL. Thus, bearing the magnitude of $\mathcal{N}_{\text{USO,Dec2},S}$ from fig. 2.36 in mind, one can safely omit this contribution.

2.4.5 Transponder-based Ranging

Summarizing the recent approximations, one obtains for the phase measurement on the master S/C in a transponder scheme the following expression:

$$\begin{aligned} \varphi_{\text{PM}|M}(t) \approx & +\omega_{\text{off},S} \cdot t \pm (\bar{\omega}_{M|M} \mp \omega_{\text{off},S}/2) \cdot 2 \cdot \rho_{\text{inst}}(t)/c_0 + \bar{\omega}_{M|M} \cdot \delta t_{\text{ifo}}(t) \\ & \pm 2\pi \cdot \delta\nu_{\text{LFN},M}(t) \cdot 2 \cdot \rho_{\text{inst}}(t)/c_0 \\ & - \omega_{\text{off},S} \cdot \delta\tau_S(t) \mp \bar{\omega}_{M|M} \cdot \delta\dot{\tau}_M(t) \cdot 2 \cdot \rho_{\text{inst}}(t)/c_0 \pm \bar{\omega}_{M|M} \cdot \Delta t_{\text{QPR,corr}} \\ & \mp \vartheta_S(t - \rho_{\text{inst}}(t)/c_0) \mp \delta\varphi_{\text{PM},S}(t - \rho_{\text{inst}}(t)/c_0) + \delta\varphi_{\text{off,USO},S} \\ & \mp \vartheta_M(t) + \Upsilon_{\text{PR},M}(t) + \delta\varphi_{\text{PM,USO},M}(t) + \delta\varphi_{\text{PM},M}(t) + \Upsilon_{\text{PM},M}(t) \\ & \mp \mathcal{O}(1/H_{\text{Loop},S}) + \text{const.}, \end{aligned} \quad (2.213)$$

The six lines contain 1) a phase ramp due to the offset frequency, the ranging signal and the interferometer instrument dependent error δt_{ifo} of both S/C, 2) the laser frequency noise, 3) relativistic terms, 4) and 5) other contributors such as effects from the wavefront overlap, transfer functions and USO induced timing errors, 6) constant bias and terms of the order $\mathcal{O}(1/H_{\text{Loop},S})$.

One should notice from the second addend in the first line in eq. (2.213) that the instantaneous range is encoded at the optical frequency $(\bar{\omega}_{M|M} \mp \omega_{\text{off},S}/2)$, which is actually the mean angular frequency $\tilde{\omega}$ between master and slave laser, i.e.

$$\tilde{\omega} = \frac{\bar{\omega}_{M|M} + \bar{\omega}_{S|S}}{2} = \bar{\omega}_{M|M} \mp \frac{\omega_{\text{off},S}}{2}. \quad (2.214)$$

In addition, the phase ramp due to the offset frequency and its relativistic modulation $(\omega_{\text{off},S} \cdot \delta\tau_S)$ need to be removed from $\varphi_{\text{PM}|M}$ to obtain a reasonable ranging measurement. This can be achieved most easily by subtracting the phase measurement of the slave S/C $\varphi_{\text{PM},S}^{(\text{CL})}$ given by eq. (2.187) from $\varphi_{\text{PM}|M}$. In total, one can transform the phase observations in a transponder scheme to the equivalent (single-way) inter-satellite distance ρ_{MS} by (cf. eq. (2.182))

$$\rho_{\text{MS}} = \frac{c_0 \cdot \varphi_{\text{PM}|M}(t) - c_0 \cdot \varphi_{\text{PM}|S}^{(\text{CL})}(t)}{\pm 2 \cdot \tilde{\omega}_{\text{est.}}} + \epsilon_{\text{SCF}} + \text{const.}, \quad (2.215)$$

where $\tilde{\omega}_{\text{est.}}$ denotes the best-knowledge or estimated mean laser frequency of master and slave laser, and ϵ_{SCF} is a scale factor error arising from the difference between $\tilde{\omega}_{\text{est.}}$ and $\tilde{\omega}$. It is remarked that the previous equation used a combination of phase measurements at the same coordinate time. Another way to define the phase-derived range is via the delayed slave measurement, which is equivalent to the previous formula in the high loop gain limit, i.e.

$$\rho_{\text{MS}} = \frac{c_0 \cdot \varphi_{\text{PM}|M}(t) - c_0 \cdot \varphi_{\text{PM}|S}^{(\text{CL})}(t - \rho_{\text{inst,est.}}(t)/c_0)}{\pm 2 \cdot \bar{\omega}_{M|M,\text{est.}}} + \epsilon_{\text{SCF}} + \text{const.}, \quad (2.216)$$

which now contains the estimated frequency of the master laser $\bar{\omega}_{M|M,\text{est.}}$ and the estimated absolute inter-satellite distance $\rho_{\text{inst,est.}}(t)$. The latter one needs to be precise to a few $\text{cm}/\sqrt{\text{Hz}}$ and can be obtained from GNSS observations. For the second approach (eq. (2.216))

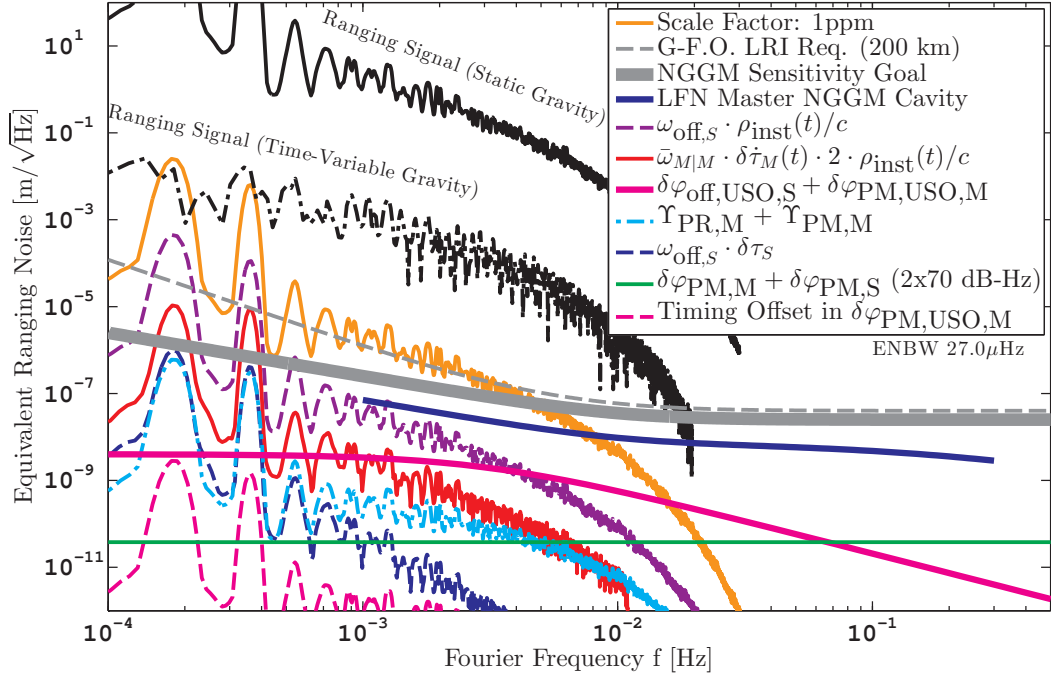


Figure 2.37: Different constituents in the transponder-based phase observable (cf. eq. (2.213)). The phase variations have been converted to (one-way) equivalent displacement variations (cf. eq. (2.214)) under the assumption of a wavelength of $\lambda = 1064$ nm. All traces are based on the NGGM baseline length $L = 100$ km, except for the requirement of the GRACE Follow-On LRI.

one might omit the simplifications shown in eq. (2.207)-(2.211) for $\varphi_{PM|M}$, because this leaves the offset frequency terms in the same form as in $\varphi_{PM|S}^{(CL)}$. The validity of eq. (2.215) becomes apparent, if one expands the phase from the slave S/C:

$$\varphi_{PM|S}^{(CL)}(t - \rho_{\text{inst,est.}}(t)/c_0) \approx \varphi_{PM|S}^{(CL)}(t) - \frac{d\varphi_{PM|S}^{(CL)}}{d\tau_S} \cdot \frac{d\tau_S}{dt} \cdot \rho_{\text{inst,est.}}(t)/c_0 \quad (2.217)$$

$$\approx \varphi_{PM|S}^{(CL)}(t) - \omega_{\text{off},S} \cdot \rho_{\text{inst,est.}}(t)/c_0 \quad (2.218)$$

The delayed slave phase measurement contains a term $\omega_{\text{off},S}$, which can cancel the corresponding term in the second addend in the first line of eq. (2.213). Thus, the ranging information is encoded at the frequency of the master laser in the combination of both phase measurements.

The distinction between the estimated optical frequency of the master S/C and of the estimated mean optical frequency between master and slave is rather of academic interest for GRACE Follow-On, since the knowledge of the laser frequency and, thus, the scale factor error is likely larger than $\omega_{\text{off},S}/\bar{\omega} \approx 10^{-7}$.

Most of the constituents of ρ_{MS} , and hence of $\varphi_{PM|M}$, are shown in fig. 2.37. The black traces at the top indicate the actual ranging signal between both S/C from the static and temporal gravity field, which have been separated for illustration in this plot. The gray dashed trace is the GRACE Follow-On LRI sensitivity with $80 \text{ nm}/\sqrt{\text{Hz}} \times \text{NSF}_1(f)$, which is based on a spacecraft separation ≤ 270 km. The other traces and the thick gray NGGM sensitivity goal of $25 \text{ nm}/\sqrt{\text{Hz}} \times \text{NSF}_2(f)$ consider a separation of 100 km. The laser frequency noise shown as thick dark blue line is based on the NGGM stabilized laser frequency noise requirement (cf. eq. (2.77)), which is far below the actual ranging signal. The scale factor error ϵ_{SCF} of 1 ppm relative to the ranging signal is the orange trace. The dashed purple line ($\omega_{\text{off},S} \cdot \rho_{\text{inst}}(t)/c_0$) demonstrates the effect of the Doppler shift in the offset frequency, however, it appears not as an error if eq. (2.216) is utilized. It would appear as an error if,

for example, the angular frequency of the master laser ($\bar{\omega}_{M|M,\text{est.}}$) would be used instead of the mean frequency of master and slave ($\bar{\omega}_{\text{est.}}$) in eq. (2.215). The red trace indicates the relativistic modulation of the master laser, e.g. due to the velocity of the S/C and due to the gravitational frequency shift of the laser light. This effect can be reduced in post-processing from the measurements, since it is a non-stochastic contribution. The solid magenta line illustrates the effect of USO timing jitter on the phase ramp on the slave satellite ($\delta\varphi_{\text{off,USO},S}$) and on the time-tags of phase samples obtained on the master satellite ($\delta\varphi_{\text{PM,USO},M}$). The shown curves assume already a post-processing correction, which means that drifts and errors of both USOs are reduced by GNSS observations (cf. sec. 2.98). At the bottom (magenta dashed trace) is the error due to the USO timing offset of 100 ps on the master, which is a second term in $\delta\varphi_{\text{PM,USO},M}$. It is negligible compared to the other delays due to the uncertainty in the transfer functions ($\Upsilon_{\text{PR},M} + \Upsilon_{\text{PM},M}$), which are shown combined by the light blue trace. It is recalled that the effect of the transfer function of the photoreceiver and phasemeter (ADC, DPPL and first decimation filter) was modeled as pure delay, which is reduced in post-processing to a value of ≈ 25 ns. The dashed dark blue trace ($\omega_{\text{off},S} \cdot \delta\tau_S$) demonstrates the effect of the relativistic modulation of the frequency offset. It would appear as an error, if one would derive the range ρ_{MS} by subtracting a phase ramp in the coordinate time ($\omega_{\text{off},S} \cdot t$) from $\varphi_{\text{PM}|M}$, instead of using the measurement from the slave S/C, which is a phase ramp with respect to the proper time ($\omega_{\text{off},S} \cdot \tau_S$). Finally, the green trace at the bottom shows the conservative phase readout noise, which would be caused by a carrier-to-noise density of 70.0 dB-Hz on both S/C. This choice is conservative, because this numerical value is the threshold for uninterrupted phase tracking (cf. sec. 2.3.7 on phasemeter), while the actual signal-to-noise ratio is expected to be higher in nominal science operation. Thus, the phase readout noise would be even lower.

Two terms from eq. (2.213) are not shown in the figure: the effects on the propagation time of the light Δt_{QPR} between the satellites and instrument induced errors δt_{ifo} . These will be addressed in subsequent sections of this thesis.

2.4.6 Transponder-based Ranging: Low Gain

The phase observable in a transponder scheme on the master S/C denoted as $\varphi_{\text{PM}|M}$ (cf. eq. (2.213)) and on the slave S/C $\varphi_{\text{PM}|S}^{(\text{CL})}$ (cf. eq. (2.187)) was formulated in the infinite gain limit ($H_{\text{loop},S} \rightarrow \infty$) of the frequency offset PLL, i.e. expanded to zeroth order in $1/H_{\text{loop},S}$. Terms due to finite gain were absorbed in $\mathcal{O}(1/H_{\text{loop},S})$.

However, the transponder scheme can also be used with low loop gain, which is quickly derived in the Laplace domain. It is recalled that the closed-loop phase measurement on the slave S/C can be written according to the block diagram in fig. 2.27 as

$$\varphi_{\text{PM},S}^{(\text{CL})}(s) = (\Phi_{\text{RX}}^c(s) - \Phi_{\text{LO}}^c(s)) \cdot H_p^c(s) \cdot H_{\text{Dec2}}^c(s) + F^c(s), \quad (2.219)$$

which holds for an arbitrary loop gain, i.e. arbitrary $H_{\text{PZT+Temp}}^c(s)$ in sec. 2.3.9, because the gain is implicitly present in the phase of the local laser light Φ_{LO}^c . The transfer function of the photoreceiver, ADC, DPPL and first decimation filter is denoted as $H_p^c(s)$, while $H_{\text{Dec2}}^c(s)$ is the transfer function of the second decimation filter. The function $F^c(s)$ contains the wavefront overlap phase ϑ^c and the USO timing jitter $\delta\varphi_{\text{PM,USO}}^c$, but it is independent of the loop gain. The phase of the received light $\Phi_{\text{RX}}^c(s)$ on the slave S/C can be written as the phase of the master laser $\Phi_M^c(s)$ delayed by the propagation time Δt_{EA} from master to slave (see event labels in fig. 2.35), i.e.

$$\Phi_{\text{RX}}^c(s) = \Phi_M^c(s) \cdot D_{EA}^c(s). \quad (2.220)$$

The phase of the light at the emission event B on the slave S/C has been stated in eq. (2.140) as

$$\Phi_B^c(s) = \frac{\Phi_{\text{LO}}^c(s)}{D_{BA}^c(s)}. \quad (2.221)$$

One can write the relation between $\varphi_{\text{PM},S}^{(\text{CL})}(s)$ and $\Phi_B^c(s)$ with eq. (2.219) and (2.221) as

$$\Phi_B^c(s) = \frac{\Phi_{\text{RX}}^c(s)}{D_{BA}^c(s)} - \frac{\varphi_{\text{PM},S}^{(\text{CL})}(s) - F^c(s)}{D_{BA}^c(s) \cdot H_p^c(s) \cdot H_{\text{Dec2}}^c(s)}. \quad (2.222)$$

The phase measurement on the master S/C can be approximated as the phase difference between the phase of the local laser and of the received light

$$\varphi_{\text{PM},M}^c(s) \approx \Phi_M^c(s) - \Phi_B^c(s) \cdot D_{BA'}^c(s), \quad (2.223)$$

where $D_{BA'}^c$ is a delay due to the propagation time from slave to master. It is easy to see that the linear combination $\Theta_{MS}(s)$ of master and slave phase measurements

$$\begin{aligned} \Theta_{MS}(s) &= \varphi_{\text{PM},M}^c(s) - X^c(s) \cdot \varphi_{\text{PM},S}^{(\text{CL})}(s) \\ &= \Phi_M^c(s) - \Phi_M^c(s) \cdot \underbrace{\frac{D_{EA}^c(s) \cdot D_{BA'}^c(s)}{D_{BA}^c(s)}}_{=D_{EA'}^c(s)} - \underbrace{\frac{D_{BA'}^c(s)}{D_{BA}^c(s)}}_{=D_{AA'}^c(s)} \cdot \frac{F^c(s)}{H_p^c(s) \cdot H_{\text{Dec2}}^c(s)}, \end{aligned} \quad (2.224)$$

yields the result in the second line (eq. (2.224)), which is independent of the loop gain, for

$$X^c(s) = \frac{D_{BA'}^c(s)}{D_{BA}^c(s) \cdot H_p^c(s) \cdot H_{\text{Dec2}}^c(s)} = \frac{D_{AA'}^c(s)}{H_p^c(s) \cdot H_{\text{Dec2}}^c(s)}. \quad (2.225)$$

The first two summands in eq. (2.224) denote the phase change of the master laser during the round-trip propagation time $\Delta t_{EA'}$. This difference contains the ranging information and is independent of the laser phase noise from the slave S/C. The last addend depending on F^c contains the USO timing jitter and the wavefront overlap phase ϑ^c from the slave S/C. The X^c in eq. (2.225) shows the required transformation of the phase measurement from the slave satellite to cancel the slave laser contributions in Θ_{MS} for an arbitrary loop gain. It consists of a one-way delay $\Delta t_{AA'}$, which is the time difference between photon reception on the slave and on the master S/C. Moreover, the effects of the transfer functions H_p^c and H_{Dec2}^c , i.e. of the photoreceiver, ADC, DPLL, and both decimation filters on the slave, need to be reversed. The reversal of $H_p^c(s) \cdot H_{\text{Dec2}}^c(s)$, which are assumed as pure delays in this thesis, has been implicitly performed in the previous sections. The effect of the transfer functions after this post-processing reversal was denoted with $\Upsilon_{\text{PR}} + \Upsilon_{\text{PM}}$ in most of the previous plots.

In fact, the transformation derived here in the Laplace domain is in agreement with the time-domain eq. (2.216), where the estimated propagation time $\rho_{\text{inst,est.}}/c_0$ corresponds to $\Delta t_{AA'}$. Thus, the laser phase variations from the slave S/C are canceled even with finite or low loop gain, if the transponder combination in eq. (2.216) is utilized for Θ_{MS} .

The phase variations in Θ_{MS} consisting of ranging information and noises such as master laser frequency fluctuations are located completely on the master side in a high gain frequency offset PLL. Thus, the ranging information is distributed asymmetrically between master and slave S/C. However, more and more phase variations appear in the slave phasemeter output, if the gain is gradually decreased. This would yield exactly the same results as in the high-gain limit, if all delays and the propagation time $\Delta t_{AA'} = \rho_{\text{inst,est.}}/c_0$ are known without errors. In practice, there is a higher noise in Θ_{MS} for a weak phaselock due to the uncertainties in the delays of the phasemeter and photoreceiver, of the propagation time and of the USO timing offset. However, the increase in noise would become only noticeable when it exceeds other noise sources.

In fact, Francis *et al.* [2015] have suggested to decrease the gain of the frequency offset PLL in the GRACE Follow-On LRI to test the so-called time-delay interferometry for LISA, which is essentially a technique to determine the propagation delays and to obtain Θ_{MS} . A comparison of the low-gain and high-gain transponder scheme and further discussion is postponed to the section after next, because an alternative functional concept is briefly addressed beforehand.

2.4.7 Passive Retro-Reflector Ranging

A passive retro-reflector concept has been suggested, for example, in [Alenia-Team, 2008] for a gravimetric mission. The idea is to replace the interferometry on the slave satellite by a passive retro-reflector, e.g. a corner cube.

As the returned light power to the master satellite scales with L^{-4} in such a concept, the maximum inter-satellite separation is limited to $L \ll 100$ km and requires a large open aperture of the retro-reflector to increase the amount of reflected light and likely a telescope on the master craft. If a large hollow corner-cube is used, diffraction effects from the edges and de-polarization effects might degrade the phasefront quality and therefore ranging performance. Furthermore, it might become difficult to place the vertex of the large retro-reflector close to the center of mass of the S/C, and hence to reduce attitude-to-ranging coupling. In addition, as there is no frequency offset imposed onto the reflected light, the interferometry on the master satellite needs to handle zero crossings of the beatnote frequency, or additional frequency shifting components need to be introduced. These points let the author of this thesis consider such a scheme to be less suited for precise inter-satellite ranging.

2.4.8 Comparison and Summary

This section 2.4 has addressed one-way ranging, dual one-way ranging, transponder-based ranging and touched briefly on passive retro-reflectors. The one-way ranging turned out to be unfeasible for a gravimetric mission, because the (laser) phase noise is not suppressed in such a scheme. One approach to mitigate this issue is to perform a round-trip measurement by sending the laser light back to the emitter S/C, e.g. by a passive retro-reflector on the distant S/C. Then one can perform a comparison between the delayed and non-delayed light phase by beating the round-trip delayed light with the local laser light, which removes the common phase, while the remaining part is, for small round-trip delays Δt , the product of instantaneous laser frequency and round-trip propagation time Δt . The delay time Δt contains the ranging information, while the instantaneous frequency of the light consists of the (constant) carrier light frequency and laser frequency noise. Thus, the observed phase is not falsified by laser phase noise anymore but by the laser frequency noise, which turns out to be beneficial for frequencies in the science measurement band ($f \ll 1$ Hz) and for S/C separations present in gravimetric missions.

Although the use of a passive retro-reflector is conceptionally simple, it turns out to be practically suboptimal due to the scaling of the returned power with the inverse fourth power of the distance L^{-4} and due to clipping of beams. Furthermore, regular zero crossings of the beatnote frequency appear due to the sinusoidal modulation of the range rate in gravimetric missions, which are difficult to handle in heterodyne interferometry. These issues can be circumvented by transponder-based concepts, where the slave S/C acts as active retro-reflector. This means the slave S/C amplifies the received light power by transmitting a power enhanced laser beam with the same phase as the received beam. It is beneficial for the master S/C and for the slave S/C, which is the transponder, if the transponder introduces a small frequency-offset into the back-reflected light, such that zero crossings of the beatnote frequencies are removed on both S/C.

The laser source on the transponder S/C can have a higher phase and frequency noise than the master laser, because the phase of the slave laser needs to be locked anyway to the phase of the incoming light field by means of a frequency offset PLL. Typically, the control loop gain can be made sufficiently high, such that the slave S/C measures simply a phase ramp due to the offset frequency, while the master S/C measures the phase ramp, the round-trip ranging information, i.e. twice the one-way Doppler shift, and the laser frequency noise of the master laser. In principle, one can discard the phase measurement of the slave S/C in on-ground processing, since the ranging information is in the data stream of the master S/C. The frequency noise of the master laser does not cancel out, which means that the master laser should be stabilized to a frequency standard such as a cavity.

It is remarked that the laser subsystems on both S/C need the capability to actuate the optical frequency with high bandwidth to achieve a high gain frequency offset PLL on the slave and to lock the laser to a frequency standard on the master. Thus, the role of master and slave S/C can be made interchangeable, if both S/C are equipped with frequency standards and frequency offset PLLs, which introduces cold-redundancy for some parts as demonstrated in the GRACE Follow-On LRI.

The transponder concept can also be used with an intermediate or low gain frequency offset PLL, where the phase measurement on the slave is not simply a phase ramp but contains also ranging information and noise. Then, the phase measurement from slave and master need to be combined with the correct delay. This delay is the light propagation time from the slave to the master S/C, in other words, one needs to evaluate the phase measurements from master and slave at slightly different instances of time. The phase difference removes the phase and frequency noise from the slave laser and the phase ramp, whereby the correct round-trip ranging information is restored. However, additional noise is practically introduced in a low gain transponder, since the delay for the synthesis of the combined phase has a limited accuracy. It should be noted that a weak phaselock still needs sufficient gain, so that the beatnote frequencies on both S/C are maintained in the measurement frequency band of the photoreceiver and phasemeter.

Major advantages of a high-gain transponder are the lower susceptibility to errors in timestamps and delays and the cancellation of laser phase noise directly in the optical domain prior to the photodiodes and digitization in contrast to a cancellation in post-processing.

Similar to the low-gain transponder is a dual one-way ranging (DOWR) approach, where data streams from both S/C are evaluated at a common (reception) time. It is being utilized in the microwave ranging of GRACE and GRACE Follow-On. The DOWR synthesis does not cancel the phase or frequency noise of a particular laser, because both wave sources are assumed to have the same noise characteristics. Instead, the DOWR removes the phase noise of both lasers symmetrically for time-scales of the one-way delay time and larger. Thus, what remains is the laser frequency noise of both lasers scaled by the one-way propagation time. The DOWR is optimal, if both lasers have the same frequency noise and are uncorrelated, because it reduces the remaining laser noise by a factor of $\sqrt{2}$. The individual phase measurements of both S/C contain the full phase noise of both wave sources, as in the low-gain transponder. Hence, the DOWR shows also a higher susceptibility to delays and timing offsets compared to the high-gain transponder.

Although the balanced distribution of phase variations on master and slave S/C in the DOWR and low-gain transponder is accompanied with higher susceptibility to timing offsets and delays, it has the advantage that the range rate induced Doppler frequency shift can be distributed onto two photoreceivers and phasemeters. The beatnote frequency of the photodiode signal on the master, i.e. the slope of the measured phase ramp, consists in a high-gain transponder concept of the round-trip Doppler shift plus the frequency offset, while in the balanced scheme it is only the one-way Doppler plus the frequency offset. Thus, the maximum relative velocity along the line-of-sight, where the beatnote frequency exceeds the measurement frequency band of photoreceiver and phasemeter, can be twice as high under optimal conditions. For example, if one considers an operational frequency band of 4 MHz..20 MHz and an offset frequency of 12 MHz, it would allow a maximum one-way Doppler shift of ± 4 MHz in a high-gain transponder and of ± 8 MHz in a DOWR scheme. These values correspond to an approximate maximum range rate of ± 4 m/s and ± 8 m/s for an optical wavelength of 1064 nm. However, the dynamic range of the high-gain transponder can be doubled as well, if a time-dependent offset frequency is used to counteract the a-priori well-known sinusoidal ranging induced Doppler shift.

Dual one-way ranging by means of optical interferometry is difficult to achieve, because the laser light on both S/C needs to be stabilized to an absolute frequency offset by a few MHz between satellites. Thus, one can not simply lock both lasers to cavity-based frequency standards, which have indistinguishable and equally spaced resonance frequencies. Further-

<p>Both S/C laser (S/C A + S/C B) same noise</p> <ul style="list-style-type: none"> → Dual One-Way Ranging: Common reception time → Frequency difference between lasers required to keep beatnote frequency in-band → No estimation of absolute distance required → Master phase: \sim Ramp + LPN(A) + LPN(B) + Doppler → Slave phase: \sim Ramp + LPN(A) + LPN(B) + Doppler → Laser phase noise cancels in post processing → Doppler distributed equally between S/C; higher range rate possible → Susceptibility to timing offsets due to high magnitude of phase measurements → Final ranging noise: \sim LFN \times L \times 2 \times 1/20 	<p>High noise (slave) and low-noise (master) laser</p> <ul style="list-style-type: none"> → cold redundancy of a frequency stabilization possible, if both S/C equipped with frequency standard <p>Option 1: High gain frequency-offset PLL on slave S/C</p> <ul style="list-style-type: none"> → Slave laser does not appear in phase measurements for high gain → No estimation of absolute distance required → Master phase: \sim Ramp + LFN(M) \times 2 \times L + 2x Doppler → Slave phase: only Ramp → Slave phase measurement in principle not required on-ground → Laser phase noise cancels in optical domain → Higher range rate possible with time-variable offset frequency → Final ranging noise: \sim LFN(M) \times L \times 2 <p>Option 2: Low gain frequency-offset PLL on slave S/C</p> <ul style="list-style-type: none"> → PLL required to keep beatnote in-band → estimation of absolute distance necessary → Master phase: \sim Ramp + LPN(M) + LPN(S) + Doppler → Slave phase: \sim Ramp + LPN(M) + LPN(S) + Doppler → Laser phase noise cancels in post processing → Doppler distributed equally between S/C; higher range rate possible → Susceptibility to timing offsets due to high magnitude of phase measurements → Final ranging noise: \sim LFN(M) \times L \times 2
--	--

Figure 2.38: Executive summary of the comparison of dual one-way ranging (left column) and of transponder-based ranging (right column). The following abbreviations are used: Laser Phase Noise (LPN); Laser Frequency Noise (LFN), which is the time-differentiated LPN; absolute inter-satellite distance (L); Master (M); Slave (S).

more, a cavity has a poor absolute frequency stability, because 1 ppm absolute frequency stability requires a mechanical stability and a manufacturing tolerance of the absolute length of the cavity at the level of 0.5 picometer (at DC), if optical light with 1 μ m wavelength is used.

An executive summary for the comparison of the relevant functional concepts is shown in fig. 2.38.

In space laser interferometry, such as in the LISA pathfinder mission and in the LISA mission concept, NPRO lasers at 1064 nm wavelength are favored, since they show a low intrinsic free-running frequency noise and a low amplitude noise, and they can be easily shifted in the optical frequency by a few per mill with temperature and piezo-electric actuators. In general, lasers can stably operate on a single longitudinal mode (frequency) only in a particular range of setpoints, which can even vary among lasers of the same batch due to manufacturing tolerances. Thus, frequency standards based on cavities are very prominent in precision metrology, since they can serve at various frequencies. In addition, they are to a large degree independent of the wavelength⁸ and of the used lasers as long as the laser can be frequency locked to the cavity resonances.

NPRO-based lasers with a cavity-based frequency stabilization likely offer the simplest means to obtain frequency stabilized light in space, not least since both components have a stand-alone value and can be developed and advanced as independent subsystems. In combination with a transponder functional concept, they enable precise laser ranging interferometry. This combination is very appealing for space missions and has been extensively studied for decades within the LISA mission and it has been qualified for flight, i.e. reached TRL 8, within the GRACE Follow-On mission by the time of this writing.

The aforementioned advantages and the maturity from the heritage of LISA and GRACE Follow-On makes transponder-based ranging with NPRO lasers and cavity-based frequency standards a good choice for future gravimetric missions, especially because the next generation of gravimetric missions will be likely not limited by ranging noise. Some operational constraints of this interferometry concept such as the maximum range rate of a few m/s can be extended with a time-variable offset frequency or even further with more complex extensions discussed in [e.motion² Team, 2014, sec. 5.3.2.3, enhanced dynamic range].

Detailed expressions for the phase observables in dual one-way ranging schemes and in

⁸The optical coatings within the cavity are wavelength dependent.

transponder-based ranging concepts have been derived from first principles in the previous sections. The constituents of the phase observable depending on the functional concept have been discussed, while the discussion of corrections to the photon time of flight and the instrument specific errors δt_{ifo} , which contain the major attitude jitter induced noise, are postponed to the next section and to sec. 2.6, respectively.

The other major contributor to the overall instrument noise is the laser phase or frequency noise. Furthermore, the analysis in the previous sections showed that the limited knowledge of the absolute laser frequency of 1 ppm yields a scale factor error, which can be plotted as an effective noise with a 1 ppm magnitude relative to the actual ranging signal. It is not a stochastic noise and can be, in principle, corrected in post-processing by estimating the optical frequency in the process of gravity field recovery. This error is specific to gravimetric missions, as in these missions the ranging information with SI unit of meters is combined with other measurements, while gravitational wave missions, for example, measure a relative distance change, i.e. dimensionless strain. It might be rather challenging to improve the 1 ppm value significantly, since in a concept with cavity-based frequency standard, discussed here, the absolute frequency is derived from the setpoint of the laser. One way to improve the knowledge on the absolute value of the wavelength is to use a dedicated instrument to measure it directly in-orbit, e.g. with a wavemeter or diffraction grating. However, these instruments can hardly exceed the 1 ppm resolution to the knowledge of the author, such that an absolute frequency standard may be more favorable.

In summary, the cavity and transponder based approach is most likely sufficient for the next gravimetric mission(s). However, as this thesis also aims to advance space laser interferometry, the following concept is proposed, which is motivated by the findings of the previous sections.

Challenges in laser interferometry discussed so far are the reduction of laser frequency noise, improvement of the absolute frequency knowledge and increase of the maximum allowed range rate. Moreover, it should be envisioned to reduce the complexity in the laser link acquisition (cf. sec. 2.3.10 and 2.6.12). The maximization of the allowed range rate was addressed priorly (see above). The knowledge of the absolute frequency can be enhanced by several orders of magnitude with an absolute frequency standard (cf. sec. 2.3.2 on optical frequency standards), e.g. the transitions in an iodine cell are known to a level of approx. 10^{-11} . This would still allow to use a transponder scheme and, for the sake of redundancy, one might want to equip both S/C with such a standard to make the role of slave and master swappable. In addition, this yields almost identical S/C, which is often advantageous in terms of the integration and testing complexity and of accompanied costs. The phase and frequency noise of a laser locked to an iodine cell is comparable to the frequency noise of a cavity (cf. sec. 2.3.2). However, if two frequency standards are present on both S/C, one could also operate them in hot redundancy with a DOWR concept. This would provide two-fold advantages: on the one hand, the laser frequency noise is reduced by $\sqrt{2}$ and, on the other hand, the laser link acquisition is simplified significantly, since a degree of freedom is removed from the acquisition search. The disadvantage is that additional frequency-shifting components are required to obtain the frequency offset between the laser beams for heterodyne interferometry. In addition, the susceptibility to timing offsets and delays is increased. However, the effect of these offsets and delays can be regarded as negligible, which has been shown as a matter of prudence in fig. 2.34. It is noted that the transponder concept could still be used as fallback option without additional hardware, if a frequency standard fails, for example. In addition, it is remarked that these changes could be made completely in the back-end of the instrument and do not require modifications of the optical layout of the interferometer, e.g. the GRACE Follow-On LRI optical benches could be reused. The advantages of such a concept justify the higher complexity introduced by additional frequency shifting components, which is a first assessment made by the author of this thesis.

2.5 Photon Time of Flight Corrections

The one-way ranging phase observable of a laser interferometer on a satellite j can be written according to the previous section as (cf. eq. (2.164))

$$\varphi_j \propto \bar{\omega}_{i|i} \cdot \tau_i(t - \Delta t_{EA}) - \bar{\omega}_{j|j} \cdot \tau_j(t - \Delta t_{BA}) + \dots + \text{const.} \quad (2.226)$$

where φ_j is the measured phase in radian, $\bar{\omega}_{i|i}$ and $\bar{\omega}_{j|j}$ are the constant optical angular frequencies with units of rad/s of the emitter and receiver S/C, respectively, Δt_{EA} and Δt_{BA} are the propagation times of the light from the respective source to the photodetection at event A . The event labels A, B, \dots used here are shown in fig. 2.30. With approximations given in eq. (2.171) one arrives at the following simplified expression

$$\varphi_j \propto \tilde{\omega} \cdot \underbrace{\Delta t_{EB}}_{\Delta t_{EA} - \Delta t_{BA}} + \dots + \text{const.}, \quad (2.227)$$

where $\tilde{\omega}$ is the mean optical angular frequency between $\bar{\omega}_{i|i}$ and $\bar{\omega}_{j|j}$. Terms depending on the beatnote frequency $\Delta\tilde{\omega}$ have been omitted in eq. (2.227), because these are significantly smaller ($\Delta\tilde{\omega}/\tilde{\omega} \approx 10^{-7}$) and have been discussed to the relevant order already in the previous sec. 2.4. The actual inter-satellite ranging information is contained in $\Delta t_{EB} \approx \Delta t_{EA}$.

The most generic expression for a propagation time is given by a line integral along the path of the photon

$$\Delta t = \int \frac{n(t(s), \vec{r}(s))}{c_n(t(s), \vec{r}(s))} ds, \quad (2.228)$$

where c_n is the instantaneous coordinate speed of light and n denotes the refractive index of the media, where the light is propagating. The light path is parameterized with a parameter s .

In the non-relativistic limit, when the proper time $\Delta\tau$ and the coordinate time Δt are equivalent, and in good approximation also in a local Lorentz frame (LLF) of a satellite, one can split the light path into segments and determine the propagation time $\Delta\tau$ from piece-wise segments by

$$\Delta\tau = \frac{\text{AOPL}}{c_0} = \frac{\sum_{\text{seg}} n_{\text{seg}} \cdot \text{GPL}_{\text{seg}}}{c_0}, \quad (2.229)$$

where AOPL is the total accumulated optical pathlength, GPL_{seg} is the geometrical pathlength of a light path segment and n_{seg} is the refractive index of the segment. The sum is taken over all segments and all quantities are referred to the LLF or the non-relativistic limit. The proper vacuum speed of light is denoted with $c_0 = 299\,792\,458$ m/s, which is equal to the coordinate speed of light c_n in the non-relativistic limit.

To simplify the succeeding calculations, the light propagation time is expressed as small variation with respect to the ideal propagation time, which is the propagation time (Δt_{PQ}) of a freely and directly traversing photon between the start and end point. Recall that in inter-satellite laser interferometry the light is guided through optical setups, so-called optical benches, which are present on both satellites. One aims to measure the distance between both satellite gravitational reference points (GRPs), e.g. the center of mass (cf. eq. (2.150)). Thus, the ideal propagation time Δt_{PQ} is defined by the event Q , which denotes the photon reception at the GRP of the receiver S/C, and event P , which is the corresponding photon emission at the GRP of the emitter S/C, such that P and Q are connected via a freely propagating photon.

In addition, in gravimetric missions one is typically interested in the instantaneous geometrical distance ρ_{inst} between the GRPs. This motivates the expression for Δt_{EB} in terms

of the desired quantity ρ_{inst} and correction as done previously, for example, in eq. (2.175):

$$\Delta t_{EB}(t) = \Delta t_{EA}(t) - \Delta t_{BA}(t) = \rho_{\text{inst}}(t)/c_0 + \text{correction} \quad (2.230)$$

$$= \underbrace{\rho_{\text{inst}}(t)/c_0 + \Delta t_{PQ,\text{corr}}(t)}_{\Delta t_{PQ}} + \delta t_{EB,\text{ifo}}(t). \quad (2.231)$$

This equation is a definition for the correction and therefore exact. The correction has been divided into a term depending on the interferometer and optical benches $\delta t_{EB,\text{ifo}}$, or in other words, on local interferometer quantities, and into a term $\Delta t_{PQ,\text{corr}}$ absorbing other variations in the time of flight between satellites, which are not covered by the non-relativistic ideal time of flight in vacuum $\rho_{\text{inst}}(t)/c_0$. Non-relativistic refers to a static scenario, i.e. non-moving satellites or parts, and to a flat space-time with the Minkowski metric tensor applying to the GCRS.

Even though the instantaneous inter-satellite distance ρ_{inst} is well-defined, it can not be measured by the satellites directly. It can only be recovered in post-processing when all observations are transformed to the GCRS and relativistic and non-relativistic effects are subtracted from the observations. If ρ_{inst}/c_0 is supplemented by $\Delta t_{PQ,\text{corr}}$, which contains relativistic corrections and corrections due to the refractive index n , one obtains the ideal range measurement between the GRPs Δt_{PQ} . However, the measurement or observation Δt_{EB} differs from Δt_{PQ} by the laser interferometric error term $\delta t_{EB,\text{ifo}}$, which is mainly because the interferometer does not measure exactly the GRP-GRP distance but the distance between interferometer reference points.

The correction terms to the photon time of flight $\Delta t_{PQ,\text{corr}}$ can be decomposed into a sum

$$\Delta t_{PQ,\text{corr}} \approx \Delta t_{\text{SR}} + \Delta t_{\text{GR}} + \Delta t_{\text{Iono}} + \Delta t_{\text{Atmo}}, \quad (2.232)$$

with special relativistic effects Δt_{SR} , general relativistic effects Δt_{GR} , effects due to the ionosphere Δt_{Iono} and due to the neutral atmosphere Δt_{Atmo} . The formulation of Δt_{corr} as a sum of different effects is an approximation, because the effects are in general coupled. Since the space-time curvature and atmospheric density is small, deviations of the light path from a straight line and deviations of c_n from c_0 are small as well. Hence, the additive approximation is justified and sufficient for the purpose of this thesis.

The rather arbitrary separation of Δt_{EB} into terms $\Delta t_{PQ,\text{corr}}$ and δt_{ifo} is driven by the idea that $\Delta t_{PQ,\text{corr}}$ vanishes in the case of the non-relativistic limit and with vacuum as medium, which eases the comparison and interrelation of δt_{ifo} with simulation results of the interferometers obtained from ray-tracing, e.g. with the AEI in-house developed `ifocad` software. In such simplified domain, optical ray- and beam-tracing is typically performed with fixed optical setups on the time scales of light propagation and δt_{ifo} is expressed with the help of accumulated optical pathlengths (cf. eq. (2.229)). Whereas the here stressed time of flight domain stressed here, allows one to evaluate relativistic effects more easily. Furthermore, one has the advantage that the corrections in $\Delta t_{PQ,\text{corr}}$ can be determined solely between the GRPs and, hence, they are independent of the state of the interferometer or of the optical layout.

The expressions Δt_{corr} and δt_{ifo} are of importance for forward-modeling, i.e. generation of realistic ranging observations in simulations, and also for the retrieval of the instantaneous range from flight telemetry with real measured phase values, e.g. in the GRACE Follow-On LRI. The term δt_{ifo} , describing the local interferometry, and the time of flight corrections Δt_{corr} are analyzed in detail in the following subsections.

2.5.1 Local Interferometry

In one-way ranging, the local interferometry correction $\delta t_{EB,\text{ifo}}$ to the photon time of flight can be expressed in a general way with the help of eq. (2.231) as

$$\delta t_{EB,\text{ifo}}(t) = -\Delta t_{PE,i} + \Delta t_{QB,j}, \quad (2.233)$$

where $\Delta t_{PE,i}$ is the correction from the emitter S/C and $\Delta t_{QB,j}$ is the correction from the receiver side. These are time differences between events shown in fig. 2.30. In the non-relativistic limit and with ideal vacuum ($\Delta t_{PQ,corr} = 0$), one can obtain a more insightful expression as follows

$$\delta t_{EB,ifo}(t) = \Delta t_{EB}(t) - \frac{\rho_{inst}(t)}{c_0} = \frac{AOPL_{EA} - AOPL_{BA} - \rho_{inst}(t)}{c_0}. \quad (2.234)$$

This equation states simply that the interferometer error is the difference between the desired GRP-GRP distance and the interferometric range measurement, which is the optical path-length difference of measurement and local oscillator beam. Thus, the local interferometry correction should be understood here as a heuristic description of all local interferometer effects, which may contain, among others, temperature or actuator induced optical pathlength changes and effects from parasitic beams affecting the phase measurement.

It is self-evident that practically $\delta t_{EB,ifo}$ can contain an unknown bias, which can not be resolved by a phase measurement. However, in case of optical simulations, where the propagation time can be written in terms of the accumulated optical pathlengths, the quantity $\delta t_{EB,ifo}$ can be determined with correct bias.

The most important effect in $\delta t_{EB,ifo}$ is probably the susceptibility to satellite rotations, which yields an attitude-to-ranging coupling. This coupling can be interpreted as an offset between the center of mass of the satellite, which is the pivot point of rotations, and the interferometer reference point, which can be understood as the fiducial point for the range measurement. The attitude-to-ranging coupling is in detail treated in sec. 2.6. It should be noted that the magnitude of $\delta t_{EB,ifo}$ is in sensible interferometers close to the instrument noise level. Thus, relativistic effects within $\delta t_{EB,ifo}$, which are a few orders of magnitude smaller, are negligible.

2.5.2 Special Relativity

The special relativistic correction Δt_{SR} in the propagation time Δt_{PQ} between the satellite GRPs accounts for the effect of the motion of the satellites in the GCRS, which includes changes due to relativistic length contraction and Sagnac-like contributions. The measured range by a ranging interferometer contains these effects and they need to be reduced from the phase observable to obtain the desired instantaneous range ρ_{inst} . It is assumed for the moment that the medium, where the light is traversing between the satellites, is vacuum with $n = 1$ and that space-time is flat, i.e. the coordinate speed of light c_n equals the proper speed of light c_0 in vacuum.

Under these assumptions, the light is propagating along a straight line in the GCRS with speed of light c_0 . The photon propagation time between the two satellites labeled i and j can be obtained from the well-known implicit light-time equation [Montenbruck & Gill, 2000, eq. (6-23)]

$$\Delta t_{PQ}(t) = \Delta t_{ij}(t) = \frac{|\vec{r}_j(t) - \vec{r}_i(t - \Delta t_{ij}(t))|}{c_0}. \quad (2.235)$$

A successive approximation by iterative means starts with $\Delta t_{ij}^{(0)} = 0$ and solves

$$\Delta t_{ij}^{(n)}(t) = \frac{|\vec{r}_j(t) - \vec{r}_i(t - \Delta t_{ij}^{(n-1)}(t))|}{c_0}. \quad (2.236)$$

The coordinate time t is the reception time of the light, which equals t_A and t_Q in the context of this and previous sections. It is assumed that the coordinate position \vec{r} , the coordinate velocity $\vec{v} = d\vec{r}/dt$ and the coordinate acceleration of $\vec{a} = d^2\vec{r}/dt^2$ of both satellites are known, such that one can approximate the position of both satellites around the measurement time

t by

$$\vec{r}(t + \epsilon) \approx \vec{r}(t) + \epsilon \cdot \vec{v}(t) + \frac{\epsilon^2 \cdot \vec{a}(t)}{2}. \quad (2.237)$$

This approximation is sufficient, since the time derivative of the acceleration is for gravimetric missions of the order of $\dot{a} \approx 0.01 \text{ m/s}^3$, which yields with $\epsilon \approx 10^{-3} \text{ sec}$ a displacement error of $\epsilon^3/6 \cdot \dot{a} \approx 10^{-12} \text{ m}$. Thus, the above expression describes the satellite position with picometer accuracy.

With given derivatives one can approximate the solution to eq. (2.236) after a few iterations as a Taylor series in c_0^{-1} by

$$\begin{aligned} \Delta t_{ij}(t) = & \frac{\rho_{\text{inst}}}{c_0} - \frac{\vec{v}_i \cdot \vec{r}_{ji}}{c_0^2} + \frac{\vec{v}_i \cdot \vec{v}_i \cdot \rho_{\text{inst}}}{2 \cdot c_0^3} + \frac{\vec{a}_i \cdot \vec{r}_{ji} \cdot \rho_{\text{inst}}}{2 \cdot c_0^3} + \frac{(\vec{v}_i \cdot \vec{r}_{ji})^2}{2 \cdot c_0^3 \cdot \rho_{\text{inst}}} \\ & - \frac{(\vec{v}_i \cdot \vec{v}_i) \cdot (\vec{v}_i \cdot \vec{r}_{ji})}{c_0^4} - \frac{\vec{a}_i \cdot \vec{v}_i \cdot \rho_{\text{inst}}^2}{2 \cdot c_0^4} - \frac{(\vec{a}_i \cdot \vec{r}_{ji}) \cdot (\vec{v}_i \cdot \vec{r}_{ji})}{c_0^4} + \mathcal{O}(c_0^{-5}, \ddot{\vec{r}}). \end{aligned} \quad (2.238)$$

These eight terms of the sum are depicted as spectral density in the upper panel of fig. 2.39 for a typical GRACE-like formation (cf. caption). The legend contains also the average (DC) part of the terms. It can be concluded that the last two terms have negligible magnitude. The first summand is the actual instantaneous range, thus, the remaining terms form the sought special relativistic correction Δt_{SR} for the one-way ranging observable, i.e.

$$\Delta t_{\text{SR}}^{(\text{OWR})} = \Delta t_{ij}(t) - \frac{\rho_{\text{inst}}}{c_0} \quad (2.239)$$

$$\approx -\frac{\vec{v}_i \cdot \vec{r}_{ji}}{c_0^2} + \frac{\vec{v}_i \cdot \vec{v}_i \cdot \rho_{\text{inst}}}{2 \cdot c_0^3} + \frac{\vec{a}_i \cdot \vec{r}_{ji} \cdot \rho_{\text{inst}}}{2 \cdot c_0^3} + \frac{(\vec{v}_i \cdot \vec{r}_{ji})^2}{2 \cdot c_0^3 \cdot \rho_{\text{inst}}} - \frac{(\vec{v}_i \cdot \vec{v}_i) \cdot (\vec{v}_i \cdot \vec{r}_{ji})}{c_0^4} \quad (2.240)$$

The corresponding correction for the dual one-way ranging scheme can be obtained in a trivial way by swapping indices, i.e.

$$\Delta t_{\text{SR}}^{(\text{DOWR})} = \Delta t_{ij}(t) + \Delta t_{ji}(t) - 2 \cdot \frac{\rho_{\text{inst}}}{c_0}. \quad (2.241)$$

This expression is shown in the central panel of fig. 2.39, where all terms were added summand-wise to maintain the same nomenclature of the traces as in the upper panel. It is noted that the first term of the correction $\Delta t_{\text{SR}}^{(\text{DOWR})}$, which is the trace labeled as $T2$ in the figure, can be written as follows

$$\frac{\vec{v}_i \cdot \vec{r}_{ji}}{c_0^2} + \frac{\vec{v}_j \cdot \vec{r}_{ij}}{c_0^2} = \frac{\vec{v}_i \cdot \vec{r}_{ji}}{c_0^2} - \frac{\vec{v}_j \cdot \vec{r}_{ji}}{c_0^2} = \frac{\vec{v}_{ji} \cdot \vec{e}_{ji}}{c_0^2} \cdot \rho_{\text{inst}} = \frac{\dot{\rho}_{\text{inst}} \cdot \rho_{\text{inst}}}{c_0^2}, \quad (2.242)$$

where $\dot{\rho}_{\text{inst}} = d\sqrt{\vec{r}_{ji}(t) \cdot \vec{r}_{ji}(t)}/dt$ is the time-derivative of the instantaneous range with respect to the GCRS coordinate time t . This $T2$ term is reduced in magnitude compared to the one-way ranging observable, because the common part of the coordinate velocities between both S/C vanishes.

The transponder scheme is characterized by a consecutive combination of propagation times, in contrast to the common reception time in DOWR, which requires a solution to

$$\Delta t_{QPR} = \Delta t_{MS}(t - \Delta t_{SM}(t)) + \Delta t_{SM}(t), \quad (2.243)$$

where the first summand indicates the propagation time from master to slave satellite (cf. the events Q and P in fig. 2.35) and the second term from slave to master (from event P to R).

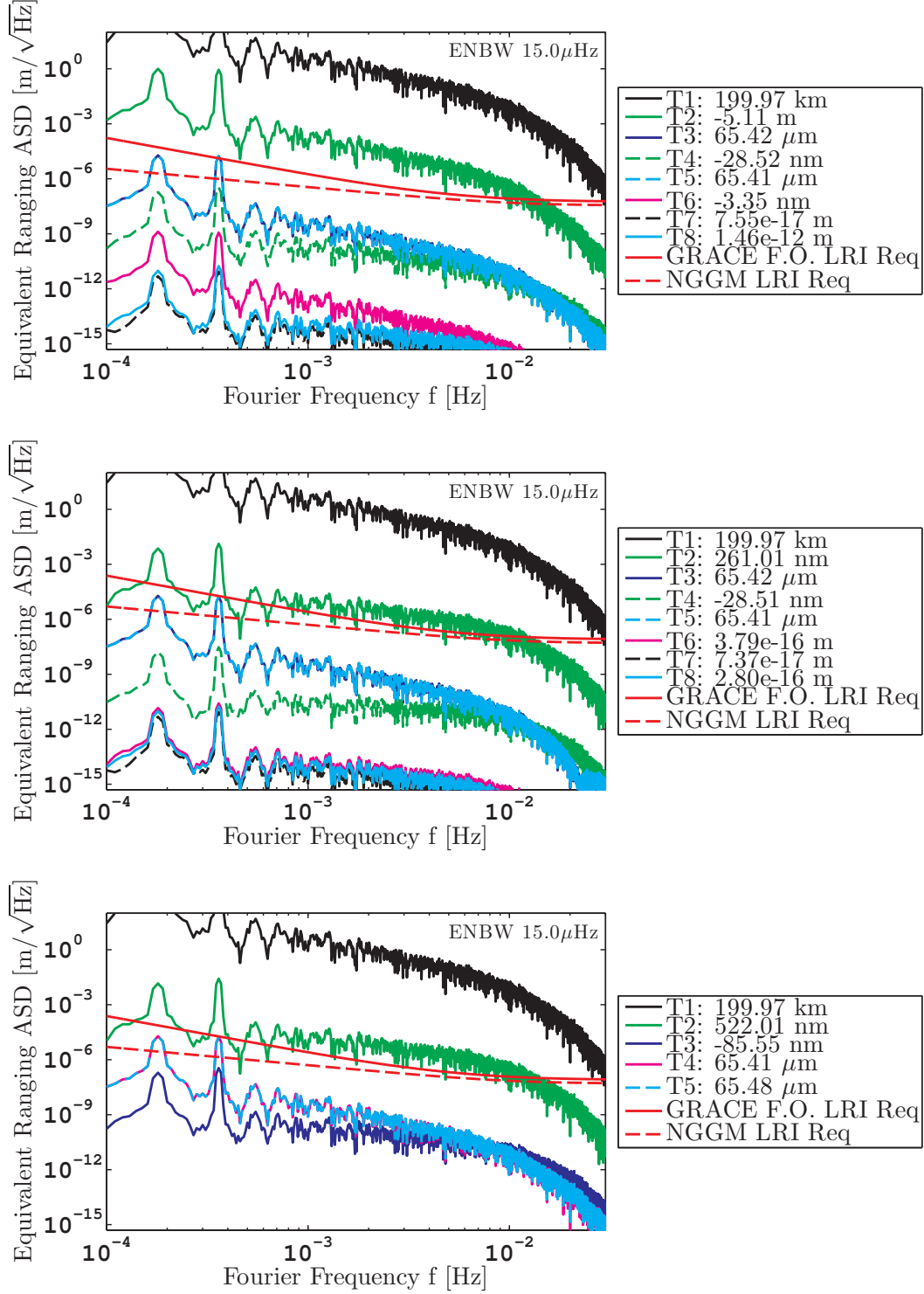


Figure 2.39: Typical spectral content of the constituents of the inter-satellite photon time of flight: the instantaneous range (traces labeled T1) and special relativistic effects in the time of flight. (**Upper panel:**) one-way ranging observable $\Delta t_{ij}(t)$ from eq. (2.238); (**Central panel:**) dual-one way ranging $(\Delta t_{ij}(t) + \Delta t_{ji}(t))/2$; (**Lower panel:**) transponder scheme Δt_{QPR} from eq. (2.244). The respective terms of the sum with units of time have been converted to an equivalent displacement. The plots are based on a simulation of a GRACE-like constellation with $L = 200$ km and $h = 400$ km. The legend contains the mean (DC) value of each addend of the sum.

With given satellite position, velocity and acceleration of slave (S) and master (M) at the reception epoch, one can obtain an approximative solution to the light-time equations as

$$\begin{aligned} \Delta t_{QPR} = & \frac{2 \cdot \rho_{\text{inst}}}{c_0} - \frac{2 \cdot \dot{\rho}_{\text{inst}} \cdot \rho_{\text{inst}}}{c_0^2} + \frac{2 \cdot \vec{a}_M \cdot \vec{r}_{SM} \cdot \rho_{\text{inst}} - \vec{a}_S \cdot \vec{r}_{SM} \cdot \rho_{\text{inst}}}{c_0^3} \\ & + \frac{(\vec{v}_S \cdot \vec{r}_{SM})^2}{c_0^3 \cdot \rho_{\text{inst}}} + \frac{2 \cdot \vec{v}_M \cdot \vec{v}_M \cdot \rho_{\text{inst}} - 2 \cdot \vec{v}_S \cdot \vec{v}_M \cdot \rho_{\text{inst}} + \vec{v}_S \cdot \vec{v}_S \cdot \rho_{\text{inst}}}{c_0^3} \\ & + \mathcal{O}(c_0^{-4}, \vec{r}), \end{aligned} \quad (2.244)$$

which is shown in the lower panel of fig. 2.39 and which defines the special relativistic correction $\Delta t_{\text{SR}}^{(\text{MS})}$.

It is repeated that the just derived special relativistic corrections $\Delta t_{\text{SR}}^{(\text{OWR})}$, $\Delta t_{\text{SR}}^{(\text{DOWR})}$ and $\Delta t_{\text{SR}}^{(\text{MS})}$ are part of the time of flight corrections $\Delta t_{PQ,\text{corr}}$, $\Delta t_{PQ,\text{corr}} + \Delta t_{P'Q',\text{corr}}$ and $\Delta t_{PQR,\text{corr}}$, which have been used in the respective phase observable in eq. (2.176), (2.181) and (2.213) in sec. 2.4 on the functional concepts.

Although the corrections Δt_{SR} depend on the instantaneous range ρ_{inst} , it is sufficient to utilize a low precision estimate of ρ_{inst} within Δt_{SR} , e.g. from GNSS observations, because the magnitude of Δt_{SR} is small as shown in fig. 2.39. Thus, it is still possible to recover a precise instantaneous range ρ_{inst} from the interferometric phase after reducing the special relativistic effects with the help of Δt_{SR} .

The dominant term of Δt_{SR} in the DOWR and transponder case is proportional to the product $\dot{\rho}_{\text{inst}} \cdot \rho_{\text{inst}}$ and this one is also corrected within the GRACE microwave ranging instrument. GRACE data processing handles this term by the so-called light-time correction ρ_{TOF} , which is provided separately in the GRACE KBR Level-1B data streams and defined by [Kim, 2000, eq. 4.39] [Wu *et al.*, 2006, App. E]

$$\rho_{\text{TOF}} = \frac{\omega_i}{\omega_i + \omega_j} \cdot \dot{\rho}_{\text{inst}} \cdot \Delta t_{ji} - \frac{\omega_i}{\omega_i + \omega_j} \cdot \eta_j \cdot \Delta t + \frac{\omega_i - \omega_j}{\omega_i + \omega_j} \cdot \eta_j \cdot \Delta t_{ij}, \quad (2.245)$$

$$= \frac{\eta_i \cdot \Delta t_{ij} \cdot \omega_i}{\omega_i + \omega_j} - \frac{\eta_j \cdot \Delta t_{ji} \cdot \omega_j}{\omega_i + \omega_j} \quad (2.246)$$

with $\eta_j = \vec{v}_j \cdot \vec{e}_{ij}$, $\eta_i = \vec{v}_i \cdot \vec{e}_{ij}$, $\dot{\rho}_{\text{inst}} = \eta_j - \eta_i$ and $\Delta t = \Delta t_{ij} - \Delta t_{ji}$. As stated in Wu *et al.* [2006], the light-time correction is derived by solving the light-cone equation (eq. (2.236)) iteratively, which most likely utilizes reduced-dynamic orbit information. The magnitude of the correction as provided in the GRACE KBR Level-1B data is shown by the red trace in fig. 2.42. It exhibits some artifacts at high frequencies, which are probably caused by some sort of filtering, but these are uncritical as they are below the microwave instrument sensitivity shown in magenta. The light-time correction has signals above the microwave instrument noise for Fourier frequencies below 3 mHz.

The GRACE light-time correction is dominated by the first addend in eq. (2.245), which is almost equivalent to the term derived here in eq. (2.242) and shown by the light blue trace in fig. 2.42. One can easily derive an expression similar in form to eq. (2.246) with $\Delta t_{ij} \approx \rho_{\text{inst}}/c_0 \cdot (1 + \eta_i/c_0)$ and $\Delta t_{ji} \approx \rho_{\text{inst}}/c_0 \cdot (1 - \eta_j/c_0)$ from the general DOWR phase observable

$$c_0 \cdot \frac{\varphi^{(\text{DOWR})}}{\omega_i + \omega_j} = \frac{\omega_i \cdot \Delta t_{ij} + \omega_j \cdot \Delta t_{ji}}{\omega_i + \omega_j} \approx \rho_{\text{inst}} + \frac{\omega_i \cdot \rho_{\text{inst}}/c_0 \cdot \eta_i - \omega_j \cdot \rho_{\text{inst}}/c_0 \cdot \eta_j}{\omega_i + \omega_j}, \quad (2.247)$$

which suggests that the propagation times Δt_{ij} and Δt_{ji} in eq. (2.245f). should be replaced by ρ_{inst}/c_0 . However, the difference is more of academic than practical relevance for microwave ranging.

2.5.3 General Relativity

In the general relativistic case, the computation is more complicated due to the non-trivial metric $g_{\alpha\beta}$ of space-time, which yields a non-uniform motion of a photon in the GCRS and

effects such as light bending. The coordinate speed of light c_n differs from the proper (local) vacuum speed of light c_0 . However, the light path between the satellites in a gravimetric mission is in good approximation still a straight line. The light bending angle towards the geocenter $\Delta\theta_{\text{gr}}$ as a function of the inter-satellite distance L is derived in appendix C as

$$\Delta\theta_{\text{gr}}(r, L) = \frac{2 \cdot GM \cdot L}{r^2 \cdot (c_0)^2} \quad (2.248)$$

which is well below 0.1 nrad for the in-line satellite constellations discussed here. It is noteworthy that the light bending falsifies also DWS measurements on the satellites, but this is uncritical due to the small magnitude. For ranging interferometry, this lateral drift of the general relativistic photon compared to the special relativistic path is not as important as the longitudinal separation due to the lower coordinate speed of light c_n , i.e. the delay. As shown in appendix C, one can compute the delay Δt_{GR} with respect to the special relativistic path in terms of three contributors

$$\Delta t_{\text{GR}}(t_i, \vec{r}_i, t_j, \vec{r}_j) = \Delta t_{\text{PM}}(t_i, \vec{r}_i, t_j, \vec{r}_j) + \Delta t_{\text{HM}}(t_i, \vec{r}_i, t_j, \vec{r}_j) + \Delta t_{\text{SM}}(t_i, \vec{r}_i, t_j, \vec{r}_j), \quad (2.249)$$

where Δt_{PM} is the delay due to Earth's monopole gravity field (cf. eq. (C.9)), Δt_{HM} is the delay due to Earth's higher moments of the gravity field (cf. eq. (C.10)) and Δt_{SM} (cf. eq. (C.9)) is the delay due to Earth's angular (spin) moment, which also curves space-time and modifies the coordinate speed of light. The Δt_{SM} is often called gravito-magnetic effect. The total propagation time of the photon is $\Delta t_{\text{GR}} + \Delta t_{\text{SR}}$ under the assumption of vacuum. The photon emission position \vec{r}_i at time t_i and photon reception location \vec{r}_j at time t_j in eq. (2.249) need to fulfill the light-time equation in a special relativistic sense, i.e.

$$\frac{|\vec{r}_i(t_i) - \vec{r}_j(t_j)|}{c_0} = t_j - t_i, \quad (2.250)$$

because the general relativistic aspect is implicitly in the propagation time.

At first, the validity of the analytical expression for Δt_{PM} , Δt_{HM} and Δt_{SM} is verified. This is performed in the following way: A typical GRACE-like satellite orbit is taken, which has a sampling time of 5s. At each epoch t a photon is launched from the location of the S/C \vec{r}_i in the direction \vec{d}_0 towards the other distant craft, i.e. along the line-of-sight. The coordinate speed of the photon c_n is determined by eq. (B.38), which fixes the initial values of the photon for a numerical integration of the geodesic equation (cf. eq. (B.27)) in the GCRS. The photon path is integrated for a propagation time $\Delta t_{\text{sim}} = 200 \text{ km}/c_0$ with a high sampling rate of 10^6 Hz . In this simulation, the metric tensor is formed by a high fidelity static gravity field model and includes the vector potential due to Earth's spin moment. The numerically determined end position of the photon $\vec{r}_{\text{end,num}}$ is compared to the analytical position obtained by

$$\vec{r}_{\text{end,ana}} = \vec{r}_i + \vec{d}_0 \cdot \underbrace{(\Delta t_{\text{sim}} + \Delta t_{\text{GR}})}_{=\Delta t_{\text{SR}}} \cdot c_0. \quad (2.251)$$

The longitudinal distance between numerical and analytical end position, i.e.

$$|(\vec{r}_{\text{end,num}} - \vec{r}_{\text{end,ana}}) \cdot \vec{d}_0|, \quad (2.252)$$

is a measure for the accuracy of the analytical expressions, if one can ensure that the numerical trajectory has a higher accuracy. The longitudinal distance refers to the projection along \vec{d}_0 and is required, since the total distance is dominated by the lateral displacement from gravitational bending. The result of the comparison is shown in terms of different constituents of Δt_{GR} in the spectral domain in fig. 2.40.

The red trace at the top shows the error, i.e. the longitudinal distance, if no general relativistic correction is performed ($\Delta t_{\text{GR}} = 0$). The mean (DC) component of the error

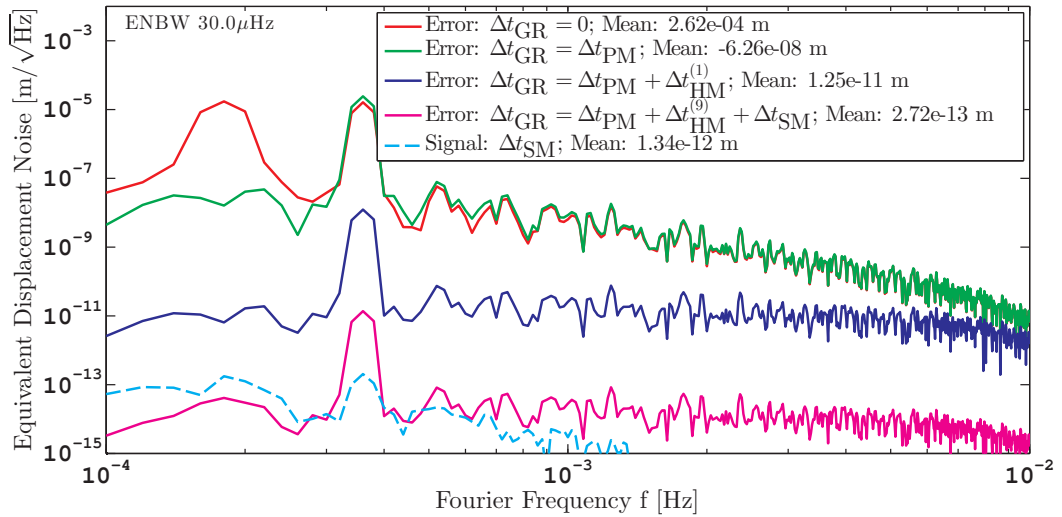


Figure 2.40: Distance as defined in eq. (2.252) between numerically determined photon end position and analytical expressions for different Δt_{GR} . The analytical model with all three contributors ($\Delta t_{\text{GR}} = \Delta t_{\text{PM}} + \Delta t_{\text{HM}} + \Delta t_{\text{SM}}$) shown by the magenta trace is expected to be the most accurate, which was confirmed by this plot. The legend contains the DC (mean) value of the underlying distance error time-series. The light blue trace shows the contribution of Earth’s spin moment term $c_0 \cdot \Delta t_{\text{SM}}$ and is not an error but a signal.

in the time-domain, which is not apparent from the spectral density plot but from the legend, amounts to 262 μm . The DC component is reduced to 62 nm and the once per orbital revolution peak is removed, if the monopole term correction ($\Delta t_{\text{GR}} = \Delta t_{\text{PM}}$) is considered (green trace). Taking into account higher moments of Earth’s gravity field to first order ($\Delta t_{\text{GR}} = \Delta t_{\text{PM}} + \Delta t_{\text{HM}}^{(1)}$) reduces the error further (dark blue trace). The correction Δt_{HM} is generally a line integral of the geopotential along the special relativistic path (cf. appendix C). Here, first order refers to an approximation of the line integral with the trapezoidal rule and evaluation of the geopotential along the photon path at two, namely emission and reception, events. The magenta trace uses a 9th order higher moment correction $\Delta t_{\text{HM}}^{(9)}$, which means that the line integral is approximated by nine segments and by evaluating the geopotential at 10 equally spaced points along the special relativistic trajectory. This reduces the magnitude of the errors further. The magenta trace contains also the correction from Earth’s spin moment Δt_{SM} . However, this gravito-magnetic effect is negligible as shown by the light blue trace. Its spectral components and the mean value are below 1 $\text{pm}/\sqrt{\text{Hz}}$ and 2 pm, respectively.

It is remarked that the numerical integration has been performed with floating-point arithmetic with double (64 bit) precision, which requires precautions regarding numerical accuracy. Due to the approx. 15 significant digits it is not possible to integrate the photon path directly in the GCRS system, however, it was integrated with respect to the special relativistic trajectory in order to avoid large numbers in the position variables. In addition, the rotation matrices for the transformation between GCRS and ITRS were implemented in a way with enhanced numerical precision⁹. This provided an accurate light path with a general-relativistic interval ds^2 close to zero even at the end position. Thus, the numerically integrated light path was considered as a good reference to determine the accuracy of the analytical expressions within the post-Newtonian approximation of the metric for the GCRS. The deviation between numerical and analytical model (magenta trace in fig. 2.40) is be-

⁹Since the time t consists of a potentially large integer part and a small fractional part, it is beneficial for the numerical precision to split the time into an integer and a fractional part and to compute the elements of the rotation matrix as a product and sum of trigonometric functions rather than as a single trigonometric function.

low 1 pm (DC) and below 10 pm/ $\sqrt{\text{Hz}}$ (AC), hence, the accuracy of the analytical model is regarded as sufficient for gravimetric missions.

The analytical model of the general relativistic effects on the time of flight have been applied in fig. 2.41 to the one-way ranging, dual one-way ranging and the transponder scheme for a GRACE-like constellation. The gravitomagnetic effect Δt_{SM} due to Earth's spin moment is direction dependent and is highly suppressed in a two-way ranging combination (dark blue trace). For the central and lower plot the terms Δt_{PM} , Δt_{HM} and Δt_{SM} were determined for both ways between the S/C separately and added term-wise.

With fig. 2.41 it can be concluded that the general relativistic effects in the propagation time manifest mainly as tones at 1/rev and 2/rev frequency, which was also the conclusion by [Turyshchev et al. \[2014\]](#). The magnitude of the tones is in the spectral domain approx. 50 $\mu\text{m}/\sqrt{\text{Hz}}$ with an equivalent noise bandwidth (ENBW) of 15 μHz , which yields a root-mean-square amplitude of

$$50 \mu\text{m}/\sqrt{\text{Hz}} \cdot \sqrt{\text{ENBW}} \approx 193 \text{ nm}_{\text{rms}}, \quad (2.253)$$

and which is far below the expected instrument tone errors (cf. sec. 1.4.5). However, the magnitude of these tones depends on the orbital parameters of both S/C such as on the orbit mismatch. Real missions likely exhibit larger sinusoidal variations, since the orbital parameter were numerically optimized in the simulation performed here. In addition, one can summarize that the general relativistic delay of the photons, often referred to as Shapiro delay, has a sub-mm DC magnitude. As the DC component is anyway not accessible to biased ranging interferometry, this effect is rather of academic relevance. However, the simulation revealed also that relativistic effects show variations of the time of flight with a continuous power distribution over Fourier frequencies, for example, with a magnitude of $> 1 \text{ nm}/\sqrt{\text{Hz}}$ at 1 mHz, which can be corrected in post-processing despite being below the anticipated instrument sensitivity.

2.5.4 Ionosphere

The satellites of a GRACE-like gravimetric mission utilize a low Earth orbit with an altitude, where the residual atmosphere contains ions and free electrons. Thus, the atmosphere is a plasma and commonly called ionosphere. A plasma has a characteristic frequency ν_p [[Chengalur et al., 2007](#), ch. 16] [[Subirana et al., 2013](#)]

$$\nu_p = \frac{1}{2\pi} \sqrt{\frac{N_e \cdot e^2}{\epsilon_0 \cdot m_e}} \approx 9 \text{ Hz} \cdot \sqrt{\frac{N_e}{1 \text{ e}^-/\text{m}^3}}, \quad (2.254)$$

where e is the electron charge, m_e is the electron mass, ϵ_0 is the vacuum permittivity and N_e is the charge number density. The ionosphere shows a maximum charge number density of $N_e \approx 10^{11}$ to $10^{12} \text{ e}^-/\text{m}^3$, which means that the ionosphere has a plasma frequency of the order of 10 MHz. Electro-magnetic waves with lower frequency are absorbed and reflected by the plasma. Light and microwaves can propagate through the ionosphere, but the propagation velocity is altered. It can be computed with the help of the wave number $k = 2\pi/\lambda$ from the approximative dispersion relation [[Subirana et al., 2013](#), ch. 5.4.1]

$$\omega^2 = c_0^2 \cdot k^2 + (2\pi\nu_p)^2 \quad (2.255)$$

as

$$v_{\text{ph}} = \frac{\omega}{k} = \sqrt{c_0^2 + \frac{(2\pi\nu_p)^2}{k^2}} = c_0 \cdot \sqrt{1 + \frac{(2\pi\nu_p)^2}{c_0^2 \cdot (2\pi/\lambda)^2}} = c_0 \cdot \sqrt{1 + \frac{\nu_p^2}{\nu^2}}. \quad (2.256)$$

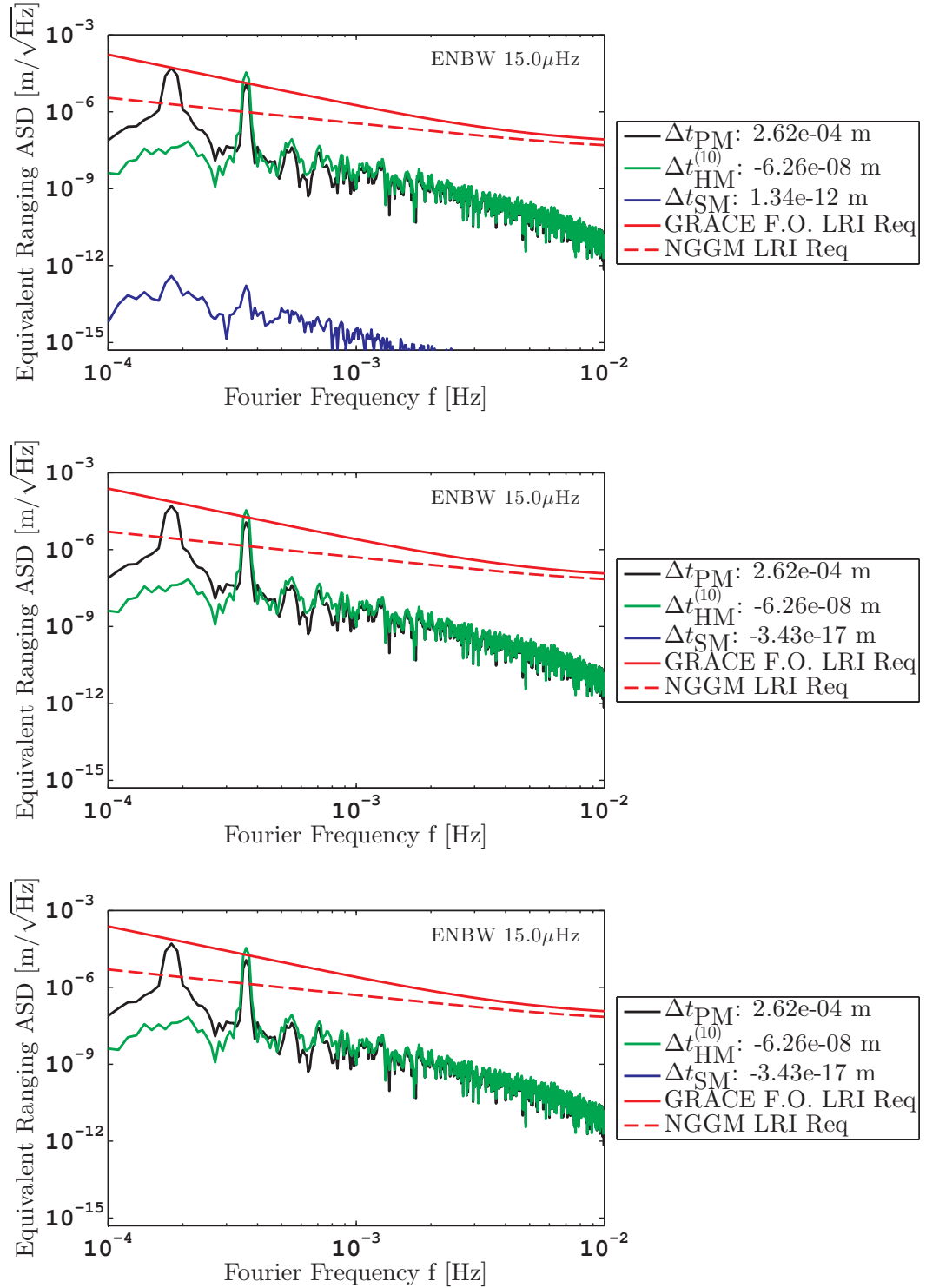


Figure 2.41: The general relativistic effects on the photon propagation time in a one-way ranging scheme (upper panel), in a dual one-way ranging concept (central panel) and in the transponder case (lower panel).

This result illustrates that the phase velocity is higher than the proper vacuum speed of light c_0 , which also implies that the refractive index of the plasma is below unity, i.e.

$$n_{\text{plasma}} = \frac{c_0}{v_{\text{ph}}} \approx c_0 \cdot \left(1 - \frac{1}{2} \frac{\nu_p^2}{\nu^2} \right) \approx 1 - \frac{40.3 \text{ Hz}^2}{\nu^2} \cdot \frac{N_e}{1 \text{ e}^-/\text{m}^3}. \quad (2.257)$$

The group velocity $v_{\text{gr}} = d\omega/dk$ is subluminal ($< c_0$) as shown in [Subirana *et al.*, 2013]. Ionospheric effects are of importance for GNSS applications, which yield an advance of the phase observation via the phase velocity, but a delay of the code measurement via the group velocity. Also microwave ranging in GRACE and GRACE-like missions is affected by the ionosphere, which has, in general, a time and position dependent electron number density N_e . The change in the propagation time of a photon can be computed with the line integral along the propagation path (cf. eq. (2.228))

$$\Delta t_{\text{iono}} \approx -\frac{40.3 \text{ Hz}^2}{\nu^2} \cdot \frac{1}{1 \text{ e}^-/\text{m}^3} \cdot \frac{1}{c_0} \cdot \underbrace{\int N_e(t, \vec{r}) ds}_{=\text{STEC}}, \quad (2.258)$$

where ν is the optical or microwave frequency of the photon and STEC is the so-called slant total electron content, which is typically given in units of $1 \text{ e}^-/\text{m}^2$ or $1 \text{ TECU} = 10^{16} \text{ e}^-/\text{m}^2$. The previous equation is derived in the special relativistic limit, i.e. the coordinate speed of light was replaced by c_0 , which is based on the valid assumption that the deviation of the actual photon path from the special relativistic path is small. Furthermore, it is mentioned that the derivation shown here considers only the first-order ionospheric effect, while higher-order corrections are possible [Hernandez-Pajares *et al.*, 2007].

The ionospheric effects are mitigated in GRACE and GRACE Follow-On microwave ranging by dual band measurements at 24 GHz (K-band) and 32 GHz (Ka-band) [Kim, 2000, sec. 2.2.3] [Ko, 2008]. With dual band measurements one obtains two phase-derived ranges

$$\rho_{\Theta, \text{K}} \approx \rho - \frac{40.3 \text{ Hz}^2}{\nu_{\text{K}}^2} \cdot \frac{1}{1 \text{ e}^-/\text{m}^3} \cdot \text{STEC} + \dots \quad (2.259)$$

$$\rho_{\Theta, \text{Ka}} \approx \rho - \frac{40.3 \text{ Hz}^2}{\nu_{\text{Ka}}^2} \cdot \frac{1}{1 \text{ e}^-/\text{m}^3} \cdot \text{STEC} + \dots, \quad (2.260)$$

which can be linearly combined to obtain the variations in the STEC as

$$\text{STEC}(t) \approx (\rho_{\Theta, \text{K}}(t) - \rho_{\Theta, \text{Ka}}(t)) \cdot \frac{-\nu_{\text{Ka}}^2 \nu_{\text{K}}^2}{\nu_{\text{Ka}}^2 - \nu_{\text{K}}^2} \cdot 1 \text{ e}^-/\text{m}^3 + \text{bias} \quad (2.261)$$

Thus, the ionospheric non-static effect can be reduced from the range measurement, while the static DC value is anyway not accessible due to the bias present in interferometry. For the sake of completeness, the one-way DC term is computed for $N_e \approx 10^{12} \text{ e}^-/\text{m}^3$, $L = 200 \text{ km}$ and $\nu = 32 \text{ GHz}$ as

$$\frac{40.3 \text{ Hz}^2}{\nu^2} \cdot \frac{N_e \cdot L/c_0}{1 \text{ e}^-/\text{m}^3} \approx \frac{8 \text{ mm}}{c_0}, \quad (2.262)$$

which is the mean advance in the photon propagation time for microwaves.

The correction term in eq. (2.261) is provided in terms of a length in meters separately in the GRACE KBR Level-1B data. It is depicted as the black solid trace in fig. 2.42. Due to the quadratic scaling of the ionospheric contributions with the radiation frequency ν , these effects are downscaled in optical interferometry by the factor

$$\left(\frac{32 \text{ GHz}}{282 \text{ THz}} \right)^2 \approx 10^{-8} \quad (2.263)$$

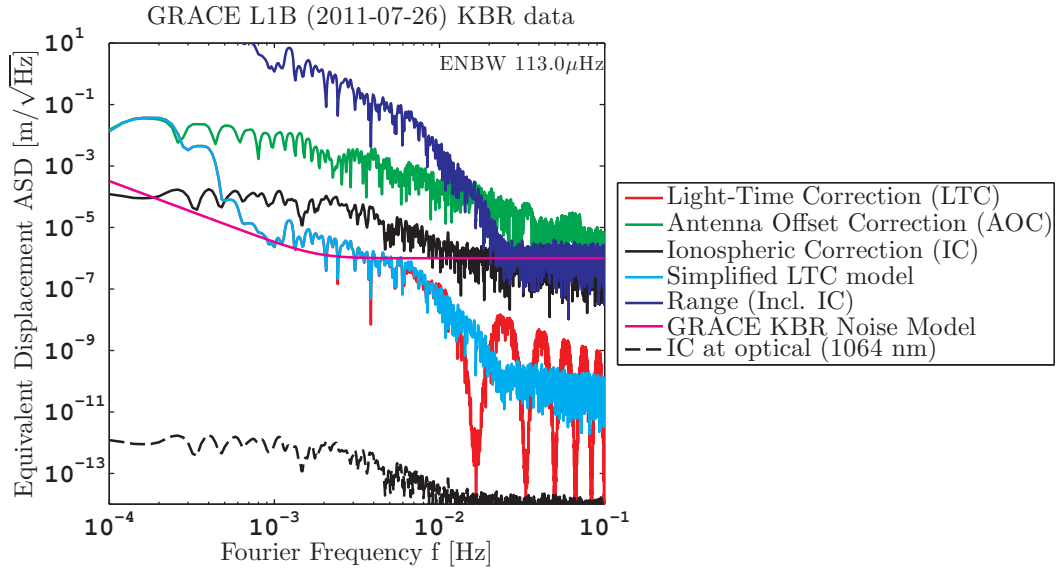


Figure 2.42: GRACE Level-1B KBR data from 26th July 2011. The antenna offset correction (green) and the light time correction (red) need to be added to the biased ranging (dark blue) as described in the GRACE data product handbook [Case *et al.*, 2010]. The light blue trace is a simplified model for the light-time correction given by $\dot{\rho} \cdot \rho / (2 \cdot c_0)$.

for light with a wavelength of 1064 nm. This makes dual band measurements or a post-processing correction of ionospheric effects unnecessary in optical interferometry (cf. dashed black trace at the bottom in fig. 2.42).

The ionospheric correction from GRACE shown in fig. 2.42 is measured in a dual one-way ranging combination, which is strictly speaking not the same as a transponder-based combination. However, it is reasonable to assume that the STEC does not change significantly over timescales of milliseconds (L/c_0) and, thus, that the DOWR and transponder STEC are approximately the same.

The other traces in fig. 2.42 show the actual KBR-derived ranging signal (dark blue trace), the attitude-to-ranging coupling via the antenna offset (green trace) and the so-called light time correction [Kim, 2000] (red trace), which are the special relativistic effects discussed in sec. 2.5.2. The light time correction in the GRACE Level-1B data shows some artifacts below the instrument sensitivity and can be approximated by the expression given in eq. (2.242), which is shown by the light trace.

2.5.5 Atmosphere

The remaining undiscussed term in eq. (2.232) influencing the photon propagation time between the satellites is the refractive index $n = n_a$ due to the residual neutral atmosphere in a low Earth orbit, which delays the light by

$$\Delta t_{\text{atmo}} \approx \frac{1}{c_0} \cdot \int_{\mathcal{P}} (n_a(t, \vec{r}) - 1) ds = \frac{1}{c_0} \cdot \int_{\mathcal{P}} \Delta n_a(t, \vec{r}) ds, \quad (2.264)$$

where the line integral is solved along the light path \mathcal{P} . The refractive index n_a of the atmosphere is close to unity for a satellite constellation in 400 km height, e.g.

$$\Delta n_a = n_a - 1 \lesssim \underbrace{10^{-14}}_{=:\Delta n_{a,\text{max}}}, \quad (2.265)$$

which can be derived from the Clausius–Mossotti relation [Choy, 2016, eq. 4.14] or the so-called Lorentz-Lorenz relation [Owens, 1967]:

$$\frac{n_a^2 - 1}{n_a^2 + 2} = B_{\text{tot}}, \quad (2.266)$$

with symbol B_{tot} being subsequently defined. For gases with small refractivity and refractive index close to unity, the following approximative solution for n_a can be used

$$n_a = 1 + \Delta n_a \approx 1 + \frac{3}{2} \cdot B_{\text{tot}}. \quad (2.267)$$

The quantity B_{tot} on the right hand side of eq. (2.266) can be computed for a mixture with atomic or molecular constituents $X \in \{O_2, N_2, O, \dots\}$ by

$$B_{\text{tot}} = \sum_X \frac{N_X}{3\epsilon_0} \cdot \alpha_X, \quad (2.268)$$

where N_X is the number density with units of m^{-3} of the atoms or molecules, α_X is the electric polarizability of the atoms or molecules with units of $\text{C} \cdot \text{m}^2/\text{V}$ and ϵ_0 is the vacuum permittivity in SI units. The number density of atoms and molecules can be obtained from an atmospheric model, e.g. the NRLMSISE00 model [Picone *et al.*, 2002], which is also often used to compute the atmospheric drag force acting on the satellite. Typical values for the number densities for different orbit heights are shown in the lower part of table 2.7, which have been derived for the year 2001 with high solar activity. The corresponding deviation of the refractive index from unity Δn_a is also shown in the table. The used polarizability α_X for the different atoms and molecules is shown in the central part of table 2.7.

Furthermore, Δn_a has been derived for the Earth’s typical sea-level atmosphere to provide a sanity check of the formulas. The result of $\Delta n_a = 274 \cdot 10^{-6}$ (last line in the lower table 2.7) is in good agreement with values from the literature such as in [Ciddor, 1996] with $\Delta n_a(\lambda = 1 \mu\text{m}) = 273 \cdot 10^{-6}$.

Thus, the upper bound $\Delta n_{a,\text{max}}$ from eq. (2.265) can be justified with the results from table 2.7. With such small $\Delta n_{a,\text{max}}$ one obtains a worst-case difference between geometrical and optical pathlength of the order of 2 nm for an inter-satellite distance of $L = 200$ km. However, such a static and small value is neither measurable nor harmful due to the inaccessible bias present in ranging interferometry. The variations of the refractive index are of importance, which yield variations in the photon time of flight and cause equivalent fluctuations in the phase-derived range measurement. For gravimetric missions the variations in the science measurement frequency band between approx. 0.18 mHz and 0.1 Hz need to be analyzed.

One can certainly assume that the variations of the refractive index are smaller than the mean (static) part $\Delta n_{a,\text{max}}$, which includes already plenty of margin, thus, the fluctuations should not exceed a root-mean squared value of 2 nm in an amplitude spectrum and $2 \text{ nm}/\sqrt{\text{Hz}}$ in an amplitude spectral density over the science measurement frequency band. A more quantitative analysis also with regard to future generations of gravimetric missions is attempted in the following.

At first, it should be noted that the refractive index deviation Δn_a is in good approximation proportional to the atmospheric density ρ_a with units of kg/m^3 . Furthermore, one can assume that the composition of the atmosphere does not change much, so that one can use

$$\Delta n_a(t, \vec{r}) \approx \Delta n_{a,\text{mean}} \cdot \frac{\rho_a(t, \vec{r})}{\rho_{a,\text{mean}}}. \quad (2.269)$$

Thus, the analysis of refractive index variations can be reduced to the analysis of atmospheric density variations. Typical variations of the refractive index along a GRACE-like polar orbit at 400 km height are shown by the magenta traces in the upper plot in fig. 2.43. These

SLA density @ 15°C	kg/m ³	1.23E+00	[1]
Avogadro Constant N _A	1/mol	6.02E+23	
Vacuum Permittivity ε ₀	C/(V·m)	8.85E-12	

Name	Units	Atoms / Molecules							Ref. / Comment
		O	N2	O2	He	Ar	H	N	
CGS [cm ³]		8.02E-25	1.74E-24	1.57E-24	2.05E-25	1.64E-24	6.67E-25	1.10E-24	[2]
Electric Polarizability α	SI [C m ² /V]	8.92E-41	1.94E-40	1.75E-40	2.28E-41	1.82E-40	7.42E-41	1.22E-40	Derived from CGS
Molar Mass M	g/mol	15.999	28.013	31.999	4.000	39.948	1.008	14.007	Periodic Table
SLA constituents mixing ratio [1]	%		78.08	20.94	0.000524	0.93			Approx.: CO ₂ , Ne, ... missing
SLA Number Density N	1/cm ³		2.06E+19	4.83E+18	9.66E+14	1.72E+17			

Year	Day of Year ¹	Height km	Atom & Molecule Number Density from NRLMISSE00 model										B _{tot}	Δn _a
			O	N2	O2	He	Ar	H	N	dimensionless	dimensionless			
2001	1	300	5.30E+08	3.57E+08	1.37E+07	9.63E+05	1.94E+05	2.76E+04	9.02E+06	4.52E-15	6.77E-15			
2001	1	350	2.64E+08	1.09E+08	3.53E+06	8.09E+05	3.57E+04	2.62E+04	4.70E+06	1.73E-15	2.59E-15			
2001	1	400	1.35E+08	3.43E+07	9.42E+05	6.84E+05	6.85E+03	2.51E+04	2.56E+06	7.23E-16	1.08E-15			
2001	1	450	7.06E+07	1.10E+07	2.58E+05	5.82E+05	1.35E+03	2.41E+04	1.43E+06	3.26E-16	4.89E-16			
2001	1	500	3.73E+07	3.61E+06	7.20E+04	4.96E+05	2.75E+02	2.31E+04	8.12E+05	1.56E-16	2.34E-16			
2001	182	300	4.67E+08	8.59E+07	4.68E+06	1.42E+07	2.38E+04	1.13E+05	2.12E+06	2.25E-15	3.37E-15			
2001	182	350	1.84E+08	8.82E+07	3.32E+06	5.58E+05	3.25E+04	3.58E+04	5.06E+06	1.31E-15	1.96E-15			
2001	182	400	9.14E+07	2.64E+07	8.35E+05	4.69E+05	5.81E+03	3.43E+04	2.69E+06	5.18E-16	7.77E-16			
2001	182	450	4.62E+07	8.06E+06	2.15E+05	3.96E+05	1.07E+03	3.28E+04	1.47E+06	2.23E-16	3.34E-16			
2001	182	500	1.01E+07	7.25E+04	1.53E+03	6.61E+06	5.91E-01	1.55E+05	3.03E+04	4.06E-17	6.09E-17			
Sea-Level Atmosphere (SLA)			2.06E+19	4.83E+18	9.66E+14	1.72E+17				1.83E-04	2.74E-04			

References

- [1] U.S. Standard Atmosphere, 1976. U.S. Government Printing Office, Washington, D.C., 1976
- [2] CRC Handbook of Chemistry and Physics: A Ready-reference Book of Chemical and Physical Data, David R. Lide

Table 2.7: Calculation of the refractive index for different orbit heights for two days within the year 2001, which was a year with high solar activity. SLA stands for sea-level atmosphere.

traces have been derived from the NRLMSISE00 atmospheric model for various different epochs in the year 2001 and 2002 to show the variability of the atmosphere. Since this model provides the composition of the atmosphere, one can directly compute the refractive index. However, as some other models may provide only the atmospheric density ρ_a , eq. (2.269) is still interesting, especially since the accelerometer data of gravimetric missions can be used to derive the atmospheric density variations [Doornbos *et al.*, 2009].

As pointed out by Zijlstra *et al.* [2005], the NRLMSISE00 and most likely other models produce a smoothed atmospheric density with little high-frequency signals and with lacking continuous background in a spectral density plot when compared to accelerometer derived densities. A typical accelerometer measurement is shown, for example, in fig. 1.25 of a previous section. Based on this figure and on the plots in [Zijlstra *et al.*, 2005], an approximate stochastic model as an upper bound was derived, which is shown by the green trace in fig. 2.43 and has the analytical form

$$\text{ASD}[\Delta n_a](f) = \Delta n_{a,\max} \cdot \text{ASD}[\rho_a/\rho_{a,\text{mean}}](f) = \Delta n_{a,\max} \cdot \frac{1}{\sqrt{1 + (f/0.2 \text{ mHz})^2}}. \quad (2.270)$$

The fluctuations of the refractive index have been multiplied by $L = 200 \text{ km}$ to obtain a displacement noise ASD with units of $\text{m}/\sqrt{\text{Hz}}$ in the figure. Thus, the upper plot of fig. 2.43 confirms the anticipation that fluctuations of the refractive index do not produce a ranging noise above approx. $2 \text{ nm}/\sqrt{\text{Hz}}$.

So far, the analysis did not properly solve the path integral in eq. (2.264) between both S/C, but the following assumption was implicitly used

$$\Delta t_{\text{atmo}} \approx \frac{1}{c_0} \cdot \int_{\mathcal{P}} \Delta n_a(t, \vec{r}) \, ds \approx \frac{\Delta n_a(t) \cdot L}{c_0}, \quad (2.271)$$

i.e. an average refractive index along the photon path was assumed. The difficulty with solving the line integral is that the atmospheric models do not properly reflect fluctuations of the atmospheric density on short spatial scales of the order of meters to 200 km. However, one can use the fact that the accelerometer aboard the S/C samples the density fluctuations along the approximate light path, not with the speed of light but with a velocity of $v \approx 7600 \text{ m/s}$. If one assumes that the spatial atmospheric density pattern does not change much over time scales of a few seconds, one can approximate the line integral by

$$c_0 \cdot \Delta t_{\text{atmo}} = \int_{\mathcal{P}} \Delta n_a(t, \vec{r}) \, ds \approx \int_{t'=t}^{t'=t+L/c_0} \Delta n_a(t', \vec{r}(t')) \cdot v \, dt', \quad (2.272)$$

which can be conveniently solved in the spectral domain as

$$c_0 \cdot \text{ASD}[\Delta t_{\text{atmo}}](f) = v \cdot \frac{\text{ASD}[\Delta n_a](f)}{2\pi f} \cdot |1 - e^{2\pi i f L/c_0}|. \quad (2.273)$$

The result is shown by the dashed dark blue trace in the upper plot of fig. 2.43. The magnitude of the dashed dark blue trace is reduced compared to the green trace, which means that the stochastic spatial variations along the photon (or satellite) path average out partly.

The fluctuations of the refractive index along the orbit $\Delta n_a(t, \vec{r}(t))$ can be expressed as function of the time, i.e. $\Delta n_a(t)$, which has a spectral density $\text{ASD}[\Delta n_a](f)$, where f is the Fourier frequency in Hz. However, an alternative method is to parameterize the fluctuations in terms of a spatial coordinate x , e.g. the position along the orbit. The time t and position x are related via $t \cdot v = x$, and thus, one has $\Delta n_a(x) = \Delta n_a(t \cdot v)$. Now one can equivalently formulate the path integral as follows

$$c_0 \cdot \Delta t_{\text{atmo}} = \int_{\mathcal{P}} \Delta n_a(t, \vec{r}) \, ds \approx \int_{x'=x}^{x'=x+L} \Delta n_a(x') \, dx', \quad (2.274)$$

while the spectral solution can be written as

$$c_0 \cdot \text{ASD}[\Delta t_{\text{atmo}}](k) = \frac{\text{ASD}[\Delta n_a](k)}{2\pi k} \cdot |1 - e^{2\pi i k L}|, \quad (2.275)$$

with k denoting the spatial frequencies with units of m^{-1} . Eq. (2.273) and (2.275) are equivalent, since

$$\text{ASD}[\Delta n_a](k) = \text{ASD}[\Delta n_a](f/v) \quad (2.276)$$

relates the fluctuations in the temporal frequency with spatial frequencies. The fractional density fluctuations or the fractional refractive index fluctuations

$$\frac{\text{ASD}[\Delta n_a](k)}{\Delta n_{a,\text{mean}}} = \frac{\text{ASD}[\rho_a](k)}{\rho_{a,\text{mean}}} \quad (2.277)$$

are shown in the lower plot of fig. 2.43 as a function of the spatial wavelength $1/k$. The domain of spatial fluctuations k is physically more adequate to describe the effects during the short photon propagation time and may allow better analysis and comparison of different atmospheric density models, because the spatial frequencies k are a property of the atmospheric models, while the temporal Fourier frequency f depends on a particular orbital velocity. It is noted that the notching features at high frequencies of the dark blue trace in the upper plot in fig. 2.43 appear for spatial fluctuations in $\Delta n_a(x)$ with a wavelength corresponding to an integer multiple of the inter-satellite distance L . Such wavelengths cancel out in the line integral.

In summary, the effect of the neutral atmosphere and the refractive index yields a small noise in the ranging measurement, which is below approx. $1 \text{ nm}/\sqrt{\text{Hz}}$ for $L = 100 \text{ km}$ even at the lower end of the science measurement frequency band. Also sinusoidal variations at integer multiples of the orbital frequency are caused by the refractive index, but they have a negligible amplitude compared to other tone errors. The effects of the neutral atmosphere discussed here likely impose a fundamental sensitivity limit in GRACE-like gravimetric missions, as these errors can not be removed by dual band measurements.

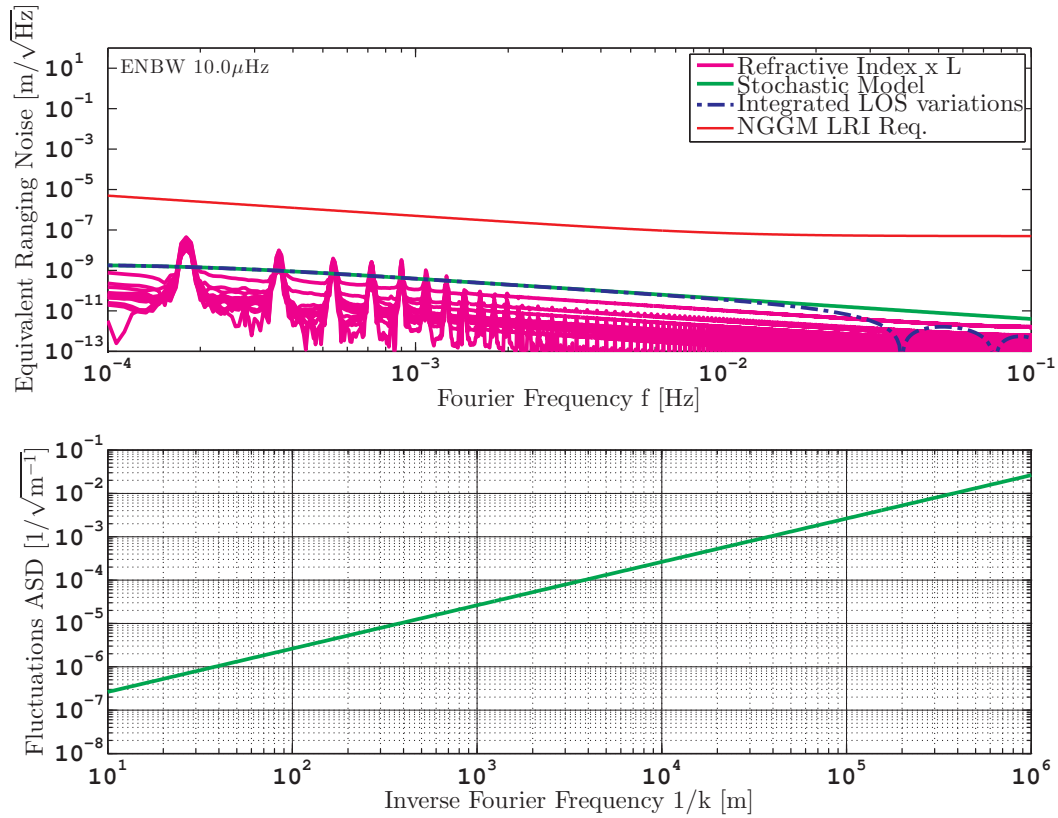


Figure 2.43: (Upper panel:) Ranging noise due to refractive index variations. (Lower panel:) Spatial spectral density of the stochastic model used to describe spatial fractional fluctuations of the atmospheric density and refractive index with units of $1/\sqrt{\text{m}^{-1}}$. Both plots assume an inter-satellite distance of $L = 200$ km.

2.6 Design Principles of Satellite-Satellite Interferometers

In the previous sections, the phase observable for the interferometric range measurement was derived for different functional concepts. Noise sources such as laser frequency noise and the USO timing jitter have been accounted for. Furthermore, relativistic and atmospheric corrections were addressed, which are required to obtain the instantaneous geometrical distance between the satellites ρ_{inst} . However, the light and its phase was mainly treated in the plane-wave approximation or within the traversing photon picture. In addition, errors due to the specifics of the optical design of the interferometers, which includes the severe coupling of satellite rotations into the range measurement, have not been discussed but absorbed in a single correction term to the photon time of flight: δt_{ifo} (cf. sec. 2.5.1). Moreover, aspects regarding the interferometric signal amplitude or signal-to-noise ratio, which are mainly driven by the available light power, have been avoided. These will be addressed in this and the following sections.

This section 2.6 is dedicated to principles of (optical) satellite-to-satellite interferometry (SSI), which are important for the design, analysis and understanding of optical ranging interferometers. At first, the coupling of satellite attitude into the range measurement is addressed with the help of reference points, which provide a geometrical meaning to the coupling factors of satellite or interferometer orientation into the pathlength. These reference points turn out to be helpful also in the further discussion of different optical layouts (cf. sec. 2.7). For sensible interferometer designs, this attitude-to-ranging coupling is the other major error source next to the laser frequency noise. The second part of this section on design principles covers the signal strength and signal-to-noise ratio of an interferometric readout, which allows one to derive detailed power link budgets for different interferometer designs in sec. 2.8. Another important aspect related to the signal strength is the laser link acquisition, which is briefly discussed in sec. 2.6.12.

2.6.1 Gaussian Beam models

The attitude-to-ranging coupling in SSI depends on the used laser beams, e.g. on their spatial modes. It is recalled that electro-magnetic waves generally have a vectorial nature and can be described by the electric field vector $\vec{E}(x, y, z) \propto \cos(2\pi\nu t)$ with time-harmonic time-dependence (cf. introduction to interferometry in sec. 2.2). Laser sources ideally provide a linear polarized Gaussian beam in TEM₀₀ mode (cf. sec. 2.3.1 on lasers), which is an eigenmode of many optical resonators present in lasers and which will be subsequently described in detail. To simplify the calculations, a scalar field theory is often used with a scalar electric-field function E given by (cf. eq. (2.16) and (2.19))

$$E(x, y, z) = |\vec{E}(\vec{r})| = E_0(\vec{r}) \cdot \cos(2\pi\nu t - \vec{k}_0 \cdot \vec{r} - \phi_E(\vec{r})), \quad (2.278)$$

where $\vec{k}_0 = k \cdot \vec{d}_0 = 2\pi/\lambda \cdot \vec{d}_0$ is the wave vector defining the normalized beam propagation direction \vec{d}_0 , ϕ_E is a term describing the phasefront and $\vec{r} = (x, y, z)^\top$ is the evaluation point of the field. Gaussian beams arise as solutions of the so-called scalar Helmholtz equation:

$$(\partial_x^2 + \partial_y^2 + \partial_z^2 + k^2) \cdot E(x, y, z) = 0, \quad (2.279)$$

under a paraxial approximation¹⁰ and under the assumption that the wavelength λ is much larger than the transversal size of the beam. The scalar Helmholtz equation follows directly from Maxwell's equations. Gaussian beams have proven to be a suitable means to describe coherent laser radiation and it is mentioned that complete orthogonal sets of Gaussian beam modes can be found, e.g. so-called Hermite-Gaussian or Laguerre-Gaussian modes, which allow to uniquely decompose arbitrary light fields into a set of modes.

¹⁰Paraxial means close to the beam axis.

The first or fundamental Gaussian beam mode is common in the Hermite-Gaussian and Laguerre-Gaussian set and it is commonly denoted as TEM₀₀. It offers a good starting point for the initial conceptual design of interferometers, as one usually tries to produce laser beams with such a mode. This mode is predestined to be used as transmit (TX) beam by an interferometer, which is explained in a moment.

A typical analytical expression for the fundamental Gaussian mode, which propagates without loss of generality along the z -direction, reads in the complex representation as

$$E^c(x, y, z) = \frac{\sqrt{2P}}{\omega_0 \cdot \sqrt{\pi}} \cdot \frac{\omega_0}{\omega(z)} \cdot e^{-\frac{(x^2+y^2)}{\omega(z)^2}} \cdot e^{-ik \cdot z - i\phi_E(\vec{r})} \cdot e^{i2\pi\nu t}, \quad (2.280)$$

where the electric field amplitude E^c has absorbed the vacuum impedance and has for this reason units $\sqrt{\text{VA}}/\text{m} = \sqrt{\text{W}}/\text{m}$ instead of V/m . The quantity P is the total optical power of the beam in watts. This convention for E^c is also used in the IFOCAD software and it allows the intensity I with units of W/m^2 to be written as the squared modulus of the electric field:

$$I(x, y, z) = |E^c(x, y, z)|^2 = \frac{2 \cdot P}{\omega_0^2 \cdot \pi} \cdot \frac{\omega_0^2}{\omega(z)^2} \cdot e^{-\frac{2 \cdot (x^2+y^2)}{\omega(z)^2}}, \quad (2.281)$$

with $\omega(z) = \omega_0 \cdot \sqrt{1 + (z/z_R)^2}$ describing the $1/e^2$ spot radius as a function of the longitudinal position z and with ω_0 denoting the $1/e^2$ waist radius, i.e. the minimum spot radius, which is located here at $z = 0$. The quantity $z_R = \pi\omega_0^2/\lambda$ is the so-called Rayleigh range. At each longitudinal position z , the intensity decays with the Gaussian function in radial direction, which means that the maximum intensity is transported along the beam axis ($x = y = 0$).

Furthermore, the phase evolution of a Gaussian beam, which is the argument of the complex-valued electric-field E^c , reads as

$$-k \cdot z - \phi_E(\vec{r}) = -k \cdot z - k \frac{x^2 + y^2}{2 \cdot R(z)} + \arctan(z/z_R) \quad (2.282)$$

with phasefront radius of curvature $R(z) = z \cdot (1 + (z_R/z)^2)$. The arctan term is the so-called Gouy phase, which can be neglected here, because this phase contribution is almost constant in the far-field ($z \gg z_R$). The radius of curvature is divergent at the waist position ($z = 0$), which means plane phasefronts are present at the location with the smallest spot size. In the far-field ($z \gg \omega_0, z \gg z_R$), the phase of a Gaussian beam approaches parabolic phasefronts, i.e.

$$\frac{x^2 + y^2}{2 \cdot R(z)} + z \stackrel{z \gg z_R}{\approx} \frac{x^2 + y^2}{2 \cdot z} + z. \quad (2.283)$$

In fact, the parabolic shape arises from the used approximations in the derivation of the Gaussian beams. In general, one can show that a confined laser beam in the near-field produces spherical phasefronts in the far field [Zhou *et al.*, 2007; Carter, 1972]:

$$\frac{x^2 + y^2}{2 \cdot R(z)} + z \stackrel{z \gg z_R}{\approx} \sqrt{x^2 + y^2 + z^2}. \quad (2.284)$$

The distinction between parabolic and spherical phasefronts is rather of academic relevance, since the difference is negligible for the interferometers discussed in this thesis.

It is noted that (ideal) fundamental Gaussian beams show a minimum beam parameter product, which is given by the waist size ω_0 and far-field divergence angle θ_{div} , i.e.

$$\omega_0 \cdot \theta_{\text{div}} = \frac{\lambda}{\pi}. \quad (2.285)$$

This means, for a fixed wavelength λ and waist size ω_0 , fundamental Gaussian beams are optimal to transport the light power along the optical axis (\vec{d}_0), since the divergence angle is

minimal. It is recalled that a confinement of radiation in the near-field yields a higher spread of the radiation in the far-field, i.e. a smaller waist size ω_0 yields a larger far-field divergence angle θ_{div} for Gaussian beams.

The minimal beam parameter product in combination with spherical phasefronts makes this type of beam a reasonable and natural choice for the transmitted (TX) light towards the distant satellite. Furthermore, Gaussian beams can be easily transformed in a well-defined way by optics, e.g. magnified by a telescope to reduce the divergence in the far-field. However, the generation of a Gaussian beam with a spot radius $\omega(z)$ requires typically that the optical path has a free aperture diameter of $6 \cdot \omega(z)$ in order to avoid clipping and associated diffraction effects. This might impose challenges regarding space and mass constraints in a space mission. Therefore, clipped Gaussian beams can also be considered as TX laser beam, which are addressed in appendix F. However, clipped Gaussian beams currently seem to be required only for missions with very low beam divergence requirements such as the LISA mission. In these missions, telescopes are used to produce a large beam with associated small divergence. It is remarked that even clipped Gaussian beams can be approximated well close to the beam axis by a fundamental Gaussian beam with slightly different beam parameters as described in appendix F.

In the following, fundamental Gaussian beams are used to describe the laser beams in interferometers. These are mathematical models, which have proven to describe the actual behavior of laser beams well. However, one should keep in mind that the Gaussian beam model is derived under a paraxial approximation and that polarization effects are omitted. In addition, a realistic description of laser beams need to consider higher-order modes, which often contain few percent of the total beam power. These inaccuracies are tolerable in an early design phase, but have to be tackled at later stages.

With clarified properties of the transmit laser beam, the differences between transmitter and receiver pointing errors can be addressed.

2.6.2 Transmitter vs. Receiver Pointing

The discussion of pointing effects in interferometry requires care, as there is no such term as *the interferometer pointing*. Reasonable SSI interferometers have a received (RX) beam axis and a transmit (TX) beam axis, which may not be co-aligned, e.g. due to a point-ahead mechanism. Furthermore, the relation of these two axes to the satellite's attitude may be non-trivial in case of an active beam steering.

If the transmit beam is misaligned with respect to the line-of-sight, which is the connecting line between the two S/C, the intensity at the receiver S/C drops as depicted in the upper sketch of fig. 2.44. At the receiver, the phasefronts have an almost spherical shape with a center of curvature ideally co-located with the CoM of the transmitter S/C and with the pivot point of rotations, so that the phase at the distant S/C does not change upon rotations.

In case of a receiver misalignment, illustrated in the lower part of fig. 2.44, the intensity stays to first order constant, because the laser beam has diverged (typically) to a size significantly larger than the S/C. However, the overlap of the laser beams at the receiver, the so-called heterodyne efficiency (cf. sec. 2.2), decreases. The misalignment between the local oscillator beam (red in fig. 2.44) and the received beam (blue) can be measured with DWS. If the rotation of the receiver is performed around a particular point, indicated with the green dot in the figure, the longitudinal phase or ranging signal as measured with both photodiodes does not change. Here, it was assumed that both photodiodes in the figure measure exactly the same signal, such that only a single green dot is present. In addition, it should be noted that the direction of the received beam in the receiver spacecraft is always along the x -axis, the line-of-sight, due to the quasi-spherical shape of phasefronts and as the waves propagate in vacuum normal to the phasefronts.

In summary, a local satellite misalignment influences the interferometric wavefront overlap, the phase and the DWS signals, while the misalignment of the transmitter, more precisely

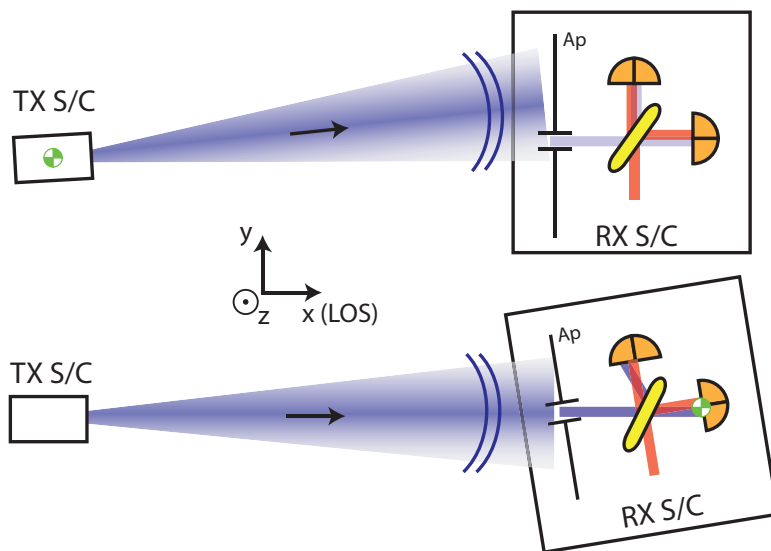


Figure 2.44: (**Upper sketch**): The transmitter S/C and TX beam are misaligned by rotation around the center of phasefront curvature, indicated with the green dot, which yields an intensity drop at the receiver. The beams on the receiver stay aligned. The phase or ranging signal at the receiver does not change, as the spherical phasefront is rotated around its center. (**Lower sketch**): The receiver is misaligned, which yields a misalignment between local oscillator beam (red) and the received beam (blue). It is noted that the beam size at the distant S/C is not up to scale as it is usually significantly larger than the satellite. The pivot point of rotation is indicated in the sketches with a green dot.

the misalignment between transmitted beam and the line-of-sight, changes the received light power. As the rotational sensing based on DWS is unaffected by the transmitter to a large extent, one can utilize DWS in a control loop for laser beam steering or for the attitude of the satellite, because DWS is affected only by local influenceable parameters. However, extensive transmitter misalignment leads to a drop of the signal amplitude below the tracking threshold of the phasemeter and to a loss of DWS and phase measurements. Furthermore, deviations of the phasefront from spherical or parabolic shape can couple transmitter misalignment and the DWS signals. Thus, for real instruments, it is essential to precisely determine the mode content of the transmit beam to be able to assess the magnitude of such disturbances.

2.6.3 Attitude-to-Ranging Coupling

The term attitude-to-ranging coupling is coined in this thesis. Other common names are tilt-to-pathlength, tilt-to-length or rotation-to-pathlength coupling. Due to this coupling mechanism, rotational degrees of freedom of a satellite, of a single component or of a test-mass produce an apparent length change in the longitudinal phase measurement. Therefore, fluctuations of the attitude can produce so-called attitude jitter noise in the phase-derived range measurement. The interferometers discussed in this thesis for gravimetric missions do not utilize an optical read-out of a test-mass, hence, attitude-to-ranging coupling refers to the attitude of the satellites, which is described in the following by three angles α , β and γ for roll, pitch and yaw, respectively. Furthermore, it is recalled that the satellites rotate around their center of mass, for example, in presence of disturbance torques.

In a DOWR and transponder-based ranging scheme, each satellite emits and receives laser light. It is assumed that the inter-satellite distance is large compared to the size of the laser beams, such that far-field approximations apply, i.e. the phasefronts are spherical at the distant S/C. The phase of the light is measured at each S/C and both measurements are subtracted to cancel the phase ramp due to the offset frequency. Moreover, the phase values

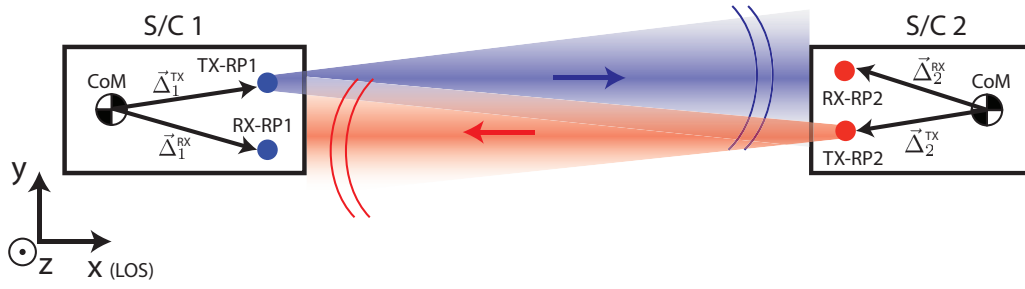


Figure 2.45: A two-way ranging scheme, where each S/C has an interferometric receiver reference point (RX RP) and a transmitter reference point (TX RP).

are scaled with the laser wavelength to obtain a displacement, i.e. the (biased) instantaneous geometrical distance $\rho = \rho_{\text{inst}}$ between the satellites (cf. sec. 2.4 on functional concepts):

$$\rho \approx \frac{1}{2} \cdot (\varphi_1 - \varphi_2) \cdot \frac{\lambda}{2\pi} \quad (2.286)$$

Relativistic effects, e.g. due to the translational motion of the satellites, have been treated in the previous sections. For the sake of simplicity, only the rotational degrees of freedom of the satellites are considered in the following generic derivation of the attitude-to-ranging coupling. A sketch of the considered setup is depicted in fig. 2.45, which shows two laterally separated beam axes. In total four points are highlighted, which are denoted as TX and RX reference points (RPs). The TX reference points are the sources of the laser beams with spherical phasefronts, i.e. the center of phasefront curvature as measured at the distant satellite. The RX reference points are the locations of point-like phase measurement systems. Specifics and technical details of the interferometer such as a local oscillator beam are omitted for the moment.

The phase φ_1 as measured by S/C 1 in this simplified scenario is proportional to the instantaneous geometrical distance between RX-RP1 and TX-RP2. If the position of the RPs is given as $\vec{\Delta}$ relative to the respective CoM, one can easily derive the following Taylor series for the pathlength coupling:

$$\varphi_1 \cdot \frac{\lambda}{2\pi} \approx \pm \rho_{1,\text{DC}} \pm (0, \gamma_1, -\beta_1) \cdot \vec{\Delta}_1^{\text{RX}} \pm \frac{1}{2} \cdot (\alpha_1, \beta_1, \gamma_1) \cdot \begin{pmatrix} 0 & 0 & 0 \\ 0 & \Delta_{1,x}^{\text{RX}} & 0 \\ 0 & 0 & \Delta_{1,x}^{\text{RX}} \end{pmatrix} \cdot \begin{pmatrix} \alpha_1 \\ \beta_1 \\ \gamma_1 \end{pmatrix} \quad (2.287)$$

$$\mp (0, \gamma_2, -\beta_2) \cdot \vec{\Delta}_2^{\text{TX}} \mp \frac{1}{2} \cdot (\alpha_2, \beta_2, \gamma_2) \cdot \begin{pmatrix} 0 & 0 & 0 \\ 0 & \Delta_{2,x}^{\text{TX}} & 0 \\ 0 & 0 & \Delta_{2,x}^{\text{TX}} \end{pmatrix} \cdot \begin{pmatrix} \alpha_2 \\ \beta_2 \\ \gamma_2 \end{pmatrix}. \quad (2.288)$$

The derivation used the fact that the inter-satellite distance is large, e.g. much larger than the size of the satellites or the lateral separation between the beam axes, and it was assumed that the rotations are performed in the order yaw-pitch-roll, i.e. they can be described with the total rotation matrix

$$\hat{R} = \hat{R}_x(\alpha) \cdot \hat{R}_y(\beta) \cdot \hat{R}_z(\gamma), \quad (2.289)$$

where α , β and γ correspond to roll, pitch and yaw rotation angles, respectively.

For this particular order, the quadratic coupling matrix becomes very simple. The signs in the Taylor series depend on the frequency ordering and are not of importance here. It is only noteworthy that the signs and the frequency ordering is reversed for S/C 2 (cf. sec. 2.4

on functional concepts), i.e.

$$\begin{aligned} \varphi_2 \cdot \frac{\lambda}{2\pi} \approx & \mp \rho_{2,\text{DC}} \pm (0, \gamma_2, -\beta_2) \cdot \vec{\Delta}_2^{\text{RX}} \pm \frac{1}{2} \cdot (\alpha_2, \beta_2, \gamma_2) \cdot \begin{pmatrix} 0 & 0 & 0 \\ 0 & \Delta_{2,x}^{\text{RX}} & 0 \\ 0 & 0 & \Delta_{2,x}^{\text{RX}} \end{pmatrix} \cdot \begin{pmatrix} \alpha_2 \\ \beta_2 \\ \gamma_2 \end{pmatrix} \\ & \mp (0, \gamma_1, -\beta_1) \cdot \vec{\Delta}_1^{\text{TX}} \mp \frac{1}{2} \cdot (\alpha_1, \beta_1, \gamma_1) \cdot \begin{pmatrix} 0 & 0 & 0 \\ 0 & \Delta_{1,x}^{\text{TX}} & 0 \\ 0 & 0 & \Delta_{1,x}^{\text{TX}} \end{pmatrix} \cdot \begin{pmatrix} \alpha_1 \\ \beta_1 \\ \gamma_1 \end{pmatrix}. \end{aligned} \quad (2.290)$$

With both phase measurements, the phase-derived range measurement ρ reads up to quadratic order in the angles as follows

$$\rho \approx \frac{1}{2} \cdot (\varphi_1 - \varphi_2) \cdot \frac{\lambda}{2\pi} \quad (2.291)$$

$$\begin{aligned} & \approx \text{const.} \pm \frac{1}{2} \cdot (0, \gamma_1, -\beta_1) \cdot (\vec{\Delta}_1^{\text{RX}} + \vec{\Delta}_1^{\text{TX}}) \\ & \pm \frac{1}{4} \cdot (\alpha_1, \beta_1, \gamma_1) \cdot \begin{pmatrix} 0 & 0 & 0 \\ 0 & \Delta_{1,x}^{\text{RX}} + \Delta_{1,x}^{\text{TX}} & 0 \\ 0 & 0 & \Delta_{1,x}^{\text{RX}} + \Delta_{1,x}^{\text{TX}} \end{pmatrix} \cdot \begin{pmatrix} \alpha_1 \\ \beta_1 \\ \gamma_1 \end{pmatrix} \\ & \pm \frac{1}{2} \cdot (0, -\gamma_2, \beta_2) \cdot (\vec{\Delta}_2^{\text{RX}} + \vec{\Delta}_2^{\text{TX}}) \\ & \pm \frac{1}{4} \cdot (\alpha_2, \beta_2, \gamma_2) \cdot \begin{pmatrix} 0 & 0 & 0 \\ 0 & \Delta_{2,x}^{\text{RX}} + \Delta_{2,x}^{\text{TX}} & 0 \\ 0 & 0 & \Delta_{2,x}^{\text{RX}} + \Delta_{2,x}^{\text{TX}} \end{pmatrix} \cdot \begin{pmatrix} \alpha_2 \\ \beta_2 \\ \gamma_2 \end{pmatrix}, \end{aligned} \quad (2.292)$$

where the first two lines of eq. (2.292) describe the attitude coupling on S/C 1 and the third and fourth line describe the attitude coupling on S/C 2.

It is noted that the transversal y and z components of the offset vectors $\vec{\Delta}_i$ couple linearly with pitch angle β and yaw angle γ , while a longitudinal offset along the x -axis ($\Delta_{1,x}$ or $\Delta_{2,x}$) couples quadratically with yaw and pitch. The roll angle α does not change the phase-derived range ρ in this simplified analysis.

In addition, it is remarked that the attitude coupling vanishes, if the satellites rotate around the centroid between the RX and the TX reference point, which means that the CoM of S/C 1 is co-located with the centroid, such that the term $(\vec{\Delta}_1^{\text{RX}} + \vec{\Delta}_1^{\text{TX}})/2$ is zero.

The attitude-to-ranging coupling was derived with the help of the simplified sketch shown in fig. 2.45. However, even in the case of a setup with a realistic interferometer, coupling factors of interferometer or satellite rotations into the range can be measured. One might be tempted to assign the measured coupling factors a geometrical meaning, for example, in terms of the offset vector $\vec{\Delta}$, which is, loosely speaking, a lever arm. This defines apparent and effective reference points for the interferometer, which have no necessary relation to the physical structure of the interferometer, i.e. they are virtual points. Of course, such an approach is only an approximation, because the coupling terms may generally have a fully populated quadratic coupling matrix, the quadratic coupling in yaw and pitch may be different or the roll-coupling may not vanish. Nevertheless, it is an interesting approach, which is followed in this thesis, since most of the attitude-to-ranging contributions can be covered with the model given in eq. (2.292).

A formal definition of the RPs is attempted as follows: RPs are pivot points of rotations, where the linear and quadratic coupling of yaw and pitch rotations into the measured phase vanish. The RX RP is defined as vanishing rotation-coupling for a phase measurement at the local rotating S/C, while the TX RP has vanishing rotation-coupling for a phase measurement at the distant (non-rotating) S/C. The RX RPs are the locations, where one would locate an equivalent ideal point-like phase measurement system instead of the complex interferometer. The TX RPs are the points, where one would place, based on phasefront observations at

the distant craft, an equivalent radiation source emitting ideal spherical waves instead of the actual transmit beam.

The motivation for reference points is to assign the linear and quadratic rotation-to-pathlength coupling factors with a geometrical meaning. These coupling factors are a major error contributor in the range measurement and key figures of inter-satellite ranging instruments. Expressing the coupling factors as a position is more vivid, in particular, it enables a systematic analysis of new interferometers and a comparison of different interferometer types. The systematic analysis should of course also include the stability and well-definedness of these points. Furthermore, it is an attempt to condense and approximate the complex interferometric setup with two points, which is only possible with simplifications, as these points typically depend on the state of the interferometer such as the temperature or the position of actuators and they are based on a linearization around an attitude set-point.

However, TX and RX reference points are properties of the interferometer and they can be used as categorization criteria. For example, if both points are located on the line-of-sight, the instrument can be denoted as an *on-axis* interferometer. Otherwise, the term *off-axis* interferometer is appropriate.

It is also repeated that the overall attitude-to-ranging coupling for a satellite depends on the centroid of RX RP and TX RP and the total attitude-to-ranging noise in the range measurement is equally driven by both satellites. Therefore, the centroid should be located close to the S/C CoM on both satellites to reduce the attitude jitter noise in the displacement measurement. Within the GRACE Follow-On LRI, this co-location has an accuracy of the order of 100 μm for the transversal y and z directions, while the line-of-sight direction has a more relaxed requirement, because this degree couples only quadratically. In fact, in the GRACE Follow-On mission, the vertex of the corner-cube is positioned at the CoM on each S/C, which equals the position of the centroid of RX- and TX RP as will be explained in sec. 2.7 on optical layouts. The effect of attitude-to-ranging coupling is depicted in terms of spectral densities in fig. 2.46, where the red trace in the lower panel shows the contribution in case of the GRACE Follow-On LRI. It has been derived from the pointing jitter simulation shown in the upper panel.

For microwave interferometry, the TX RP and RX RP are usually considered to be co-located with the antenna phase center. However, antennas have an anisotropic response and the phase center depends on the working point, e.g. the orientation of the antenna w.r.t the incident wavefronts and on the used frequency.

In optical interferometry, the determination of the RPs is also a non-trivial task as many optical components induce additional rotation-to-length coupling and moving objects such as actuators may alter the position. In the next two sub-sections, the RX and TX reference points are studied in more detail and approaches for the determination of the RPs based on sketches of the optical layouts are given. The RPs are also addressed in sec. 2.7 on optical layouts.

2.6.4 RX Reference Points

Photodiodes measure the phase of the laser light in optical interferometry. In general, each photodiode providing a longitudinal phase measurement has its own RX RP, because the attitude-to-ranging coupling factors can be determined for each photodiode individually. In addition, the reference points of different photodiodes may not be co-located. Of course, it would be appealing to directly infer the reference points from an interferometer sketch. Although this is not always possible, an empirical 3-step procedure for well-behaving and aligned interferometers, without guarantee for universal applicability, is the following:

The phasefronts arriving from the distant S/C are locally flat and appear as plane waves in front of the S/C with normal vector \vec{k} . One of these phasefronts is taken as a virtual plane (VP) as shown in fig. 2.47.

In a first step, one determines a ray originating from the VP and with direction \vec{k} , which

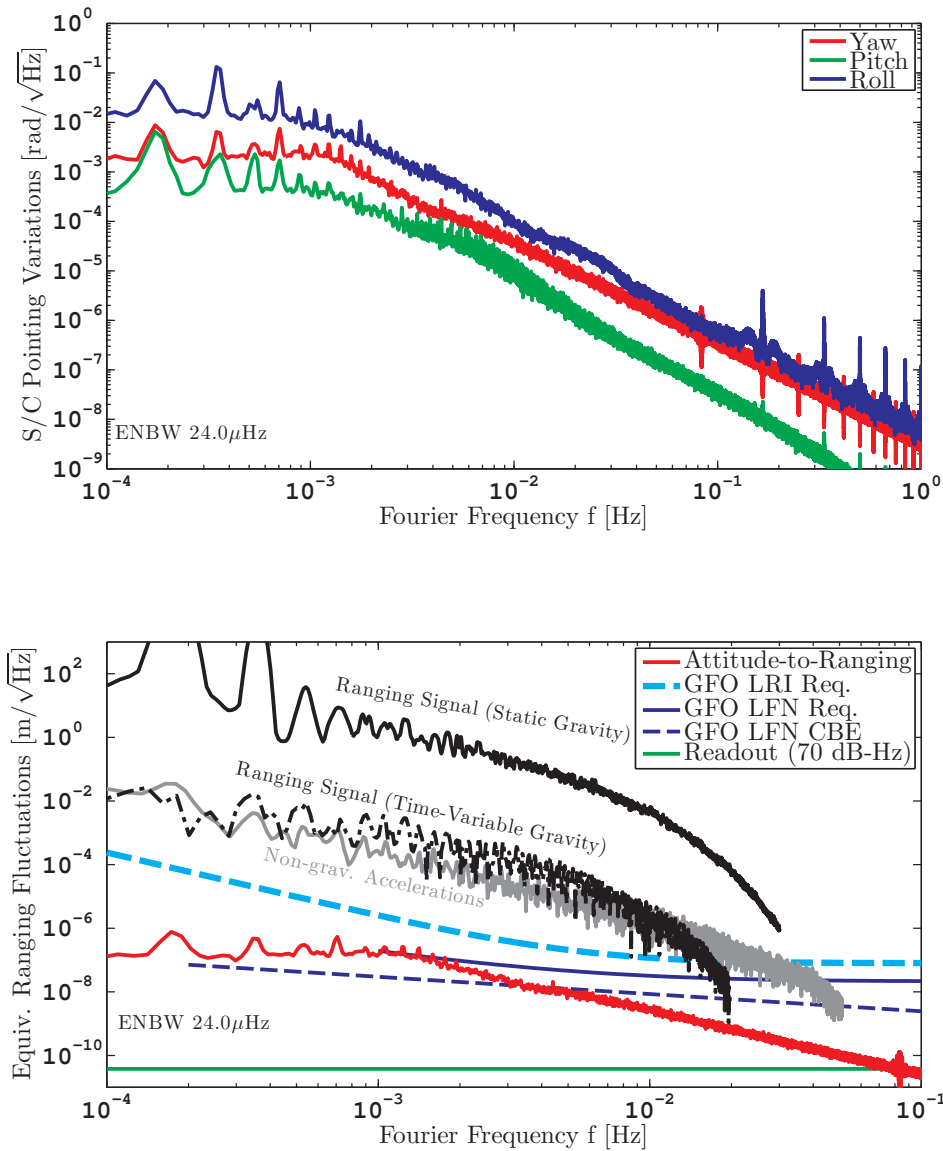


Figure 2.46: (Upper panel:) Attitude variations with respect to the line-of-sight for a single satellite. Data from a high-fidelity AOCS simulation by Airbus D&S for GRACE Follow-On. (Lower panel:) The corresponding pointing jitter noise is shown by the red trace, which includes the contributions of both satellites. A coupling of 100 $\mu\text{m}/\text{rad}$ was assumed in the lateral y and z direction, which corresponds to an offset of 100 μm between the centroid of RX RP and TX RP and the satellite CoM. The laser frequency noise (LFN) requirement and the current best estimate (CBE, 2016) are shown by the dark blue traces, which forms, together with the attitude-to-ranging coupling, the two major error contributors in inter-satellite laser ranging.

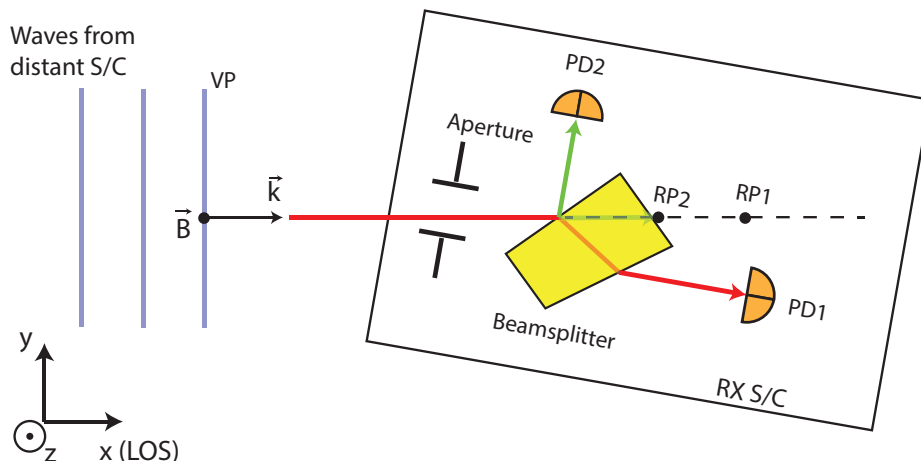


Figure 2.47: Determination of the RX reference points, RP1 for photodiode PD1 and RP2 for photodiode PD2. The intermediate point \vec{B} matches accidentally both photodiodes. The RX RPs are located on the axis \vec{k} , which propagate through the interferometer onto the center of the photodiodes. The longitudinal position on the axis is determined by the effective distance to the photodiodes. The photodiode PD1 has a longer effective distance (pathlength) due to the beamsplitter substrate, hence, RP1 has a larger separation to \vec{B} compared to RP2.

impinges onto the center of the photodiode under interest. The ray needs to propagate through the (complex) interferometer. The origin point of the ray on the VP is denoted with \vec{B} . In fig. 2.47, the point \vec{B} matches both photodiodes, which is, in general, not the case.

In a second step, the accumulated effective distance is determined, which the light ray traversed from the VP to the center of the photodiode. For purely reflective setups with flat surfaces, the effective distance is the accumulated geometrical pathlength. However, if a glass plate or an imaging system is passed, the equivalent distance is not the geometrical distance. Ideal imaging systems have zero effective distance from the input plane to the output plane. A planar beamsplitter at normal incidence with thickness d and refractive index n exhibits an effective distance of d/n . The effective distance is the B element of an ABCD ray transfer matrix.

In the last third step, the RX RP $\vec{\Delta}^{\text{RX}}$ is computed with

$$\vec{\Delta}^{\text{RX}} = \vec{B} + \frac{\vec{k}}{|\vec{k}|} \cdot d_{\text{eff,RX}}, \quad (2.293)$$

which is shown for the two photodiodes (RP1 and RP2) in fig. 2.47.

The method presented here did not consider the phase change from the local oscillator beam, i.e. it was assumed that the local oscillator beam is fixed. However, if the local oscillator is actuated to stay aligned with the RX beam and to zero DWS, the phase of the photodiode is also changed by the local oscillator. Thus, the previous expression needs to be modified to

$$\vec{\Delta}^{\text{RX}} = \vec{B} + \frac{\vec{k}}{|\vec{k}|} \cdot (d_{\text{eff,RX}} - d_{\text{eff,LO}}), \quad (2.294)$$

where $d_{\text{eff,LO}}$ is the effective distance for the local oscillator beam from the steering mirror (or the pivot point of rotation) to the photodiode center. Furthermore, it is remarked that this procedure considered that the attitude-to-ranging coupling is purely quadratic for rotations around the pivot point \vec{B} , which should apply for good-natured designs.

Another example for this procedure is shown for the GRACE Follow-On LRI design (cf. fig. 2.63), where the center of the RX aperture can be used as point \vec{B} . Then, the

effective distances for RX and LO beam are zero ($d_{\text{eff,RX}} = d_{\text{eff,LO}} = 0$), because the common imaging system images the RX aperture and the steering mirror onto the photodiode. Hence, the RX RP is at the center of the RX aperture. Even if the imaging system is removed and the individual effective distances are non-zero, the difference $d_{\text{eff,RX}} - d_{\text{eff,LO}}$ remains small, since the pathlengths from recombination beamsplitter to steering mirror and from recombination beamsplitter to aperture are almost identical. A significant shift of the RX RP would appear, if neither beam steering nor an imaging system would be present, because then eq. (2.293) would apply.

It follows from eq. (2.293) and (2.294) that the RX RP is located on the beam axis entering the satellite, however, the precise location depends on the specific optical layout. In addition, it is stressed again that the procedure stated here may not apply for all setups and the more general approach is to rotate the interferometric setup in optical simulations or even experimentally and to measure the attitude-to-ranging coupling factors directly.

2.6.5 TX Reference Points

The TX reference points have been introduced as the center of phasefront curvature (CoC) as apparent for the distant satellite (cf. upper sketch in fig. 2.48). Strictly speaking, the location of the TX RP within the satellite depends on the separation L between the satellites, although the effect is rather small within the far-field approximation ($L \gg 1$ km).

If the transmit beam is fixed in the S/C frame, i.e. no beam steering is present, rotations around the CoC do not change the phase, because a spherical phasefront is rotated around its center. The CoC is a virtual point and can be determined, in theory or in simulations, by measuring the phase at the distant satellite while rotating the local satellite around the CoM. With the linear and quadratic coupling factors one obtains the offset between the CoM and the TX RP.

Since far-field measurements are, in general, difficult, an alternative method is as follows: The transmit beam leaving the satellite is in good approximation a Gaussian beam for the interferometers considered in this thesis (cf. sec. 2.6.1). One can determine the Gaussian beam parameters, for example, the so-called complex q-parameter, at a particular position along the TX beam outside of the interferometer or satellite. With known properties of the beam, the virtual waist position of the beam on the prolonged TX beam axis can be calculated, which is the position of the CoC and of the TX RP. It is noted that the virtual waist or CoC may differ from the actual unfolded waist position, for example, if a telescope is present in the TX path. This is illustrated in the central sketch in fig. 2.48.

However, some interferometer concepts utilize active TX beam steering, which changes the direction and the light path through the S/C. This complicates the determination of the TX RP, because one needs to distinguish between attitude of the satellite and the orientation of the actuator and of the TX beam with respect to the line-of-sight, since these are non-trivially connected in interferometers with active beam steering. In the following, it is assumed that the beam steering is performed with a steering mirror, which rotates around the mirror surface center, where the laser beam is impinging (cf. lower sketch in fig. 2.48). The path along the central axis of the beam is parameterized with s , whereby $s = 0$ denotes the waist position.

The mirror pivot point is denoted with \vec{A} . At this point, the Gaussian TX beam has a phasefront radius of curvature $R(s = s_{\text{off}})$, with s_{off} being the pathlength between the waist position and point \vec{A} . The unfolded pivot point \vec{A} is denoted with $\vec{C} = (c_x, c_y, c_z)^\top$ as shown in the bottom sketch of fig. 2.48. The process of unfolding needs to account for potential imaging effects in the light path. If the steering mirror is rotated, the TX beam outside of the satellite seems to rotate around the pivot point \vec{C} . The phasefront curvature at the virtual point \vec{C} is equal to the phasefront curvature at \vec{A} . Thus, it is straightforward to compute the location of the CoC, since the distance between \vec{C} and CoC is s_{off} .

If the rotations of the satellite in roll, pitch and yaw are denoted with angles α, β and γ ,

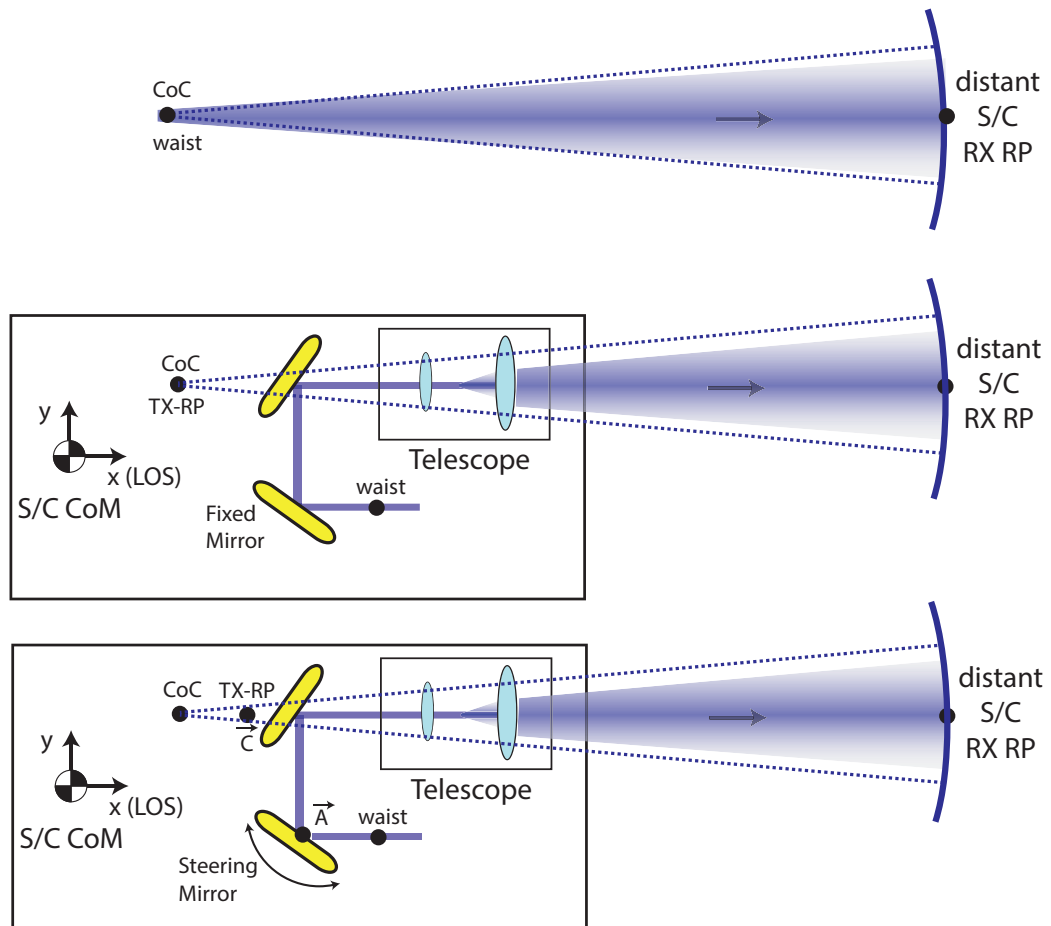


Figure 2.48: (**Upper sketch:**) Gaussian beam with almost spherical phasefront in the far-field. The waist and center of phasefront curvature (CoC) are co-located in the far-field approximation valid for inter-satellite ranging. (**Central sketch:**) Gaussian beam folded in a satellite interferometer without steering mirror. The CoC is the TX RP. It is a virtual waist position located on the transmit beam axis and corrected for imaging effects e.g. due to telescopes. The unfolded waist position would be located further to the left compared to the CoC. (**Lower sketch:**) Interferometer with steering mirror. The TX RP is denoted by point \vec{C} , which is the unfolded version of the steering mirror pivot point \vec{A} and corrected for imaging effects.

respectively, one can write the rotated position \vec{C}' of the point \vec{C} as

$$\vec{C}' = \hat{R}(\alpha, \beta, \gamma) \cdot \vec{C}, \quad (2.295)$$

where \hat{R} is a rotation matrix given in eq. (2.289). The direction of the TX beam \vec{d} is parameterized in case of lacking beam steering by

$$\vec{d} = \hat{R}(\alpha, \beta, \gamma) \cdot \vec{e}_x, \quad (2.296)$$

which means the TX beam rotates with the satellite, while in case of active beam steering it is

$$\vec{d} = \hat{R}(\delta\alpha, \delta\beta, \delta\gamma) \cdot \vec{e}_x, \quad (2.297)$$

which means the TX beam direction is inertially fixed up to some small beam pointing errors with respect to the line-of-sight denoted with $\delta\alpha, \delta\beta$ and $\delta\gamma$. The vector \vec{e}_x is the unit vector along the x -direction, which is the nominal TX beam direction and the line-of-sight.

With the direction \vec{d} and the point \vec{C}' one can compute the CoC with $-\vec{d} \cdot s_{\text{off}} + \vec{C}'$. This enables one to derive the pathlength coupling for a phase measurement at the distant S/C in absence of an active beam steering as

$$\rho \approx \text{const.} + \begin{pmatrix} 0 \\ -c_z \\ c_y \end{pmatrix} \cdot \begin{pmatrix} \alpha \\ \beta \\ \gamma \end{pmatrix} \quad (2.298)$$

$$+ \frac{1}{2} \cdot (\alpha, \beta, \gamma) \cdot \begin{pmatrix} 0 & 0 & 0 \\ 0 & c_x - s_{\text{off}} & 0 \\ 0 & 0 & c_x - s_{\text{off}} \end{pmatrix} \cdot \begin{pmatrix} \alpha \\ \beta \\ \gamma \end{pmatrix}, \quad (2.299)$$

and with TX beam steering one obtains

$$\rho \approx \text{const.} + \begin{pmatrix} 0 \\ -c_z \\ c_y \end{pmatrix} \cdot \begin{pmatrix} \alpha \\ \beta \\ \gamma \end{pmatrix} \quad (2.300)$$

$$+ \frac{1}{2} \cdot (\alpha, \beta, \gamma) \cdot \begin{pmatrix} 0 & 0 & 0 \\ 0 & c_x & 0 \\ 0 & 0 & c_x \end{pmatrix} \cdot \begin{pmatrix} \alpha \\ \beta \\ \gamma \end{pmatrix} \quad (2.301)$$

$$+ \frac{1}{2} \cdot (\delta\alpha, \delta\beta, \delta\gamma) \cdot \begin{pmatrix} 0 & 0 & 0 \\ 0 & -s_{\text{off}} & 0 \\ 0 & 0 & -s_{\text{off}} \end{pmatrix} \cdot \begin{pmatrix} \delta\alpha \\ \delta\beta \\ \delta\gamma \end{pmatrix} \quad (2.302)$$

These results illustrate that in case of a fixed TX beam in the S/C frame, the TX reference point is the center of phasefront curvature given by $\text{CoC} = (c_x - s_{\text{off}}, c_y, c_z)$, i.e. it is the unfolded waist position of the Gaussian beam, but corrected for effects from potential imaging systems. In case of active TX beam steering, the TX reference point is located at the point $\vec{C} = (c_x, c_y, c_z)$. However, if there are residual errors in the TX beam pointing with respect to the line-of-sight $(\delta\beta, \delta\gamma)$, the offset s_{off} produces changes in the measured phase, which are of quadratic order in the yaw and pitch angles. The offset s_{off} is the pathlength between the steering mirror pivot point \vec{A} and the actual waist position as shown in the lower sketch in fig. 2.48. Thus, the waist position of the laser beam should be located at the steering mirror, which is also the design baseline of the GRACE Follow-On LRI.

In summary, the TX RP is of importance for the satellite attitude-to-ranging coupling, because the coupling is determined by the centroid of RX and TX RP. For interferometers without active beam steering along the line-of-sight, such as the LISA mission, the TX RP is given by the center of the phasefront curvature as apparent in the far-field. For setups with active beam steering along the line-of-sight, such as the GRACE Follow-On LRI, the TX

RP is located at the apparent pivot point for the TX beam, which is, loosely speaking, the unfolded steering mirror pivot point. Thus, it does not depend on the phasefront or the waist position of the TX beam. However, if there are pointing errors of the TX beam with respect to the line-of-sight, caused, for example, by noise in the steering mirror, the offset s_{off} between steering mirror and waist position couples quadratically with the yaw and pitch beam pointing error.

For a numerical example of the magnitude of this induced beam jitter noise, it is assumed that the waist position is known with an accuracy of 10% of the Rayleigh range z_R and that the pointing noise with respect to the line-of-sight is of the order of $\text{ASD}[\sigma] = 5 \mu\text{rad}/\sqrt{\text{Hz}}$ in yaw and pitch. For the GRACE Follow-On LRI, the Rayleigh range is approximately $z_R = 18 \text{ m}$, which yields $s_{\text{off}} = 1.8 \text{ m}$. Furthermore, with a static offset of $\sigma_0 \approx 50 \mu\text{rad}$, this results in a noise of the order of

$$s_{\text{off}} \cdot \sigma_0 \cdot \text{ASD}[\sigma] \cdot 2 \approx 1 \text{ nm}/\sqrt{\text{Hz}}, \quad (2.303)$$

where the factor of two accounts for two satellites ($\sqrt{2}$) and for two axes ($\sqrt{2}$). Thus, the magnitude of the noise term is uncritical but noteworthy. Other pref-factors might be required, if the pointing noise $\text{ASD}[\sigma]$ is referred to the motion of a steering mirror, which often deflects the beam by twice the angle.

2.6.6 Validity and Extensions of Reference Points

Reference points have been defined in the previous sections as pivot points of vanishing attitude-to-ranging coupling for rotations around yaw and pitch axes. However, this definition holds only in an idealized case. For a particular rotation axis, there exists a line of pivot points, which is parallel to the rotation axis and where the coupling vanishes (cf. appendix E). In the non-ideal and realistic case, roll-rotations around the x -axis change the ranging signal and a line of zero coupling exists for the roll angle as well.

Furthermore, in the ideal case, yaw, pitch and roll lines intersect in a single point, however, in general, the lines are slightly skew. Hence, there is no intersection point and no reference point. This may apply for the RX RP and the TX RP. For example, in the TX path, skew lines of vanishing yaw and pitch pathlength coupling are caused by different phasefront radii of curvature along two transverse principal directions of the TX beam.

An extension of the reference points are axes or lines of vanishing coupling, which can be defined for the RX, TX and the combination of both, which is the important quantity as it determines total attitude-to-ranging coupling.

Another possible extension of the RPs are *points of minimal coupling* (POMC), which can be defined as the point closest to the lines of vanishing coupling as shown in appendix E. The magnitude of the residual attitude-to-ranging coupling at the RX-POMC and TX-POMC, the ability to measure the POMC location and the POMC position stability need to be analyzed in detail in the advanced design phase of an interferometer.

However, such an in-depth analysis for the various optical layouts shown in subsequent section 2.7 is beyond the scope of this thesis and the layouts are treated with reference points, which is sufficient in an early design phase.

2.6.7 Retro-Reflection, Point-Ahead Direction and Angle

This short sub-section addresses a design principle for interferometers, which has been used without further notice in previous sections and which applies in particular for gravimetric missions. This principle is the retro-reflection property, which interferometers need to exhibit to efficiently exchange light. Retro-reflection means here that the interferometers on the satellites send their TX beam in the direction of the received phasefronts. This can be efficiently achieved with the help of differential wavefront sensing (DWS). Furthermore, this

property motivates the use of retro-reflecting optical components within the optical layout, such as in the GRACE Follow-On LRI.

However, strictly speaking, retro-reflection is only correct if the satellites are non-moving transversally to the line-of-sight. This is because point-ahead effects play a role due to the finite speed of light c_0 and due to the non-zero time-delay Δt between photon emission at the transmitter S/C and reception at the distant S/C. Hence, the light should be emitted not exactly along the anti-parallel direction of the incoming phasefronts, but along the point-ahead direction, where the distant S/C will be located at the time of reception. The important quantity is the transversal velocity $v_{12,\perp}$ between the satellites, because it determines the point-ahead angle θ_{pa} [Sheard *et al.*, 2012]

$$\theta_{\text{pa}} \approx \frac{2 \cdot |\vec{v}_{12,\perp}|}{c_0}, \quad (2.304)$$

under the typical valid assumption $L \gg |\vec{v}_{12,\perp}| \cdot \Delta t$. The relative transversal velocity is given by

$$\vec{v}_{12,\perp} = (\vec{v}_2 - \vec{v}_1) - (\vec{v}_2 - \vec{v}_1) \cdot \vec{e}_{12}, \quad (2.305)$$

where \vec{e}_{12} is the line-of-sight direction between both satellites. Numerical values for the relative transversal velocity can be found in table 2.6.

A point-ahead angle θ_{pa} is a desired misalignment from retro-reflection and it needs to be compared to the divergence of the transmitted (Gaussian) beam θ_{TX} . The ratio $\theta_{\text{pa}}/\theta_{\text{TX}}$ is ≈ 0.01 for the exemplary gravimetric mission GRACE Follow-On as apparent from table 2.6 and indicates that the misalignment due to the point-ahead angle is acceptable without further action, while $\theta_{\text{pa}}/\theta_{\text{TX}} \approx 1$ for a LISA mission type requires a point-ahead compensation.

Because the point-ahead direction is a vectorial quantity, the point-ahead angle θ_{pa} can be decomposed into a local S/C or an interferometer coordinate frame, e.g. yaw and pitch directions. For a gravimetric in-line constellation the (negligible) point-ahead angle is mostly in pitch direction. If the point-ahead direction is constant in a local S/C or interferometer frame, a static misalignment of a mirror can induce the desired deflection. However, even a constant θ_{pa} value might still imply that the point-ahead direction changes between the different axes, which would require a dynamic point-ahead actuator.

It is summarized that the interferometers for gravimetric missions discussed here do not require a point-ahead compensation in the beam pointing, i.e. it is sufficient for the interferometers to retro-reflect the light.

2.6.8 Optical Detection Schemes

The previous sections were mainly concerned with the longitudinal phase, i.e. the ranging information, and the susceptibility to rotations and pointing. In the following sections, the signal amplitude of the interferometric phase readout is addressed, which can be used to derive the signal-to-noise ratio of the phase measurement.

To obtain an observable interference between laser beams, the beams need to be in the same polarization state and they need to be overlapped, i.e. co-located and co-aligned in their propagation direction (cf. overlap integral eq. (2.56)). The spatial overlap is typically achieved by a beamsplitter, while matching of polarization states can be performed before or after overlapping. In satellite interferometry, the interfered beams are typically detected with a quadrant photodiode, which provides DWS, DPS and the ranging (longitudinal) signals after phase-tracking (cf. sec. 2.2). Various implementations of the optical detection scheme with different degrees of redundancy can be utilized. The most common detection schemes are briefly discussed in this subsection.

The most simple setup is illustrated in scheme 1 of fig. 2.49. This scheme has only a single beamsplitter and one port of the beamsplitter is unused. Thus, the local oscillator in the open port can be used, for example, as TX beam. It is noted that the local oscillator beam

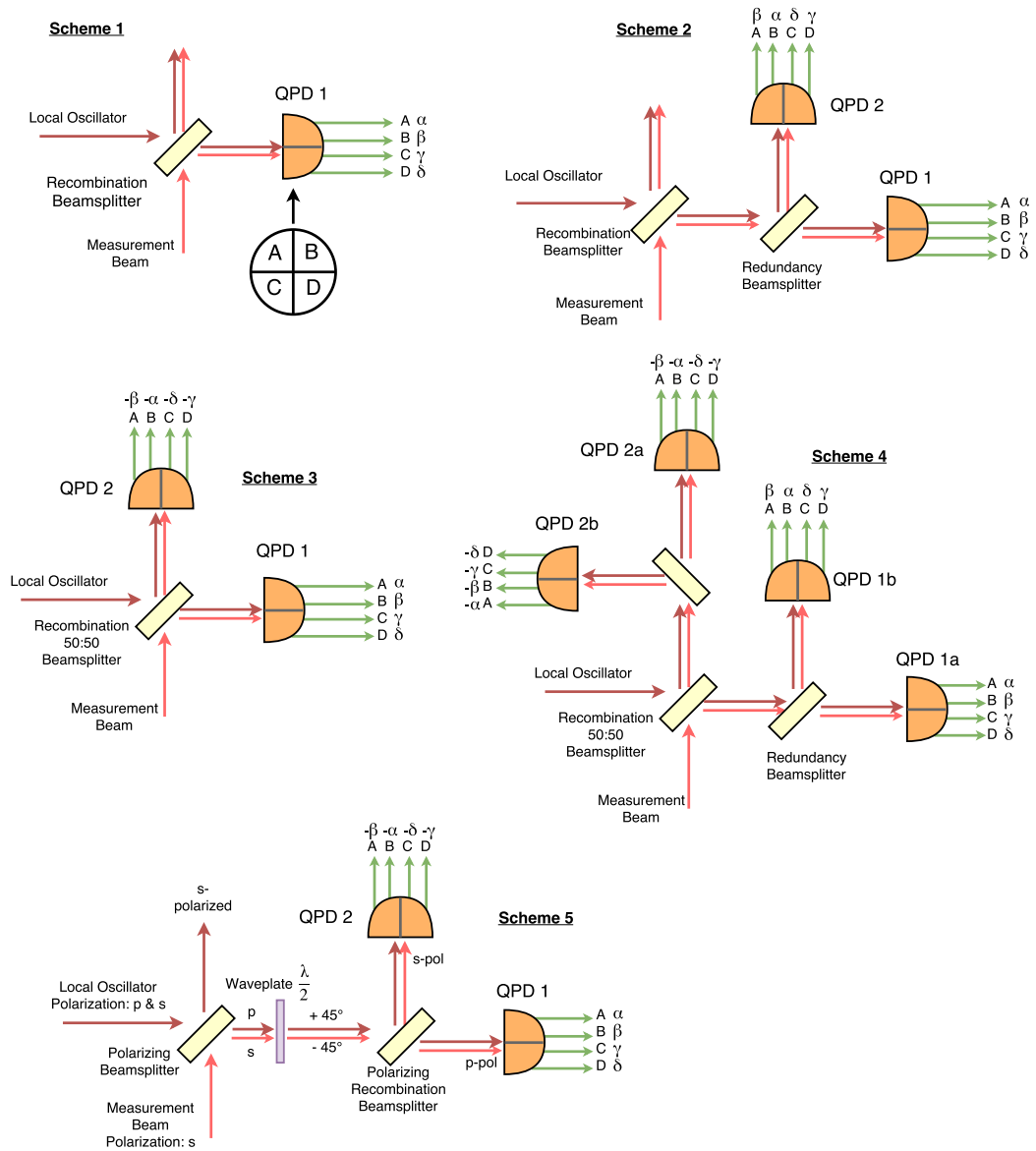


Figure 2.49: Different optical detection schemes for interferometric phase readout with required combination of photocurrents for redundant or balanced operation.

and the measurement beam are parallel in both ports, if the DWS signal is zero, i.e. both phasefronts are aligned at the photodiode. In addition, this thesis adopts the nomenclature from the GRACE Follow-On LRI project for the QPD segments, i.e. the labeling of segments (A,B,C,D) is always line-wise from left to right when looking onto the photodiode active area, with segments C and D being in the direction of the interferometer bottom baseplate¹¹. The wires of the photodiode or the photoreceiver output channels are labeled (A,B,C,D) like the segments, so that all photodiodes are inter-changeable. However, the photocurrents are labeled in this thesis with greek letters ($\alpha, \beta, \gamma, \delta$), which becomes useful when the correct combination of redundant photodiode signals is discussed.

The detection scheme 1 with a single quadrant photodiode offers no redundancy, i.e. failure of a single segment or channel implies loss of the DWS and DPS signals. Redundancy can be introduced with a second beamsplitter and photodiode, which is shown in scheme 2 of fig. 2.49. The horizontal direction appears flipped in terms of photocurrents for QPD 2 due to the additional reflection in the path of the beams towards QPD 2. To obtain a hot-redundant phase readout, the signals ($\alpha, \beta, \gamma, \delta$) of QPD 1 need to be added to the signals ($\alpha, \beta, \gamma, \delta$) of QPD 2, which means a combination of segments according to

$$(A_1, B_1, C_1, D_1) + (B_2, A_2, D_2, C_2). \quad (2.306)$$

Alternatively, one can also phase-track all 8 segments with a phasemeter, and perform the correct combination afterwards with the complex oscillation coefficients in the domain of phase and heterodyne amplitude. It is noted that the GRACE Follow-On LRI follows the redundancy scheme 2, with combination of photodiode signals prior digitization and phase-tracking in the analog electric domain. Furthermore, it is remarked that this scheme also provides an open port with a local oscillator beam aligned to the measurement beam in case of minimized DWS signals.

Another type of detection is shown in scheme 3, where only a single beamsplitter is present, i.e. no unused local oscillator beam is available anymore. The photocurrents of QPD 2 are flipped w.r.t. QPD 1, because QPD 2 has no reflection for the measurement beam. In addition, the photocurrents in QPD 2 have a phase shift of 180° , i.e. are multiplied with -1 . This phase shift between output ports of an interference-generating beamsplitter, which is often called recombination beamsplitter, follows from energy conservation. If a hot-redundant phase readout is desired, the different segments need to be subtracted according to (cf. fig. 2.49)

$$(A_1, B_1, C_1, D_1) - (B_2, A_2, D_2, C_2). \quad (2.307)$$

The heterodyne amplitudes in both ports are equal in scheme 3, if a 50:50 beamsplitter is used. This case is commonly called *balanced detection* and offers the advantage that some noise sources, most importantly the relative intensity noise, cancel out in the combined output.

Scheme 4 enables a balanced detection with full redundant readout of both anti-correlated ports, which requires 16 QPD segments.

It was assumed in the schemes 1-4 that both input beams are in the same polarization state such that interference occurs upon overlap at the beamsplitter. Scheme 5 illustrates a method, where both beams are overlapped in different polarization states, and interference is generated afterwards by a polarizing beamsplitter, which usually reflects *s*-polarized light. Again, both photodiodes have anti-correlated signals with 180° phase difference due to energy conservation. In addition, this scheme offers the advantage that the *s*-polarized part of the local oscillator input remains available, while all light of the measurement beam is used. The latter statement does not hold for schemes 1 and 2, where a part of the measurement beam is always transmitted at the first beamsplitter.

¹¹In the so-called plus orientation of a QPD. Cross-orientation is not discussed here.

A balanced detection scheme is not mandatory for gravimetric missions with $\text{nm}/\sqrt{\text{Hz}}$ sensitivity and MHz beatnotes, because the relative intensity noise is typically sufficiently small at these frequencies. The phase detection in LISA Pathfinder, which used kHz beatnotes, required balanced detection schemes to remove the relative intensity noise of the laser.

The availability of an unused local oscillator beam, which can be aligned by means of DWS with the incoming measurement (RX) beam, is typically required for interferometers with active TX beam steering such as the GRACE Follow-On LRI. Thus, scheme 1 and 2, depending on the redundancy concept of the mission, are also potential candidates for future gravimetric missions. However, since these schemes waste some part of the weak RX light, also scheme 5 is an interesting option. In fact, it will be used in an optical layout proposed here for future gravimetric missions in sec. 2.7.

In general, the selection of the optimal scheme is a difficult trade-off between the degree of redundancy, complexity and sensitivity. Further in-depth analysis of potential other detection methods and a trade-off of these would surely advance the field of inter-satellite ranging, but it was beyond the scope of this thesis. Regardless the scheme, it was pointed out in this subsection that the correct phasing and the reflection-induced flips of the segments need to be taken into account, when signals are combined in experiments or simulations. Moreover, it should be noted that the detection scheme, e.g. the number of present photodiode segments, determines the amount of noise and the signal power available for phase-tracking. In particular, it influences the carrier-to-noise density, which is addressed next.

2.6.9 Carrier-To-Noise Density C/N_0

As discussed in the section 2.3.7 on phasemeters, the carrier-to-noise density of the electric beatnote obtained by photodetection limits the phase readout sensitivity. This phase readout noise can typically be reached or measured only at high frequencies in gravimetric missions, since other noise sources such as laser frequency fluctuations or attitude-induced noise are dominating at low frequencies and the actual ranging signal is present as well.

However, the C/N_0 is still important as it represents the signal strength, e.g. dividing the C/N_0 by the bandwidth of the phase measurement system yields the signal-to-noise ratio. For the operation of a laser ranging system, the C/N_0 needs to exceed the tracking threshold for all operational conditions and over the mission lifetime, e.g. considering degradation or contamination of optics. The C/N_0 is a major driver of requirements on laser power, beam parameters and optical layout.

The C/N_0 is, in general, a property of an oscillating signal and is defined by the ratio of signal power over the noise PSD. In satellite interferometry, the oscillatory signal is obtained from the photodiode and the C/N_0 can be computed as

$$C/N_0 = \frac{I_{\text{rms}}^2}{\text{PSD}[I_{\text{PR}}] + \text{PSD}[I_{\text{SN}}] + \text{PSD}[I_{\text{RIN}}] + \text{PSD}[I_{\text{QN}}]}, \quad (2.308)$$

where the four most important noise contributors are considered.

The carrier power is given by eq. (2.54), i.e.

$$I_{\text{rms}}^2 = 4 \cdot \eta \cdot P_{\text{LO}} \cdot P_{\text{RX}} \cdot \eta_{\text{PD}} \cdot \frac{1}{2}, \quad (2.309)$$

with factor $\frac{1}{2}$ rescaling the zero-peak photocurrent to an rms-value. The heterodyne efficiency η is determined by the overlap integral (cf. eq. (2.56)) and the photodiode responsivity η_{PD} with units of A/W is a property of the photodiode. The quantities P_{RX} and P_{LO} denote the optical power of the local oscillator and of the measurement or received (RX) light beam impinging onto the active area under consideration. For the interferometers discussed within this thesis, the RX light is much weaker than the local oscillator ($P_{\text{RX}} \ll P_{\text{LO}}$).

The noise of the photoreceiver chain $\text{ASD}[I_{\text{PR}}] = \sqrt{\text{PSD}[I_{\text{PR}}]}$ has been introduced in sec. 2.3.3 on photodiodes and can be considered below $5 \text{ pA}_{\text{rms}}/\sqrt{\text{Hz}}$ for the segment of a

quadrant photodiode. The noise is assumed to be white within the measurement bandwidth for the sake of simplicity.

The shot noise (SN) results from the energy quantization of light fields. The arrival statistics of the quanta, called photons, in a (classical) electro-magnetic field obeys the well-known Poisson distribution. Furthermore, the variance $(\Delta n)^2$ of the number of arriving photons n is given by the mean number of photons in the field, $(\Delta n)^2 = \langle n \rangle$. The same holds for electrons in an electric circuit.

The single-sided shot noise power spectral density in terms of electric current I or optical power P is

$$\text{PSD}[I] = 2 \cdot e \cdot \langle I \rangle, \quad \text{PSD}[P] = 2 \cdot h\nu \cdot \langle P \rangle, \quad (2.310)$$

where $e = 1.609 \cdot 10^{-19}$ C is the electron charge, $h = 6.626 \cdot 10^{-34}$ J · s is the Planck constant and ν is the photon's frequency.

In space laser interferometry, the photons are converted into electron-hole pairs by means of the photoelectric effect with an efficiency $\eta_{\text{PD}} \leq 1$. Single photon absorption is the dominating process, on the one hand due to the band gap energy of the absorbing semi-conductor, and on the other hand due to low intensity levels. Hence, the average number of photons per unit time does not exceed the number of electrons per unit time, and the signal-to-noise ratio in the electric domain can not exceed the signal-to-noise ratio in the photon domain.

In general, heterodyne interferometry is characterized by a non-stationary number of photons arriving at the photodiode due to oscillatory intensity resulting from the interference of two fields with unequal frequency. However, due to the low power level of the received light in inter-satellite ranging, the interferometric contrast is low ($c \approx 10^{-3}$). Hence, the average number of photons is dominated by the strong local oscillator field and the shot noise can be considered white with single-sided spectral density

$$\text{PSD}[I_{\text{SN}}] = 2 \cdot e \cdot \langle I \rangle \approx 2 \cdot e \cdot \eta_{\text{PD}} \cdot P_{\text{LO}}. \quad (2.311)$$

If both interfering light fields have comparable amplitude and the interferometric contrast is high ($c \approx 1$), the resulting shot noise is cyclo-stationary [Niebauer *et al.*, 1991], which might become of interest, if additional local interferometers are used to read out the test mass position, for example.

The third noise contribution in eq. (2.308) accounts for the intensity fluctuations of the laser at once and twice the beatnote frequency, as these appear in the phase measurement at the beatnote frequency¹²

$$\begin{aligned} \text{PSD}[I_{\text{RIN}}] = & \text{PSD}[\delta P_{\text{LO}}(f)/P_{\text{LO}}] \cdot \eta_{\text{PD}}^2 \cdot P_{\text{LO}}^2 + \text{PSD}[\delta P_{\text{RX}}(f)/P_{\text{RX}}] \cdot \eta_{\text{PD}}^2 \cdot P_{\text{RX}}^2 \\ & + (\text{PSD}[\delta P_{\text{LO}}(2f)/P_{\text{LO}}] + \text{PSD}[\delta P_{\text{RX}}(2f)/P_{\text{RX}}]) \cdot \frac{\eta_{\text{PD}}^2 \cdot P_{\text{LO}} \cdot P_{\text{RX}} \cdot \eta}{4} \end{aligned} \quad (2.312)$$

$$P_{\text{RX}} \ll P_{\text{LO}} \quad \text{PSD}[\delta P_{\text{LO}}(f)/P_{\text{LO}}] \cdot (\eta_{\text{PD}} \cdot P_{\text{LO}})^2, \quad (2.313)$$

with η denoting the heterodyne efficiency. The RIN contribution at twice the heterodyne frequency vanishes in weak light interference with low interferometric contrast. The magnitude of this noise contributor can be calculated for a generic relative intensity noise requirement of $\text{PSD}[(\frac{\delta P}{P})] = 10^{-15}$ 1/Hz, which has been suggested in table 2.1 in section 2.3.1 on the laser.

The last noise term in eq. (2.308) accounts for the quantization noise arising from the digitization of the analog voltage or photocurrent. It can be described under some particular

¹²This can easily be derived by computing the photocurrent as $I = \eta_{\text{PD}} \cdot \int |E_1 + E_2|^2 dA$ with $E_i = e^{i\omega_i t} \cdot e_i(x, y) \cdot \sqrt{1 + \epsilon_{i,1} \cdot \cos((\omega_1 - \omega_2)t) + \epsilon_{i,2} \cdot \cos(2 \cdot (\omega_1 - \omega_2)t)}$, where $\epsilon_{i,1/2}$ is a small RIN amplitude at once and twice the beatnote frequency.

assumptions [Gerberding, 2014, p. 69] as white noise with amplitude spectral density as [Heinzel *et al.*, 2002]

$$\text{ASD}[U_{\text{QN}}] = \frac{U_{\text{LSB}}}{\sqrt{6 \cdot f_{s,\text{ADC}}}} = \frac{2 \cdot U_{\text{ADC,max}}}{2^N \cdot \sqrt{6 \cdot f_{s,\text{ADC}}}} \quad (2.314)$$

in units of $\text{V}_{\text{rms}}/\sqrt{\text{Hz}}$. U_{LSB} is the step size of the least-significant bit with unit of volts, N denotes the number of bits, while $f_{s,\text{ADC}}$ represents the ADC sampling frequency in Hertz. Typical numerical values of $N = 14$, $U_{\text{ADC,max}} = 10 \text{ V}$ and $f_{s,\text{ADC}} = 40 \text{ MHz}$ yield

$$\text{PSD}[U_{\text{QN}}] = (78 \text{ nV}_{\text{rms}}/\sqrt{\text{Hz}})^2 = 6.2 \cdot 10^{-15} \text{ V}_{\text{rms}}^2/\text{Hz}, \quad (2.315)$$

which can be converted to the equivalent photocurrent noise by dividing with the squared transimpedance gain, which is much larger than unity ($G_{\text{TIA}} \gg 1 \Omega$), i.e.

$$\text{PSD}[I_{\text{QN}}] = \frac{\text{PSD}[U_{\text{QN}}]}{G_{\text{TIA}}^2} \ll 6.2 \cdot 10^{-15} \text{ A}_{\text{rms}}^2/\text{Hz}. \quad (2.316)$$

Hence, in a reasonable design, the quantization noise can be made negligible compared to the equivalent current noise of the photoreceiver chain of $\approx 25 \text{ pA}_{\text{rms}}^2/\text{Hz}$ and other contributions. Furthermore, the subscript rms is dropped in the following for the sake of readability, since the numerator and denominator of the carrier-to-noise density contain rms values.

Finally, with an abbreviation for the effective power $P_{\text{eff,seg}} = \eta_{\text{seg}} \cdot P_{\text{RX,seg}}$ one can approximate the C/N_0 as

$$C/N_{0,\text{seg}} \approx \frac{2 \cdot P_{\text{LO,seg}} \cdot P_{\text{eff,seg}} \cdot \eta_{\text{PD}}}{25 \text{ pA}^2/\text{Hz} + 2 \cdot e \cdot \eta_{\text{PD}} \cdot P_{\text{LO,seg}} + 10^{-15} \text{ 1/Hz} \cdot \eta_{\text{PD}}^2 \cdot P_{\text{LO,seg}}^2}. \quad (2.317)$$

This equation holds for a single channel of the photoreceiver. This channel can be connected, for example, to a single element photodiode or to a segment of a quadrant photodiode. However, the optical power values $P_{\text{LO,seg}}$ and $P_{\text{eff,seg}}$ and the heterodyne efficiency η_{seg} need to be referred to the connected active area.

The C/N_0 from eq. (2.317) and its inverse are visualized by the magenta traces in fig. 2.50 as a function of the local oscillator power. An optimum with minimum phase readout noise is at

$$P_{\text{LO,seg}} = 0.19 \text{ mW}, \quad (2.318)$$

which is a good starting point for many interferometer designs. Based on this number, one can compute the required power per photodiode, and then the power in front of the recombination beamsplitter based on the beamsplitter transmissivity.

The C/N_0 of an individual channel of the phasemeter is of importance, since all channels need to be tracked and, hence, all channel need to exceed the minimum tracking threshold for the C/N_0 . However, the actual noise in the longitudinal phase φ_{long} or in the DWS signals (DWS_v and DWS_h) is determined by the average or difference of various segments. For example, φ_{long} is formed by the average phase of all segments of a quadrant photodiode. The averaging is typically performed within the phasemeter and can be implemented in different ways. One method is to track the four channels of a quadrant photodiode and average the phases with

$$\varphi_{\text{long}} = \frac{\varphi_A + \varphi_B + \varphi_C + \varphi_D}{4}. \quad (2.319)$$

An alternative is to weight the phase values with the corresponding heterodyne amplitude a , and form the so-called coherent sum:

$$\varphi_{\text{long}} = \arg \left(\sum_n a_n \cdot e^{i\varphi_n} \right) \quad (2.320)$$

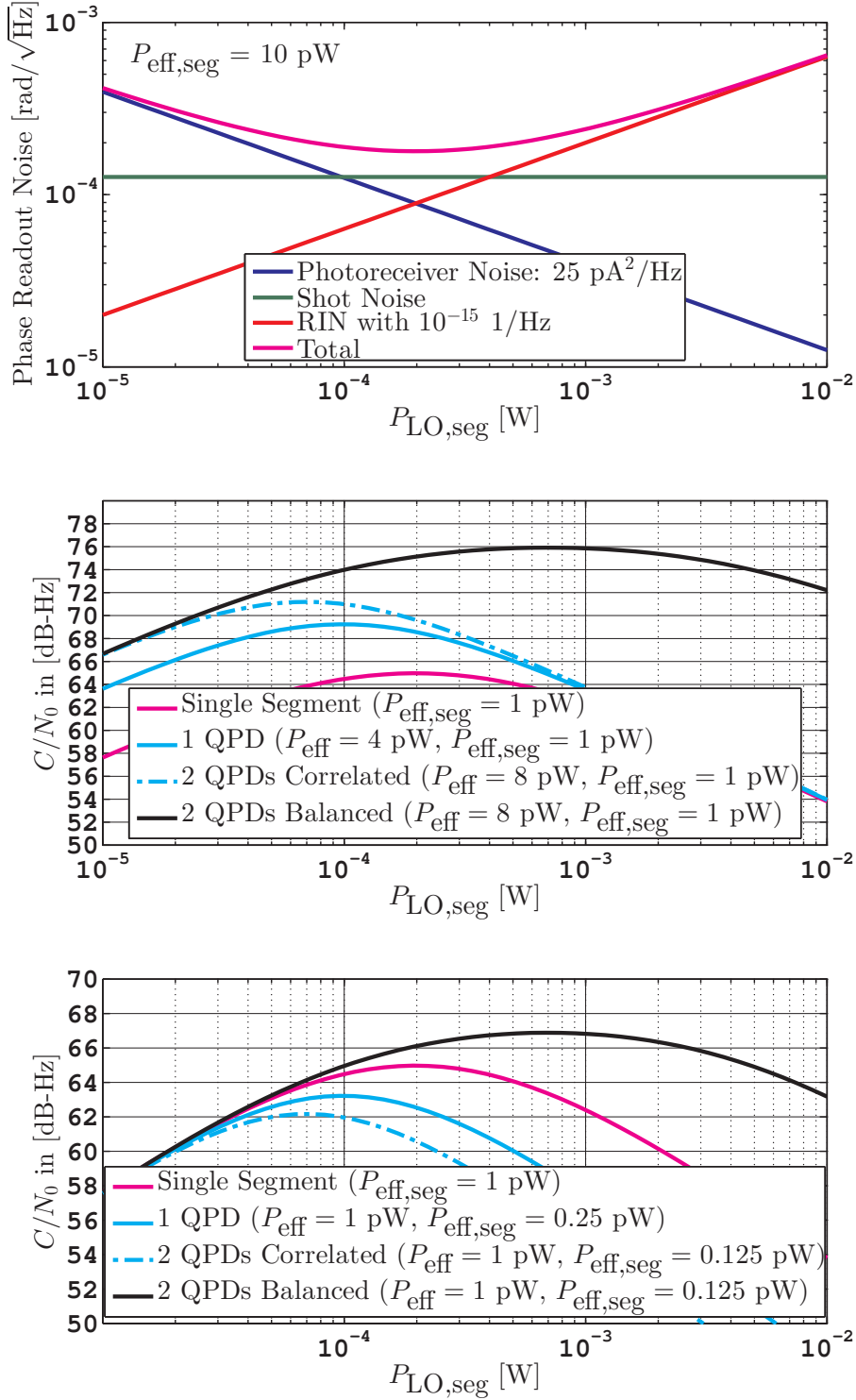


Figure 2.50: (Upper panel:) The phase readout noise (magenta trace) given by $1 \text{ rad}/\sqrt{C/N_0}$ and its constituents as a function of the local oscillator power. This plot assumes a single segment (channel) with $P_{\text{eff}} = 10 \text{ pW}$. (Central panel:) C/N_0 in dB-Hz as a function of the local oscillator power. The optimal power for a single segment is $P_{\text{LO,seg}} \approx 0.19 \text{ mW}$. A lower level causes excess photoreceiver noise, while a higher power causes an excess of RIN. The traces for the coherent sum of 4 and 8 segments have 4 and 8 times, respectively, more effective power available, i.e. 1 pW per segment. (Lower panel:) The same as the central panel, only rescaled for a total effective power of 1 pW. All plots consider a photodiode responsivity of $\eta_{\text{PD}} = 0.8 \text{ A/W}$.

Such an averaging is usually difficult to perform with the FPGA-based hardware of a phasemeter. However, a practical method is to sum the digital counts of each channel and use an additional phase-tracking loop for the sum of the segments. The resulting phase is equivalent to eq. (2.320). Furthermore, it is noted that the longitudinal phase from eq. (2.320) would be measured by an equivalent circular single-element diode in the limit of vanishing gap size between segments.

However, in practice, the difference between eq. (2.319) and (2.320) is small, because the heterodyne amplitude of all segments is usually similar.

The following expression can be used to calculate the carrier-to-noise density for the coherent sum of n_s segments

$$C/N_{0,n_s} \approx \frac{2 \cdot \eta_{\text{PD}} \cdot \left| \sum_n \sqrt{P_{\text{LO},n} \cdot P_{\text{eff},n}} \cdot e^{i\varphi_n} \right|^2}{25 \frac{\text{pA}^2}{\text{Hz}} \cdot n_s + 2 \cdot e \cdot \eta_{\text{PD}} \cdot \sum_n P_{\text{LO},n} + 10^{-15} \text{ Hz}^{-1} \cdot \eta_{\text{PD}}^2 \cdot \left| \sum_i P_{\text{LO},n} \cdot e^{i\varphi_n} \right|^2}, \quad (2.321)$$

$$\approx \frac{2 \cdot P_{\text{LO,seg}} \cdot P_{\text{eff,seg}} \cdot \eta_{\text{PD}} \cdot n_s^2}{25 \frac{\text{pA}^2}{\text{Hz}} \cdot n_s + 2 \cdot e \cdot \eta_{\text{PD}} \cdot P_{\text{LO,seg}} \cdot n_s + 10^{-15} \text{ Hz}^{-1} \cdot \eta_{\text{PD}}^2 \cdot P_{\text{LO,seg}}^2 \cdot n_s^2}, \quad (2.322)$$

which considers that the photoreceiver noise and the shot noise are uncorrelated, while the beatnote signal and the RIN are correlated among segments. This typically applies for the segments of a single quadrant photodiode (with $n_s = 4$). The simplified eq. (2.322) was derived under the assumption of similar power levels ($P_{\text{eff},n}$ and $P_{\text{LO},n}$) and similar phase φ_n among the segments of the sum.

The C/N_0 for a single quadrant photodiode (QPD) is displayed by the solid light blue trace in fig. 2.50. The central panel shows the C/N_0 for an effective power of 1 pW per segment, while the lower panel has a total effective power of 1 pW, i.e. 0.25 pW per segment. The local oscillator power on the x -axis refers to a single segment.

The previous formula can also be utilized for two redundant quadrant photodiodes ($n_s = 8$) in non-balanced detection schemes, such as scheme 2 in the previous sec. 2.6.8. In such a scheme, the photocurrents of both photodiodes are correlated and they are added to form the hot-redundant phase measurement. Furthermore, the RIN is positively correlated between both photodiodes and it remains in the hot-redundant phase combination. The summation of photodiode signals for hot-redundant operation can be performed in the analog domain prior digitization, in the digital domain prior phase-tracking or even after phase-tracking. In GRACE Follow-On, the summation is implemented within the optical bench electronics in the analog domain, since the phasemeter has only 4 AC input channels.

It is noted that in case of scheme 5 from the previous section, the beatnotes are anti-correlated on both photodiodes and the photocurrents need to be subtracted. However, the RIN is still positively correlated on both photodiodes. Thus, if the power splitting ratio between both photodiodes is 50:50, the combination of both photodiodes suppresses the RIN. For such a combination, one obtains

$$C/N_{0,n_s=8,\text{bal}} \approx \frac{2 \cdot P_{\text{LO,seg}} \cdot P_{\text{eff,seg}} \cdot \eta_{\text{PD}} \cdot 8^2}{25 \frac{\text{pA}^2}{\text{Hz}} \cdot 8 + 16 \cdot e \cdot \eta_{\text{PD}} \cdot P_{\text{LO,seg}} + \epsilon_{\text{bal}}^2 \cdot 10^{-15} \text{ Hz}^{-1} \cdot \eta_{\text{PD}}^2 \cdot P_{\text{LO,seg}}^2 \cdot 8^2}, \quad (2.323)$$

where ϵ_{bal} was introduced to describe the suppression of the RIN. The magnitude of this factor depends on the power splitting ratio at the interference-generating beamsplitter and on the similarity of both ports, which may be disturbed by decentered photodiodes, for example. A generic value of $\epsilon_{\text{bal}} = 0.1$ is assumed here. The magnitude of eq. (2.323) is shown by the black trace in fig. 2.50.

One should notice that there is no common optimal $P_{\text{LO,seg}}$ value for the coherent sum, e.g. the ranging signal, and the single segments. In this thesis, the value of the local oscillator

power is selected such that it optimizes the C/N_0 of a single segment, because the phase readout noise is not limiting the ranging sensitivity in gravimetric missions opposed to the shot-noise limited LISA mission.

With this decision and according to the central panel of fig. 2.50, one obtains the following numerical values for the C/N_0 of a single segment

$$C/N_{0,\text{seg}} = 65 \text{ dB-Hz} + 10 \cdot \log_{10} \left(\frac{P_{\text{eff,seg}}}{1 \text{ pW}} \right) \text{ dB}, \quad (2.324)$$

which means that 5 dB or equivalently approx. 3.2 pW effective power per segments is required to reach 70 dB-Hz, which was a potential phase-tracking requirement (cf. sec. 2.3.7 on phasemeter).

If an optical layout with detection scheme 2 from previous section is used, which agrees with the one used in GRACE Follow-On, for example, one can compute the C/N_0 of the longitudinal phase or of the DWS signals with

$$C/N_{0,n_s=8} = 69 \text{ dB-Hz} + 10 \cdot \log_{10} \left(\frac{P_{\text{eff,seg}}}{1 \text{ pW}} \right) \text{ dB}, \quad (2.325)$$

while

$$C/N_{0,n_s=8,\text{bal}} = 75 \text{ dB-Hz} + 10 \cdot \log_{10} \left(\frac{P_{\text{eff,seg}}}{1 \text{ pW}} \right) \text{ dB}, \quad (2.326)$$

applies for detection scheme 5 with polarizing components. Both schemes use two photodiodes and a hot-redundant summation of photodiode signals. Scheme 5 offers the advantage of a balanced detection, which suppresses the relative intensity noise of the laser light and which yields a higher C/N_0 . However, it is recommended to not rely on this gain, because this contradicts the idea of redundant operation of photodiodes, i.e. the interferometer should be capable to operate also with a single photodiode in case of failure of one diode.

In gravimetric missions, the C/N_0 is not limiting the ranging sensitivity, however, it is still an important quantity for the acquisition of the laser link (cf. sec. 2.6.12) and for the power budget of the interferometer (cf. sec. 2.8), which are subsequently addressed. The reader interested in carrier-to-noise densities and in the combination of photodiode signals is also referred to [Delgado, 2012], where this aspect is covered with regard to the LISA mission interferometry and in more detail than in this thesis.

For the calculation of the C/N_0 , the effective power P_{eff} is needed, which is discussed in the next two subsections.

2.6.10 Effective Power: RX Beam Power

The effective power P_{eff} for the C/N_0 is defined as the product of heterodyne efficiency η and of the received power P_{RX} used for the interference, which is the power of the weak beam containing the ranging information. It can be defined for the segment of a circular quadrant photodiode or for a circular photodiode (CPD), i.e.

$$P_{\text{eff,seg}} = \eta_{\text{seg}} \cdot P_{\text{RX,seg}} \quad (2.327)$$

$$P_{\text{eff,CPD}} = \eta_{\text{CPD}} \cdot P_{\text{RX,CPD}}. \quad (2.328)$$

Although the interferometer optical layouts in this thesis utilize quadrant photodiodes, the circular photodiode can be used to represent, in a good approximation, the coherent sum of the segments, which forms the longitudinal phase.

The received power P_{RX} used for the interference and photodetection had to enter the satellite and interferometer, which is assumed to happen through a circular receiver aperture with radius $r_{\text{RX,AP}}$. Since the light within the receiver aperture has effectively a constant intensity and a flat phasefront, it is a so-called *flat top* or *top hat* beam behind the aperture

and within the interferometer. The power in the receiver aperture $P_{\text{RX,AP}}$ is related to $P_{\text{RX,CPD}}$ via

$$P_{\text{RX,CPD}} = P_{\text{RX,AP}} \cdot \eta_{\text{AP} \rightarrow \text{CPD}} \cdot \eta_{\text{RX,mask,CPD}}, \quad (2.329)$$

where $\eta_{\text{AP} \rightarrow \text{CPD}}$ represents the power transfer efficiency from the receiver aperture to the circular photodiode. The term $\eta_{\text{RX,mask,CPD}}$ accounts for the ratio of light power in front of the CPD to the power in the active area of the CPD. It makes sense to require that the RX beam is smaller or equal to the size of the photodiode in order to avoid wasting of already weak light. Hence, for a circular single-element photodiode one obtains $\eta_{\text{RX,mask,CPD}} = 1$. However, if the CPD is a circular segmented quadrant photodiode with radius r_{PD} and with a small gap $g \ll r_{\text{PD}}$ between the segments, the value is approximately given by

$$\eta_{\text{RX,mask,CPD}} \approx 1 - \frac{A_{\text{gaps}}}{A_{\text{CPD}}} \approx 1 - \frac{4 \cdot g \cdot r_{\text{PD}}}{\pi r_{\text{PD}}^2}, \quad (2.330)$$

which is $\eta_{\text{RX,mask,CPD}} \approx 98.7\%$ for an ordinary 1 mm diameter diode with $g = 50 \mu\text{m}$ slit width between segments. Thus, the difference between a segmented circular photodiode and a full circular photodiode is often negligible for the RX light with assumed flat intensity.

The optical RX beam power within a segment $P_{\text{RX,seg}}$ can typically be approximated as one quarter of the power of the segmented quadrant CPD, i.e.

$$P_{\text{RX,seg}} \approx \frac{P_{\text{RX,CPD}}}{4}, \quad (2.331)$$

while more precise calculations require the integration of the light's intensity over the segment area. Of course, the previous formulas need to be adjusted to account for the actual optical layout under consideration, for example, which may contain several redundant photodiodes.

The power within the receiver aperture $P_{\text{RX,AP}}$ can be easily derived from the Gaussian beam far-field intensity for small misalignments of the TX beam with respect to the line-of-sight (cf. eq. (2.281))

$$I_{\text{RX}} \approx \frac{2 \cdot P_{\text{TX}}}{\pi \omega(L)^2} \cdot e^{-2(\beta_{\text{TX}}^2 + \gamma_{\text{TX}}^2) \cdot L^2 / \omega(L)^2} \quad (2.332)$$

and from the effective area of the aperture $A = \pi r_{\text{RX,AP}}^2 \cdot \cos\left(\sqrt{\beta_{\text{RX}}^2 + \gamma_{\text{RX}}^2}\right)$ as

$$P_{\text{RX,AP}} \approx I_{\text{RX}} \cdot \pi r_{\text{RX,AP}}^2 \cdot \left(1 - \frac{\beta_{\text{RX}}^2 + \gamma_{\text{RX}}^2}{2}\right). \quad (2.333)$$

The angles β_{TX} and γ_{TX} denote the yaw and pitch transmit beam misalignment w.r.t. the LOS, while β_{RX} and γ_{RX} are the yaw and pitch misalignment angles of the receiver. The expression $\omega(L) \approx \theta_{\text{TX,div}} \cdot L$ represents the spot size of the transmitted beam in $L \approx 100 \text{ km}$ distance, for example. P_{TX} is the transmitted laser beam power in watts. The dependency of the receiver power on the receiver misalignment β_{RX} and γ_{RX} is of quadratic order and can be neglected, since these angles are typically very small in laser interferometric applications.

Moreover, the laser beam shows a rotational symmetry and it is sufficient to consider only a single misalignment direction, e.g. with the angle α_{TX} , such that eqs. (2.332) and (2.333) lead to

$$P_{\text{RX,AP}}(\alpha_{\text{TX}}) \approx \frac{2 \cdot P_{\text{TX}} \cdot r_{\text{RX,AP}}^2}{L^2} \cdot \frac{e^{-2 \cdot \alpha_{\text{TX}}^2 / \theta_{\text{TX,div}}^2}}{\theta_{\text{TX,div}}^2}. \quad (2.334)$$

The on-axis intensity and the power in the distant S/C aperture can be maximized by decreasing the divergence $\theta_{\text{TX,div}}$ or equivalently increasing the waist size of the TX beam.

For a particular maximal TX misalignment $\alpha_{\text{TX,max}}$, the power in the distant RX aperture $P_{\text{RX,AP}}$ is maximal for

$$\theta_{\text{TX,div}} = \sqrt{2} \cdot \alpha_{\text{TX,max}} \quad (2.335)$$

with

$$P_{\text{RX,AP,max}}(\alpha_{\text{TX,max}}) \approx \frac{P_{\text{TX}} \cdot r_{\text{RX,AP}}^2}{L^2 \cdot \alpha_{\text{TX,max}}^2} \cdot 0.37 \text{ rad}^2, \quad (2.336)$$

if other parameters such as wavelength λ and total TX power P_{TX} are kept fixed. These are important relations, since an interferometer design is typically tuned to work under the worst-case assumptions such as with maximum receiver and maximum transmitter misalignment. Thus, eq. (2.335) can provide the optimal divergence of the TX beam.

Eq. (2.334) and (2.336) assume a diffraction-limited fundamental Gaussian TX beam without clipping, which means that the limiting aperture radius in the TX beam path $r_{\text{TX,AP}}$ is significantly larger than the Gaussian $1/e^2$ beam radius ω , i.e. $r_{\text{TX,AP}} > 3 \cdot \omega$. The far-field intensity in case of beam clipping is discussed in appendix F. It turns out that for a particular clipping aperture radius $r_{\text{TX,AP}}$, the on-axis power in the far-field is maximized by a Gaussian beam waist radius prior clipping of $\omega_0 = 0.892 \cdot r_{\text{TX,AP}}$. In the LISA mission context, this beam parameter maximizes the power throughput of the telescope, which is the limiting aperture. The telescope, more precisely a beam expander, has a characteristic magnification m_{T} and the largest mirror is assumed as the limiting aperture with radius $r_{\text{TAP}} = r_{\text{TX,AP}}$.

Under these assumptions, the power in the far-field aperture for a clipped Gaussian TX beam can be approximated as (cf. eq. (F.21f.))

$$P_{\text{RX,AP}}(\alpha_{\text{TX}}) \approx \frac{2 \cdot P_{\text{TX,PC}} \cdot r_{\text{RX,AP}}^2}{L^2} \cdot \left(1 - e^{-r_{\text{TAP}}^2/(\omega_{0,\text{TIN}} \cdot m_{\text{T}})^2}\right)^2 \cdot \frac{e^{-2\alpha_{\text{TX}}^2/(\theta_{\text{TX,ncg}} \cdot \psi(\omega_{0,\text{TIN}} \cdot m_{\text{T}}/r_{\text{TAP}}))^2}}{\theta_{\text{TX,ncg}}^2} \quad (2.337)$$

$$= \frac{2 \cdot P_{\text{TX,AP}} \cdot r_{\text{RX,AP}}^2}{L^2} \cdot \tanh\left(\frac{r_{\text{TAP}}^2}{2 \cdot \omega_{0,\text{TIN}}^2 \cdot m_{\text{T}}^2}\right) \cdot \frac{e^{-2\alpha_{\text{TX}}^2/(\theta_{\text{TX,ncg}} \cdot \psi(\omega_{0,\text{TIN}} \cdot m_{\text{T}}/r_{\text{TAP}}))^2}}{\theta_{\text{TX,ncg}}^2}, \quad (2.338)$$

where $\omega_{0,\text{TIN}}$ is the Gaussian $1/e^2$ waist radius in the input plane of the telescope prior magnification and $\theta_{\text{TX,ncg}}$ is the far-field divergence of a magnified non-clipped Gaussian beam, i.e.

$$\theta_{\text{TX,ncg}} = \lambda/(\pi \cdot \omega_{0,\text{TIN}} \cdot m_{\text{T}}). \quad (2.339)$$

The function ψ accounts for the increased divergence due to the clipping parameter (ratio) $\omega_{0,\text{TIN}} \cdot m_{\text{T}}/r_{\text{TAP}}$ and is given in table 2.8. The TX beam power prior clipping is denoted with $P_{\text{TX,PC}}$, while $P_{\text{TX,AP}}$ describes the clipped power, i.e. within the limiting TX aperture.

These methods to compute the far-field power for a fundamental Gaussian beam and for a clipped Gaussian beam are required for the calculation of the effective RX power and are applied in subsequent sec. 2.8 on the laser link power budget and on the determination of optimal parameters for different optical layouts. In addition, it should be noted that the optical power in the receiver aperture of a satellite is to first order independent of the receiver misalignment, but strongly dependent on the transmit beam misalignment with respect to the line-of-sight.

A word of warning is advisable concerning large TX beam misalignments. The power or intensity far away from the central beam axis is not represented correctly by the equations in this section, since only the fundamental Gaussian mode was considered and approximations were used, which hold only close to the beam axis. Furthermore, it is highly non-trivial to experimentally determine the mode content of actual laser beams precisely. Moreover, beams

delivered by optical fibers have a fiber mode [Mahrdt, 2014], which deviates from a Gaussian shape and complicates the analysis as well. Hence, the author of this thesis recommends to consider in early design studies a conservative maximum misalignment $\alpha_{\text{TX,max}}$, which does not exceed an intensity drop of $1/e^2 \approx 13.5\%$ w.r.t. the on-axis intensity, as these levels can be predicted reliably.

2.6.11 Effective Power: Heterodyne Efficiency

The heterodyne efficiency η of the interference is the second factor in the effective power (cf. eq. (2.327)). It is a function of the impinging complex electric fields E^c from local oscillator (LO) and received light (RX) and it depends on the geometry of the active area A of the photodiode or photodiode segment. The heterodyne efficiency η can be computed with help of (cf. eq. (2.56))

$$\sqrt{\eta} \cdot e^{i\varphi} = \frac{\int_A E_{\text{RX}}^c \cdot E_{\text{LO}}^{c*} dx dy}{\sqrt{(\int_A E_{\text{RX}}^c \cdot E_{\text{RX}}^{c*} dx dy) \cdot (\int_A E_{\text{LO}}^c \cdot E_{\text{LO}}^{c*} dx dy)}} = \frac{\int_A E_{\text{RX}}^c \cdot E_{\text{LO}}^{c*} dx dy}{\sqrt{P_{\text{RX}} \cdot P_{\text{LO}}}}, \quad (2.340)$$

where φ is the phase of the photodiode segment, which would be measured by a phasemeter. The star denotes complex conjugation. The heterodyne efficiency η is a real-valued quantity between 0 and 1 and a measure for the overlap or similarity between the two electric fields. Common distortions to both fields, such as a common tilt of both fields, do not alter η .

The local oscillator field can be considered as a Gaussian beam, while the received light has usually a *top hat*, also called *flat top*, shape. This indicates a constant non-zero intensity and phase in the entrance aperture and zero magnitude outside. Such an electric field has a wide angular spectrum, which causes diffraction patterns to appear upon propagation. These are typically mitigated by imaging the entrance aperture onto the active area of the photodiode, where the electric fields are measured. Imaging also implies that the beam stays centered on the photodiode upon tilts, i.e. there is no beam walk upon rotations, which allows one to use simple expressions for the electric field.

The electric field amplitude of a top hat beam with radius r_{TH} and tilted by a small angle α_{EF} can be defined in polar coordinates as

$$E_{\text{RX}}^c(r, \theta) \sim \begin{cases} e^{i \cdot 2\pi/\lambda \cdot \alpha_{\text{EF}} \cdot \cos(\theta) \cdot r}, & r \leq r_{\text{TH}} \\ 0, & r > r_{\text{TH}} \end{cases} \quad (2.341)$$

while the Gaussian local oscillator with waist at the photodiode has a functional dependency according to

$$E_{\text{LO}}^c(r, \theta) \sim e^{-r^2/\omega_{0,\text{LO}}^2}. \quad (2.342)$$

Due to the circular symmetry of the fields and the photodiode, only a tilt α_{EF} and no tip angle between the phasefronts is considered, as it simplifies the computation.

It makes sense to assume that the top hat beam formed by the RX aperture is completely imaged onto the active area of a photodiode, i.e. $r_{\text{TH}} \approx r_{\text{PD}}$, otherwise received light is wasted. The ratio between the top hat radius (= RX aperture radius) and photodiode radius provides the required magnification of the beam compressor, which is used to demagnify the flat top beam to fit the size of the photodiode, and potential other imaging optics such as telescopes. The term magnification by a factor m is also used here, if m is smaller than unity and actually a de-magnification. Any magnification of a beam size by a factor m yields a phasefront tilt magnification by $1/m$.

This duality implies that an ideal imaging system used for both beams does not change the heterodyne efficiency, if the area of the top hat beam is used for the computation of the heterodyne efficiency.

In polar coordinates, it is straightforward to compute η as the squared modulus of eq. (2.340). The polar angle θ ranges from $0..2\pi$ for a circular photodiode (CPD), which yields

$$\eta_{\text{CPD}} = \frac{8 \cdot \left| \int_{r=0}^{r_{\text{RX,AP}}} e^{-r^2/\omega_{0,\text{LO}}^2} \cdot r \cdot J_0(2\pi/\lambda \cdot \alpha_{\text{EF}} \cdot r) \, dr \right|^2}{r_{\text{RX,AP}}^2 \cdot \omega_{0,\text{LO}}^2 \cdot \left(1 - e^{-2r_{\text{RX,AP}}^2/\omega_{0,\text{LO}}^2}\right)}, \quad (2.343)$$

$$= \frac{8 \cdot \left| \int_{q=0}^1 e^{-q^2 \cdot r_{\text{RX,AP}}^2/\omega_{0,\text{LO}}^2} \cdot q \cdot J_0(2\pi/\lambda \cdot \alpha_{\text{EF}} \cdot r_{\text{RX,AP}} \cdot q) \, dq \right|^2}{\omega_{0,\text{LO}}^2/r_{\text{RX,AP}}^2 \cdot \left(1 - e^{-2r_{\text{RX,AP}}^2/\omega_{0,\text{LO}}^2}\right)}, \quad (2.344)$$

where J_0 is the Bessel function of first kind. For the second line (eq. (2.344)), the integral was recast to dimensionless boundaries, which illustrates that a magnification by a factor m , i.e. replacing

$$r_{\text{RX,AP}} \rightarrow m \cdot r_{\text{RX,AP}} \quad (2.345)$$

$$\omega_{0,\text{LO}} \rightarrow m \cdot \omega_{0,\text{LO}} \quad (2.346)$$

$$\alpha_{\text{EF}} \rightarrow \alpha_{\text{EF}}/m, \quad (2.347)$$

does not alter the heterodyne efficiency.

For $\alpha_{\text{EF}} = 0$, the heterodyne efficiency can be solved analytically:

$$\eta_{0,\text{CPD}} = \frac{2\omega_{0,\text{LO}}^2}{r_{\text{RX,AP}}^2} \cdot \tanh\left(\frac{r_{\text{RX,AP}}^2}{2 \cdot \omega_{0,\text{LO}}^2}\right). \quad (2.348)$$

The expression for $\eta_{0,\text{CPD}}$ approaches unity for $\omega_{0,\text{LO}} \gg r_{\text{RX,AP}}$, which is expected as a very large Gaussian beam has constant intensity in the central region and shows similarity to a flat top beam.

The dependency of the heterodyne efficiency on the angle α_{EF} is depicted in the left panels of fig. 2.51. The plots have been derived by numerically integrating eq. (2.343). The angle α_{EF} , where the heterodyne efficiency reaches $1/e^2$, is shown in fig. 2.52. If the waist size of the Gaussian local oscillator is smaller than approximately half the radius of the top hat ($\omega_{0,\text{LO}}/r_{\text{RX,AP}} < 0.5$), the drop in the heterodyne efficiency is nearly Gaussian with $1/e^2$ level given by the divergence angle of the local oscillator $\theta_{\text{LO}} = \lambda/(\pi \cdot \omega_{0,\text{LO}})$. A 6th order polynomial model has been derived, which enables to write an approximate solution for eq. (2.343) as a Gaussian decay

$$\eta_{\text{CPD,mod}}(\alpha_{\text{EF}}) = \eta_{0,\text{CPD}} \cdot e^{-2\alpha_{\text{EF}}^2/(\theta_{\text{LO}} \cdot \psi(\omega_{0,\text{LO}})/r_{\text{RX,AP}})^2} \quad (2.349)$$

with $\psi(x) = \sum_{i=0}^6 p_i \cdot x^i$ and coefficients p_i given in table 2.8. The model accuracy in terms of the difference $\eta_{\text{CPD,mod}} - \eta_{\text{CPD}}$ is shown in the right panels of fig. 2.51.

The heterodyne efficiency for a single segment requires evaluation of the integral in eq. (2.340) for a polar angle range of $0.. \pi/2$ for segment A, for example, which yields

$$\eta_{\text{seg,A}} = \frac{8 \cdot \left| \int_{r=0}^{r_{\text{RX,AP}}} e^{-r^2/\omega_{0,\text{LO}}^2} \cdot r \cdot (J_0(2\pi/\lambda \cdot \alpha_{\text{EF}} \cdot r) + i \cdot H_0(2\pi/\lambda \cdot \alpha_{\text{EF}} \cdot r)) \, dr \right|^2}{r_{\text{RX,AP}}^2 \cdot \omega_{0,\text{LO}}^2 \cdot \left(1 - e^{-2r_{\text{RX,AP}}^2/\omega_{0,\text{LO}}^2}\right)}, \quad (2.350)$$

$$= \eta_{\text{CPD}} + \frac{8 \cdot \left| \int_{r=0}^{r_{\text{RX,AP}}} e^{-r^2/\omega_{0,\text{LO}}^2} \cdot r \cdot H_0(2\pi/\lambda \cdot \alpha_{\text{EF}} \cdot r) \, dr \right|^2}{r_{\text{RX,AP}}^2 \cdot \omega_{0,\text{LO}}^2 \cdot \left(1 - e^{-2r_{\text{RX,AP}}^2/\omega_{0,\text{LO}}^2}\right)} \quad (2.351)$$

with H_0 denoting the so-called Struve-function. For co-aligned phasefronts, i.e. $\alpha_{\text{EF}} = 0$, the Struve-function vanishes and the value of the circular photodiode is reproduced, i.e.

$$\eta_{0,\text{seg,A}} = \eta_{0,\text{seg,B}} = \eta_{0,\text{seg,C}} = \eta_{0,\text{seg,D}} = \eta_{0,\text{CPD}}. \quad (2.352)$$

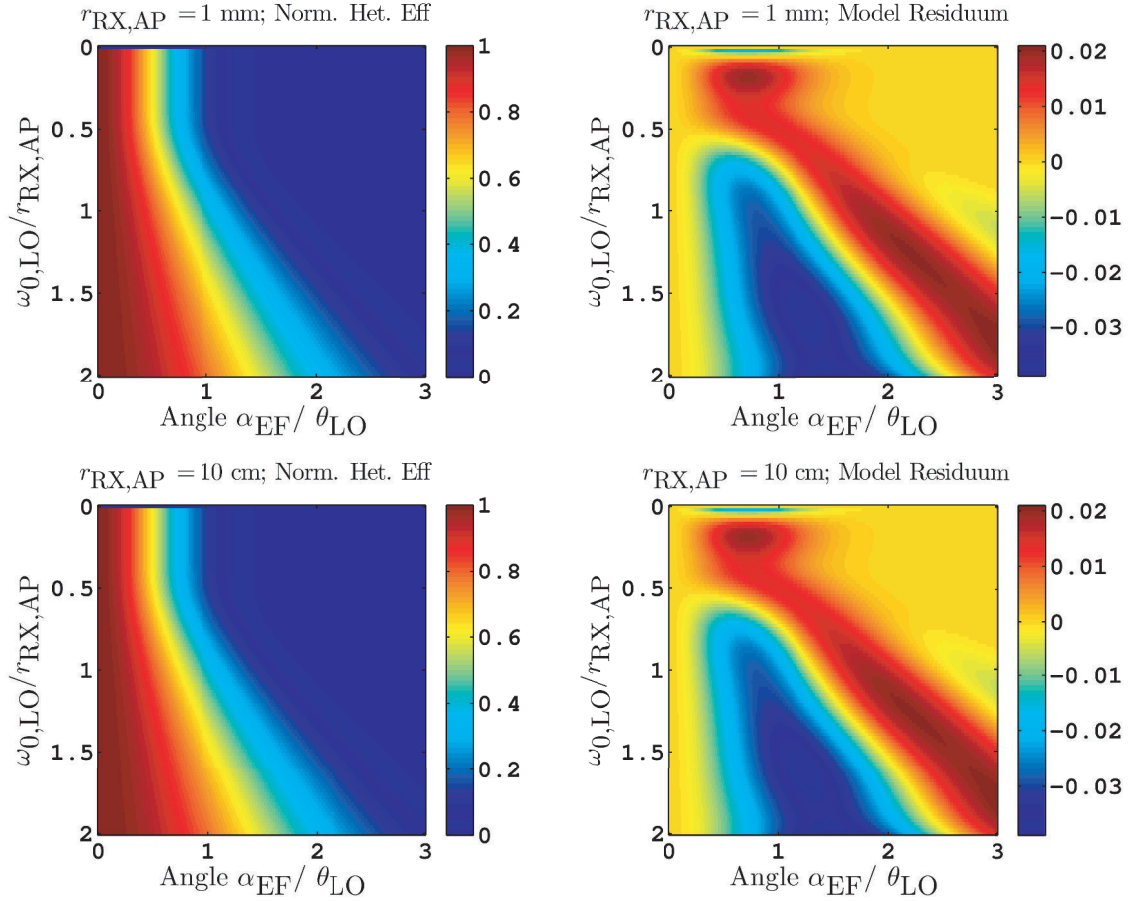


Figure 2.51: (Left panels): The heterodyne efficiency for a CPD as a function of α_{EF} and normalized at $\alpha_{\text{EF}} = 0$. For a particular value of $\omega_0/r_{\text{RX,AP}}$, the drop along the x -axis can be considered Gaussian. The x -axis is given in units of the Gaussian beam divergence $\theta_{\text{LO}} = \lambda/(\pi\omega_{0,\text{LO}})$. (Right panels): The residuum consisting of a Gaussian model (cf. eq. (2.349)) minus the actual heterodyne efficiency, as shown on the left panel. The absolute model accuracy is below 0.04. Hence, the model should not be used far away from the maximum. These plots do not depend on the used wavelength.

i	p_i	q_i	g_i
0	0.9567	1.8663	0.0051
1	1.0143	1.5448	1.7809
2	-5.0297	-8.2989	4.02283
3	10.1075	16.1162	-11.8986
4	-8.3148	-12.3148	11.1682
5	3.1866	4.3253	-4.6103
6	-0.4688	-0.5788	0.7125

Table 2.8: The coefficients of the polynomial functions $\psi(x) = \sum_{i=0}^6 p_i \cdot x^i$ for the heterodyne efficiency of a CPD, of $\psi_2(x) = \sum_{i=0}^6 q_i \cdot x^i$ for the heterodyne efficiency of a photodiode segment and of $\chi(x) = \sum_{i=0}^6 g_i \cdot x^i$ as used in eq. (2.358) and shown in fig. 2.56. These coefficients do not depend on the wavelength.

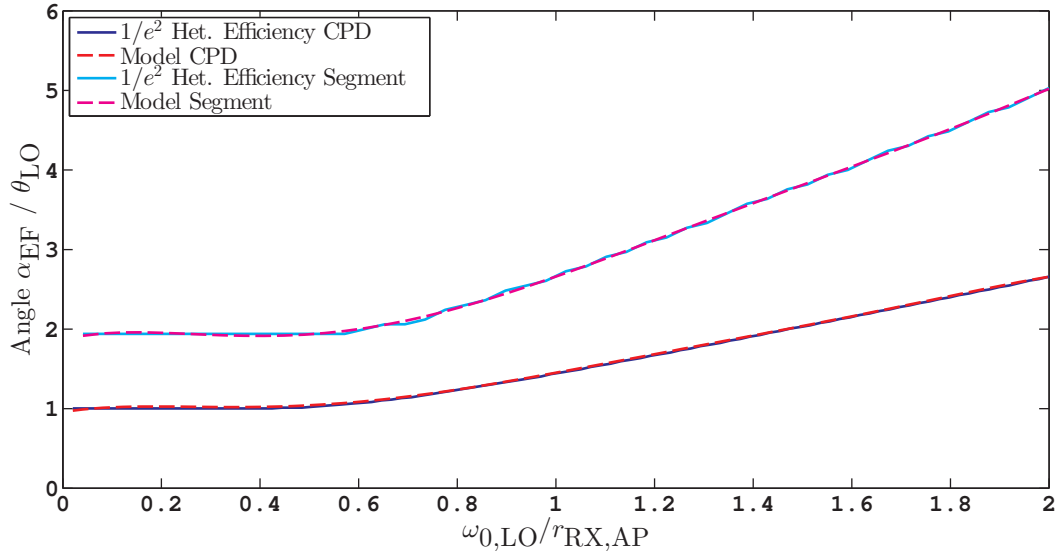


Figure 2.52: The traces indicate the phasefront tilt α_{EF} , in units of the Gaussian beam divergence $\theta_{\text{LO}} = \lambda/(\pi\omega_{0,\text{LO}})$, where the heterodyne efficiency drops to $1/e^2$ with respect to the heterodyne efficiency of non-tilted phasefronts. The dark and light blue traces consider a CPD and a segment, respectively. The red and magenta traces are polynomial fits with coefficients given in table 2.8. These plots do not depend on the used wavelength.

As the segments of a quadrant photodiode break the circular symmetry, precise calculations need to distinguish between tilt angle α_{EF} and tip angle β_{EF} and different segments, which is exemplarily shown in fig. 2.53 for GRACE-FO LRI parameters such as $\omega_{\text{LO}} = 2.5$ mm and $r_{\text{RX,AP}} = 4$ mm. The heterodyne efficiency of a single segment is not perfectly circular symmetric due to the geometrical shape of a segment.

However, the derivation of an approximative analytical model η_{seg} is attempted to ease subsequent parameter studies. This approximative model is derived for a single misalignment angle α_{EF} , i.e. $\beta_{\text{EF}} = 0$. The values for $\eta_{\text{seg,A}}(\alpha_{\text{EF}})/\eta_{0,\text{CPD}}$ obtained by numerical integration (cf. eq. (2.351)) are depicted on the left two panels of fig. 2.54 for 1 mm and 10 cm RX aperture and top hat radius. The misalignment angles α_{EF} , where the heterodyne efficiency reaches the $1/e^2$ level, are shown by the light blue trace in fig. 2.52. If a Gaussian drop of heterodyne efficiency is assumed as for the CPD case, i.e.

$$\eta_{\text{seg,approx}}(\alpha_{\text{EF}}) = \eta_{0,\text{CPD}} \cdot e^{-2\alpha_{\text{EF}}^2/(\theta_{\text{LO}} \cdot \psi_2(\omega_{0,\text{LO}}/r_{\text{RX,AP}}))^2}, \quad (2.353)$$

residuals with a magnitude of 9% appear for small ratios $\omega_{0,\text{LO}}/r_{\text{RX,AP}}$ (cf. right panels of fig. 2.54). The $\psi_2(x)$ function is a polynomial of 6th order, obtained by a fit of the data shown by the light blue trace in fig. 2.52. The polynomial coefficients are provided in table 2.8 and the model is shown by the dashed magenta trace in fig. 2.52 as well. Furthermore, the model and the accuracy of the model is illustrated in the two bottom panels of fig. 2.53.

The simple model in eq. (2.353) provides a rough and quick means to estimate η_{seg} , however, precise calculation should solve the two-dimensional integral over the area of the photodiode segments.

Another effect is studied in the following, which influences the heterodyne efficiency and is caused by a (residual) differential phasefront curvature between the RX and LO beams, which can be accounted for with a quadratic term in one of the electric field models, e.g.

$$E_{\text{RX}}^c(r, \theta) \sim e^{i \cdot 2\pi/\lambda \cdot \alpha_{\text{EF}} \cdot \cos(\theta) \cdot r} \cdot e^{i \frac{k \cdot r^2}{2 \cdot R_z}}, \quad (2.354)$$

with R_z denoting the radius of phasefront curvature. This residual curvature can be caused by imperfections of optics or by alignment tolerances. It is beneficial to express the radius of

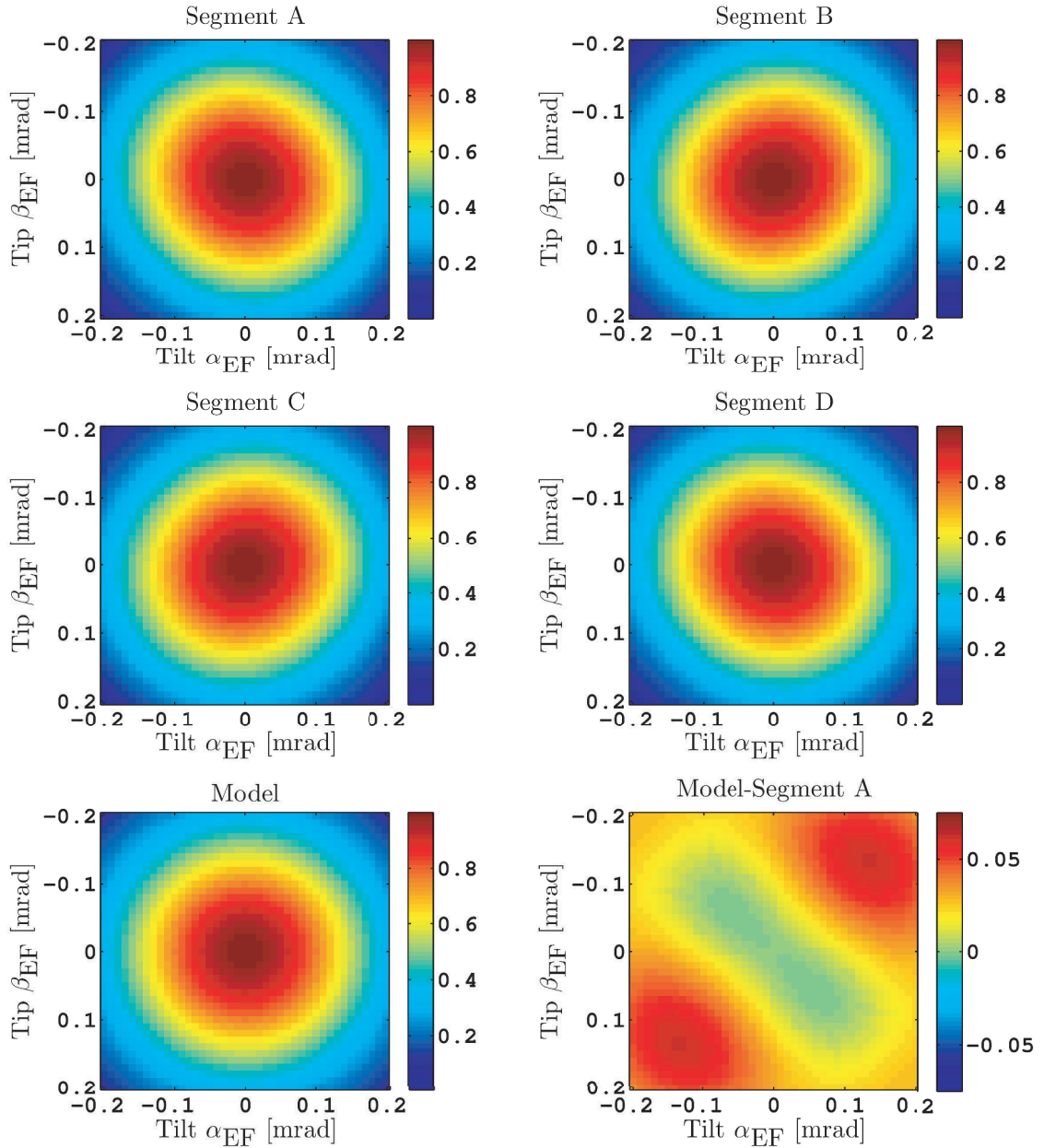


Figure 2.53: The four upper plots show the normalized heterodyne efficiency $\eta_{\text{seg}}(\alpha_{\text{EF}}, \beta_{\text{EF}})/\eta_{0,\text{CPD}}$ of single segments (A,B,C,D) as a function of tilt α_{EF} and tip β_{EF} angles for GRACE-FO LRI beam parameters, e.g. local oscillator waist radius of $\omega_{0,\text{LO}} = 2.5$ mm and $r_{\text{RX,AP}} = 4$ mm. The heterodyne efficiency has been normalized by the factor $\eta_{0,\text{seg}} = \eta_{0,\text{CPD}}$ to unity for $\alpha_{\text{EF}} = \beta_{\text{EF}} = 0$. The bottom-left panel shows the circular symmetric model given by eq. (2.353), while the bottom-right panel displays the difference between the circular symmetric model and segment A efficiency. These plots do not depend on the used wavelength.

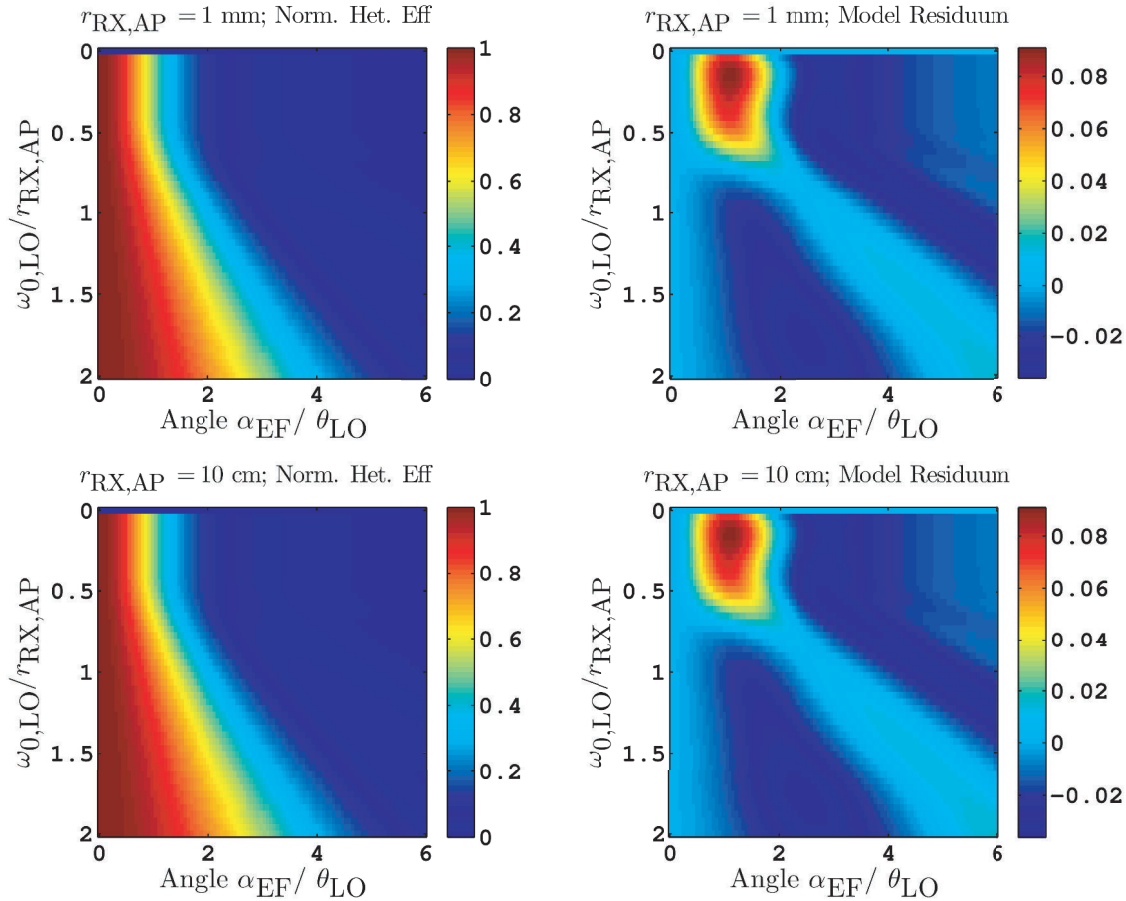


Figure 2.54: (Left panels:) The heterodyne efficiency for a photodiode segment as a function of α_{EF} , normalized at $\alpha_{EF} = 0$. For a particular value of $\omega_{0,LO} / r_{RX,AP}$ the drop can be considered approximately Gaussian. The x -axis is given in units of the Gaussian beam divergence $\theta_{LO} = \lambda / (\pi \omega_{0,LO})$. (Right panels:) The residuum consisting of a Gaussian model minus the actual heterodyne efficiency, as shown on the left panel. The accuracy of the model is poor for small ratios of $\omega_0 / r_{RX,AP}$, indicating that the drop in heterodyne efficiency does not follow exactly an Gaussian shape. These plots do not depend on the used wavelength.

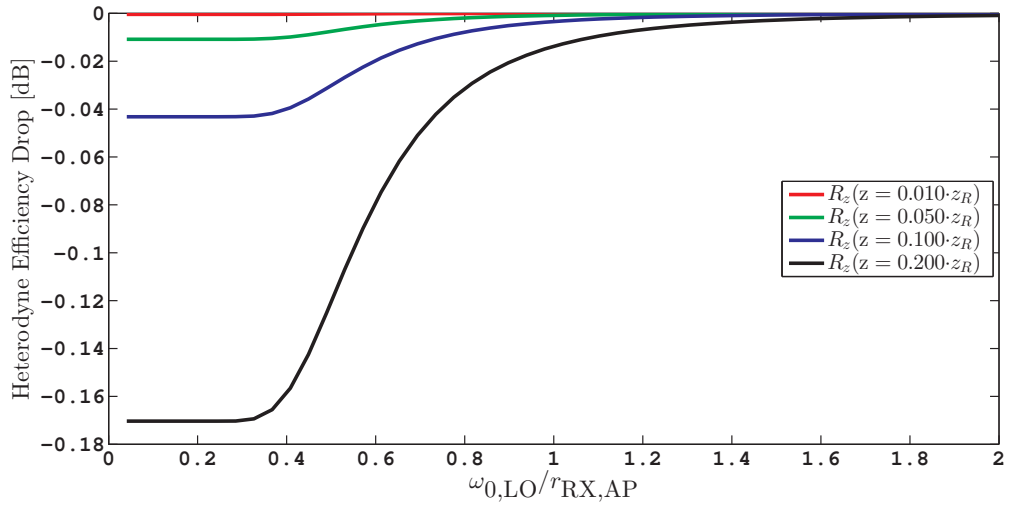


Figure 2.55: The effect of a differential phasefront curvature R_z on the heterodyne efficiency of a CPD as a function of $\omega_{0,\text{LO}}/r_{\text{RX,AP}}$. This plot considers a wavelength of 1064 nm.

curvature, which is given for a fundamental Gaussian beam as

$$R_z(z) = z \cdot \left(1 + \left(\frac{z_R}{z} \right)^2 \right), \quad (2.355)$$

in terms of the Rayleigh range z_R of the LO beam. For example, a waist offset of $\Omega = 10\% = 0.1$ of the Rayleigh range z_R corresponds to radius of curvature of

$$R_z(\Omega) = R_z(z = \Omega \cdot z_R) = R_z(z = 0.1 \cdot z_R) \approx 10 \cdot z_R = 10 \cdot \frac{\pi \cdot \omega_{0,\text{LO}}^2}{\lambda}. \quad (2.356)$$

This curvature yields a drop in the heterodyne efficiency of a CPD, which is depicted by the dark blue trace in fig. 2.55. The drop is 0.4% or 0.018 dB for a GRACE-FO LRI parameter of $\omega_{0,\text{LO}}/r_{\text{RX,AP}} \approx 0.6$, which is expressed here in decibel, because the numerical values are used in a subsequent section for the power link budget, which is more intuitive and insightful with units of decibel.

The plots for the heterodyne efficiency of a CPD (left panels in fig. 2.51) are to first order independent of a phasefront curvature, because the plots are normalized and the differential phasefront curvature does not change the way the normalized heterodyne efficiency drops upon misalignment. Thus, the previous model for the heterodyne efficiency of a CPD can still be used, but may account for the additional constant efficiency drop.

The maximum heterodyne efficiency of a single segment drops as well in the presence of a phasefront curvature, but the change is significantly smaller compared to the CPD (cf. the upper panel of fig. 2.56). Furthermore, it should be noted that the phasefront curvature parabola is centered at the inner corner of the segment and not in the center of the segment. This asymmetry causes a phase slope of

$$\frac{d\varphi}{dr} = \frac{k \cdot r_{\text{RX,AP}}}{2 \cdot R_z} = \frac{\pi \cdot r_{\text{RX,AP}}}{\lambda \cdot R_z} \quad (2.357)$$

over a segment in radial direction, which can be derived directly from geometrical considerations. Such a slope implies a non-optimal phasefront overlap and, thus, the maximum of η_{seg} is shifted in radial direction to

$$\alpha_{\text{EF,max}} = \beta_{\text{EF,max}} \approx \frac{r_{\text{RX,AP}}}{\sqrt{2} \cdot 2 \cdot R_z} \cdot \chi, \quad (2.358)$$

where the RX and LO phasefronts are as parallel as possible. The dimensionless factor χ is shown in the lower plot of fig. 2.56 and it accounts for a weighting of the curvature due to the intensity distribution of the LO beam. The factor χ depends on the parameter $\omega_{0,LO}/r_{RX,AP}$ and has been fitted with a 6th order polynomial as well (cf. table 2.8).

The heterodyne efficiency of all segments in presence of a differential phasefront curvature is shown in fig. 2.57. The position of the maximum from eq. (2.358) is shown with red dots in the four upper panels, which agrees well with the numerical data. Such a shift of the heterodyne amplitude maximum has also been observed during the testing of the GRACE Follow-On LRI. It is emphasized that the maximum of the heterodyne efficiency for the CPD (bottom-left panel), i.e. for the longitudinal phase measurement, is not shifted.

An approximate model for the heterodyne efficiency of a segment with phasefront curvature is

$$\eta_{\text{seg,approx2}}(\alpha_{\text{EF}}, \beta_{\text{EF}}) \approx \eta_{\text{seg,approx}} \left(\sqrt{(\alpha_{\text{EF}} \pm \alpha_{\text{EF,max}})^2 + (\beta_{\text{EF}} \pm \beta_{\text{EF,max}})^2} \right), \quad (2.359)$$

where the signs depend on the segment. The function $\eta_{\text{seg,approx}}$ was given in eq. (2.353). The accuracy of the model is shown on the lower right panel of fig. 2.57.

In summary, a phasefront curvature decreases the heterodyne efficiency of a circular photodiode η_{CPD} , but shifts the location of the maximum in the heterodyne efficiency of a segment η_{seg} . For aligned phasefronts of LO and RX beam ($\alpha_{\text{EF}} = \beta_{\text{EF}} = 0$), one obtains

$$\eta_{\text{CPD}} = \eta_{\text{seg,A}} = \eta_{\text{seg,B}} = \eta_{\text{seg,C}} = \eta_{\text{seg,D}}. \quad (2.360)$$

Furthermore, it is remarked that a change in the differential phasefront curvature also alters the longitudinal phase and, hence, can produce noise in a range measurement.

Other aspects of the heterodyne efficiency computation should be considered in more detailed studies of specific interferometer concepts. Namely the gaps within a segmented photodiode yield a cross-like pattern in the heterodyne efficiency, as shown in fig. 2.58. Furthermore, concentric ripples are present in the heterodyne efficiency of a CPD and of single segments, which have been omitted so far but are visible in fig. 2.58. These can be explained as follows: the main lobe of the heterodyne efficiency represents operation, where the interference pattern is mostly oscillating in-phase over the active area of the photodiode. The first zero-crossing of η indicates a full fringe on the active area, i.e. portions of the interference oscillate in-phase while other portions oscillate out-of-phase, yielding zero heterodyne amplitude in total. The second zero-crossing represents two full fringes on the active area. For example, one might want to ensure that the interferometer does not accidentally lock to the maximum of such a side lobe.

The heterodyne efficiency was written in this section as a function of the differential phasefront tilt between local oscillator and received light α_{EF} . Usually, one can relate this tilt to the pointing of the receiver satellite α_{RX} w.r.t. the line-of-sight, i.e.

$$\alpha_{\text{EF}} = \alpha_{\text{RX}} + \delta\alpha_{\text{EF,RX}}, \quad (2.361)$$

where $\delta\alpha_{\text{EF,RX}}$ is a quantity depending parameters such as steering mirror orientation or integration tolerances of the interferometer into the satellite. Hence, the effective power P_{eff} factorizes into a quantity depending on the local receiver S/C misalignment α_{RX} and a quantity depending on the TX beam misalignment α_{TX} of the distant S/C:

$$P_{\text{eff}} = \eta(\alpha_{\text{RX}} + \delta\alpha_{\text{EF,RX}}) \cdot P_{\text{RX}}(\alpha_{\text{TX}}). \quad (2.362)$$

The model for the effective power derived within this and the previous subsections is applied in sec. 2.8 on the laser link power budget. Beforehand, the laser link acquisition is addressed, which is also strongly dependent on the received power P_{RX} .

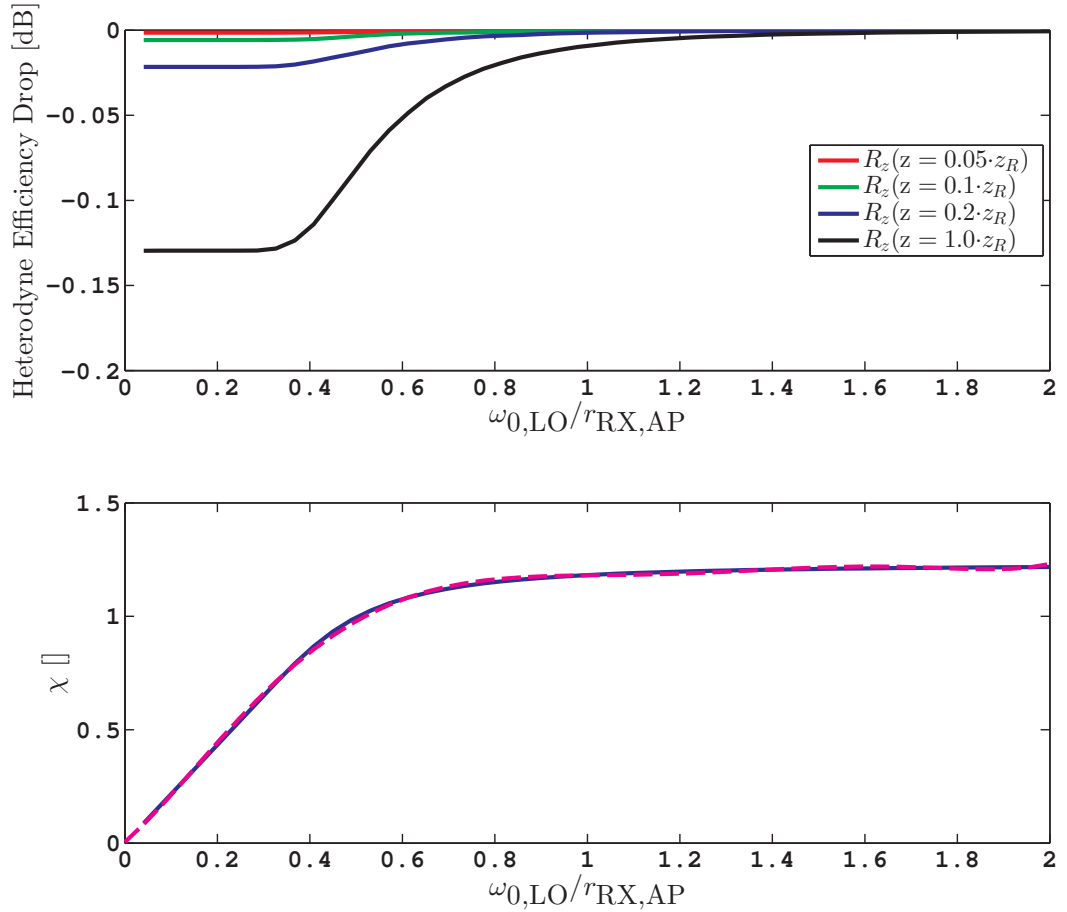


Figure 2.56: (Upper panel:) The effect of a differential phasefront curvature R_z on the maximum heterodyne efficiency of a single segment as a function of $\omega_{0,LO}/r_{RX,AP}$. The black trace indicates the maximum possible phasefront curvature of the local oscillator beam. (Lower panel:) The function χ is determined from numerical integration and by utilizing the relation given in eq. (2.358). The dashed magenta trace is a polynomial model ($\chi(\omega_{0,LO}/r_{RX,AP}) = \sum_{i=0}^6 g_i \cdot (\omega_{0,LO}/r_{RX,AP})^i$) with coefficients g_i given in table 2.8. Both plots consider a wavelength of 1064 nm.

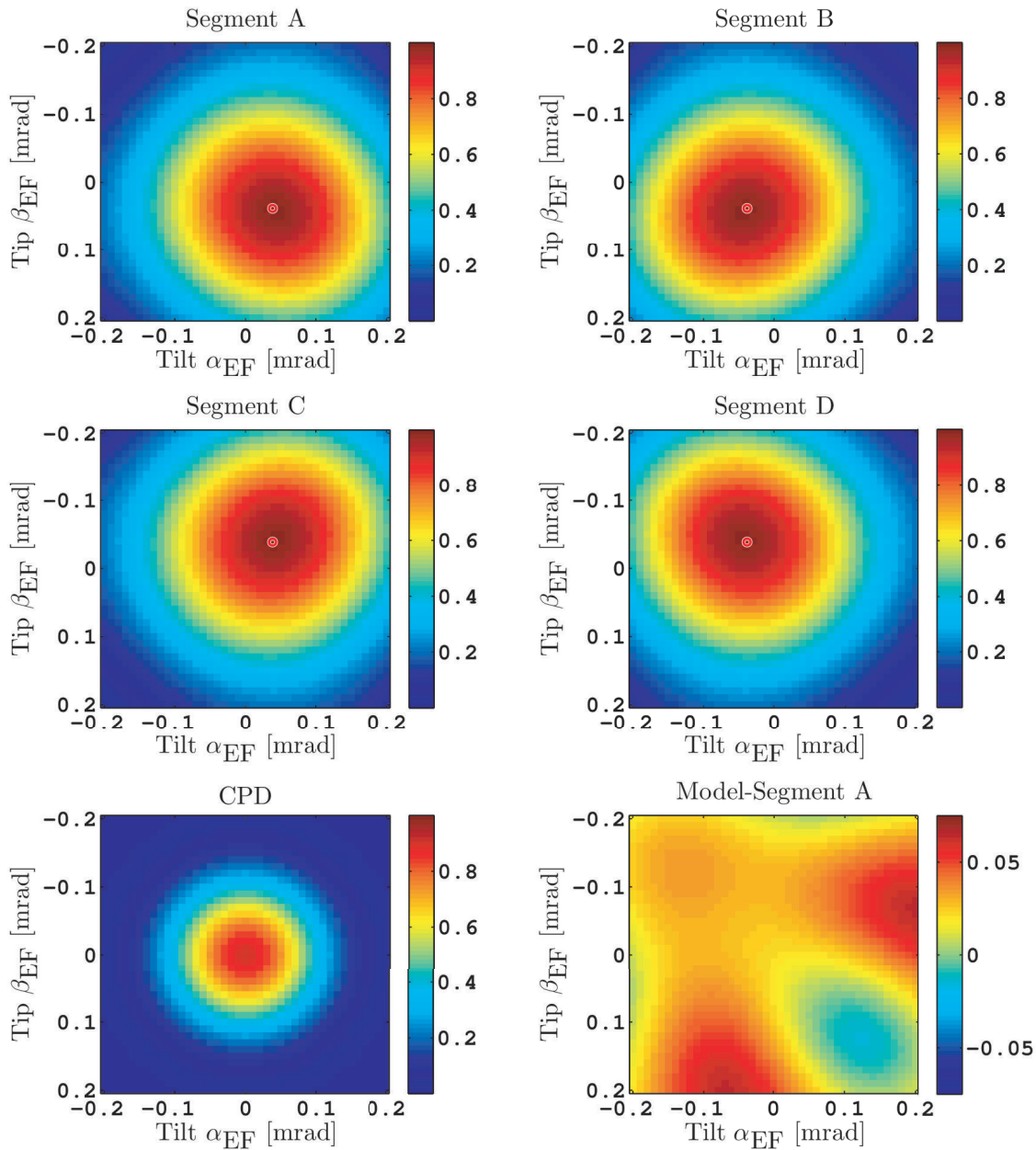


Figure 2.57: Heterodyne efficiency of segments and CPD with present strong phasefront curvature. The efficiency is normalized by the factor $\eta_{0,\text{CPD}}$. The red circles indicate the position of the maximum according to eq. (2.358). The lower-right plot shows a residual, given by the difference between the model from eq. (2.359) and segment A. The parameters used for the plots are $\omega_{0,\text{LO}} = 2.5$ mm, $r_{\text{RX,AP}} = 4$ mm, $R_z(z = z_R)$ and $\lambda = 1064$ nm.

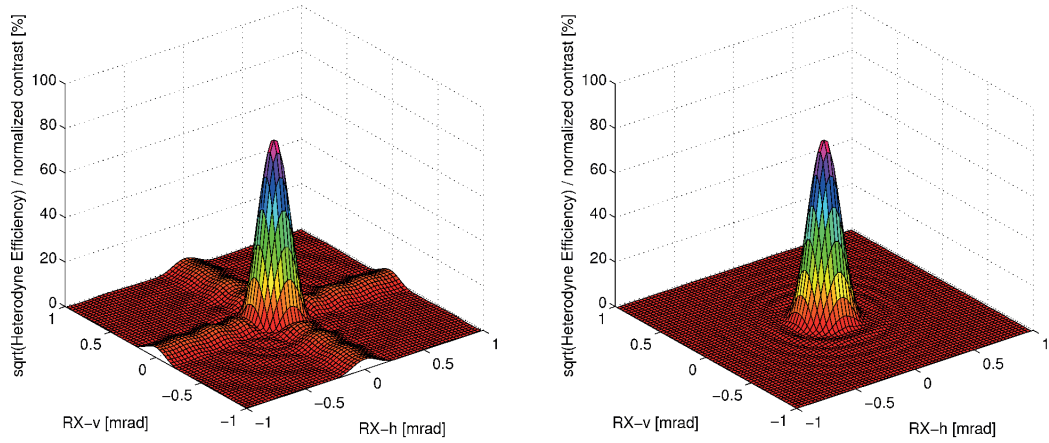


Figure 2.58: Square root of heterodyne efficiency for the coherent sum of all four quadrants with $30\ \mu\text{m}$ gap (left) and without gap (right). The surface plot is parameterized by the relative tip and tilt angle between the Gaussian beam and the flat top beam. The parameters used for the plots are $\omega_{0,LO} = 2.5\ \text{mm}$, $r_{\text{RX,AP}} = \text{PD}_r = 4\ \text{mm}$, $R_z = \infty$ and $\lambda = 1064\ \text{nm}$.

2.6.12 Laser Link Acquisition

Acquisition is the process of achieving an interferometric connection between the satellites, which enables the phasemeter to track the beatnote and to obtain DWS and longitudinal (ranging) signals. This requires that both satellites receive sufficiently high light power levels (depending on TX beam pointing) and that the interferometric contrast (depending on receiver S/C pointing) is high enough, such that the signal-to-noise-ratio is above a detection and tracking threshold. In addition, the laser frequency difference between both satellites has to be within some band, which allows the beatnote to be measured with the photoreceivers and the phasemeter.

In general, the very first (initial) acquisition is more difficult, since unknown biases in the orientation and position of all instruments are present due to the vibrations and shocks during launch, de-moisturization or zero G-effects. Once these biases are calibrated and known, a re-acquisition needs to cover a smaller uncertainty cone in the parameter space and is therefore less time consuming.

A line-of-sight (LOS) estimate is required on both satellites in both acquisition cases, which can be obtained by orbit prediction and by sensor fusion of attitude and position information (star cameras, GNSS and other sensors via AOCS). The LOS estimate is an estimation for the direction to the distant satellite and serves as starting point for the acquisition search. The difference between the LOS estimate and true LOS is the pointing error, which is dominated by the unknown static bias prior to initial acquisition.

The acquisition process is additionally complicated due to the fact that the interferometers on both satellites need to detect light at the same time, in general, without exchanging information due to the lack of real time communication.

Since the GRACE Follow-On concept has a fixed dependency between the orientation of the local oscillator beam and of the TX beam, the acquisition is a five dimensional search: two angular degrees on each satellite and the frequency difference of the lasers need to be matched simultaneously. The current acquisition strategy for GRACE Follow-On foresees that the steering mirror on each satellite scans a spatial pattern, while the laser frequency on one satellite is swept (see fig. 2.59). A non-autonomous scheme is used for the initial acquisition, also called LOS-calibration, where both satellites record the events of received light (so-called flashes) and where on-ground data processing is used to derive the bias angles between laser interferometers and LOS estimates, which determines the desired instrument misalignment

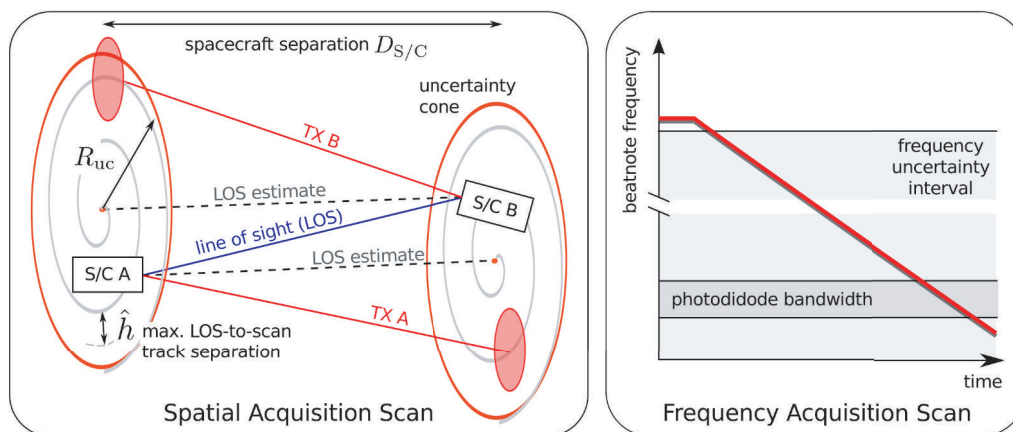


Figure 2.59: Working principle of the 5-dimensional acquisition search in the GRACE Follow-On LRI. (**Left:**) Each of the S/C performs a 2-dimensional search scan with the steering mirror to cover the uncertainty cone. (**Right:**) In parallel the laser frequency on the slave satellite is swept. Image from [Mahrdt, 2014].

and biases. Once the bias values are uploaded to the satellites, an autonomous re-acquisition is started with much smaller angular uncertainties to establish the link. Furthermore, during science operation of the LRI, a re-acquisition is initiated whenever the laser link is lost.

Extended studies have been performed on the optimal search strategy including different spatial scan patterns and coherent and incoherent detection methods of the photodetector signals [Mahrdt, 2014; Wuchenich *et al.*, 2014; Ales *et al.*, 2014]. The incoherent sum of segments has a wider acceptance angle compared to the coherent sum, i.e. the heterodyne efficiency of a segment drops more slowly with misalignment compared to a single circular photodiode (cf. previous sec. 2.6.11 on heterodyne efficiency), and might appear beneficial at the first glance. However, the coherent combination allows one to pin-point the direction of a single detection flash more accurately and was finally selected as baseline for the GRACE-FO initial acquisition.

The initial acquisition or LOS-calibration in GRACE-FO will take several hours, while re-acquisition might need up to a few minutes, although most re-acquisition events are expected to finish within a few seconds, since short interruptions of the laser link connection should not induce large pointing errors or large laser frequency offsets.

A GRACE-FO-like acquisition scheme is based on a complex five dimensional search, which requires a complex and well tested on-board software and fast beam steering capabilities. Advantageous is the detection of light from the remote satellite with the photodetectors, which also perform the measurement of the optical phase (ranging), since less optical and electrical components are required.

A significant reduction in the acquisition complexity can be achieved by an additional acquisition sensor, which splits the 5-dimensional parameter search space into three individual subsets. The sensor consists of a 2-d pixel array, e.g. a focal plane array such as CCD or CMOS, on which a part of the received light is focused. A phasefront tilt of the received light due to local S/C misalignment produces a spot, which is displaced from the sensor center, such as in a star camera or Shack-Hartmann sensor. It is an incoherent DC measurement, which does not require an additional well-aligned local oscillator beam nor a well-matched laser frequency. An a-priori ground calibration from displacement to optical angle is needed, so that the measurement can be referred to a direction. The acquisition sequence could be established as follows: at first both S/C perform in parallel a fast scan in the pointing uncertainty cone for some time, such that both acquisition sensors detect some flashes at a particular pixel location, equivalent to particular angles. These angles are used to improve

the local estimation of the line-of-sight. In a next step, each S/C aligns itself (or the LO beam) and the TX beam along the improved LOS estimate, and a frequency scan is performed until the interferometric link is established, i.e. until the phasemeter is tracking the phase of the beatnotes measured by the photodiodes. The frequency scan is required, if the absolute laser frequency is not fixed, but can be skipped if two absolute frequency standards are used in a DOWR combination (cf. sec. 2.4.8).

It is important that the optical axis of the acquisition sensor is well aligned with the interferometer axis and that it is sufficiently stable, such that the measurement from the acquisition sensor can be converted into a pointing direction for the steering mirror or spacecraft. This likely requires an accommodation of the sensor on the optical bench. Although a field-of-view for the acquisition sensor of less than $1^\circ \times 1^\circ$ ($17.4 \text{ mrad} \times 17.4 \text{ mrad}$) is sufficient, a few background stars may be present (cf. sec. 2.3.10) and need to be considered in the data processing. On the one hand, a narrow reflection coating can reduce the amount of light originating not from the distant S/C, however, on the other hand, omitting such a filter could allow to use the acquisition sensor as an additional star camera.

Two additional or supplementing ideas are mentioned for the sake of completeness, but are not considered in detail in this thesis. The first is based on a dedicated de-focus mechanism in the optical path, which increases the divergence angle of the TX beam in the acquisition phase. This may avoid a dedicated scanning of the uncertainty cone as suggested in the LISA mission [LISA-Team, 2009]. The second idea utilizes a dedicated incoherent high-power acquisition light source with wide divergence and was suggested in [e.motion² Team, 2014, sec. 4.5.1.1].

The GRACE Follow-On acquisition strategy and acquisition with a dedicated acquisition sensor are valuable options for laser interferometry in future gravimetric missions. Because the latter option is less studied, some further analysis is performed here and also in the section on the power budget of laser links.

An accurate analysis of the acquisition phase with a dedicated acquisition sensor requires knowledge on the scan pattern. However, for a preliminary analysis in the design phase, one can assume a simple rectangular $N \times M$ grid pattern of the TX beam with an angular spacing ϱ_{grid} in each direction, where the laser beam remains fixed for a time period t_h at each point. For such a scan pattern, the worst-case angular TX beam misalignment ϱ_{aq} for acquisition is diagonally in-between grid points, i.e.

$$\varrho_{\text{aq}} = \sqrt{2} \cdot \varrho_{\text{grid}}/2, \quad (2.363)$$

which can be used to compute the optical power and the number of photons arriving at the distant S/C in acquisition mode.

Furthermore, the total scan duration T given by

$$T = (t_h + t_m) \cdot N \cdot M \quad (2.364)$$

should be assessed, where t_m denotes the average time to move to the next point in the scan.

The relation between tilt of incoming wavefront α and offset Δx in the focal plane [Yuan & Long, 2003]

$$\Delta x = f \cdot \tan(\alpha) \quad (2.365)$$

can be used to evaluate the accuracy and field-of-view of the acquisition sensor design, to assess an appropriate CCD chip size and to define the lens focal length f .

The intensity distribution $I(x, y)$ in the focal plane given from a plane wave input limited at a circular aperture with radius r_{ap} is [Träger, 2012, ch. 7.2, p. 435]

$$I(x, y) = \frac{P\pi r_{\text{ap}}^2}{\lambda^2 f^2} \cdot \left(\frac{2 \cdot J_1(2\pi r_{\text{ap}} \sqrt{x^2 + y^2}/(\lambda f))}{2\pi r_{\text{ap}} \sqrt{x^2 + y^2}/(\lambda f)} \right)^2, \quad (2.366)$$

$$= \frac{P}{\pi} \cdot \left(\frac{J_1(2\pi r_{\text{ap}} \sqrt{x^2 + y^2}/(\lambda f))}{\sqrt{x^2 + y^2}} \right)^2, \quad (2.367)$$

with the incident optical power P in the aperture and with $J_1(x)$ being the Bessel function of first kind. The intensity distribution corresponds to the well known airy disk pattern, where the first zero occurs at r_{disc} [Meschede, 2008, p. 68]

$$2\pi r_{\text{ap}} \sqrt{x^2 + y^2} / (\lambda f) \approx 3.83 \Rightarrow r_{\text{disc}} = \sqrt{x^2 + y^2} \approx \frac{3.83 \cdot \lambda f}{2\pi r_{\text{ap}}}. \quad (2.368)$$

The radius of the inner disc is approx. $r_{\text{disc}} \approx 62 \mu\text{m}$ with typical values of $f \approx 0.38 \text{ m}$, $r_{\text{ap}} = 4 \text{ mm}$ and $\lambda = 1064 \text{ nm}$. A common pixel pitch of $30 \mu\text{m}$ means that the inner disc is spread over several pixels and that the centroid can be determined with sub-pixel accuracy, if the signal-to-noise ratio is sufficiently high. It is beyond the scope of this thesis to provide details on centroid determination as these methods are steadily advanced in the context of, for example, Shack-Hartmann sensors [Thomas, 2004; Vyas *et al.*, 2009] or star cameras [Samaan, 2003; Knutson, 2012].

However, an alternative method for direct centroid determination could use a template-based correlation. The ideal response of the optical system (eq. (2.366)) can be used to compute templates with a few pixels size. A single template with centered peak $I(0,0)$ may be sufficient, however, further templates with fractional pixel offsets could be envisioned. These templates can be correlated with the measured CCD image, with some interpolation even to sub-pixel accuracy. Such a template based approach allows one to define a signal-to-noise ratio for a measured spot, which is higher than the signal-to-noise ratio of a single pixel (cf. eq. (2.148)).

For the purpose of this thesis, an angular accuracy for the acquisition system of

$$\delta\alpha_{\text{req}} = 40 \mu\text{rad} \quad (2.369)$$

with a generic field-of-view of $\pm 7 \text{ mrad}$ is sufficient to establish the laser link and to account for the overall in-orbit uncertainty cone consisting of instrument misalignments (e.g. star camera sensor w.r.t. interferometer optical bench), component induced deflections (e.g. corner-cube errors or steering mirror errors), satellite pointing errors (e.g. attitude determination uncertainty), satellite position errors (e.g. orbit prediction and GNSS navigation solution uncertainty) and margin.

For such an accuracy and field-of-view, a pixel array with only 256×256 pixels seems sufficient, i.e.

$$\frac{2 \cdot 7 \text{ mrad}}{255 \text{ px}} \cdot 0.7 \text{ px} \approx 38 \mu\text{rad} < \delta\alpha_{\text{req}}, \quad (2.370)$$

if the spot center can be determined to better than 0.7 pixel, which is not very demanding.

Furthermore, with these parameters, one can verify that the aforementioned focal length $f \approx 0.38 \text{ m}$ of the lens produces a displacement on the CCD chip for the overall field-of-view. For example, considering a pixel pitch of $30 \mu\text{m}/\text{px}$, one obtains a half-width chip size of $30 \mu\text{m}/\text{px} \cdot 255 \text{ px}/2 = 3.825 \text{ mm}$. Thus, the field of view of 7 mrad is contained on the chip due to

$$f \cdot \tan(7 \text{ mrad}) = 2.7 \text{ mm} < 3.825 \text{ mm}. \quad (2.371)$$

With these simple calculations, a first initial design for an acquisition sensor could be derived. The study of the signal-to-noise ratio of the acquisition sensor is postponed to sec. 2.8 on the power budget of laser links. Beforehand, different optical layouts for interferometers are addressed.

2.7 Optical Layouts

The optical layout of a laser ranging interferometer realizes or implements a functional concept such as the dual one-way ranging or the transponder scheme, which have been discussed in

sec. 2.4 with block diagrams. The distinction into optical layouts and functional concepts has been introduced in this thesis in an attempt to systematically characterize inter-satellite ranging instruments. Furthermore, the design of optical layouts is driven by aspects and boundary conditions, which have been addressed in section 2.3 and 2.6, such as

- the attitude-to-ranging coupling, which can be expressed approximately in terms of TX and RX reference points, and which should be minimized for rotations around the S/C CoM (cf. sec. 2.6.3f.),
- the laser link acquisition, which can be reduced in complexity with a dedicated acquisition sensor (cf. sec. 2.6.12) and which usually requires the capability to point the transmit laser beams
- the point-ahead angle, which is negligible for the gravimetric missions studied in this thesis (cf. sec. 2.6.7),
- the photodiode size, which typically requires beam compressors in front of the photodiodes (cf. sec. 2.3.3 and 2.6.11),
- the carrier-to-noise density (cf. sec. 2.6.9), which is determined by the transmit beam pointing, by the local S/C or interferometer alignment and by parameters such as the laser power and the beam sizes.

Optical layouts may comprise telescopes. A telescope in the received (RX) beam path typically increases the light collecting area, which is beneficial for the carrier-to-noise density, and it is acting as a beam compressor. A telescope in the TX path typically reduces the transmit (TX) beam divergence by increasing the beam size, i.e. it acts as beam expander. This increases the optical power throughput along the axis, which is also beneficial for the carrier-to-noise density, but requires a stricter pointing of the TX beam. A common telescope instead of two single telescopes is often required due to mass, space and cost constraints in space missions. Such layouts have co-located RX and TX beam axes and are denoted in the following as *on-axis* interferometers, in contrast to *off-axis* interferometry with laterally separated axes. In an on-axis interferometer, the TX and RX reference points are located on a common axis, but they are usually separated along the axis.

Off-axis interferometers can usually be realized with fewer optical components, because of a lacking necessity for polarizing optical components. Fewer components implies less complexity, because every optical component can have various negative side effects as summarized in table 2.9. The rationale in space interferometer design is achieving the science or sensitivity goals with as few components and with as little complexity as possible.

In the next two subsections, various optical layouts, which have been found in literature, are introduced, while subsection 2.7.3 contains a discussion of the different proposed concepts. Based on the findings and the current state of knowledge, an on-axis and an off-axis layout are proposed for NGGM in sec. 2.7.4.

2.7.1 On-Axis Interferometry

In gravimetric missions, the inter-satellite distance variations between the center of mass of both S/C shall be tracked. It is a natural idea to send electro-magnetic radiation along the connecting line of both CoM to sense these variations. It is in particular useful, if a common telescope is used to enhance the received light power and to reduce the divergence of the transmitted beam as in the LISA mission concept [eLISA/NGO Team, 2012; Danzmann *et al.*, 2017]. The transmitted and received light share a common optical path. Usually one tries to minimize power losses in the transmitted path. However, due to the reversion principle in optics, the so-called Helmholtz reciprocity, this implies that most of the received light power will propagate towards the source of the TX beam. In order to avoid this, one typically exploits different polarization states of the light and uses polarizing optics to guide

Effect	Description	Counteraction / Mitigation
Temperature coupling	Mainly transmissive optics; Optical phase changes due to temperature variations; Two effects: $\Delta n/\Delta T$ value and thermal expansion of component;	Optimization of thermal stability of optical bench; glass substrates with low temperature coupling; Thin components
Attitude coupling	Transmissive optics induce an optical pathlength variation dependent on the light incidence angle; the light incidence angle might change due to spacecraft attitude (jitter), beam steering or jitter of laser beam	Compensation plates can help to reduce linear coupling, but increase quadratic coupling; Optimization of optical layout might reduce linear coupling
Power loss	Absorption within component or due to contaminant on the optical surfaces (in-orbit contamination); non-perfect coating reflectivity/transmissivity	Glass substrates with low absorption; optimization of IFO and S/C design to minimize contamination; use of high-quality coatings; sufficient margin in optical laser link budget
Ghost beams	Non-zero reflectivity produces parasitic reflections within components, which might propagate into the sensitive path	Optimization of optical layout, beam dumps, use of wedged components
Wavefront errors	Planarity or quality of surfaces influences wavefront of transmitted and reflected light	Use of high quality optics
Polarization changes	Some combination of optical components, e.g. periscopes, might rotate the polarization; polarization purity decrease due to reflection (e.g. metals)	Use of additional polarizer components; use of high quality coatings; analysis of polarization changes
Beam overlap & co-alignment	Parasitic wedges on components change direction of light (static offset): increased complexity in manufacturing (interferometer alignment)	Use of high quality substrates
Mass increase	Especially large components (telescopes) increase total optical bench mass	Use of light-weight structures, reflective vs. refractive telescopes

Table 2.9: Potential negative side effects of (additional) optical components. Some effects may cancel or may not apply in specific configurations.

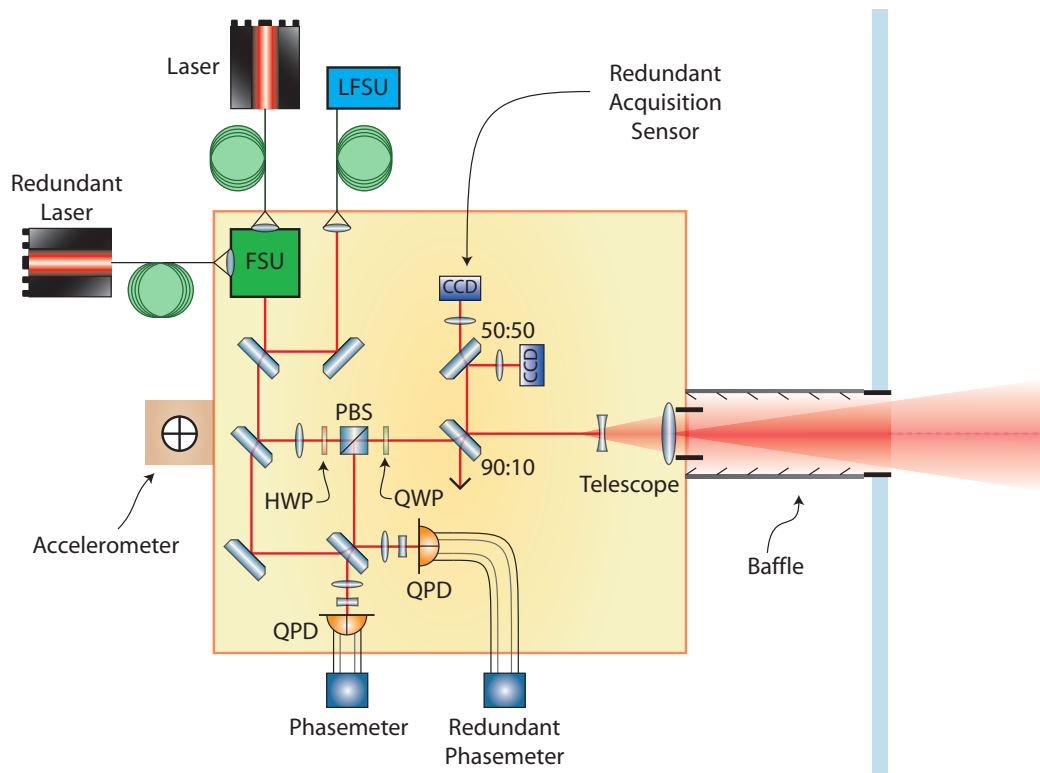


Figure 2.60: Laser interferometer concept from [e.motion Team, 2010]. FSU: Fiber Switching Unit, LFSU: Laser Frequency Stabilization Unit. HWP: Half-Wave Plate, QWP: Quarter-Wave Plate, PBS: Polarizing Beamsplitter.

most of the received light towards the photodiode and to adjust a reasonable power ratio between received beam and local oscillator field, which is used to sense the phase of the received light by means of optical mixing.

In figures 2.60-2.62 three interferometer layouts from the gravimetric mission concepts [e.motion Team, 2010], [NG2-Team, 2011] and [Alenia-Team, 2010] are shown. They are all drafted without actuators in the optical path, meaning that the local oscillator beam and the transmit beam have a stationary path through the interferometer, while the path of the received light depends on the attitude of the spacecraft. A potential misalignment between the local oscillator and received light field can be measured with DWS and needs to be counter-acted by rotating the satellite or the optical bench, such that the TX beam is sent back in the direction of the received wavefronts and to the distant S/C. Hence, the satellite can be understood as an *active retro-reflector by control*, where *active* refers to the apparent amplification of the retro-reflected light, and *control* refers to the measurement of the misalignment and correction by means of a control loop and actuators.

Accomplishing beam pointing by an optical bench rotation has the drawback, that the pivot point of the rotation needs to be co-located with the interferometer reference point¹³, which is ideally co-located with the S/C CoM. As in most cases the reference point has a fixed position w.r.t. the optical bench, the actuator needs to perform a pure rotation without any motion along the sensing axis to not disturb the displacement measurement. In addition, due to the considerable mass and moments of inertia of typical optical benches, rotations can only be performed with low actuation bandwidth and might in addition have an influence on the S/C CoM position and on other instruments such as the accelerometer.

The alternative to optical bench rotation is TX beam pointing by means of S/C rotation, which has been extensively studied within the LISA mission [eLISA/NGO Team, 2012; Danzmann *et al.*, 2017]. It is feasible in a quiet deep space environment with little disturbance

¹³centroid of RX RP and TX RP

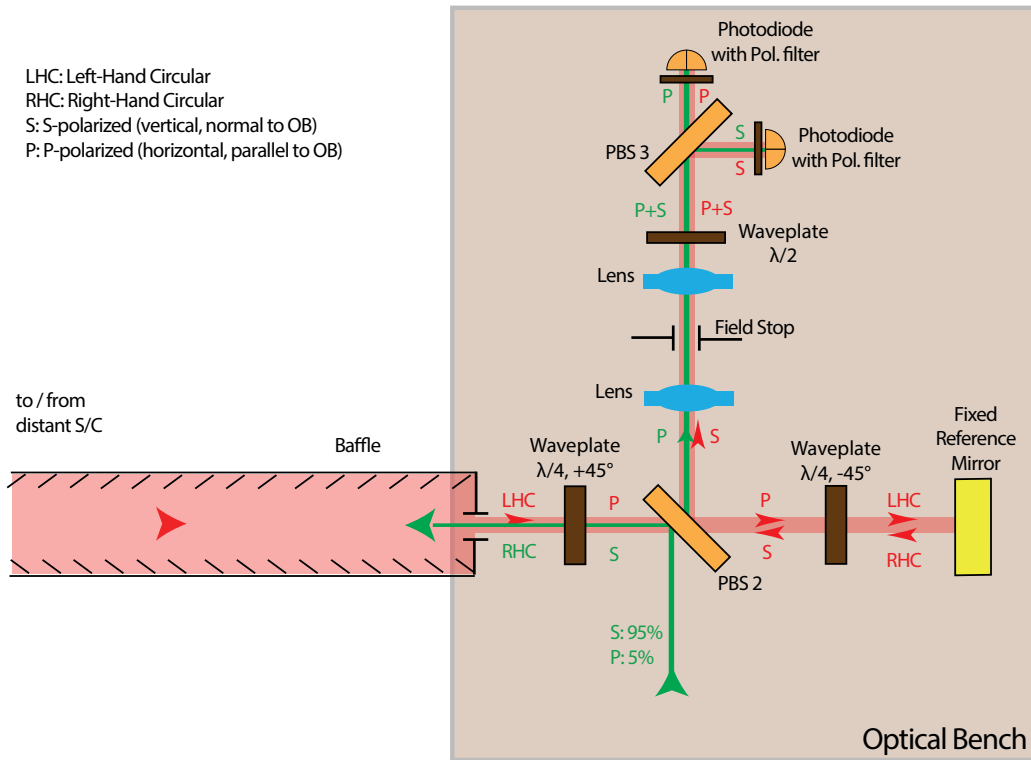


Figure 2.61: Laser interferometer concept by Airbus from [NG2-Team, 2011]. The figure has been reproduced and supplemented with the polarization states and additional labels by the author of this thesis.

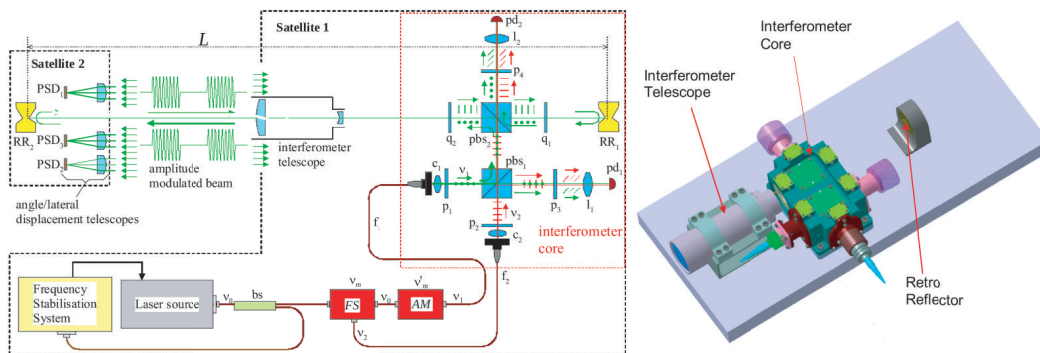


Figure 2.62: Laser interferometer concept from [Alenia-Team, 2010] by ThalesAlenia Space.

torques and where low-noise micro-Newton thruster are sufficient. In this approach, the low-noise high-bandwidth DWS signal of the interferometer, which is measuring the spacecraft tip and tilt w.r.t. the line of sight, is fed into the AOCS together with conventional attitude information from star trackers and gyroscopes, for example. The satellite uses thrusters and other available actuators to keep misalignments between RX and local oscillator (LO) beam and between TX beam and the line-of-sight small, once the laser link has been established. The interferometer and LO beams are fixed in the satellite frame, thus, TX beam pointing and spacecraft attitude are equivalent up to some static offsets. In the LISA mission, the beam pointing is more complicated due to an once-per-orbit annual variation of the inner-constellation angle, which requires an additional pointing mechanism at very low frequencies, either by rotating the telescopes, the optical bench or by using a steering mirror (in-field pointing) [Brugger *et al.*, 2014]. In addition, the point-ahead angle needs to be accounted for in LISA.

A generic requirement for the maximum tolerable yaw and pitch TX beam pointing error is $100\ \mu\text{rad}$ in gravimetric missions, which is revised in the subsequent sec. 2.8 on the laser link power budgets and optimal parameter selection. Generally, this value depends on the inter-satellite distance and on the divergence of the transmitted beam. The concept in [Alenia-Team, 2010] even requires a permissible error of only $20\ \mu\text{rad}$. Such a value could impose significant challenges on the AOCS design of a LEO craft, its actuators and sensors, particularly, if the beam pointing is performed solely by S/C rotations. However, capability of accurate pointing has been shown in other space missions, exemplary, Hubble with approx. $40\ \text{nrad}$ at an altitude of 630 km [van Woerkom, 1999], TerraSAR-X with an in-orbit pointing accuracy better than $290\ \mu\text{rad}$ ($60\ \text{arcsec}$) at 514 km height [Kahle *et al.*, 2007] or the Transition Region and Coronal Explorer (TRACE) mission with a yaw and pitch design pointing accuracy of below $100\ \mu\text{rad}$ at less than 660 km height [Zimelman *et al.*, 1995].

Next to the need for accurate S/C pointing to maintain the interferometric link, typically expressed by the maximum permissible pointing error or 3σ value, it is also beneficial to have a small attitude jitter of the S/C, as it reduces the ranging noise arising from the attitude-to-ranging coupling.

2.7.2 Off-Axis Interferometry

In this type of interferometer, the received beam and the transmit beam are separated spatially, which makes a common telescope unpractical, but reduces significantly the complexity of the optical layout due to lacking necessity for polarizing components. Hence, such a layout is only feasible, where the spacecraft separation and available laser power allows one to dismiss a common telescope (cf. subsequent section 2.8 on the laser link budget).

The off-axis interferometry scheme was first introduced in the GRACE Follow-On mission to the knowledge of the author, because the line-of-sight between the CoM of both S/C is occupied by cold-gas tanks and the microwave ranging instrument. William Folkner (NASA/JPL) initially suggested to use a hollow corner-cube retro-reflector (HCCRR) to produce the lateral offset in a so-called racetrack configuration shown in fig. 2.63. The HCCRR is called Triple Mirror Assembly (TMA) in the GRACE Follow-On project and introduces a 600 mm lateral offset between incoming and outgoing beam.

In the subsequent development of the LRI, it turned out that this racetrack concept in combination with the transponder scheme has various appealing benefits, such as

- Identical interferometer hardware on both S/C: The interferometers consisting of optical bench, triple mirror assembly (TMA) and other sub-systems (laser, frequency stabilization, phasemeter) can be made identical in terms of hardware on both spacecraft. This introduces cold redundancy for the laser frequency stabilization unit, since only one operational unit is required in the racetrack. The designation of master and slave S/C can be made interchangeable between the S/C. The operational difference between the

satellites is that the master S/C uses the cavity-based frequency reference, while the slave S/C locks its laser to the incoming field by means of a frequency-offset PLL.

- **Automatic Beam Alignment:** A steering mirror can easily be incorporated on the optical bench to align the local oscillator and the received wavefronts. This can be performed efficiently with a control loop with high gain and high bandwidth [Sheard *et al.*, 2012] by a feed back of the DWS signals of the photodiodes. The loop ensures that the beam exiting the optical bench is parallel to the received wavefronts, i.e. on the same axis as the received beam. In addition, the loop maximizes the wavefront overlap (heterodyne efficiency), and hence the signal-to-noise ratio of the phase measurement. The working principle of the steering mirror DWS control loop is shown in fig. 2.64. As the DWS signal is zeroed, the misalignment of the S/C in two dimensions w.r.t. the line-of-sight can be retrieved by measuring the steering mirror orientation.
- **TX Beam Pointing and Anti-Parallelism:** The TMA retro-reflects the powerful beam leaving the optical bench, such that it is send in the direction of the received wavefronts and hence towards the distant spacecraft. The static error in the anti-parallelism is typically dominated by the errors of the TMA such as manufacturing tolerances or temperature dependency. Other contributions from the DWS steering mirror control loop and deflections by the optical bench are significantly smaller in terms of static errors. Residual noise in the steering mirror control loop yields a small jitter in the TX beam pointing direction typically not exceeding $1 \mu\text{rad}/\sqrt{\text{Hz}}$ in a proper design . Such small TX beam pointing jitter mitigates the phasefront jitter noise in the range measurement to an uncritical level, which arises from a phasefront center of curvature offset (cf. sec. 2.6.5 on TX reference points).
- **Reference Points at the CoM:** The interferometer can be easily designed in a way that the centroid of RX and TX reference point, i.e. the effective phase center, is at the vertex of the TMA. And the TMA can be designed so that the vertex point, i.e. the intersection point of the three mirror planes, is offset from the physical structure of the assembly. This allows the accelerometer reference point to be co-located with the TMA vertex at the S/C CoM, as shown in fig. 2.63.
- **Suppression of off-racetrack contributions:** Phase changes on the path from beam launcher (FIA, Fiber injector assembly, in fig. 2.63) to the recombination beamsplitter, e.g. induced by the motion of the steering mirror, as well as on the path from the recombination beamsplitter to the photodiodes, are highly suppressed in the final ranging observable [Sheard *et al.*, 2012]. Furthermore, the final ranging observable is to first order immune to motion of the optical bench within the spacecraft.
- **Extended field-of-regard of the interferometer:** The automatic beam alignment ensures that misalignments and attitude jitter of the spacecraft w.r.t. the line-of-sight are compensated and the interferometric lock is maintained. Hence, the absolute pointing accuracy of the spacecraft can be relaxed, i.e. the absolute S/C pointing error can exceed the tight interferometer field-of-view. However, the absolute S/C pointing error needs to remain within the range of the steering mirror and within the field-of-regard of the interferometer, e.g. in order to avoid beam clipping.

The aspect from the last bullet point was required in the GRACE Follow-On mission, as the LRI is classified as a technical demonstrator and a significant modification of the AOCS was undesired. Hence, the interferometer field-of-regard was designed to account for S/C pointing errors and on-board misalignments. There is no feedback of the interferometric alignment signal such as DWS or steering mirror orientation to the AOCS in GRACE-Follow On. Although a large field-of-regard might suggest that such a feedback is not necessary, it is still beneficial to reduce the overall S/C attitude jitter w.r.t. the line-of-sight, because it mitigates the associated rotation-to-ranging noise.

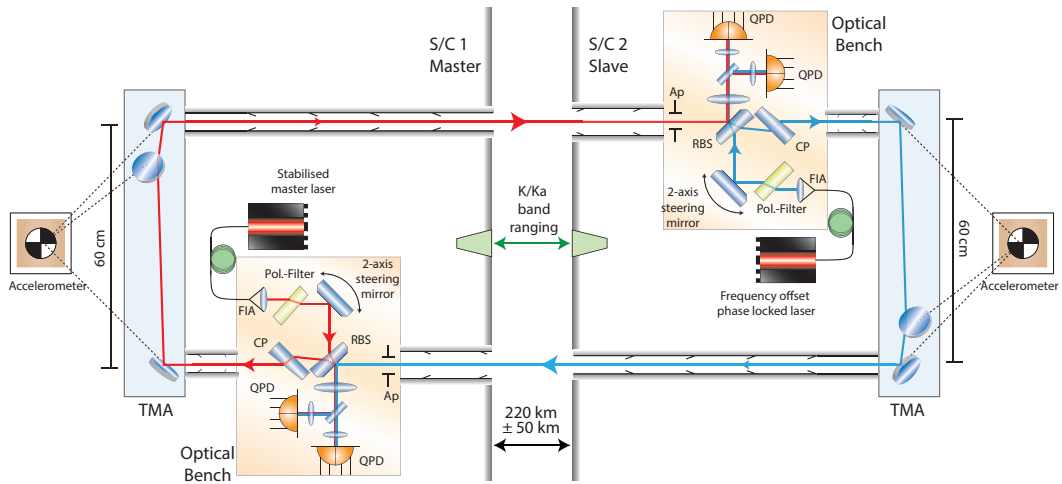


Figure 2.63: The GRACE Follow-On LRI racetrack optical layout, consisting of a master and a slave S/C. TMA: Triple Mirror Assembly, FIA: Fiber Injector Assembly, CP: Compensation Plate, RBS: Recombination Beamsplitter, Pol.-Filter: Polarization Filter. Image originally published in [Sheard *et al.*, 2012], but it has been revised and updated for this thesis.

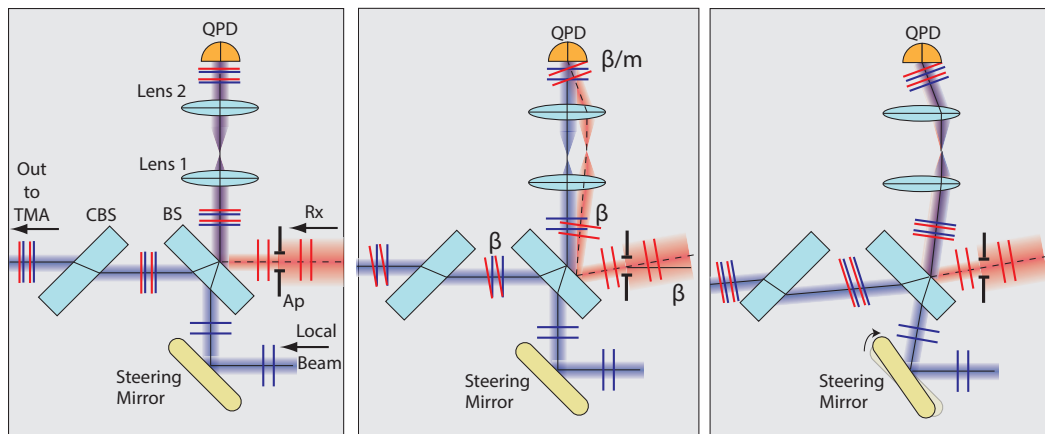


Figure 2.64: Working principle of the steering mirror DWS control loop. (**Left:**) The incoming RX field (red) is aligned with the local oscillator (blue) in front of the photodiode, which yields zero DWS signal. As the compensation plate (CBS) and beamsplitter (BS) do not induce a beam deflection, the incoming RX field is parallel to the beam leaving towards the TMA. (**Center:**) The RX field is tilted by an angle β , which yields a magnified tilt in front of the photodiode due to the beam compressor telescope ($m < 1$). The tilt is measured by DWS. The incoming RX and outgoing beam are not parallel anymore. (**Right:**) The control loop zeros the DWS signal by rotating the steering mirror. RX and outgoing beam are parallel again.

2.7.3 Discussion of Layouts

The on-axis interferometer concepts in figures 2.60-2.62 utilize polarizing components. Although polarizing optics and interferometers are commonly used in laboratory experiments, their use in a gravimetric mission needs to be assessed carefully. Experimental results by [Dehne et al. \[2009\]](#) for gravimetric applications suggest that a ranging sensitivity of $\text{nm}/\sqrt{\text{Hz}}$ is achievable, however, the effect of S/C rotations and changing incidence angles on the polarizing components has not been considered in that work to the knowledge of the author. The changes in the longitudinal phase and polarization upon varying angle-of-incidence in polarizing birefringent components such as waveplates is non-trivial to compute [[Meshksar, 2015](#)] but should be considered.

According to the figures 2.60-2.62, on-axis interferometers favor circularly polarized light for the inter-satellite path. Circular polarization is also preferred in radio communications, for example, from Space to Earth, due to the lacking necessity of polarization adjustment at the ground stations [[Freer, 1996](#), p. 55], higher suppression of multi-path signals and immunity to polarization rotation from the Faraday effect in combination with Earth's magnetic field [[Laheurte, 2012](#), ch. 7]. Furthermore, depolarization by the atmosphere plays a role in particular radio frequency bands. In optical communication links such as the Laser Communication Terminal (LCT), circular polarization is used for the TX beam [[Muehlnikel et al., 2012](#)]. However, circular polarization in phase sensitive ranging yields a susceptibility to roll rotations of the S/C due to a *cork screw*, also called *phase wind-up*, effect. A roll rotation by one degree ($\alpha = 17 \text{ mrad}$) yields a change in the phase derived range by $\alpha/(2\pi) \cdot \lambda \approx 3 \text{ nm}$ for 1064 nm light, which is uncritical but noteworthy. In case of linear polarization, such rotations alter the heterodyne amplitude but not the measured phase. On the other hand, circular polarization does not degrade the heterodyne amplitude and carrier-to-noise density at the receiver, which might be beneficial in interferometers with very low light power levels.

It is noted that the instrument in fig. 2.62 contains two interferometers: a reference interferometer, which determines the phase difference between the two frequency shifted light beams, and a science interferometer, where the actual ranging signal is obtained. In total five waveplates are used. Whereas, the layout in fig. 2.61 utilizes three waveplates. Both layouts have a similar optical configuration, where the received light passes through a quarter-waveplate, is transmitted through a polarizing beamsplitter, passes again through a quarter-waveplate, is then reflected at a flat mirror, passes again through a quarter waveplate and is finally reflected at the polarizing beamsplitter towards the photodiodes. The received light is typically weak in terms of power and in addition clipped, which yields diffraction rings while traversing. Hence, the author of this thesis prefers to keep the path simple for the RX light, e.g. as few reflections and transmissions as possible, leaving the more complex path with many components for the powerful TX beam. However, it might be beneficial to transmit a TX beam with high power as directly as possible in order to avoid parasitic thermal or stray light effects.

It is remarked that the NG2 concept seems to consider different TX polarization states for the two S/C, or in other words, the RX and the TX beam have different polarizations as shown in fig. 2.61. In case of the Alenia design, this polarization change is achieved due to the uneven number of reflections at the passive S/C, but for the transponder baseline of the NG2 concept, this implies non-identical S/C and introduces additional complexity, for example, in the ground support equipment.

The NG2 and Alenia concepts overlap the received light and the local oscillator in orthogonal linear polarization states and produce the interference by rotating both polarization states by 45 degree in front of the photodiode. These different polarization states traverse even a beam compressor prior to interference in fig. 2.61. The author of this thesis recommends to produce the interference, i.e. the same polarization state, as early as possible to maximize the common mode rejection. Otherwise, some components may produce a non-common attitude-to-ranging coupling for local oscillator and received beam, for example, due

to stress-induced birefringence in the optical components.

The e.motion layout in fig. 2.60 shows a number of additional mirrors, because the TX and LO beam are at first separated spatially. The polarizing beamsplitter is not used to overlap the LO and RX beam. This has the advantage that the beam modes of TX and LO can be independently adjusted as indicated with the small lens in front of the half-wave plate (HWP). The e.motion polarization scheme is also simpler, since only two waveplates are used and the overlapped LO and RX field interfere due to a common polarization state.

The e.motion and Alenia designs accommodate a common telescope for the TX and RX beam in contrast to the NG2 layout, which could raise the question on the necessity for polarizing optics and an on-axis system in NG2.

None of the three shown on-axis concepts utilize an active LO beam alignment mechanism, which would enhance the carrier-to-noise density upon receiver misalignment. The TX beam is fixed in the S/C frame and beam pointing is achieved by rotating the S/C or optical bench. Thus, the angular jitter of the TX beam w.r.t. the line-of-sight is driven by the considerable S/C attitude jitter present in gravimetric missions. As stated in section 2.6.5 on TX reference points, designs without TX beam steering have the TX RP at the center of phasefront curvature as apparent in the far-field at the distant satellite. The phasefront curvature can be easily determined for a small point-like laser source. However, the TX beam after a telescope has typically a low divergence, which is equivalent to a long Rayleigh range or a large waist size. Small changes in the telescope, for example induced by temperature, may lead to a significant shift in the phasefront center of curvature. Hence, the centroid of RX and TX reference point (RP) can easily vary along the line-of-sight. This offset in combination with the TX beam angular jitter could yield a noteworthy noise in the range measurement.

The exact location of the RX RP in the layouts is difficult to predict, because the telescope parameters, imaging systems and exact dimensions are not specified. For a well-behaving system, the RX RP is located on the RX beam axis as described in section 2.6.4.

For the well-studied off-axis GRACE-FO LRI layout, the RX RP is located at the center of the RX aperture, as this plane is imaged onto the photodiodes by the two lens imaging system (cf. fig. 2.63). Any rotation around this point does not change the longitudinal phase at the photodiode.

It is recalled that the GRACE-FO LRI utilizes TX and LO beam steering, thus, the TX RP is not the center of phasefront curvature but at the effective pivot point of the TX beam steering. If the procedure for the TX RP determination from sec. 2.6.5 is applied to the GRACE-FO LRI, it turns out that the TX RP is located to first order at the reflection point of the RX RP at the TMA vertex, which is due to the pathlength and lateral offset properties of the TMA and due to the design of the optical bench, i.e. equal distances from the steering mirror to the recombination beamsplitter and from the RX aperture to the recombination beamsplitter.

Taking into account second order effects, the TX RP is offset by a few millimeters along the line-of-sight, since beamsplitter and compensation plate induce a small quadratic coupling. Thus, the centroid of TX and RX RP is very close to the TMA vertex and the linear and quadratic attitude-to-ranging coupling can be minimized by co-locating TMA vertex and S/C CoM. The remaining offset in lateral direction w.r.t. the LOS is expected to be of the order of 100 μm in the GRACE-FO LRI, which couples linearly with 100 $\mu\text{m}/\text{rad}$ into the pathlength upon yaw and pitch rotations.

In the successor study for e.motion, the e.motion² proposal, the suggested interferometry layout is based on the LRI of GRACE Follow-On with modifications to account for some learned lessons [e.motion² Team, 2014]. Major differences are the use of a dedicated acquisition sensor, use of a high power laser source and feedback of the interferometry-derived attitude information into the AOCS to reduce the noise due to attitude-to-ranging coupling.

A comparison of the different layouts in tabular form is given in table 2.10. As stated in the last row, the angular jitter of the TX beam is relatively high for the on-axis interferometers

		On-Axis				Off-axis	
		LISA	NG2	e.motion	Alenia	GRACE-FO	e.motion ²
Functional Type		Transponder	Transponder	Transponder	Passive RR	Transponder	Transponder
TX Beam Pointing	Component	SM (In-Field Pointing) or Telescope or Optical Bench (out-of measurement bandwidth)				Yes (SM)	Yes (SM)
	Optical Bench	not in baseline				No	No
	S/C	Yes (in measurement bandwidth), DWS feedback into AOCS	DWS feedback into AOCS possible	DWS feedback into AOCS possible	Yes, DWS on Master, WTD on Slave S/C	no IFO feedback into AOCS; ~mrad by AOCS	Yes, IFO feedback into AOCS
Telescope		Yes, ~30 cm ϕ	No	Yes	Yes (Master S/C)	No	No
TX&RX Anti-Parallelism		by Optical Bench design & AOCS Closed Loop Performance				HCCRR 60 cm	HCCRR 30 cm
PAAM		Yes	Not req.	Not req.	Not req.	Not req.	Not req.
LO&RX Beam Alignment; SNR maximization		by S/C AOCS Pointing (bandwidth ~sub-Hz)				DWS SM Loop (bandwidth ~kHz)	
TX beam angular pointing jitter w.r.t line-of-sight		AOCS in Deep Space ~ nrad/Hz	AOCS in LEO (TBC) ~ 100 μ rad/Hz			SM DWS Loop < 5 μ rad/Hz	SM DWS Loop < 1 μ rad/Hz

Table 2.10: Comparison of various laser ranging concepts. Abbreviations: PAAM: Point-Ahead Angle Mechanism, WTD: Wavefront-Tilt-Detection, SM: Steering Mirror, IFO: Interferometer, AOCS: Attitude & Orbit Control System, LEO: Low-Earth orbit

in a low-Earth orbit, as it is determined by the AOCS or S/C pointing jitter. In combination with an undesired phasefront curvature in the far-field, this could lead to a non-negligible noise contribution.

In summary, the off-axis layout offers a simple setup with only a few optical components. Furthermore, it enables a simple implementation of active beam steering, which maximizes the carrier-to-noise density in case of a S/C misalignment, yields optimal TX beam pointing and provides a well-defined RP for the distance measurement. Moreover, the beam steering can be utilized in the acquisition phase of the interferometric link. On the other hand, the on-axis layouts allow to incorporate a single telescope in the optical path to decrease the divergence of the TX beam and to enhance the collected light power.

In the next subsection, the off-axis layout of e.motion² is revised and suggested as a potential instrument for NGGM. Furthermore, an evolved on-axis layout with most off-axis advantages is presented as alternative.

2.7.4 Proposed Layouts for NGGM

Two optical layouts of laser ranging interferometers are proposed in this subsection for future gravimetric missions. The most promising is probably the off-axis type with substantial heritage from the GRACE Follow-On LRI. It has also been suggested in [e.motion² Team, 2014] by the author of this thesis and it is shown slightly modified in fig. 2.65.

In front of the two hot-redundant photoreceivers, each containing an approx. 1 mm diameter segmented quadrant photodiode, is a two lens beam compressor, which images the optical bench RX aperture and steering mirror onto the photodiodes and adjusts the beam sizes to fit the photodiodes. Thus, the RX and LO beam have minimal beam walk on the photodiode upon tip and tilt of the beam or upon S/C rotations. In particular, the RX RP of the interferometer is located at the center of the RX aperture.

The recombination beamsplitter has a moderate reflectivity ($> 90\%$), such that most of the RX light is deflected towards the photodiodes and most of the LO light is transmitted to the retro-reflector and finally towards the distant S/C. A small wedge angle in the beamsplitter reduces the influence of ghost beams in the interferometer. However, a single 45° beamsplitter induces a lateral beam offset of the order of ± 1.5 mm and an associated non-negligible linear rotation-to-pathlength coupling of ± 1.5 mm/rad. The sign depends on the orientation of the beamsplitter. Hence, an additional beamsplitter (AqBS in fig. 2.65) with

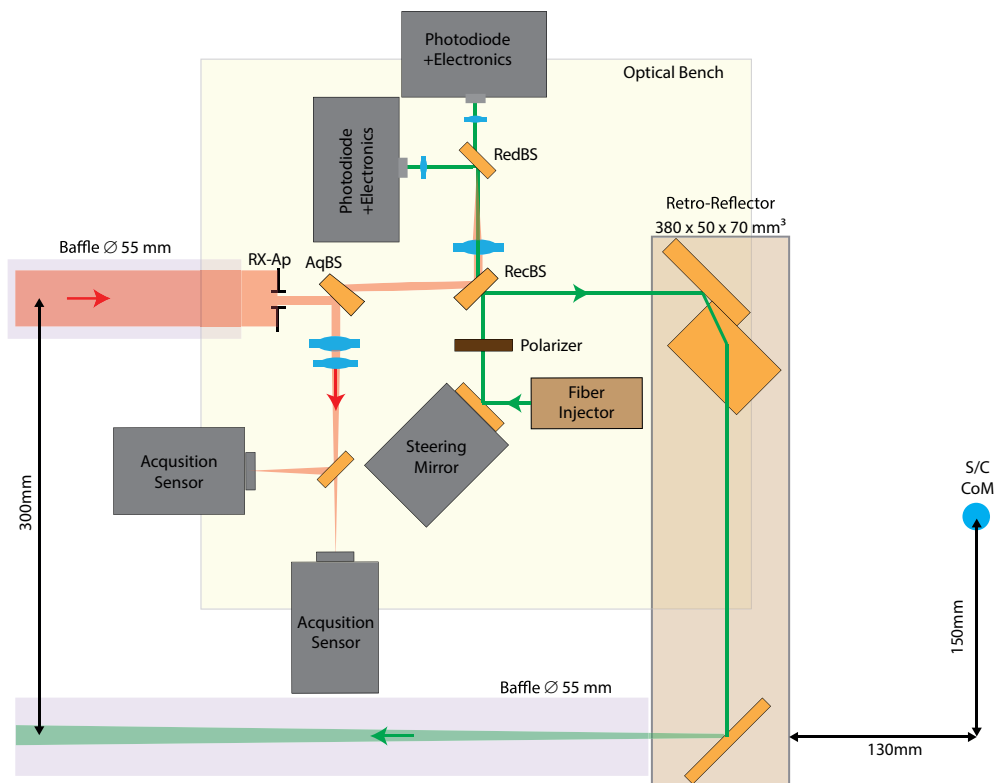


Figure 2.65: Off-axis layout with dedicated redundant acquisition sensors and with a 300 mm virtual hollow corner-cube retro-reflector. The reference point of the interferometer, given as the centroid of RX and TX reference point, is at the vertex of the retro-reflector, which is co-located with the S/C CoM. The RX reference point is located at the center of the RX aperture.

same thickness, negative wedge angle and rotated by 90 degree can be utilized to zero the linear coupling. A negative wedge angle is required, since both components in transmission should not deflect the light. With this configuration, the RX beam at the aperture and the TX beam entering the corner-cube are co-aligned along the same axis. It is noted that this co-alignment means that the TX beam has no lateral offset with respect to the RX beam, which is an important feature for the determination of the TX RP position.

In the GRACE-FO layout, the additional beamsplitter features anti-reflective coatings on both sides and is called compensation plate. It is located in the TX beam path (cf. fig. 2.63). However, in the layout proposed here, the additional beamsplitter is partially reflective in the RX path, so that it branches off some light power for the acquisition sensors. Although this compensation plate or second beamsplitter cancels the linear coupling, it doubles the small quadratic coupling, which is less critical.

The dimensions of the corner-cube are reduced significantly to 300 mm lateral offset compared to the GRACE Follow-On LRI with 600 mm, which eases the ground testing (cf. sec. 2.3.5) and should allow a final co-alignment error of less than 20 μ rad with a more rigid HCCR design.

The special properties of the corner-cube (cf. sec. 2.3.5) yield a TX RP location, which is approximately the reflection point of the RX RP at the retro-reflector vertex. Thus, the centroid of the TX and the RX RP is approximately at the vertex and at the S/C CoM. The *approximately* refers to a small offset of the order of millimeters in the less critical LOS direction, which is caused by the quadratic coupling arising from the two beamsplitters in the racetrack. If the beamsplitters are very thin, the quadratic coupling vanishes, and the TX RP is exactly at the reflection point of the RX RP at the TMA vertex. However, this holds only if the distance between the RX aperture and the recombination beamsplitter equals the distance between the steering mirror and the recombination beamsplitter (which is unfortunately not very well represented in fig. 2.63).

An alternative and of course less mature optical layout is shown in fig. 2.66, which serves as starting point for further discussion. It accommodates a common refractive telescope for the RX and TX path, which could also be easily changed into a reflective telescope. Furthermore, the telescope could be removed if not required. This on-axis design has been derived from the off-axis layout by simply replacing the hollow corner-cube retro-reflector with the on-axis retro-reflector discussed in sec. 2.3.5. In addition, a deflection mirror in the baffle, in front of the telescope, has been incorporated to shift the interferometer RP into the S/C CoM. Some further changes such as wave plates and recombination beamsplitter with polarization dependent coatings are applied to appropriately adjust the interference light power levels. This on-axis design utilizes a steering mirror, which provides automatic beam alignment and proper control of TX beam direction. Hence, most of the off-axis or racetrack advantages are preserved along with the potential advantages of a telescope.

As the telescope images the telescope aperture onto the virtual intermediate aperture, and the beam compressor images the intermediate aperture onto the photodiodes, the RX RP is located virtually at the center of the telescope aperture (purple dot in the center of the telescope aperture in fig. 2.66). However, due to the mirror in the baffle, the virtual RX RP is unfolded into the point labeled S/C CoM. Rotations of the S/C around its CoM produce a pure tilt of the RX beam and no piston effect in the telescope aperture, in the intermediate aperture and at the photodiode. Thus, the RX RP is at the S/C CoM.

It is assumed that the local oscillator beam waist is located at the steering mirror in fig. 2.66, as in the racetrack configuration. One focal plane of the retro-reflector (RR) lens coincides with the RR-mirror surface of M2. The other focal plane is co-located with the steering mirror and with the virtual intermediate aperture, since both distances are matched. Due to the telescope, the TX RP in the virtual intermediate aperture is imaged further into the telescope aperture center. Hence, there are three fix-points of the LO/TX beam upon steering mirror rotations: the reflection point of the steering mirror, which is the pivot point of the steering mirror rotation, the center of the virtual intermediate aperture and the center

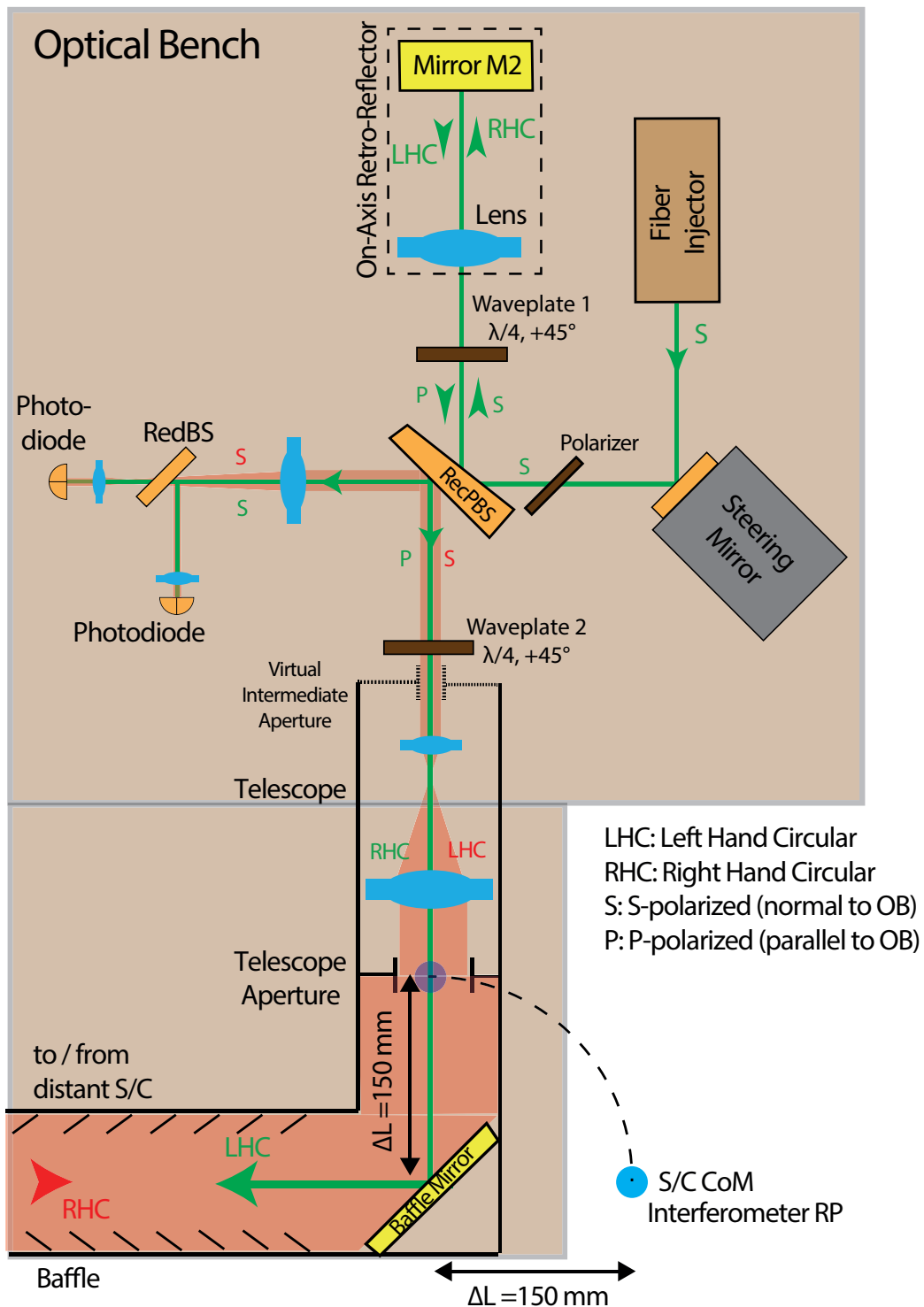


Figure 2.66: On-axis interferometer layout with on-axis retro-reflector and common TX and RX telescope. The recombination beamsplitter (RecBS) has a polarization dependent coating. The polarization states of the different beam paths are provided. The purple dot in the telescope aperture center is the virtual RX and TX RP, which is unfolded into the S/C CoM. Some RX light is transmitted at the recombination beamsplitter (not shown).

of the telescope aperture. Thus, the TX RP is virtually in the center of the telescope aperture but unfolded into the S/C CoM as the RX RP.

The distance ΔL between the telescope aperture and the baffle mirror defines the distance between the interferometer RP and the baffle mirror. Hence, due to the baffle mirror, an optical layout is obtained, where the interferometer RP, which is given by the centroid of TX and RX RP, is physically separated from the optical bench (OB) and baffle structure.

There is no compensation plate in the on-axis layout, because the TX beam traverses the recombination beamsplitter twice in different directions, which cancels the linear coupling. Furthermore, the recombination beamsplitter can have a small wedge angle to suppress ghost beams on the photodiodes. The polarizing recombination beamsplitter has a reflectivity close to unity for s -polarized light and is almost transparent for p -polarized light.

Figure 2.66 shows no acquisition sensor for the sake of simplicity, but it can be easily implemented. For example, one can place a polarizing acquisition beamsplitter between wave plate 2 and the recombination beamsplitter, such that some fraction of the s -polarized RX light is transmitted onto the acquisition sensor, while most of the RX light and the TX light is reflected, which does not induce additional attitude-to-ranging coupling and avoids losses in the TX path.

In addition, it should be noted that one might be able to remove the baffle mirror, if a reflective telescope is used in an appropriate configuration.

Unfortunately, the off-axis and the on-axis designs (cf. fig. 2.65 and 2.66) transmit some of the weak received light at the recombination beamsplitter. The loss can be mitigated by overlapping the RX and LO beams in different polarization states with a polarizing recombination beamsplitter as shown in fig. 2.67. However, this requires an additional wave plate and a polarizing coating on the redundancy beamsplitter. It is remarked that the same technique can be utilized in an off-axis layout as well (not shown).

Another noteworthy constraint is present in both layouts, off-axis and on-axis, which concerns the spatial beam modes. So far, the LO laser beam mode used for the interference was equal to the beam mode entering the telescope (on-axis) or leaving towards the distant S/C (off-axis/racetrack). It is not possible to add a beam expander in the TX path in the racetrack layout, since the telescope magnifies also the angular variations and would falsify the TX beam pointing. However, it is easy to see in the on-axis layout, that the retro-reflector ABCD matrix (cf. sec. 2.3.5) can be modified with a curved mirror M2 to produce a magnification of the laser beam by a factor m_{RR} , i.e.

$$\begin{pmatrix} -1 & 0 \\ 0 & -1 \end{pmatrix} \rightarrow \begin{pmatrix} -m_{RR} & 0 \\ 0 & -1 \end{pmatrix}, \quad (2.372)$$

which does not alter the beam direction. Even in an off-axis design it is likely possible to change the TX beam mode by a two-lens system, as long as the ABCD matrix for the overall TX path is of the form of eq. (2.372). However, such an extension needs to be analyzed thoroughly regarding phase errors and attitude-to-ranging coupling within the field of regard of the TX beam.

The optical layouts presented here are further elaborated with the help of laser link power budgets, which allow in the end to derive the optimal interferometer parameter such as laser beam sizes and aperture sizes.

2.8 Laser Link Power Budgets

A power budget of a laser link is an indispensable tool in the design process of ranging interferometers. It shows the allocation of available optical power in the laser link, in particular, the amount received by the photodiodes. Such a link budget is typically a table with available optical (input) laser power, losses in the optical path and the final received optical power. However, it can easily be extended to contain or account for

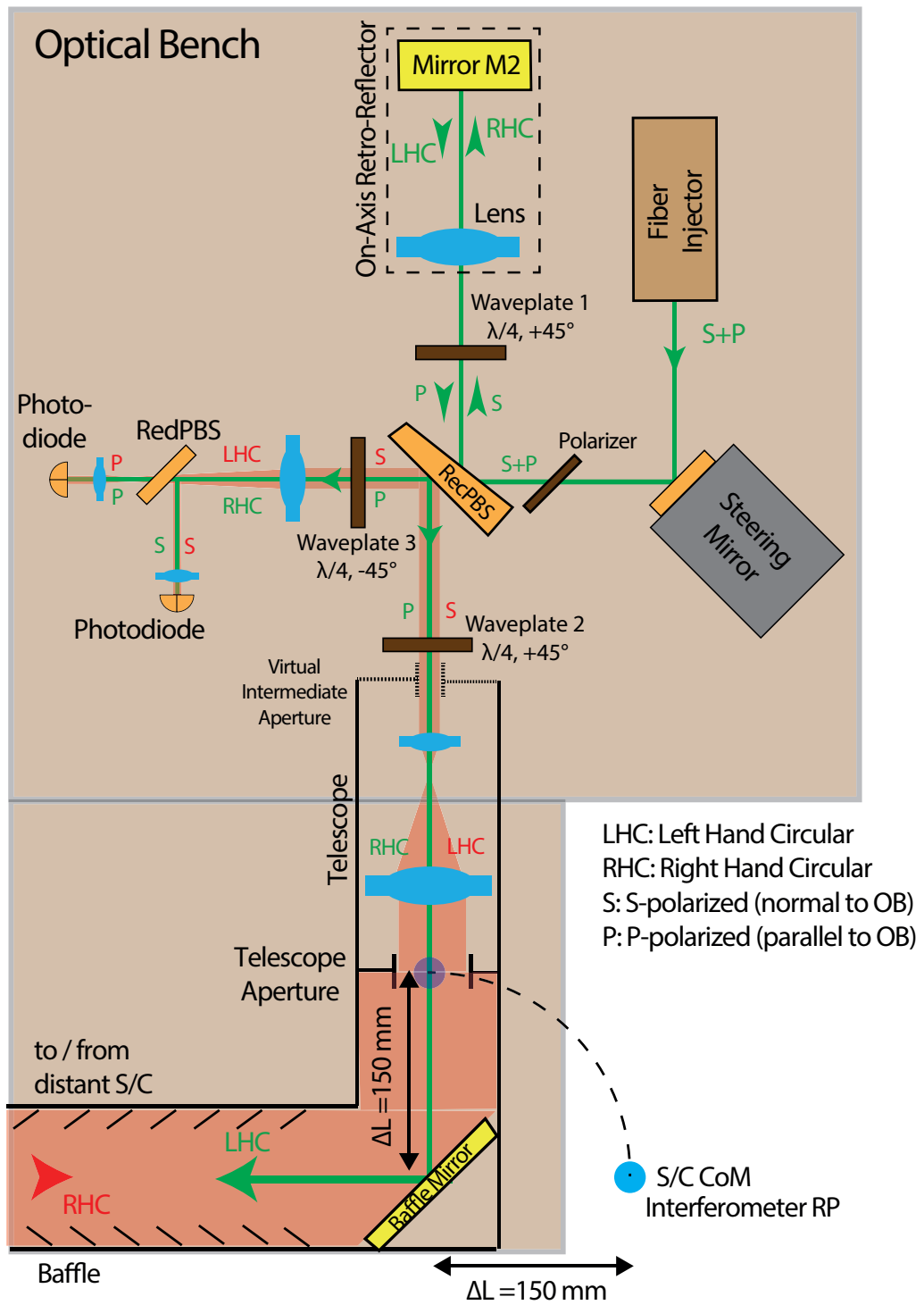


Figure 2.67: On-axis layout without transmission loss of the RX light at the recombination beamsplitter. Based on fig. 2.66.

- beam modes, i.e. sizes of the beams,
- photodiode properties such as photodiode responsivity,
- noise levels of the photoreceiver and of the laser light, such as the relative intensity noise,
- expected wavefront overlap of the interference pattern, i.e. the heterodyne efficiency,
- misalignment of beams and/or of the S/C.

With this information, an otherwise purely optical link budget can account for the transition into the electric domain and enables to derive the carrier-to-noise density, i.e. the signal-to-noise ratio of the instrument. Hence, such budgets directly provide information on the feasibility of particular designs as the carrier-to-noise density needs to exceed a tracking threshold, for example.

A comprehensive and precise budget can be created with computer-aided spreadsheets, which can use formulas and allow to assess the effect of parameter changes such as sizes of apertures, beams or telescopes or the noise level of the photoreceivers. Such budgets easily become a tabular representation of the whole interferometer.

Different columns of the budget can be used to evaluate different operational states of the interferometers and satellites, e.g. with different misalignment angles or between the worst case and the best or high case, which represent the minimal and maximal possible power levels, respectively.

Exemplary laser link budgets for the two proposed optical layouts (cf. fig. 2.65 and 2.67) are given in tables 2.11-2.14.

The rows of the budgets are arranged in categories:

- *constants*: natural physical constants and parameters intended not to change, e.g. because some formulas are valid only for particular parameter values,
- *fixed*: parameters and noise levels, which are constant throughout the budget (in all columns),
- *case*: parameters such as S/C misalignment angles or parameters strongly changing between the columns, e.g. from worst to high case,
- *setup*: design parameters of the interferometer,
- *computed*: quantities automatically computed within the spreadsheet.

The classification into categories *fixed*, *case* and *setup* parameters is not strict and may be changed, for example, if further constraints or boundary conditions exist. Here, the assignment was motivated by the subsequent optimization of *setup* parameters in sec. 2.8.4.

2.8.1 Off-Axis Interferometer

Tables 2.11 and 2.12 contain the power budget for the off-axis or racetrack layout. The table columns represent a GRACE-FO LRI-like setup and a NGGM interferometer in worst and high case, which is shown in fig. 2.65. The two *setup* parameters in rows 28 and 29 are the beam waist radius of the local oscillator $\omega_{0,LO}$, which is equal to the transmit (TX) beam mode $\omega_{0,TX}$, and the RX aperture radius $r_{RX,AP}$. The number of surfaces traversed by the beams are given in rows 14-17. These numbers are required to calculate the loss arising from an eventual degradation of optical surfaces due to molecular and particulate contamination, which is considered here in a simplified manner with a constant loss per surface in row 22. Although one percent loss of optical power per traversed surface might appear conservative, this value already leads to a desired advantage for less complex layouts with only a few optical components.

Row	Type Name	Unit	~ GFO LRI	NGGM Worst-Case	NGGM High-Case	Ref./Formula		
1	constants	Wavelength λ	m	1.06E-06	1.06E-06	1.06E-06		
2		Photon energy	eV	1.17	1.17	1.17		
3		Electron charge	J	1.87E-19	1.87E-19	1.87E-19		
4		Speed of light c	C	1.60E-19	1.60E-19	1.60E-19		
5			m/s	3.00E+08	3.00E+08	3.00E+08		
6	fixed	Transmittance T_{ACS-BS}	[]	0.95	0.95	0.95	acq. sensor BS	
7		# of QPD segments	[]	8	8	8		
8		Loss per QPD (Gap, Clipping)	[]	0.03	0.03	0.03		
9		Responsivity QPD η_{PD}	A/W	0.8	0.8	0.8	Sec. 2.3.3	
10		RIN	1/Hz	1.00E-015	1.00E-015	1.00E-015	Sec. 2.3.1	
11		Photoreceiver noise	pA ² /Hz	25	25	25	eq. (2.80)	
12		QPD radius	mm	0.5	0.5	0.5	Sec. 2.3.3	
13		Frequency Stabilization Laser Power Requirement $P_{FreqStab}$	mW	3	3	3		
14		# Surfaces from Laser to RecBS: n_a	[]	5	5	5		
15		# Surfaces from RecBS to QPD: n_b	[]	6	6	6		
16		# Surfaces from RecBS to TX-Exit: n_c	[]	4	4	4		
17		# Surfaces from RX-AP to RecBS: n_d	[]	2	2	2		
18		case	Available laser power @ worst case/EOL P_{laser}	mW	30	100	100	
19			Laser polarization purity / polarizer transmission $T_{polarizer}$	[]	0.98	0.98	1	
20			Reflectivity Retro Reflector T_{RR}	[]	0.92	0.92	0.99	
21			Ifo Polarization Overlap η_{Pol}	[]	0.98	0.98	0.98	at photodiode
22			Contamination per surface: T_{CSurf}	[]	0.990	0.990	1.000	transmissivity
23	S/C Separation L		km	200	150	70		
24	RX-LO Phasefront Curvature in terms of "Waist Position Offset / Rayleigh Range" Ω		[]	0.10	0.10	0.00	eq. (2.356)	
25	Laser Power Scaling BOL/EOL: G_{BOL}		[]	1	1	3	(for high-case)	
26	RX S/C misalignment α_{RX}		μ rad	100	133	0		
27	TX S/C misalignment α_{TX}		μ rad	100	133	0		
28	setup	Radius Waist $\omega_{0,LO} = \omega_{0,TX}$	mm	2.50	2.00	2.00		
29		RX Aperture Radius $r_{RX,AP}$	mm	4	3	3		
30	computed	Laser Splitting Ratio: Freq.Stab. / OB	[]	0.10	0.03	0.03	via (18) & (13)	
31		Optical Power at Optical Bench: P_{OB}	mW	27.00	97.00	291.00	(25)*(18)*(1-(30))	
32		Optimal LO Power: $P_{LO,seg}$	mW	0.20	0.20	0.20	cf. fig. 2.50	
33		Optimal $P_{LO,total}$ @RecBS	mW	1.68	1.68	1.68	via (32) & (7)	
35		Beam Divergence Θ_{LO}	μ rad	135.47	169.34	169.34	via (25)	
36		Beam Divergence Θ_{TX}	μ rad	135.47	169.34	169.34	via (25)	
37		IFO Clipping Param. $\zeta = \omega_{0,LO} / r_{RX,AP}$	[]	0.63	0.67	0.67		
38		$\Psi_2(c)$ for Heterodyne Efficiency	[]	2.02	2.07	2.07	eq. (2.353)	
39		Optimal Recombination Beamsplitter LO Transmission (@Worst Case)	%	7.10	1.98	1.98		
34		Actual $P_{LO,seg}$ with G_{BOL}	mW	0.20	0.20	0.68	at BOL & high-case	
40		Power P_{TX} leaving S/C: $P_{TX} = P_{TX,PC}$	mW	20.66	78.31	282.40	Sec. 2.8.3	
41		RX-LO Phasefront Radius of Curvature (RoC): $Rz(\Omega)$	m	186.38	119.29	Infinity	cf. (24)&eq. (2.356)	
42		χ for RoC	[]	1.09	1.12	1.12	eq. (2.358)	
43		Angular Offset in Het. Efficiency Maximum due to RoC	μ rad	8.28	9.93	0.00	eq. (2.358)	
44		Beam Compressor Demagnification	[]	8.00	6.00	6.00	via (28) and (12)	
45		Noise Spectral Density	A_{rms}^2/Hz	1.03E-22	1.03E-22	4.90E-22	Sec. 2.6.9	
46	Carrier Power of Segment ($P_{eff}=1pW$)	A_{rms}^2	3.23E-16	3.23E-16	1.08E-15	Sec. 2.6.9		

Table 2.11: Part 1 of 2 of the laser link budget for the off-axis concept (cf. fig. 2.65)

47	Type Name	Unit	~ GFO LRI	NGGM Worst-Case	NGGM High-Case	Ref./Formula	
49	C/N0 ($P_{\text{eff}} = 1 \text{ pW}$), Single Segment	Hz/pW	3.14E+06	3.14E+06	2.20E+06	via (45) & (46)	
50	Power in RX-Aperture With $\alpha_{\text{TX}} = 0$	pW	900.53	2184.74	36175.30	Perfect Pointing	
51	RX power drop due to α_{TX}	[]	0.34	0.29	1.00	eq. (2.334)	
52	Max. Het. Efficiency $\eta_{0,\text{seg}}$	[]	0.67	0.72	0.72	eq. (2.348)	
53	Het. Eff. Drop due to RoC & α_{RX}	[]	0.73	0.72	1.00	eq. (2.353)	
54	Het. Eff. Drop due to Polarization	[]	0.98	0.98	0.98	= (21)	
55	Transmission Efficiency RX-Aperture to QPD-Segment	[]	0.096	0.101	0.109	includes splitting into segments	
56		Hz	4.37E+07	1.02E+08	6.15E+09		
57	Final C/N0 – Single Segment	dB-Hz	76.40	80.09	97.89		
58	Acquisition Sensor						
59	# of Ac. Sensors	[]		2	2	cf. Optical Layout	
60	Readout Noise	e ⁻		150	150		
61	Dark Noise	e ⁻ /sec		10000	10000		
62	Well Capacity	e ⁻		120000	120000	Sec. 2.3.10	
63	# of ADC bits	[]		12	12		
64	Responsivity ACS	A/W		0.6	0.6		
65	RX Aperture Radius $r_{\text{RX,AP}}$	mm		3	3	(28)	
66	Integration Time of Sensor	ms		0.2	0.2		
67	Stop Duration per Scan Point	ms		1	1	Sec. 2.6.12	
68	Avg. Hop-Time between Points	ms		2	2		
69	Optical Losses ACS-BS to ACS	%		5	5		
70	ACS Field-of-View (FOV)	$\mu\text{rad}, \pm$		3000	3000		
71	# of Pixels x & y dimension	[]		256	256		
72	ACS – Focal Length	m		0.38	0.38		
73	Worst-Case Closest Approach (WCCA) Angular Separation	μrad		140	140	Sec. 2.6.12	
74	Pixel Pitch	μm		30	30	Chip Spec.	
75	Angular Resolution / Pixel	$\mu\text{rad}/\text{px}$		23.53	23.53		
76	ACS dimensions in x & y	mm, \pm		3.825	3.825	via (71) & (74)	
77	Maximum displacement @ FOV	mm, \pm		1.14	1.14	via (70) & (72)	
78	Spot radius on chip	μm		82.15	82.15		
79		px		2.74	2.74	eq. (2.368)	
80	# of Scan Pattern Points	[]		121	121	via (70) & (73)	
81	Total Duration of Scan	sec		0.36	0.36		
82	Power in RX-AP – WCCA	pW		556.84	9220.19		
83	Energy in RX-AP – WCCA	J		5.57E-13	9.22E-12		
84	# Photons in RX-AP – WCCA	[]		2.98E+006	4.94E+007		
85	Signal Photons for all ACS – WCCA	[]		1.42E+005	2.35E+006	Hot Redundancy	
86	Signal Electrons for each ACS	e ⁻		4.25E+004	7.04E+005		
87	Signal Electrons per Frame per ACS	e ⁻		8.50E+003	1.41E+005	Worst-Case	
88	Signal Electrons per Frame per Pixel	e ⁻		1133.70	18771.92		
89	Used ADC Capacity for Signal Pixel	%		0.95	15.64		
90	Noise RMS per Px per ACS	e ⁻ (rms)		153.74	203.16		
91	SNR of pixel per frame per ACS	[]		7.37	92.40		

Table 2.12: Part 2 of 2 of the laser link budget for the off-axis concept (cf. fig. 2.65). Abbreviations: ACS: Acquisition (Sensor), BS: Beamsplitter, QPD: Quadrant Photodiode, RecBS: Recombination Beamsplitter, BOL: Beginning of life, EOL: End of life, WCCA: worst-case closest approach, OB: Optical Bench, RoC: Phasefront Radius of Curvature, RX-AP: RX Aperture

Based on the development of the ESA High-Stability-Laser system (cf. sec. 2.3.1 on the laser) and in accordance with the e.motion² study, a laser power of 100 mW has been selected as end-of-life value in row 17. The required laser power for the frequency stabilization is specified with 3 mW in row 13. The budget assumes a degradation of the laser power from beginning to the end of the mission by a factor of 3 as shown in row 25. The TX beam and the receiver S/C misalignment angles are 133 μ rad for the NGGM worst case in rows 26 and 27.

The photoreceiver characteristics from rows 9-11 are used to calculate the electric current noise density in row 45 and the optimal local oscillator power per segment in row 32, which maximizes the carrier-to-noise density (cf. sec. 2.6.9). Furthermore, this allows the optimal local oscillator power at the recombination beamsplitter to be computed in row 33 and, hence, the optimal reflectivity of the recombination beamsplitter can be determined as shown in row 39. Another interesting parameter is the required de-magnification of the beam compressor, which is computed in row 44.

The effective power, which depends on the receiver S/C misalignment, on the transmit beam misalignment and on the heterodyne efficiency is computed with the methods discussed in sec. 2.6.10f. At first, the heterodyne efficiency is calculated for aligned phasefronts ($\alpha_{RX} = 0$, row 52). Then, the drop due to the phasefront tilt and due to a potential phasefront curvature mismatch, which is specified in row 24, is calculated in row 53. This drop accounts also for the shift in the maximum position of the heterodyne efficiency (cf. sec. 2.6.11). Moreover, a generic heterodyne efficiency drop of 2% accounts for an eventual polarization mismatch in row 54.

The main result of the laser link budget is the carrier-to-noise density for a single segment given in rows 56 and 57 in table 2.12, which is the product of the rows 49-55. With the selected NGGM worst case parameters for the inter-satellite separation $L = 150$ km from row 23 and with the available laser power of 100 mW from row 18, one obtains approx. 80 dB-Hz for the carrier-to-noise density, which has a sufficient 10 dB margin to the tracking requirement of 70 dB-Hz (cf. eq. (2.127)).

An exemplary budget for the acquisition sensor is starting from row 58. A rectangular acquisition scan pattern is assumed. Each S/C scans the 6 mrad \times 6 mrad uncertainty space specified in row 70 by pointing the TX beam with the steering mirror. The beam is assumed to stop at each scan point for a duration defined in row 67, while the transition time between points is given in row 68. The angular separation between the TX beam and the actual distant S/C may be zero, if the TX beam points accidentally in the correct direction. However, under worst case assumptions, the closest approach should be bound by the threshold in row 73, which yields in combination with the field-of-view from row 70 the number of grid points in the scan pattern in row 80. The total scan duration in row 81 should be sufficient short to ensure a quick acquisition, which is fulfilled with 0.36 s in this design.

The focal length in row 72 of the acquisition sensor optics is selected such that the spot size on the sensor illuminates several pixels as shown in row 79. Furthermore, the FoV does not exceed the dimensions of the sensor (cf. rows 76 vs. 77), which has been addressed in sec. 2.6.12 on the laser link acquisition.

The worst case angular separation in row 73, the noise characteristics of the acquisition sensor in rows 60-63 and the sensor integration time in row 66 are used to compute the expected signal to noise ratio in row 91 of the illuminated signal pixels in the acquisition phase. The final SNR of the whole spot can be expected even larger, as information from multiple pixels is combined, but such a calculation was beyond the scope of this budget.

2.8.2 On-Axis Interferometer

The on-axis laser link budget in table 2.13 and 2.14 has been structured in the same way as the off-axis budget, which eases comparison of both setups. The number of optical surfaces traversed by the laser beams is higher in rows 14-17 compared to the racetrack design, which

increases the losses in the TX and RX path with regard to degradation of optical surfaces. However, the disadvantage is mostly compensated by the smaller losses at the recombination beamsplitter, since almost all RX light can be reflected with the polarization dependent coatings. This fact is especially appealing for interferometers with low laser power, since the optimal beamsplitter transmission is 7.1 % with a 30 mW laser and 2.0 % with a 100mW laser (cf. row 39 in table 2.11), which means that 7.1 % or 2.0 % of the RX light power is lost in an off-axis design without polarization dependent coatings.

An end-of-life and worst-case laser power of 25 mW was considered for the on-axis design as shown in row 18 in table 2.13, which is further split into 3 mW for the laser frequency stabilization shown in row 13 and 1.68 mW for the local oscillator in row 40. Most of the remaining light power (14.20 mW, row 47) is transmitted through the telescope and leaving towards the distant S/C (13.92 mW, row 49).

The four *setup* parameters in the on-axis budget are the waist radius of the local oscillator $\omega_{0,LO}$ in row 28, the telescope magnification m_T in row 29, the magnification of the retro-reflector m_{RR} in row 30, which is kept at 1 throughout this thesis, and the radius of the telescope aperture r_{TAP} in row 31. The constraint $m_{RR} = 1$ yields the relation $\zeta = \zeta_2$. The ratio $\zeta = \omega_{0,LO}/(r_{TAP}/m_T)$ in row 34 is important for the computation of the interference, i.e. heterodyne efficiency, while $\zeta_2 = m_T \cdot m_{RR} \cdot \omega_{0,LO}/r_{TAP}$ in row 35 is the clipping ratio of the TX beam at the telescope and is important for the computation of the transmit beam divergence and the rejected power at the telescope.

The same noise levels for the photoreceivers are assumed as in the off-axis budget, which yields a normalized carrier-to-noise density of $3.14 \cdot 10^6 \text{ Hz} \approx 65 \text{ dB-Hz}$ per picowatt effective power and per photodiode segment. The final C/N_0 values are listed in row 64 and indicate for 80 μrad TX and RX misalignment a satisfying 14.3 dB margin to the phasemeter tracking threshold of 70 dB-Hz (cf. eq. (2.127)).

These power budgets show that the on-axis and the off-axis layouts are feasible, however, they represent only a snapshot for a particular parameter set and do not provide much insight, for example, on similarities or differences of both interferometer types. Furthermore, the selection of the numerical values for the *setup* parameters is not justified. However, with the budgets and the underlying formulas, one can easily derive analytical expressions for the carrier-to-noise density as a function of the *setup* parameters, for example. Then, the expressions can be used to perform a parametric study, which is the outline for the next two subsections.

2.8.3 Budget Analysis: Carrier-To-Noise Density

Based on the power budgets in the previous subsections, one can write the carrier-to-noise density C/N_0 for the on-axis and off-axis interferometers as product of four terms, i.e.

$$C/N_0 = \frac{10^{65/10} \text{ Hz}}{1 \text{ pW}} \cdot \frac{2}{\pi L^2} \cdot P_{\text{TX,PC}} \cdot G_{\text{ifo}}. \quad (2.373)$$

The first factor is the carrier-to-noise density of the interferometric readout normalized to 1 pW effective power, while the other three terms form the actual effective power. The local oscillator power and the recombination beamsplitter transmission were optimized in the budgets to maximize the carrier-to-noise density to the $65 \text{ dB-Hz} = 65 \text{ dB(Hz)} = 10^{65/10} \text{ Hz}$ value, which is referred to 1 pW effective power on a photodiode segment (cf. sec. 2.6.9). This 65 dB(Hz/pW) value might be a few dB higher for a sophisticated low-noise phase readout system, or a few dB lower, if the interferometer is operated at a sub-optimal working point, for example, with slightly higher or lower local oscillator power.

Since the total C/N_0 in eq. (2.373) should fulfill the tracking threshold requirement of 70 dB-Hz (cf. eq. (2.127)), the effective power needs to exceed 3.16 pW or 5 dB(pW). The effective power is a function of the inter-satellite separation L , the second term in eq. (2.373), and of the transmitted power $P_{\text{TX,PC}}$, the third term. The last factor G_{ifo} has units of m^2

Row	Type	Name	Unit	NGGM Worst-Case	NGGM High-Case	Ref./Formula
1	constants	Wavelength λ	m	1.06E-06	1.06E-06	
2		Photon energy	eV	1.17	1.17	
3		Electron charge	C	1.60E-19	1.60E-19	
4		Speed of light c	m/s	3.00E+08	3.00E+08	
5		Transmittance T_{ACS-BS}	[]	0.95	0.95	acq. sensor BS
6	fixed	# of QPD segments	[]	8	8	
7		Loss per QPD (Gap, Clipping)	[]	0.03	0.03	
8		Responsivity QPD η_{PD}	A/W	0.8	0.8	Sec. 2.3.3
9		RIN	1/Hz	1.00E-015	1.00E-015	Sec. 2.3.1
10		Photoreceiver noise	pA ² /Hz	25	25	eq. (2.80)
11		QPD radius	mm	0.5	0.5	Sec. 2.3.3
12		Frequency Stabilization Laser Power Requirement $P_{FreqStab}$	mW	3	3	
13		# Surfaces from Laser to RecBS: n_a	[]	5	5	
14		# Surfaces from RecBS to QPD: n_b	[]	8	8	
15		# Surfaces from RecBS to TX-Exit: n_c	[]	19	19	
16		# Surfaces from RX-AP to RecBS: n_d	[]	7	7	
17		Available laser power @ worst case/EOL P_{laser}	mW	25	25	
18		case	Laser polarization purity / polarizer transmission $T_{polarizer}$	[]	0.98	1
19	Reflectivity Retro-Reflector T_{RR}		[]	0.92	0.99	
20	Ifo Polarization Overlap η_{pol}		[]	0.02	0.02	at photodiode
21	Contamination per surface: T_{CSurf}		%	0.99	1	transmissivity
22	S/C Separation L		km	150	75	
23	RX-LO Phasefront Curvature in terms of "Waist Position Offset / Rayleigh Range" Ω		[]	0.10	0.00	eq. (2.356)
24	Laser Power Scaling BOL/EOL: G_{BOL}		[]	1	1.1	(for high-case)
25	RX S/C misalignment α_{RX}		μ rad	80	0	
26	setup	TX S/C misalignment α_{TX}	μ rad	80	0	
27		Radius Waist $\omega_{0,LO}$	mm	1.00	1.00	
28		Telescope Magnification m_T	[]	4	4	
29		RR-Magnification: m_{RR}	[]	1	1	
30		Telescope Radius r_{TAP}	mm	10	10	
31	computed	Intermediate Aperture Radius r_{IAP}	mm	2.5	2.5	via (29) & (31)
32		Waist at IAP of TX beam: $\omega_{0,IAP}$	mm	1	1	via (28) & (30)
33		IFO Clipping Param. $\zeta = \omega_{0,LO} / r_{RX,AP}$	[]	0.40	0.40	for (44); Het. Eff.
34		Tel. Clipping Param.: $\zeta_2 = m_T \cdot \omega_{0,IAP} / r_{TAP}$	[]	0.40	0.40	for (36) & (43)
35		$\Psi_1(\zeta_2)$ for clipped Gaussian diffraction	[]	1.02	1.02	eq. (F.23)
36		Laser Spitting Ratio: Freq.Stab. / OB	[]	0.12	0.12	via (18) & (13)
37		P_{laser} to Optical Bench	mW	22.00	24.20	(25)*(18)*(1-(37))
38		Optimal $P_{LO,seg}$	mW	0.20	0.20	cf. fig. 2.50
39		Optimal $P_{LO,total}$ @RecBS	mW	1.68	1.68	via (39) & (7)
40		Actual $P_{LO,seg}$	mW	0.20	0.22	at BOL & high-case
41		Beam Divergence Θ_{LO}	μ rad	338.68	338.68	via (28)
42		(Clipped) Divergence Θ_{TX}	μ rad	86.56	86.56	eq. (F.23)
43		$\Psi_2(\zeta)$ for Heterodyne Efficiency	[]	1.91	1.91	eq. (2.353)
44		Optimal Recombination Beamsplitter Transmission (@Worst Case)	%	8.89	8.89	

Table 2.13: Part 1 of 2 of the laser link budget for the on-axis concept (cf. fig. 2.67).

46	Type	Name	Unit	NGGM Worst-Case	NGGM High-Case	Ref./Formula
47	computed	TX Power prior Clipping: $P_{TX,PC}$	mW	14.20	21.83	cf. Appendix F
48		Rejected Power by Telescope	mW	0.00	0.00	
49		Power leaving S/C : $P_{TX,AP}$	mW	14.20	21.83	
50		RX-LO Phasefront Radius of Curvature (RoC): $R_z(18)$	m	29.82	2952624.67	cf. (24)
51		χ for RoC	[]	0.84	0.84	eq. (2.358)
52		Angular Offset in Het. Efficiency Maximum due to RoC	μrad	24.93	0.00	eq. (2.358)
53		Beam Compressor Demagnification	[]	5.00	5.00	via (12) & (32)
54		Noise Spectral Density	A_{rms}^2/Hz	1.01E-22	1.11E-22	Sec. 2.6.9
55		Carrier Power of Segment ($P_{eff}=1\text{pW}$)	A_{rms}^2	3.16E-16	3.48E-16	Sec. 2.6.9
56		C/N0 ($P_{eff} = 1 \text{ pW}$, Single Segment)	Hz/pW	3.14E+06	3.13E+06	via (54) & (55)
57		Power in RX-Aperture With $\alpha_{TX} = 0$	pW	16778.60	103177.49	Perfect Pointing
58		RX Power Drop due α_{TX}	[]	0.18	1.00	eq. (2.334)
59		Max. Het. Efficiency $\eta_{0,seg}$	[]	0.32	0.32	eq. (2.348)
60		Het. Eff. Drop due to RoC & α_{RX}	[]	0.95	1.00	eq. (2.353)
61		Het. Eff. Drop due to Polarization	[]	0.98	0.98	= (21)
62		Transmission Efficiency RX-Aperture to QPD-Segment	[]	0.096	0.112	includes splitting into segments
63			Hz	2.72E+08	1.13E+10	
64		Final C/N0 – Single Segment	dB-Hz	84.34	100.52	

Table 2.14: Part 2 of 2 of the laser link budget for the on-axis concept (cf. fig. 2.67). Abbreviations: RoC: Phasefront Radius of Curvature, IAP: Intermediate aperture (image plane of telescope), RR: Retro-Reflector. For further abbreviations see table 2.12.

and depends strongly on the interferometer design and beam parameters. However, the first three terms are generic and apply for all interferometer types.

For the off-axis design with non-clipped Gaussian beams, the $P_{TX,PC}$ value is given by P_{TX} as stated in row 40 of table 2.11. In the on-axis layout with a telescope, the Gaussian beams may be clipped by the telescopes. For this case, the link budget shows the TX power prior clipping $P_{TX,PC}$ and the power in the TX aperture $P_{TX,AP}$, i.e. leaving the S/C (cf. rows 47 and 49 in table 2.14).

Although it may appear counter-intuitive at the first glance to use the prior-clipping value ($P_{TX,PC}$) in eq. (2.373), it is advantageous, because $P_{TX,PC}$ does not depend on *setup* parameters such as the size of the laser beams or the size of the telescope. It is self-evident that the product $P_{TX,PC} \cdot G_{ifo}$ needs to be formulated consistent to obtain the correct results.

The optical power $P_{TX,PC}$ has a functional dependence on the laser power P_{laser} according to

$$P_{TX,PC} \approx \kappa \cdot (P_{laser} - P_{freq.stab.} - P_{LO}), \quad (2.374)$$

where κ denotes the transmission efficiency from fiber injector on the optical bench to the TX beam prior eventual clipping. $P_{TX,PC}$ is reduced by $P_{freq.stab.} \approx 3 \text{ mW}$, which is the required light power for the laser frequency stabilization unit, and by the local oscillator power $P_{LO} \approx 1.68 \text{ mW}$ required for local interference. The 1.68 mW are split onto 8 photodiode segments in the interferometers considered here. The racetrack configuration with only a few surfaces in the optical path has a higher $\kappa \approx 0.8$ value compared to the on-axis design with $\kappa \approx 0.6$. For on-axis layouts, the power value $P_{TX,PC}$ is related to the power leaving the limiting aperture $P_{TX,AP}$ by

$$P_{TX,AP} = P_{TX,PC} - P_{rej}, \quad (2.375)$$

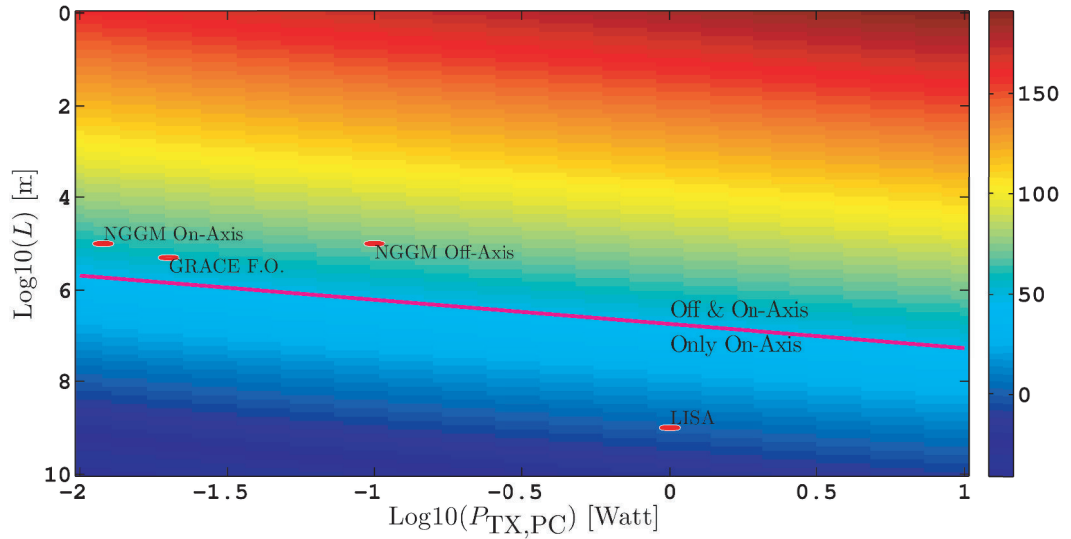


Figure 2.68: The first three terms of eq. (2.373) as a function of the S/C separation L and transmitted optical power $P_{\text{TX,PC}}$ prior-clipping on a logarithmic scale. The color function denotes $10 \cdot \log_{10}(10^{6.5} \text{ Hz}/1 \text{ pW} \cdot 2/(\pi L^2) \cdot P_{\text{TX,PC}})$, i.e. it has units of $\text{dB}(\text{Hz}/\text{m}^2)$. The magenta line indicates the $45 \text{ dB}(\text{Hz}/\text{m}^2)$ values, which is a soft limit for the feasibility of off-axis or telescope-free designs as discussed in the next sec. 2.8.4.

where P_{rej} is the rejected light power due to beam clipping (cf. eq. (F.19)).

Figure 2.68 illustrates the magnitude of the first three factors in eq. (2.373) as a function of the S/C separation L and laser TX power $P_{\text{TX,PC}}$, which are both independent of the interferometer type. Gravimetric missions reach a value of approx. $60 \text{ dB}(\text{Hz}/\text{m}^2)$, while LISA mission parameters are in the region of $0 \text{ dB}(\text{Hz}/\text{m}^2)$. From this plot and from the desired carrier-to-noise density of $70 \text{ dB}(\text{Hz})$, one can derive requirements on the interferometer-describing factor G_{ifo} , which has units of m^2 and which can be written as the product of five terms:

$$G_{\text{ifo}} = G_{\text{RX}} \cdot G_{\text{collect}} \cdot G_{\alpha_{\text{TX}}} \cdot \eta_{0,\text{seg}} \cdot G_{\alpha_{\text{RX}}}. \quad (2.376)$$

The first term G_{RX} denotes the efficiency of the optical power transfer from the receiving aperture to the photodiode segment and includes the polarization overlap (cf. row 21 in table 2.11). The term G_{collect} describes the interferometer's ability to collect light and depends on the size of the receiving aperture and on the TX beam divergence. Furthermore, G_{collect} contains the effect of the rejected power, if the TX beam is clipped at the telescope. The maximum heterodyne efficiency $\eta_{0,\text{seg}}$ is derived for perfectly aligned phasefronts and depends on the size of the RX aperture and on the beam modes. The terms $G_{\alpha_{\text{TX}}}$ and $G_{\alpha_{\text{RX}}}$ denote the intensity and heterodyne efficiency drop upon transmitter α_{TX} and receiver α_{RX} misalignment, respectively. Analytical expressions for the terms are provided in the next subsection.

The link budgets from tables 2.11-2.14 have been condensed and rewritten in table 2.15 in terms of the quantities shown in eq. (2.373) and (2.376). The lower part of the table is simply a decibel representation of the upper part, i.e. all values are computed as $10 \cdot \log_{10}(x)$ of the values from the upper part. Decibel is, in general, a controversial unit and should be avoided in interferometric applications, where optical light power is used to produce a sinusoidal voltage, since field quantities ($20 \cdot \log_{10}(x)$) and power quantities ($10 \cdot \log_{10}(x)$) are not easily distinguishable. However, the logarithmic scale offers the advantage that a multiplicative chain can be expressed as an illustrative sum. Since all dB values are accompanied by the non-dB values, the dB scale is exceptionally used here.

As apparent from table 2.15, the factor G_{RX} is approximately 0.10 for all designs. It is dominated by the splitting into the eight photodiode segments and contains some other

			GFO LRI like	NGGM: Worst-case		
				Off-Axis	On-Axis	
	RX S/C misalignment α_{RX}	μrad	100	133	80	
	TX S/C misalignment α_{TX}	μrad	100	133	80	
	Laser power P_{laser}	mW	30	100	25	
1	Basic C/N_0	Hz/pW	3.14E+06	3.14E+06	3.14E+06	
2	$P_{TX,PC} (P_{\text{Laser}})$	pW	2.07E+10	7.83E+10	1.42E+10	
3	S/C Separation L	1/m ²	1.59E-11	2.83E-11	2.83E-11	
4	G_{ifo}	Efficiency: G_{RX}	[]	9.38E-02	9.89E-02	9.41E-02
5		G_{collect}	m ²	2.74E+03	9.86E+02	4.18E+04
6		RX Power drop due to α_{TX}	[]	3.36E-01	2.91E-01	1.81E-01
7		Heterodyne efficiency: $\eta_{0,\text{seg}}$	[]	6.69E-01	7.19E-01	3.19E-01
8		Het. Eff. drop due to α_{RX}	[]	7.32E-01	7.17E-01	9.49E-01
9	Total	Hz	4.37E+07	1.02E+08	2.72E+08	
		dB-Hz	76.40	80.09	84.34	
10	Basic C/N_0	db-Hz/pW	64.97	64.97	64.97	
11	$P_{TX,PC} (P_{\text{Laser}})$	dB-pW	103.15	108.94	101.52	
12	S/C Separation L	dB-m ⁻²	-107.98	-105.48	-105.48	
13	G_{ifo}	Efficiency: G_{RX}	dB	-10.28	-10.05	-10.26
14		G_{collect}	dB-m ²	34.38	29.94	46.21
15		RX Power drop due to α_{TX}	dB	-4.73	-5.36	-7.42
16		Heterodyne efficiency: $\eta_{0,\text{seg}}$	dB	-1.74	-1.43	-4.97
17		Het. Eff. drop due to α_{RX}	dB	-1.36	-1.45	-0.23
18	Sum	dB-Hz	76.40	80.09	84.34	

Table 2.15: Condensed laser link budgets for the different interferometer designs. The lower part of the table is a logarithmic representation (dB) of the upper part.

minor losses, e.g. due to the acquisition sensors. The gain in the RX power due to lacking RX transmission at the recombination beamsplitter in the on-axis design is mostly compensated by the additional contamination losses due to the higher number of traversed optical surfaces.

The remaining last four terms in eq. (2.376) depend strongly on *setup* parameters in the link budget such as beam sizes or the telescope magnification. The determination of optimal parameters for the different optical layouts, which maximize G_{ifo} , is covered in the following subsection.

2.8.4 Optimal Parameter Selection

The rationale in the selection of the *setup* parameters is to ensure operation of the interferometer under worst-case conditions, for example, for a maximal misalignment of the transmitter S/C α_{TX} , which implies a misalignment of the TX beam w.r.t. the LOS, and for a maximal misalignment of the receiver S/C α_{RX} w.r.t. the LOS. The cost function for the optimization can be defined as

$$G_{\text{setup}}(\alpha_{TX}, \alpha_{RX}, \dots) := \frac{G_{\text{ifo}}}{G_{RX}} = G_{\text{collect}} \cdot G_{\alpha_{TX}} \cdot \eta_{0,\text{seg}} \cdot G_{\alpha_{RX}}. \quad (2.377)$$

Since each S/C acts as receiver and transmitter at the same time and both S/C of the laser link are equitable, the misalignment angles of the transmitter (α_{TX}) and of the receiver (α_{RX}) can be considered equal for the worst-case analysis. This does not mean that α_{RX} and α_{TX} have the same effect on G_{setup} , but that the misalignment of both S/C is similar. Generally, the laser beam misalignment and the S/C pointing error need to be considered in the yaw and pitch directions, however, a simplified analysis with rotational symmetric laser beams is used here.

In the off-axis layout, the beam mode used as the local oscillator is equal to the beam mode transmitted towards the distant S/C. Here, the beam mode is defined by the waist size

$\omega_{0,LO} = \omega_{0,TX}$ of a fundamental Gaussian beam. The size of the flat top beam is determined by the RX aperture radius $r_{RX,AP} = r_{AP}$. With these *setup* parameters, one can write G_{setup} with units of m^2 for the off-axis layout as follows

$$G_{\text{setup}}(\alpha_{TX}, \alpha_{RX}, \omega_{0,LO}, r_{AP}) = \frac{\pi r_{AP}^2}{\theta_{TX}^2} \cdot e^{-2\frac{\alpha_{TX}^2}{\theta_{TX}^2}} \cdot \frac{2\omega_{0,LO}^2 \tanh\left(\frac{r_{AP}^2}{2\omega_{0,LO}^2}\right)}{r_{AP}^2} \cdot e^{-2\frac{(\alpha_{RX} + \alpha_{RoC})^2}{\theta_{LO}^2 \cdot \Psi_2^2}} \quad (2.378)$$

$$= \frac{\pi^3 \cdot \omega_{0,LO}^4}{\lambda^2 \cdot \zeta^2} \cdot e^{-2\frac{\alpha_{TX}^2 \cdot \pi^2 \cdot \omega_{0,LO}^2}{\lambda^2}} \cdot 2\zeta^2 \tanh(1/(2\zeta^2)) \cdot e^{-2\frac{(\alpha_{RX} + \alpha_{RoC})^2 \cdot \pi^2 \cdot \omega_{0,LO}^2}{\lambda^2 \cdot \Psi_2(\zeta)^2}}, \quad (2.379)$$

where $\zeta = \omega_{0,LO}/r_{AP}$ is used as an abbreviation (cf. row 37 in table 2.11). The recast from eq. (2.378) to (2.379) used the fact that the TX beam divergence θ_{TX} is equal to the LO beam divergence θ_{LO} . The four single product terms in eq. (2.379) correspond to G_{collect} , $G_{\alpha_{TX}}$, $\eta_{0,\text{seg}}$ and $G_{\alpha_{RX}}$, respectively. The function is depicted in fig. 2.69, where the four upper panels are based on the heterodyne efficiency of a single segment of the photodiodes, while the lower four lower panels show the efficiency for a circular photodiode or the coherent sum of four segments. The heterodyne efficiency of a single segment is computed with the help of the polynomial Ψ_2 -function, which was derived from a fit to results obtained by the electric field overlap integral (cf. sec. 2.6.11). In addition, it is recalled the heterodyne efficiency of a segment is susceptible to a phasefront curvature mismatch between RX and LO beam, which causes a shift in the position of the maximum heterodyne efficiency. This angular shift is denoted with $\alpha_{RoC} = \alpha_{EF,\text{max}}$ (cf. eq. 2.358) and is based on the assumption, that the differential phasefront curvature is caused by a longitudinal shift in the LO waist position of $\Omega = 10\%$ of the Rayleigh range.

The parameters $\zeta \approx 0.7$ and $r_{AP} = 3$ mm are selected for the NGGM off-axis layout within this thesis, i.e. these are the values in the laser link budget. These parameters result in a slightly smaller Gaussian waist radius of $\omega_{0,LO} \approx 2$ mm compared to the GRACE Follow-On LRI (2.5 mm), which eases on-ground measurements of the mode content of the laser beams. Furthermore, for a misalignment of $\alpha_{TX} = \alpha_{RX} = 130 \mu\text{rad}$, these values yield $G_{\text{setup}} \approx 22 \text{ dB}(\text{m}^2)$, which is fairly close to the overall maximum at this misalignment (cf. fig. 2.69)

The upper-left panel in fig. 2.69 shows a $G_{\text{setup}} \approx 28.5 \text{ dB}(\text{m}^2)$ value for non-misaligned S/C in case of the NGGM off-axis parameter set, which agrees with the values provided in table 2.15 (sum of rows 14 and 16). Some regions are blank or blue in fig. 2.69, as they are considered undesirable by the author of this thesis. These regions mark the parameter space, where

- the local oscillator waist radius is higher than 3 mm, which would require an interferometer optical bench with large optical components. In addition, it is difficult to characterize precisely the mode content of such large beams due to the long Rayleigh range.
- the heterodyne efficiency drops below 0.13, i.e. $\eta_{\text{seg}} = \eta_{0,\text{seg}} \cdot G_{\alpha_{RX}} < 0.13$. This indicates, for example, that only a small region of the RX or of the LO beam is used in the interference, which increases the susceptibility of the interferometric readout to localized wavefront distortions.
- the factor $G_{\alpha_{TX}}$ is smaller than 0.13. This means the Gaussian TX beam intensity is evaluated far away from the central axis and it can not be predicted reliably unless a precise model of the mode content of the TX beam is available.

It is remarked that the total carrier-to-noise density C/N_0 in units of $\text{dB}(\text{Hz})$ can be obtained by adding up $G_{RX} \approx 0.1 = -10 \text{ dB}$ with the colorbar values from fig. 2.68 and from fig. 2.69 (upper four panels). Furthermore, the overall maximum value for G_{setup} in the upper-left panel of fig. 2.69 is approx. $35 \text{ dB}(\text{m}^2)$, which can be understood as a soft limit

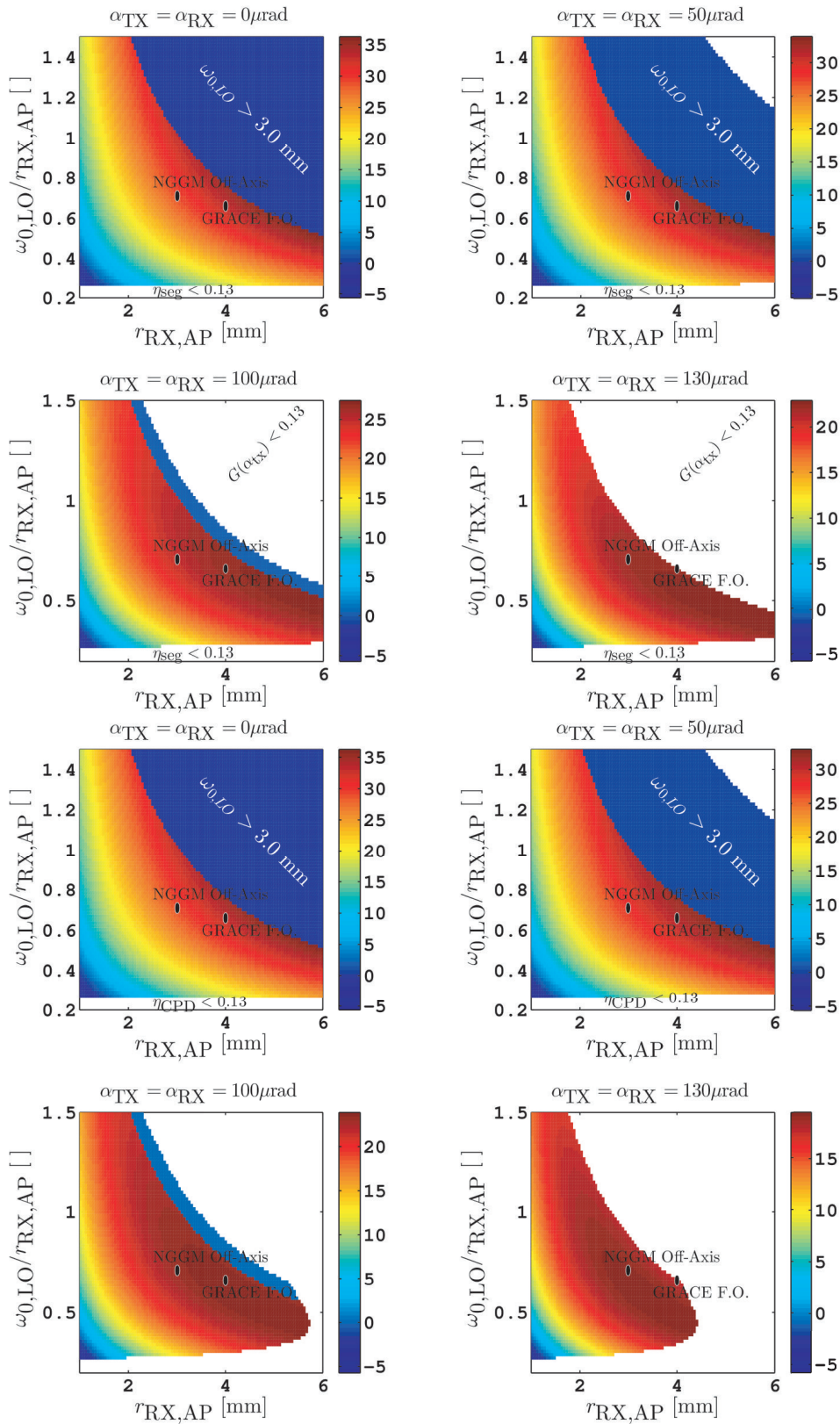


Figure 2.69: G_{setup} is shown for the off-axis (racetrack) layout based on the heterodyne efficiency of a **single photodiode segment** (upper four panels) and of a **circular photodiode** (lower four panels). The color function is defined as $10 \cdot \log_{10}(G_{\text{setup}})$, i.e. it has units of dB(m²). White areas denote parameter regions, where the heterodyne efficiency η or $G_{\alpha_{TX}}$ is below 0.13. The blue region at the upper right in the sub-plots denotes the parameter space in which the Gaussian local oscillator waist radius is larger than 3 mm. For this region, G_{setup} was artificially set to 0 dB(m²). This figure considers a wavelength λ of 1064 nm.

for the capability of off-axis layouts. In combination with $G_{\text{RX}} \approx -10$ dB and the tracking threshold of 70 dB(Hz/m²), this leads to the magenta 45 dB(Hz/m²) limit line in fig. 2.68. However, it is a soft limit as it depends on the rather empirical limit given by the maximum LO and TX waist radius of 3 mm and it considers error-free pointing of the interferometers ($\alpha_{\text{TX}} = \alpha_{\text{RX}} = 0$).

For the sake of completeness, the four lower panels in fig. 2.69 show G_{setup} with the heterodyne efficiency of a circular photodiode instead of a single segment. These plots are obtained from a modified eq. (2.379), where Ψ_2 is replaced by Ψ_1 and α_{RoC} is set to zero. At higher misalignment angles, more regions are blank compared to the panels for the single segment in fig. 2.69, because the heterodyne efficiency of the circular photodiode falls off more quickly with misalignment than the efficiency of a single segment (cf. sec. 2.6.11 on heterodyne efficiency).

The on-axis layouts have the advantage that a common telescope can be used, which can enhance the light-collecting area and reduce the divergence of the TX beam. The telescope aperture radius r_{TAP} , which defines the light-collecting area, and the telescope magnification m_T (cf. row 29 in table 2.13) are assumed as *setup* parameters in the power budget. Moreover, the LO waist size $\omega_{0,\text{LO}}$ is a free parameter to be analyzed. The LO beam is used for the interference with the top hat beam, which has a radius of r_{TAP}/m_T at the recombination beamsplitter. In addition, one part of the LO beam is sent through the on-axis retro-reflector (cf. fig. 2.66), which may produce a magnification by m_{RR} , and through the telescope, which further magnifies the beam by m_T . The formed TX beam may be clipped by r_{TAP} , which would increase the far-field divergence of the TX beam and which would cause some power loss due to the clipping.

Similar to eq. (2.379), the on-axis layout figure of merit can be defined for the parameter optimization as

$$\begin{aligned}
 G_{\text{setup}}(\alpha_{\text{TX}}, \alpha_{\text{RX}}, \omega_{0,\text{LO}}, r_{\text{TAP}}, m_T) &:= \frac{G_{\text{ifo}}}{G_{\text{RX}}} = G_{\text{collect}} \cdot G_{\alpha_{\text{TX}}} \cdot \eta_{0,\text{seg}} \cdot G_{\alpha_{\text{RX}}} \\
 &= \frac{\pi r_{\text{TAP}}^2 \cdot (1 - e^{-r_{\text{TAP}}^2/(\omega_{0,\text{LO}} m_T m_{\text{RR}})^2})^2}{\theta_{\text{TX,ncg}}^2} \cdot e^{-2 \frac{\alpha_{\text{TX}}^2}{\theta_{\text{TX,div}}^2}} \cdot \frac{2\omega_{0,\text{LO}}^2 \tanh\left(r_{\text{IAP}}^2/(2\omega_{0,\text{LO}}^2)\right)}{r_{\text{IAP}}^2} \\
 &\quad \cdot e^{-\frac{2(m_T \alpha_{\text{RX}} + \alpha_{\text{RoC}})^2}{\theta_{\text{LO}}^2 \cdot \Psi_2^2}} \tag{2.380}
 \end{aligned}$$

$$\begin{aligned}
 &= \underbrace{\frac{\pi^3 r_{\text{TAP}}^2 \cdot \omega_{0,\text{LO}}^2 m_T^2 \cdot (1 - e^{-1/\zeta^2})^2}{\lambda^2}}_{=G_{\text{collect}}} \cdot \underbrace{e^{-2 \left(\frac{\alpha_{\text{TX}} \cdot \pi \cdot \omega_{0,\text{LO}} \cdot m_T \cdot \Psi_1(\zeta_2)}{\lambda} \right)^2}}_{=G_{\alpha_{\text{TX}}}} \\
 &\quad \cdot \underbrace{2\zeta^2 \tanh\left(1/(2\zeta^2)\right)}_{\eta_{0,\text{seg}}} \cdot \underbrace{e^{-\frac{2(m_T \alpha_{\text{RX}} + \alpha_{\text{RoC}})^2 \cdot \pi^2 \cdot \omega_{0,\text{LO}}^2}{\lambda^2 \cdot \Psi_2(\zeta)^2}}}_{G_{\alpha_{\text{RX}}}}. \tag{2.381}
 \end{aligned}$$

For the sake of simplicity, the on-axis retro-reflector is assumed to maintain the beam mode, i.e. $m_{\text{RR}} = 1$. Hence, the zeta parameters $\zeta = \omega_{0,\text{LO}}/r_{\text{IAP}} = m_T \cdot \omega_{0,\text{LO}}/r_{\text{TAP}}$ and $\zeta_2 = m_{\text{RR}} \cdot m_T \cdot \omega_{0,\text{LO}}/r_{\text{TAP}}$ are equal. However, the zeta parameters have a different meaning, i.e. $\Psi_2(\zeta)$ is used to compute the heterodyne efficiency of a photodiode segment, while ζ_2 is the clipping parameter at the telescope and used in combination with $\Psi_1(\zeta_2)$ to calculate the beam divergence $\theta_{\text{TX,div}}$ of the clipped Gaussian beam (cf. appendix F). The non-clipped Gaussian beam divergence is $\theta_{\text{TX,ncg}} = \lambda/(\pi \cdot m_{\text{RR}} \cdot m_T \cdot \omega_{0,\text{LO}})$.

The G_{collect} factor in eq. (2.381) contains the expression $(1 - e^{-1/\zeta^2})^2$, which accounts for the rejected light power at the telescope due to clipping. In addition, is noted that the phasefront tilt at the photodiodes α_{RX} is magnified by m_T due to the telescope as apparent from the last term $G_{\alpha_{\text{RX}}}$ in eq. (2.381).

Numerical values of G_{setup} for a potential NGGM on-axis design with a convenient LO waist radius of $\omega_{0,\text{LO}} = 1$ mm are shown in fig. 2.70. The selected 20 mm diameter telescope

with a magnification of $m_T = 4$ yields a flat top beam radius of 2.5 mm on the optical bench. This flat top beam is imaged onto the photodiodes with 0.5 mm radius by the beam compressor with a de-magnification factor of 5 (cf. row 53 in table 2.14). The upper-left panel of fig. 2.70 indicates a magnitude of $G_{\text{setup}} \approx 41 \text{ dB(m}^2\text{)}$ for non-misaligned S/C with the selected NGGM on-axis parameters, which is approx. 10 dB higher than in the off-axis layout. With a larger telescope, the value can be increased to 80 dB(m²), for example, required for LISA-like missions.

However, the on-axis gain in the effective power is accompanied by a faster decay of the power with S/C misalignment, i.e. stricter pointing requirements. The selected parameters for the NGGM on-axis layout are optimal for a misalignment of approx. 80 μrad , which complies with the accuracy of the acquisition sensor and with the co-alignment accuracy of a compact on-axis retro-reflector.

The parameter space with $\zeta = \zeta_2 > 2.0$ or $\zeta = \zeta_2 < 2.0$ is excluded from the plots, because the functions Ψ_1 and Ψ_2 have been computed only within these ranges. In addition, white areas show undesired areas with $G_{\alpha_{\text{RX}}} < 0.13$ or with $G_{\alpha_{\text{TX}}} < 0.13$.

The parameters selected here should not be considered as a final decision, but as a starting point for further discussion. Further analysis is desirable, for example, related to a possible change in the TX beam mode via a magnification in the retro-reflector $m_{\text{RR}} \neq 1$. Furthermore, it is stressed that the on-axis layout proposed in this thesis can also be used without a telescope. This might be appealing, because the co-alignment of RX and TX field can be verified more easily in on-axis concepts, where the beams are not separated by a large amount. Moreover, the footprint of the interferometer in the S/C can be made smaller, since only a single baffle is required.

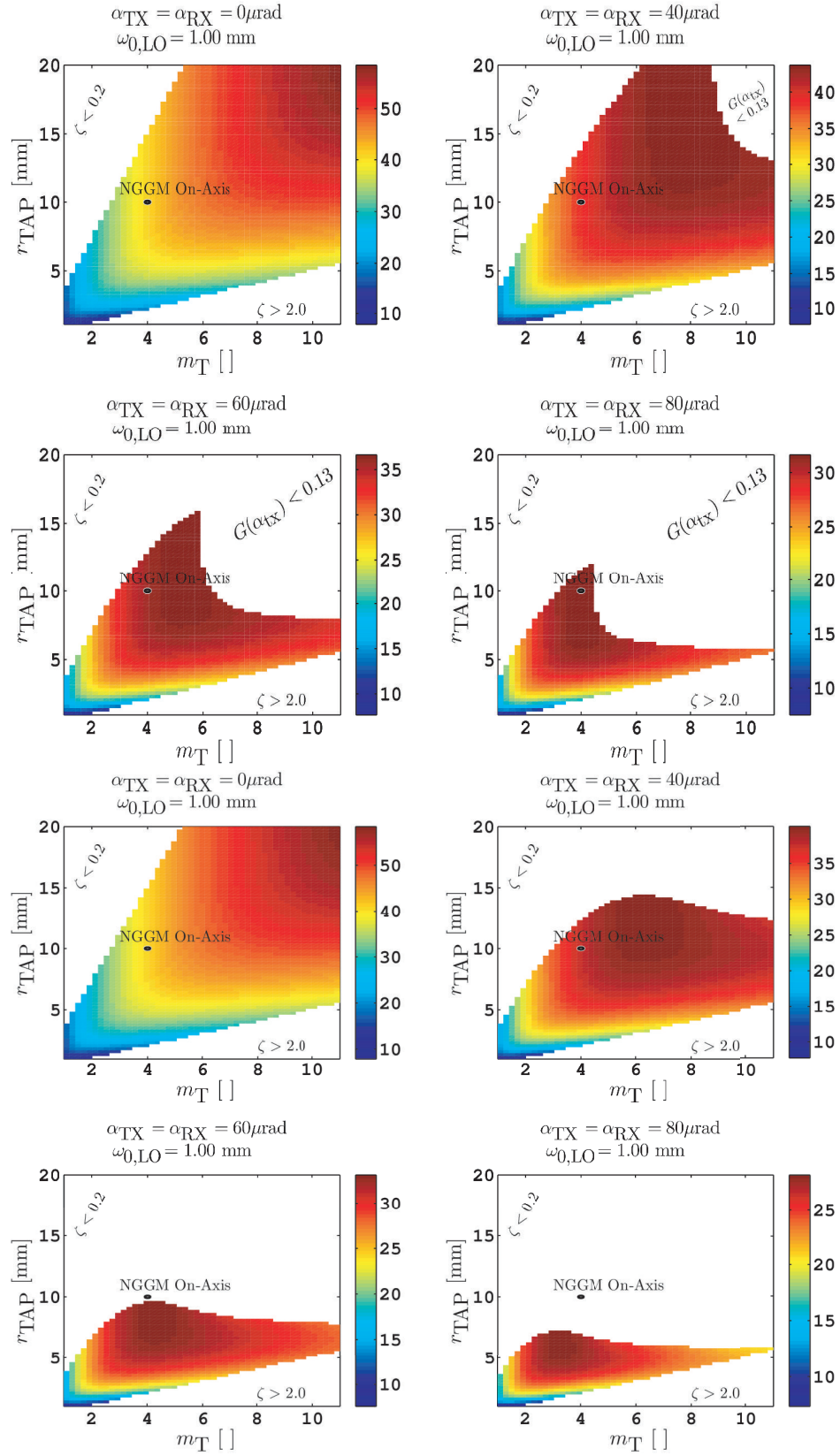


Figure 2.70: G_{setup} is shown for the on-axis layout with $\omega_{0,LO} = 1 \text{ mm}$ based on the heterodyne efficiency of a **single photodiode segment** (upper four panels) and of a **circular photodiode** (lower four panels). The color function is defined as $10 \cdot \log_{10}(G_{\text{setup}})$, i.e. units of $\text{dB}(\text{m}^2)$. Please note that the colorbar is different for all sub-plots. White areas denote parameter regions with $\zeta > 2$, $\zeta < 0.2$, $G_{\alpha_{TX}} < 0.13$ or $G_{\alpha_{RX}} < 0.13$. This figure considers a wavelength λ of 1064 nm .

2.9 Summary & Conclusion

The second part of this thesis (chapter 2) discussed design considerations for laser interferometry aboard current and potential future gravimetric satellite missions. Laser interferometers in this context are used to measure distance variations between the satellites. This chapter started with a brief introduction to relativity (sec. 2.1), because one aspect of this thesis was to derive a relativistically correct description of the phase-derived range measurement. These relativistic effects need to be characterized and understood, since one might want to remove them in post-processing to obtain the instantaneous geometrical distance between the satellites, which is often used in gravity field recovery. In addition, these effects need to be considered in the forward-modeling, where one aims to simulate realistic phase observations.

The introductory part included a description of phase-tracking and the interferometric signals such as the longitudinal phase, which contains the ranging information, the differential wavefront sensing (DWS) signals and the differential power sensing (DPS) signals (cf. sec. 2.2). The relation between the photocurrent and the light fields was formulated taking into account the vectorial nature of electro-magnetic waves (cf. eq. (2.56)), which is not commonly found in the literature to the knowledge of the author. This enables one to simulate and evaluate precisely polarization effects in laser interferometers, which immediately suggests an extension of the work performed by Meshksar [2015] with the more precise equations.

In section 2.3, various subsystems of typical laser interferometers were addressed such as laser sources, photodiodes and frequency standards for the optical and electrical domains. The two most prominent optical frequency standards are based on the macroscopic mechanical stability of optical cavities, and on the energy transition levels of atoms, e.g. so-called iodine cells. It was pointed out that both standards achieve approximately the same stability but differ in accuracy. For example, cavities show a poor accuracy, because they can stabilize light at various absolute frequencies, i.e. resonances occur at equidistantly separated frequencies. On the one hand, this is beneficial, since a cavity can be used at different frequencies and wavelengths, but on the other hand, the absolute frequency needs to be deduced by other means.

It was attempted to provide an overview on the state-of-the-art technology of interferometer subsystems available for space missions together with the key figures such as noise levels. Variations of some systems were also addressed, for example, on-axis retro-reflectors as alternative to corner-cubes in section 2.3.5. Mathematical models were provided where applicable for the subsystems, e.g. for the phase obtained by a phasemeter, for the photocurrent from photoreceivers or for the signal strength. In addition, it was briefly mentioned (cf. sec. 2.3.4) that a single frequency standard serving after conversion at optical and electrical frequencies would be beneficial, since it could tie GNSS, laser ranging, time stamping and eventual microwave measurements to a single frequency source. However, this requires the use of a complex frequency comb, which is likely beyond the scope of the next generation of gravimetric missions.

To cope with the complexity and variety of different laser interferometers, their description and modeling was divided into a description of the functional concepts (cf. sec. 2.4), into effects arising from the light propagation between satellites (cf. sec. 2.5), and into contributions from the optical layout and implementation (cf. sec. 2.6f.). The discussion of functional concepts encompassed one-way ranging, dual one-way ranging, transponder-based ranging and briefly ranging based on passive retro-reflectors. Mathematical descriptions of the phase observables were derived under consideration of the subsystems' transfer functions and relativistic effects. These effects manifest in gravimetric missions as a variation of the proper time, which influences the phase of the laser light and the time-stamping of phase samples, and as a variation of the propagation time of light between the satellites, which was discussed in section 2.5.2 and 2.5.3. It turned out that a precise description of the phase observable is best accomplished through a description of the phase in terms of the propagation time between events, which differs from the typical domain of optical pathlengths utilized in

non-relativistic optical simulations.

The different terms in the analytical expressions for the phase observables in section 2.4 were visualized with the help of spectral densities. These plots include traces for the effects of USO timing errors, transfer functions of phasemeter and photoreceiver, laser frequency noise and relativistic phase modulations, among others. In addition, the plots allow the magnitude of these effects to be compared with the expected ranging signal from the gravity field. As laser interferometry and interferometry by means of microwaves show similarities, it was appropriate to provide a comparison of both technologies in section 2.4.3 on dual one-way ranging. Furthermore, it should be mentioned that the mathematical description in section 2.4 and 2.5 yields the recipe for the conversion of the phase measurement aboard the satellites to the instantaneous geometrical distance between the satellites in GRACE Follow-On and future missions.

With regard to this conversion, it turned out that the knowledge of the absolute laser frequency or wavelength is likely a limiting quantity in future gravimetric missions. In interferometers with cavity-based frequency standards, the absolute frequency of the laser needs to be deduced from the setpoint of the laser, which limits the fractional accuracy of the wavelength to an approximate magnitude of 1 ppm. Thus, this uncertainty yields an effective noise with a 1 ppm magnitude relative to the actual ranging signal. One option to circumvent this issue is to fit this scale factor in the process of gravity field recovery, but the more desirable approach is to achieve a better a-priori knowledge on the wavelength and frequency. This can be accomplished through an absolute frequency standard such as one based on an iodine cell.

Subsequently in section 2.4.8, a comparison of the transponder and the dual one-way ranging (DOWR) scheme was provided, which also summarized the relevant functional concepts. It was pointed out that a DOWR approach with an absolute frequency standard could be beneficial for future gravimetric missions, since it would improve the scale factor and reduce one of the major noise sources in laser ranging interferometry, the laser frequency noise, by a factor of $\sqrt{2}$. Furthermore, this would simplify the acquisition phase of laser interferometers, since the differential frequency between the lasers would be fixed. However, the DOWR approach would require more frequency shifting components in the interferometer back-end to obtain beatnote frequencies of correct magnitude, whereby the required changes in the optical layouts are expected to be marginal. In addition, it was stressed that the transponder scheme, which is a well-established and mature technique used within the LISA development and GRACE Follow-On mission could still be applied as fallback option to add (more) redundancy, e.g. in case of failure of one optical frequency standard.

Section 2.5 treated apparent variations of the range measurement due to the inter-satellite propagation of light, which included effects from special relativity, general relativity, ionosphere and (neutral) atmosphere. The relativistic effects on the phase measurements can be reduced with the formulas presented here, so that the instantaneous geometrical distance between the satellites is obtained. The ionospheric effects are uncritical in optical laser interferometry due to the reciprocal scaling of these disturbances with the radiation frequency. The atmospheric effects, which arise due to the deviation of the refractive index from unity in a low Earth-orbit, are also uncritical for gravimetric mission with an approximate height of 400 km. It should be mentioned that the Faraday effect, which causes the polarization of light to rotate in a magnetic field, such as the geomagnetic field, was not assessed in this thesis, but may be worth to analyze in future work.

In section 2.6, some principles of the interferometer design were discussed: the attitude-to-ranging coupling, which is typically the second major error contributor in satellite laser interferometry, and the carrier-to-noise density of interferometers, which describes loosely speaking the signal-to-noise ratio of the measurement and needs to exceed a tracking threshold. The attitude-to-ranging coupling (cf. sec. 2.6.3f.) was described with the help of reference points, which express the coupling factors in terms of an equivalent geometrical offset of the pivot point of rotations or the center of mass from the fiducial of the range measurement. It

was pointed out that one can not describe the complete coupling with reference points and extensions such as the points of minimal coupling (cf. appendix E) have been introduced. However, the approximation with reference points is sufficient for design studies and for a comparison of different optical layouts as conducted here.

The carrier-to-noise density of a phase measurement aboard a S/C depends on the noise of the phase readout system (cf. sec. 2.6.9), on the amount of the received light, which is influenced by the TX beam misalignment (cf. sec. 2.6.10), and on the receiver S/C misalignment (cf. sec. 2.6.11). Although a general analytical closed-form solution for the carrier-to-noise density is not achievable, approximative expressions were obtained, which account for effects such as a differential phasefront curvature between the interfering light fields or the photodiode size. The analytical models eased the subsequent parametric studies and the derivation of power budgets for the laser links.

A further aspect, the laser link acquisition, was briefly covered in section 2.6.12, which is a complex procedure in GRACE Follow-On. Future missions could use dedicated acquisition sensors to reduce the complexity, which have been analyzed regarding their accuracy and signal-to-noise ratio in this thesis.

A short survey of optical layouts was given in section 2.7. The layouts have been categorized into on-axis and off-axis types with the help of reference points. The GRACE Follow-On LRI is the prototype of an off-axis interferometer. It is a mature design utilizing corner-cube retro-reflectors. It shows various advantages such as an automatic beam alignment, which maximizes the local carrier-to-noise density and ensure correct pointing of the TX beam, which in turn maximizes the optical power at the distant S/C. In addition, the layout discriminates pathlength fluctuations outside of the racetrack in the final phase observable. On-axis interferometers (cf. sec. 2.7.1) have been suggested in literature and allow to use a single telescope in the RX and TX beam path, which enhances the light collecting area and decreases the TX beam far-field divergence for the detriment of stricter pointing requirements. Various optical layouts have been assessed regarding their complexity, advantages and disadvantages in section 2.7.3. Based on this assessment, an on-axis and an off-axis optical layout have been suggested in section 2.7.4 for application in potential future gravimetric missions. The proposed off-axis design includes minor modifications in comparison to the GRACE Follow-On LRI such as a smaller corner-cube retro-reflector and a dedicated acquisition sensor. The on-axis design has been derived from the well-studied off-axis layout by replacing the corner-cube with an on-axis retro-reflector. This preserves the advantages such as beam steering and, in addition, it allows a telescope to be implemented in the interferometer, if required.

The last section 2.8 analyzed the carrier-to-noise density of the proposed optical layouts with the help of power budgets. A power budget of a laser link allows one to assess the feasibility of a particular interferometer design as the budget takes into account the available laser power, the satellite separation, pointing errors and so forth. Such a budget is also used within the GRACE Follow-On LRI project and the learned lessons were incorporated into the budgets shown here, so that they provide a good starting point for the development of future ranging instruments. The exemplary budgets of the proposed on-axis and off-axis design were compared in sec. 2.8.3 and the parameter space, where telescope-free designs are feasible, was derived. In addition, the functional relations present in the budgets were extracted and it was shown how to perform a parametric study to derive optimal parameters for the beam mode, aperture size or telescope magnification (cf. sec. 2.8.4) of the interferometer. These values might need to be refined in later stages of the design, if further constraints or requirements become apparent. However, with the presented formalism this should be straightforward.

Although various aspects of the interferometer design were addressed in this thesis, it is by far not a complete description. The description of various further error and potential noise contributors was beyond the scope of this work, which includes among others: ghost beams in the interferometer, effects arising from the non-Gaussian beam mode in local interferometry and in the far-field phase, supply voltage fluctuations, temperature induced errors, the

Faraday effect and the parasitic Sagnac effect. However, the most important errors, which are sufficient for the conceptual design of interferometers, have been addressed in this thesis.

Appendix A

NGGM Drag Compensation: Accelerometer Saturation and Propellant

The technical note presented in this section was initially written during the e.motion² study under *NGGM-AEI-TN-004-V2* in February 2014. It was revised and slightly adopted for this thesis. The aim is to analyze GRACE Level-1B accelerometer data to assess eventual occurrences of accelerometer saturation in a potential e.motion² accelerometer. In addition, the propellant consumption for a drag-compensation or drag-free concept is estimated. The analysis is restricted to linear accelerations.

A.1 Accelerometer

The current e.motion² baseline assumes a GOCE-like servo-accelerometer with a sensitivity of $4 \cdot 10^{-11} \text{ m}/(\text{s}^2\sqrt{\text{Hz}})$ in the sensitive along-track and radial direction and a less-sensitive cross-track axis with a noise of $4 \cdot 10^{-10} \text{ m}/(\text{s}^2\sqrt{\text{Hz}})$. The GOCE pre-launch design sensitivity is approximately one order of magnitude better [Alenia-Team, 2008, p. 101], whereby the actual in-orbit performance is at $1 \cdot 10^{-11} \text{ m}/(\text{s}^2\sqrt{\text{Hz}})$ for the ultra-sensitive axis [Stummer, 2013, p. 83]. The dynamic range of the measurement is assumed here to be $\pm 4 \cdot 10^{-6} \text{ m/s}^2$ or $8 \cdot 10^{-6} \text{ m/s}^2$ as peak-to-peak value, which is of the same order as the GOCE accelerometer with $\pm 6 \cdot 10^{-6} \text{ m/s}^2$ [Visser, 2009].

A.2 GRACE Level 1B data

To assess the magnitude of non-gravitational accelerations the Level-1B data of the GRACE-A and GRACE-B accelerometer was analyzed for an 11-year period, i.e. from 7th April 2002 to 7th April 2013. For each day, the mean, the maximum and the minimum acceleration along the three axes was computed from the 1 Hz data. Data samples with reduced quality were omitted, i.e. with a non-zero quality flag. This flag is set upon interpolation of missing samples or upon abnormal proof mass bias voltage. The data has been corrected for scale factors and biases according to [Bettadpur, 2009], whereby one should note that these corrections are only accurate for data before the 31st of March 2009, since the corrections were obtained by a fit with data until this date. The results are shown in fig. A.1 and fig. A.2. One notices that the variations of non-gravitational accelerations for time scales smaller than one day, which are given by the difference between maximum and minimum value, are small compared to the assumed accelerometer dynamic range, especially in the relevant along-track direction. Since the atmospheric density and, hence, the air drag are influenced by the solar and geomagnetic activity, one can explain the *quiet* along-track period between day 1500 and 3000 in fig. A.3 with a low solar activity.

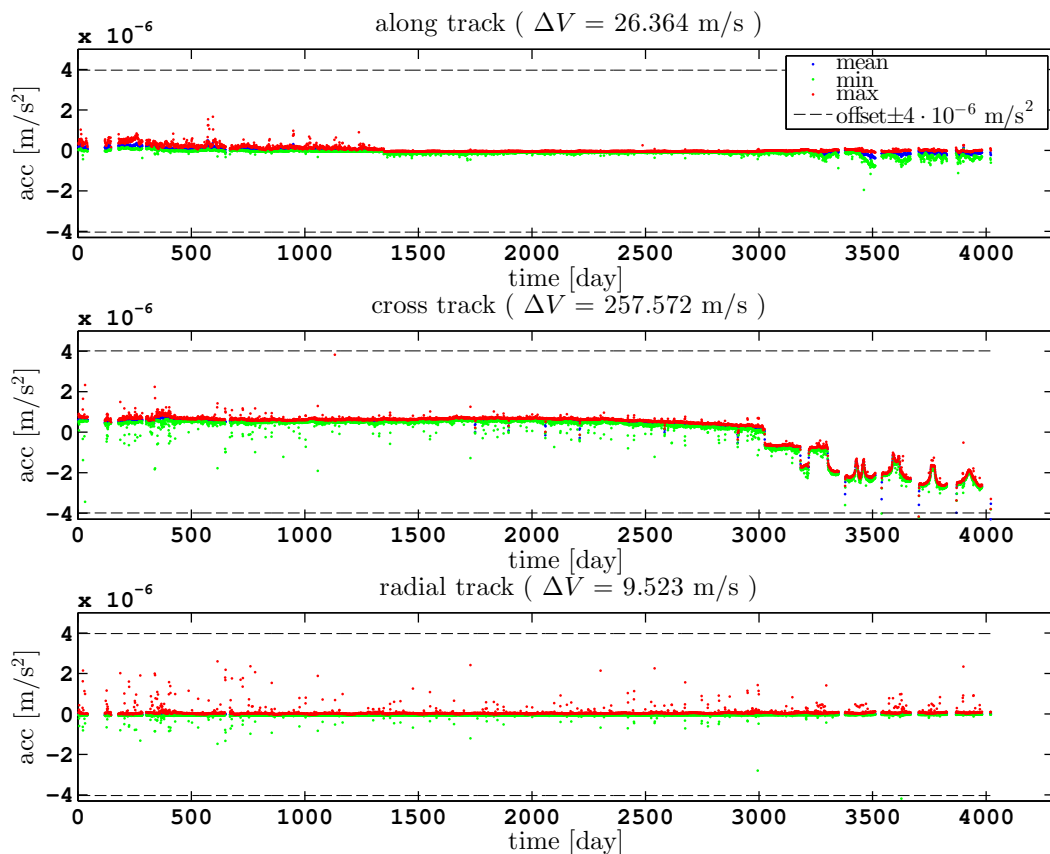


Figure A.1: GRACE-A accelerometer data is shown for a period of 11 years. The x-axes start at 7th April 2002. The dashed horizontal lines indicate the biased dynamic range of the e.motion² accelerometer.

A small step at day 1350 (December 2005) is visible in the along track direction, which is due to a swapping maneuver of the satellites. Since the satellites rotated by 180 degree along the radial (yaw) direction, the sign of the air drag changed.

The steps and jumps visible after 3000 days, in particular in the cross-track direction, are partly caused by changes in the spacecraft temperature control and accelerometer turn-off periods imposed by the reduced battery capacity¹.

The cross-track direction is the less sensitive axis of the accelerometer [Case *et al.*, 2010]. Most of the spikes in the radial and cross-track direction are assumed to be caused by high-frequency perturbations on the spacecraft, e.g. by twangs [Peterseim, 2014], by electric current fluctuations induced by heater switching or by thruster activation. For the e.motion² study, it is assumed that these disturbances can be significantly reduced by design.

The GRACE orbit height decreased from 500 km in 2002 to approx. 450 km in 2013. An increased drag due to orbital decay could not be observed in the accelerometer data in this analysis. However, for e.motion², with an orbit height between 420 km and 430 km an increased atmospheric density should be considered. According to [Montenbruck & Gill, 2000], the average atmospheric density is approx. 2 times higher in 420 km than in 460 km for mean solar activity. An additional safety factor of 3 is assumed, and that all non-gravitational accelerations in the along-track direction scale with orbit height, which yields fig. A.4. The radial and cross-track components of the GRACE Level-1B data are dominated by perturbations and not by typical non-gravitational surface forces such as air drag, solar radiation pressure and Earth's albedo [Frommknecht, 2008]. These components are considered to be less susceptible to accelerometer saturation.

Based on fig. A.4, one can state that an e.motion² accelerometer will not saturate, even

¹private communication, Jakob Flury, Institut für Erdmessung, Universität Hannover, January 2012

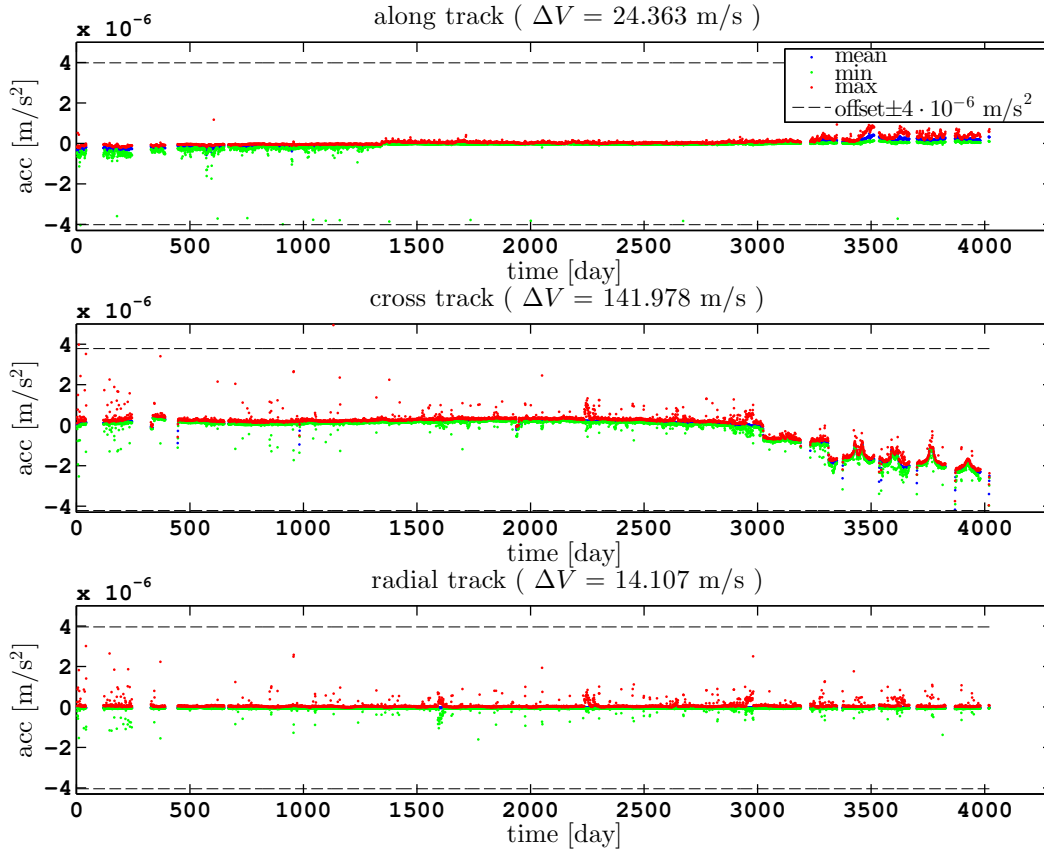


Figure A.2: GRACE-B accelerometer data is shown for a period of 11 years. The x-axes start at 7th April 2002. The dashed horizontal lines indicate the biased dynamic range of the e.motion² accelerometer. Some very few points are outside of the plot axes and were omitted.

if a constant thrust is used for drag-compensation over 11 years, except for some very short periods, e.g. at day 595 with strong solar flares (cf. fig. A.3).

A.3 Propellant

The absolute mean acceleration in along-track direction for the GRACE-A data in fig. A.1 is $8.2 \cdot 10^{-8} \text{ m/s}^2$, which results for a period of 3694 days (10.5 years)² in a total ΔV of

$$\Delta V = 26 \text{ m/s.}$$

These values are in good agreement with modeled values considering air drag, solar radiation pressure and Earth's albedo [Frommknecht, 2008]. Models for the GRACE non-gravitational accelerations in along-track direction provide accelerations of the order of $1 \cdot 10^{-7} \text{ m/s}^2$, which corresponds to approximately $50 \mu\text{N}$ for a satellite with 500 kg mass and a total ΔV of 35 m/s for the 10.5 year period.

To compensate for these forces, approximately 30 kg propellant with a specific impulse of 60 s is required. However, one should be aware of the fact that the solar cycle 24 (starting March 2008) was very weak and that the air drag was very low for the GRACE satellites. Assuming a scaling factor of 6 for e.motion² due to the lower altitude and increased solar activity, the required propellant mass is of the order of 150 kg to 200 kg for a satellite of 500 kg mass.

²3694 days is the number of valid daily samples, while most plots in this document show 4021 days, which is the day number after 7th April 2002.

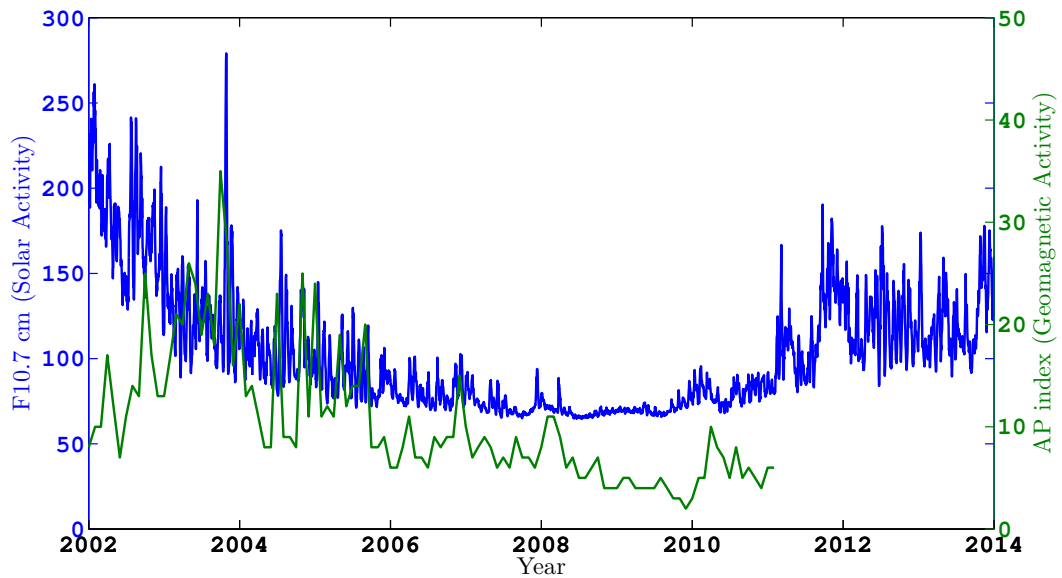


Figure A.3: The solar and geomagnetic activity is shown, which is based on data from NGDC Space Weather Website (<ftp://ftp.ngdc.noaa.gov>). The x-axis starts at 7th April 2002.

A.4 Summary

This analysis showed that accelerometer saturation will most likely not appear for an altitude between 420 km and 430 km, even if drag compensation is dismissed at all. However, to avoid orbital decay and to maintain the orbit repeat cycles, drag compensation is required. A simple feed-forward control with almost fixed thrust seems sufficient. An AOCS drag compensation within the measurement band and accelerometer feedback is not necessary with regard to accelerometer saturation.

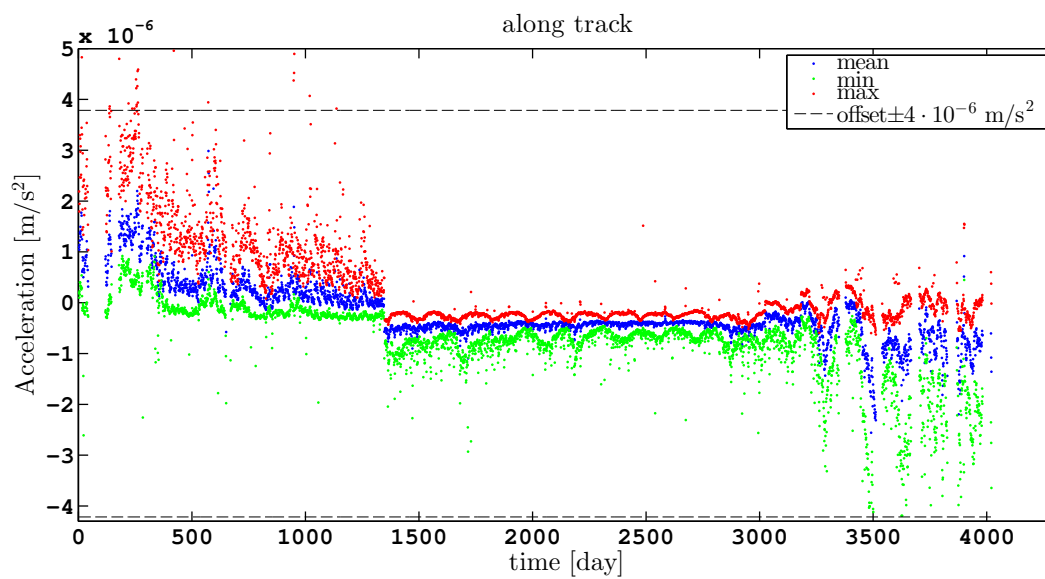


Figure A.4: The minimum, maximum and mean non-gravitational accelerations for 420 km orbit height are shown, which apply for a potential e.motion² mission. These values are derived by rescaling the upper plot in fig. A.1 with a factor of 6. The dashed horizontal lines indicate the biased dynamic range of the e.motion² accelerometer. The bias is removed by drag compensation in e.motion². The x-axis starts at 7th April 2002.

Appendix B

Relativistic Quantities

Throughout this thesis the sign convention $\eta_{\alpha\beta} = \text{diag}(-1, +1, +1, +1)$ is employed as used by [Kopeikin *et al.*, 2011]. The Greek indices such as α and β range from 0..3, while Latin letters like m and n denote spatial components and range from 1..3. In this section c_0 denotes the proper speed of light in vacuum with a numerical value of 299 792 458 m/s, whereby the coordinate speed of light is c_n . Furthermore, the Euclidean norm is used for three dimensional spatial vectors showing a vector arrow, e.g. \vec{r} .

The metric tensor $g_{\alpha\beta}$ of the Earth in the GCRS is approximated by a Post-Newtonian expansion as [Turyshev *et al.*, 2014] [Soffel & Langhans, 2012, p.54]

$$g_{\alpha\beta} = \eta_{\alpha\beta} + h_{\alpha\beta}, \quad (\text{B.1})$$

with

$$h_{00} = \frac{2W}{c_0^2} - \frac{2W^2}{c_0^4} + \mathcal{O}(c_0^{-6}) \quad (\text{B.2})$$

$$h_{0m} = h_{m0} = -\frac{4V^m}{c_0^3} + \mathcal{O}(c_0^{-5}) \quad (\text{B.3})$$

$$h_{mm} = \frac{2W}{c_0^2} + \mathcal{O}(c_0^{-4}) \quad (\text{B.4})$$

where W is Earth's scalar gravitational potential (cf. eq. (1.1), $W=U$) and $\vec{V} = V^m$ is a vector potential accounting for Earth's spin moment, which also curves space-time. Tidal contributions from other celestial bodies are not considered here.

Let us denote coordinates in the co-rotating geocentric frame (ITRF) with

$$\tilde{x}^\alpha = (c_0 \cdot T, X, Y, Z) = (c_0 \cdot T, \vec{\tilde{x}}) = (\tilde{x}^0, \tilde{x}^1, \tilde{x}^2, \tilde{x}^3)^\top, \quad (\text{B.5})$$

and in the GCRS as

$$x^\alpha = (c_0 \cdot t, x, y, z) = (c_0 \cdot t, \vec{r}) = (x^0, x^1, x^2, x^3)^\top, \quad (\text{B.6})$$

where the common four-vector notation from relativity is used. The relation between both frames is considered to be given by

$$c_0 \cdot T = c_0 \cdot t, \quad \vec{\tilde{x}} = \hat{R}_z(\omega_e \cdot t) \cdot \vec{r}, \quad (\text{B.7})$$

where ω_e is a constant angular velocity of Earth's rotation. The rotation matrix $\hat{R}_z(\omega_e \cdot t) = \hat{R}(t)$ is the 3-d rotation matrix around the z -axis transforming a vector from GCRS to ITRF frame in a simplified way. Proper conversions between both frames are described in the IERS conventions [Petit *et al.*, 2010] and include corrections due to precession, nutation and polar motion.

In Earth's co-rotating frame, the gravitational potential W is considered time-independent, while all partial derivatives can be written as

$$\frac{\partial W}{\partial T} = 0, \quad \frac{\partial W}{\partial X} = \tilde{a}_x, \quad \frac{\partial W}{\partial Y} = \tilde{a}_y, \quad \frac{\partial W}{\partial Z} = \tilde{a}_z, \quad (\text{B.8})$$

where the gravitational acceleration vector $\vec{a} = (\tilde{a}_x, \tilde{a}_y, \tilde{a}_z)^\top$ in the ITRF frame can be computed from the spherical harmonic expansion of Earth's gravity field.

The partial derivative with respect to the coordinate time t of the GCRS can be computed as

$$\frac{\partial W}{\partial t} = \underbrace{\frac{\partial W}{\partial T}}_{=0} \frac{\partial T}{\partial t} + \underbrace{\frac{\partial W}{\partial X}}_{\tilde{a}_x} \frac{\partial X}{\partial t} + \underbrace{\frac{\partial W}{\partial Y}}_{\tilde{a}_y} \frac{\partial Y}{\partial t} + \underbrace{\frac{\partial W}{\partial Z}}_{\tilde{a}_z} \frac{\partial Z}{\partial t} \quad (\text{B.9})$$

$$= \vec{a}^\top \cdot \frac{\partial \vec{x}}{\partial t} = \vec{a}^\top \cdot \left(\frac{\partial \hat{R}}{\partial t} \cdot \vec{r} + \hat{R}(t) \cdot \underbrace{\frac{\partial \vec{r}}{\partial t}}_{=0} \right) \quad (\text{B.10})$$

$$= \vec{a}^\top \cdot \underbrace{\hat{R}^\top \cdot \frac{\partial \hat{R}}{\partial t}}_{-\vec{\omega} \times} \cdot \vec{r} \quad (\text{B.11})$$

$$= -\vec{a}^\top \cdot (\vec{\omega} \times \vec{r}) = w_e \cdot y \cdot a_x - w_e \cdot x \cdot a_y, \quad (\text{B.12})$$

where the rotated acceleration $\vec{a} = (a_x, a_y, a_z)^\top = \hat{R}^\top \cdot \vec{\tilde{a}}$ and the angular velocity vector of Earth's rotation $\vec{\omega} = (0, 0, \omega_e)^\top$ were introduced. The vector \vec{a} is the coordinate acceleration in the GCRS system, which can be used to numerically integrate satellite orbits, while $\vec{\tilde{a}}$ is the acceleration vector in the ITRF system. This follows from the spatial partial derivatives:

$$\frac{\partial W}{\partial x^m} = \underbrace{\frac{\partial W}{\partial T}}_{=0} \frac{\partial T}{\partial x^m} + \underbrace{\frac{\partial W}{\partial X}}_{\tilde{a}_x} \frac{\partial X}{\partial x^m} + \underbrace{\frac{\partial W}{\partial Y}}_{\tilde{a}_y} \frac{\partial Y}{\partial x^m} + \underbrace{\frac{\partial W}{\partial Z}}_{\tilde{a}_z} \frac{\partial Z}{\partial x^m} \quad (\text{B.13})$$

$$= \vec{a}^\top \cdot \underbrace{\frac{\partial \vec{x}}{\partial x^m}}_{=\hat{R}} \quad (\text{B.14})$$

$$\vec{\nabla} W = \vec{a}^\top \cdot \hat{R} = \vec{a}^\top. \quad (\text{B.15})$$

The vector potential \vec{V} , which is present in the metric tensor, is usually approximated as [Turyshev *et al.*, 2014, eq. 5]

$$\vec{V}(t, \vec{r}) \approx \frac{GM}{2 \cdot |\vec{r}|^3} \cdot \vec{S} \times \vec{r} + \mathcal{O}(x^{-4}, c^{-2}), \quad (\text{B.16})$$

with Earth's spin moment \vec{S} , i.e. angular momentum per unit of mass, given in a good approximation by the angular momentum of a sphere:

$$\vec{S} \approx \frac{2}{5} \cdot R_e^2 \cdot \omega_e \cdot \begin{pmatrix} 0 \\ 0 \\ 1 \end{pmatrix} \approx 1.18 \cdot 10^9 \text{ m}^2/\text{s} \cdot \begin{pmatrix} 0 \\ 0 \\ 1 \end{pmatrix} \quad (\text{B.17})$$

where $R_e \approx 6378 \text{ km}$ is Earth's radius and $\omega_e \approx 7.29 \cdot 10^{-5} \text{ rad/s}$ is Earth's angular rate. A more precise value for the moment is $|\vec{S}| \approx 9.80 \cdot 10^8 \text{ m}^2/\text{s}$ [Petit *et al.*, 2010, p. 156], which follows from Earth's moments of inertia. In some succeeding equations, the abbreviation ξ is used as defined by

$$\vec{\xi} = \frac{GM}{2} \cdot \frac{2}{5} \cdot R_e^2 \cdot \begin{pmatrix} 0 \\ 0 \\ 1 \end{pmatrix}, \quad (\text{B.18})$$

which has the norm $\xi = |\vec{\xi}| = |\vec{S}|/\omega_e \cdot GM/2$.

The Christoffel symbols of second kind, which are required to formulate the equations of motion in the context of general relativity, are [Kopeikin *et al.*, 2011, eq. 3.34]

$$\Gamma^\mu_{\alpha\beta} = \frac{1}{2} \cdot g^{\mu\lambda} \cdot \left(\frac{\partial g_{\lambda\alpha}}{\partial x^\beta} + \frac{\partial g_{\lambda\beta}}{\partial x^\alpha} - \frac{\partial g_{\alpha\beta}}{\partial x^\lambda} \right), \quad (\text{B.19})$$

$$= \frac{1}{2} \cdot g^{\mu\lambda} \cdot \left(\frac{\partial h_{\lambda\alpha}}{\partial x^\beta} + \frac{\partial h_{\lambda\beta}}{\partial x^\alpha} - \frac{\partial h_{\alpha\beta}}{\partial x^\lambda} \right), \quad (\text{B.20})$$

where again the Einstein sum convention was utilized, i.e. the expression on the right hand side is summed over λ ranging from 0..3. The dual metric $g^{\mu\lambda}$ is the inverse of the metric tensor $g_{\mu\lambda}$. The partial derivatives of the metric tensor with respect to $(c_0 \cdot t, x, y, z)$ are required to compute the Christoffel symbols $\Gamma^\mu_{\alpha\beta}$, which can be written for the GCRS as

$$h_{00,t}^{(1)} = w_e \cdot y \cdot a_x - w_e \cdot x \cdot a_y \quad (\text{B.21})$$

$$h_{00,t}^{(2)} = 2 \cdot (w_e \cdot y \cdot a_x - w_e \cdot x \cdot a_y) \cdot W/c_0^2 \quad (\text{B.22})$$

$$\frac{\partial h_{\alpha\beta}}{\partial c_0 t} = 2/c_0^3 \cdot \begin{pmatrix} h_{00,t}^{(1)} + h_{00,t}^{(2)} & 0 & 0 & 0 \\ 0 & h_{00,t}^{(1)} & 0 & 0 \\ 0 & 0 & h_{00,t}^{(1)} & 0 \\ 0 & 0 & 0 & h_{00,t}^{(1)} \end{pmatrix}, \quad (\text{B.23})$$

$$\frac{\partial h_{\alpha\beta}}{\partial x} = 2/c_0^2 \cdot \begin{pmatrix} a_x - 2a_x \cdot W/c_0^2 & \frac{-6\omega_e \xi xy}{c_0 \cdot r^5} & \frac{-2\omega_e \xi \cdot (r^2 - 3x^2)}{c_0 \cdot r^5} & 0 \\ \frac{-6\omega_e \xi xy}{c_0 \cdot r^5} & a_x & 0 & 0 \\ \frac{-2\omega_e \xi \cdot (r^2 - 3x^2)}{c_0 \cdot r^5} & 0 & a_x & 0 \\ 0 & 0 & 0 & a_x \end{pmatrix}, \quad (\text{B.24})$$

$$\frac{\partial h_{\alpha\beta}}{\partial y} = 2/c_0^2 \cdot \begin{pmatrix} a_y - 2a_y \cdot W/c_0^2 & \frac{2\omega_e \xi \cdot (r^2 - 3y^2)}{c_0 \cdot r^5} & \frac{+6\omega_e \xi xy}{c_0 \cdot r^5} & 0 \\ \frac{2\omega_e \xi \cdot (r^2 - 3y^2)}{c_0 \cdot r^5} & a_y & 0 & 0 \\ \frac{+6\omega_e \xi xy}{c_0 \cdot r^5} & 0 & a_y & 0 \\ 0 & 0 & 0 & a_y \end{pmatrix}, \quad (\text{B.25})$$

$$\frac{\partial h_{\alpha\beta}}{\partial z} = 2/c_0^2 \cdot \begin{pmatrix} a_z - 2a_z \cdot W/c_0^2 & \frac{-6\omega_e \xi yz}{c_0 \cdot r^5} & \frac{+6\omega_e \xi xz}{c_0 \cdot r^5} & 0 \\ \frac{-6\omega_e \xi yz}{c_0 \cdot r^5} & a_z & 0 & 0 \\ \frac{+6\omega_e \xi xz}{c_0 \cdot r^5} & 0 & a_z & 0 \\ 0 & 0 & 0 & a_z \end{pmatrix}, \quad (\text{B.26})$$

where the abbreviation $r = |\vec{r}|$ was used. It is recalled that tidal accelerations from Sun and Moon were neglected here.

Finally, the geodesic equation describing the motion of a test particle, such as a photon or a satellite, reads in the GCRS as [Kopeikin *et al.*, 2011]

$$\ddot{x}^k = d^2 x^k / dt^2 = -\Gamma^\mu_{\alpha\beta} \cdot \dot{x}^\alpha \cdot \dot{x}^\beta + \frac{1}{c_0} \Gamma^0_{\alpha\beta} \cdot \dot{x}^\alpha \cdot \dot{x}^\beta \cdot \dot{x}^k, \quad (\text{B.27})$$

where k ranges from 1..3 and denotes the spatial components. \ddot{x}^0 is in fact zero, which can be used to validate the implementation. The equation is convenient for numerical integration and the expansion up to c_0^{-2} is given here:

$$\ddot{x} = a_x + c_0^{-2} \cdot (-3a_x v_x^2 - 8\omega_e \xi v_y / r^3 - 4a_y v_x v_y + a_x v_y^2 - 4a_z v_x v_z + a_x v_z^2 - 4a_x W + 12\omega_e \xi v_y (x^2 + y^2) / r^5 + 12\omega_e \xi v_z yz / r^5 + 3v_x \omega_e \cdot (a_y x - a_x y)) \quad (\text{B.28})$$

$$\ddot{y} = a_y + c_0^{-2} \cdot (8\omega_e \xi v_x / r^3 + a_y v_x^2 - 4a_x v_x v_y - 3a_y v_y^2 - 4a_z v_y v_z + a_y v_z^2 - 4a_y W - 12\omega_e \xi v_z xz / r^5 - 12\omega_e \xi v_x (x^2 + y^2) / r^5 + 3v_y \omega_e \cdot (+a_y x - a_x y)) \quad (\text{B.29})$$

$$\ddot{z} = a_z + c_0^{-2} \cdot (a_z v_x^2 + a_z v_y^2 - 4a_x v_x v_z - 4a_y v_y v_z - 3a_z v_z^2 - 4a_z W + 12\omega_e \xi v_y xz / r^5 - 12\omega_e \xi v_x yz / r^5 + 3v_z \omega_e \cdot (a_y x - a_x y)), \quad (\text{B.30})$$

which can be written in compact vector form as

$$\ddot{\vec{r}} = \vec{a} + \vec{a}_{\text{PPN}} \quad (\text{B.31})$$

$$= \vec{a} + \dot{\vec{r}} \cdot \frac{3 \cdot (\vec{a} \cdot (\vec{\omega} \times \vec{r}))}{c_0^2} \quad (\text{B.32})$$

$$+ \vec{a} \cdot \frac{(|\dot{\vec{r}}|^2 - 4 \cdot W)}{c_0^2} - \dot{\vec{r}} \cdot \frac{4 \cdot (\vec{a} \cdot \dot{\vec{r}})}{c_0^2} - (\vec{\xi} \times \dot{\vec{r}}) \cdot \frac{4\omega_e}{c_0^2 \cdot |\vec{r}|^3} - (\dot{\vec{r}} \times \vec{r}) \cdot \frac{12\omega_e \cdot (\vec{\xi} \cdot \vec{r})}{c_0^2 \cdot |\vec{r}|^5}. \quad (\text{B.33})$$

It is remarked that the here presented relativistic correction \vec{a}_{PPN} equals the formula from the IERS convention [Petit *et al.*, 2010, eq. (10.12)], if the acceleration \vec{a} in the relativistic correction \vec{a}_{PPN} is considered only for Earth's monopole gravity field and $\vec{\xi} = \vec{S}/\omega_e \cdot GM/2$ is used. Then, the first c_0^{-2} term vanishes in line (B.32), since $\vec{a} \parallel \vec{r}$. However, the here derived equations are more general and agree with the results given in [Zschocke, 2016, eq. (20)].

We wish now to derive the coordinate speed of light for vacuum c_n in the GCRS, which differs from the speed of light c_0 apparent in a local Lorentz frame. Therefore, we assume the following coordinate four velocity of the photon

$$\frac{dx^\alpha}{dt} = (c_0, \vec{d}_0 \cdot c_n)^\top, \quad (\text{B.34})$$

where \vec{d}_0 is the normalized propagation direction of the photon, \vec{r} is the 3-d position of the photon and t is the coordinate time in the GCRS. One might be tempted to write the coordinate speed of light as $c_n = c_0/n_{\text{gr}}$, where n_{gr} is an apparent refractive index in the GCRS, which is caused by the space-time curvature and slows down the photon.

The interval ds^2 of a world line of a massless particle vanishes (cf. sec. 2.1), i.e.

$$ds^2 = g_{\alpha\beta}(t, \vec{r}) \cdot dx^\alpha \cdot dx^\beta = 0. \quad (\text{B.35})$$

which yields a single equation to solve after dividing with dt^2 , i.e.

$$0 = g_{mn}(t, \vec{r}) \cdot dx^m/dt \cdot dx^n/dt \quad (\text{B.36})$$

$$= c_0^2 \cdot g_{00} + \vec{G} \cdot \vec{d}_0 \cdot c_n \cdot c_0 + c_n^2 \cdot g_m, \quad (\text{B.37})$$

where the post-Newtonian metric definition from eqs. (B.1)-(B.4) was used to rewrite $g_m = g_{11} = g_{22} = g_{33}$ and $\vec{G} = 2 \cdot (g_{01}, g_{02}, g_{03})^\top$. The quadratic equation can be solved and the solution with positive propagation velocity is taken:

$$c_n = c_0 \cdot \sqrt{\frac{1 - h_{00}}{1 + h_m} + \frac{(\vec{G} \cdot \vec{d}_0)^2}{4 \cdot (1 + h_m)^2}} - c_0 \cdot \frac{\vec{G} \cdot \vec{d}_0}{2 \cdot (1 + h_m)}, \quad (\text{B.38})$$

where the metric perturbation h_{mn} was inserted for the metric tensor g_{mn} according to eq. (B.1). In addition, one has $h_m = h_{11} = h_{22} = h_{33}$. The argument of the square-root is positive, since $\vec{G} = -8\vec{V}/c_0^3$, h_m and h_{00} are close to zero. Thus, the coordinate speed of light is always positive.

Appendix C

General Relativistic Delay of Light

In the context of general relativity, the light path is not a straight line, since light and photons follow a geodesic. This yields effects such as gravitational bending of light. Furthermore, the coordinate speed of light c_n of the GCRS differs from the proper speed of light c_0 . However, for light in a low Earth orbit, the difference between c_0 and c_n does not exceed 1 m/s. It is well known that the acceleration of light-like particles is twice the acceleration of slow ($\ll c_0$) objects: *Einstein predicted that the amount of light bending by the Sun is twice that given by a Newtonian theory of gravity* [Kopeikin *et al.*, 2011, Preface]. Thus, if light is sent between low Earth orbiters, the photons and the phasefronts are bended towards the geocenter with a constant acceleration of $2 \cdot GM/r^2$. The approximate deflection angle $\Delta\theta_{\text{gr}}$ can be easily determined as

$$\Delta\theta_{\text{gr}}(r, L) = \frac{2 \cdot GM/r^2 \cdot L/c_0}{c_0} = \frac{2 \cdot GM \cdot L}{r^2 \cdot (c_0)^2}, \quad (\text{C.1})$$

which is for a LEO application ($r = 6371 + 400$ km) with $L = 200$ km well below 0.1 nrad. This small value justifies the assumption that the light path \mathcal{P} in a gravimetric mission is nearly a straight line, which can be parameterized by a parameter $\lambda \in [0, 1]$:

$$\vec{r}_{\text{ph}}(\lambda) = \vec{r}_j' + (\vec{r}_i - \vec{r}_j') \cdot \lambda, \quad (\text{C.2})$$

where \vec{r}_j' denotes the position of the photon emission, i.e. the start position, and \vec{r}_i denotes the position of the light reception, i.e. the end position. The primes illustrate simply the event or position at an earlier time with respect to the reception instance. We wish to compute the propagation time Δt of a photon between start and end position. Therefore, one can utilize the line integral

$$\Delta t = \int_{\mathcal{P}} \frac{n(t, \vec{r}_{\text{ph}})}{c_n(t, \vec{r}_{\text{ph}})} ds, \quad (\text{C.3})$$

where n denotes the refractive index of the medium and c_n is the coordinate speed of light. The light propagation is assumed to be in vacuum ($n = 1$), which yields

$$\begin{aligned} \Delta t &= \int_{\mathcal{P}} c_n^{-1}(t, \vec{r}_{\text{ph}}) ds = \int_{\lambda=0}^1 c_n^{-1}(t, \vec{r}_{\text{ph}}) \cdot \left| \frac{d\vec{r}_{\text{ph}}}{d\lambda} \right| d\lambda \\ &= |\vec{r}_i - \vec{r}_j'| \cdot \int_{\lambda=0}^1 c_n^{-1}(t, \vec{r}_{\text{ph}}) d\lambda. \end{aligned} \quad (\text{C.4})$$

The coordinate speed of light from eq. (B.38) is recast in terms of the geopotential W and vector potential V accounting for Earth's angular momentum (cf. eq. (B.16))

$$c_n = \sqrt{\frac{c_0^6 - 2 \cdot c_0^2 \cdot W^2 + 4 \cdot W^3 + 16 \cdot (\vec{V} \cdot \vec{d}_0)^2}{(c_0^2 + 2 \cdot W)^2}} + \frac{4 \cdot \vec{V} \cdot \vec{d}_0}{c_0^2 + 2 \cdot W}, \quad (\text{C.5})$$

which allows to obtain the following approximate formula for the inverse coordinate speed of light

$$c_n^{-1} = \frac{1 + 2 \cdot W/c_0^2 - 4 \cdot \vec{V} \cdot \vec{d}_0/c_0^3}{c_0} + \mathcal{O}(c_0^{-5}), \quad (\text{C.6})$$

where \vec{d}_0 is the normalized propagation direction of the photon in the GCRS. The geopotential W can be separated into the dominating central term and higher moments (HM) of the gravity field, i.e.

$$W(t, \vec{r}) = \frac{GM}{|\vec{r}(t)|} + W_{\text{HM}}(t, \vec{r}). \quad (\text{C.7})$$

The higher moments of the gravity field are time-dependent due to the rotation of the Earth, however, on time-scales of the light propagation time ($\ll 1$ s) the field can be often regarded as constant.

Plugging eq. (C.6) into eq. (C.4) yields

$$\begin{aligned} \Delta t \approx & \underbrace{\frac{|\vec{r}_i - \vec{r}_j'|}{c_0}}_{\Delta t_{\text{SR}}} + \underbrace{2 \cdot \Delta t_{\text{SR}} \cdot \int_{\lambda=0}^1 \frac{GM}{c_0^2 \cdot |\vec{r}_{\text{ph}}(\lambda)|} d\lambda}_{\Delta t_{\text{PM}}} \\ & + \underbrace{2 \cdot \Delta t_{\text{SR}} \cdot \int_{\lambda=0}^1 \frac{W_{\text{HM}}(t(\lambda), \vec{r}_{\text{ph}}(\lambda))}{c_0^2} d\lambda}_{\Delta t_{\text{HM}}} + \underbrace{\Delta t_{\text{SR}} \cdot \int_{\lambda=0}^1 \frac{-4 \cdot \vec{V}(\vec{r}_{\text{ph}}(\lambda)) \cdot \vec{d}_0}{c_0^3} d\lambda}_{\Delta t_{\text{SM}}}, \quad (\text{C.8}) \end{aligned}$$

where Δt_{SR} is the classical propagation time from special relativity, Δt_{PM} is the gravitational delay due to Earth's central gravity field, Δt_{HM} are corrections from higher moments of the gravity field and Δt_{SM} is the delay or advancement due to Earth's spin moment. It is noted that Δt_{PM} is always positive, i.e. a delay.

The integral for Δt_{PM} can be solved analytically [Turyshev *et al.*, 2014, eq. (21)]:

$$\Delta t_{\text{PM}} = \frac{2 \cdot GM}{c_0^3} \cdot \ln \left(\frac{|\vec{r}_i| + \vec{d}_0 \cdot \vec{r}_i}{|\vec{r}_j'| + \vec{d}_0 \cdot \vec{r}_j'} \right) \quad \text{with} \quad \vec{d}_0 = \frac{\vec{r}_i - \vec{r}_j'}{|\vec{r}_i - \vec{r}_j'|}, \quad (\text{C.9})$$

which is commonly called Shapiro time delay in literature.

The higher moments (HM) of the gravity field in terms of spherical harmonics can be considered as well. Turyshev *et al.* [2014] derived analytical expressions for the quadrupole moments. However, for a more general approach one can simply solve the line integral using the trapezoidal rule and discretized sampling of the photon path, i.e.

$$\Delta t_{\text{HM}}^{(N-1)} = \frac{2}{c_0^2} \cdot \sum_{n=1}^{N-1} \frac{W_{\text{HM}}(t_n, \vec{r}_{\text{ph}}(\lambda_n)) + W_{\text{HM}}(t_{n+1}, \vec{r}_{\text{ph}}(\lambda_{n+1}))}{2} \cdot (t_{n+1} - t_n). \quad (\text{C.10})$$

The first order solution $\Delta t_{\text{HM}}^{(1)}$ uses the geopotential $W_{\text{HM}} = W - GM/r$ at two events, namely at the photon emission location \vec{r}_j' at coordinate time $t_1 = t_j$ and at the photon reception event \vec{r}_i with time $t_N = t_j$. This solution can be easily extended with higher N for a denser sampling of the photon path. The time dependence of the gravitational potential W_{HM} over time scales of the photon propagation is practically negligible and can be omitted for the sake of computational effort.

The integrand of the last term Δt_{SM} concerning Earth's spin moment can be recast with the help of eq. (B.16) and (B.18) into

$$\vec{V}(\vec{r}_{\text{ph}}(\lambda)) \cdot \vec{d}_0 = \left(\vec{\xi} \times \frac{\vec{r}_{\text{ph}}(\lambda)}{|\vec{r}_{\text{ph}}(\lambda)|^3} \right) \cdot \vec{d}_0 = \vec{\xi} \cdot \left(\frac{\vec{r}_j' + \vec{d}_0 \cdot c_0 \cdot t_{\text{SR}} \cdot \lambda}{|\vec{r}_{\text{ph}}(\lambda)|^3} \times \vec{d}_0 \right) \quad (\text{C.11})$$

$$= \vec{\xi} \cdot \left(\frac{\vec{r}_j'}{|\vec{r}_{\text{ph}}(\lambda)|^3} \times \vec{d}_0 \right) = (\vec{\xi} \times \vec{r}_j') \cdot \vec{d}_0 \cdot \frac{1}{|\vec{r}_{\text{ph}}(\lambda)|^3}. \quad (\text{C.12})$$

With this simplification one can approximate the line integral for Δt_{SM} by the trapezoidal rule to first order, i.e.

$$\Delta t_{\text{SM}} \approx -\frac{4}{c_0^3} \cdot (\vec{\xi} \times \vec{r}_j') \cdot \vec{d}_0 \cdot \left(\frac{1}{|\vec{r}_j'|^3} + \frac{1}{|\vec{r}_i|^3} \right) \cdot \frac{1}{2}. \quad (\text{C.13})$$

The magnitude of Δt_{SM} is much smaller than Δt_{PM} and Δt_{HM} , which justifies the approximation of the integral.

Appendix D

Polarization and Phase Changes within the GRACE-FO TMA

The following analysis was initially performed in 2012 within the GRACE Follow-On LRI project and resulted in an internal technical note, which was also re-printed in the (unpublished) master thesis of the author of this thesis. As the analysis is also applicable for potential future gravimetric missions, it has been revised and updated for this thesis.

This appendix chapter analyzes polarization and phase effects of three mirrors, which are aligned in a corner-cube configuration. Different mirror materials are considered. Various papers exist on polarization effects of corner-cube retro-reflectors [Player, 1988; Liu & Azzam, 1997; Scholl, 1995; Liu & Azzam, 1997]. Unfortunately, the authors usually use local beam coordinate frames, which are aligned with corner-cube faces, while the analysis here is focused on space-fixed polarization states and takes into account phase changes upon rotations of the corner-cube, which alter an interferometric displacement measurement.

For this analysis, the ifocad [Kochkina *et al.*, 2013] software¹ was extended to allow polarization tracing of beams. A 3-d Jones-matrix formalism as described in [Yun *et al.*, 2011] was used to compute the output polarization vector for different mirror materials. The complex reflectivity and transmittance coefficients for each mirror are computed from well-known Fresnel equations. A detailed description of the implementation can be found in the master thesis by Meshksar [2015].

D.1 Setup

An optical bench with normal vector in $+x$ direction is assumed as shown in fig. D.1. The initial beam direction is $+z$. After three reflections at the mirror surfaces of the corner-cube, the outgoing beam is anti-parallel to the incoming beam. This property is independent of corner-cube orientation as long as the mirror surfaces are hit by the beams. The geometrical pathlength of a beam is also invariant under rotations of the corner-cube around the intersection point of all three mirror planes, which is commonly called vertex.

In the GRACE-FO mission the so-called Triple Mirror Assembly (TMA) is used, which is a hollow corner-cube, where unused mirror surface areas are removed. With other words, the TMA consists of three separated mirrors, whereby all mirror planes are mutually perpendicular. The positions of the mirrors and the normal vectors of the mirror planes define the vertex position.

In [STI-TMA, 2013] the following mirror configuration is given, which was used in this

¹A ray- and beam-tracing software framework developed at the AEI

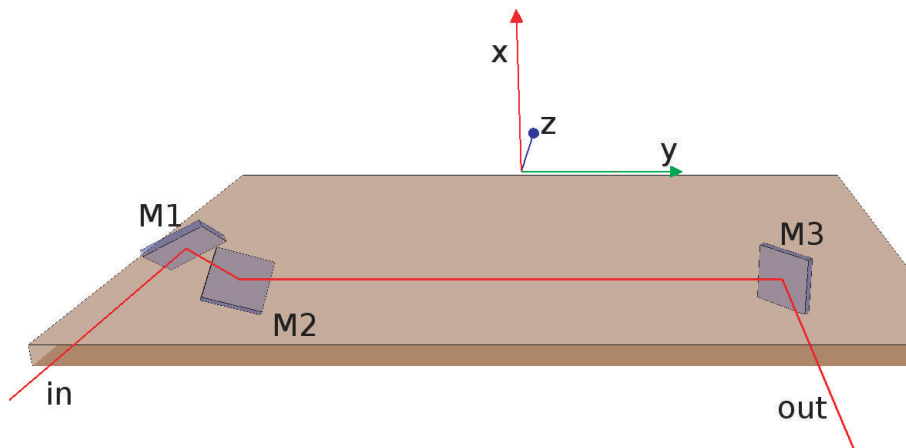


Figure D.1: Coordinate frame and mirror location used in the simulation.

analysis².

$$\vec{c}_1 = \begin{pmatrix} 24.000 \\ -300.000 \\ -333.941 \end{pmatrix} \text{mm}, \quad \vec{c}_2 = \begin{pmatrix} -24.000 \\ -266.058 \\ -300.000 \end{pmatrix} \text{mm}, \quad \vec{c}_3 = \begin{pmatrix} -24.000 \\ 300.000 \\ -300.000 \end{pmatrix} \text{mm} \quad (\text{D.1})$$

$$\vec{n}_1 = \begin{pmatrix} -1/\sqrt{2} \\ 0.5 \\ -0.5 \end{pmatrix}, \quad \vec{n}_2 = \begin{pmatrix} 1/\sqrt{2} \\ 0.5 \\ -0.5 \end{pmatrix}, \quad \vec{n}_3 = \begin{pmatrix} 0 \\ -1/\sqrt{2} \\ -1/\sqrt{2} \end{pmatrix} \quad (\text{D.2})$$

The body diagonal of the corner-cube is given by $\vec{n}_d = (\vec{n}_1 + \vec{n}_2 + \vec{n}_3)/\sqrt{3}$, which is here not parallel to the input beam direction. This case is referred to as non-normal incidence in the literature.

In nominal TMA alignment, the laser beam is reflected at the center of each mirror. The separation between in- and outgoing beam is 600 mm. The origin of the coordinate system coincides with the vertex of the TMA as shown in fig. D.1.

The angle of incidence (AOI) at each mirror is dependent on the orientation of the corner-cube. In nominal case, the AOIs at M1, M2 and M3 are 60.0° , 60.0° , 45.0° , respectively. The linear polarization states s (perpendicular, german “senkrecht”) and p (parallel) are defined with respect to the optical bench and correspond to the polarization vectors $\vec{P}_s = (1, 0, 0)^\top$ and $\vec{P}_p = (0, 1, 0)^\top$, respectively (cf. fig. D.1), for a normalized input wave vector $\vec{k} = (0, 0, +1)^\top$. The first two components of the polarization vector form the so-called Jones vector, if the propagation direction is along the z-direction.

D.2 Material constants

The laser beams are reflected at the mirrors, which consist of a single thick layer of metal in this simulation. The (real) refractive indices and the extinction coefficients for considered metals are shown in fig. D.2. Using a wavelength of 1064 nm yields refractive indices shown in table D.1. A hypothetical highly-absorbing material with $n = 1.4 + i \cdot 200$ was added to the list. It represents an ideal mirror, where the reflection is maximal for all incidence angles and for s- and p-polarization.

²reversed normal vectors were used, because normal vectors point outwards in IFOCAD

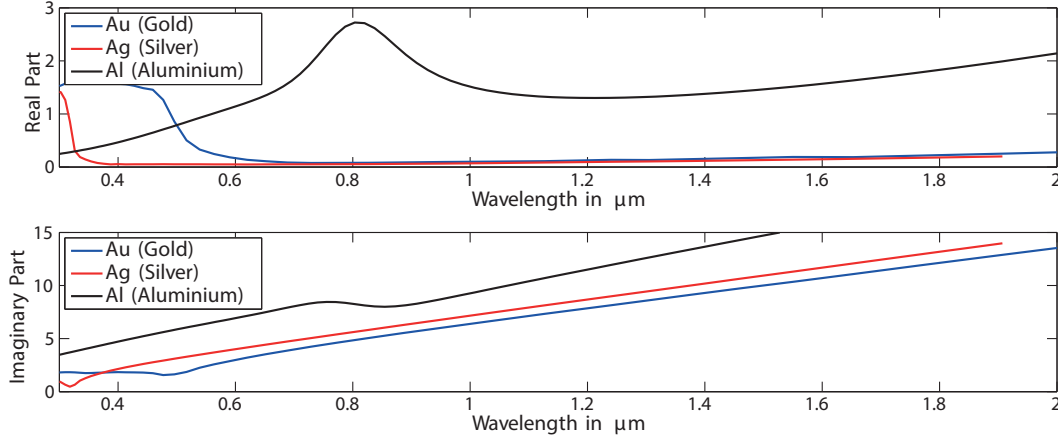


Figure D.2: The real and imaginary part of the refractive index is shown for different materials. The data is taken from the web database <http://refractiveindex.info>, which used [Babar & Weaver, 2015] for gold and silver and [Rakić *et al.*, 1998] for aluminum.

Material	Real refractive index	Extinction coefficient
Gold (Au)	0.10444	6.8635
Silver (Ag)	0.076623	7.6481
Aluminum (Al)	1.3850	9.9911
Highly-Absorbing (HA)	1.4000	200.0

Table D.1: Refractive indices used in the simulation.

D.3 Polarization Matrices

The polarization matrix $\hat{\mathbb{P}}$ describes the change of a polarization vector \vec{P}_{in} upon reflection or transmission at an interface. Furthermore, it transforms the wave vector \vec{k}_{in} , i.e.

$$\hat{\mathbb{P}}\vec{P}_{\text{in}} = \vec{P}_{\text{out}}, \quad \hat{\mathbb{P}}\vec{k}_{\text{in}} = \vec{k}_{\text{out}}. \quad (\text{D.3})$$

The polarization matrix of an optical system such as a corner-cube is the product of single polarization matrices $\hat{\mathbb{P}} = \hat{\mathbb{P}}_3 \cdot \hat{\mathbb{P}}_2 \cdot \hat{\mathbb{P}}_1$ [Yun *et al.*, 2011], where the single matrices represent the reflection at the mirrors and dependent on the actual angle of incidence. The final polarization matrix is only valid for a particular input wave vector \vec{k}_{in} , but it is independent of the input polarization vector. The polarization matrices for the different material scenarios are:

$$\hat{\mathbb{P}}_{\text{Au}} = \begin{pmatrix} 0.984261 \cdot e^{60.6312^\circ i} & 0.027838 \cdot e^{54.3342^\circ i} & 0.000000 \cdot e^{0.0000^\circ i} \\ 0.027753 \cdot e^{-113.9657^\circ i} & 0.985004 \cdot e^{56.4564^\circ i} & 0.000000 \cdot e^{0.0000^\circ i} \\ 0.000000 \cdot e^{0.0000^\circ i} & 0.000000 \cdot e^{0.0000^\circ i} & 1.000000 \cdot e^{180.0000^\circ i} \end{pmatrix} \quad (\text{D.4})$$

$$\hat{\mathbb{P}}_{\text{Ag}} = \begin{pmatrix} 0.990536 \cdot e^{54.6290^\circ i} & 0.022811 \cdot e^{48.5298^\circ i} & 0.000000 \cdot e^{0.0000^\circ i} \\ 0.022769 \cdot e^{-120.9513^\circ i} & 0.991034 \cdot e^{50.7644^\circ i} & 0.000000 \cdot e^{0.0000^\circ i} \\ 0.000000 \cdot e^{0.0000^\circ i} & 0.000000 \cdot e^{0.0000^\circ i} & 1.000000 \cdot e^{180.0000^\circ i} \end{pmatrix} \quad (\text{D.5})$$

$$\hat{\mathbb{P}}_{\text{Al}} = \begin{pmatrix} 0.906446 \cdot e^{41.3447^\circ i} & 0.012409 \cdot e^{51.1810^\circ i} & 0.000000 \cdot e^{0.0000^\circ i} \\ 0.012175 \cdot e^{-120.8918^\circ i} & 0.912236 \cdot e^{38.2639^\circ i} & 0.000000 \cdot e^{0.0000^\circ i} \\ 0.000000 \cdot e^{0.0000^\circ i} & 0.000000 \cdot e^{37.2159^\circ i} & 1.000000 \cdot e^{180.0000^\circ i} \end{pmatrix} \quad (\text{D.6})$$

$$\hat{\mathbb{P}}_{\text{HA}} = \begin{pmatrix} 0.999722 \cdot e^{2.1238^\circ i} & 0.000035 \cdot e^{2.6968^\circ i} & 0.000000 \cdot e^{0.0000^\circ i} \\ 0.000035 \cdot e^{-176.8981^\circ i} & 0.999744 \cdot e^{1.9561^\circ i} & 0.000000 \cdot e^{0.0000^\circ i} \\ 0.000000 \cdot e^{0.0000^\circ i} & 0.000000 \cdot e^{0.0000^\circ i} & 1.000000 \cdot e^{180.0000^\circ i} \end{pmatrix} \quad (\text{D.7})$$

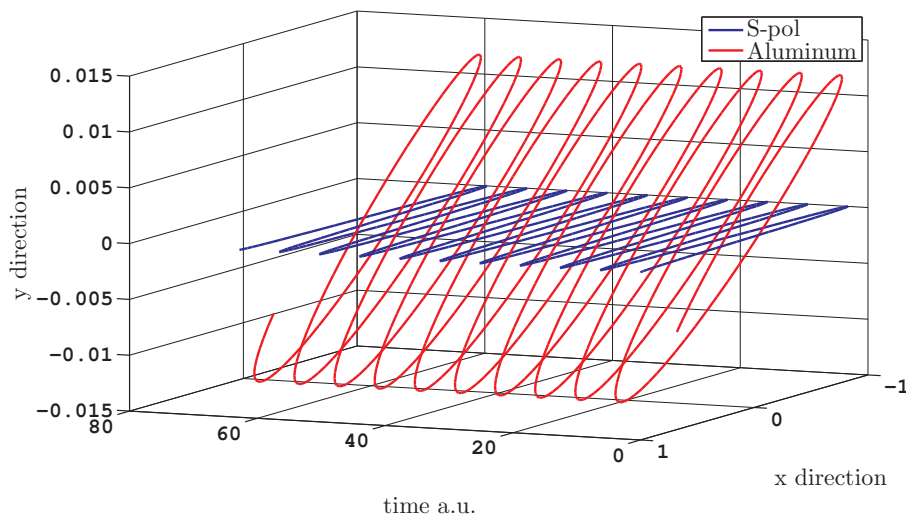


Figure D.3: The direction of electric field vector is shown for a s-polarized field as blue line and of the polarization given in eq. (D.8) as red line. Please note that the axis scale is not equal for both transversal direction.

The first column of the polarization matrices corresponds to the outgoing polarization for s-polarized input. The second column for the p-polarized case. For example, the polarization vector of a s-polarized input beam will be transformed by the TMA in case of aluminum mirrors into

$$\vec{P} = (0.906446 \cdot e^{41.3447^\circ i}, 0.012175 \cdot e^{-120.8918^\circ i}, 0)^\top. \quad (\text{D.8})$$

The corresponding electric field vector (direction) is shown in fig. D.3 (red), which is denoted here as elliptical left-circulating³. The input s-polarization is the dark blue trace. It is noted that the ellipticity appears highly exaggerated in the plot due to an unequal scale of the axes. The corresponding p-polarized electric field amplitude is only 0.012 V/m for a s-polarized input of 1 V/m, which is in terms of optical power only $0.012^2 \approx 1.4 \cdot 10^{-4}$.

D.4 TMA Polarization Change

The outgoing polarization ellipses for p- and s-polarized inputs are depicted in fig. D.4 for the different materials as given by the matrices eqs. (D.4)-(D.7). Other helpful numerical values can be found in table D.2. The de-polarization or polarization extinction ratio (PER), which is defined here as ratio of optical power in one linear input polarization to the orthogonal linear polarization at the output, is similar for s- and p-polarized input. However, in the case of silver or gold, the retardation is almost 0° or 180° for the p-input, which means that the output polarization is almost linear. The reflectivity is also higher for p-polarized input in these cases. Silver shows the highest reflectivity in the table. In fact, p-polarization and a silver coating is used within GRACE Follow-On and it is also a reasonable choice for future missions. The actual GRACE-FO TMA coating is named CZ322 by Cassidian Optronics GmbH, which is a proprietary space-qualified product. It comprises next to the silver base also a protective layer against space corrosion.

Although the polarization state is altered by a TMA, the changes are not severe, as less than one percent of power is transformed into the orthogonal polarization state. This yields a small decrease in heterodyne amplitude, because the effective power in the right mode and polarization is reduced. Furthermore, the light in the wrong polarization state might have a different phase and is transmitted to the distant craft. This is uncritical, if the

³two contradicting conventions exist for the sense of rotation

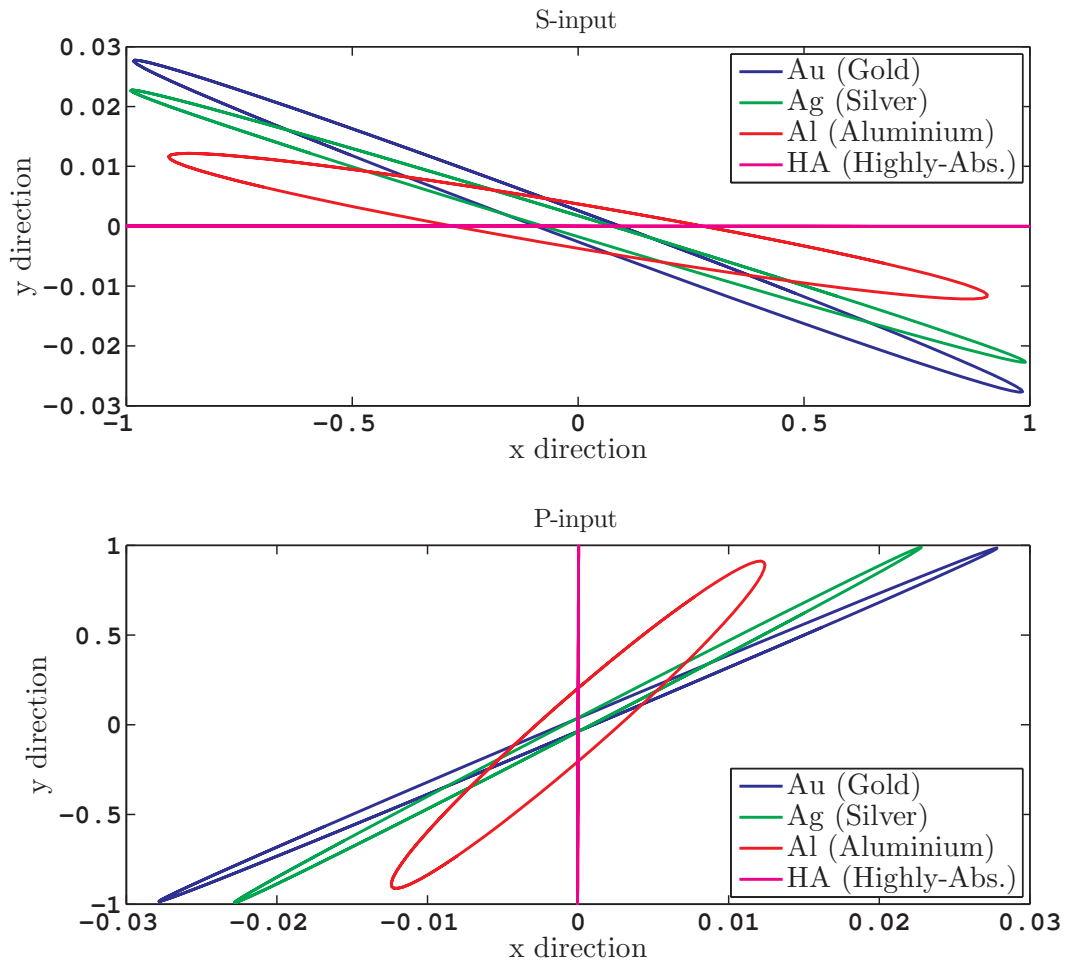


Figure D.4: Output polarization states for a TMA with different mirror materials for s-polarized input (upper plot) and p-polarized input (lower plot). Please note the unequal axes scale.

	Aluminum	Silver	Gold	Highly-Absorb.
In-Power	1.000000	1.000000	1.000000	1.000000
Power-Out-s	0.821644	0.981161	0.968769	0.999444
Power-Out-p	0.000148	0.000518	0.000770	0.000000
PER	-37.4 dB	-32.8 dB	-31.0 dB	-89.0 dB
P_a	0.821785	0.981678	0.969536	0.999444
P_b	0.003367	0.001738	0.002572	0.000001
Ellipticity Angle $ \chi $	0.23°	0.10°	0.15°	0.00°
Phase Difference s-p	-162.24°	-174.60°	-172.47°	-179.02°
Ellipse Rot. Angle Φ	0.73°	1.31°	1.61°	0.00°
Polarization Type	weakly elliptical left-circulating			linear
In-Power	1.000000	1.000000	1.000000	1.000000
Power-Out-s	0.000154	0.000520	0.000775	0.000000
Power-Out-p	0.832174	0.982148	0.970233	0.999488
PER	-37.3 dB	-32.8 dB	-31.0 dB	-89.0 dB dB
P_a	0.832324	0.982668	0.971007	0.999488
P_b	0.002531	0.000881	0.001015	0.000000
Ellipticity Angle $ \chi $	0.17°	0.05°	0.06°	0.00°
Phase Difference s-p	-12.92°	2.12°	-0.71°	-0.74°
Ellipse Rot. Angle Φ	0.76°	1.62°	-1.39°	0.00°
Polarization Type	weakly ellipt. right-circulat.	almost linear		linear

Table D.2: Polarization parameter of outgoing beams for s-input (upper table) and p-input (lower table). P_a is the power of the major axis, while P_b is the power of the minor axis of the polarization ellipse. The polarization extinction ratio is computed as $\text{PER} = 10 \cdot \log_{10}(P_{\perp\text{in}}/P_{\text{in}})$, where P_{in} is the output power in the input polarization. The ellipticity angle is defined as $|\chi| = \arctan(\sqrt{P_b/P_a})$.

receiver local oscillator is perfectly p-polarized. However, in the presence of S/C attitude jitter, in particular roll rotations by an angle u_{RX} , the receiver senses the phase of the wrong polarization. A worst case assessment considering a phase difference of 90° between main and disturbing polarization state and a relative power of $\Delta P = 0.1$ in the wrong polarization yields the following phase-derived displacement coupling

$$\rho = \frac{\lambda}{2\pi} \arg \left(\sqrt{1 - \Delta P} \cdot \cos(u_{\text{RX}}) + \sqrt{\Delta P} \cdot \sin(u_{\text{RX}}) \cdot e^{i\pi/2} \right) \quad (\text{D.9})$$

$$\approx \frac{\lambda}{2\pi} \cdot \frac{u_{\text{RX}}}{\sqrt{1/\Delta P - 1}} \approx 56 \text{ nm/rad} \cdot u_{\text{RX}}, \quad (\text{D.10})$$

where $\lambda = 1064 \text{ nm}$ was used. The result illustrates that the effect is uncritical for gravimetric missions, since other couplings such as the attitude-to-pathlength typically have a larger magnitude.

D.5 TMA Rotation Induced Phase Changes

The geometrical pathlength of a beam passing through a corner-cube is independent of rotations around its vertex. However, the phase of the light changes upon reflection at an interface with non-vanishing imaginary part of the refractive index, which is the so-called extinction coefficient. Metallic mirrors generally have a non-vanishing extinction coefficient. Furthermore, the phase change is in general dependent on the angle of incidence (AOI) and appears also in mirrors with a dielectric multilayer coating [Apfel, 1982; Delay, 2015]. However, such dielectric mirrors are not considered in this section.

The phase change upon reflection is already apparent from the phases in the polarization matrices in eqs. (D.4)-(D.7). In the previous section, receiver misalignment and the effect of a rotated local oscillator polarization was considered. Here, a misalignment of the local satellite is taken into account, which yields a change in the AOI for particular interferometers such as the GRACE-FO LRI. The changing AOI induces phase changes and leads to an apparent displacement change in an interferometric measurement. The effect is estimated by rotating the TMA around the vertex by angles u, v, w along the x, y and z axis, respectively, from -1 mrad to $+1 \text{ mrad}$. These angles correspond to yaw, pitch and roll, respectively. The phase in the polarization matrices is computed for different AOIs and the first numerical derivative was derived, which can be translated into a pathlength coupling factor with units of m/rad . The results are shown in table D.3.

The phase changes in the correct polarization, i.e. p-p or s-s, are less than $1 \mu\text{m/rad}$ and negligible compared to other linear coupling factors present in laser interferometry. The phase changes of the opposite polarization, i.e. the cross-terms s-p and p-s, are larger, but they are not severe, because the phase of the wrong polarization is not measured in case of perfectly aligned receiver and local oscillator. If the receiver is slightly misaligned by a roll-angle u_{RX} , the coupling is suppressed by the low relative power, i.e. $\sin(u_{\text{RX}}) \cdot \sqrt{\Delta P}$, as shown in eq. (D.9)

Hence, one can conclude that the TMA induced phase changes upon reflection for the simulated mirror types are uncritical. However, metallic mirrors require a protective coating, which was not considered here. Furthermore, it might be of interest to analyze the effects in dielectric mirrors as well.

	Aluminum				Silver		
In-Out	u	v	w		u	v	w
s-s	0.054	0.000	0.000		0.069	-0.001	0.001
p-p	0.019	0.000	0.000		0.024	0.001	-0.001
s-p	-0.002	5.458	-0.668		-0.000	4.165	-0.494
p-s	0.068	-5.459	0.670		0.092	-4.165	0.494
	Gold				Highly-Absorbing		
In-Out	u	v	w		u	v	w
s-s	0.075	-0.001	0.001		0.0	0.0	0.0
p-p	0.027	0.001	-0.001		0.0	0.0	0.0
s-p	-0.001	3.73	-0.435		0.0	97.429	-13.995
p-s	0.101	-3.730	0.435		0.0	-97.429	13.995

Table D.3: Coupling factors in units of $\mu\text{m}/\text{rad}$ due to a TMA orientation induced phase change. A wavelength of 1064 nm was used.

Appendix E

Relation between TMA Co-Alignment, Vertex and POMC

This analysis was initially performed in 2013 within the GRACE Follow-On LRI context and resulted in an internal technical note, which was also re-printed in the (unpublished) master thesis of the author. As the analysis is also applicable for potential future gravimetric missions, it has been revised and updated for this thesis.

In this appendix chapter, the effect of mirror misalignments in a hollow corner-cube retro-reflector (HCCRR) is analyzed with regard to beam parallelism and to coupling coefficients of rotations into the pathlength. A single pre-defined light path is considered as shown in fig. D.1, i.e. it is assumed that the light is reflected at the three mirrors in a pre-defined order. The analysis is based on analytical raytracing and the plane-wave approximation. Polarization effects of corner-cubes, refractive index changes or spatial extension of laser light are omitted.

The analysis was carried out with the help of the symbolic mathematical computation program `Mathematica` developed by Wolfram Research.

E.1 Analytical Raytracing

In the beginning, some basic ideas of analytical raytracing are introduced, which are deployed in the next subsections. Throughout this appendix chapter, computations are performed in the Euclidean space \mathbb{R}^3 , meaning that vectors have three components and matrices have the dimension 3×3 , which are shown with a hat, e.g. \hat{R} .

A laser beam is defined as a straight line with a beam direction \vec{d} and with beam origin at position \vec{p} . Moreover, the beam is parameterized by an independent parameter l , so that points along the beam are given by

$$\vec{b}(l) := \vec{p} + l \cdot \vec{d}. \quad (\text{E.1})$$

A mirror is defined in this appendix chapter as a plane, which is given by a mirror center \vec{c} and by a mirror normal vector \vec{n} . It is recalled that the points on a plane \vec{x} can be parameterized using the so-called Hessian normal form with $M(\vec{c}, \vec{n}, \vec{x}) = 0$, where the function M is given by

$$M(\vec{c}, \vec{n}, \vec{x}) := \vec{n} \cdot \vec{x} - \vec{c} \cdot \vec{x}, \quad (\text{E.2})$$

with $\vec{x} = (x, y, z)^\top$ being the position vector. When a light ray is reflected at a mirror, its direction is changed according to

$$\vec{d}_{\text{out}} = \hat{D}(\vec{n}) \cdot \vec{d}_{\text{in}}, \quad (\text{E.3})$$

with

$$\hat{D}(\vec{n}) := -\hat{R}(180^\circ, \vec{n}), \quad (\text{E.4})$$

where $\hat{R}(180^\circ, \vec{n})$ is a rotation matrix for a rotation around the axis \vec{n} by 180° . The intersection or reflection point of a ray at a mirror can be computed by solving

$$M(\vec{c}, \vec{n}, \vec{b}(l)) = M(\vec{c}, \vec{n}, \vec{p} + l \cdot \vec{d}) = 0 \quad (\text{E.5})$$

for the parameter l , which yields

$$l_s = L(\vec{c}, \vec{n}, \vec{p}, \vec{d}) := \frac{(\vec{c} - \vec{p}) \cdot \vec{n}}{\vec{n} \cdot \vec{d}}. \quad (\text{E.6})$$

The intersection point can be found with eq. (E.1) as $\vec{b}(l_s)$. All these functions can be easily implemented in an algebraic manipulation program.

E.2 The Nominal Setup

We analyze the propagation of a light ray through a hollow corner-cube retro-reflector consisting of three mirrors M_1, M_2 and M_3 , which are given by the following nominal mirror centers \vec{c}_i and mirror normal vectors \vec{n}_i :

$$\vec{c}_1 := \begin{pmatrix} 300.0 \\ 300.0 \\ -24.0 \end{pmatrix} \text{mm}, \quad \vec{c}_2 := \begin{pmatrix} 300.0 \\ -266.0588745 \\ -24.0 \end{pmatrix} \text{mm}, \quad \vec{c}_3 := \begin{pmatrix} 333.9411255 \\ -300.0 \\ 24 \end{pmatrix} \text{mm}, \quad (\text{E.7})$$

$$\vec{n}_1 := \begin{pmatrix} 1/\sqrt{2} \\ -1/\sqrt{2} \\ 0 \end{pmatrix}, \quad \vec{n}_2 := \begin{pmatrix} 0.5 \\ 0.5 \\ 1/\sqrt{2} \end{pmatrix}, \quad \vec{n}_3 := \begin{pmatrix} 0.5 \\ 0.5 \\ -1/\sqrt{2} \end{pmatrix}. \quad (\text{E.8})$$

These numerical values apply for the Triple Mirror Assembly (TMA) of the GRACE Follow-On LRI. The setup is depicted in fig. D.1, but for this appendix chapter the coordinate frame was rotated compared to appendix D, so that the nominal input beam direction points along the x -axis and the order of mirrors was reversed. This changes yield no physical or computational advantage but are due to an inconsistency in notation, since the analysis in this chapter was independently performed of the analysis in the previous chapter.

The nominal vertex \vec{V}_{nom} of the corner-cube, in other words the intersection point of all three mirror planes, can be computed by the formula [Glassner, 2013, p. 305]

$$\vec{V}_{\text{nom}}(\vec{c}_1, \vec{n}_1, \vec{c}_2, \vec{n}_2, \vec{c}_3, \vec{n}_3) := \quad (\text{E.9})$$

$$\frac{(\vec{c}_1 \cdot \vec{n}_1) \cdot (\vec{n}_2 \times \vec{n}_3) + (\vec{c}_2 \cdot \vec{n}_2) \cdot (\vec{n}_3 \times \vec{n}_1) + (\vec{c}_3 \cdot \vec{n}_3) \cdot (\vec{n}_1 \times \vec{n}_2)}{|\vec{n}_1 \vec{n}_2 \vec{n}_3|}, \quad (\text{E.10})$$

where $|\vec{n}_1 \vec{n}_2 \vec{n}_3|$ is the determinant of a matrix, which contains the vectors \vec{n}_1, \vec{n}_2 and \vec{n}_3 in the columns. In the case of an ideal corner-cube without mirror misalignments, the nominal vertex is located at the coordinate origin $(0, 0, 0)^T \text{mm}$ for the particular numerical values given here.

We assume the initial input ray into the corner-cube is defined by

$$\vec{b}_0(l) := \vec{p}_0 + l \cdot \vec{d}_0 = \begin{pmatrix} x_0 \\ 300.0 + y_0 \\ -24.0 + z_0 \end{pmatrix} \text{mm} + l \cdot \begin{pmatrix} -1 \\ 0 \\ 0 \end{pmatrix}, \quad (\text{E.11})$$

where $x_0 > 300.0 \text{mm}$ is a variable for the distance between the corner-cube and the origin of the ray. The parameters y_0, z_0 describe a lateral displacement of the initial ray w.r.t. the

nominal optical axis given by $y_0 = z_0 = 0$. The input ray \vec{b}_0 is reflected at M_1 and forms a ray called \vec{b}_1 , which is reflected at M_2 and forms ray \vec{b}_2 , which is again reflected at M_3 and forms the final ray \vec{b}_3 . The nominal angles of incidence are 45° , 60° and 60° on M_1 , M_2 and M_3 , respectively.

In addition, a virtual plane is used, which is normal to the direction of the initial ray \vec{b}_0 , and intersects with the origin of the initial ray. The final ray \vec{b}_3 intersects with the virtual plane and is terminated at that point. In total, one obtains four ray segments through the corner-cube and starting and ending at the virtual plane. The first ray length l_0 can be computed using eq. (E.6) as

$$l_0 = L(\vec{c}_1, \vec{n}_1, \vec{p}_0, \vec{d}_0). \quad (\text{E.12})$$

This allows to write ray \vec{b}_1 as

$$\vec{b}_1(l) = \vec{p}_1 + l \cdot \vec{d}_1 = \vec{b}_0(l_0) + l \cdot \hat{D}(\vec{n}_1) \cdot \vec{d}_0. \quad (\text{E.13})$$

The ray segment length l_1 can be computed again using eq. (E.6). Iteratively, one can derive all beams until \vec{b}_3 . The final beam \vec{b}_3 is a function of all mirrors. Its direction can be written as

$$\vec{d}_3 = \hat{D}(\vec{n}_3) \cdot \hat{D}(\vec{n}_2) \cdot \hat{D}(\vec{n}_1) \cdot \vec{d}_0, \quad (\text{E.14})$$

where \vec{d}_0 is simply the initial ray direction $(-1, 0, 0)^\top$. Since the nominal setup consists of an error-free retro-reflector, the final direction is anti-parallel to the incoming beam:

$$\vec{d}_3 = \begin{pmatrix} 1 \\ 0 \\ 0 \end{pmatrix}, \quad (\text{E.15})$$

which follows directly from the fact that

$$\hat{D}(\vec{n}_3) \cdot \hat{D}(\vec{n}_2) \cdot \hat{D}(\vec{n}_1) = -\hat{1} \quad (\text{E.16})$$

for three mutually orthogonal and normalized vectors \vec{n}_1 , \vec{n}_2 and \vec{n}_3 (cf. eq. (E.4)). A precondition is that the normal vectors \vec{n}_1 , \vec{n}_2 and \vec{n}_3 form a left-handed system, which applies for the here analyzed corner-cube.

The final beam intersects with the virtual plane at

$$\vec{b}_3(l_3) = \begin{pmatrix} x_0 \\ -300.0 - y_0 \\ 24.0 - z_0 \end{pmatrix}, \quad (\text{E.17})$$

showing that the corner-cube produces a lateral displacement of 600 mm in y -direction and 48 mm in z -direction (when $y_0 = z_0 = 0$). The accumulated geometrical pathlength ρ through the setup is the sum of all segments:

$$\rho = l_0 + l_1 + l_2 + l_3. \quad (\text{E.18})$$

It simplifies in the nominal setup to $2 \cdot x_0$, which is twice the distance between virtual plane and vertex. With eq. (E.18) one can compute a lengthy analytical expression for the pathlength, which depends on the mirror positions and orientations.

E.3 TMA Rotations

The effect of TMA rotations is investigated by introducing the rotation angles u for roll around the x -axis, v for pitch around the y -axis, and w for yaw around the z -axis. The combined rotation matrix

$$\hat{R}(u, v, w) = \hat{R}\left(+u, (1, 0, 0)^\top\right) \cdot \hat{R}\left(+v, (0, 1, 0)^\top\right) \cdot \hat{R}\left(+w, (0, 0, 1)^\top\right), \quad (\text{E.19})$$

is composed of elementary rotation matrices for rotations around the x , y and z direction. Since the angles u, v, w are small, the rotation matrices are commuting and the order of rotations does not matter. This holds only up to linear order in the angles. If quadratic terms are considered, the expressions are generally dependent on the used convention for rotations.

The TMA mirrors rotate around a pivot point $\vec{\delta} = (\delta x, \delta y, \delta z)^\top$ and not around the coordinate origin or the nominal TMA vertex. The transformation of each mirror can be written as

$$\vec{n}_i(u, v, w) = \hat{R}(u, v, w) \cdot \vec{n}_i, \quad (\text{E.20})$$

$$\vec{c}_i(u, v, w) = \hat{R}(u, v, w) \cdot (\vec{c}_i - \vec{\delta}) + \vec{\delta}. \quad (\text{E.21})$$

Since rotations of all three normal vectors maintain the orthogonality of the vectors, the final beam direction is invariant under TMA rotations:

$$\vec{d}_3 = \hat{D}(\vec{n}_3(u, v, w)) \cdot \hat{D}(\vec{n}_2(u, v, w)) \cdot \hat{D}(\vec{n}_1(u, v, w)) \cdot \vec{d}_0 = \begin{pmatrix} 1 \\ 0 \\ 0 \end{pmatrix}. \quad (\text{E.22})$$

The pathlength ρ is a lengthy expression, therefore, it is expanded in a series up to second order in u, v, w :

$$\begin{aligned} & \rho(\vec{c}_1(u, v, w), \vec{n}_1(u, v, w), \vec{c}_2(u, v, w), \vec{n}_2(u, v, w), \vec{c}_3(u, v, w), \vec{n}_3(u, v, w)) \\ & \approx 2 \cdot x_0 + \begin{pmatrix} 0 \\ 2 \cdot \delta z \\ -2 \cdot \delta y \end{pmatrix} \cdot \begin{pmatrix} u \\ v \\ w \end{pmatrix} + \begin{pmatrix} 0 \\ -\delta x \\ -\delta x \end{pmatrix} \cdot \begin{pmatrix} u^2 \\ v^2 \\ w^2 \end{pmatrix}. \end{aligned} \quad (\text{E.23})$$

The first term is again twice the distance between virtual plane and vertex, which is generally not accessible in interferometry due to the integer ambiguity of the phase. The second term contains the linear coupling and the third term describes the quadratic coupling of rotations into the pathlength. It is remarked that the expression is equal to the coupling obtained in section 2.6.3 on reference points, which was derived not in the context of retro-reflectors. This implies that the here analyzed ideal corner-cube has actually a reference point, where rotation-to-pathlength coupling around arbitrary or all axes vanishes. In fact, the reference point is the vertex position, i.e. $\vec{\delta} = \vec{V}_{\text{nom}}$. This cannot be presumed in general, since the coupling around different rotation axes may not be the same. It is evident that the offset $(\delta x, \delta y, \delta z)$ between the pivot point of rotation and the vertex should be minimized to reduce the coupling of (spacecraft) rotations into the geometrical and optical pathlength.

E.4 TMA mirror misalignment

So far, the coupling was computed for an error-free corner-cube. In this subsection, the mirrors are misaligned with respect to their nominal orientation. It is advised to incorporate the misalignments for each mirror in a frame, which has the same origin as the nominal vertex $\vec{V}_{\text{nom}} = (0, 0, 0)^\top$, but with axes along the normal vectors of the mirrors. In this TMA frame,

the mirror centers become

$$\begin{aligned}\vec{c}_{1,\text{loc}} &:= \hat{R}_{\text{TMA} \rightarrow \text{SC}}^{-1} \cdot (\vec{c}_1 - \vec{V}_{\text{nom}}) + \vec{V}_{\text{nom}} = \begin{pmatrix} 0 \\ 316.970563 \\ 283.029437 \end{pmatrix} \text{mm}, \\ \vec{c}_{2,\text{loc}} &:= \hat{R}_{\text{TMA} \rightarrow \text{SC}}^{-1} \cdot (\vec{c}_2 - \vec{V}_{\text{nom}}) + \vec{V}_{\text{nom}} = \begin{pmatrix} 400.264069 \\ 33.941125 \\ 0 \end{pmatrix} \text{mm}, \\ \vec{c}_{3,\text{loc}} &:= \hat{R}_{\text{TMA} \rightarrow \text{SC}}^{-1} \cdot (\vec{c}_3 - \vec{V}_{\text{nom}}) + \vec{V}_{\text{nom}} = \begin{pmatrix} 448.264069 \\ 0 \\ 33.941125 \end{pmatrix} \text{mm},\end{aligned}\tag{E.24}$$

$$\tag{E.25}$$

and the normal vectors transform to

$$\begin{aligned}\vec{n}_{1,\text{loc}} &:= \hat{R}_{\text{TMA} \rightarrow \text{SC}}^{-1} \cdot \vec{n}_1 = \begin{pmatrix} 1 \\ 0 \\ 0 \end{pmatrix}, \\ \vec{n}_{2,\text{loc}} &:= \hat{R}_{\text{TMA} \rightarrow \text{SC}}^{-1} \cdot \vec{n}_2 = \begin{pmatrix} 0 \\ 0 \\ 1 \end{pmatrix}, \\ \vec{n}_{3,\text{loc}} &:= \hat{R}_{\text{TMA} \rightarrow \text{SC}}^{-1} \cdot \vec{n}_3 = \begin{pmatrix} 0 \\ 1 \\ 0 \end{pmatrix}.\end{aligned}\tag{E.26}$$

The rotation matrix for the transformation from the spacecraft frame to the TMA frame is given by

$$\hat{R}_{\text{TMA} \rightarrow \text{SC}}^{-1} := \begin{pmatrix} \leftarrow & \vec{n}_1 & \rightarrow \\ \leftarrow & \vec{n}_3 & \rightarrow \\ \leftarrow & \vec{n}_2 & \rightarrow \end{pmatrix} = \hat{R}(-\alpha, \vec{q}),\tag{E.27}$$

where the order of vectors was swapped to obtain a right-handed system and a matrix determinant of +1. The rotation axis \vec{q} is the eigenvector of $\hat{R}_{\text{TMA} \rightarrow \text{SC}}^{-1}$ to the eigenvalue +1, while the angle of rotation $-\alpha$ can be computed using the trace of the matrix:

$$\text{tr}(\hat{R}_{\text{TMA} \rightarrow \text{SC}}^{-1}) = 1 + 2 \cdot \cos(-\alpha).\tag{E.28}$$

For each mirror, small tip and tilt misalignments are introduced, which are denoted in the following by angles α_i and β_i . This yields

$$\begin{aligned}\vec{n}_{1,\text{loc}}^e &:= \begin{pmatrix} 1 \\ \alpha_1 \\ \beta_1 \end{pmatrix}, \\ \vec{n}_{2,\text{loc}}^e &:= \begin{pmatrix} \alpha_2 \\ \beta_2 \\ 1 \end{pmatrix}, \\ \vec{n}_{3,\text{loc}}^e &:= \begin{pmatrix} \alpha_3 \\ 1 \\ \beta_3 \end{pmatrix}.\end{aligned}\tag{E.29}$$

Finally, the error-prone normal vectors are transformed back into the original (spacecraft) frame according to

$$\vec{n}_i^e := \hat{R}_{\text{TMA} \rightarrow \text{SC}} \cdot \vec{n}_{i,\text{loc}}^e = \hat{R}(+\alpha, \vec{q}) \cdot \vec{n}_{i,\text{loc}}^e.\tag{E.30}$$

The new vertex is denoted as *true* vertex and can be derived from eq. (E.10)

$$\vec{V}_{\text{true}}(\vec{c}_1, \vec{n}_1^e, \vec{c}_2, \vec{n}_2^e, \vec{c}_3, \vec{n}_3^e) \stackrel{\text{linearized}}{\approx} \begin{pmatrix} \begin{pmatrix} 224.132 \\ 200.132 \\ 224.132 \end{pmatrix} \cdot \vec{\alpha} + \begin{pmatrix} 200.132 \\ 16.9706 \\ 16.9706 \end{pmatrix} \vec{\beta} \\ \begin{pmatrix} -224.132 \\ 200.132 \\ 200.132 \end{pmatrix} \cdot \vec{\alpha} + \begin{pmatrix} -200.132 \\ 16.9706 \\ 16.9706 \end{pmatrix} \vec{\beta} \\ \begin{pmatrix} 0. \\ 283.029 \\ -316.971 \end{pmatrix} \cdot \vec{\alpha} + \begin{pmatrix} 0. \\ 24.0 \\ -24.0 \end{pmatrix} \vec{\beta} \end{pmatrix} \text{ mm/rad}, \quad (\text{E.31})$$

with $\vec{\alpha} = (\alpha_1, \alpha_2, \alpha_3)^\top$ and $\vec{\beta} = (\beta_1, \beta_2, \beta_3)^\top$ being the mirror misalignments in radian. The true vertex is accessible, e.g. by measuring the mirror planes physically with a coordinate measurement machine, while the nominal vertex \vec{V}_{nom} is purely virtual and not a good reference point anymore.

It is anticipated that the relative error angles γ_1 , γ_2 and γ_3 between the mirror planes are a helpful quantity, which are often denoted as dihedral angles in literature:

$$\vec{\gamma} = \begin{pmatrix} \gamma_1 \\ \gamma_2 \\ \gamma_3 \end{pmatrix} = \begin{pmatrix} \alpha_1 + \alpha_3 \\ \alpha_2 + \beta_1 \\ \beta_2 + \beta_3 \end{pmatrix} = \begin{pmatrix} \pi/2 - \sphericalangle(\vec{n}_1^e, \vec{n}_3^e) \\ \pi/2 - \sphericalangle(\vec{n}_1^e, \vec{n}_2^e) \\ \pi/2 - \sphericalangle(\vec{n}_2^e, \vec{n}_3^e) \end{pmatrix}. \quad (\text{E.32})$$

E.4.1 Anti-Parallelism Errors

The retro-reflection property of corner-cubes is exploited in laser interferometry such as in the GRACE Follow-On LRI. However, the retro-reflected beam is not anti-parallel to the incident beam in a corner-cube with misaligned mirrors. This effect is assessed in this subsection. Therefore, eq. (E.30) and eq. (E.21) are combined to obtain the error-prone mirror normal vectors upon spacecraft or TMA rotations, i.e.

$$\vec{n}_i^e(u, v, w) = \hat{R}(u, v, w) \cdot \vec{n}_i^e, \quad (\text{E.33})$$

which are used to derive the final dimensionless beam direction

$$\vec{d}_3 = \hat{D}(\vec{n}_3^e(u, v, w)) \cdot \hat{D}(\vec{n}_2^e(u, v, w)) \cdot \hat{D}(\vec{n}_1^e(u, v, w)) \cdot \vec{d}_0 \stackrel{\text{linearized}}{\approx} \begin{pmatrix} 1 \\ 0 \\ 0 \end{pmatrix} + \begin{pmatrix} 0 & 0 & 0 \\ -\sqrt{2} & -\sqrt{2} & 0 \\ 1 & -1 & \sqrt{2} \end{pmatrix} \vec{\gamma} \cdot \frac{1}{\text{rad}} \quad (\text{E.34})$$

$$+ \begin{pmatrix} 0 & 0 & 0 \\ -u + v & u - v & -\sqrt{2} \cdot u - \sqrt{2} \cdot v \\ -\sqrt{2} \cdot u + w & -\sqrt{2} \cdot u - w & -\sqrt{2} \cdot w \end{pmatrix} \vec{\gamma} \cdot \frac{1}{\text{rad}^2}, \quad (\text{E.35})$$

where one can see that in case of no misalignments ($\vec{\gamma} = 0$), the outgoing beam direction is $(1, 0, 0)^\top$, i.e. perfectly anti-parallel. The second term provides the dependency of the outgoing beam direction w.r.t. the mirror misalignment angles. The last term shows that the beam direction can depend on the spacecraft or TMA orientation u , v , w . However, the effect is rather small, since γ_i has a typical magnitude of μrad and u , v , w of mrad . The static misalignment given by the second term has coefficients of the order of 1, meaning that a mirror misalignment angle of 1 μrad causes a beam deflection of the order of 1 μrad .

The static misalignment matrix in the second term was independently verified by numerical raytracing using IFOCAD and it has been partly verified in laboratory experiments

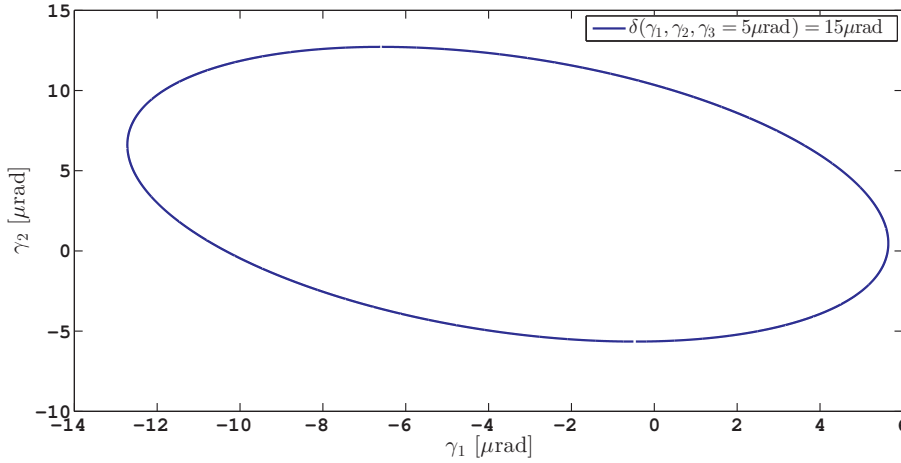


Figure E.1: The required accuracy for the alignment of the two angles γ_1 and γ_2 in a TMA is shown in terms of an error ellipse for the particular assumptions given in the text.

[Schütze, 2014, sec. 4.2.5.3]. The matrix can be used to derive the following half-cone beam deflection angle δ

$$\delta = \sqrt{\delta_y^2 + \delta_z^2} = \sqrt{2 \cdot (\gamma_1 + \gamma_2)^2 + (\gamma_1 - \gamma_2 + \sqrt{2} \cdot \gamma_3)^2}, \quad (\text{E.36})$$

where the following misalignment angles δ_y and δ_z were used

$$\begin{pmatrix} 0 \\ \delta_y \\ \delta_z \end{pmatrix} = \begin{pmatrix} 0 & 0 & 0 \\ -\sqrt{2} & -\sqrt{2} & 0 \\ 1 & -1 & \sqrt{2} \end{pmatrix} \vec{\gamma} \cdot \frac{1}{\text{rad}}. \quad (\text{E.37})$$

Example: Application to TMA requirements

For this example, it is assumed that a requirement of $\delta \leq 15 \mu\text{rad}$ for the total beam deflection due to a TMA is given and that the two close-by mirrors M_2 and M_3 are aligned with an error below $\gamma_3 = 5 \mu\text{rad}$. Thus, eq. (E.36) can be used to derive the error ellipse for the remaining angles γ_1 and γ_2 , which is shown in fig. E.1. If both angles are within the ellipse, the total beam deflection δ is $\leq 15 \mu\text{rad}$.

Also Yoder [1958] derived the beam deflection due to corner-cube errors. In the paper it is stated that misalignment angles $|\gamma_i|$ below θ result in a maximum beam deflection of $3.26 \cdot \theta$. However, one can show with eq. (E.36) that the total error is bound by $3.41 \cdot \theta$, if $\gamma_1 = -\gamma_2 = \gamma_3 = \theta$. The cause of this discrepancy was not further investigated, but might be due to the present non-normal incidence into the TMA. Normal incidence is often used in literature on corner-cubes and means that the incident ray direction \vec{d}_0 is parallel or anti-parallel to the cube-diagonal $\vec{n}_d = (\vec{n}_1 + \vec{n}_2 + \vec{n}_3)/\sqrt{3}$.

E.4.2 Pathlength errors of a misaligned TMA

This subsection discusses the changes in the accumulated geometrical pathlength of a light beam, which passes through a corner-cube retro-reflector with misaligned mirrors. Such a corner-cube has a true vertex position \vec{V}_{true} . In this section, it is assumed that rotations of the retro-reflector are performed around the pivot point $\vec{V}_{\text{true}} + \vec{\delta}$, where $\vec{\delta} = (\delta x, \delta y, \delta z)^\top$ is

a small offset vector. The pathlength coupling can be obtained as

$$\rho(\vec{c}_1(u, v, w), \vec{n}_1^e(u, v, w), \vec{c}_2(u, v, w), \vec{n}_2^e(u, v, w), \vec{c}_3(u, v, w), \vec{n}_3^e(u, v, w)) \approx 2 \cdot x_0 + \frac{2 \cdot \delta z \cdot v}{\text{rad}} - \frac{2 \cdot \delta y \cdot w}{\text{rad}} \quad (\text{E.38})$$

$$+ \begin{pmatrix} \sqrt{2} \cdot y_0 + 1.0 \cdot z_0 \\ \sqrt{2} \cdot y_0 - 1.0 \cdot z_0 \\ \sqrt{2} \cdot z_0 \end{pmatrix} \cdot \vec{\gamma} \cdot \frac{1}{\text{rad}} \quad (\text{E.39})$$

$$+ u \cdot \begin{pmatrix} 266.1 \text{ mm} + (y_0 - \delta y) + \sqrt{2}(z_0 - \delta z) \\ -333.9 \text{ mm} - (y_0 - \delta y) + \sqrt{2}(z_0 - \delta z) \\ 424.3 \text{ mm} + \sqrt{2}(y_0 - \delta y) \end{pmatrix} \cdot \vec{\gamma} \cdot \frac{1}{\text{rad}^2} \quad (\text{E.40})$$

$$+ v \cdot \begin{pmatrix} -300.0 \text{ mm} - y_0 + \delta x \\ 300.0 \text{ mm} + y_0 - \delta x \\ 424.3 \text{ mm} + \sqrt{2}(y_0 + \delta x) \end{pmatrix} \cdot \vec{\gamma} \cdot \frac{1}{\text{rad}^2} \quad (\text{E.41})$$

$$+ w \cdot \begin{pmatrix} 24.0 \text{ mm} - z_0 + \sqrt{2}\delta x \\ -24.0 \text{ mm} + z_0 + \sqrt{2}\delta x \\ -33.94 \text{ mm} + \sqrt{2}z_0 \end{pmatrix} \cdot \vec{\gamma} \cdot \frac{1}{\text{rad}^2}, \quad (\text{E.42})$$

The line (E.38) is the nominal TMA coupling given in eq. (E.23). The next line vanishes, if the lateral beam offset y_0 and z_0 is zero. Since all quantities are static in this term, it is negligible. The next three lines provide the TMA orientation dependent coupling. This linear coupling is less than $25 \mu\text{m}/\text{rad}$ for all rotations, if a magnitude of $5 \cdot 10^{-5}$ rad is assumed for the dihedral angles γ . As this linear coupling w.r.t. yaw, pitch and roll rotations can be compared to, for example, the TMA vertex offset coupling, it is beneficial to rewrite it in form of partial derivatives:

$$\begin{pmatrix} \partial\rho/\partial u \\ \partial\rho/\partial v \\ \partial\rho/\partial w \end{pmatrix} = 1 \text{ mm}/\text{rad}^2 \cdot \begin{pmatrix} 266.059 & -333.941 & 424.264 \\ -300.0 & +300.0 & 424.264 \\ 24.0 & -24.0 & -33.9411 \end{pmatrix} \cdot \vec{\gamma} \quad (\text{E.43})$$

$$+ \begin{pmatrix} 0 & -\gamma_1 + \gamma_2 - \sqrt{2}\gamma_3 & -\sqrt{2}\gamma_1 - \sqrt{2}\gamma_2 \\ \gamma_1 - \gamma_2 + \sqrt{2}\gamma_3 & 0 & 2 \\ \sqrt{2}\gamma_1 + \sqrt{2}\gamma_2 & -2 & 0 \end{pmatrix} \cdot \begin{pmatrix} \delta x \\ \delta y \\ \delta z \end{pmatrix} \cdot \frac{1}{\text{rad}^2}, \quad (\text{E.44})$$

where no lateral beam offset ($y_0 = z_0 = 0$) was assumed. One should notice that mirror misalignments $\vec{\gamma}$ induce a roll pathlength coupling ($\partial\rho/\partial u$), however, it can be compensated by a large value for δy and/or δz . On the other side, the yaw and pitch (v and w) coupling can be minimized by small adjustment of δy and δz due to the 2 elements in the matrix. Hence, one cannot zero the linear coupling for all rotations by a set of $\delta x, \delta y, \delta z$, or in other words, the matrix in line (E.44) is not invertible due to a vanishing determinant.

In the linear approximation (eq. (E.43)-(E.44)) and for a particular rotation axis, there is a plane of pivot points, where the linear coupling vanishes. For example, for rotations in roll direction, the points of the plane ($\delta x, \delta y, \delta z$) need to fulfill

$$1 \frac{\text{mm}}{\text{rad}^2} \cdot \begin{pmatrix} 266.059 \\ -333.941 \\ 424.264 \end{pmatrix} \cdot \vec{\gamma} + \begin{pmatrix} 0 \\ -\gamma_1 + \gamma_2 - \sqrt{2}\gamma_3 \\ -\sqrt{2}\gamma_1 - \sqrt{2}\gamma_2 \end{pmatrix} \cdot \begin{pmatrix} \delta x \\ \delta y \\ \delta z \end{pmatrix} \cdot \frac{1}{\text{rad}^2} = 0. \quad (\text{E.45})$$

Moreover, it is noted that the rotation axis is always in the plane of zero coupling.

If one extends the coupling also to quadratic terms, i.e.

$$\begin{pmatrix} \partial^2 \rho / \partial u^2 \\ \partial^2 \rho / \partial v^2 \\ \partial^2 \rho / \partial w^2 \end{pmatrix} = 1 \text{ mm/rad}^3 \cdot \begin{pmatrix} 224.132 & -200.132 & -16.9706 \\ -212.132 & -212.132 & 0 \\ -12.0 & +12.0 & -16.9706 \end{pmatrix} \cdot \vec{\gamma} \quad (\text{E.46})$$

$$+ \frac{1}{2} \begin{pmatrix} 0 & \sqrt{2} \cdot (\gamma_1 + \gamma_2) & -\gamma_1 + \gamma_2 - \sqrt{2}\gamma_3 \\ -2 & 0 & \gamma_1 - \gamma_2 + \sqrt{2}\gamma_3 \\ -2 & -\sqrt{2} \cdot (\gamma_1 + \gamma_2) & 0 \end{pmatrix} \cdot \begin{pmatrix} \delta x \\ \delta y \\ \delta z \end{pmatrix} \cdot \frac{1}{\text{rad}^3},$$

one can reduce the plane of zero coupling to a line of zero coupling, where the direction of the line is the rotation axis.

Seeking for solution with vanishing linear and quadratic coupling, one arrives at the following three lines

$$\vec{l}_u(t) \approx \begin{pmatrix} t \\ \frac{634.0 \cdot (\gamma_1^2 + \gamma_1 \gamma_2) + 48.0 \cdot (\gamma_2 + \gamma_1) \cdot \gamma_3}{-3\gamma_1^2/2 - \gamma_1(\gamma_2 + \sqrt{2}\gamma_3) - 3\gamma_2^2/2 + \sqrt{2}\gamma_2\gamma_3 - \gamma_3^2} + 300.0 \\ \frac{-412.0\gamma_1^3 + 60.0\gamma_1^2\gamma_2 + 508.0\gamma_1\gamma_2^2 - 24.0\gamma_3^2 \cdot (\gamma_1 + \gamma_2) - 634.0\gamma_1\gamma_3(\gamma_1 + \gamma_2) + 36.0\gamma_2^3}{(-3\gamma_1^2/2 - \gamma_1(\gamma_2 + \sqrt{2}\gamma_3) - 3\gamma_2^2/2 + \sqrt{2}\gamma_2\gamma_3 - \gamma_3^2) \cdot (\gamma_1 + \gamma_2)} \end{pmatrix} \cdot 1 \text{ mm} \quad (\text{E.47})$$

$$\vec{l}_v(t) \approx \begin{pmatrix} -212.132 \cdot (\gamma_1 + \gamma_2) \\ t \\ 150.0 \cdot (\gamma_1 - \gamma_2) - 212.132\gamma_3 \end{pmatrix} \cdot 1 \text{ mm} \quad (\text{E.48})$$

$$\vec{l}_w(t) \approx \begin{pmatrix} -12.0 \cdot (\gamma_1 - \gamma_2) - 16.9705\gamma_3 \\ 12.0 \cdot (\gamma_1 - \gamma_2) - 16.9705\gamma_3 \\ t \end{pmatrix} \cdot 1 \text{ mm} \quad (\text{E.49})$$

for roll rotations by an angle u around the x -axis, for pitch rotations by an angle v around the y -axis and for yaw rotations by an angle w around the z -axis. t is simply the dimensionless parameter of the line. The solution for l_u is divergent for a perfectly aligned TMA, because the pathlength coupling vanishes and rotations around arbitrary points have zero coupling.

It is noted that the closest approach between the v and w lines occurs for \vec{l}_v at

$$\vec{l}_v \approx \begin{pmatrix} -212.132 \cdot (\gamma_1 + \gamma_2) \\ 12.0 \cdot (\gamma_1 - \gamma_2) - 16.9705\gamma_3 \\ 150.0 \cdot (\gamma_1 - \gamma_2) - 212.132\gamma_3 \end{pmatrix} \cdot 1 \text{ mm} \quad (\text{E.50})$$

and for \vec{l}_w at

$$\vec{l}_w \approx \begin{pmatrix} -12.0 \cdot (\gamma_1 - \gamma_2) - 16.9705\gamma_3 \\ 12.0 \cdot (\gamma_1 - \gamma_2) - 16.9705\gamma_3 \\ 150.0 \cdot (\gamma_1 - \gamma_2) - 212.132\gamma_3 \end{pmatrix} \cdot 1 \text{ mm}, \quad (\text{E.51})$$

which differ slightly in the x -coordinate.

This illustrates that a corner-cube with misaligned mirrors has a non-zero rotation-to-pathlength coupling (for yaw and pitch), even if the pivot point coincides with the true vertex. The arising question on the optimal pivot point for interferometric measurements is addressed in the next subsection.

E.5 Point of Minimal Coupling for a misaligned TMA

The point of minimal coupling (POMC) is the pivot point of rotations, where the rotation-to-pathlength coupling is minimal. As there are (typically) three different rotation types, e.g. roll, pitch and yaw, and the coupling cannot be zeroed at the same time for all of them for a real TMA with mirror misalignments, one needs to define a metric in form of weights.

For example, one seeks for a solution for $\delta x, \delta y, \delta z$ given by the linear eq. (E.44) and quadratic eq. (E.47):

$$\begin{aligned} & \widehat{W} \cdot \left(\begin{array}{c} 1 \frac{\text{mm}}{\text{rad}^2} \cdot \begin{pmatrix} 266.059 & -333.941 & 424.264 \\ -300.0 & +300.0 & 424.264 \\ 24.0 & -24.0 & -33.9411 \end{pmatrix} \\ 1 \frac{\text{mm}}{\text{rad}^3} \cdot \begin{pmatrix} 224.132 & -200.132 & -16.9706 \\ -212.132 & -212.132 & 0 \\ -12.0 & +12.0 & -16.9706 \end{pmatrix} \end{array} \right) \cdot \vec{\gamma} \\ & = -\widehat{W} \cdot \left(\begin{array}{c} \frac{1}{\text{rad}^2} \cdot \begin{pmatrix} 0 & -\gamma_1 + \gamma_2 - \sqrt{2}\gamma_3 & -\sqrt{2}\gamma_1 - \sqrt{2}\gamma_2 \\ \gamma_1 - \gamma_2 + \sqrt{2}\gamma_3 & 0 & 2 \\ \sqrt{2}\gamma_1 + \sqrt{2}\gamma_2 & -2 & 0 \end{pmatrix} \\ \frac{1}{2\text{rad}^3} \cdot \begin{pmatrix} 0 & \sqrt{2} \cdot (\gamma_1 + \gamma_2) & -\gamma_1 + \gamma_2 - \sqrt{2}\gamma_3 \\ -2 & 0 & \gamma_1 - \gamma_2 + \sqrt{2}\gamma_3 \\ -2 & -\sqrt{2} \cdot (\gamma_1 + \gamma_2) & 0 \end{pmatrix} \end{array} \right) \cdot \begin{pmatrix} \delta x \\ \delta y \\ \delta z \end{pmatrix}. \end{aligned} \quad (\text{E.52})$$

A diagonal 6×6 weight matrix \widehat{W} is assumed with weights w_1, w_2, w_3 for the linear terms and with weights w_4, w_5, w_6 for the quadratic terms. The over-determined system can be solved in a least-squares sense, and the solution can be linearized to linear order in γ_i , which yields

$$\vec{\delta}_{\text{POMC}} = \begin{pmatrix} \delta x \\ \delta y \\ \delta z \end{pmatrix} \approx \begin{pmatrix} -\frac{212.13 \cdot (\gamma_1 + \gamma_2) \cdot w_5 + 12.0 \cdot (\gamma_1 - \gamma_2) \cdot w_6 + 16.9706 \cdot \gamma_3 \cdot w_6}{w_5 + w_6} \\ 12.0 \cdot (\gamma_1 - \gamma_2) - 16.9705 \cdot \gamma_3 \\ 150.0 \cdot (\gamma_1 - \gamma_2) - 212.132 \cdot \gamma_3 \end{pmatrix} \cdot 1 \text{ mm/rad}. \quad (\text{E.53})$$

The solution in this approximation does not depend on the weights $w_1..w_4$, thus, not on the information from the roll-coupling (w_1 and w_4). Only the weights w_5 and w_6 appear in the x -component. For equal weights $w_5 = w_6$, the x -component simplifies to $-112.066\gamma_1 - 100.066\gamma_2 - 8.4853\gamma_3$. The result in eq. (E.53) is the point of minimal coupling (POMC), which is given with respect to true vertex, i.e. the position of the POMC is $\vec{\delta}_{\text{POMC}} + \vec{V}_{\text{true}}$. The residual rotation-to-pathlength coupling for rotations around the POMC is to linear order given by

$$\begin{pmatrix} \partial\rho/\partial u \\ \partial\rho/\partial v \\ \partial\rho/\partial w \end{pmatrix} \approx 1 \text{ mm/rad}^2 \cdot \begin{pmatrix} 266.059 & -333.941 & 424.264 \\ 0 & 0 & 0 \\ 0 & 0 & 0 \end{pmatrix} \cdot \vec{\gamma}, \quad (\text{E.54})$$

which was experimentally determined for the GRACE Follow-On TMA in [Schütze, 2014, sec. 4.2.5.1] and agrees well with the here presented formula.

Appendix F

Far-Field of Clipped Gaussian Beams

This appendix chapter contains a derivation of the far-field intensity of a symmetrically clipped Gaussian beam. The derivation uses a scalar field and omits polarization effects or the vectorial nature of light. Moreover, it is assumed that the Gaussian beam is clipped at the waist position with a circular aperture in the xy -plane, while the beam propagates along the z -axis. The intensity I with units of W/m^2 of a non-clipped Gaussian beam at the waist position ($z = 0$) with optical power P is

$$I(x, y, z = 0) = I_{\text{waist}}(x, y) = \frac{2}{\pi \cdot w_0^2} \cdot P \cdot e^{-2(x^2+y^2)/w_0^2}, \quad (\text{F.1})$$

while the far-field (FF) intensity with units of W/m^2 at distance L is given by

$$I(x, y, z = L) = I_{\text{FF}}(x, y) \approx \frac{2}{\pi \cdot L^2 \cdot \theta_{\text{div}}^2} \cdot P \cdot e^{-2(x^2+y^2)/(L \cdot \theta_{\text{div}})^2}, \quad (\text{F.2})$$

where the divergence angle $\theta_{\text{div}} = \lambda/(\pi \cdot \omega_0)$ was used. The $1/e^2$ waist radius is commonly denoted as ω_0 , which is required to be larger than the wavelength λ . The electric field of a Gaussian beam at the waist position can be considered real-valued, because the phasefront is flat. In addition, it is assumed that the electric field E has units of $\sqrt{\text{VA}}/\text{m}$, i.e. the vacuum impedance is absorbed in the electric field. This allows to write the electric field E simply as the square root of the intensity

$$E_{\text{waist}}(x, y) = \sqrt{I_{\text{waist}}(x, y)}. \quad (\text{F.3})$$

From Fourier optics it is well known that the 2-d Fourier transform of the electric field provides a plane wave decomposition, sometimes called the angular spectrum [Goodman, 2005, sec. 3.10.3]. Furthermore, the irradiance (intensity) distribution in the far-field is proportional to the squared modulus of the Fourier transform [Shannon *et al.*, 2005]. This is shown in cartesian coordinates by computing the squared modulus as

$$|\mathcal{F}[E_{\text{waist}}(x, y)](k_x, k_y)|^2 = \left| \int_{x=-\infty}^{+\infty} \int_{y=-\infty}^{+\infty} E_{\text{waist}}(x, y) \cdot e^{-i2\pi(k_x \cdot x + k_y \cdot y)} \, dx \, dy \right|^2 \quad (\text{F.4})$$

$$= 2\pi \cdot P \cdot w_0^2 \cdot e^{-2 \cdot (k_x^2 + k_y^2) \cdot \pi^2 \cdot w_0^2} \quad (\text{F.5})$$

$$= \frac{2 \cdot \lambda^2}{\pi \cdot \theta_{\text{div}}^2} \cdot P \cdot e^{-2 \cdot (k_x^2 + k_y^2) \cdot \lambda^2 / \theta_{\text{div}}^2}. \quad (\text{F.6})$$

By comparing eq. (F.6) and eq. (F.2) one obtains the useful relation of the angular frequencies k_x and k_y to the far-field position as

$$k_x \cdot \lambda = x/L = \theta_x, \quad k_y \cdot \lambda = y/L = \theta_y. \quad (\text{F.7})$$

Furthermore, the far-field intensity can be written as follows

$$I_{\text{FF}}(x, y) = \frac{1}{\lambda^2 \cdot L^2} \cdot \left| \mathcal{F}[E_{\text{waist}}(x, y)](k_x = \frac{x}{\lambda \cdot L}, k_y = \frac{y}{\lambda \cdot L}) \right|^2. \quad (\text{F.8})$$

For symmetrical clipping of the beam at a circular aperture it is advised to use polar coordinates (r, ψ) . In these coordinates, the electric field $E_{\text{waist}}(r, \psi) = E_{\text{waist}}(r \cdot \cos(\psi), r \cdot \sin(\psi))$ can be transformed into the spectral domain with

$$|\mathcal{F}[E_{\text{waist}}(r, \psi)](k_r, k_\psi)|^2 = \left| \int_{r=0}^{+\infty} \int_{\psi=0}^{+2\pi} E_{\text{waist}}(r, \psi) \cdot r \cdot e^{i2\pi k_r \cdot r \cdot \cos(\psi - k_\psi)} \, d\psi \, dr \right|^2 \quad (\text{F.9})$$

$$= \frac{8\pi \cdot P}{\omega_0^2} \left| \int_{r=0}^{+\infty} r \cdot e^{-r^2/\omega_0^2} \cdot J_0(2\pi k_r \cdot r) \, dr \right|^2 \quad (\text{F.10})$$

$$= 2\pi \cdot P \cdot \omega_0^2 \cdot e^{-2k_r^2 \cdot \pi^2 \cdot \omega_0^2} \quad (\text{F.11})$$

$$= \frac{2P \cdot \lambda^2}{\pi \cdot \theta_{\text{div}}^2} \cdot e^{-2k_r^2 \cdot \lambda^2 / \theta_{\text{div}}^2}, \quad (\text{F.12})$$

where $J_0(x)$ is the Bessel function of first kind. Again, the far-field intensity is obtained by multiplying the squared modulus of the Fourier transform with $1/(L^2 \cdot \lambda^2)$:

$$I_{\text{FF}} = \frac{1}{\lambda^2 \cdot L^2} \cdot |\mathcal{F}[E_{\text{waist}}(r, \psi)](k_r, k_\psi)|^2. \quad (\text{F.13})$$

Furthermore, the angular component k_r can be written as

$$k_r \cdot \lambda = \sqrt{\theta_x^2 + \theta_y^2} = \sqrt{x^2 + y^2}/L. \quad (\text{F.14})$$

To account for clipping, the electric field E_{waist} needs to be multiplied with the transmittance function of the circular aperture, which is a rectangular box function in radial direction. The radius of the clipping aperture is labeled as r_{ap} . Hence, the far-field behind the aperture can be determined by changing the integral limit from $+\infty$ to r_{ap} in eq. (F.10) to account for the aperture, i.e.

$$I_{\text{FF}}(k_r) = \frac{1}{\lambda^2 \cdot L^2} \cdot \frac{8\pi \cdot P}{\omega_0^2} \left| \int_{r=0}^{r_{\text{ap}}} r \cdot e^{-r^2/\omega_0^2} \cdot J_0(2\pi k_r \cdot r) \, dr \right|^2 \quad (\text{F.15})$$

$$I_{\text{FF}}(x, y) = \frac{1}{\lambda^2 \cdot L^2} \cdot \frac{8\pi \cdot P}{\omega_0^2} \left| \int_{r=0}^{r_{\text{ap}}} r \cdot e^{-r^2/\omega_0^2} \cdot J_0(2\pi/\lambda \cdot \sqrt{x^2 + y^2}/L \cdot r) \, dr \right|^2. \quad (\text{F.16})$$

It is remarked that the same integral as in eq. (F.16) appeared in sec. 2.6.11 on the heterodyne efficiency, where a polynomial approximation was derived. It will be utilized subsequently. Moreover, to avoid confusion, we write the power P more precisely as the power of the beam prior clipping P_{PC} and we label the $1/e^2$ waist radius ω_0 as the non-clipped Gaussian (ncg) quantity $\omega_{0,\text{ncg}}$.

Unfortunately, there is no general analytical solution for the integral in eq. (F.16). A special case for the on-axis intensity, $k_r = 0$, can be obtained as

$$I_{\text{FF,OnAxis}} = \frac{P_{\text{PC}}}{L^2} \cdot \frac{2\pi \cdot \omega_{0,\text{ncg}}^2}{\lambda^2} \cdot \left(1 - e^{-r_{\text{ap}}^2/\omega_{0,\text{ncg}}^2} \right)^2, \quad (\text{F.17})$$

which agrees with well-known results as, for example, given in [Barke, 2015, p. 34]. The on-axis intensity can be maximized for a given aperture radius r_{ap} with

$$\omega_{0,\text{ncg}} = 0.892135 \cdot r_{\text{ap}}, \quad (\text{F.18})$$

which is independent of the used wavelength. The result is well known from the LISA mission concept, where the transmit Gaussian beam is clipped due to the finite size of the telescope. It

states the optimal relation of telescope size to transmit beam waist radius after magnification (but before or without clipping), i.e. the waist radius at the telescope input plane $\omega_{0,\text{in}}$ times the telescope magnification (m).

The optical power within the aperture P_{ap} can be computed as

$$P_{\text{ap}} = P_{\text{PC}} - P_{\text{rej}} = P_{\text{PC}} \cdot \left(1 - e^{-2 \cdot r_{\text{ap}}^2 / \omega_{0,\text{ncg}}^2}\right), \quad (\text{F.19})$$

which is slightly different from the factor appearing in eq. (F.17). The term P_{rej} is called the rejected power by the aperture or by the telescope throughout this thesis.

The two left panels in fig. F.1 show the dimensionless far-field intensity as a function of r_{ap} and of the non-clipped Gaussian (ncg) $1/e^2$ radius $\omega_{0,\text{ncg}} = \omega_{0,\text{in}} \cdot m$. The optimal ratio as specified in eq. (F.18) is shown as magenta line. On this line approx. 8% of the power is rejected due to the aperture, which is shown on the right side of fig. F.1. Losses higher than 20% are considered as unpractical and are left blank in the right panels.

Combining eq. (F.19) and (F.17) yields with the help of a complex identity for the hyperbolic tangent:

$$I_{\text{FF,OnAxis}} = \frac{P_{\text{ap}}}{L^2} \cdot \frac{2\pi \cdot \omega_{0,\text{ncg}}^2}{\lambda^2} \cdot \tanh\left(\frac{r_{\text{ap}}^2}{2\omega_{0,\text{ncg}}^2}\right) = \frac{P_{\text{ap}}}{L^2} \cdot \frac{2}{\pi \cdot \theta_{\text{ncg}}^2} \cdot \tanh\left(\frac{r_{\text{ap}}^2}{2\omega_{0,\text{ncg}}^2}\right). \quad (\text{F.20})$$

The dependency of the far-field intensity as a function of the beam misalignment $\theta \approx r/L$ has been computed by numerical integration of eq. (F.16). The result is shown in the two left panels of fig. F.2 for two different aperture radii r_{ap} . The misalignment angle θ on the x -axis is expressed in units of the divergence angle of the non-clipped Gaussian beam $\theta_{\text{ncg}} = \lambda/(\pi \cdot \omega_{0,\text{ncg}})$, while the waist radius $\omega_{0,\text{ncg}}$ on the y -axis is expressed in units of the clipping aperture radius r_{ap} . The intensity (and color function) is normalized to unity at $\theta = 0$.

The upper parts ($\omega_{0,\text{ncg}}/r_{\text{ap}} < 0.5$) of the left plots in fig. F.2, where the clipping aperture is significantly larger than the beam, show a Gaussian intensity decay with $1/e^2$ radius given by θ_{ncg} , i.e. the intensity drops to $1/e^2$ for $\theta/\theta_{\text{ncg}} = 1$. However, if the beam size is comparable or larger than the clipping aperture, the divergence of the clipped beam increases due to diffraction. The divergence angle, i.e. the angle where the far-field intensity dropped to a level of $1/e^2$, is shown as blue trace in fig. F.3. A polynomial fit up to 6th order has been performed, which yields the red trace.

This allows to write the far-field intensity of a clipped Gaussian beam as a function of the beam misalignment θ as

$$I_{\text{FF}}(\theta) = \frac{P_{\text{PC}}}{L^2} \cdot \frac{2\pi \cdot \omega_{0,\text{ncg}}^2}{\lambda^2} \cdot \left(1 - e^{-r_{\text{ap}}^2 / \omega_{0,\text{ncg}}^2}\right)^2 \cdot e^{-2\theta^2 / (\theta_{\text{ncg}} \cdot \psi(\omega_{0,\text{ncg}}/r_{\text{ap}}))^2}, \quad (\text{F.21})$$

$$= \frac{P_{\text{ap}}}{L^2} \cdot \frac{2\pi \cdot \omega_{0,\text{ncg}}^2}{\lambda^2} \cdot \tanh\left(\frac{r_{\text{ap}}^2}{2\omega_{0,\text{ncg}}^2}\right) \cdot e^{-2\theta^2 / (\theta_{\text{ncg}} \cdot \psi(\omega_{0,\text{ncg}}/r_{\text{ap}}))^2}, \quad (\text{F.22})$$

where the function $\psi(x) = \sum_{i=0}^6 p_i \cdot x^i$ and the coefficients p_i are given in table 2.8 in sec. 2.6.10. The function $\psi(x)$ does not depend on the used wavelength λ for practical considerations¹ and provides an approximation for the actual far-field divergence θ_{div} of the clipped Gaussian beam via

$$\theta_{\text{div}} = \theta_{\text{ncg}} \cdot \psi(\omega_{0,\text{ncg}}/r_{\text{ap}}). \quad (\text{F.23})$$

The absolute accuracy of eq. (F.21) is better than 0.04 for reasonable input parameters, which is as shown on the two right panels in fig. F.2. However, for large misalignment angles and a small intensity with respect to the on-axis intensity, where $\psi < 0.1$, the relative accuracy of the model is poor and the ψ -approximation should be replaced by a precise (numerical) solution of the integral eq. (F.16).

¹as long as the wavelength is larger than the waist size of the beam.

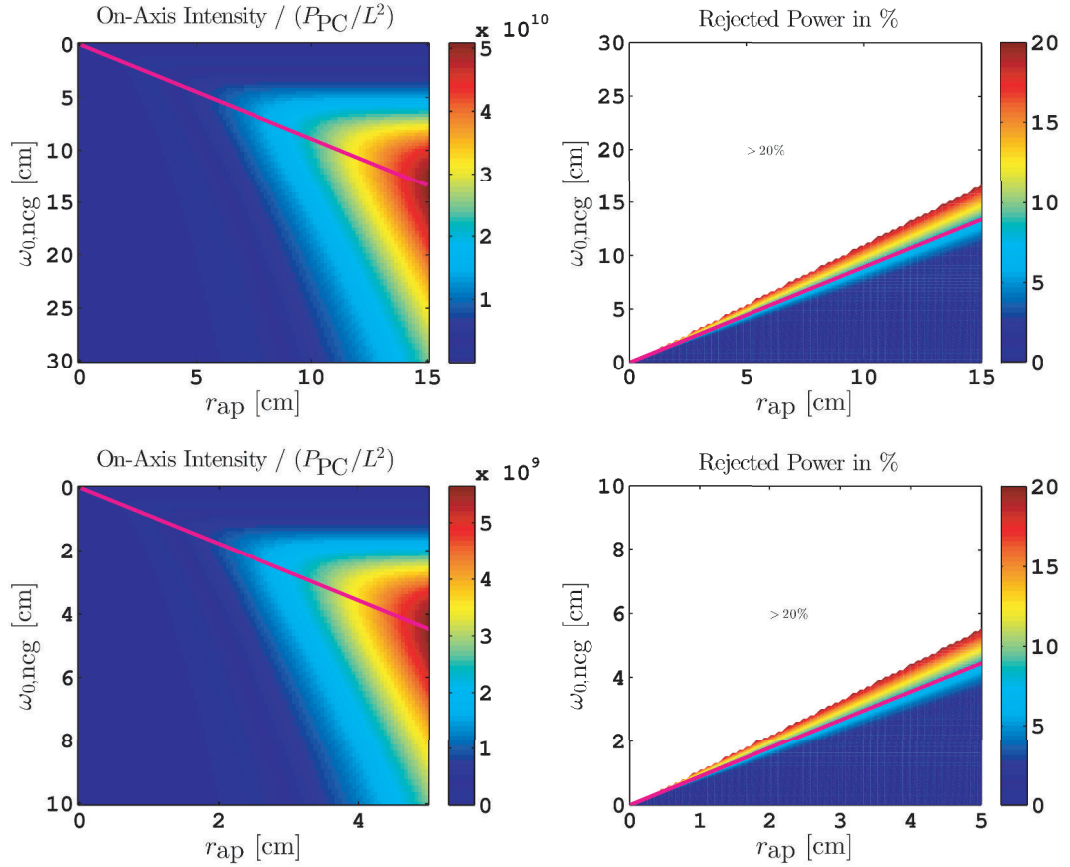


Figure F.1: The two left panels show the dimensionless far-field on-axis intensity as a function of the clipping aperture radius r_{ap} and of the non-clipped Gaussian (ncg) $1/e^2$ radius ω_0 . To obtain an intensity with units of W/m^2 , the color function needs to be multiplied with the optical power P_{PC} of the non-clipped beam and divided by the squared distance L^2 . The maximum intensity for a particular r_{ap} is shown as magenta line. The two right panels show the loss (or rejection) due to the aperture in terms of optical power. The color function is clipped at 20% to improve readability. The upper and lower subplots differ only in the shown parameter space. A wavelength of 1064 nm was used in these plots, which scales the absolute value (colorbar) on the left panels.

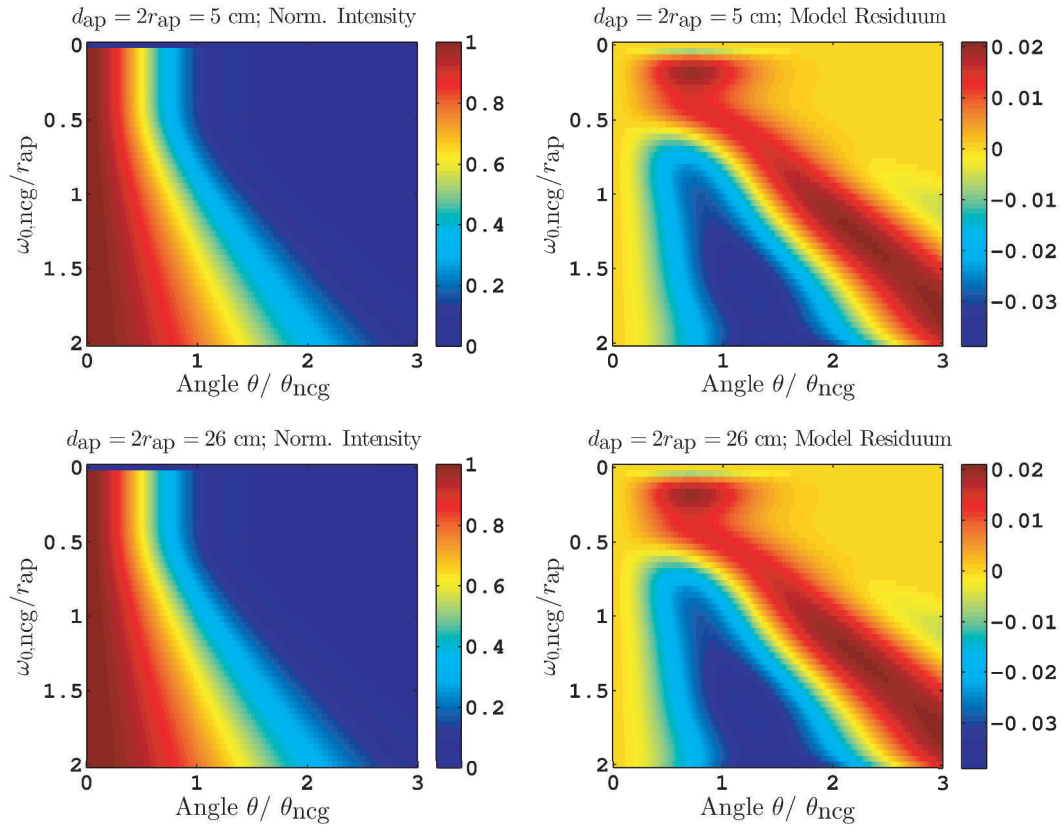


Figure F.2: The two left panels show the normalized far-field intensity drop upon misalignment by angle θ as a function of the Gaussian beam radius $\omega_{0,\text{ncg}}$. The right panels show the residuum, if a Gaussian model is subtracted from the intensity shown on the left side. The upper and lower subplots differ only in the shown parameter space. Due to the normalization, these plots are independent of the wavelength.

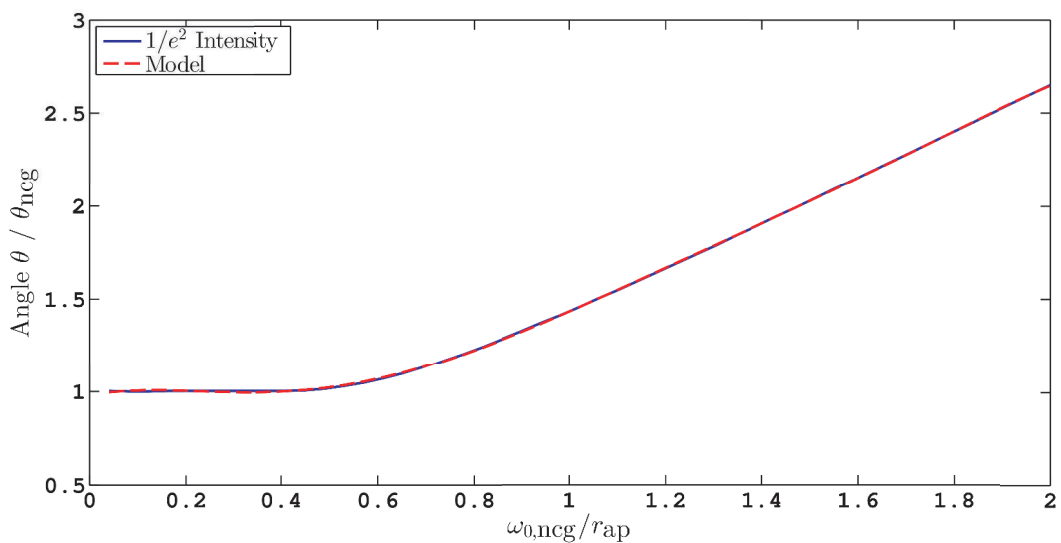


Figure F.3: Far-field divergence angle of a clipped Gaussian beam as a function of the clipping parameter $\omega_{0,\text{ncg}} / r_{\text{ap}}$. This plot is independent of the wavelength.

Curriculum Vitae

Vitali Müller

CONTACT
INFORMATION

Havemannstr. 5
30165 Hannover, Germany
E-Mail: mail@vimu.de
Born on 6th January 1986 in Omsk/Russia

EDUCATION

University of Hannover, Germany

PhD student, research assistant, and QUEST HALOSTAR stipend holder at the Max Planck Institute for Gravitational Physics (Albert Einstein Institute) and the Institute for Gravitational Physics, Leibniz Universität Hannover (Germany), 2013-2017

- Thesis Topic: *Design Considerations for Future Geodesy Missions and for Space Laser Interferometry*, July 2017

Master of Science in Physics, 2010-2013; Master thesis at the Max Planck Institute for Gravitational Physics (Albert Einstein Institute) and the Institute for Gravitational Physics, Leibniz Universität Hannover (Germany)

- Thesis Topic: *Simulations for LISA & GRACE-Follow-On: Satellite constellations at Lagrangian points for LISA-like missions & Interferometer simulations for the GRACE Follow-On mission*, April 2013

Bachelor of Science in Physics, 2007-2010; Bachelor thesis at the Max Planck Institute for Gravitational Physics (Albert Einstein Institute) and the Institute for Gravitational Physics, Leibniz Universität Hannover (Germany)

- Thesis Topic: *Orbit Simulation Toolkit - OSTK - Documentation of Models, Methods and Implementation*, September 2010

Clemens August Gymnasium, Cloppenburg, Germany

Abitur, secondary school education, 2001-2006

Kolleg Sankt Thomas Gymnasium, Vechta, Germany

Secondary school education, 1997-2001

Grundschule Essen i.O. and Grundschule Bevern, Germany

Primary school education, 1993-1997

REFEREED
JOURNAL
PUBLICATIONS

1. D. Schütze, G. Stede, V. Müller, O. Gerberding, T. Bandikova, B. S. Sheard, G. Heinzel, and K. Danzmann “Laser beam steering for GRACE Follow-On intersatellite interferometry.” *Opt. Express*, 22, 24117-24132 (2014).
2. D. Schütze, V. Müller, and G. Heinzel, “Precision absolute measurement and alignment of laser beam direction and position”, *Appl. Opt.* 53, 6503-6507 (2014).
3. Daniel Schütze, Vitali Müller, Gunnar Stede, Benjamin S. Sheard, Gerhard Heinzel, Karsten Danzmann, Andrew J. Sutton, and Daniel A. Shaddock, “Retroreflector for GRACE follow-on: Vertex vs. point of minimal coupling”, *Opt. Express* 22, 9324-9333 (2014).
4. Kochkina, Evgenia and Heinzel, Gerhard and Wanner, Gudrun and Müller, Vitali and Mahrtdt, Christoph and Sheard, Benjamin and Schuster, Sönke and Danzmann, Karsten, “Simulating and optimizing laser interferometers”, *Proc. of the 9th LISA Symposium, Link* (2013).
5. Y. Wang, D. Keitel, S. Babak, A. Petiteau, M. Otto, S. Barke, F. Kawazoe, A. Khalaidovski, V. Müller, D. Schütze, H. Wittel, K. Danzmann, and B. F. Schutz, “Octahedron configuration for a displacement noise-cancelling gravitational wave detector in space”, *Phys. Rev. D* 88, 104021 (2013).

PUBLISHED
REPORTS

1. Gruber, Th.; Murböck, M.; NGGM-D Team: “e.motion: Earth System Mass Transport Mission (Square) - Concept for a Next Generation Gravity Field Mission”; Deutsche Geodätische Kommission der Bayerischen Akademie der Wissenschaften, Reihe B, *Angewandte Geodäsie*, Vol. 2014, Heft 318, C.H. Beck, ISBN (Print) 978-3-7696-8597-8, ISSN 0065-5317, 2014; Chapter 5 by V. Müller

Acknowledgments

I have joined the Albert-Einstein-Institute in Hannover in my third semester as an undergraduate physics student. Since the first day, I have enjoyed every day in this pleasant and professional environment, which allowed me to learn from world-class scientists, which continuously feeds my curiosity through the talks, lectures and discussions with colleagues and which has shaped me in the last years.

This open-minded and unique place is the merit of Prof. Dr. Karsten Danzmann to whom I am very thankful for giving me the opportunity to be part of it, for holding exciting lectures in my first semesters and for his supervision and mentoring.

I owe deep gratitude to my direct supervisor Prof. Dr. Gerhard Heinzel, who is my teacher, mentor and colleague. His ideas, experience, patience and sessions of playing devil's advocate motivated me and enabled this thesis.

I would like to thank my colleagues and friends in the GRACE Follow-On LRI group for the enjoyable atmosphere, sharing of ideas, support and fruitful discussions: Alexander Görth, Germán Fernández Barranco, Gunnar Stede and my former colleagues Benjamin Sheard, Christina Bogan, Christoph Mahrtdt and Daniel Schütze.

I wish to express my gratitude to Heather Audley and Olaf Hartwig for proof reading my thesis. Your help is highly appreciated.

Moreover, I thank the research school IMPRS, geo-Q, QUEST and QUEST Halostar for supporting me in the last years.

Last but not least, I am very lucky to have my patient and supportive wife and my encouraging parents. Thank you all!

The author would like to thank the DFG Sonderforschungsbereich (SFB 1128: geo-Q) Relativistic Geodesy and Gravimetry with Quantum Sensors, for financial support. The author was supported by the centre for Quantum Engineering and Space Time research (QUEST) at University of Hannover, Germany.

Bibliography

- AEI-TN. 2011. *Internal Report: Optical Bench EBB Design Definition File, Opto-Electronics & Alternative Beam Compressors*. technical note. Albert-Einstein-Institut Hannover. LOB-AEI-TN-008.
- Ai, Chiayu, & Smith, Kenneth L. 1992. Accurate measurement of the dihedral angle of a corner cube. *Appl. Opt.*, **31**(4), 519–527.
- Alenia-Team. 2008. *GO-TN-AI-0027: Performance Requirements And Budgets For The Gradiometric Mission*. Tech. rept. Thales-Alenia Space.
- Alenia-Team. 2010. *Assessment of a Next Generation Mission for Monitoring the Variations of Earth's Gravity (SD-RP-AI-0688. 22/DEC/2010)*. Tech. rept. Thales Alenia Space.
- Ales, Filippo, Gath, Peter F, Fitzsimons, Ewan D, Dörr, Simon, Johann, Ulrich, & Braxmaier, Claus. 2014. Designing & Simulating Signal Acquisition for Inter-Satellite Laser Links. *In: Proceedings of the 10th LISA Symposium, Florida*.
- Ales, Filippo, Mandel, Oliver, Gath, Peter, Johann, Ulrich, & Braxmaier, Claus. 2015. A phasemeter concept for space applications that integrates an autonomous signal acquisition stage based on the discrete wavelet transform. *Review of Scientific Instruments*, **86**(8).
- Alloin, D.M., & Mariotti, J.M. 1994. *Adaptive Optics for Astronomy*. Springer.
- Alnis, J., Matveev, A., Kolachevsky, N., Udem, Th., & Hänsch, T. W. 2008. Subhertz linewidth diode lasers by stabilization to vibrationally and thermally compensated ultralow-expansion glass Fabry-Pérot cavities. *Phys. Rev. A*, **77**(May), 053809.
- Apfel, Joseph H. 1982. Phase retardance of periodic multilayer mirrors. *Appl. Opt.*, **21**(4), 733–738.
- Armano, M, *et al.* 2015. A Strategy to Characterize the LISA-Pathfinder Cold Gas Thruster System. *Journal of Physics: Conference Series*, **610**(1), 012026.
- Armano, M., *et al.* 2016a. Constraints on LISA Pathfinder's self-gravity: design requirements, estimates and testing procedures. *Classical and Quantum Gravity*, **33**(23), 235015.
- Armano, M., *et al.* 2016b. Sub-Femto-*g* Free Fall for Space-Based Gravitational Wave Observatories: LISA Pathfinder Results. *Phys. Rev. Lett.*, **116**(Jun), 231101.
- Babar, Shaista, & Weaver, J. H. 2015. Optical constants of Cu, Ag, and Au revisited. *Appl. Opt.*, **54**(3), 477–481.
- Bandikova, T. 2015. *The Role of Attitude Determination for Inter-satellite Ranging*. Ph.D. thesis, Fachrichtung Geodäsie und Geoinformatik der Leibniz Universität Hannover.
- Bandikova, Tamara, & Flury, Jakob. 2014. Improvement of the GRACE star camera data based on the revision of the combination method. *Advances in Space Research*, **54**(9), 1818 – 1827.

- Barke, S. 2015. *Inter-Spacecraft Frequency Distribution for Future Gravitational Wave Observatories*. Ph.D. thesis, Leibniz Universität Hannover, Albert-Einstein-Institut.
- Barke, S., Brause, N., Bykov, I., Esteban Delgado, J. J., Enggaard, A., Gerberding, O., Heinzl, G., Kullmann, J., Pedersen, S. M., & Rasmussen, T. 2014. *LISA metrology system-final report*. Tech. rept. DTU Space / AEI Hannover / Axcon ApS / ESA. available at <http://hdl.handle.net/11858/00-001M-0000-0023-E266-6>.
- Barranco, Germán Fernández, Gerberding, Oliver, Schwarze, Thomas S., Sheard, Benjamin S., Dahl, Christian, Zender, Bernd, & Heinzl, Gerhard. 2017. Phase stability of photoreceivers in intersatellite laser interferometers. *Opt. Express*, **25**(7), 7999–8010.
- Barrett, Brynle, Geiger, Rémy, Dutta, Indranil, Meunier, Matthieu, Canuel, Benjamin, Gauguet, Alexandre, Bouyer, Philippe, & Landragin, Arnaud. 2014. The Sagnac effect: 20 years of development in matter-wave interferometry. *Comptes Rendus Physique*, **15**(10), 875 – 883. The Sagnac effect: 100 years later / L’effet Sagnac : 100 ans après.
- Barthelmes, F. 2009. *Definition of Functionals of the Geopotential and Their Calculation from Spherical Harmonic Models: Theory and Formulas Used by the Calculation Service of the International Centre for Global Earth Models (ICGEM)*. Tech. rept. GFZ, Helmholtz-Zentrum, ICGEM.
- Baur, O., Bock, H., Höck, E., Jäggi, A., Krauss, S., Mayer-Gürr, T., Reubelt, T., Siemes, C., & Zehentner, N. 2014. Comparison of GOCE-GPS gravity fields derived by different approaches. *Journal of Geodesy*, **88**(10), 959–973.
- Bender, P. L., Wiese, D. N., & Nerem, R. S. 2008. A possible Dual-GRACE mission with 90 degree and 63 degree inclination orbits. *In: Proceedings, 3rd International Symposium on Formation Flying, Missions and Technologies. European Space Agency Symposium Proceedings, ESA SP-654*. Noordwijk, The Netherlands: ESA, for ESA. JILA Pub. 8161.
- Bender, PL, Brilliet, A, Ciufolini, I, Cruise, AM, Cutler, C, Danzmann, Karsten, Folkner, WM, Hough, J, McNamara, PW, Peterseim, M, *et al.* 1998. *LISA. Laser Interferometer Space Antenna for the detection and observation of gravitational waves. An international project in the field of Fundamental Physics in Space*. Tech. rept. Max-Planck-Institut für Quantenoptik.
- Bender, P.L., Nerem, R.S., & Wahr, J.M. 2003. Possible Future Use of Laser Gravity Gradiometers. *Space Science Reviews*, **108**(1-2), 385–392.
- Bertiger, W. I., Bar-Sever, Y. E., Christensen, E. J., Davis, E. S., Guinn, J. R., Haines, B. J., Ibanez-Meier, R. W., Jee, J. R., Lichten, S. M., Melbourne, W. G., Muellerschoen, R. J., Munson, T. N., Vigue, Y., Wu, S. C., Yunck, T. P., Schutz, B. E., Abusali, P. A. M., Rim, H. J., Watkins, M. M., & Willis, P. 1994. GPS precise tracking of TOPEX/POSEIDON: Results and implications. *Journal of Geophysical Research: Oceans*, **99**(C12), 24449–24464.
- Bettadpur, Srinivas. 2009. *Recommendation for a-priori Bias & Scale Parameters for Level-1B ACC Data (Version 2)*. Tech. rept. JPL.
- Bezdek, A., Sebera, J., Klokočnik, J., & Kostelecký, J. 2014. Gravity field models from kinematic orbits of CHAMP, GRACE and GOCE satellites. *Advances in Space Research*, **53**(3), 412–429.
- Bieg, B. 2015. Polarization properties of a metal corner-cube retroreflector. *Fusion Engineering and Design*, **96**, 729–732.

- BIPM. 2007. *Recommended Values Of Standard Frequencies For Applications Including The Practical Realization Of The Metre And Secondary Representations Of The Definition Of The Second*. Tech. rept. Bureau International des Poids et Mesures (BIPM). available at http://www.bipm.org/utils/common/pdf/mep/M-e-P_I2_532.pdf.
- Björck, A. 1996. *Numerical Methods for Least Squares Problems*. Society for Industrial and Applied Mathematics.
- Boisvert, Joseph, Isshiki, Takahiro, Sudharsanan, Rengarajan, Yuan, Ping, & McDonald, Paul. 2008. Performance of very low dark current SWIR PIN arrays. *Pages 69400L–69400L of: SPIE Defense and Security Symposium*. International Society for Optics and Photonics.
- Boroson, Don M. 1993. LITE engineering model-I: operation and performance of the communications and beam-control subsystems. *Proc. SPIE*, **1866**, 73–82.
- Brugger, Christina, Broll, Bernhard, Fitzsimons, Ewan, Johann, Ulrich, Jonke, Wouter, Lucarelli, Stefano, Nikolov, Susanne, Voert, Martijn, Weise, Dennis, & Witvoet, Gert. 2014. An Experiment to test In-Field Pointing for eLISA. *Page 10 of: Proc of the International Conference on Space Optics*, vol. 7.
- Bykov, Iouri, Delgado, Esteban, Jose, Juan, Marin, Antonio Francisco Garcia, Heinzl, Gerhard, & Danzmann, Karsten. 2009. LISA phasemeter development: advanced prototyping. *In: Journal of Physics: Conference Series*, vol. 154.
- Canuto, Enrico S. 2008. Drag-free and attitude control for the GOCE satellite. *Automatica*, **44**(7), 1766–1780.
- Carter, William H. 1972. Electromagnetic field of a Gaussian beam with an elliptical cross section. *JOSA*, **62**(10), 1195–1201.
- Case, K., G., Kruizinga, & Wu, S.-C. 2010. *GRACE Level 1B Data Product User Handbook*. Tech. rept. Jet Propulsion Laboratory, California Institute of Technology.
- Cervantes, F Guzman, Livas, J, Silverberg, R, Buchanan, E, & Stebbins, R. 2011. Characterization of photoreceivers for LISA. *Classical and Quantum Gravity*, **28**(9), 094010.
- Cesare, S. 2002. *Performance Requirements And Budgets For The Gradiometric Mission*. Tech. rept. Thales-Alenia Space. GO-TN-AI-0027.
- Chen, Haiqin, Jiang, Yanyi, Fang, Su, Bi, Zhiyi, & Ma, Longsheng. 2013. Frequency stabilization of Nd:YAG lasers with a most probable linewidth of 0.6 Hz. *J. Opt. Soc. Am. B*, **30**(6), 1546–1550.
- Chen, J. L., & Wilson, C. R. 2008. Low degree gravity changes from GRACE, Earth rotation, geophysical models, and satellite laser ranging. *Journal of Geophysical Research: Solid Earth*, **113**(B6).
- Chen, J.L., Wilson, C.R., & Seo, Ki-Weon. 2009. S2 tide aliasing in GRACE time-variable gravity solutions. *Journal of Geodesy*, **83**(7), 679–687.
- Cheng, Minkang, Ries, John C., & Tapley, Byron D. 2011. Variations of the Earth’s figure axis from satellite laser ranging and GRACE. *Journal of Geophysical Research: Solid Earth*, **116**(B1).
- Chengalur, J.N., Gupta, Y., & Dwarakanath, K.S. 2007. *Low Frequency Radio Astronomy*. National Centre for Radio Astrophysics. textbook.

- Choy, T.C. 2016. *Effective Medium Theory: Principles and Applications*. International Series of Monographs on Physics. Oxford University Press.
- Christophe, B. 2013. GRACE & GOCE experience. *In: Proceedings of MICROSCOPE colloquium II, Paris, 29-30 January 2013*.
- Chwalla, M, Danzmann, K, Barranco, G Fernández, Fitzsimons, E, Gerberding, O, Heinzl, G, Killow, C J, Lieser, M, Perreux-Lloyd, M, Robertson, D I, Schuster, S, Schwarze, T S, Tröbs, M, Ward, H, & Zwetz, M. 2016. Design and construction of an optical test bed for LISA imaging systems and tilt-to-length coupling. *Classical and Quantum Gravity*, **33**(24), 245015.
- Ciddor, Philip E. 1996. Refractive index of air: new equations for the visible and near infrared. *Applied optics*, **35**(9), 1566–1573.
- Dahle, C., Flechtner, F., Gruber, C., König, D., König, R., Michalak, G., & Neumayer, K.-H. 2012. *GFZ GRACE Level-2 Processing Standards Document for Level-2 Product Release 0005*. Tech. rept. GFZ. available at <http://doi.org/10.2312/GFZ.b103-12020>.
- Dahle, Christoph, Flechtner, Frank, Gruber, Christian, König, Daniel, König, Rolf, Michalak, Grzegorz, & Neumayer, Karl-Hans. 2014. GFZ RL05: An Improved Time-Series of Monthly GRACE Gravity Field Solutions. *Pages 29–39 of: Observation of the System Earth from Space - CHAMP, GRACE, GOCE and future missions*. Advanced Technologies in Earth Sciences. Springer Berlin Heidelberg.
- Danzmann, K., *et al.* 2017. *Laser Interferometer Space Antenna (LISA): A proposal in response to the ESA call for L3 mission concept*. Tech. rept. LISA Consortium. available at https://www.elisascience.org/files/publications/LISA_L3_20170120.pdf.
- Danzmann, Karsten, *et al.* 2007. *LISA Pathfinder: Einstein's Geodesic Explorer*. Tech. rept. ESA. available at <http://sci.esa.int/science-e/www/object/doc.cfm?fobjectid=40573>.
- d'Arcio, L, Bogenstahl, J, Dehne, M, Diekmann, C, Fitzsimons, ED, Fleddermann, R, Granova, E, Heinzl, G, Hogenhuis, H, Killow, CJ, *et al.* 2010. Optical bench development for LISA. *In: ICSO 2010-International Conference on Space Optics*.
- Dehne, Marina, Cervantes, Felipe Guzmán, Sheard, Benjamin, Heinzl, Gerhard, & Danzmann, Karsten. 2009. Laser interferometer for spaceborne mapping of the Earth's gravity field. *Journal of Physics: Conference Series*, **154**(1), 012023.
- Delay, Michael. 2015. *Whitepaper: Practical Aspects of Mirror Usage in Optical Systems for Biology – Part1*. Tech. rept. Semrock Inc.
- Delgado, Esteban. 2012. *Laser ranging and data communication for the laser interferometer space antenna*. Ph.D. thesis, Granada: Universidad de Granada; Albert-Einstein-Institut.
- Delva, P., Meynadier, F., Le Poncin-Lafitte, C., Laurent, P., & Wolf, P. 2012 (April). Time and frequency transfer with a MicroWave Link in the ACES/PHARAO mission. *Pages 28–35 of: European Frequency and Time Forum (EFTF), 2012*.
- Diekmann, Christian. 2013. *Development of Core Elements for the LISA Optical Bench: Electro-optical Measurement Systems and Test Devices*. Ph.D. thesis, Gottfried Wilhelm Leibniz Universität Hannover, Albert-Einstein-Institut.
- Dinges, H.W., Burkhard, H., Lösch, R., Nickel, H., & Schlapp, W. 1992. Refractive indices of InAlAs and InGaAs/InP from 250 to 1900 nm determined by spectroscopic ellipsometry. *Applied Surface Science*, **54**, 477 – 481.

- Ditmar, Pavel, Teixeira da Encarnação, João, & Hashemi Farahani, Hassan. 2012. Understanding data noise in gravity field recovery on the basis of inter-satellite ranging measurements acquired by the satellite gravimetry mission GRACE. *Journal of Geodesy*, **86**(6), 441–465.
- Dobslaw, Henryk, Bergmann-Wolf, Inga, Dill, Robert, Forootan, Ehsan, Klemann, Volker, Kusche, Jürgen, & Sasgen, Ingo. 2015. The updated ESA Earth System Model for future gravity mission simulation studies. *Journal of Geodesy*, **89**(5), 505–513.
- Doornbos, E., Förster, M., Fritsche, B., van Helleputte, T., van den IJssel, J., Koppenwallner, G., Lühr, H., Rees, D., & Visser, P. 2009. *ESTEC contract 21022/07/NL/HE Air density models derived from multi-satellite drag observations – Final Report*. Tech. rept. DEOS / TU Delft scientific report 01/2009. TU Delft.
- Doringshoff, K., Mohle, K., Nagel, M., Kovalchuk, E.V., & Peters, A. 2010 (April). High performance iodine frequency reference for tests of the LISA laser system. *Pages 1–6 of: EFTF-2010 24th European Frequency and Time Forum*.
- Drever, R.W.P., Hall, J.L., Kowalski, F.V., Hough, J., Ford, G.M., Munley, A.J., & Ward, H. 1983. Laser phase and frequency stabilization using an optical resonator. *Applied Physics B*, **31**(2), 97–105.
- Dunn, C., Bertiger, W., Bar-Sever, Y., Desai, S., Haines, B., Kuang, D., Franklin, G., Harris, I., Kruizinga, G., Meehan, T., Nandi, S., Nguyen, D., Rogstad, T., Thomas, J.B., Tien, J., Romans, L., Watkins, M., Wu, S.-C., Bettadpur, S., & Kim, J. 2003. Instrument of Grace. *GPS World*, March.
- Edwards, CH., Wallace, N.C., Tato, C., & van Put, P. 2004. The T5 ion propulsion assembly for drag compensation on GOCE. In: *Second International GOCE User Workshop "GOCE, The Geoid and Oceanography"*.
- Einstein, A. 1916. *Näherungsweise Integration der Feldgleichungen der Gravitation*. Sitzungsberichte der Königlich Preussischen Akademie der Wissenschaften zu Berlin. Verlag der Königlich Akademie der Wissenschaften.
- Eisele, A. 2014. *Millimeter-Precision Laser Rangefinder Using a Low-Cost Photon Counter*. Karlsruhe Series in Photonics and Communications / Karlsruhe Institute of Technology, Institute of Photonics and Quantum Electronics (IPQ). KIT Scientific Publishing.
- eLISA/NGO Team. 2012. *NGO Assessment Study Report (Yellow Book) ESA/SRE (2011) 19*. Tech. rept. European Space Agency.
- Elliffe, EJ, Bogenstahl, Johanna, Deshpande, Amruta, Hough, James, Killow, Christian, Reid, Stuart, Robertson, David, Rowan, Sheila, Ward, Harry, & Cagnoli, Geppo. 2005. Hydroxide-catalysis bonding for stable optical systems for space. *Classical and Quantum Gravity*, **22**(10), S257.
- Ellmer, Matthias. 2011. *Optimization of the orbit parameters of future gravity missions using genetic algorithms*. MSc thesis, Universität Stuttgart, Holzgartenstr. 16, 70174 Stuttgart.
- Elsaka, Basem. 2010. *Simulated satellite formation flights for detecting the temporal variations of the Earth's gravity field*. Ph.D. thesis, Bonn, Univ., Diss., 2010.
- e.motion Team. 2010. *e.motion: Earth System Mass Transport Mission*. Tech. rept. Nansen Environmental and Remote Sensing Center, Norway. In Response to Call for Proposals for Earth Explorer Opportunity Mission EE-8 (ESA/EXPLORER/COM-3/EE-8 October 2009).

- e.motion² Team. 2014. *e.motion square: Earth System Mass Transport Mission (Square) - Concept for a Next Generation Gravity Field Mission* -. DKG Reihe B. Final Report of Project “Satellite Gravimetry of the Next Generation (NGGM-D)”; B 318; available at https://dgk.badw.de/fileadmin/user_upload/Files/DGK/docs/b-318.pdf.
- Esterhuizen, S., Franklin, G., Hurst, K., Mannucci, A., Meehan, T., Webb, F., & Young, L. 2009. TriG-A GNSS Precise Orbit and Radio Occultation Space Receiver. *In: Proc of the 22nd International Technical Meeting Of The Satellite Division Of The Institute Of Navigation (IonGnss2009)*. Institute of Navigation.
- Fackler, U. 2005. *GRACE - Analyse von Beschleunigungsmessungen*. Diploma thesis, IAPG, TU München. IAPG-FESG no. 20.
- Ferre-Pikal, Eva S., & Walls, Fred L. 2001. *Frequency Standards, Characterization*. John Wiley & Sons, Inc.
- Feynman, R.P., Leighton, R.B., & Sands, M. 2013. *The Feynman Lectures on Physics, Desktop Edition Volume I*. Basic Books.
- Flechtner, Frank, Neumayer, Karl-Hans, Dahle, Christoph, Dobslaw, Henryk, Fagiolini, Elisa, Raimondo, Jean-Claude, & Güntner, Andreas. 2016. What Can be Expected from the GRACE-FO Laser Ranging Interferometer for Earth Science Applications? *Surveys in Geophysics*, **37**(2), 453–470.
- Foulon, B. 2013. Development status of the electrostatic accelerometer for the GRACE-FO mission. *In: GRACE Science Team Meeting, 2013, Austin, USA; Presentation*.
- Francis, Samuel P, Shaddock, Daniel A, Sutton, Andrew J, de Vine, Glenn, Ware, Brent, Spero, Robert E, Klipstein, William M, & McKenzie, Kirk. 2015. Tone-assisted time delay interferometry on GRACE Follow-On. *Physical Review D*, **92**(1), 012005.
- Freer, J. 1996. *Computer Communications And Networks, 2nd Edition*. CRC Press. Taylor & Francis.
- Frommknecht, B. 2008 (01). *Integrated sensor analysis of the GRACE mission*. Ph.D. thesis, Fakultät für Bauingenieur- und Vermessungswesen, TU München.
- Frommknecht, B, Oberndorfer, H, Flechtner, F, & Schmidt, R. 2003. Integrated sensor analysis for GRACE - development and validation. *Advances in Geosciences*, **1**, 57–63.
- Gale, Patrick. 2008. *Application Note: Estimating laser diode lifetimes and activation energy*. Tech. rept. ILX Lightwave / Newport.
- Gans, P. 1992. *Data Fitting in the Chemical Sciences: By the Method of Least Squares*. Wiley.
- Gerberding, O. 2014. *Phase Readout for Satellite Interferometry*. Ph.D. thesis, Leibniz Universität Hannover, Albert-Einstein-Institut.
- Gill, K., Axer, M., Dris, S., Grabit, R., Macias, R., Noah, E., Troska, J., & Vasey, F. 2005. Radiation hardness assurance and reliability testing of InGaAs photodiodes for optical control links for the CMS experiment. *Nuclear Science, IEEE Transactions on*, **52**(5), 1480–1487.
- Glassner, A.S. 2013. *Graphics Gems*. Graphics Gems - IBM. Elsevier Science.
- Goldman, MA. 1996. Ball retro-reflector optics. *NRAO GBT Memo Series*, **148**.
- Goodman, J.W. 2005. *Introduction to Fourier Optics*. McGraw-Hill physical and quantum electronics series. W. H. Freeman.

- Gruber, Th., Bamber, J. L., Bierkens, M. F. P., Dobslaw, H., Murböck, M., Thomas, M., van Beek, L. P. H., van Dam, T., Vermeersen, L. L. A., & Visser, P. N. A. M. 2011. Simulation of the time-variable gravity field by means of coupled geophysical models. *Earth System Science Data Discussions*, **4**(1), 27–70.
- Gurfil, P., & Seidelmann, P.K. 2016. *Celestial Mechanics and Astrodynamics: Theory and Practice*. Astrophysics and Space Science Library. Springer Berlin Heidelberg.
- Gusarov, Andrei I., Doyle, Dominic, Hermanne, Alex, Berghmans, Francis, Fruit, Michel, Ulbrich, Gerd, & Blondel, Michel. 2002. Refractive-index changes caused by proton radiation in silicate opticalglasses. *Appl. Opt.*, **41**(4), 678–684.
- Hansen, C.N. 2002. *Understanding Active Noise Cancellation*. Taylor & Francis.
- Harvey, Nate. 2016. GRACE star camera noise. *Advances in Space Research*, **58**(3), 408 – 414.
- He, Wenjun, Fu, Yuegang, Zheng, Yang, Zhang, Lei, Wang, Jiake, Liu, Zhiying, & Zheng, Jianping. 2013. Polarization properties of a corner-cube retroreflector with three-dimensional polarization ray-tracing calculus. *Appl. Opt.*, **52**(19), 4527–4535.
- Heinzel, Gerhard. 2002. *Presentation: "The LTP interferometer and Phasemeter" at Journées du GREX 2004 in Nice, 28/10/2004*. Presentation. AEI Hannover.
- Heinzel, Gerhard, Rüdiger, Albrecht, & Schilling, Roland. 2002. *Spectrum and spectral density estimation by the Discrete Fourier transform (DFT), including a comprehensive list of window functions and some new at-top windows*. Tech. rept. Albert-Einstein-Institute Hannover.
- Helmert, F.R. 1880. *Die mathematischen und physikalischen Theorien der höheren Geodäsie, Band I*. Teubner.
- Helmert, F.R. 1884. *Die mathematischen und physikalischen Theorien der höheren Geodäsie, Band II*. Teubner.
- Hernandez-Pajares, M, Juan, JM, Sanz, J, & Orús, R. 2007. Second-order ionospheric term in GPS: Implementation and impact on geodetic estimates. *Journal of Geophysical Research: Solid Earth*, **112**(B8).
- Herrmann, Sven. 2008. *A Michelson-Morley test of Lorentz invariance using a rotating optical cavity*. Ph.D. thesis, Mathematisch-Naturwissenschaftliche Fakultät I, Humboldt-Universität zu Berlin.
- Hildebrand, Ulrich. 2005. *Fiber optic components in the Laser Communications Terminal on TerraSAR-X*. Presentation at The First ESA-NASA Working Meeting on Optoelectronics:- Fiber Optic System Technologies in Space, 5th and 6th October.
- Holst, G.C., & Lomheim, T.S. 2011. *CMOS/CCD Sensors and Camera Systems*. SPIE Press monograph. JCD Publishing.
- Horwath, Martin, Lemoine, Jean-Michel, Biancale, Richard, & Bourgoigne, Stéphane. 2010. Improved GRACE science results after adjustment of geometric biases in the Level-1B K-band ranging data. *Journal of Geodesy*, **85**(1), 23–38.
- Hulse, R. A., & Taylor, J. H. 1975. Discovery of a pulsar in a binary system. *apjl*, **195**(jan), L51–L53.
- IEEE. 1999. IEEE Standard Definitions of Physical Quantities for Fundamental Frequency and Time Metrology - Random Instabilities. *IEEE Std 1139-1999*.

- Iess, Luciano, Di Benedetto, Mauro, Marabucci, Manuela, & Racioppa, Paolo. 2012. Improved Doppler tracking systems for deep space navigation. *In: Proc of the 23rd International Symposium on Space Flight Dynamics*.
- Inácio, Pedro, Ditmar, Pavel, Klees, Roland, & Farahani, Hassan Hashemi. 2015. Analysis of star camera errors in GRACE data and their impact on monthly gravity field models. *Journal of Geodesy*, **89**(6), 551–571.
- Jäggi, A, Sośnica, K, Thaller, D, & Beutler, G. 2012. Validation and estimation of low-degree gravity field coefficients using LAGEOS. *In: Proceedings of 17th ILRS Workshop, Bundesamt für Kartographie und Geodäsie*, vol. 48.
- Jarrige, J, Thobois, P, Blanchard, C, Elias, P-Q, Packan, D, Fallerini, L, & Noci, G. 2014. Thrust measurements of the Gaia mission flight-model cold gas thrusters. *Journal of Propulsion and Power*, **30**(4), 934–943.
- Jekeli, Christopher. 1999. The determination of gravitational potential differences from satellite-to-satellite tracking. *Celestial Mechanics and Dynamical Astronomy*, **75**(2), 85–101.
- Johannessen, J.A., Balmino, G., Le Provost, C., Rummel, R., Sabadini, R., Sünkel, H., Tscherning, C.C., Visser, P., Woodworth, P., Hughes, C., Legrand, P., Sneeuw, N., Perosanz, F., Aguirre-Martinez, M., Rebhan, H., & Drinkwater, M. 2003. The European Gravity Field and Steady-State Ocean Circulation Explorer Satellite Mission Its Impact on Geophysics. *Surveys in Geophysics*, **24**(4), 339–386.
- Joshi, Abhay M., Heine, Frank, & Feifel, Thomas. 2006. Rad-hard ultrafast InGaAs photodiodes for space applications. *Proc. SPIE*, **6220**, 622003–622003–14.
- Jäggi, A., Bock, H., Prange, L., Meyer, U., & Beutler, G. 2011. GPS-only gravity field recovery with GOCE, CHAMP, and GRACE. *Advances in Space Research*, **47**(6), 1020 – 1028.
- Kahle, R, Kazeminejad, B, Kirschner, M, Yoon, Y, Kiehling, R, & D’Amico, S. 2007. First in-orbit experience of TerraSAR-X flight dynamics operations. *In: Proceedings of 20th International Symposium on Space Flight Dynamics, Annapolis, Maryland, USA, 24-28 September, 2007*. NASA.
- Kasdin, N.J., & Paley, D.A. 2011. *Engineering Dynamics: A Comprehensive Introduction*. Princeton University Press.
- Kawamura, Seiji, LCGT-Collaboration, & DECIGO-Working-Group. 2009. Japanese Gravitational Wave Detectors: LCGT and DECIGO. *Page JTua5 of: Frontiers in Optics 2009/Laser Science XXV/Fall 2009 OSA Optics & Photonics Technical Digest*. Optical Society of America.
- Kessler, Thomas, Legero, Thomas, & Sterr, Uwe. 2012. Thermal noise in optical cavities revisited. *JOSA B*, **29**(1), 178–184.
- Kim, Jeongrae. 2000. *Simulation study of a low-low satellite-to-satellite tracking mission*. Ph.D. thesis, The University of Texas at Austin.
- Klinger, Beate, & Mayer-Gürr, Torsten. 2016. The role of accelerometer data calibration within GRACE gravity field recovery: Results from ITSG-Grace2016. *Advances in Space Research*, **58**(9), 1597 – 1609.
- Knutson, Matthew Walter. 2012. *Fast star tracker centroid algorithm for high performance CubeSat with air bearing validation*. Ph.D. thesis, Massachusetts Institute of Technology.

- Ko, U.D. 2008. *Analysis of the Characteristics of GRACE Dual One-way Ranging System*. Ph.D. thesis, University of Texas at Austin.
- Ko, Ung-Dai, & Tapley, B.D. 2010 (March). Computing the USO frequency instability of GRACE satellites. *Pages 1–8 of: Aerospace Conference, 2010 IEEE*.
- Kochkina, Evgenia, Heinzl, Gerhard, Wanner, Gudrun, Müller, Vitali, Mahrtdt, Christoph, Sheard, Benjamin, Schuster, Sönke, & Danzmann, Karsten. 2013. Simulating and optimizing laser interferometers. *Pages 291–292 of: Proc. of the 9th LISA Symposium*.
- Konopliv, Alex S., Park, Ryan S., Yuan, Dah-Ning, Asmar, Sami W., Watkins, Michael M., Williams, James G., Fahnstock, Eugene, Kruizinga, Gerhard, Paik, Meegyeong, Strelakov, Dmitry, Harvey, Nate, Smith, David E., & Zuber, Maria T. 2013. The JPL lunar gravity field to spherical harmonic degree 660 from the GRAIL Primary Mission. *Journal of Geophysical Research: Planets*, **118**(7), 1415–1434.
- Koop, Radboud, & Rummel, Reiner. 2007. *The future of satellite gravimetry*. Tech. rept. ESA-ESTEC.
- Kopeikin, S., Efroimsky, M., & Kaplan, G. 2011. *Relativistic Celestial Mechanics of the Solar System*. Wiley.
- Kramer, H.J. 2002. *Observation of the Earth and Its Environment: Survey of Missions and Sensors*. Engineering online library. Springer Berlin Heidelberg.
- Kusche, J. 2003. A Monte-Carlo technique for weight estimation in satellite geodesy. *Journal of Geodesy*, **76**(11-12), 641–652.
- Kusche, J., Schmidt, R., Petrovic, S., & Rietbroek, R. 2009. Decorrelated GRACE time-variable gravity solutions by GFZ, and their validation using a hydrological model. *Journal of Geodesy*, **83**(10), 903–913.
- Kusche, Jürgen. 2007. Approximate decorrelation and non-isotropic smoothing of time-variable GRACE-type gravity field models. *Journal of Geodesy*, **81**(11), 733–749.
- Laheurte, J.M. 2012. *Compact Antennas for Wireless Communications and Terminals: Theory and Design*. ISTE. Wiley.
- Langley, Richard B. 1997. GPS receiver system noise. *GPS world*, **8**(6), 40–45.
- Lindh, Marcus. 2014. *Development and implementation of star tracker electronics*. MSc thesis, KTH, School of Electrical Engineering (EES), Space and Plasma Physics.
- LISA-Team. 2009. *Laser Interferometer Space Antenna (LISA) Mission Concept*. Tech. rept. ESA and NASA. LISA-PRJ-RP-0001, available at <https://lisa.nasa.gov/Documentation/LISA-PRJ-RP-0001.pdf>.
- Liu, Jian, & Azzam, RMA. 1997. Polarization properties of corner-cube retroreflectors: theory and experiment. *Applied optics*, **36**(7), 1553–1559.
- Liu, X. 2008. *Global gravity field recovery from satellite-to-satellite tracking data with the acceleration approach*. PhD thesis, Publications on geodesy. New series. Nederlandse Commissie voor Geodesie.
- Loomis, Bryant D., Nerem, R.S., & Luthcke, S.B. 2012. Simulation study of a follow-on gravity mission to GRACE. *Journal of Geodesy*, **86**(5), 319–335.
- LSC. 2016. Observation of Gravitational Waves from a Binary Black Hole Merger. *Phys. Rev. Lett.*, **116**(Feb), 061102. LIGO Scientific Collaboration (LSC).

- Mahrtdt, Christoph. 2014. *Laser link acquisition for the GRACE follow-on laser ranging interferometer*. Ph.D. thesis, Leibniz Universität Hannover, 2014, Albert-Einstein-Institut.
- Malykin, Grigorii B. 2000. The Sagnac effect: correct and incorrect explanations. *Physics-Uspekhi*, **43**(12), 1229.
- Marque, Jean-Pierre, Christophe, Bruno, & Foulon, Bernard. 2010. Accelerometers for GOCE: one year of in-orbit results. In: *Proceedings of GPHYS SYMPOSIUM, 22-24 June 2010, Paris (France)*.
- Matsuo, Koji, Chao, Benjamin F., Otsubo, Toshimichi, & Heki, Kosuke. 2013. Accelerated ice mass depletion revealed by low-degree gravity field from satellite laser ranging: Greenland, 1991–2011. *Geophysical Research Letters*, **40**(17), 4662–4667.
- Mavis, David, Cox, Bill, Adams, Dennis, & Greene, Richard. 1998. A reconfigurable, non-volatile, radiation hardened field programmable gate array (FPGA) for space applications. In: *Military and Aerospace Applications of Programmable Devices and Technologies Conference*.
- Mayer-Gürr, T. 2006 (Oct.). *Gravitationsfeldbestimmung aus der Analyse kurzer Bahnbögen am Beispiel der Satellitenmissionen CHAMP und GRACE (in german)*. Ph.D. thesis, University Bonn, Germany.
- McRae, Terry G., Ngo, Silvie, Shaddock, Daniel A., Hsu, Magnus T. L., & Gray, Malcolm B. 2013. Frequency stabilization for space-based missions using optical fiber interferometry. *Opt. Lett.*, **38**(3), 278–280.
- Meehan, Tom, Esterhuizen, Stephan, Franklin, Garth, Tien, Jeffrey, Young, Larry, Bachman, Brian, Munson, Tim, Robison, David, & Stecheson, Ted. 2012. Development status of NASA's TriG GNSS science instrument. In: *Proc of the IROWG-2 Workshop, 28th March – 3rd April 2012, Estes Park, Colorado*.
- Meschede, D. 2008. *Optics, Light and Lasers: The Practical Approach to Modern Aspects of Photonics and Laser Physics*. Physics textbook. Wiley.
- Meshksar, N. 2015. *Optical Simulations for Laser Interferometry Considering Polarisation Effects*. MSc thesis, Leibniz Universität Hannover, Albert-Einstein-Institut.
- Misner, C.W., Thorne, K.S., & Wheeler, J.A. 1973. *Gravitation*. Gravitation. W. H. Freeman.
- Monsky, A. 2010. *Understanding Interferometric Drag-free Sensors in Space Using Intelligent Data Analysis Tools*. Ph.D. thesis, Leibniz Universität Hannover, Albert-Einstein-Institut.
- Montenbruck, O., & Gill, E. 2000. *Satellite Orbits: Models, Methods and Applications*. Springer Berlin Heidelberg.
- Montenbruck, Oliver, van Helleputte, Tom, Kroes, Remco, & Gill, Eberhard. 2005. Reduced dynamic orbit determination using GPS code and carrier measurements. *Aerospace Science and Technology*, **9**(3), 261 – 271.
- Morrison, Euan, Meers, Brian J., Robertson, David I., & Ward, Henry. 1994. Automatic alignment of optical interferometers. *Appl. Opt.*, **33**(22), 5041–5049.
- Muehlnikel, Gerd, Kämpfner, Hartmut, Heine, Frank, Zech, Herwig, Troendle, Daniel, Meyer, R., & Philipp-May, S. 2012. The Alphasat GEO Laser Communication Terminal Flight Acceptance Tests. In: *Proc. International Conference on Space Optical Systems and Applications (ICSOS)*.

- Murböck, Michael, Pail, Roland, Daras, Ilias, & Gruber, Thomas. 2014. Optimal orbits for temporal gravity recovery regarding temporal aliasing. *Journal of Geodesy*, **88**(2), 113–126.
- Naeimi, M. 2013. *Inversion of Satellite Gravity Data Using Spherical Radial Base Functions*. Ph.D. thesis, Fachrichtung Geodäsie und Geoinformatik, Leibniz Universität Hannover.
- Nagano, Shigeo, Yoshino, Taizoh, Kunimori, Hiroo, Hosokawa, Mizuhiko, Kawamura, Seiji, Sato, Takashi, & Ohkawa, Masashi. 2004. Displacement measuring technique for satellite-to-satellite laser interferometer to determine Earth's gravity field. *Measurement Science and Technology*, **15**(12), 2406.
- Nagano, Shigeo, Hosokawa, Mizuhiko, Kunimori, Hiroo, Yoshino, Taizoh, Kawamura, Seiji, Ohkawa, Masashi, & Sato, Takashi. 2005. Development of a simulator of a satellite-to-satellite interferometer for determination of the Earth's gravity field. *Review of Scientific Instruments*, **76**(12).
- NG2-Team. 2011. *Assessment of a Next Generation Mission to Monitor the Variations of Earth's Gravity Field, Final Report, ESA contract: 22672/09/NL/AF*. Tech. rept. Astrium EADS.
- Nicholson, T. L., Campbell, S. L., Hutson, R. B., Marti, G. E., Bloom, B. J., McNally, R. L., Zhang, W., Barrett, M. D., Safronova, M. S., Strouse, G. F., Tew, W. L., & Ye, J. 2015. Systematic evaluation of an atomic clock at 2×10^{-18} total uncertainty. *Nature Communications*, **6**(2015-04), 6896.
- Nicklaus, K, Herding, M, Wang, X, Beller, N, Fitzau, O, Giesberts, M, Herper, M, Barwood, GP, Williams, RA, Gill, P, *et al.* 2014a. High stability Laser for next generation gravity missions. *Page 10 of: International Conference on Space Optics*, vol. 7.
- Nicklaus, K, Herding, M, Baatzsch, A, Dehne, M, Diekmann, C, Voss, K, Gilles, F, Guenther, B, Zender, B, Boehme, S, *et al.* 2014b. Optical Bench Of The Laser Ranging Interferometer On Grace Follow-On. *Page 10 of: International Conference on Space Optics*, vol. 7.
- Niebauer, TM, Schilling, Roland, Danzmann, Karsten, Rüdiger, Albrecht, & Winkler, Walter. 1991. Nonstationary shot noise and its effect on the sensitivity of interferometers. *Physical Review A*, **43**(9), 5022.
- Notcutt, Mark, Ma, Long-Sheng, Ludlow, Andrew D., Foreman, Seth M., Ye, Jun, & Hall, John L. 2006. Contribution of thermal noise to frequency stability of rigid optical cavity via Hertz-linewidth lasers. *Phys. Rev. A*, **73**(Mar), 031804.
- Numata, Kenji, Kemery, Amy, & Camp, Jordan. 2004. Thermal-Noise Limit in the Frequency Stabilization of Lasers with Rigid Cavities. *Phys. Rev. Lett.*, **93**(Dec), 250602.
- Numata, Kenji, Chen, Jeffrey R, & Camp, Jordan. 2010. Fiber laser development for LISA. *Page 012043 of: Journal of Physics: Conference Series*, vol. 228. IOP Publishing.
- Ogawa, Ryoko. 2010. *Transient, seasonal and inter-annual gravity changes from GRACE data: Geophysical modelings*. Ph.D. thesis, Hokkaido University.
- Ott, Melanie N, Coyle, Donald Barry, Canham, John S, & Leidecker Jr, Henning W. 2006. Qualification and issues with space flight laser systems and components. *Pages 61001V–61001V of: Lasers and Applications in Science and Engineering*. International Society for Optics and Photonics.
- Owens, James C. 1967. Optical refractive index of air: dependence on pressure, temperature and composition. *Applied optics*, **6**(1), 51–59.

- Peck, Edson R. 1962. Polarization Properties of Corner Reflectors and Cavities. *J. Opt. Soc. Am.*, **52**(3), 253–257.
- Peterseim, Nadja. 2014. *TWANGS – High-Frequency Disturbing Signals in the 10 Hz Accelerometer Data of the GRACE Satellites*. Dissertation, Technische Universität München.
- Petit, G., Luzum, B., Rotation, International Earth, & Service, Reference Systems. 2010. *IERS Conventions: (2010)*. IERS technical note. Verlag des Bundesamtes für Kartographie und Geodäsie.
- Picone, JM, Hedin, AE, Drob, D Pj, & Aikin, AC. 2002. NRLMSISE-00 empirical model of the atmosphere: Statistical comparisons and scientific issues. *Journal of Geophysical Research: Space Physics*, **107**(A12).
- Player, MA. 1988. Polarization properties of a cube-corner reflector. *Journal of Modern Optics*, **35**(11), 1813–1820.
- Pollack, S E, & Stebbins, R T. 2006. Demonstration of the zero-crossing phasemeter with a LISA test-bed interferometer. *Classical and Quantum Gravity*, **23**(12), 4189.
- Pour, Siavash Iran, Reubelt, Tilo, & Sneeuw, Nico. 2013. Quality assessment of sub-Nyquist recovery from future gravity satellite missions. *Advances in Space Research*, **52**(5), 916 – 929.
- Qian, S.E. 2016. *Optical Payloads for Space Missions*. Wiley.
- Rakić, Aleksandar D., Djurišić, Aleksandra B., Elazar, Jovan M., & Majewski, Marian L. 1998. Optical properties of metallic films for vertical-cavity optoelectronic devices. *Appl. Opt.*, **37**(22), 5271–5283.
- Ray, R.D., Rowlands, D.D., & Egbert, G.D. 2003. Tidal Models in a New Era of Satellite Gravimetry. *Space Science Reviews*, **108**(1-2), 271–282.
- Reubelt, Tilo, *et al.* 2014. *Observation of the System Earth from Space - CHAMP, GRACE, GOCE and future missions: GEOTECHNOLOGIEN Science Report No. 20*. Berlin, Heidelberg: Springer Berlin Heidelberg. Chap. Future Gravity Field Satellite Missions, pages 165–230.
- Rindler, W. 2012. *Essential Relativity: Special, General, and Cosmological*. Theoretical and Mathematical Physics. Springer Berlin Heidelberg.
- Rummel, R., Flury, J., Haagmans, R., Hughes, C., Grand, P. Le, Schrama, E., Sneeuw, N., Vermeersen, B., & Woodworth, P. 2003 (01). *Scientific objectives for future geopotential missions*. tech. report; study for ESA contract 396 2/01/NL/GS. ESA.
- Samaan, Malak Anees. 2003. *Toward Faster And More Accurate Star Sensors Using Recursive Centroiding And Star Identification*. Ph.D. thesis, Texas A&M University.
- Sanjuán, J. 2009. *Development and validation of the thermal diagnostics instrumentation in LISA Pathfinder*. Ph.D. thesis, Polytechnic University Barcelona.
- Schlie, J., Murböck, M., & Pail, R. 2015 (01). Feasibility Study of a Future Satellite Gravity Mission Using GEO-LEO Line-of-Sight Observations. *Pages 123–130 of: Marti, U. (ed), Gravity, Geoid and Height Systems. Proceedings of the IAG Symposium GGHS2012, October 9-12, 2012, Venice, Italy. Part III. IAG Symposia*, vol. 141.
- Schnabel, R, Britzger, M, Brückner, F, Burmeister, O, Danzmann, K, Duck, J, Eberle, T, Friedrich, D, Luck, H, Mehmet, M, Nawrodt, R, Steinlechner, S, & Willke, B. 2010. Building blocks for future detectors: Silicon test masses and 1550 nm laser light. *Journal of Physics: Conference Series*, **228**(1), 012029.

- Scholl, Marija S. 1995. Ray trace through a corner-cube retroreflector with complex reflection coefficients. *JOSA A*, **12**(7), 1589–1592.
- Schreiber, K.U., Klügel, T., Velikoseltsev, A., Schlüter, W., Stedman, G.E., & Wells, J.-P.R. 2009. The Large Ring Laser G for Continuous Earth Rotation Monitoring. *Pure and Applied Geophysics*, **166**(8-9), 1485–1498.
- Schreiber, U., Schneider, M., Rowe, C.H., Stedman, G.E., & Schlüter, W. 2001. Aspects Of Ring Lasers As Local Earth Rotation Sensors. *Surveys in Geophysics*, **22**(5-6), 603–611.
- Schuldt, T., Keetman, A., Doringshoff, K., Reggentin, M., Kovalchuk, E., Nagel, M., Gohlke, M., Johann, U., Weise, D., Peters, A., & Braxmaier, C. 2012 (April). An ultra-stable optical frequency reference for space applications. *Pages 554–558 of: European Frequency and Time Forum (EFTF), 2012*.
- Schuster, Sönke, Tröbs, Michael, Wanner, Gudrun, & Heinzl, Gerhard. 2016. Experimental demonstration of reduced tilt-to-length coupling by a two-lens imaging system. *Optics Express*, **24**(10), 10466–10475.
- Schutz, B. 2009. *A First Course in General Relativity*. Cambridge University Press.
- Schütze, Daniel. 2014. *Intersatellite Laser Interferometry: Test Environments for GRACE Follow-on*. Ph.D. thesis, Leibniz Universität Hannover, Albert-Einstein-Institut.
- Schwander, T. 2006. New 808nm High Power Laser Diode Pump Module for Space Applications. *In: ESA Special Publication*, vol. 621.
- Sechi, G, Buonocore, M, Cometto, F, Saponara, M, Tramutola, A, Vinai, B, Andrè, G, & Fehringer, M. 2011. In-flight results from the drag-free and attitude control of GOCE satellite. *In: Proceedings of the IFAC 2011 Congress, Milan*.
- Seeber, G. 2003. *Satellite Geodesy*. Walter de Gruyter.
- Seefelder, W. 2002. *Lunar Transfer Orbits Utilizing Solar Perturbations and Ballistic Capture*. Luft- und Raumfahrt. Utz, Wiss.
- Shaddock, D., Ware, B., Halverson, P. G., Spero, R. E., & Klipstein, B. 2006. Overview of the LISA Phasemeter. *AIP Conference Proceedings*, **873**(1), 654–660.
- Shannon, R.R., Shack, R., Harvey, J.E., & Hooker, R.B. 2005. *Robert Shannon and Roland Shack: Legends in Applied Optics*. Press Monograph. SPIE Press.
- Sheard, B.S., Heinzl, G., Danzmann, K., Shaddock, D.A., Klipstein, W.M., & Folkner, W.M. 2012. Intersatellite laser ranging instrument for the GRACE follow-on mission. *Journal of Geodesy*, **86**(12), 1083–1095.
- Shiozawa, T. 2013. *Classical Relativistic Electrodynamics: Theory of Light Emission and Application to Free Electron Lasers*. Advanced Texts in Physics. Springer Berlin Heidelberg.
- Sirtori, Carlo. 2002. Applied physics: Bridge for the terahertz gap. *Nature*, **417**(6885), 132–133.
- Sneeuw, Nico. 2000. *A semi-analytical approach to gravity field analysis from satellite observations*. Ph.D. thesis, Technische Universität München.
- Sneeuw, Nico, Flury, Jakob, & Rummel, Reiner. 2005. Science Requirements On Future Missions And Simulated Mission Scenarios. *Pages 113–142 of: Future Satellite Gravimetry and Earth Dynamics*. Springer New York.

- Snyder, J. J. 1975. Paraxial ray analysis of a cat's-eye retroreflector. *Appl. Opt.*, **14**(8), 1825–1828.
- Soffel, M., & Langhans, R. 2012. *Space-Time Reference Systems*. Astronomy and Astrophysics Library. Springer Berlin Heidelberg.
- STI-TMA. 2013 (04). *TMA Mirror Assembly Specification (internal document)*, LRI-STI-SP-010. Tech. rept. SpaceTech Immenstaad (STI) GmbH, Germany.
- Stummer, C. S. 2013 (01). *Gradiometer data processing and analysis for the GOCE mission*. Ph.D. thesis, Fakultät für Bauingenieur- und Vermessungswesen, TU München.
- Subirana, J.S., Zornoza, J.M.J., Hernández-Pajares, M., Agency, European Space, & Fletcher, K. 2013. *GNSS Data Processing*. ESA TM, no. Bd. 1. ESA Communications.
- Sugimoto, Nobuo, & Minato, Atsushi. 1996. Optical Characteristics of the Retroreflector in Space for the Advanced Earth Observing Satellite. *Optical Review*, **3**(2), 62–64.
- Swenson, Sean, & Wahr, John. 2006. Post-processing removal of correlated errors in GRACE data. *Geophysical Research Letters*, **33**(8).
- Tapley, Byron D., Bettadpur, Srinivas, Ries, John C., Thompson, Paul F., & Watkins, Michael M. 2004. GRACE Measurements of Mass Variability in the Earth System. *Science*, **305**(5683), 503–505.
- Thomas, J.B. 1999. *An Analysis of Gravity-Field Estimation Based on Intersatellite Dual-1-Way Biased Ranging*. Tech. rept. Jet Propulsion Laboratory, National Aeronautics and Space Administration.
- Thomas, S. 2004 (10). Optimized centroid computing in a Shack-Hartmann sensor. *Pages 1238–1246 of: Advancements in Adaptive Optics*, vol. 5490.
- Thompson, R., Folkner, W.M., de Vine, G., Klipstein, W.M., McKenzie, K., Spero, R., Yu, N., Stephens, M., Leitch, J., Pierce, R., Lam, T.T.-Y., & Shaddock, D.A. 2011 (May). A flight-like optical reference cavity for GRACE follow-on laser frequency stabilization. *Pages 1–3 of: Frequency Control and the European Frequency and Time Forum (FCS), 2011 Joint Conference of the IEEE International*.
- Tien, Jeffrey Y, Okihiro, Brian Bachman, Esterhuizen, Stephan X, Franklin, Garth W, Meehan, Thomas K, Munson, Timothy N, Robison, David E, Turbiner, Dmitry, & Young, Lawrence E. 2012. TriG: Next Generation Scalable Spaceborne GNSS Receiver. *In: Presentation; Institute of Navigation 2012 International Technical Meeting; 30 Jan - 1 Feb 2012; Newport Beach, CA; Algeria*.
- Träger, F. 2012. *Springer Handbook of Lasers and Optics*. Springer Berlin Heidelberg.
- Traub, Martin, Plum, Heinz-Dieter, Hoffmann, Hans-Dieter, & Schwander, Thomas. 2007. Spaceborne fiber coupled diode laser pump modules for intersatellite communications. *Proc. SPIE*, **6736**, 673618–673618–9.
- Tröbs, M. 2005. *Laser Development and Stabilization for the Spaceborne Interferometric Gravitational Wave Detector LISA*. Ph.D. thesis, Leibniz Universität Hannover, Albert-Einstein-Institut.
- Tröbs, Michael, d’Arcio, Luigi, Heinzl, Gerhard, & Danzmann, Karsten. 2009. Frequency stabilization and actuator characterization of an ytterbium-doped distributed-feedback fiber laser for LISA. *J. Opt. Soc. Am. B*, **26**(5), 1137–1140.

- Turyshev, Slava G., Sazhin, Mikhail V., & Toth, Viktor T. 2014. General relativistic laser interferometric observables of the GRACE-Follow-On mission. *Phys. Rev. D*, **89**(May), 105029.
- Van Helleputte, T. 2011 (Jan.). *The integration of spaceborne accelerometry in the precise orbit determination of low-flying satellites*. Ph.D. thesis, Technical University Delft.
- van Lonkhuyzen, M., Klees, R., & Bouman, J. 2002. Regularization for the Gravity Field Recovery from GOCE Observations. *Pages 117–122 of: Gravity, Geoid and Geodynamics 2000*. International Association of Geodesy Symposia, vol. 123. Springer Berlin Heidelberg.
- van Woerkom, P Th LM. 1999. High-accuracy spacecraft observatory motion: a primer for attitude control development (IAF-99-A.4.01). *50th International Astronautical Congress : 4 - 8 Oct 1999, Amsterdam, The Netherlands*.
- Vig, John R. 2014. *Quartz Crystal Resonators and Oscillators for Frequency Control and Timing Applications - A Tutorial*, Rev. 8.5.6.2. Presentation. IEEE.
- Visser, P.N.A.M. 2009. GOCE gradiometer: estimation of biases and scale factors of all six individual accelerometers by precise orbit determination. *Journal of Geodesy*, **83**(1), 69–85.
- Visser, P.N.A.M., Sneeuw, N., & Gerlach, C. 2003. Energy integral method for gravity field determination from satellite orbit coordinates. *Journal of Geodesy*, **77**(3-4), 207–216.
- Vyas, Akondi, Roopashree, MB, & Prasad, BR. 2009. Optimization of existing centroiding algorithms for Shack Hartmann sensor. *arXiv preprint arXiv:0908.4328*.
- Wallace, Neil, Jameson, Peter, Saunders, Christopher, Fehringer, Michael, Edwards, Clive, & Floberghagen, Rune. 2011. The GOCE ion propulsion assembly-lessons learnt from the first 22 months of flight operations. *Pages 1–21 of: Proc of the 32nd International Electric Propulsion Conf*.
- Wallat, C, & Schön, S. 2016. Phase only PPP and multi-antenna solutions for improved kinematic LEO orbits. *In: Proceedings of the 8th ESA Navitec 2016,14.-16.12.2016, ESA/ESTEC, The Netherlands*, vol. 1.
- Wand, Vinzenz. 2007. *Interferometry at low frequencies: Optical phase measurement for LISA and LISA Pathfinder*. Ph.D. thesis, Gottfried Wilhelm Leibniz Universität Hannover, Albert-Einstein-Institut.
- Wang, F. 2003. *Study on center of mass calibration and K-band ranging system calibration of the GRACE mission*. Ph.D. thesis, The University of Texas at Austin.
- Wang, Furun, Bettadpur, Srinivas, Save, Himanshu, & Kruizinga, Gerhard. 2010. Determination of Center-of-Mass of Gravity Recovery and Climate Experiment Satellites. *Journal Of Spacecraft And RocketS*, **47**(2), 371–379.
- Wanner, Gudrun. 2010. *Complex optical systems in space: numerical modelling of the heterodyne interferometry of LISA Pathfinder and LISA*. Ph.D. thesis, Leibniz Universität Hannover, Albert-Einstein-Institut.
- Weaver, Gregory, Reinhart, Matthew, & Miranian, Mihran. 2004. *Developments in ultra-stable quartz oscillators for deep space reliability*. Tech. rept. Johns Hopkins University Applied Physics Laborator. 36th Annual Precise Time and Time Interval (PTTI) Meeting.
- Weaver, Gregory, Garstecki, Jeffrey, & Reynolds, Samuel. 2010. *The Performance Of Ultra-Stable Oscillators For The Gravity Recovery And Interior Laboratory (Grail)*. Tech. rept. Johns Hopkins University Applied Physics Laborator.

- Weigelt, M., van Dam, T., Jäggi, A., Prange, L., Tourian, M. J., Keller, W., & Sneeuw, N. 2013. Time-variable gravity signal in Greenland revealed by high-low satellite-to-satellite tracking. *Journal of Geophysical Research: Solid Earth*, **118**(7), 3848–3859.
- Weinbach, Ulrich, & Schön, Steffen. 2013. Improved GRACE kinematic orbit determination using GPS receiver clock modeling. *GPS Solutions*, **17**(4), 511–520.
- Wiese, David N., Visser, Pieter, & Nerem, Robert S. 2011. Estimating low resolution gravity fields at short time intervals to reduce temporal aliasing errors. *Advances in Space Research*, **48**(6), 1094 – 1107.
- Wu, S.-C., Kruizinga, G., & Bertiger, W. 2006. *Algorithm Theoretical Basis Document for GRACE Level-1B Data Processing V1.2*. Tech. rept. JPL. available at ftp://podaac.jpl.nasa.gov/allData/grace/docs/ATBD_L1B_v1.2.pdf.
- Wuchenich, Danielle M. R., Mahrtdt, Christoph, Sheard, Benjamin S., Francis, Samuel P., Spero, Robert E., Miller, John, Mow-Lowry, Conor M., Ward, Robert L., Klipstein, William M., Heinzl, Gerhard, Danzmann, Karsten, McClelland, David E., & Shaddock, Daniel A. 2014. Laser link acquisition demonstration for the GRACE Follow-On mission. *Opt. Express*, **22**(9), 11351–11366.
- Yang, B, & Friedsam, H. 1999. *Ray-tracing studies for a whole-viewing-angle retroreflector*. Tech. rept. Argonne National Lab. Argonne, Ill.
- Yeh, Hsien-Chi, Yan, Qi-Zhong, Liang, Yu-Rong, Wang, Ying, & Luo, Jun. 2011. Inter-satellite laser ranging with homodyne optical phase locking for Space Advanced Gravity Measurements mission. *Review of Scientific Instruments*, **82**(4).
- Yoder, PR. 1958. Study of light deviation errors in triple mirrors and tetrahedral prisms. *JOSA*, **48**(7), 496–499.
- Yoon, Y., Montenbruck, O., & Kirschner, M. 2006. Precise Maneuver Calibration Satellites for remote sensing. *In: Proceedings Of The International Symposium On Space Technology And Science*, vol. 25.
- Yuan, Jie, & Long, Xingwu. 2003. CCD-area-based autocollimator for precision small-angle measurement. *Review of scientific instruments*, **74**(3), 1362–1365.
- Yun, Garam, Crabtree, Karlton, & Chipman, Russell A. 2011. Three-dimensional polarization ray-tracing calculus I: definition and diattenuation. *Appl. Opt.*, **50**(18), 2855–2865.
- Zehentner, N., & Mayer-Gürr, T. 2013. *Kinematic orbits for GRACE and GOCE based on raw GPS observations*. Poster presented at the IAG Scientific Assembly 2013, 1.-6. September 2013, Potsdam, Germany.
- Zhang, D. 2012. *Advanced Mechatronics and MEMS Devices*. Microsystems. Springer New York.
- Zhou, Guoquan, Ni, Yongzhou, & Zhang, Zhongwei. 2007. Analytical vectorial structure of non-paraxial nonsymmetrical vector Gaussian beam in the far field. *Optics communications*, **272**(1), 32–39.
- Zhu, L., & Jekeli, C. 2007. Combining Gravity and Topographic Data for Local Gradient Modeling. *Pages 288–295 of: Dynamic Planet*. International Association of Geodesy Symposia, vol. 130. Springer Berlin Heidelberg.

- Ziemer, John K, Randolph, Thomas M, Gamero-Castaño, Manuel, Hruby, Vlad, Connolly, William, Demmons, Nathaniel, Ehrbar, Eric, Martin, Roy, Roy, Tom, Spence, Douglas, *et al.* 2007. Flight hardware development of colloid microthruster technology for the space technology 7 and LISA missions. *In: Proc of the 30th International Electric Propulsion Conference, IEPC-2007-288, Florence, Italy.*
- Zijlstra, Mark, Theil, Stephan, & Scheithauer, Silvia. 2005. Model for Short-term Atmospheric Density Variations. *Pages 489–494 of: Earth Observation with CHAMP.* Springer Berlin Heidelberg.
- Zimbelman, Darrell, Wilmot, Jonathan, & Evangelista, Solomon. 1995. The attitude control system design for the transition region and coronal explorer mission. *In: Proceedings of AIAA/USU Conference on Small Satellites.*
- Zschocke, Sven. 2016. Light propagation in the gravitational field of N arbitrarily moving bodies in the 1.5 PN approximation for high-precision astrometry. *Physical Review D*, **93**(10), 103010.